XLII ANNUAL MEETING OF THE OPTICAL SOCIETY OF INDIA

OSI - International Symposium on Optics (OSI-ISO 2018)

19 - 22 September 2018

INDIAN INSTITUTE OF TECHNOLOGY KANPUR

ABSTRACTS

Advisory Committee

Arvind (IISER Mohali)
G. S. Agarwal (Texas A&M University)
Kallol Bhattacharya (University of Calcutta)
Wojteck J. Bock (University of Quebec)
R. Boyd (University of Rochester)
Stefan Enoch (Institut Fresnel, Marseilles)
Stavroula Foteinopoulou (University of New Mexico)
Ajoy Ghatak (NASI, Allahabad)
A.K. Gupta (IRDE, Dehradun)
Alex I. Gaeta (Columbia University)
Laxmi Narayan Hazra (University of Calcutta)
G. Ravindra Kumar (TIFR, Mumbai)
Akhlesh Lakhtakia (Pennsylvania State University)
Benjamin Lionel (IRDE, Dehradun)
Olivier J.F. Martin (EPF Lausanne)
Bishnu Pal (Bennet University / IIT Delhi)
C.S. Narayanamurthy (IIST, Thiruvananthapuram)
Sir John B. Pendry (Imperial College London)
Reji Philip (Raman Research Institute, Bengaluru)
D. Narayana Rao (University of Hyderabad)

Technical Program Committee

S. Balaji (IIT Madras)
Ayan Banerjee (IISER Kolkata)
Shivkiran Bhaktha (IIT Kharagpur)
Shanti Bhattacharya (IIT Madras)
Shubananda Chakrabarti (IIT Bombay)
Dibakar roy Chowdhury (Mahindra Ecole, Hyderabad)
Bijoy K. Das (IIT Madras)
Ritwick Das (NISER Bhubaneswar)
Tarak Nath Dey (IIT Guwahati)
A.V. Gopal (TIFR, Mumbai)
Nirmalya Ghosh (IISER Kolkata)
Rajan Jha (IIT Bhubaneshwar)
Joby Joseph (IIT Delhi)
Kedar Khare (IIT Delhi)
Pavan Kumar (IISER Pune)
Naveen Nischal (IIT Patna)
K. Divakara Rao (BARC Vishakapatnam)
Amarendra Sarma (IIT Guwahati)
Kushal Kumar Shah (IISER Bhopal)
Kamal Priya Singh (IISER Mohali)
R.P. Singh (PRL, Ahmedabad)
Rakesh Kumar Singh (IIST Thiruvananthapuram)
Ranjan Singh (NTU Singapore)
B.V.R. Tata (University of Hyderabad)
S.K. Varshney (IIT Kharagpur)
Anurag Sharma (IIT Delhi)
Kehar Singh (Formerly IIT Delhi)
Ravindra K. Sinha (CSIO, Chandigarh)
Nirmal K. Viswanathan (University of Hyderabad)

Local Organization Committee of IIT Kanpur

Convenor: S. Anantha Ramakrishna (Physics)
Co-convenor: Harshwardhan Wanare (Physics)
Co-convenor: Saikat Ghosh (Physics)
General Secretary: J. Ramkumar (Mechanical Engg.)
Treasurer: Kumar Vaibhav Srivastava (Electrical Engg.)

Members:

- D. Goswami (Chemistry)
- Shilpi Gupta (Electrical Engg.)
- Anand Kumar Jha (Physics)
- J. N. Moorthy (Chemistry)
- G. Rajshekhar (Electrical Engg.)
- Pratik Sen (Chemistry)
- Saurabh Mani Tripathi (Physics)
- R. Vijaya (Physics)

Program schedule for the OSI-ISO 2018

19 Sept. 2018	Reception for Invited speakers, Chairs and regular OSI members		
	20 Sept. 2018	21 Sept. 2018	22 Sept. 2018
Breakfast	7:30-8:30	7:30-8:30	7:30-8:30
Opening ceremony	9.00-9.30 Chief Guest: Lionel Benjamin (IRDE)		
Techno-commercial	9:30-9:45 ATOS		
		E.C.G Sudarshan memorial Plenary session: 9:00-9:50 N. Mukunda	
Plenary 1	9.50- 10.40 Stefan Enoch		9:00-9:50 Ravindra Kumar
Techno-commercial		9:50-10:05 ATOS	
Plenary 2		10:05-10:55 Yuri S. Kivshar	9:50-10:40 Gautam Vemuri
Tea break	10.40-11.00	10:55- 11.05	10:40- 11.00
Session 1	11.00 – 13:00	11:05 -13:10	11:00-13:10
Lunch	13:00-14:00	13:10-14:00	13:10-14:00
Session 2	14:00 – 15:40	14:00 – 16:00	14:00 – 16:00
Tea break	XXXX	XXXX	16:00 – 16:20
	16:00 – 17:00	16:00 – 17:00	Concluding session and High Tea
Session 3	POSTERS + TEA Paper # 1 to # 90 17:00 – 18:30	POSTERS + TEA Paper # 91 to # 195 17:00 – 18:30	
	18:15 – 19:15 General meeting of the Optical Society of India		
Distinguished lifetime Lecture & felicitation	19:15 -20:15 Ajoy Ghatak	19:00 -20:00 Kehar Singh	
Posters + DINNER	20:15-22:00	20:00-22:00	

Program schedule for the OSI-ISO 2018

20 Sept. 2018,
Day – 1 Session -1:

	Parallel session A A: Guided wave optics	Parallel session B B: Photonics materials	Parallel session C C: Light & Imaging
Invited 35 mins	Bijoy Das	Yidong Chong	Joby Joseph
Techno-comm 10 min			
Invited 35 mins	David Grojo	Praveen C. Ramamurthy	Ajay Kumar
Oral 15 min	Paper # 127	Paper # 161	Paper # 20
Invited 35 min	Myeongsoo Kang	Rajadurai Chandrasekhar	Paper # 37 (Oral)
			Paper # 86 (Oral)

Day – 1 Session -2:

	Parallel session A A2: OAM & Polarization	Parallel session B B2: Metamaterials & Plasmonics	Parallel session C C1: Optical devices and Systems
Invited 35 mins	P. Senthil Kumaran	Achanta Venu Gopal	Rakesh Kumar Singh
Invited 35 mins	Sankalpa Ghosh	Alexander Iskandar	Rajan Jha
Oral 15 min	Paper # 83	Paper # 168	Paper # 36
Invited 35 min	Nirmal Viswanathan	Sulabha Kulkarni	Shanti Bhattacharya
Tea break			
Invited 35 mins	R.P. Singh	Ritwick Das	C. S. Narayanamurthy
Oral 15 min	Paper # 7	Paper # 101	Paper # 85
Oral 15 min	Paper # 14	Paper # 146	Paper # 92

Program schedule for the OSI-ISO 2018

21 Sept. 2018,
Day – 2 Session – 1 :

	Parallel session A Laser & Polarization	Parallel session B Metamaterials	Parallel session C C: Biomedical Appln
Invited 35 mins	Hari Babu Srivastava	Ravi Hegde	Anabela de Silva
Oral 15 min	Paper # 119	Paper # 69	Paper # 88
Invited 35 mins	Naveen Nischal	Basudev Lahiri	A. R. Ganesan
Oral 15 min	Paper # 54	Paper # 58	Paper # 113
Oral 15 min	Paper # 136	Paper # 43	Paper # 133

Day – 2 session -2:

	Parallel session A A1: Quantum Optics	Parallel session B B1: Materials & Micro/nano fabrication	Parallel session C: C: Biomedical Appln. and imaging
Invited 35 mins	Arvind	Ganapati Subramania	Renu John
Invited 35 mins	Aranyabhuti Bhattacharjee	Subhananda Chakrabarti	Murali Chilakapati
Oral 15 min	Paper # 15	Paper # 72	Paper # 64
Invited 35 min	Amarendra Sarma	Ayan Banerjee	Paper # 113 (Oral)
			Paper # 114 (Oral)
Tea break			Light – matter interaction/sensors
Invited 35 mins	Shubrangshu Dasgupta	Rajesh Kumar	Dibakar Roy Chowdhury
Oral 15 min	Paper # 23	Paper # 99	Paper # 164
Oral 15 min	Paper # 195	Paper # 80	Paper # 162
Oral 15 min	Paper # 186	Paper # 33	Paper # 160

Program schedule for the OSI-ISO 2018

22 Sept. 2018,
Day – 3, Session – 1:

	Parallel session A: Memorial session for Prof. Porsezian	Parallel session B B: THz Photonics and spectroscopy	Parallel session C C2: Lasers and NLO
Invited 35 mins	P.K. Panigrahi	Ranjan Singh	Reji Philip
Oral 15 min	Paper # 27	Paper # 82	Paper # 193
Invited 35 mins	Shailendra K. Varshney	P.K. Datta	D. Narayana Rao
Oral 15 min	Paper # 110	R.K. Sinha (Invited)	Mrinmay Pal (Invited)
Oral 15 min	Paper # 48		

Day – 3 session -2:

	Parallel session A Optical devices	Parallel session B Optical materials & effects	Parallel session C: Atmospheric phenomena
Invited 35 mins	Vinod Karar	Anand Kumar Jha	Raghavendra Prasad
Oral 15 min	Paper # 166	Paper # 183	Paper # 62
Invited 35 min	Kallol Bhattacharya	Paper # 10 (Oral)	Paper # 19 (Oral)
		Paper # 45 (Oral)	Paper # 79 (Oral)
Oral 15 min	Paper # 103	Paper # 66	Paper # 89
Oral 15 min	Paper # 115		

Day – 3 Concluding session

- Concluding remarks by OSI officials
- Announcement and distribution of Best student paper, best poster awards to students
- Vote of thanks by General Secretary
- High Tea

LIFETIME DISTINCTION LECTURES

OSI-ISO 2018 manuscript No.
(L1)

Evolution of quantum theory and Entanglement

Ajoy K. Ghatak

Abstract. The talk will briefly discuss the evolution of various theories of light which eventually led to quantum theory and concepts associated with it. It will also discuss the EPR Paradox and a simple derivation of Bells inequality.

Professor Meghnad Saha Fellow of NASI
Formerly Indian Institute of Technology, Delhi
Email: ajoykghatak@gmail.com

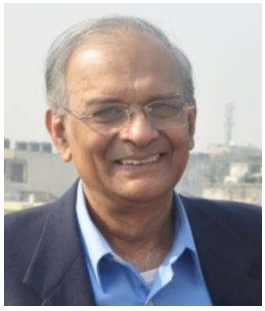

Prof. Ajoy Ghatak is currently Professor MeghnadSaha Fellow of NASI (The National Academy of Sciences, India). He received his BSc from Agra College, M.Sc from Delhi University and PhD from Cornell University. After a short tenure as a Research Associate at Brookhaven National Laboratory, he joined IIT Delhi in 1966. Professor Ghatak has research interests in Fiber Optics & Quantum Mechanics. He has authored several books including his undergraduate text on ***OPTICS*** which has been translated to Chinese and Persian.
His other books include *Quantum Mechanics: Theory & Applications* (coauthored with Professor S. Lokanathan), *Fiber Optics*, *Lasers, Optical Electronics* (all 3 coauthored with Professor K. Thyagarajan) and a popular book on *AlbertEinstein: The Story of a Genius.* He is recipient of several awards including the 2008 SPIE Educator award in recognition of "*his unparalleled global contributions to the field of fiber optics research, and his tireless dedication to optics education worldwide..",* the 2003 Esther Hoffman Beller award (instituted by The Optical Society of America) in recognition of his "*outstanding contributions to optics education ...",* the 2003 Khwarizmi award, the International Commission for Optics 1998 Galileo Galilei award and also the CSIR 1979 S.S. Bhatnagar award for "*outstanding contributions in physical sciences".*

OSI-ISO 2018 manuscript No.
(L2)

Optical Cryptography for Information Security: A Personal Tour (2000-2018)

Kehar Singh

Abstract. In recent years, the march of optics/photonics has posed a serious challenge to the supremacy of digital electronics-centered technology, benefitting numerous areas of science and engineering. Cryptography which has been traditionally an area of computer science and engineering, is also no exception. Due to inherent advantages of parallel processing and increased key-space provided by optical techniques, optical cryptography has made rapid inroads into the areas hitherto dominated by digital electronics. The proposed talk aims at presenting glimpses of some aspects of optical cryptography such as double random phase encoding and its variants using various integral transforms such as Fourier-,Fresnel-,Mellin-,gyrator-,and Hartley transforms as also their fractionalized versions. Systems based on photorefractive-,and digital holography, and structured phase masks would also be discussed. Vulnerability of the cryptosystems for some type of attacks would be briefly mentioned. The talk is aimed at presenting glimpses of some systems, based mainly on the researches carried out by the author's groups at IIT Delhi and NorthCap University Gurugram.

Formerly Indian Institute of Technology, Delhi
E-mail: keharsiitd@gmail.com

Prof. Kehar Singh served IIT Delhi since 1965 in various capacities, including Head Physics Deptt., and Dean Post Graduate Studies and Research. He was an 'Academic visitor' at the Imperial College London (1969-70) and visited /carried out research for short periods at British Scientific and Industrial Research Association Ealing, Queen's Univ. Belfast , and N. P. L. Teddington (UK). He served as CLUSTER Chair at the Swiss Federal Inst. of Technology, Lausanne (Switzerland) in Dec. 2002. Until June 30, 2011 he served as an Emeritus Fellow at IIT Delhi where he continued to teach and carry out research. Since 2011, he has been working as anHony. Distinguished Research Professor at the NorthCap University, Gurgaon (Haryana) where he mentors a group of faculty members. He also served as Chairman of the Research Council of IRDE (DRDO) Dehradun, and is a

member of the Research Council of N.P.L. Delhi. Since May 2015, he has been serving as an Associate Editor of the journal 'Optics Express'. He is also engaged in popularizing optics and photonics by giving special lectures at various technical institutions, especially in the NCR.

Prof. Singh as an active researcher and educator, created infrastructural facilities for teaching and research at IITD in his areas of specialization: Photonics/Information Optics (Image formation and evaluation, Dynamic holography, Nonlinear photorefractives, Optical correlators, Holographic storage, Nanophotonics, Singular optics and Optical encryption). He has authored / co-authored nearly 350 peer reviewed research papers, besides approx. 70 review articles in books and and journals, and 60 papers in confer. proceedings. He has mentored 35 doctoral students besides supervising 75 M.Tech.,M.Sc., and B.Tech. student projects, and had been the backbone of the M. Tech. program in Applied Optics at IITD, ever since its inception in 1966.

His awards include: S. S. Bhatnagar-, Galileo Galilei- (ICO), 'Opt.Soc.India'-'Life Time Achievement' and Golden Jubilee 'Distinguished Service Award' of IIT Delhi. He was also honored in 2011 under the golden jubilee "Honoring the Mentor' program of IITD. He is a Fellow of OSA, SPIE, INAE, OSI, and LASSI and served as President OSI , LASSI, ISCA (Physical Sci. Sec.) Prof. Singh is an international advisory member of editorial boards of Optical Review (Japan), J. Optics (India), and Computer Optics (Russia). He also served on the editorial boards of Optics & Lasers in Engg. (Elsevier) and Indian J. Pure Appl. Phys. (CSIR). He has been serving as a reviewer of research papers for several journals of repute and has given approx. 95 invited lectures in various international and national conferences, besides having been associated as member of organizing/technical committees of several conferences. He was one of the Directors of the II Winter College in Optics held at ICTP, Trieste, Italy during Feb-March, 1995. Prof. Singh's research work has attracted funding from a number of agencies such as DST, MHRD, and DRDO. He has served on many committees of the Govt. of India notably the 'Environmental Impact Assessment Committee' for thermal power stations.

As technical chair of the Int'l Confer.on 'Optics and Optoelectronics'(Dehradun, 1998), Prof. Singh co-edited a two volume proceedings of the confer. and SPIE vol. 3729, 'Selected papers from International Conference on Optics and Optoelectronics'98' He was also technical co-chair of the Int'l confer. on Optics and Opto-electronics (Dehradun, 2005), co-chair Advisory Committee of the OSI confer. (2012, IITD), and Chair Technical Program Committee, OSI's Int'c conference held in 2017 at GJUST Hisar. He is also Chair Int'l Advisory Committee of the upcoming confer. on Photonics at IIT Delhi. Prof Singh has edited / co-edited 2 special issues on 'Photorefractives and their applications' of J. Optics (India), 4 issues on 'Optical pattern recognition' and 'Optical information security' of Asian J. Physics, and two book; 'Perspectives in Engineering Optics' and "Those Were the Days; Personal Recollections of Former Faculty Members of IIT Delhi " . Prof. Singh has also served as a member/chair of several national committees of the MHRD, CSIR, ISRO, and DRDO. Besides having served as a consultant to some industries/organizations, he has also been a consultant on security holograms to some state Govts. in India.

PLENARY LECTURES

OSI-ISO 2018 manuscript No.
(K1)

Metamaterials, transformation optics and some applications beyond optics

Stefan Enoch

Abstract. After a brief presentation of research conducted at Institut Fresnel in Marseille in optics and photonics we will focus mainly on the work we did on photonic crystals and metamaterials. Nanophotonics is a highly topical field of modern optics that has created new exciting technological opportunities in many areas. Managing light propagation or near-field light-matter interactions at a subwavlength nanoscale level provides new avenues to develop devices. Photonic crystals have been introduced to control spontaneous emission but have also the ability to control light propagation. Metamaterials have been proposed as a potential solution to have a perfect control on light propagation but able to enhance emission or conversion of light. For example, the Near Zero Index metamaterials have been proposed to design directive emitters. More recently so-called hyperbolic metamaterials have been intensively studied. It has been shown that hyperbolic metamaterials could lead to negative refraction and superlensing. The dispersion relation display hyperbolic features (i. e. isofrequency dispersion relation is a hyperbola) and, thus, could lead to diverging density of states and enhancement of spontaneous emission.

I will also introduce the transformation optics and it's well know application to invisibility with example of application for plasmonics.

We will also briefly show how these concepts could be used for other wavelength for example for MRI applications or other type of waves leading us to waterwave cloaking or seismic protection.

Institut Fresnel, Marseilles
E-mail: stefan.enoch@fresnel.com

OSI-ISO 2018 manuscript No.
(K2)

E C G Sudarshan's contribution to Quantum Optics: the Optical Equivalence Theorem

N. Mukunda

Abstract. E C G Sudarshan discovered the Diagonal Representation inquantum optics, and the Optical Equivalence Theorem that it leads to,in 1963.This talk recalls the historical context in which theseresults appeared.Emil Wolf's creation of the classical theory ofpartially coherent fields, the impact of the experimental discovery ofthe Hanbury Brown Twiss effect, and Leonard Mandel's semi classicaltheory of photo electron counting statistics, will be brieflyrecalled. Against this background,we outline Glauber's quantum theoryof partially coherent optical fields , and the special role played bycoherent states .The Diagonal Representation is then described, andthe Optical Equivalence Theorem stated . Its use in distinguishingbetween 'classical' and 'non classical' states within quantum theory ,basic to quantum optics,is outlined and illustrated through several examples.

IISc, Bengaluru
E-mail: nmukunda@gmail.com

OSI-ISO 2018 manuscript No.
(K3)

All-dielectric resonant meta-optics and nanophotonics

Yuri Kivshar

Abstract. Metamaterials---artificial electromagnetic media that are structured on the subwavelength scale---were initially suggested for the realisation of negative-index media, and later they became a paradigm for engineering electromagnetic space and controlling propagation of electromagnetic waves. However, applications of metamaterials in optics are limited due to inherent losses in metallic element employed for the realisation of artificial optical magnetism. Recently, we observe

the emergence of a new field of *all-dielectric resonant meta-optics* aiming at the manipulation of strong optically-induced electric and magnetic Mie-type resonances in dielectric and semiconductor nanostructures with relatively high refractive index. Unique advantages of dielectric resonant nanostructures over their metallic counterparts are low dissipative losses and the enhancement of both electric and magnetic fields that provide competitive alternatives for plasmonic structures including optical nanoantennas, efficient biosensors, passive and active metasurfaces, and functional metadevices. This talk will summarize the most recent advances in all-dielectric resonant meta-optics including active nanophotonics as well as the recently emerged fields of topological photonics and nonlinear metasurfaces.

Australian National University, Australia
E-mail:yuri.kivshar@anu.edu.au

OSI-ISO 2018 manuscript No.
(K4)

Extreme light - spin offs for optics and photonics

G. Ravindra Kumar

Abstract. High intensity, ultrashort light pulses ('extreme light') are revolutionizing science and technology in very exciting ways, whether it is laboratory simulation of astrophysical phenomena, relativistic optics, particle acceleration on a table top, real time x-ray diffraction of molecules, lithography and medical therapies for cancer [1,2] . Such pulses can heat a piece of matter to intra-stellar temperatures ***at*** high density. It is this feature of ultrashort pulses that helps us devise compact, novel radiation sources for applications.

We will review the basics of this interaction and then present some novel efforts in the generation of x-ray sources that can be applied to studies in other branches of science. High harmonic emission from gaseous sources has been well established as a source in the VUV - soft x-ray region [3]. Hard x-ray sources, however are based mainly on solid target plasmas. Here, great progress has been made by the discovery that the nano spatial scale has a very important role play in the interaction of intense, pulsed light with matter. We will see how nanoparticles [4], nanowires [5, 6] and sub wavelength structures [7] influence the generation of very high energy electrons, which in turn generate hard x-rays.

It is also interesting to see that the study of the x-ray emission process itself is leading to great advances in attosecond dynamics in atoms, molecules and solids [3]. We will conclude by presenting the emergence of high efficiency table top sources at the other extreme, namely terahertz region [8]

References:

[1] G. Ravindra Kumar, “Intense, ultrashort light and dense, hot matter”, Current Trends in Science, Ed: N. Mukunda, Indian Academy of Sciences Platinum Jubilee Special, p311 (2009).

(Also in Pramana- Journal of Physics, 73, p 113-155 (2009)) [Review]

[2] G. Chatterjee et al., Nat. Communs 8, 15970 (2017)

[3] G Vampa and T Brabec 2017 J. Phys. B: At. Mol. Opt. Phys. 50 083001 [Review]

[4] P.P.Rajeev et al., Phys. Rev. Lett. 90, 115002(2003);

[5] S. Mondal et al., Phys. Rev.B 83, 035408 (2011)

[6] D. Sarkar et al., APL Photonics 2, 066105 (2017)

[7] S. Kahaly et al. Phys.Rev.Lett. 101, 145001 (2008)

[8] I. Dey et al., Nat Communs 8, 1184 (2017)

Tata Institute of Fundamental Research, Mumbai 400 005
E-mail: grk@tifr.res.in

OSI-ISO 2018 manuscript No.
(K5)

Non-hermitian dynamics in delay-coupled semiconductor lasers

Gautam Vemuri

Abstract. We will describe our work on realization of a non-hermitian Hamiltonian system in time-delay coupled semiconductor lasers. The experimental system consists of two lasers, operated under identical conditions with a small frequency detuning between them, which are bidirectionally coupled through optical injection. The effective Hamiltonian for this system is non-hermitian, and reminiscent of a parity-time (PT) symmetric Hamiltonian. The dynamical response of the intensity of the lasers as a function of detuning between them reveals characteristics of a PT symmetric system. Numerical simulation of the nonlinear rate equation model that describes our system is compared to the experimental results. An analytic theory of the system is also formulated by employing the Lambert W function, which makes very specific predictions about the behavior of the system and its dependence on the time-delayed coupling. Excellent agreement between experiments, theory and simulations is found.

Indiana University Purdue University Indianpolis
Email: gvemuri@iupui.edu

INVITED LECTURES

OSI-ISO 2018 manuscript No.
(I1)

Multiphoton Bell's inequalities

Arvind

Abstract. Bell's inequalities are used to capture the non-local aspects of bipartite quantum systems. Original formulations of Bell's inequalities was for two spins and most of the initial experiments were done using two photons. We describe Bell type inequalities which are formulated for radiation modes rather than for photons and which can be applied to a wide variety of quantum states of the radiation field. We show how these inequalities can bring out the non-local and hence the non-classical aspects of various Gaussian and non-Gaussian radiation states.

Indian Institute of Science Education and Research Mohali
E-mail: arvind@iisermohali.ac.in

OSI-ISO 2018 manuscript No.
(I2)

Microlithography using micro-bubbles manipulated using thermo-optical tweezers

Subhrokoli Ghosh . Basudev Roy. Ayan Banerjee

Abstract. We have developed a micro-lithography technique exploiting directed self assembly driven by a laser induced microbubble generated in thermo-optical tweezers, where we have been able to pattern soft polymers such as oxometalates and a variety of other entities in conjunction with the oxometalates on a glass substrate. These include fluorescent dyes, catalysts, organic monomers, metallic nanoparticles such as carbon nanotubes, and even biological moieties such as antigens and antibodies. Our idea stems from the fact that a microbubble grown in a (typically) aqueous dispersion of a material by thermo-optical tweezers induces convective flows of the material that

self-assembles at the bubble's base and then undergoes a phase transition to crystallize and thereby form permanent patterns as the bubble is translated by the tweezers. The microbubble is grown by using a laser wavelength where the material to be patterned absorbs. Thus, we have already made considerable progress in preparing plastic electronic circuits, where we have simultaneously synthesized, doped, and patterned conducting polymers such as poly-pyrrole and poly-aniline in-situ – starting from the parent monomers. The most recent advancement has been in direct patterning of biological entities, which reveal the potential of this technique as a new method of fast and low-cost lithography for preparing micro-patterns of diverse materials.

IISER Kolkata
E-mail: ayan@iiserkol.ac.in

OSI-ISO 2018 manuscript No.
(I3)

Near Field Interferometric Phase Coherence Mapping after a Quantum Quench of a Bose-Einstein Condensate in an optical Lattice using Talbot Interferometry

Aranya B Bhattacherjee

Abstract. Controlling and manipulating coherence in different systems is one of the primary goals of modern research. In cold atom physics, interferometry has proved to be a powerful tool to explore coherence. Here a near-field interferometeric technique based on the Talbot effect is described, which allows us to probe the phase coherence of ultracold atoms in an optical lattice for well defined distances. The gradual build-up of phase coherence after a quantum quench of a Bose–Einstein condensate in a one-dimensional optical lattice is demonstrated. The results indicate that the phase coherence after the quench builds like a diffusive process. The possibility to probe finite-range phase correlations in a quantum gas offers many possibilities for the study of non-equilibrium dynamics.

Department of Physics, Birla Institute of Technology and Science, Pilani, Hyderabad Campus, India
E-mail:aranyabhuti@googlemail.com

OSI-ISO 2018 manuscript No.
(I4)

Full field birefringence microscopy using a rotating polarizer

Kallol Bhattacharya

Abstract. This work aims to provide a novel method to characterize and analyze microscopic birefringent samples in terms of its magnitude of retardance and its fast axis orientation with the help of a rotating analyzer. Moreover, it is possible to estimate the Stokes parameters using a simple algorithm thus developed. The simulated and experimental results thus presented are in good agreement with the proposed theory.

Department of Applied Optics and Photonics, University of Calcutta, Kolkata 700106
E-mail: kbaop@caluniv.ac.in

***"Refer to paper number 180 for more* details"**

OSI-ISO 2018 manuscript No.
(I5)

Diffractive Optics on Fibre Facets

Shanti Bhattacharya

Abstract. Diffractive optics enables the compact manipulation of light, as well as possesses the ability to manipulate light in ways impossible with refractive optics. Fibre optics allows access to difficult to reach places, and also makes systems more compact. In this paper, we look at how fibre optics and diffractive optics can be combined, creating sub-systems that can potentially transform the size and functionality of optical systems.

Keywordsdiffractive optics, lithography, direct laser writing, sub-wavelength gratings, polarization manipulation, complex light generation

In this work, we will briefly review work by other groups [1-3] on fabricating diffractive optics on a fibre facet, before presenting detailed results from our group [4]. Different fabrication techniques, such as Focused Ion Beam and Direct laser writing have been used to write the structures and the advantages of each method will be highlighted. Results of elements that generate complex light or manipulate polarization will be presented.

References

1. X. Zhenwei, G. Shecheng, L.Ting, F. Shengfei, Z. Zhang, L. Fan, Z. Jianbo, L. Zhaohui and Y. Xiaocong, "Integrated (de)multiplexer for orbital angular momentum fiber communication," Photon. Res. **6**, 743-749 (2018)

2. T. Gissibl, M. Schmid and H. Giessen, "Spatial beam intensity shaping using phase masks on single-mode optical fibers fabricated by femtosecond direct laser writing," Optica, **3**(4), 448 (2016).

3. T. Gissibl, S. Thiele, A. Herkommer and H. Giessen, "Sub-micrometre accurate free-form optics by three-dimensional printing on single-mode fibers," Nat. Comm., **7** 11763 (2016).

4. P. Vayalamkuzhi, S. Bhattacharya, U. Eigenthaler, K. Keskinbora, C. T. Samlan, M. Hirscher, J. P. Spatz, and N. K. Viswanathan, "Direct patterning of vortex generators on fiber tip using a focused ion beam," Opt. Lett. **41**(10), 2133-2136 (2016).

Department of Electrical Engineering, IIT Madras, Chennai – 600 036, India
E-mail:shantib@iitm.ac.in

OSI-ISO 2018 manuscript No.
(I6)

Strain-coupled homogeneous and heterogeneous In(Ga)As quantum dot heterostructures for detector and photovoltaic applications

Subhananda Chakrabarti*. Debiprasad Panda . Debabrata Das . Harshal Rawool . Sandeep Madhusudan Singh

Abstract. A new perspective of strain-coupled quantum dot (QD) heterostructures is reported in this study, which will be the motivation for future generation infrared focal plane arrays (IR-FPAs) and solar cells. The Stranski-Krastanov and Submonolayer (SML) QDs have numerous independent advantages as the intersubband IR detectors. The homogeneously coupled SK QDIP with a new

growth strategy is reported in this study, which has an ultranarrow spectral response. However, the heterogeneously coupled SK-SML QD has a broad response in the IR region, which might be suitable for the IR detection along with intersubband solar cell (IBSC) application. The lower dark current exhibited by these QD heterostructures is also reported in this study, which attributes a better vertical confinement of carriers in the QD.

---

*Department of Electrical Engineering, Indian Institute of Technology Bombay, Mumbai, INDIA-400076
E-mail: subho@ee.iitb.ac.in

OSI-ISO 2018 manuscript No.
(I7)

Non-Linear Optical Organic Micro-Resonators

Rajadurai Chandrasekar

Abstract. Bottom-up molecular self-assembly technique has emerged as one of the powerful methods to produce miniaturized organic photonic structures, such as optical waveguides, lasers, resonators, filters, circuits and modulators. Optical waveguides and modulators are used to control the light propagation down to microscale and modulate the light propagation speed, respectively. In optical resonators their mirror-like geometry allows them to tightly trap the photons by repeated total internal reflection at the air-matter interface and act as optical gain media exhibiting high-quality factor (Q) with the low optical loss. We have been performing single-particle micro-PL spectroscopy studies to exploit the geometrical features of diverse self-assembled organic structures for photonic applications. In my talk, I will discuss some original results achieved in our group in linear and non-linear optical organic optical waveguide and microresonators useful for signal enhancement, sensing and lasing applications.

Functional Molecular Nano/Micro Solids Laboratory, School of Chemistry, University of Hyderabad, Hyderabad – 500046, INDIA
E-mail:r.chandrasekar@uohyd.ac.in

OSI-ISO 2018 manuscript No.
(I8)

Overview of Biomedical Raman spectroscopy

C. Murali Krishna

Abstract. Conventional diagnosis involves clinical examination followed by relevant biochemical/microbiological/pathological examinations which rely on symptoms suggesting diagnosis of existing disease. Such late diagnosis is often prone to poor prognosis, emphasizing early diagnosis for better prognosis. Monitoring of treatment response is another crucial aspect of disease management. Accurate evaluation and monitoring of treatment response lead to better disease management and towards personalized medicine. In this context, Raman spectroscopy has been explored in biomedical applications, as it is better suited due to attributes such as sensitivity to biochemical composition, objective, rapid, no external labelling/sample preparation, and most importantly in vivo/in situ on line applications. This paper presents an overview of in vivo Raman spectroscopy studies and explorations on exfoliated cells and body fluids showcasing aspects of diagnosis/screening, treatment response in cancers.

Cancer Research Institute (CRI), Advanced Center for Treatment, Research and Education in Cancer (ACTREC)Tata Memorial Center (TMC) Navi Mumbai
E-mail:mchilakapati@actrec.gov.in, pittu1043@gmail.com

***"Refer to paper number 22 for more* details"**

OSI-ISO 2018 manuscript No.
(I9)

Nonlinear topological lattices

Yidong Chong

Abstract. When lattices with topologically nontrivial phases are extended into the nonlinear regime, a variety of novel phenomena can be observed. I discuss the phenomenon of "topological solitons", a new class of solitons confined by a self-generated topological gap. Next, I discuss our recent experimental work on the implementation of a nonlinear transmission line(NLTL) metamaterial based on the nonlinear SSH lattice, showing that harmonic generation in a left-handed NLTL can be greatly increased by the presence of a topological edge state.

Nanyang Technological University, Singapore
E-mail: seewhydee@gmail.

OSI-ISO 2018 manuscript No.
(I10)

Quantitative PhotoAcoustic Imaging of Biological Tissues: Accessing to Multiphysics Informational Content

Anabela da Silva

Abstract. Photoacoustic (PA) offers promising perspectives in probing and imaging subsurface absorbing structures in biological tissues. The principle consists in heating the tissues with pulsed light sources. When an absorbing heterogeneity, such as a tumor, more absorbing than normal tissues, is present, the optical energy absorbed is partly dissipated into heat accompanied with microdilatations that generate acoustic pressure waves, the intensity of which is related to the amount of absorbed energy. This acoustic wave propagates in biological tissues without any scattering. Hence the photoacoustic signal measured at the periphery can be time reversed to access the map of the pressure at initial time, directly related to the spatial distribution of the absorption coefficient, in 3D if tomographic measurements are considered (PAT). If, furthermore, spectroscopic measurements are performed, within the so-called therapeutic window (600-900 nm), this technique allows to monitor the local molecular composition of the tissues (oxy- or deoxy-hemoglobin, lipids, water…). Because PA collected signals are resulting from a multi-wave phenomenon, they contain the signatures of both optical and acoustic contrasts of the probed tissues. Our research focusses on developing new strategies to retrieve the maximum information from the multiwaves measured signals. The different methodological strategies and experimental developments conducted in our group are presented.

Aix Marseille Univ, CNRS, Centrale Marseille, Institut Fresnel, Marseille, France
E-mail: anabela.dasilva@fresnel.fr

OSI-ISO 2018 manuscript No.
(I11)

Design and modeling of thermo-optic phase-shifters for integrated silicon photonics

Bijoy Krishna Das

Abstract. With the advent of silicon photonics technology, various design architectures of thermo-optic phase shifters are being used and proposed for switching and reconfigurable device

applications Two important figure-of-merits (FOMs) of a thermo-optic phase shifter seriously considered so far are its switching power Pπ (electrical power require for π phase-shift) and switching time τ (rise/fall time), respectively. Besides these, effective footprint of a switching cell and its operating temperature are going to play important roles for a large-scale photonic integrated circuit. Therefore, it is essential to develop a generic model to analyze the performance of a thermo-optic phase-shifter in terms of its all essential FOMs.

In this talk, we will address first the various reported design of thermo-optic phase shifters in silicon-on-insulator platform. Thereafter, we will introduce a couple of characteristics parameters useful for modeling a thermo-optic waveguide phase-shifter. These characteristics parameters are then extracted from numerical simulation results and subsequently shown to be consistent with experimental results. Finally, we will be going to present experimental results of a broadband thermo-optic switching cell and an attractive wavelength band add-drop multiplexer/switching device fabricated recently at IIT Madras.

Department of Electrical Engineering, IIT Madras, Chennai – 600 036, India
E-mail:bkdas@ee.iitm.ac.in

OSI-ISO 2018 manuscript No.
(I12)

Tamm-plasmon-polaritons in periodic and aperiodic photonic crystals

Mukesh K. Shukla . Ritwick Das

Abstract. One dimensional (1D) periodic photonic geometries are optical analogues of widely-investigated counterparts in condensed-matter physics. They exhibit dispersion curves which are bounded within the Brilliouin zone boundary and describes the evolution of electromagnetic (em) field in the wavevector (k)-space. Due to the cyclic evolution, the em-field picks up a quantized geometric phase or alternately `Zak'-phase while moving between equivalent points within the photonic pass bands. Such investigations have revealed topological photonic insulators and topologically-protected optical surface states. This feature, however, is not apparent in a quasi-periodic or deterministically aperiodic system. In the present work, we discuss and provide a plausible route to define `Zak'-phase in a 1D quasi-periodic (Fibonacci) lattice.

School of Physical Sciences, National Institute of Science Education and Research, HBNI, Jatni - 752050, India
E-mail: ritwick.das@niser.ac.in

***"Refer to paper number 67 for more* details"**

OSI-ISO 2018 manuscript No.
(I13)

Quantum dots on metal-dielectric interface: a novel architecture for quantum information processing

Shubhrangshu Dasgupta

Abstract. A generic architecture based on quantum emitters on metal-dielectric interface to generate photons in nonclassical states will be presented. The photons emitted into the surface plasmon (SP) mode from the initially excited emitters radiate out in free space, and when detected at two detectors, exhibit anti-coalescence - a clear signature of nonclassicality. One can also obtain a two-emitter Heisenberg-type coupling, suitable for realization of emitter-based quantum gates, thanks to their common coupling to the SP mode.

Department of Physics, Indian Institute of Technology Ropar
E-mail: sdasgupta@iitrpr.ac.in

OSI-ISO 2018 manuscript No.
(I14)

Methods of Ultrafast Optical Characterization for Photonic, Electronic and Magnonic Applications

Sayantan Bhattacharya. Nikita Porwal. P K Datta

Abstract. The origin of electronic and optical properties of materials is a complex interplay between lattice, electronic and spin degrees of freedom that generally occur on a timescale that ranges from 10−18 to 10−9 s (or longer).With a revolutionary technological improvement in the field of ultrafast lasers, shorter time domain laser pulses with broader band-with become available for high resolution ultrafast spectroscopic techniques. Shorter the pulse become, the resolution goes higher. Experimental time resolved optical techniques to characterize the dynamic properties of photonic, electronic and magnonic systems in femtosecond time scale have transformed our understanding of these materials. In this report we will be discussing about such few techniques which enable us to

measure quantitates like ultrafast decay path ways of electrons, spin dynamics and absorption of low energy quasi-particles. Development and experimental intricacies of Transient absorption spectroscopy (TAS), THz-time domain spectroscopy (THz-TDS) and Time resolved magneto optical kerr (TR-MOKE) will be discussed thoroughly along with representative data that we have published in recent years.

An acquisition of aTi: Sapphire amplifier system (Libra-He) along with femtosecond optical parametric amplifier(TOPAS-Prime) at IIT Kharagpur have fuelled a flurry of activities in the field of ultrafast dynamics. The experimental methods that are being used for the ultrafast dynamical characterization of various optical, electronic and magnetic processes in materials are discussed. Transient absorption Spectroscopy(TAS) with tunable optical pump and white light super continuum covering a spectral range of 350-1400nm and with a temporal resolution of 100fsis used to identify different electronic processes and their rates in 2D layer materials (Carbon based and transitional metal di-chalcogenides). Total temporal scan window of is 4ns and it is achieved using eight pass probe beam through a retro-reflector sitting on the top a motorized delay stage. Transmitted or reflected signal is collected using a fiber coupledspectrometer connected to Si photodiode array (MS-260i, Oriel Instrument).An optical chopper, in synchronization with the spectrometer, operating at 500 Hz is used to modulate the pump beam. The pump-probe measurements are taken on the samples in a cuvette of path length 2 mm having a magnetic stirring system. A differential change in absorbance (ΔA) is measured from the difference.Transient absorption data of graphene oxide (GO) and reduced graphene oxide (RGO) dispersion is reproduced from the reference [1] in figure 1(a) and (b) where the samples are pumped at 415 nm with 3μJ pulse energy.

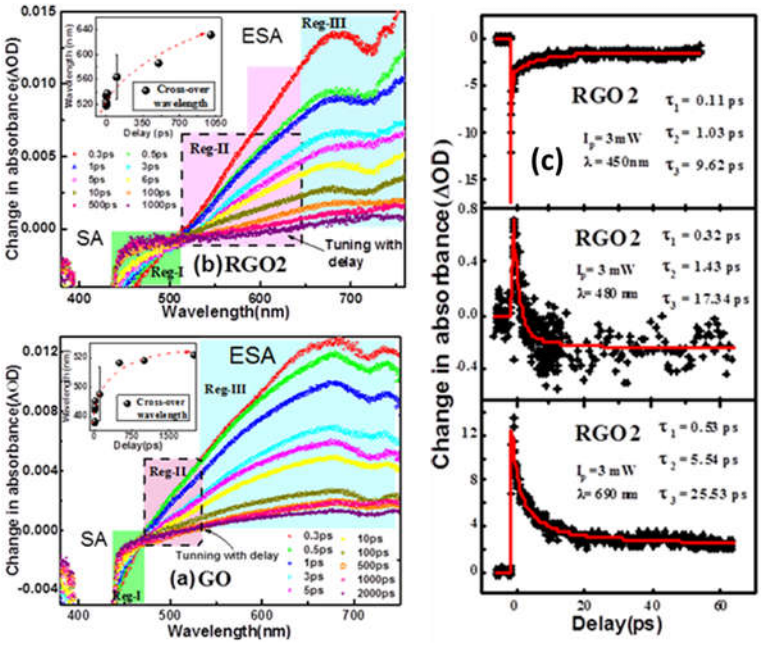

Figure 1 Transient absorption spectra of (a) as grown GO, (b) RGO2 with 415 nm pump at 3mW average pump power.(c) Decay kinetics of RGO2 at probe wavelength of 450nm,480nm and 690nm

THz time domain spectroscopy(THz-TDS) with THz range of 0.2-3.0 THz and spectral resolution of 500 MHz is developed to identify combination phonon modes in doped GaSe crystals. THz is generated using an optical rectification process in <110> cut ZnTecrystal and THz is detected using same crystal by means of electro-optic sampling method.As the THz cycle is of picosecond duration

and the probe beam is in femtosecond duration, the whole THz cycle is traced with the probe by moving the delay stage using an automated code written in LabVIEW 2012 environment. The THz

generation and detection set-up is kept inside a Plexiglas box.Representative time domain and frequency domain data of THz field is presented in figure 2 for air reference, pure GaSe and In, Cr doped GaSe from ref 2. FFT of time domain data is taken for one cycle of the THz pulse and the absolute value of the data isplotted in Figure 2 (b).

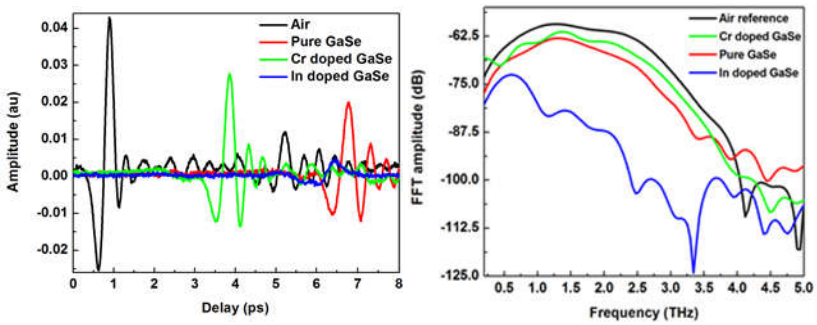

Figure 2THz field in (a) time domain , (b) frequency domain for all GaSe samples and air reference

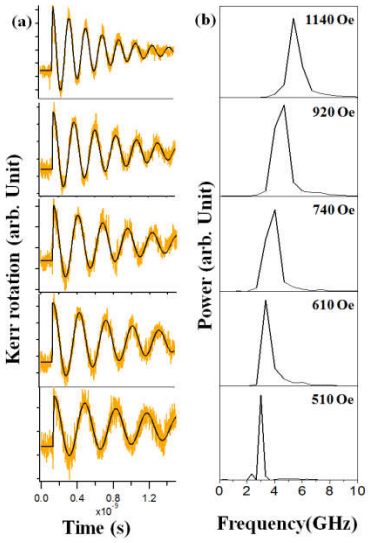

Time resolved magneto-optical Kerr set-up is developed to measure spin wave frequencies with spectral resolution of 500 MHz in Permalloy film of various thicknesses. The TR-MOKE set up is based upon two-colour collinear optical pump-probe geometry.A static magnetic field is applied at a small angle (~10^0) to the sample plane, the in-plane component of which is defined as the bias field H. The magnitude of in-plane component of this field has to be large enough to saturate the magnetization. The time varying polar Kerr rotation is measured at room temperature by using an optical bridge detector and a lock-in amplifier in a phase sensitive manner.Figure 3 shows the background subtracted Kerr rotation data (yellow color) with fitting (black color) with varying in-plane bias magnetic field for Py 30 nm thin film sample and (b) shows the corresponding FFT spectra of the sample. We observe uniform frequency mode of the sample and the precession spin wave frequency significantly decreases with the decrease in the in-plane bias magnetic fieldsand thus confirms the magnetic origin of the spin wave mode of the sample.

A highly accurate Z-scan set-up is also developed with a laser pulse of 150 fs at 1 kHz repetition rate at the wavelength of 808 nmtomeasurereal and imaginary part of third order optical nonlinearity due to electronic processes in reduced graphene oxide [3].Lock-in amplifier and motorized translational stage are incorporated in LabVIEW 2012 environment for automation and averaging of data. Pulse-to-pulse fluctuation is taken care of using reference data from photodiode. Before taking measurements, z-scan set up is calibrated using a slandered sample (CS2).

Reference:
1. S.Bhattacharya, A.Ghorai, S.Raval, M.Karmakar,A.Midya, S. K. Ray, and P. K. Datta, A comprehensive dual beam approach for broadband control of ultrafast optical nonlinearity in reduced graphene oxide. Carbon 134, 80-91 (2018).
2. A. C. Das, S. Bhattacharya, M.Jewariya, S.S. Prabhu, K. CMandal, T.Ozaki, P. K. Datta, Identification of Combination Phonon Modes in Pure and Doped GaSe Crystals by THz Spectroscopy, IEEE J. Sel. Top. Quantum Electron.23 (4), 1-7 (2017).
3. S.Bhattachraya, R.Maiti , A. C. Das, S.Saha, S.Mondal, S. K. Ray, S. N. B. Bhaktha, and P. K. Datta, Efficient control of ultrafast optical nonlinearity of reduced graphene oxide by infrared reduction, J. App. Phy 120, 013101 (2016).

Dept. of Physics, IIT Kharagpur-721302
E-mail: pkdatta@phy.iitkgp.ac.in

OSI-ISO 2018 manuscript No.
(I15)

Measurement and Characterization of higher order human ocular aberrations

A.R. Ganesan

Abstract. The aberrations in the optics of the human eye which degrade the quality of the image and hence vision can be categorized into lower and higher order aberrations. The lower order aberrations are the defocus and astigmatism which contribute up to 92% of the total aberration. This is commonly measured using a slit lamp apparatus and vision correction is done by spectacles or contact lenses. The higher order aberrations include spherical aberration, horizontal and vertical coma, curvature and so on. The measurement and correction of higher order aberrations would result in improved visual quality.

The talk would present the design and development of an indigenous Shack-Hartmann Wavefront Sensor which can measure wavefront phase profiles in real-time. The system can measure wavefront tilts to an accuracy of 2 μ radians, surface profiles down to λ/50, and aberration terms upto 4^{th} order Zernike polynomials. Higher order ocular aberrations caused by the eye's optics have been quantified using the wavefront sensor, which provides data for adaptive correction in retinal imaging, laser surgery, and vision correction. The experimental results of higher order aberration measurement and compensation would be presented.

Department of Physics, Indian Institute of Technology Madras Chennai 600036, INDIA
E-mail: arg@iitm.ac.in

OSI-ISO 2018 manuscript No.
(I16)

Theoretical studies of the ultra-cold BEC in a crossed cavity system

Sankalpa Ghosh

Abstract. Recently a supersolid-phase of ultra cold atoms was observed in crossed cavity system by the ETH Group In this talk we plan to theoretically analyze ultra cold atoms in such crossed cavity system. We derive the effective Bose-Hubbard hamiltonian for such ultra cold atoms in a cross-cavity system and also try to find out the mean field description of such supersolid phases in the appropriate limit.

Indian Institute of Technology Delhi
E-mail: sankalpa@physics.iitd.ac.in

OSI-ISO 2018 manuscript No.
(I17)

Quasicrystal based metamaterials and their applications

Achanta Venu Gopal

Abstract. By combining periodic structures with multiple periods one may achieve broadband response. However, the polarization and launch angle dependence are still limited by the constituent lattices. Designing a truly random pattern with broadband, dispersionless response is not trivial. Quasiperiodic structures can be designed for a particular wavelength response. They offer broadband dispersionless response. I will present applications of quasi periodic metamaterials for anti-reflection, Goos-Hanchen shift of a wave packet, and to modulate the magneto-optical properties of ferromagnetic thin films and electrical properties of organic semiconductors. Broadband response is also possible in sub-wavelength structures with multi-shaped elements of different sizes. While different shapes offer polarization independence, different sizes offer broadband response. I will present such broadband, launch angle and polarization independent near perfect absorber.

Tata Institute of Fundamental Research, HomiBhabha Road, Mumbai 400005 INDIA
E-mail:achanta@tifr.res.in

OSI-ISO 2018 manuscript No.
(I18)

Exceeding the threshold of ultrafast laser writing in bulk Si: opening the horizon for 3D silicon photonics

David Grojo

Abstract. An important challenge in the field of three-dimensional ultrafast laser processing is to achieve in the bulk structuring of silicon and narrow gap materials. Attempts by increasing the energy of infrared ultrashort pulses have simply failed. Our solution is inspired by solid-immersion microscopy to produce hyper-focused beams which are intrinsically free from aberrations and associated with an extreme energy confinement deep into the matter. Its validity is demonstrated by controlled refractive index modifications inside silicon. This opens a way to the direct writing of 3D monolithic devices for silicon photonics and provides perspectives for new strong-field physics and warm-dense-matter experiments.

CNRS / Aix-Marseille Universite
E-mail:david.grojo@univ-amu.fr

***"Refer to paper number 4 for more* details"**

OSI-ISO 2018 manuscript No.
(I19)

Flat Optics - Computational Techniques for designing Wide-area Metasurfaces

Ravi Hegde

Abstract. Recent work in plasmonic and all-dielectric metasurfaces point to the intriguing possibility of ultraflat optics.A drastic reduction in device bulk, the possibility of dynamic tuning and novel functionalities not realizable with standard optics continues to drive further research. The

design of metasurfaces is particularly challenging - considering the large number of free parameters. In this talk, I will discuss our recent work in the development of computational techniques to enable rapid design of these complex optical devices. Specifically, I focus on the design and optimization of ultraflat spectral filters, beam deflectors and lenses.

Indian Institute of Technology Gandhinagar
E-mail: hegder@iitgn.ac.in

OSI-ISO 2018 manuscript No.
(I20)

Plasmonic Cylindrical Nanoshell and Its Sensing Applications

Alexander A. Iskandar

Abstract. Metal Nano Particles of core–shell structures have attracted growing research interest. It allows the introduction of an additional parameter of shell thickness invoking the plasmon hybridization (PH) effect between inner and outer surface plasmons, as well as the core size giving rise to the cavity dependent effects. This structure therefore offers increased sensing tunability. Further, a symmetry breaking of the core-shell structure us expected to introduce additional features of the scattered wave characteristics promising among others, the potential of directed wave sensing applications.

Presented in this talk are several of our research results on cylindrical plasmonic system, including a system of metallic nanotube for complementary high-performance sensing of gases and liquids, metallic cylindrical multishell system of highly sensitive responses with large Figure of Merit and non-concentric metallic cylindrical nanoshell and its directed wave sensing performance.

Physics of Magnetism and Photonics Research Division, InstitutTeknologi,BandungJl, Ganesa 10, Bandung 40132, Indonesia
E-mail: iskandar@fi.itb.ac

***"Refer to paper number 35 for more* details"**

OSI-ISO 2018 manuscript No.
(I21)

Acoustic sensor based on post processed optical fiber

Rajan Jha

Abstract. Optical microfiber based sensing technology is mainly utilized for chemical and biological sensing; for sensing physical parameters it is rarely used. Hence, microfibers for sensing physical parameters such as curvature and acoustic sensing have been carried out [1-4]. These curvature sensors have shown advantages such as high sensitivity, high resolution, negligible hysteresis, very low temperature sensitivity and high stability. Another advantage is that the performance parameters of these sensors can be easily tailored in accordance with the application.

These results encouraged us to utilize these structures for acoustic sensing. We started with the inline MZI structure and demonstrated a hydrophone system which shows a sensitivity of 14.02 nm/kPa and a minimum detectable pressure of 651 μPa/√Hz in the low-frequency range (<100 Hz). Further, a tapered micro-tip in cantilever configuration with cantilever length of 15 mm act as an optical microphone and shows a sensitivity of 10.63 mV/Pa or -159.5 dB re1 V/μPa at 250 Hz with a noise-limited minimum detectable pressure of 19.1 mPa/√Hz [5]. Apart from these diaphragm free structures, a low-cost acoustic sensor using tapered SMF structure attached to a nitrile diaphragm is also studied for acoustic frequency measurement. Even with this simple design, the sensor shows an acoustic sensitivity of 36 mV/kPa and a minimum detectable pressure of 21.11 Pa/√Hz at 2500 Hz [6].

With the advantage of fairly simple fabrication of the sensor head and cost effectiveness, such sensor can be deployed for example in iron and steel industry to monitor the workplace noise to protect employees from unnecessarily high exposure. Additionally, such system can open a new window for underwater defense and bioacoustics applications.

References

[1] S. Dass and R. Jha, “Micrometer Wire Assisted Inline Mach – ZehnderInterferometric Curvature Sensor,” IEEE Photonics Technol. Lett., vol. 28, no. 1, pp. 31–34, 2016.

[2] S. Dass, J. N. Dash, and R. Jha, “Intensity modulated SMF cascaded tapers with a hollow core PCF based microcavity for curvature sensing,” J. Opt., vol. 18, no. 3, p. 035006, 2016.

[3] S. Dass and R. Jha, “Microfiber-Wrapped Bi-Conical-Tapered SMF for Curvature Sensing,” IEEE Sensors Journal, vol. 16, no. 10.pp. 3649–3652, 2016.

[4] S. Dass and R. Jha, “Bending Sensor Based on Square Knot Resonator,” IEEE Photonics Technol. Lett., DOI: https://doi.org/10.1109/LPT..2857200, 2018.

[5] S. Dass and R. Jha, “Micro-tip Cantilever as Low Frequency Microphone,” Sci. Rep., 8, pp. 12701-6, 2018.

[6] S. Dass and R. Jha, “Tapered Fiber Attached Nitrile Diaphragm based Acoustic sensor,” J. Light.Technol., vol. 35, no. 24, pp. 5411–5417, 2017.

Nanophotonics and Plasmonics Laboratory, School of Basic Sciences,IIT Bhubaneswar, Argul 752050, India
E-mail: rjha@iitbbs.ac.in

OSI-ISO 2018 manuscript No.
(I22)

Nano-photonic Structures through Phase controlled Interference Lithography and its applications

Joby Joseph

Abstract. Wide applications of photonic structures, and large scale realization of photonic devices demand a cost-effective, high spatial resolution, accurate and easy pattern transfer method to fabricate such structures in 1D, 2D and 3D over large area. Out of many, Interference lithography (IL) based method is very cost effective where, fast and large area patterning is possible. However, conventional IL becomes multi-step process for the realization of 2D and 3D complex photonic structures. Further, the realization of complex photonic structures such as chiral, quasicrystal and motheye involves multiple beams with a control over either the phase or polarization that leads to inclusion of multiple optical components. We investigate a reconfigurable and scalable phase controlled interference lithography approach leading to fabrication of simple as well as complex photonic structures with submicrometerperiodic features, in a single step over large area. Fabrications of various photonic structures with feature sizes ranging from ~300nm to many microns have been achieved. The presentation gives an overview of the technique of phase controlled interference lithography for photonic structure fabrication, and describes some applications which have been realized through these photonic structures.

Department of Physics, Indian Institute of Technology Delhi, New Delhi-110016.
E-mail: joby@physics.iitd.ac.in

OSI-ISO 2018 manuscript No.
(I23)

Optical Coherence Tomography: Clinical Applications

Renu John

Abstract. This paper provides a broad overview of the recent advances made in the field of optical coherence tomography (OCT) in clinical diagnosis. The use of imaging modalities for surgical guidance and interventions has resulted in improved patient outcome and a reduction in patient

morbidity. If the surgeon is provided with the ability to view or image tissue intraoperatively, then collateral damage to normal tissue can be minimized. We discuss our results w.r.t. ex vivo imaging of surgically resected tumors from gastro enteric patients. We demonstrate how clear tumor margins could guide a surgeon for desired tumor-free outcomes post-surgery.

Department of Biomedical Engineering, Indian Institute of Technology Hyderabad, Kandi 502285
E-mail: renujohn@iith.ac.in

OSI-ISO 2018 manuscript No.
(I24)

Nonlinear frequency conversion of sound and light in micro/nano-scaled photonic systems

Myeong Soo Kang

Abstract. Micro/Nano-scaled systems can exhibit various types of nonlinear phenomena by very tiny input driving pump powers. In particular, nonlinear coupling between different optical/mechanical modes is not only an interesting subject of fundamental research in the field of micro/nano-optics/mechanics but an important operating principle of various functional optical/mechanical devices. In this talk, I will present some recent effort to enhance the nonlinear coupling strength to create high-efficiency nonlinear optical/mechanical mode coupling even at very small optical/mechanical powers and to understand the underlying physics of the resulting phenomena.

Department of Physics, Korea Advanced Institute of Science and Technology, 291 Daehak-ro, Yuseong-gu, Daejeon 34141, Republic of Korea
E-mail: mskang@kaist.ac.kr

OSI-ISO 2018 manuscript No.
(I25)

Technologies Used in Head Up Displays for Fighter Aircraft

Vinod Karar

Abstract. Fighter aircrafts flying at supersonic speeds, doing maneuvering, flying at low height at high speed, handling of multiple activities and operation of aircraft, flight and combat leaves pilot with lot of workload. In earlier days, conventional cockpits used to have the traditional style analog dials and gauges which used to provide single information at a time. Their use also used to make the pilot divert his attention several times for monitoring of flight information in different directions. The hassle was reduced to great lengths with the advent of glass cockpits. A glass cockpit uses several displays driven by flight management systems like: Head-Up Display (HUD), Helmet Mounted Displays (HMD), Multi-function display (MFD), Gun Sights etc. to display flight and weapon aiming information as needed. The glass cockpit provides maximum information with minimal hassle to any pilot. The HUD or HMD (which is essentially a kind of HUD used on helmet) eases his/her workload by providing flight, aircraft and weapon information in his/her line of sight. This means that the flight-weapon information and outside information both are focused at infinity thus avoiding need to refocus pilot's attention on near and far field. This enhances situational awareness of pilot tremendously. That's why HUD has been designated as primary flight instrument of a fighter aircraft installed in the glass cockpit.

A head-up display gives pilots the access to the critical flight information needed to safely fly the aircraft while allowing them to focus their attention outside the cockpit for potential conflicts or threats. The combiner glass is coated with a unique material or combination materials that reflects the green wavelength but allows everything else, such as the scenery outside, to pass through, appearing quite naturally.

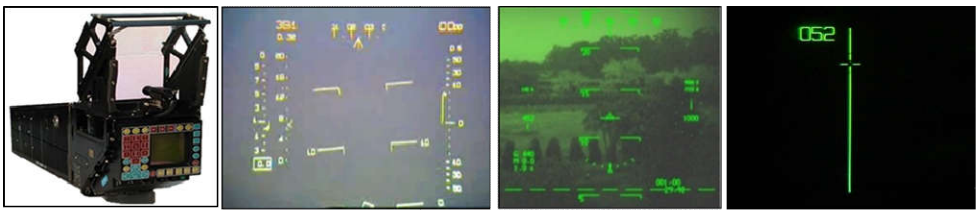

(a) Typical Head Up Display (b) Day mode stroke flight symbology (c) Night mode stroke over raster symbology (d) Standby sight symbology

HUD interfaces electrically with Mission Computer of the aircraft and displays flight symbology as well as Forward Looking Infrared Camera (FLIR) captured IR video of the outside environment. Like aircraft, not all HUD designs are same. One important difference is field of view. This refers to the angle of view which a pilot can view on left and right side while looking in forward direction through beam combiners. Because aircraft don't always fly where the nose is pointed, a wider field of view allows the HUD to accurately project data at the edges of the display in strong crosswinds. As each type of cockpit has different spatial geometry based on the aircraft class and built, the HUD construction in terms of opto-mechanical layout, critical optical and combiner's coating design changes drastically. The HUD display day mode stroke symbology, low visibility mode stroke in raster and the standby sight in case of failure of mission computer to guide pilot in emergency

situations. They are built with real time communication with pilot directly through MC and Multi-Functional Up-Front Control Panel and continuous health monitoring of the subsystems.

The HUD/HMD is an amalgamation of multiple disciplines involving electronics, software, optics, material science, human engineering, aesthetic aspects, etc. and its design & construction require highly specialized skill set. There is a range of display device technologies which could be utilized in HUD or HMD construction such as active matrix liquid crystal display (AMLCD), digital light engine (DLE), cathode ray tube (CRT), organic light emitting diode (OLED), grating light valve (GLV), etc. They along with the associated electronics and software need to be ruggedized for operation in harsh electromagnetic interference and compatibility requirements, and electrical and environmental requirements. The collimating optics could be constructed as refractive optics with spherical, aspheric and freeform optical components, or as reflective optics using waveguide or light field optics resulting in varying form factors and achievable optical specifications. The other crucial part of technology in HUD or HMD is beam combiners which could be a semi-reflective thin film combiner with flat, graded or rugate type coating or could be powered or unpowered holographic combiner. To achieve a contrast ratio of better than 1.2 even when the ambient luminance is of order of 35,000 cd/m2, the combination of display device, optics and beam combiner technology need to be suitably chosen. The innovative electro-optics design and distortion correction algorithms result in achieving of very accurate and precise symbol positioning accuracy, which decides apart from others the weapon aiming accuracy as well, of order of 1.5mR.

CSIR-Central Scientific Instruments Organisation, Chandigarh
E-mail: vkarar@rediffmail.com

OSI-ISO 2018 manuscript No.
(I26)

Technologies Trends in Electro-optical & Thermal imaging Instrumentations

Ajay Kumar

Abstract. Electro-optical instruments play a vital role in modern defence systems especially in day and night vision devices, laser based devices, fire control systems, surveillance systems, stabilization systems etc. Instruments Research and Development Establishment (IRDE) at Dehradun is a premier DRDO laboratory working on advanced electro-optical instrumentation for strengthening armed forces including Army, Navy and Air-force of the country. These systems have potential applications in surveillance & reconnaissance, target acquisition & engagement, night patrolling, vehicle driving, missile guidance, and missile warning.

IRDE has been engaged in developing vision systems for different parts of electromagnetic spectrum ranging from visible, SWIR, MWIR, LWIR etc. Many systems based on thermal imaging

technology have been evolved to get rid of night blindness of the armed forces. Apart from this, IRDE has realized numerous image intensifier tube based night vision instruments which are undergoing production at various production centers across the country. IRDE has also established state-of-the-art infrastructure for design and development of laser based instruments such as laser range finders, designators, and seekers. Some the laser based instrumentation realized by IRDE will be presented

A majority of these electro-optical systems need to be mounted on a stabilized platform for their deployment in the field. In this regard, IRDE has established world class facilities for development and testing of gimbaled platform for various field applications with high accuracy, which is required for accurate tracking, surveillance and fire control systems. Several such systems will be presented

These electro-optical systems require precision optical components for high quality imaging, beam delivery, and tracking in visible, SWIR and IR spectrum. IRDE has complete facilities to design, fabricate and characterize various kind of optical components (such as, conventional spherical, aspheric, and freefrom) of sizes ranging from millimeters to several meters.

Apart from these activities, IRDE has been venturing into futuristic emerging technologies, which may find immense defence applications in the near future. These technologies include Micro-optics, Nanophotonics, Integrated Optics, Nonlinear Optics, Holography, Tera Hertz, and Adaptive Optics. The size and weight of a future defence system would be reduced with better performance by exploiting these technologies. A number of new areas of research are also being taken up at IRDE to further supplement existing expertise. The emerging technologies would be useful in developing next generation camouflaging, countermeasures, explosive detection, and sensing devices.

In this presentation, a brief overview of activities going on at IRDE Dehradun will be given.

Instruments Research & Development Establishment, Raipur Road, Dehradun – 248 008
E-mail: ajay@irde.drdo.in

OSI-ISO 2018 manuscript No.
(I27)

Hybrid Silicon Photonic Devices for Switching and Memory Applications

Rajesh Kumar*.Shubham Singh. Nadir Ali.Aditi Sharma

Abstract. Silicon photonics is on the forefront to lead photonics technology for short and long reach optical communication. Multi-and fully-functional optical chips require integration of active and passive photonic components and devices on a single chip. Many photonic components and devices with extremely high performance have been demonstrated that can be integrated on a single chip and

many are either missing or have poor performance. Photonic memories, buffers and switches that are non-volatile in nature and consume lesser power while having ultra-low footprint are in the category of later. The talk will focus on novel solutions potentially useful for chip to chip and long reach communication using non-volatile phase change material Ge2Sb2Te5 integrated on silicon photonic platform. Such devices can be realized at current optical communication wavelength of 1.55 μm as well as emerging window of optical communication around 2 μm.

Indian Institute of Technology Roorkee, Roorkee-247667, India
*E-mail: rajeshfph@iitr.ac.in

"Refer to paper number 106 for more **details"**

OSI-ISO 2018 manuscript No.
(I28)

Optically Tuned Anisotropic, Plasmonic, Multitasking Nanostructures

Sulabha Kulkarni

Abstract. In the condensed matter Physics one always talks about structure-property correlation. However, one talks about structure-size-shape-properties correlation in nanoscience. The properties of nanomaterials, either semiconductors, metals or metal oxides depend on material, structure as well as size and shape. This gives an opportunity to obtain a huge variety of materials with similar building blocks!

Metal nanoparticles of silver and gold, rightly termed as Plasmonic particles are no exception. They can be obtained as spherical particles, rods, cubes, prisms, wires, spears and platelets to name a few. Although there are few reports on lithographically achieved shape control, many research groups prefer a wet chemical route to obtain the plasmonic particles.

Amongst the different methods developed to obtain anisotropic particles, seed mediated growth is very facile. Starting with the seeds ~ 2-3 nm in size one can choose different paths to end up with various shapes and sizes of gold or silver nanoparticles. Reaction parameters like temperature, pH, concentrations of precursors, use of surfactants along with the methodology and technique help in achieving the final goal. Once the size and shape control is achieved even self assembly of these materials can occur under certain conditions adding to the advantages of these materials. Here, we will discuss some examples of plasmonic nanostructures.

Gold as well as silver are unreactive (noble) metals in their bulk form due to their completely filled electronic 4d (only for Ag) and 5d shells (for Au). However, these particles are very reactive at the nanoscale. The nanoparticles of Au and Ag can be used in sensing applications as well as for

catalysis. We have synthesized Au-Cu alloy nanostars and embedded them in Polyaniline (PANI). The nanocomposite thus fabricated was used as the ammonia gas sensor. A different type of nanocomposite ammonia sensor using coreshell of silica (rod)-gold nanoparticles in PVA proved to be even better and selective for ammonia gas. Another kind of sensors, which use the optical properties of gold and silver also were made. Novel silica-silver core-shell particles were fabricated to detect E-coli in water with very high sensitivity. Surface Plasma Resonance (SPR) characteristic of silver was used here to detect instantaneously even the low level of water pollution. Another optical ultra sensitive sensor was due to self-assembly of vertically aligned gold nanorods. Due to their superlattice arrangement over large area of few micrometers these nanorods generated strong electric field between them (hot spots). These were used to detect ultra low concentrations of glucose and TNT, using Surface Enhanced Raman Spectroscopy (SERS). Gold nanorods were also used in the laser welding of the tissues. Here the advantage is taken of the tunable longitudinal SPR, which can be easily tuned to the wavelength of the laser. This helps in having strong absorption of laser power at the required spot in the tissue.

More interesting galvanic replacement type of gold nanoparticles also can be synthesized using silver nanocubes. Silver nanocubes themselves were used in organic solar cell, which showed improved efficiency.

Briefly, gold and silver nanoparticles of variety of shapes and sizes were synthesized and used to demonstrate the application potential of plasmonic particles in different fields. This is only a glimpse of what can be done with plasmonic particles. Many more morphologies and their applications are possible with gold and silver nanoparticles.

Centre for Materials for Electronics Technology, Pune
E-mail: skknano@gmail.com

OSI-ISO 2018 manuscript No.
(I29)

Nanoscale Chemical Imaging of Plasmonic Modes beyond the Diffraction Limit

Basudev Lahiri

Abstract. The ability to image plasmonic and photonic modes of nanomaterials at the nanoscale level is fundamental for their applications in numerous areas including solar energy harvesting and single molecule sensing. Present day high-resolution imaging techniques – such as Atomic Force Microscopy (AFM) and Scanning Electron Microscopy (SEM) can provide accurate information on the structure (morphology) of nanomaterials. However, the information regarding their chemical compositions are usually obtained over a large-scale area, typically using Infrared (IR) spectroscopic

techniques [usually, tens of micrometer for Fourier Transform Infrared Spectroscopy (FTIR)]. These conventional spectroscopic techniques suffer from diffraction limits in probing materials of dimensions smaller than their operating wavelengths − thereby producing inaccurate information that fails to correlate between the physical and chemical properties of nanomaterials – thus, inhibiting their proper development.

The Photo Thermal Induced Resonance (PTIR) is a new technique that overcomes the limitations of conventional spectroscopy by combining the lateral resolution of Atomic Force Microscopy with the chemical specificity of IR spectroscopy to produce chemical images at nanoscale levels. PTIR is a versatile nano-imaging and characterization technique that is fast, accurate and can be used over a variety of materials. In this talk, I will discuss the mechanisms of the PTIR method and describe how to image the bright and dark plasmonicmodes of nanoscale Split Ring Resonators (SRRs). I will also demonstrate the application of PTIR for chemical imaging of Polymer Nanocomposites and mapping their local absorption enhancements.

Nano Bio Photonics Group, Dept. of Electronics & Electrical Communication Engineering, IIT Kharagpur
E-mail: blahiri@ece.iitkgp.ac.in

OSI-ISO 2018 manuscript No.
(I30)

Wave propagation analysis through pseudo random phase plate (mimicking atmospheric turbulence) for imaging

Christi Jose . J Sreelakshmi . Pramod Panchal . C S Narayanamurthy

Abstract. Imaging through atmospheric turbulence is challenging due to the temporal fluctuations of refractive index spoiling quality image of distant object. In this paper we report some of our experimental investigations by propagating different class of beams through a Pseudo Random Phase Plate (PRPP) mimicking Kolmogorov type atmospheric turbulence and its influence on imaging.

Applied and Adaptive Optics Laboratory, Department of Physics, IIST, Valiamala(PO), Trivandrum - 695547
E-mail: c_s_narayanamurthy@rediffmail.com

OSI-ISO 2018 manuscript No.
(I31)

Vector beam with required phase-only functions for asymmetric image encryption

Naveen Kumar Nishchal

Abstract. With the technological evolution enormous amount of information/data is being created, stored, and exchanged. This requires efficient security system for secure storage and secure transmission. Digital schemes for information security already in use are being researched further considering improvement in terms of robustness and speed. Optical cryptosystems are being developed owing to their inherent features in terms of speed and security. The techniques have attracted increased attention of researchers after the report of first pioneering work; double random phase encoding (DRPE) was reported in 1995. Since then a large number of techniques have been demonstrated. At a later stage, the DRPE scheme was proved vulnerable due to involved linearity in the method. To overcome the weakness, optical asymmetric cryptosystems have been proposed. In which, the encoded spectrum (may be Fourier, Fresnel, fractional Fourier, gyrator) is amplitude- and phase-truncated. The amplitude-truncated part is stored as decryption key and phase-truncated part is further encoded and the process is repeated. In this process, different keys are used for encryption (encryption keys) and during the encryption process, 'decryption keys' are generated. The encryption keys are not required for retrieval of original information. Use of decryption keys and following the correct process results original data/image. To further strengthen the technique, phase retrieval algorithm has been applied for generating phase-only functions and used as keys. In this paper, the emphasis will be on optical asymmetric encryption schemes based on generation of vector beams with non-uniform arbitrary polarization distribution. The proposed scheme is based on the vector beam generator which uses the modified phase retrieval algorithm for controlling the phase of the generated vector beam. Stokes polarimetry of the generated vector beam is carried out to obtain the ciphertext and one of the keys. The encryption process can be achieved optically, while the decryption can be done numerically.

Department of Physics, Indian Institute of Technology Patna, Bihta, Patna-801 106, INDIA
E-mail: nkn@iitp.ac.in

OSI-ISO 2018 manuscript No.
(I32)

Fiber Laser and Supercontinuum Source – Versatility in Light Domain

Mrinmay Pal

Abstract. Fiber lasers have seen progressive developments in terms of spectral coverage, brightness and beam quality, output power, pulse energy and width since the first demonstration of a glass fiber laser in 1964. Their applications have extended into a variety of fields like industrial, medical, scientific and strategic sectors. In my presentation, recent development on fiber laser will be briefly reviewed and current activities at CSIR-CGCRI on CW, Q-switched and mode-locked fiber lasers with pulse dynamics will be addressed. The whole landscape of supercontinuum generation changed in the mid-1990s with the invention of photonic crystal fibers (PCF). The special micro-structures of these PCFs have a number of benefits like endlessly single-mode nature, dispersion tailoring and high non-linear property. The most notable one is the ability to tailor the dispersion properties. In my presentation, details of silica PCF fabrication and development of supercontinuum source will be presented.

CSIR-Central Glass & Ceramic Research Institute
E-mail: mpal@cgcri.res.in

OSI-ISO 2018 manuscript No.
(I33)

On the contributions of Prof. Porsezian

Prashanta K Panigrahi

Abstract. Prof. Porsezian's research encompassed a wide classes of non-linear systems associated with optics. Generation of optical solitons and solitary waves and their physical properties have been studied by him and his collaborators leaving behind research mile-stones which will stand alone. The instability of their systems and associated physical aspects had been an area of deep interest to him. The generation of rogue waves and superluminal light owe their origin to this modulational instability. In this reminiscence, we will touch upon some of their notable research areas of Prof. Porsezian's brief career.

Indian Institute of Science Education and Research Kolkata
E-mail: pprasanta@iiserkol.ac.

OSI-ISO 2018 manuscript No.
(I34)

Expansion dynamics of ultrafast laser produced metal plasmas

Reji Philip

Abstract. The properties of laser-produced plasma plumes from metallic targets are under extensive investigation owing to a wide variety of applications. Recently, we have comprehensively studied the dynamics of the expansion of laser produced metal plasmas into a vacuum chamber for background pressures ranging from 10-5 to 102 Torr, employing the diagnostic tools of optical emission spectroscopy, fast gated time-resolved imaging, ion time of flight measurements, and surface morphology analysis. Comparative studies of ultrashort pulse (fs) laser ablation (ULA) and short pulse (ns) laser ablation (SLA) have been carried out. While the electron temperature and number density of the plasma can be calculated from optical emission spectra, plume bifurcation due to the propagation of fast and slow species can be studied from time-resolved ICCD images. The expanding plasma shows a spherical morphology for plumes produced by smaller beam sizes, and a cylindrical morphology for those produced by larger beam sizes. Linear, shock wave and drag models have been used to understand plume expansion dynamics in the low, intermediate and high background pressure regions respectively. Ion current and dynamics have been measured using a Faraday Cup and the signals are compared for both ULA and SLA, from which the SLA plasma is found to be the more efficient ion source. These studies are of potential importance for variety of applications, including ion beam generation, pulsed laser deposition, laser welding and micromachining.

Raman Research Institute, C.V. Raman Avenue, Sadashivanagar, Bangalore 560080, India
E-mail: reji@rri.res.in

OSI-ISO 2018 manuscript No.
(I35)

Visible Emission Line Coronagraph (VELC) on India's First Space Solar Mission AdityaL1– Design and realization challenges

B. Raghavendra Prasad

Abstract. VELC-Aditya(L1) is an internally occulted space solar coronagraph with simultaneous imaging, spectroscopy and spectro-polarimetry channels close to the solar limb. The primary science goals of this mission are (1) Diagnostics of the coronal and coronal loops plasma (Temperature,

Velocity, & Density), (2) Heating of the corona, (3) Development, dynamics & origin of CME's, (4) Studies on the drivers for space weather and (5) Measurement of coronal magnetic fields in the corona (not planned by any mission so far). VELC is designed to image solar corona from ±1.05Ro to ±3Ro (Ro: solar radius) with a plate scale of 2.5"/pixel. It has multi-slit spectroscopic channels at three emission lines namely 530.3nm, 789.2nm and 1074.7nm with spectral resolution of 65mÅ, 95mÅ and 150mÅ respectively. It has dual-beam spectro-polarimetry at 1074.7nm for magnetic field measurements. FOV for spectroscopy and spectro-polarimetry is from ±1.05Ro to ±1.5Ro. The pay-load consists of 40 optical elements, four large format detectors and multi-operational mechanisms. The stringent demands on design, realization of subsystems, integration and finally the calibration challenges will be discussed in this talk.

Principal Investigator, VELC-AdityaL1
Indian Institute of Astrophysics, Bangalore
E-mail: brp@iiap.res.in

OSI-ISO 2018 manuscript No.
(I36)

Opto-electronic enhancement in nano-structured thin film photovoltaic devices

Jagdish A K . Kumar M P. D Roy Mahapatra . Gopalkrishna Hegde . Praveen C Ramamurthy

Abstract.thinNano-structured platforms have been explored in the context of enhanced absorption in photovoltaic systems [1, 2]. However facile fabrication of nanostructures remains a challenge. Also identification of important device length-scales over which nano-scale effects result in enhanced and combined opto-electronic performance is a problem seldom addressed. We present our work on

identification of enhancement mechanisms in both the optical and electrical domains, in a proof of concept polymer photovoltaic system shown schematically in Figure 1(a). The experiments are carried out a nano-structured platforms fabricated by facile methods involving template-based moulding.

The nanostructured device are seen to result in a significantly improved photocurrent, as seen from the external quantum efficiency curves in Figure 1(b) and the enhanced absorptance of the structured architecture in Figure 1(c). We see that the enhancement in due to simultaneous improvements in optical absorptance and charge transport.

Further we also present our findings on the effects of the length scales of the various layers in the device architecture and the consequent trade-offs between nano-structured enhancement and increased parasitic losses with nanostructures. This leads to design rules for geometry and material selection in the general context of thin film photovoltaic devices. Further, our novel fabrication method opens up a simplified experimental method to make device quality nano-patterned substrates at an applied level, and studying nano-scale phenomena at the fundamental level.

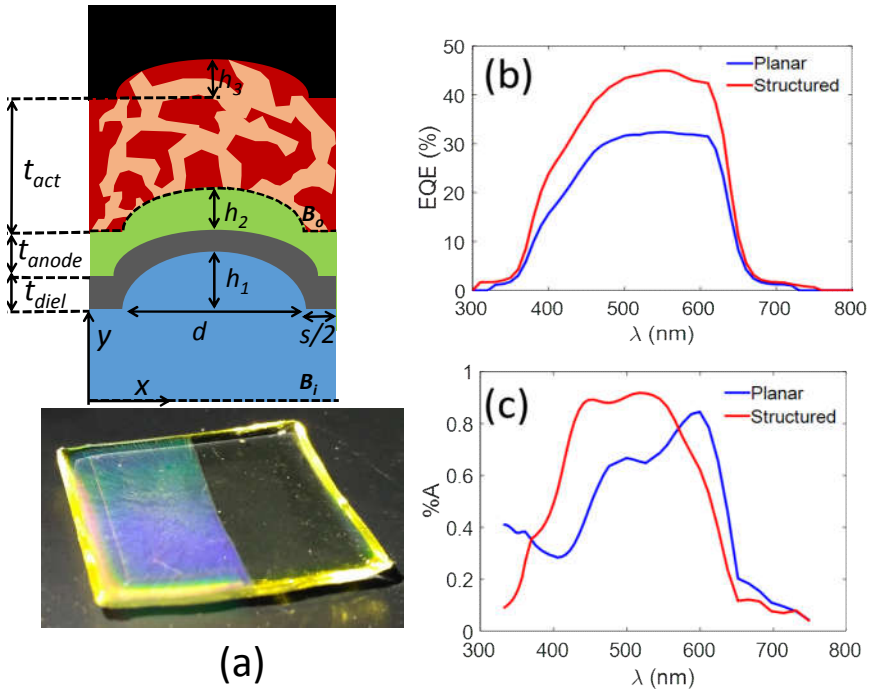

Fig. 1 (a) Schematic device architecture employed (above) and structured substrate (below), (b) External quantum efficiency of planar and structured devices, (c) Computed absorptances of planar and structured devices.

Example References

[1] S. Mokkapati and K. Catchpole, "Nanophotonic light trapping in solar cells," Journal of applied physics, vol. 112, p. 101101, 2012.

[2] J. Nelson, The physics of solar cells vol. 1: World Scientific, 2003.

Indian Institute of Science, Bangalore, India 560012
E-mail:praveen@iisc.ac.in

OSI-ISO 2018 manuscript No.
(I37)

Laser induced subwavelength periodic surface structures and their application towards broad band absorption and super-hydrophobic surfaces

D. Narayana Rao

Abstract. Femtosecond (fs) laser direct writing (LDW) has been touted as an excellent technique for creating subsurface structures on metals, semiconductors and dielectrics and has led to many advanced applications. We are going to present our recent results on fabrication of laser induced sub-wavelength periodic structures (LIPSS) also known as ripples on various materials like diamond, Si, Ge, Ti, Al, and Ag by fs LDW technique. Several theories have been proposed in literature to explain the observed sub-wavelength features and we take a look at some of these explanations and see how they support our results. The presentation will also show how the surface reflectivities can be reduced over a very broad range of wavelengths making them useful in imaging systems. The surface modifications also lead to super-hydrophobicity.

School of Physics, University of Hyderabad, Prof. C. R. Rao Road, Gachibowli, Hyderabad-500046, India
E-mail:dnrsp@uohyd.ac.in

OSI-ISO 2018 manuscript No.
(I38)

Thin Film Sensing with Terahertz Metamaterials

Sabyasachi Banerjee[1]. Maidul Islam[2] . Ch. Sai Amith[1]. Jagan Mohan Suraboina[2] . Gagan Kumar[2] . Dibakar Roy Chowdhury[1]

Abstract. We investigate thin film sensing capabilities of various terahertz (THz) metamaterial structures, one comprising of an array of asymmetric double split gap ring resonators (SRR) and the other having simple rectangular SRRs. The sensitivity and corresponding figure of merit (FoM) of the odd and even resonant modes are analyzed with respect to different thicknesses of the coated analyte film. Such studies should be very useful for the development of metamaterial based sensing devices in near future.

[1]Mahindra EcoleCentrale, Hyderabad, Telangana, India, 500043
[2]Department of Physics, IIT Guwahati, Assam, India, 781039
E-mail:dibakar.roychowdhury@mechyd.ac

OSI-ISO 2018 manuscript No.
(I39)

Unconventional Photon Blockade in Cavity Optomechanics

Amarendra Kumar

Abstract. Single-photon sources are in high demand as its necessary for possible applications of photons in quantum information processing and quantum communication. Photon blockade (PB) is one of the ways of obtaining single photons. Using PB one can produce sub-Poissonian light from a cavity, driven by a classical light field. In this talk I, starting with the basics, will discuss about various novel schemes proposed by our research group to obtain photon blockade in various optomechanical set up [2]. I will also discuss about our recent proposal to achieve photon blockade in three-mode optomechanical systems [3].

References:

[1] T. C. H. Liew and V. Savona, Phys. Rev. Lett. 104, 183601 (2010).

[2] B. Sarma and A. K. Sarma, Phys. Rev. A 96, 053827 (2017).

[3] B. Sarma and A. K. Sarma, arXiv: 1805.02218 (2018).

Indian Institute of Technology Guwahati
E-mail:aksarma@iitg.ac.in

OSI-ISO 2018 manuscript No.
(I40)

Angular momentum transfers in spin-orbit beams

P.Senthilkumaran

Abstract. We deal here few mechanisms in which the spin and orbital angular momentums can be transferred to spin-orbit beams. Depending on the type of the angular momentum that is transferred the type of the singularity also undergo changes. This has been explained using circular basis representation of polarization singularities. It is planned to introduce the phase singularities and the orbital angular momentum of photons. Types of angular momentums are introduced. Generation

and detection methods are described. How the transfer of one type of momentum transforms a beam is discussed and some of the interesting results are presented in this talk.

Department of Physics,Indian Institute of Technology Delhi
E-mail: P.Senthilkumaran@physics.iitd.ac.in

OSI-ISO 2018 manuscript No.
(I41)

Optically probing nanomechanical effects of light-fluid interaction

Kamal P. Singh

Abstract. While the photons momentum in vacuum is well established, the nature of photons momentum inside a transparent dielectric medium, such as water, is still debated for over a century known as the Minkowski-Abraham controversy. In this talk, I will shed light on this long-standing puzzle by employing direct interferometry on tiny fluid drops capable of resolving nanomechanical effects of light on an air-fluid interfaces. With our high precision data we unambiguously validate the century-old Minkowski theory for a general angle of incidence. The possibility of existence of Abraham momentum is systematically examined experimentally. We discuss our recent attempts to achieve sub-nm precision and non-invasive characterization (thermal, elastic, viscous etc) of complex biological fluids.

Dept. of Physical Sciences, IISER Mohali, Mohali, Punjab 140306, India
Email: kps.iiserm@gmail.com

OSI-ISO 2018 manuscript No.
(I42)

Coherence waves interference to overcome phase recovery challenge: in optical, crystallography and X ray imaging

Rakesh Kumar Singh

Abstract. Coherence function behaves like a wave and follows two-four dimensional wave equations. Utilizing this feature, available resources of the optical signal processing can be used for the coherence. Moreover, coherence waves give liberty to design and develop lensless configurations for optical, electron beams, X rays. Recently, we have come up with new methods using interference of the coherence waves to overcome phase recovery in a non-iterative manner. Our technique makes use of the Hanbury Brown-Twiss (HBT) approach. In this paper, we discuss issues, developments and our contributions on phase recovery with a lensless geometry. Applications of coherence wave interference in the correlation holography, Stokes holography and single pixel Hybrid correlation holography are also highlighted. Based on our experience in the optical domain, we believe and propose to apply interference of the coherence waves in areas like crystallography and X ray Imaging.

Indian Institute of Technology (BHU), Varanasi
E-mail: krakeshsingh@gmail.com

OSI-ISO 2018 manuscript No.
(I43)

Ultrafast dual-channel switching and ultrathin superconducting metamaterials

Yogesh Kumar Srivastava[1,2]. Ranjan Singh[1,2]

Abstract. In this work, we demonstrate all-optical dual-channel switching of sharp Fanoresonances excited in superconducting asymmetric split ring resonators. Upon irradiation with optical pump, the ultrasensitive Cooper pairs in superconductor undergo dual dissociationrelaxationdynamics within a single superconductivity restoration cycle and lead to dual switching windows in picoseconds

timescale. The extreme sensitivity of Cooper pairs to external perturbations enable access to such unique dual switching features, which can be readily engineered by varying the substrate properties. Moreover, we introduce a thinnest superconducting terahertz metamaterial. We demonstrate that superconducting metamaterials of thickness 25 nm supports excitation of Fanoresonances while metallic samples of identical thickness do not show any Fano resonance. Upon irradiation with optical pump, ultrathin superconducting metamaterials show extremely low threshold switching. Our results manifest new ways to realize extremely low threshold ultrafast dual channel switchable devices.

---

[1]Division of Physics and Applied Physics, School of Physical and Mathematical Sciences, Nanyang Technological University, 21 Nanyang Link, Singapore 637371, Singapore.
[2]Center for Disruptive Photonic Technologies, The Photonics Institute, Nanyang Technological University, 50 NanyangAvenue, Singapore 639798, Singapore.
E-mail: ranjans@ntu.edu.sg

***"Refer to paper number 34 for more* details"**

OSI-ISO 2018 manuscript No.
(I44)

Statistics of Heralded Twisted Single Photons

Nijil Lal[1, 2].Ayan Biswas[1,2]. Ali Anwar[1].Anindya Banerji[1].R. P. Singh[1]

Abstract. Using spontaneous parametric down conversion with vortex pump, we generate heralded single photons carrying orbital angular momentum (OAM). We study the variation of the second order quantum coherence function with the topological charge of twisted single photons.

---

[1]Quantum Science and Technology Laboratory, Physical Research Laboratory, Ahmedabad – 380054, India
[2]Indian Institute of Technology, Palaj, Gandhinagar, Gujarat, India
E-mail: rpsingh@prl.res.in

OSI-ISO 2018 manuscript No.
(I45)

Slow light enabled nanophotonic devices on Photonic Crystal Platform

Ravindra K. Sinha

Abstract. Slow light refers to reduction of the group velocity of the light wave propagating in a medium. This leads to increased light matter interaction strength, which enables increased time delay for optical signals as a key functionality for processing, storing and buffering optical signals. Photonic Crystal line defect waveguide is one of the most suitable platforms to generate and control the slow light. The dispersion curve of guided modes is used to determine the group velocity of light wave propagating through them. The realization of slow light effect in Photonic Crystal line defect waveguide due to flattening of dispersion curve can be achieved by numerous ways such as by changing hole sizes and shapes, infiltrating with dielectric material and by adjusting the position of holes adjacent to the waveguides. In this invited talk, Photonic crystal line defectwaveguides in silicon on insulator (SOI) platform will be described and the method to obtain optimized structuralparameters for the design of (i) optical buffer in terms of delaybandwidth product (ii) Time and wavelengthdivision multiplexure (iii) Optical spectral switch and (iv) generation of optical soliton at incredibly low optical power will be covered.

CSIR-Central Scientific Instruments Organisation, Chandigarh
E-mail: dr_rk_sinha@yahoo.com

OSI-ISO 2018 manuscript No.
(I46)

Laser based Systems: Recent Developments at LASTEC

H. B. Srivastava*. A. K. Razdan. M. N. Reddy. Rahul Bhatt

Abstract. LASTEC is a DRDO laboratory working in the field of Laser based systems. Multiple Laser technologies are being pursued at LASTEC. Some of these technologies have matured to some extent and accordingly a few systems, based on them, have been developed. These include Optical target locator, Laser Fence, Explosive Detectors called 'Pre-emptor', Ordinance Disposal system called 'LORDS', etc. These systems are at various stages of Trials, Evaluations and Improvisations.

A number of new technological initiatives are also being pursued. LIDAR systems fall under this category. Specifically, the technologies related to stand-off detection of clouds, aerosols, chemical agents and explosives have become very important.

LIDAR involves transmitting 'Pulse Laser' radiation into the atmosphere and measuring the 'backscattered radiation' with time. Depending on the specific variants and associated algorithms, this 'back-scattered' signal provides the information about the clouds / aerosols as well as the pollutants /chemical agent present in the atmosphere. The knowledge about these has become very important not only due to the impact of global climate on human health but also because of the current security situation, where chemical threats have become a reality.

Mie-Scattering based algorithm is used for vertical profiling of clouds and aerosols. By including the measurement of depolarization as well as Raman channels, the shape and optical properties of aerosol can be detected. Such a system can also find the water vapour content in the atmosphere.

Differential Absorption Lidar [DiAL] technique is used for identification and quantification of hazardous chemical agent in the atmosphere. A number of important pollutants, chemical warfare agents (CWA) and toxic chemicals absorb electromagnetic radiation in the mid infra-red region. Hence the detection of such molecules is possible if the laser wavelengths are transmitted in this wavelength band [mid-infrared]. For evaluation of DiAL based system, the simulants are used, which provide the exact spectroscopic signature of the respective chemical species.

Besides LIDAR technology, high power Laser is another key area in which LASTEC is working towards achieving the self-reliance. A Fiber Laser system, up to 1 KW, has been realized. For scaling up the power, multiple beams need to be combined. Out of many alternatives of Beam combining, the 'Spectral Beam Combining' is being pursued.

The talk will include design, development and testing aspects of the above technologies.

---

*Director, Laser Science & Technology Centre, Metcalfe House, Delhi
E-mail: director@lastec.drdo.in

OSI-ISO 2018 manuscript No.
(I47)

Nanophotonics for Tailoring Propagation, Emission and Topological behavior of Light

GanapathiSubramania

Abstract. Nanophotonic architectures such as photonic crystals and metamaterials have become key players in modern photonics. They offer hitherto unprecedented capabilities combined with great versatility to control various properties of light-propagation, polarization, emission and photon statistics. They have become increasingly important for chipscale photonics. In this talk, I will

present research carried out along with my colleagues in this area using photonic crystals and metamaterials at Sandia. In particular, I will provide a broad overview of our work covering three-dimensional photonic crystals operating in the visible, light emission from three-nitride nanowire two-dimensional photonic crystal arrays, metal-dielectric epsilon-near-zero metamaterials at visible wavelengths and non-resonant, broadband ultrasubwavelength light confinement structures. I will follow this overview with two of our more recent efforts. One, is on fabrication and spectroscopy of site-selective III-nitride quantum dots for quantum light sources using photo-electro-chemical etch. This approach for deterministic placement can potentially lead to quantum light sources with deterministic properties, important for quantum information processing. The other is on our efforts towards achieving topologically non-trivial photonic structures. Topological photonic structures exhibit one-way scatter-free light transport that can have important applications in optical and quantum communications.

Semiconductor materials and device sciences, Sandia National Laboratories, Albuquerque, NM 87185
E-mail:gssubra@sandia.gov

OSI-ISO 2018 manuscript No.
(I48)

Revisiting Multimode Optical Fibers: Nonlinear Applications

Shailendra K. Varshney

Abstract. In this talk, I'd review the nonlinear interactions in multimode optical fibers with few recent examples. Multimode optical fibers have been the preferred choice for local area optical network due to various reasons. Over the last few years, these fibers have gained significant interest in nonlinear regime due to large possibilities of intermodal phase matching, leading to interesting nonlinear phenomenon such as intermodal four-wave mixing, cascaded stimulated Raman scattering, intermodal modulation instabilities and many more.

Dept. of E&ECE, IIT Kharagpur
E-mail: skvarshney@ece.iitkgp.ac.in

OSI-ISO 2018 manuscript No.
(I49)

Investigation of exceptional point in a non-Hermitian system

Nirmal K. Viswanathan

Abstract. Exceptional points (EPs), the singularities of non-Hermitian systems, where both the eigenvalue and eigenvector coalesce, have been under intense investigation due to the unusual topology of its eigenmodes. The EPs have been demonstrated and characterized in a variety of physical systems leading to unidirectional light propagation, PT symmetry breaking, selective optical amplification. The recent article by Berry and Dennis [1] brought together the underlying physics of EPs in biaxial crystals under different conditions. The singular axes or EPs occur along directions where the birefringence and dichroism are equal in magnitude, and their principal planes make 45° angle with each other. The complex dynamics of the EPs is studied carefully, which leads to a fine control of the EPs and the associated chiral dynamics [2]. Our results on EPs is expected to generate several intricate features to further the emerging interest in topological optics and photonics.

School of Physics, University of Hyderabad, Hyderabad 500046, India
E-mail: nirmalsp@uohyd.ac.in

***"Refer to paper number 147 for more* details"**

Contributed Papers

OSI-ISO 2018 manuscript No.
(1)

Splicing of SMF and MOF: Loss Evaluation Using Enhanced Analytical Field Model

Dinesh Kumar Sharma. Anurag Sharma. Saurabh Mani Tripathi

Abstract The majority of optical fiber devices such as detectors and switches use standardized telecom fiber connectors. Therefore, most of the practical applications of specialty fibers, including microstructured optical fibers (MOFs), require a reliable and repeatable low-loss splicing with standard single-mode fiber (SMF). Although strongly demanded such splices are still one of the fundamental issues for realistic MOFs based applications due to completely different inner structures of SMF and MOFs. Using enhanced version of the analytical field model, we have evaluated splice losses between MOF and SMF without considering the effect of air-holes collapse at the joint interface. However, collapsing of air-holes can facilitate to reduce the mode-field mismatch, and thus lowering the losses. Therefore, we have also evaluated splice losses taking into account the effect of shrinking of air-holes at the splice interface. For comparison, we have included results based on finite-element method.

Keywords Splice loss. Microstructured optical fiber. Enhanced field model. Single-mode fiber

I. Introduction

The performance and integrity of optical fiber based devices and systems are often critically dependent on optical coupling between interconnected fibers/waveguides. Fusion splicing has been widely used to interconnect different fibers, and the splicing quality plays an important role on performance of devices in various applications. Furthermore, high mechanical strength at splicing joint is critical, for ensuring excellent long-term fiber device reliability, essential for applications such as undersea optical transmission and gyroscopes. Recent, emerging specialty optical fibers such as large-mode area fibers and microstructured optical fibers (MOFs) also referred as photonic crystal fibers [1] pose a new challenge to fusion splicing technology because of their distinct characteristics. New splicing techniques are required and more in-depth understanding of optical characteristics at splice joint is required. When two dissimilar fibers are fusion spliced together, a longitudinally varying transition region at splice joint is created. For a given fiber pair, efficient light coupling depends on proper optimization of splice joint. The waveguide transition at splice joint leads to optical field change when light propagates through space. As a result, an optical transmission loss occurs at the splice joint. For studying the fundamental modal characteristics of high-index core triangular MOF with circular air-holes in air/silica microstructured cladding, we have developed an improved field model [2], and have achieved appreciably good agreement between experimental and numerical results; reflecting the strength of field model, equipped well to take into account the field asymmetries around the air-holes. In this paper, we aim to illustrate optical characteristics of interconnected joint when two dissimilar fibers such as MOF and classical step-index fiber are spliced together, and to estimate coupling loss by using enhanced field model [2]. Also, we have evaluated splicing losses taking into account the effect of collapse of air-holes at the joint interface between the fibers. We have checked the accuracy of our results with those based on full-vector finite-element method (FEM), as available in the literature.

Dinesh Kumar Sharma
School of Vocational Studies and Applied Sciences, Gautam Buddha University, Greater Noida - 201312, India
E-mail: dk81.dineshkumar@gmail.com

II. Enhanced field model

We have considered the following trial electric field with $A, \alpha, \alpha_1, \sigma, B, \alpha_2$ and η as the field parameters, associated with 6-fold rotational symmetric of the hexagonal lattice [2]:

$$E_t(r,\varphi) = e^{-\alpha r^2} - \left(A e^{-\alpha_1 (r-\sigma\Lambda)^2} \left(1 + \cos 6\varphi\right) \right) - \left(B e^{-\alpha_2 \left(r - \eta\Lambda\sqrt{3}\right)^2} \left(1 - \cos 6\varphi\right) \right) \quad (1)$$

where Λ is termed as pitch. Using variational method for guided scalar modes, optimized values of model parameters have been obtained during the process of optimization.

III. Results and discussion

Using enhanced field model, we have evaluated splice losses based on overlap integral of optical field amplitudes of guided modes in interconnected fibers such as high-index core MOF and SMF-28 fiber [3], assuming that both fibers are perfectly aligned. Splice losses as a function of pitch is shown in Fig. 1 at λ = 1.55 μm for d/Λ = 0.40. For demonstrating the performance of enhancement in the field model, we have also included results based on earlier developed field model, termed as 1-Ring Model [4]. For checking the accuracy of results, we have also included results based on full-vector FEM [3].

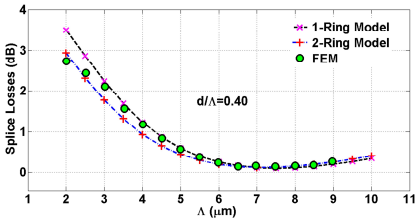

Fig. 1. Splice losses as a function of pitch.

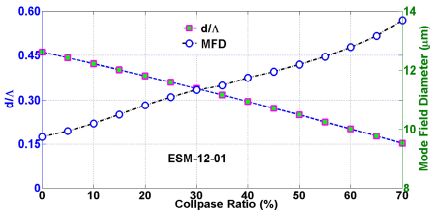

Fig. 2. MFD and d/Λ against degree of collapse ratio.

The MOF/SMF splicing loss is mainly caused by mode-field mismatch, and it is possible to match mode-field diameters (MFDs) of SMF and MOF by collapsing the air-holes of MOF. During splicing process, air-holes of MOF shrink, and the relation between air-hole size and pitch can be given by [5]: $\Lambda/\Lambda_0 = \left[\sqrt{3}/2 - \pi/4 \left(d_0/\Lambda_0\right)^2 \Big/ \sqrt{3}/2 - \pi/4 \left(d/\Lambda\right)^2 \right]^{0.5}$; where Λ_0 and d_0 are initial values of pitch and air-hole size, respectively. The MFD of an MOF increases linearly with Λ and decrease with increase in d/Λ ratio, and the relation is given by; $d/\Lambda = d_0(1-\delta) \Big/ \Lambda_0 \sqrt{1 - \rho\left(d_0/\Lambda_0\right)^2 + \rho\left(d_0(1-\delta)/\Lambda_0\right)^2}$; where $\rho = \pi\sqrt{3}/6$ is a constant, and the collapse ratio of air-holes is given by $\delta = \left(d_0 - d\right)/d_0$ with $0 \le \delta \le 1$. The results evaluated by using enhanced field model, for solid-core ESM-12-01 MOF [5] with Λ = 8.0 μm and $d/\Lambda = 0.46$, is shown in Fig. 2. The MFD of ESM-12-01 MOF is enlarged from ~6 μm to ~12 μm, when the collapse ratio changes from 0% to 55%. The MFD of SMF-28e [5] is ~10 μm. It can be depicted from Fig. 2, that the enlarged mode field of MOF can match that of SMF-28e, when air-hole collapse ratio is 60%-70%.

IV. Conclusion

Using enhanced version of field model, we have evaluated splice losses between index-guiding MOFs, and traditional step-index single-mode fiber. Enhanced field model is significantly better for modelling the azimuthal variation of modal characteristics for the MOFs, particularly, when modal field spreads deeper into the holey cladding. We have checked the accuracy of our results with those based on full-vector FEM.

References

[1] J.C. Knight, T.A. Birks, P.St.J. Russell, and D.M. Atkin, Opt. Lett. 21, 1547 (1996).
[2] D.K. Sharma and A. Sharma, Opt. Commun. 366, 127 (2016).
[3] Y.L. Hoo, W. Jin, J. Ju, and H.L. Ho, Microw. & Opt. Technol. Lett. 40, 378 (2004).
[4] D.K. Sharma and A. Sharma, Opt. Quant. Electron. 44, 415 (2012).
[5] T. Zhu, F. Xiao, L. Xu, M. Liu, M. Deng, and K.S. Chiang, Opt. Exp. 20, 24465 (2012).

Design of Multi-band Terahertz Metamaterial

S.Sasi Princy[1], E.Manikandan[1]*, B.S.Sreeja[1], S.Radha[1]
[1]Department of ECE, SSN College of Engineering, Chennai – 603110, India
*E-mail: manikandane@ssn.edu.in, drop4mani@gmail.com, +91-8939517252

Abstract

This work presents the design of multi-band terahertz metamaterial using two hexagonal shaped split ring resonators. The designed structure provides bandstop characteristics at five frequencies 0.08THz, 0.142THz, 0.285THz, 0.39THz and 0.4725THz respectively for transverse electric mode. The numerical simulation results show that the design has obtained polarization dependent transmission characteristics.

Keywords: Terahertz, multi-band, metamaterial, sensing

Introduction

Terahertz (THz) is the band of frequencies i.e. 100GHz to 30THz lies between microwave and infrared regions. Initially it has been used widely in the field of astronomy but the advancements in the technology made its utilization in number of fields such as communication, medical, security, non destructive testing etc.[1]. The development in the metamaterials will provide a solution for obtaining the polarimetric devices in the terahertz range[2]. Metamaterials are an artificial electromagnetic structure which consists of a periodic array of the metallic unit cell with each dimension in the order of sub-wavelength of the operation. These metamaterials have exotic properties such as negative refraction, backward propagation, cloaking and so forth and are of great interest in the terahertz field where it is mainly used for sensing, imaging, modulation, etc.[3–5].

Design

The schematic representation of the proposed multi-band terahertz metamaterial is depicted in Fig1.The structure consist of two layers: a PTFE dielectric substrate and on top copper based metallic resonators. The thickness of the dielectric and metallic patch is 0.25mm and 0.5µm respectively. The dimensions of the designed metamaterial structure are as follows: p=0.5mm, d=30µm, g=40µm, w=30µm, r1=180µm and r2=240µm.

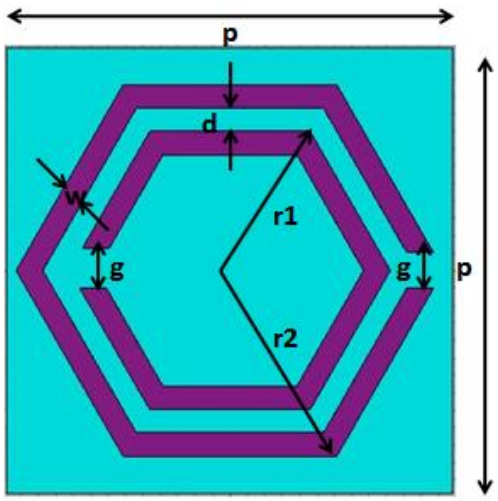

Fig1. Schematic representation of the proposed multi-band terahertz metamaterial

Results and Discussions

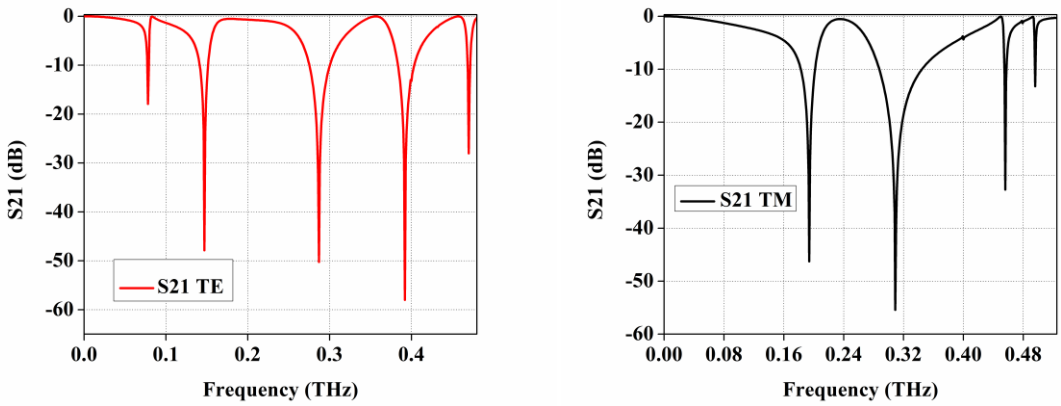

Fig2.Transmission characteristics of the proposed terahertz metamaterial for TE and TM polarization

Conclusions

A five band terahertz metamaterial is designed and its numerical evaluation is reported using CST Microwave studio software. The designed structure has polarization dependent transmission behavior which finds importance for making polarimetric components. The numerical simulation results reveal that the structure has angle independent operation in all the resonances.

References

1. M. Tonouchi, Nat. Photonics **1**, 97 (2007).
2. W. M. Zhu, A. Q. Liu, T. Bourouina, D. P. Tsai, J. H. Teng, X. H. Zhang, G. Q. Lo, D. L. Kwong, and N. I. Zheludev, Nat. Commun. **3**, (2012).
3. W. Withayachumnankul and D. Abbott, IEEE Photonics J. **1**, 99 (2009).
4. W. Xu, L. Xie, and Y. Ying, Nanoscale (2017).
5. S. RoyChoudhury, V. Rawat, A. H. Jalal, S. N. Kale, and S. Bhansali, Biosens. Bioelectron. **86**, 595 (2016).

Exceeding the threshold of ultrafast laser writing in bulk Si: opening the horizon for 3D silicon photonics

David Grojo

Aix-Marseille University, CNRS, LP3 UMR 7341, Marseille, France

david.grojo@univ-amu.fr

Abstract

An important challenge in the field of three-dimensional ultrafast laser processing is to achieve in the bulk structuring of silicon and narrow gap materials. Attempts by increasing the energy of infrared ultrashort pulses have simply failed. Our solution is inspired by solid-immersion microscopy to produce hyper-focused beams which are intrinsically free from aberrations and associated with an extreme energy confinement deep into the matter. Its validity is demonstrated by controlled refractive index modifications inside silicon. This opens a way to the direct writing of 3D monolithic devices for silicon photonics and provides perspectives for new strong-field physics and warm-dense-matter experiments.

Keywords: Femtosecond laser, material processing, laser writing, ultrafast optics, nonlinear propagation, nonlinear ionization

An important challenge in the field of three-dimensional (3D) ultrafast laser processing is to achieve permanent modifications in the bulk of silicon (Si) and narrow-gap materials. Attempts by increasing the energy of infrared ultrashort pulses with conventional laser machining configurations have failed [1-3].

We concentrate on the limitations experienced in femtosecond interactions at 1300-nm wavelength to fully identify their origins. We focus our experimental investigations on the 3D reconstruction of the nonlinear pulse propagation and ionization of Si under tight focusing configurations. By comparison with simulations [4], we quantify the strong nonlinear and plasma effects in the pre-focal region causing the limitations [5]. With an extrapolation of the energy density that could be delivered with hyper-NA values (up to 3.5 in Si), we show that solid immersion focusing provides a solution to achieve ultrafast optical breakdown in Si [5].

By repeatedly illuminating the center of a Si sphere with pulses focused at apparent NA near 3, we exceed the breakdown threshold with sub-100 fs pulses. As illustrated with figure 1, we measure with an infrared phase microscopy arrangement a highly-localized negative change of the refractive index that allows envisioning the fabrication of photonic microdevices.

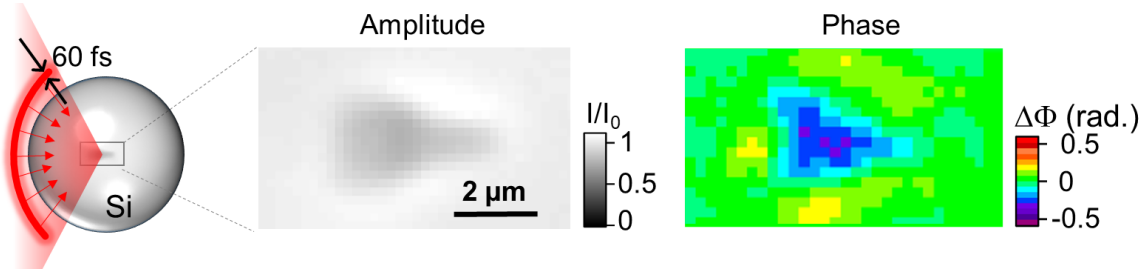

(a) (b) (c)

Figure 1: Refractive index modification achieved in the bulk of silicon with ultrashort pulses. (a) Sketch of the configuration for micro-modifications created at the centre of silicon spheres using focused 60-fs laser pulses with the hyper-NA value of 2.97. (b) Bright-field infrared images of a modification for 1000 applied laser pulses of 20 nJ energy. (c) Corresponding phase image indicating a local change of the silicon refractive index $\Delta n<-0.07$.

Beyond this proof-of-concept demonstration, we translate the experiment with the astigmatic solid-immersion lens (ASIL) configuration consisting in focusing the laser radiation through an hemispherical Si sample while ensuring an appropriate optical contact with a planar wafer. This makes possible to achieve similar modifications in Si wafers with a long working distance focusing objective of modest NA (<0.3). This represents a critical step towards technological developments.

We expect that refractive index engineering by ultrafast laser writing will open the new possibilities of 3D architectures and monolithic Si platforms for silicon photonics and it can change the way the microsystems are today designed and fabricated in this field.

Acknowledgments
This project has received funding from the Euro- pean Research Council (ERC) under the European Union's Horizon 2020 research and innovation program (Grant Agreement No. 724480).

References

[1] V. V Kononenko, V. V Konov, and E.M. Dianov, **Opt. Lett.** 37, 3369 (2012).
[2] A. Mouskeftaras, A. V. Rode, R. Clady, M. Sentis, O. Utéza, and D. Grojo, **Appl. Phys. Lett.** 105, 191103 (2014).
[3] D. Grojo, A. Mouskeftaras, P. Delaporte, and S. Lei, **J. Appl. Phys.** 117, 153105 (2015).
[4] V.Y. Fedorov, M. Chanal, D. Grojo, and S. Tzortzakis, **Phys. Rev. Lett.** 117, 43902 (2016).
[5] M. Chanal, V.Y. Fedorov, M. Chambonneau, R. Clady, S. Tzortzakis, and D. Grojo, **Nature Commununications** 8, 773 (2017).

OSI-ISO 2018 manuscript No.
(7)

Novel polarization singularity lattice structures

Sushanta Kumar Pal · P. Senthilkumaran

Abstract : Polarization singularity lattices exhibit richer features and varieties than phase vortex lattices. Phase and polarization engineering technique can be used to realize lattices consisting of only C-points or only V-points of different Stokes indices. In this article we discuss the generation of polarization singularity lattice structures embedded with both integral and half integral C-points. These lattice structures are unique as the occurrence of integral C-point is rare. Interestingly all the C-points in the lattice patterns are of same handedness irrespective of the index of the C-points. The feasibility of these lattice structures are based on sign principle.

Keywords Interference, Polarization, Optical Vortices, C-point.

Star, lemon and monstar are the generic polarization singularities (C-points) in two dimensional ellipse fields [1–3]. These are isolated singular points in the spatially varying polarization distributions, where the orientation of the azimuth is indeterminate. The C-points can have positive or negative, integral or half integral index values. They can be of left or right handed and can be dark or bright. C-points with half integral index values are more common, whereas C-points with integral index values are rare.

We present interference of six phase engineered radially polarized plane beams for generation of various lattice structures. The wave vectors of these six beams are symmetric and lie on the surface of a cone such that, $\mathbf{k_j} = \frac{2\pi}{\lambda}\{\cos(\xi_j)\sin(\theta), \sin(\xi_j)\sin(\theta), \cos(\theta)\}$, where j is the beam number and $j = 1-6$. The angle between any of these wave vectors and k_z-axis is $\theta = 0.15°$ and ξ_j is the angle between the projection of a wave vector onto the transverse plane and the k_x axis. In the transverse plane the electric field vectors of these six interfering beams are oriented in a radial fashion. The resultant

Department of physics, Indian Institute of Technology Delhi, New Delhi 110016, India.
E-mail: sushanta1985@gmail.com

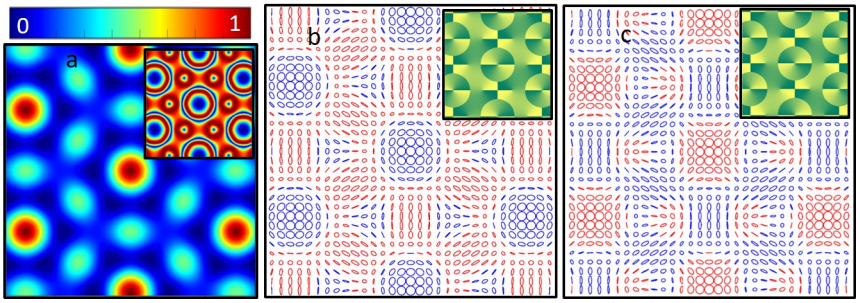

Fig. 1 Six-beam interference: (a) Intensity distribution; (b, c) polarization distributions

field of six phase engineered vector beams can be written as $\mathbf{E_R} = \sum_{j=1}^{6} \mathbf{E_j} = \sum_{j=1}^{6} \hat{r} e^{i(\mathbf{k_j}\cdot\mathbf{r}+2j\pi/6)}$. The resultant six-beam interference intensity distribution is shown in Fig. 1(a) and S_{12} Stokes intensity is shown as inset.

Normalized Stokes parameters (S_1,S_2,S_3) are widely used to describe the states of polarization in an optical field [4]. Complex Stokes field $S_{12} = S_1 + iS_2$ can be used to identify polarization singularities. In the S_{12} phase distribution, the polarization singularities appear as phase vortices of different topological charges. The resultant polarization distribution for the interference of six phase engineered radially polarized vector beams is shown in Fig. 1(b) and the corresponding S_{12} Stokes phase distribution is shown as inset. The polarization distribution is embedded with both integral and half integral C-points. In the S_{12} Stokes phase distribution the integral C-points appear as phase vortices of charge $(+2)$, whereas the half integral C-points appear as phase vortices of charge (-1) respectively. In the polarization distribution the left and right handed regions are depicted by red and blue colors respectively. Interestingly both integral and half integral C-points are of same handedness. The index inversed polarization distribution of Fig. 1(b) is shown in Fig. 1(c) [5].

In conclusion we present two novel polarization singularity lattice structures, in six-beam interference, based on phase and polarization engineering methods. Lattices populated with both integral and half integral index C-points are demonstrated. The effect of half waveplate on polarization distribution is also analyzed. The salient features of these lattice structures are discussed.

References

1. I. Freund, M. S. Soskin, and A. I. Mokhun, "Elliptic critical points in paraxial optical fields," Opt. Commun. **208**, 223–253 (2002).
2. I. Freund, "Polarization singularity indices in Gaussian laser beams," Opt. Commun. **201**, 251–270 (2002).
3. R. W. Schoonover, and T. D. Visser, "Creating polarization singularities with N-pinhole interferometer," Phys. Rev. A **79**, 043809 (2009).
4. D. Goldstein, *Polarized Light* (CRC Press, Florida, USA 2011).
5. S. K. Pal, Ruchi and P. Senthilkumaran, "Polarization singularity index sign inversion by a half-wave plate," Appl. Opt. **56**, 6181–6190 (2017).

OSI-ISO 2018 manuscript No.
(8)

Dynamics of nonequilibrium two mode Dicke model

Aranya B Bhattacherjee · Deepti Sharma

Abstract We investigate the collective dynamics and dynamical phases of the two-mode non-equilibrium Dicke model. The collective interaction of the ensemble of atoms with all the modes is the determining factor for the superradiant phase transition. The critical condition to observe the superradiant phase transition is derived and it is found that tuning one of the mode influences the dynamics associated with the other mode.

Keywords Superradiant phase transition · two-mode Dicke model · Dynamical phase diagram

PACS 37.30.+i · 42.50.-p · 42.50.Pq

1 Introduction

The collective and coherent effects of many atoms interacting with a radiation field is described by the Dicke model [1,2,3]. The collective and cooperative interaction between light and matter is realized only when the spatial dimensions of the ensemble of atoms are smaller than the wavelength of the radiation field. The Dicke model undergoes a second-order quantum phase transition as the coupling between the atoms and the radiation mode reaches a specific critical value.In this work, we investigate the non-equilibrium dynamics of the two-mode Dicke model.

Aranya B Bhattacherjee
Department of Physics, BITS Pilani, Hyderabad Campus, India
E-mail: aranyabhuti@hyderabad.bits-pilani.in

Deepti Sharma
School of Physical Sciences, Jawaharlal Nehru University, New Delhi-110067, India

2 Multimode equilibrium Dicke model

We consider a system composed of N identical two level atoms confined in an optical cavity interacting with a certain finite number of cavity modes. All atoms have the same transition frequency Ω. The atoms are coupled to the j^{th} cavity mode via a dipole interaction with a coupling constant λ_j. In terms of the collective spin operators, the effective Hamiltonian is written as

$$H = \sum_j \omega_j a_j^\dagger a_j + \Omega J_z + \frac{(J_+ + J_-)}{\sqrt{N}} \sum_j \lambda_j (a_j^\dagger + a_j). \tag{1}$$

Here ω_j is the frequency of the j^{th} mode and $a^\dagger(a_j)$ is the creation (annihilation) operator of the j^{th} cavity mode.

3 Mean field analysis of the critical condition for superradiant phase transition and the dynamics

The energy function $E(\alpha_j, \theta)$ in terms of the coherent photon states $\alpha_j e^{i\phi_j}$, coherent spin 1/2 state $|z, \theta\rangle$, fractional population difference z and mean photon number α_j^2 in the j^{th} mode is derived as

$$E(\alpha_j, \theta) = \sum_j \omega_j \alpha_j^2 + \frac{\Omega N \cos\theta}{2} + \sqrt{N} \sin 2\theta \sum_j \lambda_j \alpha_j \cos\phi_j. \tag{2}$$

Minimizing $E(\alpha_j, \theta)$ with respect to α_j and θ, we get the critical condition to observe the multimode Dicke superradiance

$$\sum_j \frac{\lambda_j^2 \cos^2\phi_j}{\omega_j} = \frac{\Omega}{4}. \tag{3}$$

For a single mode, Eqn. (3) reproduces the critical coupling constant $\lambda_c = \sqrt{\omega\Omega}/2$ [4].

This indicates that the collective interaction of the ensemble of atoms with all the modes is the determining factor for the superradiant phase transition instead of interaction with each individual mode. In the mean field approximation for two modes, we numerically solve the equations of motion for the variables $n_j = \alpha_j^2$, ϕ_j, θ and z. The results are shown in Fig.1 which illustrates the time evolution of the photon numbers $n_1(t)$ and $n_2(t)$. Fig.1a shows superradiance in both the modes which satisfies the inequality $\sum_{j=1,2} \frac{\lambda_j^2 \cos^2\phi_j}{\omega_j} > \frac{\Omega}{4}$ while Fig.1b shows absence of superradiance, since it satisfies the inequality $\sum_{j=1,2} \frac{\lambda_j^2 \cos^2\phi_j}{\omega_j} < \frac{\Omega}{4}$.

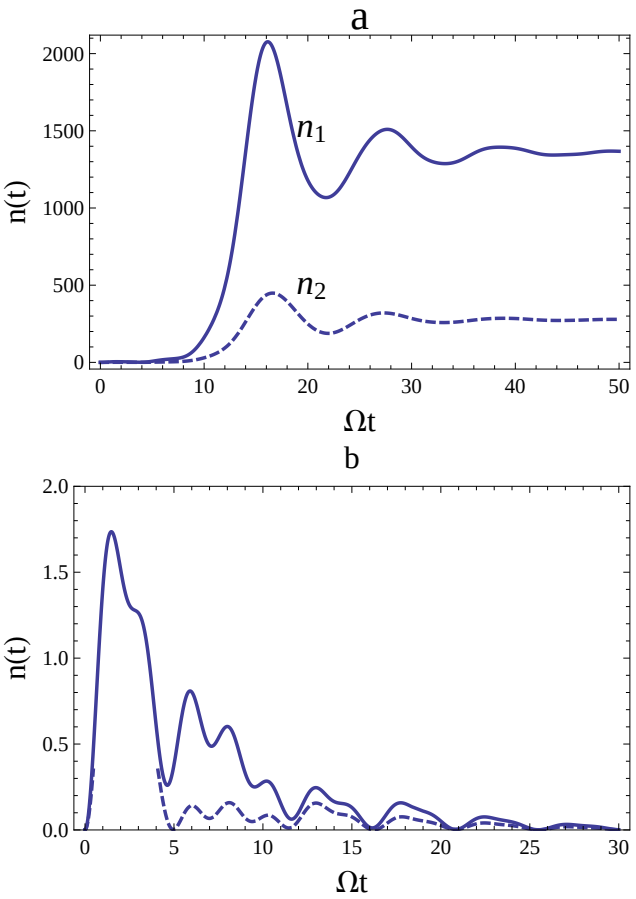

Fig. 1 Time evolution of the photon numbers n_1 and n_2 for $\omega_1 = \Omega$, $\omega_2 = 0.8\Omega$, $\kappa_1 = \kappa_2 = 0.35\Omega$. For plots $1a$, $\lambda_1 = 0.55\Omega$, $\lambda_2 = 0.2\Omega$. For plots $1b$, $\lambda_1 = 0.36\Omega$ and $\lambda_2 = 0.32\Omega$.

4 Dynamical phase diagram and time evolution

The critical condition for superradiant phase transition for two modes taking into account the decay of the cavity modes is

$$\frac{\lambda_1^2\omega_1}{\kappa_1^2+\omega_1^2} + \frac{\lambda_2^2\omega_2}{\kappa_2^2+\omega_2^2} = \frac{\Omega}{4}. \tag{4}$$

Here κ_1 and κ_2 are the decay rates of the two modes.

We consider the instability of the initial state $a_j = 0$ and $J_z = -N/2$ by rewriting the operators $a - j$, J_+, J_- as a sum of mean field part and a small fluctuation [5]. Analysis reveals that the initial state becomes unstable exactly when the critical condition for the Dicke superradiance is satisfied. The dynamical phase diagram thus obtained is depicted in the contour plot of Fig.2. The time evolution of $J_z(t)$ at the points J_1,J_2,J_3 and J_4 marked in

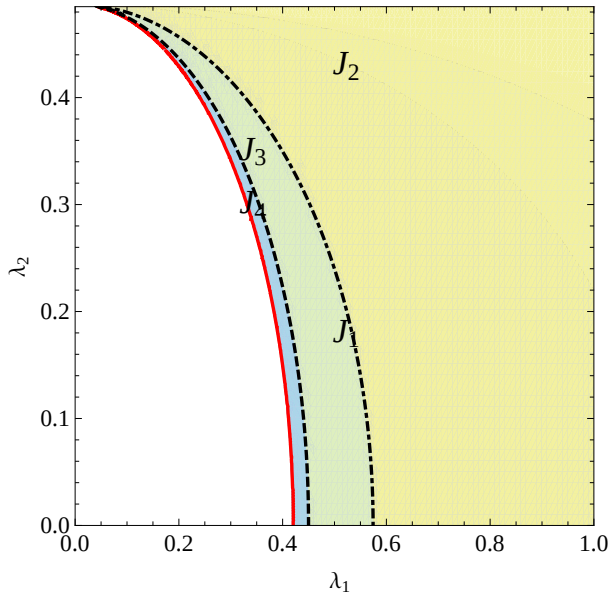

Fig. 2 Dynamical phase diagram for $\omega_2 = 0.8\Omega$, $\kappa_1 = \kappa_2 = 0.35\Omega$, $N = 10^4$.The white region is the stable non-superradiant region. The red solid line is the boundary separating the stable region from the unstable region for $\omega_1 = 0.3\Omega$. The dashed boundary line is $\omega_1 = 0.2\Omega$ and the dashed-dotted boundary line is for $\omega_1 = 0.1\Omega$.

the phase diagram are shown in Fig.3. The fluctuations destabilize the initial state and a complex time evolution takes place. At the points J_1, J_2 and J_3, the system stays in its initial state for a certain duration before it goes into the superradiant state and reaches its stable attractor. On the other hand, the initial state at the point J_4 remain stuck since the critical condition is not satisfied for superradiant phase transition.

5 Conclusions

In this work, we have explored the collective dynamics of an ensemble of atoms interacting with two modes in an optical cavity. The collective interaction of the ensemble of atoms with all the modes is the determining factor for the superradiant phase transition instead of interaction with each individual mode. The collective effect is also evident from the fact that presence of a second mode influences the dynamics of the first mode.

6 acknowledgments

A. Bhattacherjee acknowledges support from BITS Pilani, Hyderabad Campus. D. Sharma acknowledges financial support from the Jawaharlal Nehru University under the university scholarship scheme.

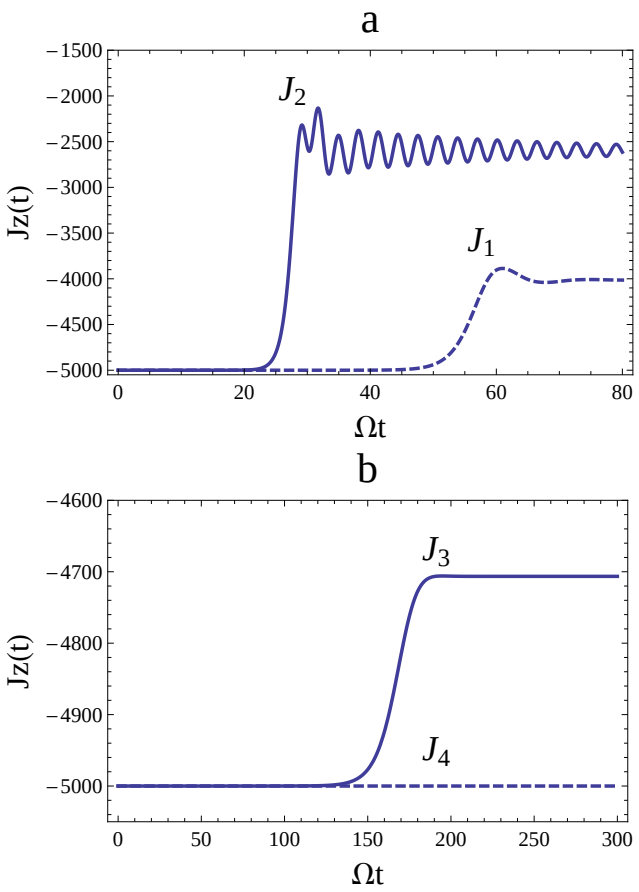

Fig. 3 Time evolution in the superradiant regime (J_1,J_2 and J_3) and the stable regime (J_4) with initial conditions $a_1 = a_2 = 0$ and $J_z = -N/2$.

References

1. R. H. Dicke, "Coherence in spontaneous radiation processes," Phys. Rev. **93**, 99-110 (1954).
2. B. M. Garraway, "The Dicke model in quantum optics: Dicke model revisited," Phil. Trans. R. Soc. A **369**, 1137-1155 (2016).
3. A. B. Bhattacherjee, "Non-equilibrium dynamical phases of the two-atom Dicke model," Phys. Letts. A **378**, 3244-3247 (2014).
4. C. Emary and T. Brandes, "Chaos and quantum phase transition in the Dicke model," Phys. Rev. E **67**, 066203 (2003).
5. M. J. Bhaseen, J. Mayoh, B. D. Simons and J. Keeling, "Dynamics of nonequilibrium Dicke models," Phys. Rev. A **85**, 013817 (2012).

A comparative study of LMR/SPR based tapered fiber optic sensors: A mathematical modelling

Vikas, R. K. Verma

Department of Physics, Central University of Rajasthan

NH-8 Bandarsindri, Ajmer-30581 Rajasthan (India)

Corresponding author's e mail: rkverma@curaj.ac.in

Abstract:

In present study, theoretical evaluation of Lossy mode resonance (LMR) based tapered fiber optic sensor have been carried out. Indium tin oxide (ITO) is used as a LMR active material and deposited over unclad portion of tapered fiber core. We have analyzed the effect of five different taper profiles viz. exponential-linear, linear, parabolic, Gaussian and quadratic on the sensitivity of the tapered fiber optic sensor. It was observed that among five different taper profiles exponential-linear profile has maximum sensitivity and quadratic profile has the least value. Also, it is found that the sensitivity increases with increasing the taper ratio. To compare LMR and surface plasmon resonance (SPR) based tapered fiber optic sensors, platinum and copper are used as SPR active materials.

Keywords: Lossy mode resonance, Surface plasmons and Indium Tin Oxide (ITO)

Theory: In recent few years, conducting metal oxides are being used as a substitute of conventionally used metals for making sensing probes. These metal oxides are capable of exciting several lossy modes. The resonant excitation of lossy modes is also extremely sensitive towards change in surrounding refractive index. Apart from that a large number of modifications have been proposed in the structure of the optical fiber for its better performance. Tapering of the optical fiber is one of the famous techniques used for sensitivity enhancement. In our present study, we have used principle of attenuated total reflection (ATR) on Kretschmann configuration[1] on a step index multimode fiber with tapered core. The schematic diagram of the tapered fiber optic probe on a PCS (plastic cladded silica) fiber is shown in figure 1. We have conceptualized the deposition of thin layers of ITO/Pt/Cu on unclad portion of tapered fiber core. Wavelength interrogation scheme has been used. The dispersion relations can be calculated using Drude model as given in reference[2][3]. Transmitted power is calculated using N-layer Matrix method as calculated in reference[4]. Sensitivity is defined as the change in resonance wavelength per unit change in Refractive index of the sensing medium[4]

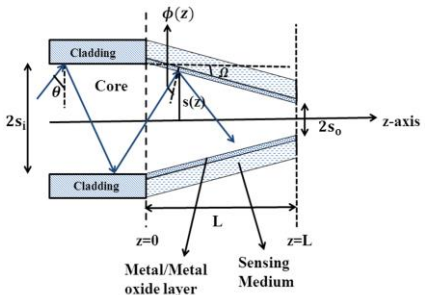

Fig. 1 Schematic diagram of a typical tapered fiber optic probe

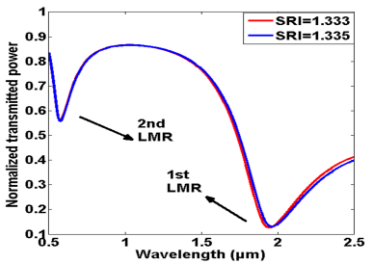

Fig. 2: Transmission spectra for ITO coated tapered fiber optic sensors at taper ratio 1.0

Results and Discussion:

For LMR to occur, we have used ITO of film thickness 90nm. Similarly, for excitation of surface plasmons the thickness used is 90nm for platinum and 35nm for copper. The metal oxide/metal coated fiber optic probe is kept in direct contact with surrounding medium of refractive indices varied from 1.333 to 1.335. Fig. 2 shows the transmission spectra for ITO coated tapered fiber optic sensors at taper ratio 1.0 for two different refractive index of surrounding medium (SRI) i.e. 1.333 and 1.335. It shows that there is red shift in resonance wavelength if we increase the SRI. From Fig. 3 and Fig. 4 it is clear that, using ITO, for exp-linear profile sensitivity corresponding to first lossy mode is 8.53μm/RIU and for platinum and copper it is 4.875μm/RIU and 2.41μm/RIU respectively at taper ratio 1.0 i.e. without tapering. We have also analyzed the effect of taper ratio on performance of the sensor. The taper ratio is increased in steps of 0.1. It is observed that, for ITO maximum sensitivity is 12.005μm/RIU at taper ratio 1.7 and for platinum and copper it is 6.39μm/RIU and 3.665μm/RIU respectively at taper ratio 2.0. This is due to reason that with increasing the taper ratio the angle of incidence in the transition taper region approaches the critical angle leading to a larger value of penetration depth of the evanescent wave and hence stronger coupling between evanescent wave and lossy modes results in higher value of sensitivity. The sensitivity also varies with variation in taper profile. It was observed that among all five profiles, exponential-linear taper profile has the maximum value of the sensitivity. Thus, LMR based tapered fiber optic sensors using ITO gives 2.5 fold enhancement of sensitivity than conventionally used SPR based tapered fiber optic sensors.

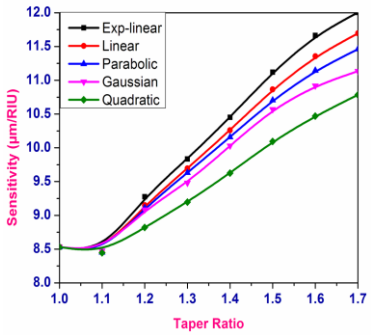

Fig. 3 Variation of sensitivity with taper ratio for different taper profiles for ITO

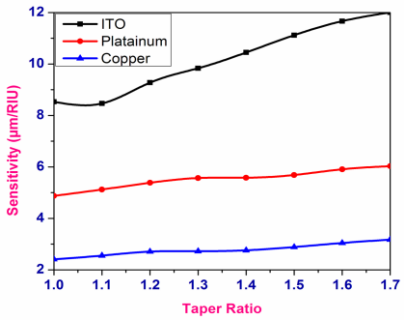

Fig. 4 Sensitivity comparison of a LMR and SPR based tapered fiber optic probe for exp-linear profile

Acknowledgements: One of the author Mr Vikas yadav is thankful to Department of Science and Technology (DST) for INSPIRE fellowship

References:

1. E. Kretschmann and H. Raether, Z. Naturforsch. **23**, 2135 (1968).
2. K. Shah, N. K. Sharma, and V. Sajal, Optik. **135**, 50 (2017).
3. A. K. Sharma and B. D. Gupta, Journal of Applied Physics. **101**, 093111(2007).
4. R. K. Verma, A. K. Sharma, and B. D. Gupta, Opt. Commun. **281**, 1486 (2008).

OSI-ISO 2018 manuscript No.
(10)

Low-threshold, stable lasing in gold-coated nanoporous anodic alumina membranes

Anjani Kumar Tiwari[1,†] · **Saleem Shaik**[2] · **S. Anantha Ramakrishna**[1]

Abstract We report optically pumped waveguide lasing in 1.8 μm thick nanoporous anodic alumina membrane. The nanoporous structure is fabricated using double anodization of aluminum sheet. Rhodamine dye dissolved in methanol is infiltrated in the membrane which automatically fills the nanopores and maintains a continuous flow of dye by wetting effect. The reflectivity of the membrane is improved by depositing a thin gold layer on its top surface. The reflection spectrum of the membrane consists of a series of Fabry-Perot resonances which is shifted by varying its thickness. While doing so, the pump laser wavelength is matched with one of the peak and valley of the Fabry-Perot resonances. Whenever the pump wavelength matches with one of the reflection minima of the membrane, the coupling of the pump light maximizes leading to a higher optical gain in the system. In this case, we observed a low threshold, stable and intense lasing from the nanoporous anodic alumina membrane.

Keywords Nanoporous anodic alumina · Fabry-Perot resonance · Waveguide lasing · Random lasing

An optical cavity containing an amplifying medium with sufficient gain can produce coherent emission. Of late, there has been a keen interest in extracting laser-like emission from various kinds of microstructures such as planar microcavities, nanowires, photonic microcavities, waveguides, dye-doped aerosols, and even randomly distributed scatterers [1–3]. Higher Q-factor cavities with smaller gain volume can significantly improve the performance of these devices by offering low threshold lasing. However, a tiny cavity will have a modest gain volume, which yields a lower output emission. To some extent, the performance of an amplifying microcavity can further be improved by the efficient coupling of the pump light. Herein, we report the consequence of the effective coupling of the incident laser in dye loaded nanoporous anodic alumina (NAA) membrane [4]. A highly transparent NAA membrane is prepared by anodizing a 200 μm thick aluminum sheet at 40 V in 0.3 M oxalic acid at a temperature of 3^o C. The thickness of the membrane, pore diameters, and pore lengths are controlled by varying the anodization

1. Department of Physics, Indian Institute of Technology Kanpur, Kanpur 208016, India
†E-mail: tiwari.tifr@gmail.com
2. Department of Materials Science and Engineering, Indian Institute of Technology Kanpur, Kanpur 208016, India

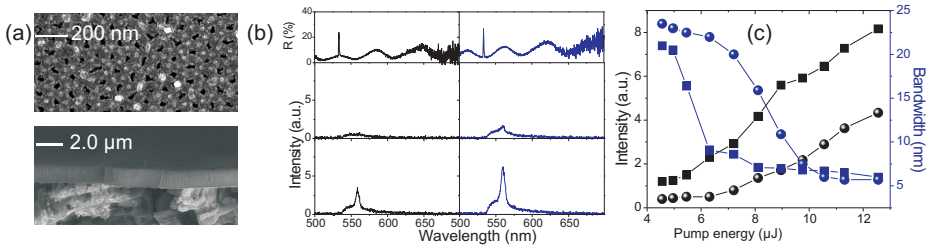

Fig. 1 (a) FESEM image of the NAA membrane, top panel: surface view, bottom panel: cross-section view. (b) Top panel: reflection spectrum, the pump laser wavelength is matched with the reflection maximum (black curve) and minimum (blue curve). Corresponding emission spectrum at $E_p = 5.5$ μJ (middle panel) and at $E_p = 10.6$ μJ (bottom panel). (c) Plot of pump energy versus the output intensity and bandwidth when the reflection maximum (circle) and minimum (square) is matched with the pump laser.

parameters. Post-fabrication, a thin layer of gold (20 nm) is deposited on its top surface to provide the better confinement for light residing inside the membrane.

The top panel in Fig. 1(a) shows the field emission scanning electron microscope (FESEM) images of the NAA membrane. The nanopores are arranged in a hexagonal fashion, and the average diameter and interpore spacing are about 40 nm and 100 nm respectively. The open ends of nanopores in the gold-coated membrane is still visible which allows loading of laser dye and ensures its continuous flow on the NAA surface. The Rhodamine dye is excited using an Nd:YAG laser ($\lambda = 532.8$ nm, rep rate = 10 Hz, and pulse width = 700 ps). The coupling of the pump laser is varied by changing the thickness of the membrane. The top panel in Fig. 1(b) shows the reflection spectrum of the membrane infiltrated with dye dissolve methanol solution. The black curve corresponds to the reflection curve when the peak of the Fabry-Perot profile matches with the pump laser while the blue curve represents the case when the minimum of the reflection profile matches with the pump laser. In the former case, the coupling of the pump light is lesser since the reflection is maximum near 532.8 nm. Consequently, it leads to a lower gain in the membrane, while we have a larger gain in the latter case. The middle panel and the bottom panel show the consequent emission at $E_p = 5.5$ μJ and $E_p = 10.6$ μJ respectively. The emission is more prominent when the pump wavelength matches with one of the reflection minima. Fig. 1(c) shows the variation of output intensity and its bandwidth as a function of excitation energy. The circles present the case discussed in the left panel of Fig. 1(b). A clear lasing threshold is evident at $E_p = 8.3$ μJ, above which the output intensity shows rapid growth, and the bandwidth collapses. The square symbol depicts the case discussed in the right panel of Fig. 1(b), herein lasing starts at $E_p = 6.0$ μJ. Overall, the lasing threshold decreases by 30 % in the latter case.

Acknowledgements We acknowledge DST, India through project No. DST/PHY/20130147. AK Tiwari also thanks DST for the INSPIRE Faculty Award (DST/INSPIRE/04/2016/002068).

References

1. K. J. Vahala, Optical microcavities, Nature (London) 424, 839-846 (2003).
2. J. J. Zayhowski, Microchip lasers, Optical materials 11, 255-267 (1999).
3. A. K. Tiwari, S. Mujumdar, Random lasing over gap states from a quasi-one-dimensional amplifying periodic-on-average random superlattice, Phys. Rev. Lett. 111, 233903 (2013).
4. A. K. Tiwari, S. Shaik, S. A. Ramakrishna, Lasing in dye-infiltrated nanoporous anodic alumina membranes, Appl. Phys. B 124-127 (2018).

Planar photonic crystal as a polarizer for the out-of-plane incidence of light

Pratyasha Sahani[1] **· R. Vijaya**[2]

Abstract A planar photonic crystal is modeled to demonstrate the polarizing properties of light incident from a plane outside the plane of its periodicity. The analysis is done for a square lattice configuration in a symmetric as well as in an asymmetric background. The structure can be used to polarize the radiating modes within certain incident frequency intervals. The resonant coupling of the radiating modes with the incoming modes at different out-of-plane incident angles which ultimately comprises the polarized output modes is studied. The structural engineering helps to operate it as a polarizer for wide incident frequency intervals as well as for wide angle incidence of light near the wavelength of 1550nm, which is relevant for optical communications. We also discuss if the polarizer operates in reflection or transmission or in both configurations.
Keywords (050.5298) Planar photonic crystal; (240.5440) Polarizer; (260.1180) Out-of-plane incidence

[1] Introduction

The planar photonic crystal (also known as the two-dimensional (2D) photonic crystal slab (PCS) of finite thickness) has a periodic variation of refractive index in the plane of the slab and a homogeneous refractive index along the direction orthogonal to the slab [1]. Several groups have discussed the *in-plane* control of the polarization of light in a 2D PCS of finite thickness [2, 3], but there is no report for an *out-of-plane* incidence of light. This work is based on the latter possibility which is explained by using the property of the light line and Fano resonances. Being able to polarize light incident from outside the plane with specialized transmission / reflection characteristics will enable its usage as a micro-optical component in miniaturized optical set-ups.

[2] Modeled structure and computational result

The simulation is performed with BandSOLVE module of RSoft^{TM} based on the plane-wave expansion method and the band diagram is computed using the 'supercell technique' [4]. The structure has an optimal thickness d of $(0.400 \pm 0.007)a$ and an optimal r/a of 0.300, where r is the radius of air holes and a is the lattice constant. For our work, we have chosen a supercell dimension of 4*period, spatial resolution in steps of 16 and a spectral resolution of 10^{-10}.

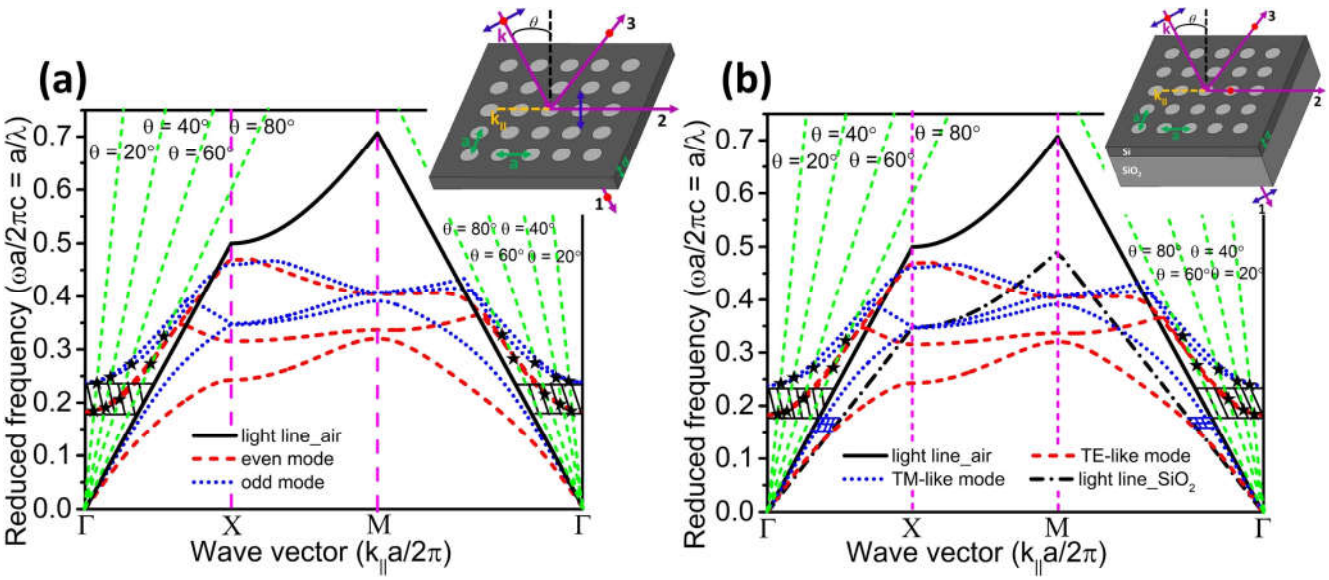

Fig. 1 Projected band diagram of the lowest three bands of both TE-like (even) and TM-like (odd) modes of light in a 2D PCS with a square array of air holes embedded in the PCS placed in (a) a symmetric, and (b) an asymmetric background. The figures also show the coupling between the leaky slab modes of band 2 with the incoming modes at a few angles θ. The insets in (a) and (b) show the schematic of the operation when the light is incident from outside the plane in a symmetric and an asymmetric PCS respectively.

Pratyasha Sahani[1] and R. Vijaya[1,2]

[1]Department of Physics, Indian Institute of Technology Kanpur, Kanpur 208016, India
[2]Centre for Lasers and Photonics, Indian Institute of Technology Kanpur, Kanpur 208016, India

E-mail: *pratyasa@iitk.ac.in*, *rvijaya@iitk.ac.in*

In Fig. 1(a), we use ray 1 and ray 3 respectively for the out-of-plane transmitted and reflected light and ray 2 for the in-plane transmitted light. The same for a PCS sandwiched between air (superstrate), and SiO_2 (substrate) is shown in Fig. 1(b). The frequency intervals shown by the hatched regions are summarized in Table 1 and represent the reduced frequencies which will get polarized and emerge in reflection or transmission directions for light incident from outside the plane of the PCS. Guided modes can be polarized too and are not discussed here. A similar analysis can be applied to other 2D lattice configurations such as triangular lattice and honeycomb lattice.

Table 1 Detailed frequency intervals as shown by the hatched regions in Fig. 1 for which the symmetric as well as the asymmetric PCS can behave as a polarizer for the radiating modes. Along the XM-direction of the square lattice, there are no radiating modes.

Nature of the PCS	High symmetry direction	Selected frequency interval	Description of the polarizing mode
Symmetric PCS shown in Fig. 1(a)	ΓX	$0.182 \le \omega a/2\pi c \le 0.237$	Radiating, even (TE-like), *reflection and transmission*
	MΓ	$0.182 \le \omega a/2\pi c \le 0.237$	Radiating, even (TE-like), *reflection and transmission*
Asymmetric PCS shown in Fig. 1(b)	ΓX	$0.182 \le \omega a/2\pi c \le 0.238$	Radiating from air-Si and Si-SiO_2 interfaces, even (TE-like), *reflection and transmission*
		$0.137 \le \omega a/2\pi c \le 0.182$	Radiating from Si-SiO_2 interface, odd (TM-like), *transmission*
	MΓ	$0.182 \le \omega a/2\pi c \le 0.238$	Radiating from air-Si and Si-SiO_2 interfaces, even (TE-like), *reflection and transmission*
		$0.140 \le \omega a/2\pi c \le 0.182$	Radiating from Si-SiO_2 interface, odd (TM-like), *transmission*

For an out-of-plane incidence, subject to a proper $k_{||}$ matching between the leaky slab modes and the incoming modes represented by different θ, there can be resonant coupling between them indicated by the black stars in Fig. 1 and the leaky slab modes will excite. These correspond to *Fano resonances* [5, 6] which will only increase the light intensity and will not affect the above polarization results.

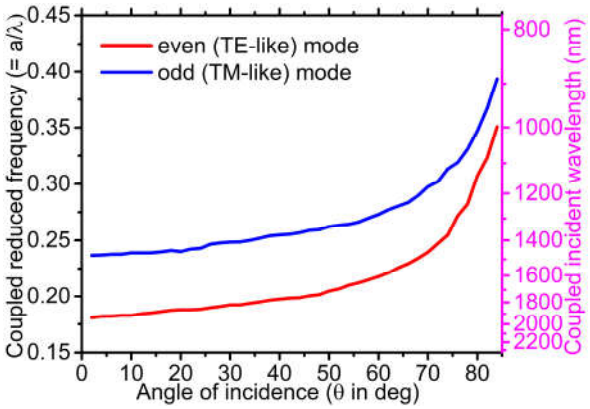

Fig. 2 Coupled reduced frequencies (left y-axis) and the coupled incident wavelengths for a = 350nm (right y-axis) of both even and odd modes at various angles of incidence when the out-of-plane incident light has an in-plane component along ΓX-direction of the square lattice in a symmetric PCS.

The variation of the coupling frequencies and wavelengths with different angles of incidence is shown in Fig. 2. Fig. 2 shows the variation of selected reduced frequencies and incident wavelengths which are resonantly coupled to incident modes at different angles of incidence when $k_{||}$ is along ΓX-direction of the square lattice and are additionally included in polarized modes. For a = 350nm the relevant wavelength range will be near 1500nm. The flatness of the curve indicates wide angle operation for the odd polarized modes. This is also true when $k_{||}$ is along MΓ-direction because for the square lattice |ΓX| = |MΓ|. The whole discussion is applicable to an asymmetric PCS as well.

[3] Conclusion

In conclusion, we have presented a 2D PCS which can polarize the radiating modes of light and we have identified the relevant frequency ranges for polarized light only in transmission and in both reflection and transmission. The structural engineering ensures that the PCS can be used as a polarizer for odd modes for a wide angle of incidence at 1550nm if the lattice constant is 350 nm.

Acknowledgments The authors acknowledge the funding from Science and Engineering Research Board, India (sanction number: EMR/2015/001450).

[4] References

[1] L. Prodan , R. Hagen, P. Gross, R. Arts, R. Beigang, C. Fallnich, A. Schirmachcher, L. Kuipers, and K. J. Boller, "Mid-IR transmission of a large-area 2D silicon photonic crystal slab", J. Phys. D: Appl. Phys., 41, 135105 (2008)

[2] R. K. Sinha, and Y. Kalra, "Design of optical waveguide polarizer using photonic band gap", Opt. Express, 14, 10790-94 (2006)

[3] M. Zhang, R. Malureanu, A. C. Kruger, and M. Kristensen, "1x3 beam splitter for TE polarization based on self-imaging phenomena in photonic crystal waveguides", Opt. Express, 18, 14944-9 (2010)

[4] Shi S, Chen C, and Prather W, "Plane-wave expansion method for calculating band structure of photonic crystal slabs with perfectly matched layers", J. Opt. Soc. Am. A, 21, 1769-75 (2004)

[5] K. V. Ummer, and R. Vijaya, "Spectral characterization of silicon photonic crystal slab using out-of-plane light coupling arrangement", Appl. Phys. B, 124, 136 (2018)

[6] M. F. Limonov, M. V. Rybin, A. N. Poddubny, and S. Kivshar, "Fano resonances in photonics", Nature Photonics, 11, 543-54 (2017)

Measurement of optical rotation due to chiral sample using inhomogeneously-polarized light beam

Rashmi Ranjan Suna, C.T. Samlan and Nirmal K. Viswanathan*
School of Physics, University of Hyderabad, Hyderabad 500046, India
*Corresponding author: nirmalsp@uohyd.ac.in

Abstract

We have experimentally demonstrated a novel method of using inhomogeneously polarized light beam generated using a birefringent wedge pair to measure optical rotation due to quartz rotator. The underlying mechanism of non-separability between the state-of-polarization and spatial-mode degrees of freedom of the optical beam results in spatially periodic variation in polarization ellipse orientation. This translates into fringe shift when a polarizer placed in the output beam path is rotated. The quartz rotator sample kept before the fixed analyser influences this fringe shift which provides an accurate information regarding the optical rotation angle and hence its chirality.

Key Words: Birefringent wedge pair, Optical rotation, Polarization ellipse, Fringe shift

Introduction

One of the ways to characterize chiral molecules, an important constituent of life on earth, is to measure the optical rotation (OR) angle [1], the rotation of plane of polarization of light passing through it. The polarimetry method, consisting of polarizer-analyzer combination sandwiching the chiral medium, is typically used to measure the OR due to chiral medium [1]. However, the measurement sensitivity limitation of the polarimetry method and the requirement for large volume of chiral material has motivated researchers in recent times to search for alternate measurement techniques.

Probing optical chirality to measure OR angle using inhomogeneously polarized light beam [2] has recently been demonstrated to be advantageous over probing with homogeneously polarized light beam [3,4]. Here we generate inhomogeneously polarized light beam having a spatial periodicity in the polarization ellipse orientation [5] using a combination of birefringent wedge pair (BWP) [6] and a λ/4-plate at suitable orientation. The BWP is made of two wedge-shaped birefringent plates with their fast-axis oriented at 90° to one another. To detect the spatial periodicity in the state-of-polarization (SoP) in the beam cross-section, we place a linear polarizer after the beam exits the BWP. The intensity variation is banded, mimicking interference fringe, but is polarization encoded. When a chiral sample is introduced in the beam path in-between the BWP and oriented analyzer, the shift in the fringes is measured to calculate the optical rotation. A Fourier fringe analysis method is used on the measured fringe pattern to extract accurately the OR angle. Large number of fringes in the field-of-view offers additional advantage to average over them to improve the measurement accuracy.

Experimental details and Results

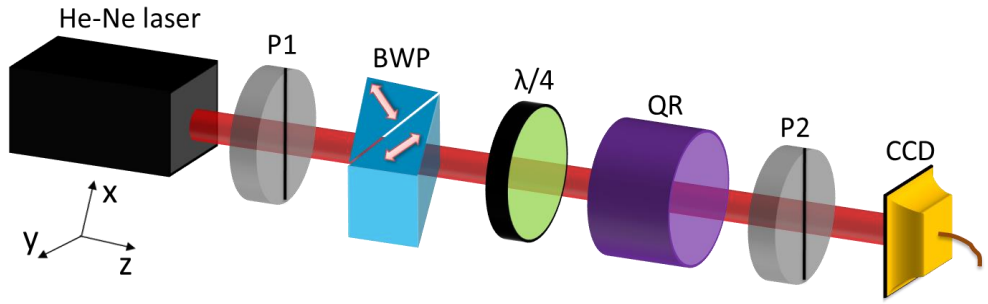

Fig.1. Schematic of the experimental setup. P1, P2: Glan-Thompson polarizer; BWP: Birefringent wedge pair; λ/4: Quarter wave plate; QR: Quartz rotator; CCD: Camera.

Schematic of the experimental setup is shown in Fig. 1. The Gaussian beam from He-Ne laser (λ=632.8 nm) passes through a Glan-Thompson polarizer P1 to produce vertically polarized light. The uniformly polarized beam passes through the BWP resulting in the output beam that is inhomogeneously polarized with spatial periodicity in ellipticity

[5]. The spatially varying ellipticity in the beam cross-section is converted to spatially varying ellipse orientation [5] by passing the beam through oriented quarter wave plate(QWP). Stokes polarimetry measurements on the output beam are carried out to verify the variations in the SoP in the beam cross-section, to make it suitable for OR measurement. An analyzer placed after the QWP converts the variation in the SoP to intensity interference fringes shown in Fig. 2 (a). Further, when the analyser is rotated the fringes move in linear direction, indicating a field gradient in the beam cross-section, an essential requirement for its use to measure OR angle. Now, keeping the analyser orientation fixed, we introduce quartz rotator in the beam path and the interference fringes are recorded using the CCD camera. Interference fringes recorded for three different quartz rotators with different OR angles are shown in Fig. 2 (b) – (d). From the recorded intensity images, we extract phase change at a fixed position (indicated by red colour box) using Fourier fringe analysis. The phase difference at a fixed position in the fringe cross-section without and with the QRs gives the required information of the OR angle. The values obtained are tabulated below and are found to agree well with the given values.

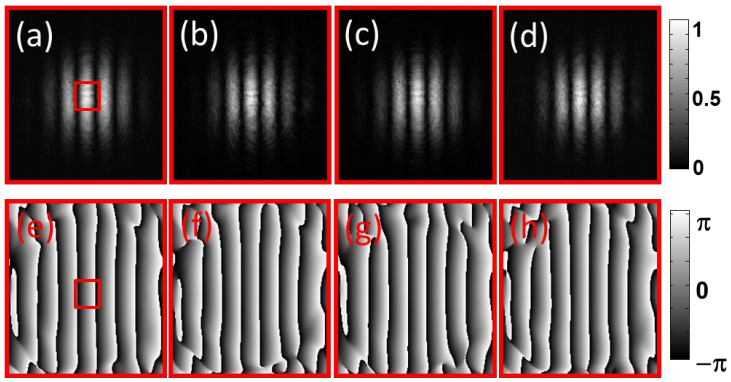

Table1

Quartz rotator	OR-angle (Specified)	OR-angle (Measured)
1	$9.789^0 \pm 0.02^0$	$9.701^0 \pm 0.001^0$
2	$-11.845^0 \pm 0.02^0$	$-11.929^0 \pm 0.001^0$
3	$-2.056^0 \pm 0.02^0$	$-2.107^0 \pm 0.001^0$

Fig.2. Recorded intensity images (a) without QR and (b)-(d) with 3 different QRs; (e)-(h) phase information extracted from the intensity images.

Summary

We have demonstrated a novel way to accurately measure the OR angle of chiral sample like quartz rotator using inhomogeneously polarized beam generated using a BWP as a viable alternate to the polarimetry method. The advantages of the technique include no moving parts, high sensitivity, which can be tuned based on the requirements and large number of fringes, suitable for averaging to improve measurement accuracy.

Acknowledgements
The authors acknowledge Science and Engineering Research Board (SERB) for continued financial support for this research and Dr. Kumar, Digipol Technologies, USA for quartz rotator samples. RRS acknowledges RGNF-SRF from University Grants Commission (UGC).

Reference list

1. E. Hecht, Optics, 4th ed., Pearson education, Addison Wesley publication (2002).
2. Q. Zhan, "Cylindrical vector beams: from mathematical concepts to applications," Adv. Opt. Photon. 1, 1–57 (2009).
3. C.T. Samlan, R.R. Suna, D.N. Naik and N.K. Viswanathan, "Spin-orbit beams for optical chirality measurement," Appl. Phys. Lett., 112, 031102 (2018).
4. X. Qiu, L. Xie, X. Liu, L. Luo, Z. Zhang and J. Du, "Estimation of optical rotation of chiral molecules with weak measurements," Opt. Lett. 41, 4032(2016).
5. D. Goldstein, Polarized light, CRC press (2016).
6. C.T. Samlan, N.K. Viswanathan, ''Generation of vector beams using a double-wedge depolarizer: Non-quantum entanglement," Optics and Lasers in Engineering, 82, 135–140 (2016).

Experimental realization of a fiber based Michelson interferometer for FBG sensor interrogation

Deepa Srivastava[1], Ishita Bhutani[2], and Bhargab Das[1,*]
[1]Advanced Materials and Sensors Division, CSIR-Central Scientific Instruments Organization (CSIO), Chandigarh-160030, India
[2]Department of Amity School of Applied Sciences, Amity University Rajasthan, India
***Corresponding author: bhargab.das@csio.res.in**

Abstract: We report here the experimental demonstration of a fiber based Michelson interferometer as a promising technique for fiber Bragg grating (FBG) sensor Bragg wavelength shift measurement. Fiber interferometers for FBG sensor interrogation are extremely appropriate for dynamic strain measurement applications in the areas of vibration analysis and acoustics due to their advantages in terms of wide bandwidth, high resolution and tunable sensitivity. Fiber interferometers perform phase sensitive measurement of Bragg wavelength shift which is recorded as intensity variations at the output end. A Michelson interferometer with optical path difference of ~ 4.7 *mm* is thus designed and fabricated using simple fiber optic components consisting of a 2×2 fiber 3dB coupler and two Faraday rotator mirrors. The polarization states of the two reflected light beams are controlled by the two FRMs leading to better interference visibility. Experimental results on the measurement of acoustic signal generated Bragg wavelength modulation is presented as a proof of concept.
Keywords: Fiber optic sensors, Fiber Bragg gratings, Interferometry, Wavelength conversion devices, Interrogation techniques.

1. Introduction

Since its first appearance almost a 30 years ago, optical fiber Bragg grating based (FBG) sensors have become an indispensable tool for high sensitivity measurement of both static and dynamic strain with detection limits ranging from 10^{-9} to 10^{-6} $\varepsilon\, Hz^{-1/2}$, where ε is the fractional length change [1]. Such low level strain measurement is of utmost importance in many research fields encompassing underwater acoustic array detectors, structural health monitoring etc. The widespread popularity of FBG sensors are due to its well-known attributes of electromagnetic immunity, long distance sensing, wavelength selectivity, environmental endurance, reduced size, and multiplexing capability. In its simplest form, an FBG consists of periodic perturbation of optical fiber core refractive index (RI) which acts as a filter reflecting a narrow wavelength range centered about a peak wavelength, known as Bragg wavelength (λ_B), given by, $\lambda_B = 2n_{eff}\,\Lambda$. Here, n_{eff} is the effective refractive index and Λ is the grating period. The principle of sensing using FBG is based on the fact that any external perturbation that has the ability to affect either the refractive index (n_{eff}) and/or grating period (Λ) can be measured using FBG as a sensor. The effect of external perturbation is manifested as a change $\Delta\lambda_B$ of the Bragg wavelength.
The measurement of Bragg wavelength shift has been the subject of substantial research and several methods have been developed *e. g.* Fabry-Perot tunable filter, unbalanced fiber interferometer, edge filter, CCD spectrometer, matched FBGs etc. It has been established previously that interferometric interrogation principle realized with an unbalanced fiber interferometer offers the highest sensitivity measurement among the known techniques [1-5]. This fiber interferometer based wavelength interrogation method has additional advantages of wide-bandwidth, high-resolution, tunable-sensitivity etc. and is more suitable for dynamic measurement of strain as required in the fields of vibration and acoustics. Mach-Zehnder interferometer (MZI) is the most commonly used configuration for this purpose [1-5]. Another well-known two-beam interferometric configuration that is frequently used in bulk optics domain is the Michelson interferometer (MI). In this article, we present experimental results of a designed and fabricated fiber based MI utilized as a FBG sensor interrogation technique. For dynamic strain induced modulation in the FBG sensor Bragg wavelength denoted by $\Delta\lambda_B\, sin\,\omega t$**,** the phase-shift modulation of the fiber interferometer can be represented as:

$$\Delta\phi(t) = -\frac{2\,\pi\ \mathrm{OPD}}{\lambda^{\,2}}\Delta\lambda_B\, sin\,\omega t = -\frac{2\,\pi\ \mathrm{OPD}}{\lambda^{\,2}}\ \gamma\ \Delta\varepsilon\ sin\,\omega t \qquad (1)$$

Where $\Delta\varepsilon$ is the dynamic strain modulation, γ is the strain-to-wavelength shift responsivity, $OPD = n_{eff}d$ is the optical path difference between the two arms and *d* is the physical length imbalance.
The output intensity of the MI can be expressed as:

$$I(\lambda_B) = A[1 + k\cos\Delta\phi(t)] \qquad (2)$$

where, *A* is proportional to the input intensity and system loses and *k* is the interference fringe visibility.

2. Experimental Results and Discussion:

The experimental set up realized for performing MI based FBG sensor interrogation is shown in Fig. 1 (a). The MI is designed using simple fiber optic components cosisting of a 2×2 fiber 3dB coupler and two Faraday rotator mirrors (FRM). The use of FRMs as mirrors also controls the polarization states of the two reflected light beams leading to better interference visibility. It is important to realize that in order to maintain temporal coherence between the interfering light beams travelling through the two arms of MI, the interferometer path difference must

be less than the effective cohrence length of the light signal reflected from the FBG sensor. Fig. 1(b) shows the power spectrum of the fabricated MI as recorded in an optical spectrum analyzer (OSA). Noting the wavelength seperation between two consecutive peaks (~ 0.49 *nm*), the resultant *OPD* of the MI is calculated to be ~ 4.7 *mm*. This is smaller than the effective coherence length of the Bragg reflected light signal (FWHM~0.19 *nm*) as well as matches very well with the theoretical optimum OPD for maximum sensitivity suggested by Weiss *et al.* [5]. The FBG sensor reflected light spectrum is shown is Fig. 1(c). Furthermore, in order to demonstrate the Bragg wavelength modulation measurement with the MI based phase-sensitive detection scheme, the FBG sensor is glued onto a cantileve plate. Light from a broad band source with wavelength range: 1525 to 1565 *nm* is directed to the FBG sensor through an optical circulator and the reflected light signal is then goes to the MI. Sound signal from a generic speaker exicte vibrations in the cantilever plate inducing dynamic strain modulations which in turn results into Bragg wavelegth modulation. The output intensity of the fiber interferometer is then detected with the help of an InGaAs PIN photodiode and an in-house facricated transimpedance amplifier. A data acqusition (DAQ) device is used to record the analog intererence signal for further digital processing and analaysis.

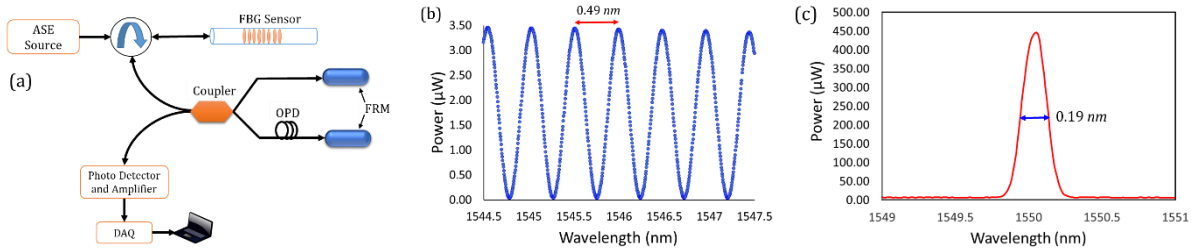

Fig. 1 (a) Schematic diagram of experimental set-up for Michelson interferometer bases FBG sensor interrogation principle. FRM: Faraday rotator mirror; OPD: Optical path difference; ASE: Broadband light source; DAQ: Data acquisition card; **(b)** Power spectrum of the designed and fabricated Michelson interferometer. The OPD is estimated to be ~ 4.7 *mm*. **(c)** Reflection spectrum of FBG sensor; Bragg wavelength ~ 1550 *nm* and FWHM is ~ 0.19 *nm*.

The FBG sensor attached cantilever plate is excited with sound signals of various frequencies ranging from 200 to 1000 Hz. Enhanced response is observed at around the resonant mode frequencies of the cantilever plate arrangement. Fig. 2(a) shows the temporal response recorded by the photodetector for the MI based FBG sensor interrogation system while applying a continuous sinusoidal sound signal of 800 Hz. The red sinusoidal curve shows the fitted data on the experimental time signal. The power spectral density (PSD) of the time signal is shown in Fig. 2(b) wherein the sharp peak is observed at 800 Hz. The peak-to-baseline height is ~ 43 dB. In conclusion, we have experimentally demonstrated the working principle of a fiber based Michelson interferometer for FBG sensor Bragg wavelength shift detection for dynamic strain modulation measurement. The experimental results demonstrate the feasibility of MI based FBG sensor interrogation technique which can also be extended for an FBG sensor array configuration.

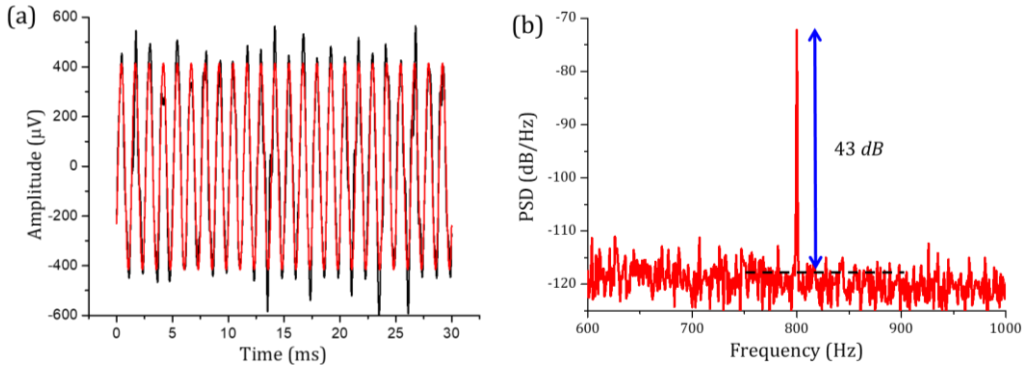

Fig. 2 Fiber MI based FBG sensor interrogation results. **(a)** Temporal response at the interferometer output for sinusoidal sound signal of 800 Hz. The red sinusoidal curve is the fitted data. **(b)** Power spectral density (PSD) of the time signal. Peak-to-baseline height at 800 Hz is ~ 43 dB.

References

[1]. S. Yin, P. B. Ruffin, and F. T. S. Yu (Eds.), *Fiber optic sensors*, 2nd Edition (CRC Press, Taylor and Francis Group, 2008).

[2]. A. D. Kersey, M. A. Davis, H. J. Patrick, M. LeBlanc, K. P. Koo, C. G. Askins, M. A. Putnam, and E. J. Friebele, *J. Lightwave Technol.* 15, 1442 (1997).

[3]. B. Das, A. P. Narayan, and U. Tiwari, *12th International Conference on Fiber Optics and Photonics*, OSA Technical Digest (online) (Optical Society of America 2014), Paper M4A.17.

[4]. B. Das and V. Chandra, *Appl. Opt.* **55,** 8287 (2016).

[5]. D. Srivastava, U. Tiwari, and B. Das, *Opt. Commun.* 410, 88 (2018).

OSI-ISO 2018 manuscript No.
(14)

Evolution of fractional-charge vortex beam in the near-field

Sujai Matta[1], Pramitha Vayalamkuzhi[2], Dinesh N. Naik[3] and Nirmal K. Viswanathan[1*]
[1]School of Physics, University of Hyderabad, Hyderabad 500046, India
[2]Department of Electrical Engineering, IIT Madras, Chennai 600036, India
[3]Department of Physics, IIST, Thiruvananthapuram 695547, India
Corresponding author:*nirmalsp@uohyd.ac.in

Abstract
Controlling and understanding the behavior of fractional charge optical vortices (FC-OV) during free-space propagation is of fundamental importance. The FC-OVs are structurally unstable during propagation and in the far-field most of the anticipated intricate dynamics are lost, mostly due to diffraction-related smoothing of optical fields and measurement limitations. We carry out measurements using a near-field scanning optical microscope (NSOM) to gain information on the propagation dynamics of FC-OV. The evolution of fractional vortices is theoretically investigated using angular spectrum method and theoretical results are found to match well with the experimental measurements.

Keywords: Singular optics, Optical Vortices, Spiral phase plate, Near-field scanning optical Microscope.

Introduction

The study of the wavefront dislocation or optical vortices in light fields initiated by the work of Nye and Berry [1] and its angular momentum aspects due to Allen et al., [2] has enriched tremendously the research areas of singular optics and optical angular momentum. The optical vortices have helical phase structure around the singularity and have zero intensity at the vortex [3]. These beams are generated by illuminating a spiral phase plate (SPP) with a Gaussian beam and are typically described by $exp(il\varphi)$ term where, φ is the azimuthal angle and l its topological charge [4]. In the recent years, work on the fractional charged vortices has gained attention, which is of fundamental interest. Fractional charged vortices exhibit a line discontinuity due to non-integer topological charge. Berry [5] theoretically explained and analyzed the evolution and strength of the fractional charged vortices containing alternate chain of charges having complex phase structure along the discontinuity line. It was subsequently verified experimentally in the far-field by generating the half-integer fractional charge using spatial light modulator (SLM) [6]. Here we measure the evolution of fractional charge vortices in the near-field since these are unstable structures and some intricate dynamics may be lost in the far-field due to measurement related limitations. The intensity distribution is measured by scanning at different Z-planes along the free-space propagation and are recorded within a few micro-meter range using near-field scanning optical microscope (NSOM) [7]. The NSOM measurements enabled us to resolve the alternate chains of the fractional charged vortices with high spatial resolution and are reported here. The spatial evolutions dynamics are modeled using the formalism based on angular spectrum method.

Experiment and Results

To study the near-field evolution of the fractional charge vortex beam, we used a SPP (diameter of 10µm) etched on the core of the optical fiber (SMF-28 with mode-filed diameter of 10.4±0.8µm at 1550nm,) using the ion beam lithography [8]. The device is fabricated to operate at 632.8 nm wavelength to generate a single charge optical vortex beam. However, we used it with Ar^+ laser to realize fractional order vortices. To obtain the high spatial resolution intensity images with in the near-field, we used MultiView 4000 NSOM (M/s Nanonics imaging limited). The device is fixed using a fiber holder at the sample stage of the NSOM and the laser beam is coupled into the fiber to generate a desired fractional charge optical vortex out of the SPP device. The schematic diagram of the experimental setup is shown in Fig.1.

The output beam is scanned at different Z-planes along propagation direction using NSOM probe (tip diameter of 100 nm with a resonance frequency of 36.41 kHz). This probe is mounted on a mechanical strip which can be positioned on the sample using XY piezo drivers and the stepper motor is used to move along Z-axis. The transverse field distribution of the output optical beam (20µm x 20µm) is recorded at different Z-planes with a step size of 1µm up to 7µm in z-axis. The tip is attached to optical fiber which transmits the output optical field to the photomultiplier tube (PMT) detector.

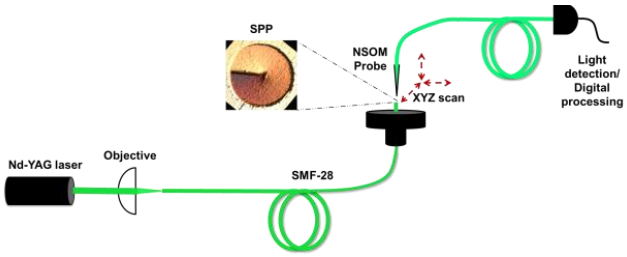

Fig.1. Schematic of the experimental setup.

The Ar^+ laser operated at wavelengths of 532nm, 514nm, and 488nm are coupled in to the fiber with SPP device and the output beam from the device is measured at different Z-planes. With the design wavelength different from the operational wavelength we could realize different fractional charges (l) of 1.189, 1.23, and 1.297 using this arrangement.

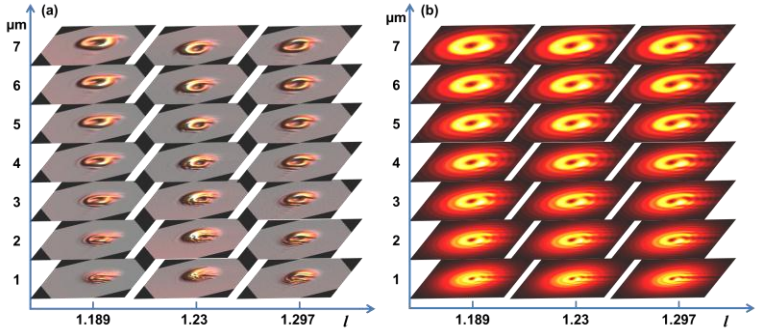

Fig.2. (a) Experimentally recorded, (b) simulated intensity images fractional charge vortices as a function of propagating distance.

The experimentally measured NSOM images are shown in Fig.2. (a). The near-field measurements enabled us to capture fractional charged vortices with high spatial resolution. As the beam propagates, the alternative chains of fractional charges merged with each other, losing the crucial information, as anticipated from far-field measurement. Also, as we increase the fractional value of the beam, the radial line gets darker and the alternate chain of charges moves towards the center of the core. We also simulated the propagation of fractional charged vortices theoretically using angular spectrum method [9] and the results are shown in Fig. 2 (b). The experimental results are found to match with the theoretical results.

Acknowledgements

SM acknowledges University Grants Commission (UGC), India for research fellowship. PV thanks Max Planck Society, Department of Science and Technology (DST) and Indo German Science and Technology Center (IGSTC) for the financial support. The authors acknowledge DST- Fund for Improvement of S & T Infrastructure (FIST) for the purchase of NSOM facility.

Reference list

1. J.F. Nye and M.V. Berry, Proc. R. Soc. Lond. A 336, 165(1974)
2. L. Allen, M.W. Beijersbergen, R.J.C. Spreeuw, and J.P. Woerdman, Phys. Rev. A 45, 8185(1992)
3. N.R. Heckenberg, R. McDuff, C.P. Smith, and A.G. White, Opt. Lett. 17, 221(1992)
4. M.W. Beijersbergen, R.P.C. Coerwinkel, M. Kristensen, J.P. Woerdman., Optics Communications 112, 321(1994)
5. M.V. Berry, J.Opt. A: Pure Appl. Opt. 6, 259 (2004)
6. J. Leach, E. Yao, and M.J. Padgett, New J. Phys. 6, 1(2004)
7. B. Hecht, B. Sick, and U.P. Wild, J. Chem. Phys. 112, 7761(2000)
8. P. Vayalamkuzhi, S. Bhattacharya, U. Eigenthaler, K. Keskinbora, C. T. Samlan, M. Hirscher, J. P. Spatz, and N. K. Viswanathan. Opt. Lett. 41, 2133 (2016)
9. S. Matta, P. Vayalamkuzhi, D.N. Naik and N.K. Viswanathan. J. Opt. 20, 075604 (2018)

OSI-ISO 2018 manuscript No.
(15)

Role of coherence and control of entanglement longevity in a two qubit system

Namitha C V · S V M Satyanarayana

Abstract We investigate the entanglement dynamics of a two identical dipole interacting two qubit system couple to a vacuum field. The entanglement of mixed states suffer finite time death when it undergoes decoherence. In order to understand the role of coherence of the initial state on entanglement dynamics, we constructed two classes of X states; one class with only one photon coherence and the other with only two photon coherence. We investigate the entanglement longevity of both class of X states by defining the time over which the state remains disentangled after Entanglement Sudden Death (ESD) ($\tau_R - \tau_D$) for different interatomic distances. We show that the state with high two photon coherence and high atomic dipole interaction have high entanglement longevity and are better resource for quantum information applications.

Keywords Quantum entanglement · Decoherence · ESD · Coherence

PACS 03.65.Yz

The applications of quantum information processing strongly relies on the entanglement between quantum systems [1]. Real system suffers decoherence due to the inevitable interaction with the surrounding environment. It leads to the degradation of entanglement and in some cases undergoes a finite time death of entanglement called Entanglement Sudden Death (ESD) [2]. In this paper we consider an open system with two identical two level atoms couple through dipole forces and interact with a vacuum bath under Markov approximation. The time evolution of the system is governed by the Lehmberg-Agarwal master equation [3, 4]. In order to understand the role of coherence on entanglement

Department of Physics, Pondicherry University, Puducherry 605 014, India
Tel.:+91-413-2654631
E-mail: svmsatya@gmail.com

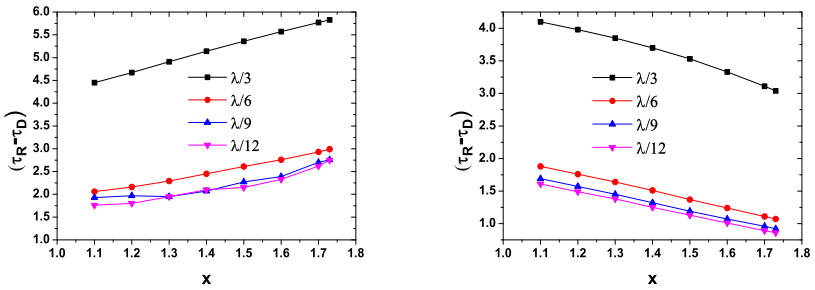

(a) single photon coherence state (b) two photon coherence state

Fig. 1 The time over which the state remains disentangled ($\tau_R - \tau_D$) during evolution is plotted for different coherence parameter (x) in the case of (a) single photon and (b) two photon coherence states with different interatomic distance ($r_{12} = \lambda/3, \lambda/6, \lambda/9$ and $\lambda/12$)

.

dynamics, we construct two classes of X states, one class with only one photon coherence and the other with only two photon coherence [5]. The class of X states with one photon (X_1) and two photon (X_2) coherence states are respectively given by

$$X_1 = \begin{pmatrix} \frac{1}{6} & 0 & 0 & 0 \\ 0 & \frac{1}{6} & \frac{x}{6} & 0 \\ 0 & \frac{x}{6} & \frac{1}{2} & 0 \\ 0 & 0 & 0 & \frac{1}{6} \end{pmatrix}, \qquad X_2 = \begin{pmatrix} \frac{1}{2} & 0 & 0 & \frac{x}{6} \\ 0 & \frac{1}{6} & 0 & 0 \\ 0 & 0 & \frac{1}{6} & 0 \\ \frac{x}{6} & 0 & 0 & \frac{1}{6} \end{pmatrix}; \; 0 \leq x \leq 1.73 \tag{1}$$

The states are entangled for $1 < x \leq 1.73$. We investigate the entanglement longevity by studying $\tau_R - \tau_D$, the time over which the state remains disentangled; where τ_D and τ_R are ESD and revival time respectively. It can be seen from fig. 1 that $\tau_R - \tau_D$ decreases with decrease in r_{12} for any value or type of coherence. $\tau_R - \tau_D$ increases with increase in coherence for states with one photon coherence. For states with two photon coherence, $\tau_R - \tau_D$ decreases with increase in coherence. These features are valid for all interatomic distances. Thus, we conclude that the states with high two photon coherence and high dipole interaction are better entanglement resources for their use in quantum information processing under noisy environments inducing decoherence.

References

1. M A Nielsen and I L Chuang, Quantum Computation and Quantum Information, (Cambridge: Cambridge University Press) (2000).
2. Ting Yu and J H Eberly, The End of an Entanglement, Science, **316**, 555-57 (2007).
3. R H Lehmberg, Radiation from an N-Atom System. I. General Formalism, Phys.Rev.A., **2**, 883 ; Phys.Rev.A. **2** 889 (1970).
4. Z Ficek, R Tanas and S Kielich, Quantum beats and superradiant effects in the spontaneous emission from two nonidentical atoms, Physica, **146A**, 452-82 (1987).
5. Namitha C V and S V M Satyanarayana, Role of initial coherence on entanglement dynamics of two qubit X states, J.Phys.B:At.Mol.Opt.Phys., **51** 045506 (2018).

OSI-ISO 2018 manuscript No.
(16)

Spin-induced orbital-Hall effect of light in inhomogeneous medium

T. Pradeep Chakravarthy and Nirmal K. Viswanathan*
School of Physics, University of Hyderabad, Hyderabad 500046, India
*Corresponding author: nirmalsp@uohyd.ac.in

Abstract

Propagation of paraxial beam of light through an inhomogeneous medium like a GRIN rod couples its spin angular momentum $(\sigma = \pm, \text{SAM})$ and orbital angular momentum $(l = \pm, \text{OAM})$ degrees of freedom of light. This leads to a large variety of manifestation of effects due to spin-orbit interaction (SOI) including spin-to-orbital angular momentum conversion, intrinsic and extrinsic spin-Hall and orbital-Hall effect that are of emerging interest both from fundamental understanding and applications point of view. Breaking the propagation symmetry of the system for OAM beam results in a spin-induced orbital Hall effect of light owing to the refractive index gradient. We report here different spin-induced orbital-Hall effect due to propagation of circularly polarized OAM beam through GRIN rod and measured using orthogonal spin projection.

Key Words: Spin-orbit interaction of light, Inhomogeneous media, spin-Hall effect of light.

Introduction

Spin-orbit interactions of light manifests itself as geometric phase accumulation for circularly polarized (CP) Gaussian beam propagation through twisted trajectory resulting in a transverse spin dependent splitting of the output optical field, known as SHEL [1]. The refractive index inhomogeneity in a GRIN rod couples the spatial and polarization degrees of freedom. Introduction of OAM beams through this media couples the spin, intrinsic and extrinsic orbital angular momenta leading to the observation of different type of SOI which depends on the path, OAM charge and spin of the optical beam. We present here our theoretical calculation and experimental results.

Theory

Maintaining the excitation and propagation symmetry of light beam through the GRIN rod, a right circularly polarized $(\text{RCP}, \sigma = -1)$ Gaussian beam generates an optical vortex beam of topological charge l = +2 in orthogonal left circular polarization $(\text{LCP}, \sigma = +1)$ basis and vice versa, due to Rytov-Vladimirskii-Berry (RVB) type geometric phase accumulation. Breaking the symmetry, by off-axis launching, the polarized Gaussian beam experiences refractive index gradient resulting in a transverse, spin dependent shift of the optical beam position known as spin-Hall effect of light (SHEL) [2]. Equivalently, the off-axis propagation of optical vortex beam with helical phase front experiences refractive index gradient resulting in OAM-dependent beam shift dependent on the ± l charge of the vortex beam, known as the orbital-Hall effect of light owing to orbit – orbit interaction (OOI) of light [3].The shift in the centre of gravity is calculated for displacement of input beam position $r_s = y_s$ as [4]

$$\langle Y \rangle = 0, \langle X \rangle = -l_i f y_s \frac{3B \sin^4 \theta_c}{2A\left(4 - 3\cos\theta_c - \cos^3 \theta_c\right)} \qquad (1)$$

Where, f is the focal length of the GRIN rod, θ_c is the acceptance angle of light into the GRIN rod and l_i is the charge of the incident OAM beam. As the topological charge of OAM beams is increased from $l = \pm 1$ to $l = \pm 3$ the resulting Orbital Hall effects increases linearly with launch offset, as can be seen from eqn. (1).

In addition, the on-axis propagation of RCP vortex beam through the GRIN rod couples with the SAM, intrinsic (I) and extrinsic (E) OAM of the beam, resulting in SAM-IOAM enabled spin-to-orbital angular momentum conversion of light in LCP basis, distinct from SOI such that the charge of output optical vortex increases if $l\sigma_i = +$ and decrease if $l\sigma_i = -$. The off-axis propagation of CP OAM beams couples the SAM, IOAM and EOAM, resulting in spin-induced orbital Hall effect (SOHE) of light. The shift in the centre of gravity of the output beam in orthogonal CP basis is calculated for displacement of input beam position $r_s = y_s$ using [4]

$$\langle Y \rangle = 0, \langle X \rangle = -(l_i + l_\sigma)\, fy_s \frac{3B\sin^4\theta_c}{2A(4-3\cos\theta_- - \cos^3\theta_-)} \qquad (2)$$

Where, l_σ is the OAM of generated optical vortex in orthogonal spin projection for input CP beams due to SOI and l_i is the charge of input OAM beam.

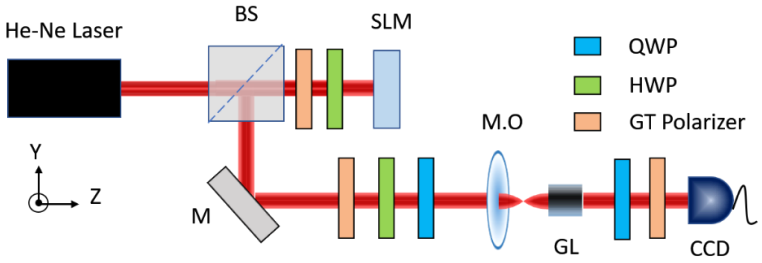

Fig.1. Schematic of the experimental setup to investigate the spin-induced orbital Hall effect in GRIN rod.

Experimental details and Results

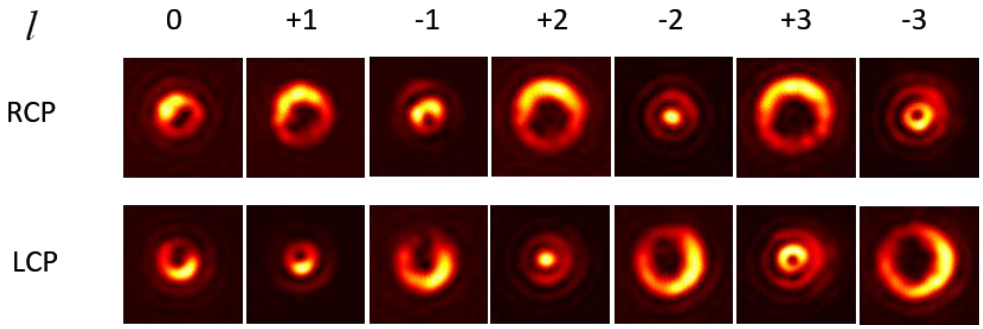

Fig.2. Experimentally measured spin-induced orbital Hall effect for RCP/LCP input beams with different topological charges.

The Gaussian output beam from He-Ne laser is incident on phase-only spatial light modulator (SLM) to generate OAM beams with different topological charge. The OAM beams are launched on to the GRIN rod using 5-axis micro-positioner and the output optical field is projected in orthogonal circular SOP using QWP and analyser. The off-axis propagation of CP OAM beams through GRIN rod resulted in the spin-induced orbital Hall effect and upon flipping sign of OAM beams, the center of gravity of the beam shift either increases or decreases. The beam shift of the output optical field increases if $l_i\sigma = +$ and decreases if $l_i\sigma = -$ reflected as beam size change, as can be seen in the Fig 2. A special case arises for charge ± 2 for LCP/RCP beams resulting in Gaussian beam in orthogonal spin projection as shown in the Fig 2. The SOI- IOAM enabled spin to orbital angular momentum conversion of light results in this spin induced orbital Hall effect of light for the broken symmetry of system.

Acknowledgments
The authors acknowledge Science and Engineering Research Board (SERB), India for continued financial assistance to this area of research and TPC acknowledges DST-INSPIRE for research fellowship.

References

1. Bliokh, K. Yu, et al. "Spin-orbit interactions of light." *Nature Photonics* 9.12, 796-808 (2015).
2. Bliokh, Konstantin Y. "Geometrodynamics of polarized light: Berry phase and spin Hall effect in a gradient-index medium." *Journal of Optics A: Pure and Applied Optics* 11.9 (2009).
3. Bliokh, Konstantin Y., and Anton S. Desyatnikov. "Spin and orbital Hall effects for diffracting optical beams in gradient-index media." *Physical Review A* 79.1, 011807 (2009).
4. Bliokh, Konstantin Y., et al. "Spin-to-orbital angular momentum conversion in focusing, scattering, and imaging systems." *Optics express* 19.27 26132-26149 (2011).

Large Kerr nonlinearity in a four-level quantum well under the regime of electromagnetically induced transparency

Sajia Yeasmin*, Sabanam Talukdar and Nitu Borgohain
Department of Physics, University of Science and Technology, Meghalaya
Techno City, Baridua, 9th Mile, Ri-Bhoi, Meghalaya-793101, India
*Email: sajiayeasmin97@gmail.com

Abstract: We present an investigation on linear and nonlinear susceptibilities of a four-level asymmetric multiple quantum well, wherein a weak probe pulse and two strong control laser beams are interacting in an N-type excitation scheme. We report the existence of large third-order susceptibility of magnitude $\sim 10^{-12}\, m^2/V^2$ within an electromagnetically induced transparency window. By changing the Rabi frequencies of the control fields, the peak values of the susceptibilities can be shifted to different frequencies.

Keywords: Electromagnetically induced transparency; Multiple quantum well; Optical susceptibility; Rabi frequency; Control detuning; Density matrix formalism.

1. Introduction

In recent years, the semiconductor quantum wells (QW) have received much attention of the research community of nonlinear optics, because of their potential applications in optoelectronic and photonic devices [1]. QW systems possess intrinsic properties like large optical dipole moments, high nonlinear coefficients and wide adjustable parameter that offer large flexibility in device design. In view of the realization of quantum coherence and interference effects by optical pulses in quantum wells, very high nonlinearity at negligible absorption are expected in these systems, which may efficiently persuade different nonlinear optical phenomena. Recently, electromagnetically induced transparency (EIT), a technique which eliminates the effect of linear absorption in an opaque medium, via quantum interference, is studied extensively in QW systems to obtain enhanced Kerr nonlinearity, steeped dispersion, reduction of group velocity etc. [2-4]. Further developments have resulted in the realization of efficient four-wave mixing, optical switching, slow optical solitons [2] etc. in different three- and four-level QW systems. Therefore, in the present work, we plan to execute an investigation of linear and nonlinear susceptibilities in a four-level quantum well system with emphasis to the effects of control field parameters.

2. Physical model and governing equation

We consider an asymmetric four-level multiple quantum well (MQW) nanostructure [5] which is interacting in an N-type configuration with three laser fields as shown in Fig. 1(a). The model consists of a deep GaAs well whose thickness is 7.1 nm and is adjacent to two shallow 6.8 nm thick AlGaAs wells separated by two AlGaAs barriers of thickness 2.0 nm and 2.5 nm, respectively. Between the deep well and the continuum there is an AlGaAs barrier with 0.7 nm thickness. The shallow well which is in left side is in contact with an AlGaAs barrier of 10 nm.

To analyze the light-matter interaction process in the system, we adopt the density matrix formalism. Under a rotating wave approximation, we proceed with the same process as described in [4], which led to the expressions of first (linear) and third-order (nonlinear) susceptibilities as

$$\chi^{(1)} = -\frac{N|\mu_{13}|^2}{\hbar\epsilon_0}\left(\frac{D_p(0)}{D(0)}\right), \tag{1}$$

$$\chi^{(3)} = \frac{N|\mu_{13}|^4}{4\hbar^3\epsilon_0}\left(\frac{\{|\Omega_c(\Delta_p-\Delta_c+\Delta_d+i\gamma_{41})|^2+|D_p(0)|^2+|\Omega_c\Omega_d|^2\}D_p(0)}{|D(0)|^2 D(0)}\right). \tag{2}$$

where N is carrier density, μ_{13} is dipole moment due toprobe field, Ω_c and Ω_d are Rabi frequencies of the control fields, Δ_p, Δ_c and Δ_d are detunings of the probe and control fields, $D_p(0)$ and $D(0)$ terms are functions of Ω_c, Ω_d, Δ_p, Δ_c, Δ_d and decay rates γ_{21}, γ_{31}, and γ_{41}.

3. Results and discussions

To start with, we first take the system parameters as follows: $N = 10^{23}\, m^{-3}$, $\varepsilon_0 = 8.854 \times 10^{-12} C^2 N^{-1} m^{-2}$, $\mu_{13} = 17.76 \times 10^{-28}\, Cm$, $\omega_p = 2.337 \times 10^{15} s^{-1}$, and the decay parameters $\gamma_{21} = 0.5 \times 10^{13} s^{-1}$, $\gamma_{31} = 1.00 \times 10^{13} s^{-1}$, and $\gamma_{41} = 1.00 \times 10^{13} s^{-1}$. We first focus on the linear or first-order susceptibility which leads to the EIT phenomena. The imaginary and real parts of $\chi^{(1)}$ characterize, respectively, the absorption and dispersion (or refractive index) of the probe field. In panel (i) of Fig. 1(b), we plot the imaginary part of $\chi^{(1)}$ as a function of Δ_p for different values of Rabi frequencies of the first control field (Ω_c). From figure, it is seen that, in absence of Ω_c, the probe pulse is greatly absorbed showing a large peak around probe field resonance $\Delta_p = 0$, but in presence of Ω_c, the absorption peak splits into two parts, which is the signature of formation of EIT window. The suppression of the absorption is caused by the quantum destructive interference effect, which is driven by the strong control field Ω_c. Simultaneously, in panel (ii) of Fig. 1(b), where real part of $\chi^{(1)}$ is plotted with respect to Δ_p, shows a steep negative slope around ($\Delta_p = 0$) in

absence of Ω_c, but when Ω_c starts growing, the $Re(\chi^{(1)})$ profile dramatically possess a positive slope. This indicates the change of the sign of the group velocity from negative to positive. In all above investigations, we kept the second control field OFF, i.e., $\Omega_d = 0$. Next, to check the effect of the second control filed Ω_d, we plot $Im(\chi^{(1)})$ and $Re(\chi^{(1)})$with respect toΔ_p, for different values of Ω_d, at a fixed value of $\Omega_c (= 3 \times 10^{13} s^{-1})$, which are depicted in panels (i) and (ii) of Fig. 1(c), respectively. From panel (i) it is seen that, with the enhancement of Ω_d, another absorption peak appears around $\Delta_p = 0$, thereby creating two EIT windows. Meanwhile, the $Re(\chi^{(1)})$ is also seen to be possess a very steep negative slope at around $\Delta_p = 0$. This result demonstrates that it is possible change the sign of group velocity of the probe pulse, multiple times by regulating the control field Rabi frequencies.

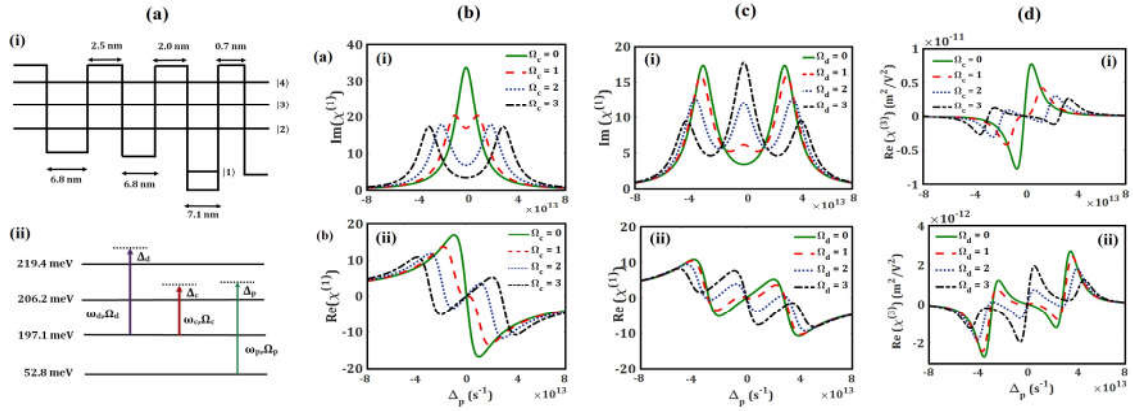

Figure 1: **(a)** Schematic of the band structure of a single period of the quantum well, (i) conduction band energy level diagram, (ii) N-type excitation scheme. **(b)** Imaginary (i), and real (ii) parts of $(\chi^{(1)})$as functions of Δ_p for different values $\Omega_c$at $\Omega_d = 0$. **(c)** Imaginary (i), and real (ii) parts of $(\chi^{(1)})$as functions of Δ_p for different values $\Omega_d$at $\Omega_c = 3 \times 10^{13} s^{-1}$. **(d)** Real (i) parts of $(\chi^{(3)})$as functions of Δ_p for different values $\Omega_c$at $\Omega_d = 0$, and imaginary (ii) part of $(\chi^{(3)})$as functions of Δ_p for different values Ω_d at $\Omega_c = 3 \times 10^{13} s^{-1}$.Other system parameters are mentioned in the text.

Next, we proceed to the investigation of third-order susceptibility $Re(\chi^{(3)})$. First we plot the profiles of $Re(\chi^{(3)})$ for different values of first control field (Ω_c), in absence of second control field $(\Omega_d = 0)$, as depicted in panel (i) of Fig. 1(d). In the figure, it is seen that though, initially, in absence of any control fileds, $Re(\chi^{(3)})$ possess a positive slope at around zero probe detuning $(\Delta_p = 0)$, but with the increase of the first control field (i. e. , $\Omega_c > 0$), the profile of $Re(\chi^{(3)})$ splits into two peaks, and the separation between these two peaks increases with increase in Ω_c. In order to study the influence of second control field (Ω_d) on $Re(\chi^{(3)})$, we plot panel (ii) of Fig. 1(d). In this figure, it is seen that, under the effect of Ω_d, $Re(\chi^{(3)})$ develops another peak at around zero probe detuning. Comparing panel (i) of Fig. 1(d) with panel (i) of Fig. 1(b) and panel (ii) of Fig. 1(d) with panel (i) of Fig. 1(c), it is seen that, the all changes in $Re(\chi^{(3)})$ occurs under EIT regime. The important point to note is that the QW possesses third-order susceptibility of magnitude $Re(\chi^{(3)}) \sim 10^{-12} m^2/V^2$, at EIT window. Comparing this with previously reported values, such as $\sim 10^{-16} m^2/V^2$ in GaAs quantum disc [6] and $\sim 10^{-14} m^2/V^2$ in GaAs/AlGaAs QW [3], we can claim that, the QW system adopted in the present work, may possess large third-order susceptibility. The large value of $Re(\chi^{(3)})$ could be very interesting in the view point of efficient observation of nonlinear phenomena in this QW system.

4. Conclusion

In conclusion, we have identified the existence of large third-order susceptibility in the quantum well system whose magnitude is as large as$\sim 10^{-12}\ m^2/V^2$. By changing the Rabi frequencies of the control fields, the peak value susceptibilities can be obtained at different frequencies. The large value of third-order susceptibility maybe utilized for observation of different nonlinear optical phenomena efficiently under EIT condition.

Acknowledgement: Authors acknowledge the moral and financial support of Shri Mahbubul Hoque, Chancellor, University of Science and Technology, Meghalaya.

References

[1]. A. M. Fox, Contemp. Phys. 37, 111-125 (2006).
[2]. C. Zhu, G. Huang, Phys. Rev. B 80, 235408 (2009).
[3]. X. Hao, W. X.Yang, X. Lü, J. Liu, P. Huang, C. Ding, X. Yang, Phys. Lett. A 372, 7081-7085 (2008).
[4]. N. Borgohain, S. Konar, J Appl. Phys. 119, 213103 (2016).
[5]. C. R. Lee, Y. Li, F. K. Men, C. Pao, Y. Tsai, J. Wang, Appl. Phys. Lett. 86, 201112 (2005).
[6]. C. H. Liu, K. X. Guo, C. Y. Chen, B. K. Ma, Physica E 15, 217 – 228 (2002).

OSI-ISO 2018 manuscript No.
(18)

Spin-induced orbital-Hall effect of light in inhomogeneous medium

T. Pradeep Chakravarthy and Nirmal K. Viswanathan*
School of Physics, University of Hyderabad, Hyderabad 500046, India
*Corresponding author: nirmalsp@uohyd.ac.in

Abstract

Propagation of paraxial beam of light through an inhomogeneous medium like a GRIN rod couples its spin angular momentum $(\sigma = \pm, \text{SAM})$ and orbital angular momentum $(l = \pm, \text{OAM})$ degrees of freedom of light. This leads to a large variety of manifestation of effects due to spin-orbit interaction (SOI) including spin-to-orbital angular momentum conversion, intrinsic and extrinsic spin-Hall and orbital-Hall effect that are of emerging interest both from fundamental understanding and applications point of view. Breaking the propagation symmetry of the system for OAM beam results in a spin-induced orbital Hall effect of light owing to the refractive index gradient. We report here different spin-induced orbital-Hall effect due to propagation of circularly polarized OAM beam through GRIN rod and measured using orthogonal spin projection.

Key Words: Spin-orbit interaction of light, Inhomogeneous media, spin-Hall effect of light.

Introduction

Spin-orbit interactions of light manifests itself as geometric phase accumulation for circularly polarized (CP) Gaussian beam propagation through twisted trajectory resulting in a transverse spin dependent splitting of the output optical field, known as SHEL [1]. The refractive index inhomogeneity in a GRIN rod couples the spatial and polarization degrees of freedom. Introduction of OAM beams through this media couples the spin, intrinsic and extrinsic orbital angular momenta leading to the observation of different type of SOI which depends on the path, OAM charge and spin of the optical beam. We present here our theoretical calculation and experimental results.

Theory

Maintaining the excitation and propagation symmetry of light beam through the GRIN rod, a right circularly polarized $(\text{RCP}, \sigma = -1)$ Gaussian beam generates an optical vortex beam of topological charge l = +2 in orthogonal left circular polarization $(\text{LCP}, \sigma = +1)$ basis and vice versa, due to Rytov-Vladimirskii-Berry (RVB) type geometric phase accumulation. Breaking the symmetry, by off-axis launching, the polarized Gaussian beam experiences refractive index gradient resulting in a transverse, spin dependent shift of the optical beam position known as spin-Hall effect of light (SHEL) [2]. Equivalently, the off-axis propagation of optical vortex beam with helical phase front experiences refractive index gradient resulting in OAM-dependent beam shift dependent on the ± l charge of the vortex beam, known as the orbital-Hall effect of light owing to orbit – orbit interaction (OOI) of light [3].The shift in the centre of gravity is calculated for displacement of input beam position $r_s = y_s$ as [4]

$$\langle Y \rangle = 0, \langle X \rangle = -l_i f y_s \frac{3B \sin^4 \theta_c}{2A\left(4 - 3\cos\theta_c - \cos^3 \theta_c\right)} \qquad (1)$$

Where, f is the focal length of the GRIN rod, θ_c is the acceptance angle of light into the GRIN rod and l_i is the charge of the incident OAM beam. As the topological charge of OAM beams is increased from $l = \pm 1$ to $l = \pm 3$ the resulting Orbital Hall effects increases linearly with launch offset, as can be seen from eqn. (1).

In addition, the on-axis propagation of RCP vortex beam through the GRIN rod couples with the SAM, intrinsic (I) and extrinsic (E) OAM of the beam, resulting in SAM-IOAM enabled spin-to-orbital angular momentum conversion of light in LCP basis, distinct from SOI such that the charge of output optical vortex increases if $l\sigma_i = +$ and decrease if $l\sigma_i = -$. The off-axis propagation of CP OAM beams couples the SAM, IOAM and EOAM, resulting in spin-induced orbital Hall effect (SOHE) of light. The shift in the centre of gravity of the output beam in orthogonal CP basis is calculated for displacement of input beam position $r_s = y_s$ using [4]

$$\langle Y \rangle = 0, \langle X \rangle = -(l_i + l_\sigma) f y_s \frac{3B \sin^4 \theta_c}{2A(4 - 3\cos\theta_- - \cos^3 \theta_-)} \quad (2)$$

Where, l_σ is the OAM of generated optical vortex in orthogonal spin projection for input CP beams due to SOI and l_i is the charge of input OAM beam.

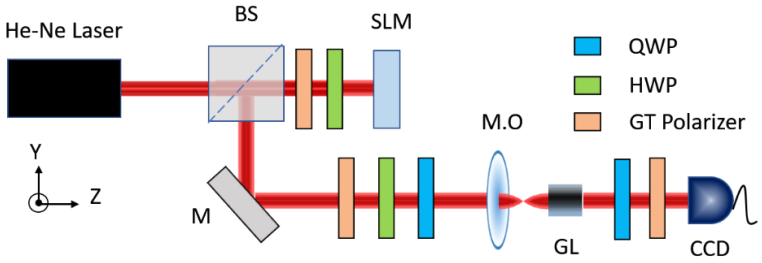

Fig.1. Schematic of the experimental setup to investigate the spin-induced orbital Hall effect in GRIN rod.

Experimental details and Results

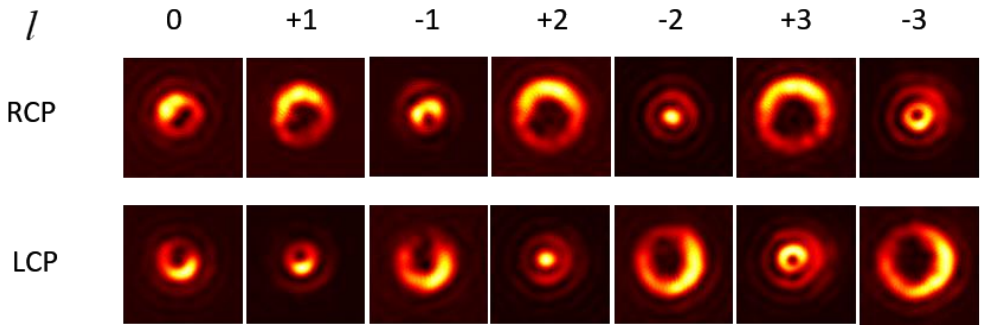

Fig.2. Experimentally measured spin-induced orbital Hall effect for RCP/LCP input beams with different topological charges.

The Gaussian output beam from He-Ne laser is incident on phase-only spatial light modulator (SLM) to generate OAM beams with different topological charge. The OAM beams are launched on to the GRIN rod using 5-axis micro-positioner and the output optical field is projected in orthogonal circular SOP using QWP and analyser. The off-axis propagation of CP OAM beams through GRIN rod resulted in the spin-induced orbital Hall effect and upon flipping sign of OAM beams, the center of gravity of the beam shift either increases or decreases. The beam shift of the output optical field increases if $l_i\sigma = +$ and decreases if $l_i\sigma = -$ reflected as beam size change, as can be seen in the Fig 2. A special case arises for charge ± 2 for LCP/RCP beams resulting in Gaussian beam in orthogonal spin projection as shown in the Fig 2. The SOI- IOAM enabled spin to orbital angular momentum conversion of light results in this spin induced orbital Hall effect of light for the broken symmetry of system.

Acknowledgments

The authors acknowledge Science and Engineering Research Board (SERB), India for continued financial assistance to this area of research and TPC acknowledges DST-INSPIRE for research fellowship.

References

1. Bliokh, K. Yu, et al. "Spin-orbit interactions of light." *Nature Photonics* 9.12, 796-808 (2015).
2. Bliokh, Konstantin Y. "Geometrodynamics of polarized light: Berry phase and spin Hall effect in a gradient-index medium." *Journal of Optics A: Pure and Applied Optics* 11.9 (2009).
3. Bliokh, Konstantin Y., and Anton S. Desyatnikov. "Spin and orbital Hall effects for diffracting optical beams in gradient-index media." *Physical Review A* 79.1, 011807 (2009).
4. Bliokh, Konstantin Y., et al. "Spin-to-orbital angular momentum conversion in focusing, scattering, and imaging systems." *Optics express* 19.27 26132-26149 (2011).

Large Kerr nonlinearity in a four-level quantum well under the regime of electromagnetically induced transparency

Sajia Yeasmin*, Sabanam Talukdar and Nitu Borgohain
Department of Physics, University of Science and Technology, Meghalaya
Techno City, Baridua, 9th Mile, Ri-Bhoi, Meghalaya-793101, India
*Email: sajiayeasmin97@gmail.com

Abstract: We present an investigation on linear and nonlinear susceptibilities of a four-level asymmetric multiple quantum well, wherein a weak probe pulse and two strong control laser beams are interacting in an N-type excitation scheme. We report the existence of large third-order susceptibility of magnitude $\sim 10^{-12}\, m^2/V^2$ within an electromagnetically induced transparency window. By changing the Rabi frequencies of the control fields, the peak values of the susceptibilities can be shifted to different frequencies.

Keywords: Electromagnetically induced transparency; Multiple quantum well; Optical susceptibility; Rabi frequency; Control detuning; Density matrix formalism.

1. Introduction

In recent years, the semiconductor quantum wells (QW) have received much attention of the research community of nonlinear optics, because of their potential applications in optoelectronic and photonic devices [1]. QW systems possess intrinsic properties like large optical dipole moments, high nonlinear coefficients and wide adjustable parameter that offer large flexibility in device design. In view of the realization of quantum coherence and interference effects by optical pulses in quantum wells, very high nonlinearity at negligible absorption are expected in these systems, which may efficiently persuade different nonlinear optical phenomena. Recently, electromagnetically induced transparency (EIT), a technique which eliminates the effect of linear absorption in an opaque medium, via quantum interference, is studied extensively in QW systems to obtain enhanced Kerr nonlinearity, steeped dispersion, reduction of group velocity etc. [2-4]. Further developments have resulted in the realization of efficient four-wave mixing, optical switching, slow optical solitons [2] etc. in different three- and four-level QW systems. Therefore, in the present work, we plan to execute an investigation of linear and nonlinear susceptibilities in a four-level quantum well system with emphasis to the effects of control field parameters.

2. Physical model and governing equation

We consider an asymmetric four-level multiple quantum well (MQW) nanostructure [5] which is interacting in an N-type configuration with three laser fields as shown in Fig. 1(a). The model consists of a deep GaAs well whose thickness is 7.1 nm and is adjacent to two shallow 6.8 nm thick AlGaAs wells separated by two AlGaAs barriers of thickness 2.0 nm and 2.5 nm, respectively. Between the deep well and the continuum there is an AlGaAs barrier with 0.7 nm thickness. The shallow well which is in left side is in contact with an AlGaAs barrier of 10 nm.

To analyze the light-matter interaction process in the system, we adopt the density matrix formalism. Under a rotating wave approximation, we proceed with the same process as described in [4], which led to the expressions of first (linear) and third-order (nonlinear) susceptibilities as

$$\chi^{(1)} = -\frac{N|\mu_{13}|^2}{\hbar\epsilon_0}\left(\frac{D_p(0)}{D(0)}\right), \tag{1}$$

$$\chi^{(3)} = \frac{N|\mu_{13}|^4}{4\hbar^3\epsilon_0}\left(\frac{\{|\Omega_c(\Delta_p-\Delta_c+\Delta_d+i\gamma_{41})|^2+|D_p(0)|^2+|\Omega_c\Omega_d|^2\}D_p(0)}{|D(0)|^2 D(0)}\right). \tag{2}$$

where N is carrier density, μ_{13} is dipole moment due toprobe field, Ω_c and Ω_d are Rabi frequencies of the control fields, Δ_p, Δ_c and Δ_d are detunings of the probe and control fields, $D_p(0)$ and $D(0)$ terms are functions of Ω_c, Ω_d, Δ_p, Δ_c, Δ_d and decay rates γ_{21}, γ_{31}, and γ_{41}.

3. Results and discussions

To start with, we first take the system parameters as follows: $N = 10^{23}\, m^{-3}$, $\varepsilon_0 = 8.854 \times 10^{-12} C^2 N^{-1} m^{-2}$, $\mu_{13} = 17.76 \times 10^{-28}\, Cm$, $\omega_p = 2.337 \times 10^{15} s^{-1}$, and the decay parameters $\gamma_{21} = 0.5 \times 10^{13} s^{-1}$, $\gamma_{31} = 1.00 \times 10^{13} s^{-1}$, and $\gamma_{41} = 1.00 \times 10^{13} s^{-1}$. We first focus on the linear or first-order susceptibility which leads to the EIT phenomena. The imaginary and real parts of $\chi^{(1)}$ characterize, respectively, the absorption and dispersion (or refractive index) of the probe field. In panel (i) of Fig. 1(b), we plot the imaginary part of $\chi^{(1)}$ as a function of Δ_p for different values of Rabi frequencies of the first control field (Ω_c). From figure, it is seen that, in absence of Ω_c, the probe pulse is greatly absorbed showing a large peak around probe field resonance $\Delta_p = 0$, but in presence of Ω_c, the absorption peak splits into two parts, which is the signature of formation of EIT window. The suppression of the absorption is caused by the quantum destructive interference effect, which is driven by the strong control field Ω_c. Simultaneously, in panel (ii) of Fig. 1(b), where real part of $\chi^{(1)}$ is plotted with respect to Δ_p, shows a steep negative slope around ($\Delta_p = 0$) in

absence of Ω_c, but when Ω_c starts growing, the $Re(\chi^{(1)})$ profile dramatically possess a positive slope. This indicates the change of the sign of the group velocity from negative to positive. In all above investigations, we kept the second control field OFF, i.e., $\Omega_d = 0$. Next, to check the effect of the second control filed Ω_d, we plot $Im(\chi^{(1)})$ and $Re(\chi^{(1)})$with respect toΔ_p, for different values of Ω_d, at a fixed value of $\Omega_c (= 3 \times 10^{13} s^{-1})$, which are depicted in panels (i) and (ii) of Fig. 1(c), respectively. From panel (i) it is seen that, with the enhancement of Ω_d, another absorption peak appears around $\Delta_p = 0$, thereby creating two EIT windows. Meanwhile, the $Re(\chi^{(1)})$ is also seen to be possess a very steep negative slope at around $\Delta_p = 0$. This result demonstrates that it is possible change the sign of group velocity of the probe pulse, multiple times by regulating the control field Rabi frequencies.

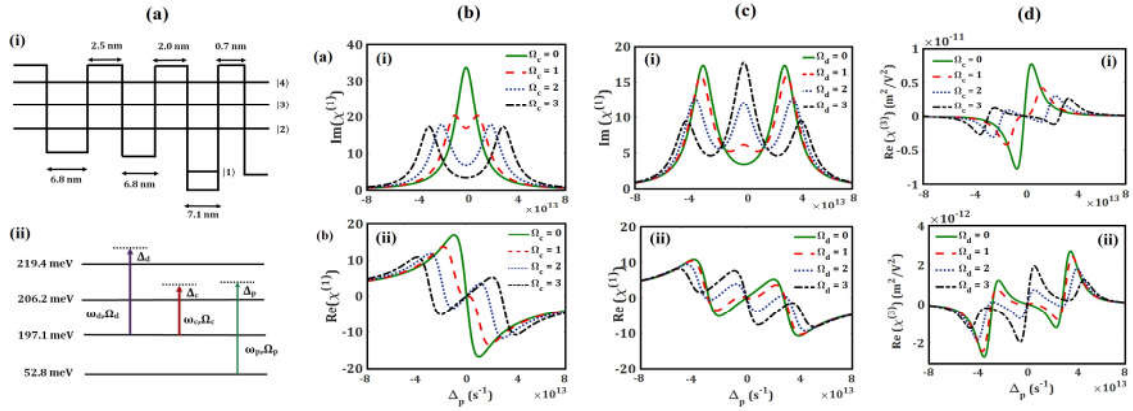

Figure 1: **(a)** Schematic of the band structure of a single period of the quantum well, (i) conduction band energy level diagram, (ii) N-type excitation scheme. **(b)** Imaginary (i), and real (ii) parts of $(\chi^{(1)})$as functions of Δ_p for different values $\Omega_c$at $\Omega_d = 0$. **(c)** Imaginary (i), and real (ii) parts of $(\chi^{(1)})$as functions of Δ_p for different values $\Omega_d$at $\Omega_c = 3 \times 10^{13} s^{-1}$. **(d)** Real (i) parts of $(\chi^{(3)})$as functions of Δ_p for different values $\Omega_c$at $\Omega_d = 0$, and imaginary (ii) part of $(\chi^{(3)})$as functions of Δ_p for different values Ω_d at $\Omega_c = 3 \times 10^{13} s^{-1}$.Other system parameters are mentioned in the text.

Next, we proceed to the investigation of third-order susceptibility $Re(\chi^{(3)})$. First we plot the profiles of $Re(\chi^{(3)})$ for different values of first control field (Ω_c), in absence of second control field $(\Omega_d = 0)$, as depicted in panel (i) of Fig. 1(d). In the figure, it is seen that though, initially, in absence of any control fileds, $Re(\chi^{(3)})$ possess a positive slope at around zero probe detuning $(\Delta_p = 0)$, but with the increase of the first control field (i. e. , $\Omega_c > 0$), the profile of $Re(\chi^{(3)})$ splits into two peaks, and the separation between these two peaks increases with increase in Ω_c. In order to study the influence of second control field (Ω_d) on $Re(\chi^{(3)})$, we plot panel (ii) of Fig. 1(d). In this figure, it is seen that, under the effect of Ω_d, $Re(\chi^{(3)})$ develops another peak at around zero probe detuning. Comparing panel (i) of Fig. 1(d) with panel (i) of Fig. 1(b) and panel (ii) of Fig. 1(d) with panel (i) of Fig. 1(c), it is seen that, the all changes in $Re(\chi^{(3)})$ occurs under EIT regime. The important point to note is that the QW possesses third-order susceptibility of magnitude $Re(\chi^{(3)}) \sim 10^{-12} m^2/V^2$, at EIT window. Comparing this with previously reported values, such as $\sim 10^{-16} m^2/V^2$ in GaAs quantum disc [6] and $\sim 10^{-14} m^2/V^2$ in GaAs/AlGaAs QW [3], we can claim that, the QW system adopted in the present work, may possess large third-order susceptibility. The large value of $Re(\chi^{(3)})$ could be very interesting in the view point of efficient observation of nonlinear phenomena in this QW system.

4. Conclusion

In conclusion, we have identified the existence of large third-order susceptibility in the quantum well system whose magnitude is as large as$\sim 10^{-12}\ m^2/V^2$. By changing the Rabi frequencies of the control fields, the peak value susceptibilities can be obtained at different frequencies. The large value of third-order susceptibility maybe utilized for observation of different nonlinear optical phenomena efficiently under EIT condition.

Acknowledgement: Authors acknowledge the moral and financial support of Shri Mahbubul Hoque, Chancellor, University of Science and Technology, Meghalaya.

References

[1]. A. M. Fox, Contemp. Phys. 37, 111-125 (2006).
[2]. C. Zhu, G. Huang, Phys. Rev. B 80, 235408 (2009).
[3]. X. Hao, W. X.Yang, X. Lü, J. Liu, P. Huang, C. Ding, X. Yang, Phys. Lett. A 372, 7081-7085 (2008).
[4]. N. Borgohain, S. Konar, J Appl. Phys. 119, 213103 (2016).
[5]. C. R. Lee, Y. Li, F. K. Men, C. Pao, Y. Tsai, J. Wang, Appl. Phys. Lett. 86, 201112 (2005).
[6]. C. H. Liu, K. X. Guo, C. Y. Chen, B. K. Ma, Physica E 15, 217 – 228 (2002).

Parametrical study of near and far field numerical reconstruction methods in digital holography

Gaurav Dwivedi[1, 2], Lavlesh Pensia[1, 2], Raj Kumar [1, 2, *]

[1]CSIR – Central Scientific Instruments Organisation Chandigarh-160030, India

[2]Academy of Scientific and Innovative Research (AcSIR), CSIR-CSIO, Chandigarh-160030, India

[*]Corresponding author: raj.optics@csio.res.in

Extended Abstract

Numerical reconstruction is a constituent part of digital holography in which both amplitude and phase of recorded object is recreated using scalar diffraction computation. Among several numerical reconstruction methods; e.g. Rayleigh – Sommerfeld diffraction integral, Fresnel diffraction method, angular spectrum method, convolution method etc., two of the most frequently used numerical reconstruction methods are angular spectrum and Fresnel diffraction method. Both the methods are preferred as they are Fourier transform based techniques and so provide less effort in computation. But, they suffer due to limitations on propagation distance during reconstruction. Although, angular spectrum method is an exact technique in which reconstructed image size does not change with distance, it works only in near field and generates aliasing error after a certain distance. On the other hand, Fresnel diffraction method is an approximation of Rayleigh-Sommerfeld integral and works only in far field. Contrary to angular spectrum method, in Fresnel diffraction method, the reconstruction distance depends on pixel resolution and computation window size and thus reconstructed image size becomes smaller as reconstruction distance increases.

In this paper, numerical reconstruction methods i.e. multistep Fresnel diffraction method to counter the problem of variable size of reconstructed image with propagation distance and combination of angular spectrum and Fresnel diffraction methods for near and far field propagation are studied. The two methods are compared experimentally with conventional angular spectrum and Fresnel diffraction methods in terms of accuracy and reconstruction quality.

Keywords

Numerical reconstruction, digital holography, reconstruction distance, accuracy, reconstruction quality

Acknowledgments

Authors are thankful to Department of Science and Technology, Government of India, New Delhi for financial support for this research work under HoloCam project (Grant No. DST/TSG/NTS/2015/59).

Reference list

- M. K. Kim, SPIE reviews, 018005, 1 (2010)
- D. Wang, J. Zhao, F. Zhang, G. Pedrini, and W. Osten, App. Opt., D12, 47 (2008)
- P. Ferraro, S. De Nicola, G. Coppola, A. Finizio, D. Alfieri, and G. Pierattini, Opt. Lett., 854, 29 (2004)
- C. Liu, D. Wang, and Y. Zhang, Opt. Engg., 105802, 48 (2009)

Coherence waves interference to overcome phase recovery challenge: in optical, crystallography and X ray imaging

Rakesh Kumar Singh

Department of Physics, Indian Institute of Technology (BHU), Varanasi, 221005, Uttar-Pradesh, India

krakeshsingh.phy@iitbhu.ac.in, krakeshsingh@gmail.com

Acknowledgement: Author acknowledges support from the IIT (BHU), Indian Institute of Space Science and Technology (IIST), and Science and Engineering Research Board (SERB)- EMR/2015/001613. Contributions of research students from the IIST are also acknowledged.

Abstract: Coherence function behaves like a wave and follows two-four dimensional wave equations. Utilizing this feature, available resources of the optical signal processing can be used for the coherence. An interference of the coherence waves can be utilized to develop non-iterative phase recovery methods for optical to matter waves. Moreover, *coherence waves* give liberty to design and develop *lensless* configurations for optical, electron beams, X rays.

Recently, we have come up with new methods using interference of the coherence waves to overcome phase recovery in a non-iterative manner. Our technique makes use of the *Hanbury Brown-Twiss* (HBT) approach. In this paper, we discuss issues, developments and our contributions on phase recovery with a lensless geometry. Applications of coherence wave interference in the correlation holography, Stokes holography and single pixel Hybrid correlation holography are also highlighted. Based on our experience in the optical domain, we believe and propose to apply interference of the coherence waves in areas like crystallography and X ray Imaging.

Key Words: Lensless Imaging, Phase retrieval, Coherence, Single pixel Imaging, Fourier spectrum

Introduction

Light fields are inherently of a statistical nature and correlations play significant role in characterizing the light. In particular, the cross correlation of the random fields at two points, is a complex quantity and known as coherence function [1]. The complex coherence behaves like a wave and several tools and techniques of the optical signal processing can be extended to the coherence waves [2]. In this paper, we highlight application of the coherence waves in a phase recovery and discuss how this technique can be applied in other areas of imaging such as crystallography and X ray.

Consider an example of an incoherent source and description of the spatial coherence. The size and shapes of incoherent source tailor the coherence function according to the propagation kernel. For example, coherence function in the far field is a Fourier transform of the incoherent source. Therefore, a complex coherence function carries signature of the Fourier spectrum of the source. Measurement of the coherence requires interferometric approach wherein two points intensity correlation, i.e. the Hanbury Brown-Twiss approach, plays an important role due to high stability and simplicity [1]. However, the HBT approach provides only modulus square of the Fourier spectrum and phase information is lost. There have been attempts to recover the phase of the Fourier spectrum using iterative techniques. On the other hand, we have proposed non-iterative techniques to recover the complex Fourier spectrum using the HBT approach [3, 4]. Basic theoretical explanation of the technique and possible applications are discussed in coming section.

Principle:

Consider propagation of the light from a source(s) as shown in Figure. The complex field at the detector plane is written as $E(p) = \int G(r, p)E(r)dr$ (1)

where, $G(r, p)$ is propagation kernel, $E(r)$ and $E(p)$ represents the complex field at the source and observation planes respectively. Consider a relation between coherence function and intensity cross-covariance as:

$$\left\langle \Delta I(p_1)\Delta I(p_2)\right\rangle = \left|\left\langle E(p_1)E^*(p_2)\right\rangle\right|^2 \qquad (2)$$

where < > represents ensemble average, * complex conjugate and $\Delta I = I - \left\langle I(p)\right\rangle$ is fluctuation of intensity over its mean value. If we assume that source is composed of two independent incoherent sources as shown in Fig. therefore

$$\left\langle \Delta I(p_1)\Delta I(p_2)\right\rangle = \left|\left\langle E_o(p_1)E_o^*(p_2)\right\rangle + \left\langle E_R(p_1)E_R^*(p_2)\right\rangle\right|^2 \qquad (3)$$

Eq. (3) represents interference of the coherence waves which can be used for phase recovery applications such as in lensless imaging through random scattering medium, crystallography and X ray imaging.

Results and Discussion:

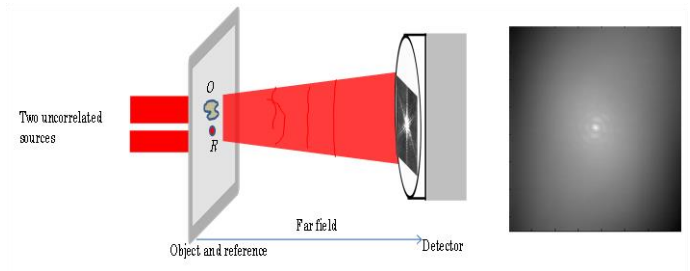

Fig. Formation of fringes in the intensity correlation structure due to interference of coherence waves generated from two incoherent sources

Fig. shows superposition of coherence waves coming from two un-correlated sources. A two dimensional result shown in extreme right of the Fig. represents an experimental result of the intensity correlation fringes due to interference of two coherence waves. Formation of the intensity correlation fringes is realized in a complete lensless geometry and makes a lensless Fourirer transform hologram. Moreover, such geometry helps to achieve spatial stationarity of the random field even in the Fresnel domain from the random source plane [4]. The intensity correlation can be utilized to develop various new and un-conventional imaging systems such as correlation holography, Stokes holography and single pixel imaging [3-5]. Similar requirements also exist in x ray and electron beam diffraction where knowledge of the *complex Fourier spectrum* is desired for different reasons. Based on our experience in the optical domain, we propose to apply the coherence wave interference in the *x ray imaging* and *electron beam*.

References:

1. L. Mandel, E. Wolf, Optical Coherence and Quantum Optics (Cambridge University Press, 1995)
2. A. W. Lohman, D. Medlovic, G. Shabtay, J. Opt. Soc. Am. 16, 359 (1999)
3. R. K. Singh, Opt. Lett. 42, 2515 (2017)
4. R. K. Singh, S. Vyas, Y. Miyamoto, J. Opt. 19, 115705 (2017)
5. D. Singh, R. K. Singh, Opt. Express 26, 10801 (2018)

Overview of Biomedical Raman spectroscopy

Dr. C. Murali Krishna
Chilakapati Lab,
Cancer Research Institute (CRI)
Advanced Center for Treatment, Research and Education in Cancer (ACTREC)
Tata Memorial Center (TMC)
Navi Mumbai
mchilakapati@actrec.gov.in, pittu1043@gmail.com

Conventional diagnosis involves clinical examination followed by relevant biochemical/microbiological/pathological examinations which rely on symptoms suggesting diagnosis of existing disease. Such late diagnosis is often prone to poor prognosis, emphasizing early diagnosis for better prognosis. In addition to disease diagnosis/screening, monitoring of treatment response is another crucial aspect of disease management. Accurate evaluation and monitoring of treatment response lead to better disease management and towards personalized medicine. In this context, optical spectroscopy methods such as laser-induced-fluorescence, FTIR, Raman and diffused reflectance are some of the most widely pursued as potential alternatives/adjuncts. The discovery of Raman Effect, in the year 1928, demonstrated that the analysis of inelastically scattered light from the simplest molecule H_2O could provide unique fingerprint of molecular structure. With advent of lasers and CCDs, Raman spectroscopy of even weakly scattering samples like tissues and cells is easy. And Raman spectroscopy hasbeen explored in biomedical applications, as it is better suited due to attributes such as sensitivity to biochemical composition, objective, rapid, no external labelling/sample preparation, and most importantly in vivo/in situ on line applications.

Paper presents an overview of in vivo Raman spectroscopy studies and explorations on less invasive samples (exfoliated cells and bodyfluids) showcasing aspects of diagnosis/screening, treatment response in cancers[1-8].

Key words: Optical diagnosis, Raman spectroscopy, Optical biopsy, Theranostics.

Reference:

1. P. Kumar and C. Murali Krishna, in Oral Cancer Detection: Novel Strategies and Clinical Impact , Ed: Prashanth Panta , (Springer-Verlag, 2018) , DOI /10.1007/978-3-319-61255-3
2. A. Malik, A. Sahu, S. Singh, A. Deshmukh, D. Nair, S. Nair, P.Chatturvedi, C. Murali Krishna, Head&Neck (2017),DOI 10.1002/hed.24884
3. C. Murali Krishna and A. Sahu, Cancer Research(2017), 10.1158/0008-5472.CAN-16-3206
4. K. Mehta, A. Atak, A. Sahu, S.Srivastava, C.Murali Krishna , Analyst (2018) , 10.1039/C8AN00224J
5. S. P. Singh, Hunain Alam, Crismita Dmello, Milind M. Vaidya, R.R. Dasari, C. Murali Krishna, Journal of Biophotonics(2017), 10.1002/jbio.201600249
6. A. Sahu, Nikhila, S. Sawant and C. Murali Krishna, Analyst (2015), 10.1039/C4AN01860E .
7. A Hole, G Tyagi, A Sahu, R Shaikh, C.Murali Krishna,Vibrational Spectroscopy (2018) , 10.1016/j.vibspec.2018.07.001.
8. A. Sahu, V. Pai, P. Gera, A. Dubey, G.Tyagi, M. Mahimkar, C. Murali Krishna, Journal of Biomedical Optics(2017), 10.1117/1.JBO.22.11.115003.

OSI-ISO 2018 manuscript No.
(23)

Effect of quantum channels on quantum networks: A case study on Quantum Fourier Transformation

Prajit Dhara[1], S. Sivakumar[2]

Abstract Quantum Fourier Transform is an important part of many other quantum algorithms. If the circuitry for performing the transform is not ideal, the output is not reliable. The effect of three important classes of quantum channels, namely, phase flip, bit flip and bit-phase flip, on the output is studied in this report. Effect of these channels is quantified in terms of quantum state fidelity, which measures the deviation of the Fourier transformed state in realistic circuits from the expected ideal output. It is found that the fidelity decreases drastically with increasing input size and depends on the type of channel. This implies that the resource requirement for error correction scales nonlinearly with problem size.

Keywords Quantum Fourier Transform · Quantum channel · Fidelity

Quantum algorithms perform better than classical algorithms in specific problem classes. Certain intractable problems (mostly belonging to the **NP** class) in the classical domain, have polynomial time solutions in the quantum framework. Prime factorization of large numbers [1] and data search in a unsorted data structure [2] are two famous examples which have highly efficient quantum computing algorithms.

Quantum algorithms are implemented using quantum circuits or networks, made of quantum gates in tandem. An ideal circuitry is not influenced by external disturbances, *i.e.*, they are closed systems. However, it is impossible to achieve perfect isolation. These imperfections may lead to processes such as bit flip, phase flip, bit-phase flip and dissipation. Such non-unitary processes are accounted for in the operator sum representation [3]. In this study, we have explored the delirious effects of these processes on Quantum Fourier Transform (QFT).

We compare the ideal QFT ρ of an input state with its channel-affected QFT σ. The deviation between ρ and σ is quantified using quantum fidelity, given by tr $\left(\sqrt{\rho^{1/2}\sigma\rho^{1/2}}\right)$. The dependence of fidelity on system size (n), error probabilities (p) and error types (X, Z, Y) have been studied. For a fixed error probability, a large set of randomly initialized states were used as input states. The effect of channels on randomly initialized states, as system size increases, gives a few indicators regarding the general behavior of fidelity. For random states, the bit-phase flip channel affects the system the most, as this channel leads to the lowest fidelity. However, the standard deviation is lesser compared to those in the case of bit flip and phase flip channels. To determine a more general behavior of the effect of these channels, it is beneficial to study their effects on the computational basis states. By examining which states are more susceptible to the effect of channels, algorithms can be tailored to avoid the susceptible states. While increase of error probability p affects the fidelity more, it is found that some basis states are more prone to be affected by the channels. Based on the observations from Fig. 1, the mean of fidelities for the bit flip and bit-phase flip errors, is almost a constant for the various basis states. The dependence of fidelity on p is shown in Figs. 2a and 2b, (bit + bit-phase) and phase flip respectively. Important lesson from these profiles is that the reliable (closeness of p to unity) performance of gates is a stringent requirement as the system size increases. For instance, fidelity as high as 0.98 is possible with a error probability $(1-p) = 0.02$ if the system size is 3. However, when the same architecture is scaled to size 6, the fidelity drops to 0.85. It deteriorates further as the system size increases. It is possible to get a best fit curve for the profiles shown in Fig. 2. As the error probability increases, the fidelity of the transformed state decreases. With the increase in system size, as required for scalability to handle large inputs, the fidelity deteriorates as

[1] Department of Electrical and Electronics Engineering,
BITS Pilani, Pilani 333031
E-mail: prajitdhara1@gmail.com
[2] Indira Gandhi Centre for Atomic Research,
Kalpakkam 603102
E-mail: palakadsiva@gmail.com

a modulated exponential of the system size. An equation of the form $f = a(1-x)^{-b}\exp(c(1-x))$, where x is the error probability, provides the best fitting functions among those evaluated. In conclusion, quantum error correction is required in equally large measure which scales nonlinearly with the system size and p. Requirement for an almost ideal quantum circuitry for implementing quantum algorithms has been highlighted in our study.

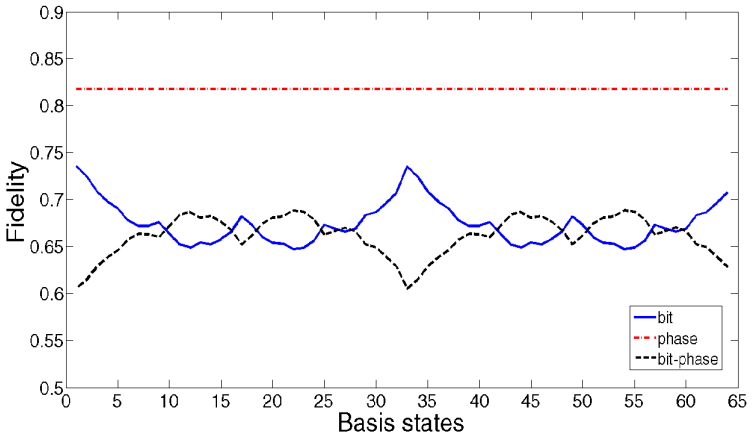

Fig. 1: Fidelity trends for various kinds of error vs. basis state; Basis states are marked by their decimal notation; n=6 p=0.9

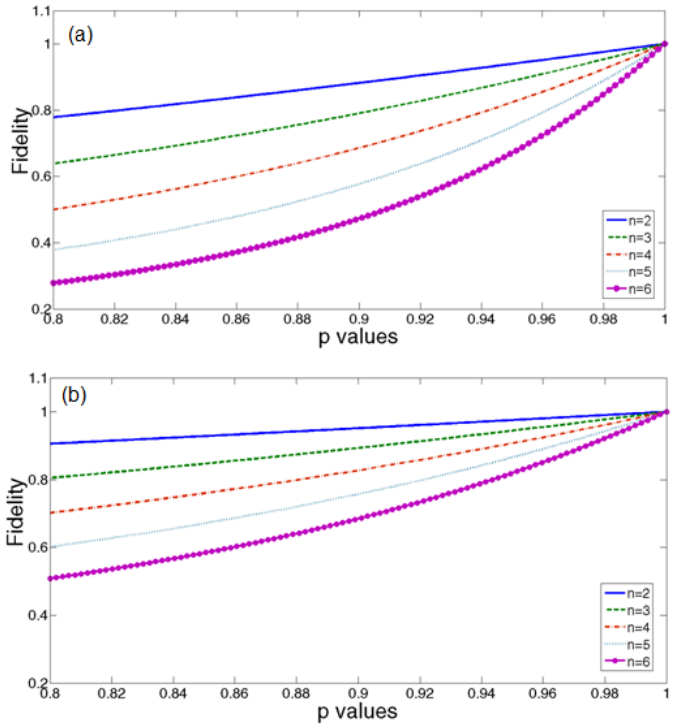

Fig. 2: Average fidelity trends with respect to p values for various system size (n) (a) Mean of bit and bit-phase flip (b) Phase flip

References

1. Peter W. Shor. Polynomial-Time Algorithms for Prime Factorization and Discrete Logarithms on a Quantum Computer. *Proceedings of the 35th Annual Symposium on Foundations of Computer Science, IEEE Computer Society Press*, pages 124–134, 1995.
2. Lov K. Grover. Quantum mechanics helps in searching for a needle in a haystack. *Physical Review Letters*, 79(2):325–328, 1997.
3. Michael A. Nielsen and Isaac L. Chuang. *Quantum Computation and Quantum Information*. Cambridge Press, 2000.

Design and development of spatial profile analysis method for authenticating security holograms

Sajan Ambadiyil,[1*] Avinash Kumar Jha[2],V.P.Mahadevan Pillai[3]
[1]Center for Development of Imaging Technology, Thiruvanthapuram-695027, Kerala, India
[2] School of Electrical Science, Hindustan Institute of Technology and Science, Padur-603103, Chennai, India
[2]Department of Optoelectronics, University of Kerala, Thiruvanthapuram-69558, Kerala, India
[1]ambadycdit@gmail.com

Abstract

The spread of hologram technology through embossed holograms as anti-counterfeit devices in every sector has aggravated the counterfeiter to make imitation or counterfeiting of the same. Unfortunately, there has been very little development in the area of methods to establish the authenticity of the security hologram itself. Hence, there is always need of a robust method to verify security hologram; which does not require special steps to be taken during production of the security hologram and should be able to work on any security hologram. We have made an invention, using spatial profile analysis exploiting the analogy between uniqueness associated with security hologram and fingerprint and apply feature score matching method similar to biometric recognition techniques for authenticating the security hologram. The invention can be applied to any hologram as it utilises the comparison of the spatial profile of a genuine hologram with a sample hologram to be verified.

Keywords

Security hologram, Authentication, Spatial profile analysis, Biometric recognition techniques.

Since Steve Benton's invention of the rainbow hologram in 1968 and development of mass development method by recording a surface relief in photoresist and mass-production by embossing the relief in a polymer (1979), holograms have been first choice to be applied as a security feature and ensuring the authenticity of documents and products. However, there has been very little development in the area of methods to establish the authenticity of the hologram itself. The spread of hologram technology through embossed holograms as anti-counterfeit devices in every sector has aggravated the counterfeiter to make imitation or counterfeiting of the same. Initially, hologram counterfeits are produced from the artworks and conventional recording method. The evolution of computer-generated holograms increases the number of hologram counterfeiting. Also, the technological advancement made in the availability of associated equipment at a cheaper cost. Now the embossed holograms are turning out to be getting easier to counterfeit. There are several straightforward, simple, and inexpensive ways to counterfeit the kinds of holograms currently used in documents and products. A skilled holographer in collaboration with the graphic artist can make optical copies of holograms that are very difficult to distinguish from the originals. Even though it may be impossible to make a perfect counterfeit of a hologram, it is not very difficult for a skilled, well-equipped holographer to make a counterfeit that will pass a cursory inspection by an untrained person. Also, as the embossed hologram is in bumps or pits on the plastic, just peel it off and use it as a mould for mechanical copying. The reproduction won't be perfect, but no one knows what they are supposed to look like well enough to tell the difference. And, once a good master copy has been made, high-quality replicas are very easy to make. Hence, to serve the holograms and other diffractive optical variable image device as an anti-counterfeit role, it is necessary to

identify a fast and efficient automated analysing and authentication method in the forensic level to detect counterfeits. Thus there is always need of a robust method to verify hologram; which does not require special steps to be taken during production of the hologram that can work on any hologram and should be free from the constraints related to experimental set up for verifying the hologram.

We have made an invention, using spatial profile analysis exploiting the analogy between uniqueness associated with security hologram and fingerprint and apply feature score matching method similar to biometric recognition techniques for authenticating the security hologram. The principle of the proposed method involves the comparison of the spatial profile of the holograms with that of a reference one. The analysis of the spatial profile of the security hologram will be done with the help of a scanning/image acquisition device. 3D profiles of holograms converted into the 2D images and the corresponding data matrix are extracted using image processing technique. Using this output, authentication of holograms can be performed. The present invention overcomes the drawback present in the prior art systems by applying a digital image processing technique to authenticate the hologram so that the effect of the physical parameter such as angle of incidence, type of incidence light, the position of the detector etc. are not present. Also, the present invention does not require any specific steps to be followed during the production of the hologram; neither has it needed any prior information about the hologram. As it utilizes software based computation, the possibility of human error during observation is eliminated. Further, the invention can be applied to any hologram as it utilises a comparison of the spatial profile of a genuine hologram with a sample hologram to be verified.

References

1. Stephen P McGrew, International Symposium and Product Presentation for Optical Information Storage and Display, Switzerland (1987).
2. Stephen P McGrew, Proc. SPIE Vol. 1210, pp. 66-76.
3. R N Jagtap, A H Ambre, Indian Journal of Engineering and Material Sciences, Vol. 13, (2006).
4. Tim Thompson and Sue Black. (CRC Press, London, 2007), pp. 57-72
5. Ravi. J, K. B. Raja, Venugopal. K. R. International Journal of Engineering Science and Technology (2009)

Specular-Reflection Based Position Measurement Technique

Ravi Dhawan[1*], Rushal Shah[2], Nitin Kawade[1,2], Biswaranjan Dikshit[1,2]
[1]Homi Bhabha National Institute, Anushaktinagar, Mumbai-400094, India
[2]Laser & Plasma Technology Division, Bhabha Atomic Research Centre, Mumbai-400085, India
*Email: ravidhawan273@gmail.com

Abstract

Using the principle of specular-reflection from metallic target surfaces, a precise non-contact based position sensing technique is brought forward in this paper. In this technique, a laser is projected at an angle and a portion of the specular light band from the target is collected by the lens and focused on the centre fiber of linear fiber array coupled to the CCD camera. As the position of target changes, there is the shift of the image spot across the fiber array and correspondingly to the CCD Camera. The position change of target is inferred from the centre of image spot using Fourier Phase Shift method at CCD camera. A position resolution of 500 µm for 6 mm range was achieved for the selected optical linear fiber array. The given system can be used in industrial environments having EMI, nuclear radiations as the camera can be placed remotely.

Keywords

Non-contact position sensing, Linear fiber array, CCD camera, Centroid measurement.

Introduction

Laser-based measurement techniques have many advantages over the others in industrial environments. These advantages include non-contact, non-destructive, fast and harsh environment adaptive measurement techniques. Position measurement is a common task in various industrial applications such as the location of the tool on a work-piece in coordinate measurement machines, differential gear alignment in automobiles etc [1]. Most of object surfaces in industry are made of polished metal. These materials are likely to reflect laser light in a mixed diffuse and specular way as shown in Fig 1. The intensity of reflected and diffused light depends on the characteristics of the target surface such as roughness, gloss etc. Light band emerges with a reflection pattern and light intensity distribution is based on the rough surface scattering theory. For position measurement of metallic target surfaces, a portion of this specular light is captured via lens and is focussed to the detector. As the target changes its position, the image spot at the detector also changes. The detector can be CCD or Position Sensing Detector (PSD) based on the application and resolution required. Thus, change in target position can be measured. However, sometimes due to the EMI/EMC or nuclear radiation environment it is difficult to place electronic components and measurement is needed to be done remotely [2]. In this paper, above-mentioned property of specular light intensity based change in position of the target is investigated by using optical linear fiber array coupled with the CCD camera. The position change information is inferred by calculating the centroid of image spot using Fourier Phase shift technique [2, 3]. For the given linear fiber array resolution of 500 µm was achieved for the range of 6 mm.

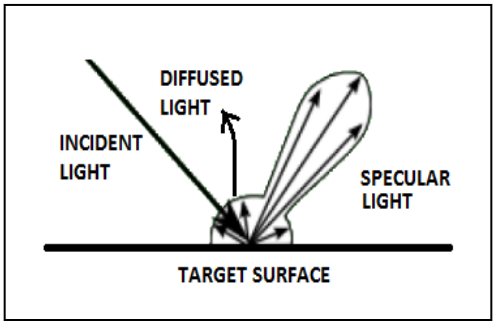

Fig. 1 Schematic of light scattering from the metallic target surface

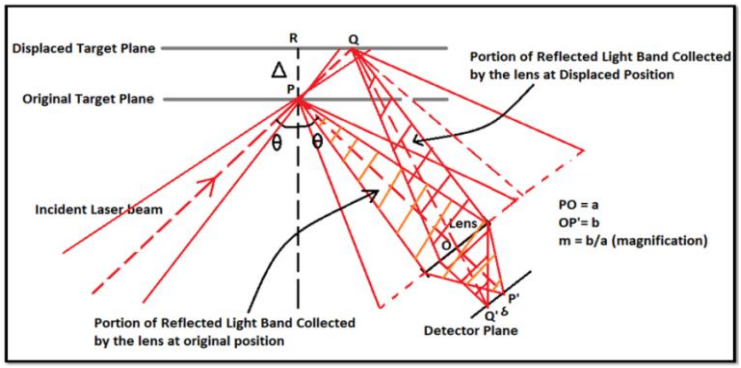

Fig. 2 Schematic of specular-reflection based position measurement

System Description & Experimental Setup

From Fig 2 the relation between target position change Δ and image position change δ is given as,

$$\Delta = \frac{\delta \times \cos\theta}{m} \quad (1)$$

Where, m = magnification of lens. For θ = 45˚, $\delta = \sqrt{2} \times m \times \Delta$ (2)

The pitch of the linear fiber array used in our system is 250 µm. This linear fiber array acts as transmitting position information to CCD where the algorithm measures the position information. Substituting the value of δ as 250 µm, we get:

$$m = \frac{176.5}{\Delta} \quad (3)$$

For Δ = 500 µm, the magnification of the system is 0.3535. The relation between a and b from Fig 2 comes out as, b= 0.3535a. Using Lens formula, focal length f comes out as 19.58 mm for a = 75 mm. For experimentation, f = 20 mm.

The experimental setup consists of the aluminium target fixed on the linear movable stage. A laser (λ = 650 nm, 2.3V, 30 mA) is inclined and focused at the target surface at an angle of 45°. From the target surface, the lens placed at an angle of 45° from the normal captures the portion of a band of reflected laser light as shown in Fig 2. This portion of reflected light is collected by the lens and is focused at the centre fiber of linear fiber array (Step Index Fiber 12 fibers of Core = 50 µm, Clad = 125 µm, Pitch = 250 µm, Numerical Aperture = 0.2, Length = 5 m). The CCD does the detection of the image spot from the individual fibers of linear fiber array at the other end. There are various techniques for measuring the centre of image spot which includes centre of intensity, least square technique, Fourier series etc. We selected Fourier series method to obtain the centroid of image spot, as it offers a robust technique for solving for the centre of a symmetric curve. The algorithm is based on the detection of the phase shift in the Fourier domain, i.e., the spatial frequency domain.

Results

An aluminium target fixed on the micrometer was displaced. As the position of target changes, there is corresponding change in the image spot position at the linear fiber array takes place via lens. The CCD camera connected to the other end of linear optical fiber array acquires the image of shifted laser spot continuously based on the change of target position. An algorithm based on Fourier series method to calculate the centroid of the laser spot. The calibration is done in terms of pixel values as shown in Fig 3 and the position of unknown target was measured as shown in Fig 4.

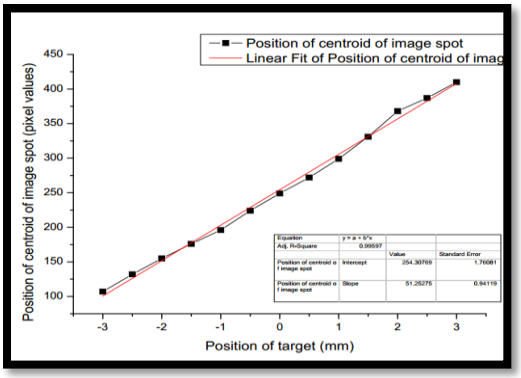

Fig. 3 Calibration Curve

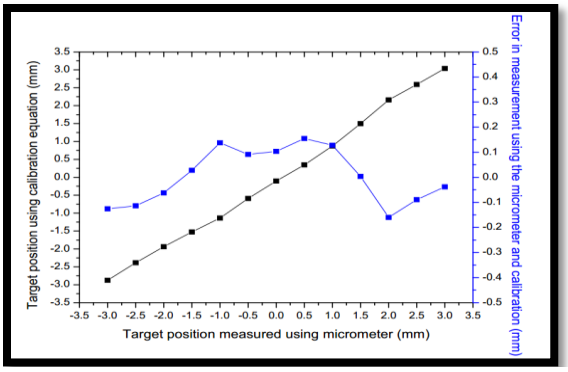

Fig. 4 Measured data after calibration along with the error

Conclusion

In this paper, specular reflection based technique for position measurement of the target is investigated. The given technique is useful for the non-contact measurement and can be used in environment with EMI and radiation. In our measurement system, the range of 6 mm with the resolution of 500 µm was achieved. The maximum error in the measurement range was 300 µm.

References

1. G. Berkovic, E. Shafir, Adv. in Optics and Photonics, 4, 441 (2012).
2. R. Dhawan, R. Shah, N. Kawade, B. Dikshit, Optik, 139, 355 (2017).
3. J. P. Fillard, Opt. Eng. 31(11), 2465 (1992).

Suppression of modulation instability by control field in a three-level quantum well nanostructure

Nitu Borgohain
Department of Physics, University of Science and Technology, Meghalaya-793101, India
Email: nituborgohain.ism@gmail.com

Abstract: In this paper, the effect of control field Rabi frequency on modulation instability of a probe field is investigated in a three-level quantum well system under an electromagnetically induced transparency regime. The system is found to be stable against modulation instability for small control field intensities whereas the growth of modulation instability gradually reduces for large intensities of the control field.

Keywords: Semiconductor quantum well, electromagnetically induced transparency, Rabi frequency, modulation instability.

Introduction

Modulation instability (MI) is a fundamental nonlinear phenomenon which is observed in diverse fields like fluid dynamics, plasma physics, nonlinear optics [1-4], etc. MI refers to an exponential growth of weak perturbations of a continuous wave resulting from interplay between the dispersion and the nonlinearity. Due to MI, in time domain, the wave disintegrates during propagation, leading to filamentation of pulse trains and in spectral domain, it results the generation of frequency sidebands around the central frequency of the pump pulse. From its discovery [5] in optical fibers, MI has been studied extensively, due to their potential applications in frequency generation, optical switching and laser techniques.

Recently, several nonlinear optical phenomena originating from quantum coherent and interference, such as, electromagnetically induced transparency (EIT), gain without inversion (GWI), slow light, Kerr nonlinearity, optical soliton etc., have been studied extensively in semiconductor quantum wells (SQW). The devices based on SQWs possess intrinsic properties like large optical dipole moments, high nonlinear coefficients and wide adjustable parameter that offer large flexibility in device design. Though, the study of MI in QWs still rare, but recently, the effects of higher-order dispersion and nonlinearity on MI in SQWs have been studied [6,7]. In this paper we have investigated the influence of control field intensity on MI gain spectrum of a weak probe field, results of which may have important applicability in nonlinear optics.

Theoretical Framework

For this study, a three-level asymmetric double quantum well (ADQW) system, same as referred in [8], which is depicted in Fig. 1(a). The system consists of two GaAs QWs of thickness 6.4 nm and 3.5 nm, respectively, which are separated by a 1.5 nm tunnel barrier. On the left hand side of the wide well, there is a 1.0 nm AlGaAs barrier followed by a 36 nm thick AlGaAs layer. On the right hand side of the narrow well, there is a 1.5 nm AlGaAs barrier. A weak probe pulse of angular frequency ω_p couples the transition $|1\rangle \rightarrow |3\rangle$ and a strong continuous wave control beam of angular frequency ω_c couples the transition $|2\rangle \rightarrow |3\rangle$, in a Λ-type excitation scheme.

Here, adopting density matrix formalism, under rotating wave approximation, and proceeding with same process as described in [7], the standard nonlinear Schrödinger equation governing the evolution of the probe pulse is obtained

$$i\frac{\partial\tilde{\Omega}_p}{\partial z} - \frac{1}{2}\beta_2\frac{\partial^2\tilde{\Omega}_p}{\partial T^2} + W\left|\tilde{\Omega}_p\right|^2\tilde{\Omega}_p = 0, \tag{1}$$

where $\tilde{\Omega}_p$ is envelope of the probe field, associated with probe field Rabi frequency $\Omega_p \left(=\frac{\mu_{13}E_p}{\hbar}\right)$, E_p is the probe electric field and μ_{13} is the dipole moment for $|1\rangle \rightarrow |3\rangle$ transition. The term β_2 is group velocity dispersion (GVD) which accounts for the dispersion contribution to the propagating wave. We ignored third-order dispersion term, since it has no contribution to MI [7]. The term W represents the nonlinear coefficient. Both β_2 and W are the functions of probe field detuning Δ_p, control field Rabi frequency $\Omega_c \left(=\frac{\mu_{23}E_c}{\hbar}\right)$, and decay rates γ_{21} and γ_{31}, detail expressions of which can be found elsewhere [7].

The modulation instability of the probe field has been investigated via a standard approach [9], where a steady-state solution, with small perturbation contribution to the amplitude is considered, which leads to a dispersion relation

$$K^2 + \beta_2|\mathrm{W}|\mathrm{P}_0\Omega^2 - \frac{1}{4}\beta_2^2\Omega^4 = 0, \tag{2}$$

where P_0 is the input power of the continuous wave. The MI gain, at any frequency of perturbation Ω, is defined as $g(\Omega) = 2 \times \text{Imaginary part of } (K)$ which can be written as

$$g(\Omega) = 2\left(\beta_2|\mathrm{W}|\mathrm{P}_0\Omega^2 - \frac{1}{4}\beta_2^2\Omega^4\right)^{1/2}. \tag{3}$$

We are now in a position to investigate the MI spectra, with emphasis to the effect of control Rabi frequency.

Results and discussion

For this investigation, the system parameters are taken as follows: Carrier density $N = 10^{24}\ m^{-3}$, dipole moment $\mu_{13} = 20.0 \times 10^{-29}\ mC$, probe frequency $\omega_p = 26.0 \times 10^{13} s^{-1}$, decay rates $\gamma_{21} = 1.0 \times 10^{12} s^{-1}$ and $\gamma_{31} = 0.5 \times 10^{12} s^{-1}$. MI results from the interplay between dispersion and nonlinearity. Using equation (3), we have investigated the effect of different values of control filed Rabi frequencies (Ω_c) on MI of the probe field, which are depicted in Figure 1(b). Panel (i) of Fig. 1(b) depicts that the MI gain for $\Omega_c/\gamma_{21} = 1.0$, possess a gradual increase of the gain with increase in power P_0. Interestingly, in panel (ii) of Fig. 1(b), which depicts the MI gain at $\Omega_c/\gamma_{21} = 1.9$, it is seen that though the gain increases with power, but the spectral width has reduced. Panel (iii) of Fig. 1(b) depicts the MI growth for $\Omega_c/\gamma_{21} = 3.5$, where it is seen that, the gain reduces in comparison to the previous cases, but the width of the MI spectrum increases. In panel (iv) of Fig. 1(b), which has been plotted for $\Omega_c/\gamma_{21} = 4.0$, reveals that though the gain is minimum, but the spectral distribution is still significantly large. Therefore, the control field Rabi frequency plays a significant role in the growth of MI.

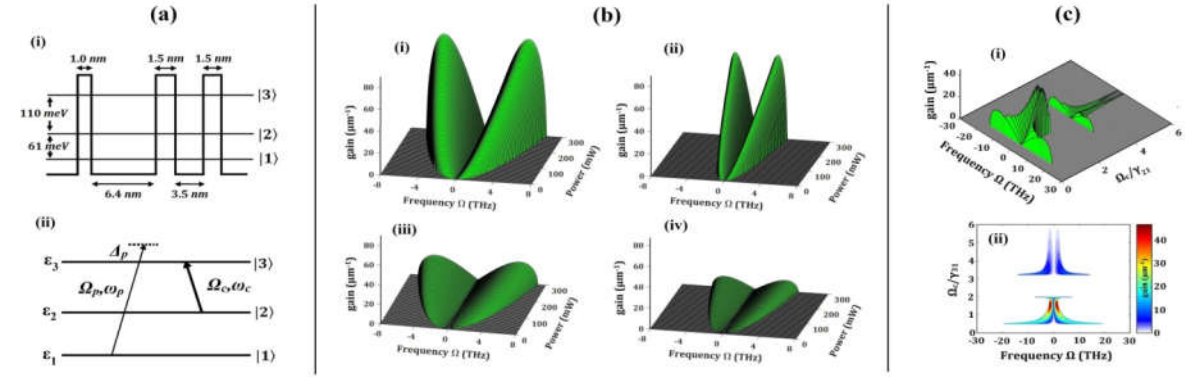

Figure 1: ***(a)*** *The MQW adopted in this study. (i) Conduction band energy level diagram of a single period of MQW, and (ii) Λ-type excitation scheme of the MQW.* ***(b)*** *Modulation instability gain spectra as functions of instability frequency Ω and input probe powers, at four different values of Ω_c/γ_{21}: (i) $\Omega_c/\gamma_{21} = 1.0$, (ii) $\Omega_c/\gamma_{21} = 1.9$, (iii) $\Omega_c/\gamma_{21} = 3.5$, (iv) $\Omega_c/\gamma_{21} = 4.0$.* ***(c)*** *Modulation instability gain spectra as functions Ω and Ω_c/γ_{21}: (i) Variation of instability gain, and (ii) 2D contour plot representing the distribution of MI spectrum at different values of Ω_c/γ_{21}.*

In order to have a clear picture how MI behaves at different control field Rabi frequencies at a fixed power, we have plotted Fig. 1(c). Panel (i) of Fig. 1(c) depicts the MI gain spectra for a series of control field Rabi frequencies (Ω_c) at a fixed power $P_0 = 200$ mW. It is evident form panel (i) that for small values of Rabi frequencies, such as $\Omega_c/\gamma_{21} \lesssim 0.5$, the MI is absent. The instability start developing at around $\Omega_c/\gamma_{21} \gtrsim 0.5$, and disappears again for $\Omega_c/\gamma_{21} \approx 2.0$ to 3.0. From $\Omega_c/\gamma_{21} \approx 3.0$ onwards, the MI gain spectra gradually decreases. For better clarity, we present the spectral distribution of MI gain with control field Rabi frequencies in the form of 2D contour plots in panel (ii) of Fig. 1(c). From the contour plot in panel (ii), it is seen that, MI gain possess wider spectra at around $\Omega_c/\gamma_{21} \approx 0.5$ and ≈ 3.2, whereas gain maximize at around $\Omega_c/\gamma_{21} \approx 1.5$. For smaller values $\Omega_c/\gamma_{21} \lesssim 0.5$, and mid-values $\Omega_c/\gamma_{21} \approx 2.0$ to 3.0, the probe field remains stable against MI. For larger values $\Omega_c/\gamma_{21} \gtrsim 5.0$ the MI gain gradually suppressed. Thus, the control field Rabi frequency has a great control over modulation instability of probe field.

Conclusion

To conclude, it is shown that the control field Rabi frequency has a great influence on the modulation instability of a probe field, interacting in a three-level asymmetric double quantum well system. The probe field remains stable against modulation instability for particular values of control filed Rabi frequencies. This investigation may have potential applications in optoelectronic devices made from semiconductor quantum well systems.

Acknowledgment: Author thanks Sri M. Hoque, Chairman, USTM for financial and moral support. Author specially acknowledges Prof. S. Konar, BIT, Mesra, Ranchi for his encouragement.

References

[1]. T. B. Benjamin, J. E. Feir, J. of Fluid Mech. 27 417 (1967).
[2]. Y. H. Ichikawa, T. Suzuki, T Taniuti, J. Phys. Soc. Jpn. 34, 1089 (1973).
[3]. G. P. Agrawal, Nonlinear fiber optics, 5th ed, Academic Press, California, (2013).
[4]. V. E. Zakharov, L. A. Ostrovsky, Physica D 238, 540 (2009).
[5]. A. Hasegawa, Opt. Lett. 9, 288-290 (1984)
[6]. S. Swetanshumala, S. Konar, A. Biswas, Appl. Phys. B 111, 53-64 (2013).
[7]. N. Borgohain, S. Konar, J. of Appl. Phys. 119, 213103 (2016).
[8]. H. Sun, S. Gong, Y. Niu, S. Jin, R. Li, Z. Xu, Phys. Rev. B 74 155314 (2006).
[9]. R. V. J. Raja, K. Porsezian, and K. Nithyanandan, Phys. Rev. A 82, 013825 (2010).

Wavevector distribution of Fluorescence and SERS in a Film Coupled Plasmonic Nanowire Cavity

Sunny Tiwari[1,#], Adarsh B Vasista[1], Harsh Jog[1], Tal Heilpern[2], Mathew E Sykes[2], Deepak K Sharma[1], Shailendra K Chaubey[1], Gary P Weiderrecht[2], Stephen K Gray[2], G V Pavan Kumar[1,3]

[1]Deaprtment of Physics, Indian Institute of Science Education and Research, Pune-411008, India

[2]Center for Nanoscale Materials, Argonne National Laboratory, Argonne-60439, USA

[3]Center for Energy Science, Indian Institute of Science Education and Research, Pune-411008, India

[#]Email address: sunny.tiwari@students.iiserpune.ac.in

Abstract

The emission properties of the molecules confined in a cavity can be very different compared to their behaviour in an isolated homogenous environment. The emission rate as well as their emission direction can be tuned depending on the magnitude and polarization of the local electric field present in the cavity. Here in, we discuss the effect of an elongated one dimensional plasmonic cavity, silver nanowire placed on a gold film, on the molecular emission from the gap between nanowire and the film [1]. The Nile blue molecules, present in the cavity give both surface enhanced Raman scattering and fluorescence signals, which overlap in the wavelength or energy domain. But when studied in the momentum space of the outcoupled emission, surface enhanced Raman scattering and fluorescence outcouple at different wavevectors. The fluorescence of the molecules was mainly confined to higher values of in-plane wavevectors, whereas the SERS signal was distributed along all the wavevectors.

Keywords

Fourier microscopy, energy-momentum spectroscopy, SERS, plasmons

Acknowledgments

Authors thank Ms.Vandana Sharma and Ms.Chetna Taneja for helpful discussions.

Reference list

- Differential Wavevector Distribution of Surface-Enhanced Raman Scattering and Fluorescence in a Film-Coupled Plasmonic Nanowire Cavity.

Adarsh B Vasista, Harsh Jog, Tal Heilpern, Mathew E Sykes, Sunny Tiwari, Deepak K Sharma, Shailendra K Chaubey, Gary P Weiderrecht, Stephen K Gray, G V Pavan Kumar, Nano Lett.,2018,18(1), pp 650-655

Reorientation Dynamics of avian Red Blood Cells in an Optical Trap

Praveen P[1], Nagesh B V[2] , Shruthi S Iyengar[1], Chetana D[1], Ashwini Bhat[1],
B M Veeregowda[3], Sarbari Bhattacharya[1] and Sharath Ananthamurthy[4,1]*

[1]Department of Physics, Jnanabharathi Campus, Bangalore University, Bangalore 560056
[2]Department of Physics, M S Ramaiah Institute of Technology, MSR Nagar, MSRIT Post, Bangalore 560054
[3]Department of Veterinary Microbiology, Veterinary College, Hebbal, Bangalore 560024
[4]School of Physics, University of Hyderabad, Hyderabad 500046
email:sasp@uohyd.ac.in.com

Abstract

We report here on the reorientation dynamics of the avian Red Blood Cell (aRBC) a structure ellipsoidal in shape and which has a non-uniform distribution of birefringence across its diameter. We find that in linearly polarized light, an aRBC shows a dual reorientation behaviour with the first reorientation about the major axis and the second about the minor axis so as to align its major axis along the laser propagation direction. Under circularly polarized OT, about 70% of the trapped cells showed both first and second flips and the rest showed only the first flip. The dynamics under elliptically polarized light reveals that the extent of the second flip depends on the degree of ellipticity of the polarized light.

Keywords:

Avian Red Blood Cells, Optical Tweezer, Polarization of light, Reorientation-dynamics

Introduction

Any asymmetric microstructure maximizes its volume along the region of highest electric field when trapped in an Optical Trap (OT) [1]. Furthermore, if the trapped object is birefringent along with being asymmetrically shaped, then, apart from maximizing its volume along the region of highest electric field, the optic axis of the trapped micro-object also becomes aligned along the linear polarization direction. In a previous study [2], we found that a human Red Blood Cell which is biconcave in shape and birefringent, acquires an edge-on orientation with respect to the laser beam propagation direction, and subsequently, stays rotationally bound to the linear polarization direction. In another study carried out by us previously, we showed that avian red cells which have an overall ellipsoidal shape are also birefringent and have a contrasting distribution of the birefringence across the cellular volume when compared with the human RBC [3]. Therefore, it is interesting to investigate the trapping dynamics of aRBC under OTs of different polarizations.

Experimental Details

The details of the setup used by us is discussed elsewhere [2]. Briefly, we used a 1064nm laser that was focused down to a diffraction-limited spot using an oil-immersion objective of Numerical Aperture 1.4. The trapped micro-objects were imaged using a camera of resolution 2.1MP run at 15 frames per second. Blood sample was collected aseptically from the wing vein of an adult layer chicken into an equal volume of Alsever's solution and was washed twice at 2000 rpm using a table top centrifuge. The washed aRBCs were stored at 4˚C by adding 2ml of sterile Phosphate Buffered Saline (PBS) of pH 7.4. About 10µl of this solution was suspended in 1.5ml of PBS solution. About 10µl of this solution is further diluted with 400µl of PBS and loaded in a sample holder made by sticking an o-ring of diameter 1 cm and thickness 1mm on a glass slide. The sample holder was slightly overfilled and another glass slide was kept on top to make the whole arrangement air-tight.

Results and Discussion

a) Linearly Polarized Laser

The reorientation dynamics of an aRBC is captured in the sequence of images in Fig. 1.1 and 1.2. An aRBC shows a dual reorientation in a linearly polarized OT with the I reorientation about the major axis and the II reorientation about the minor axis so as to align its major axis along the beam propagation direction in the final equilibrium orientation.

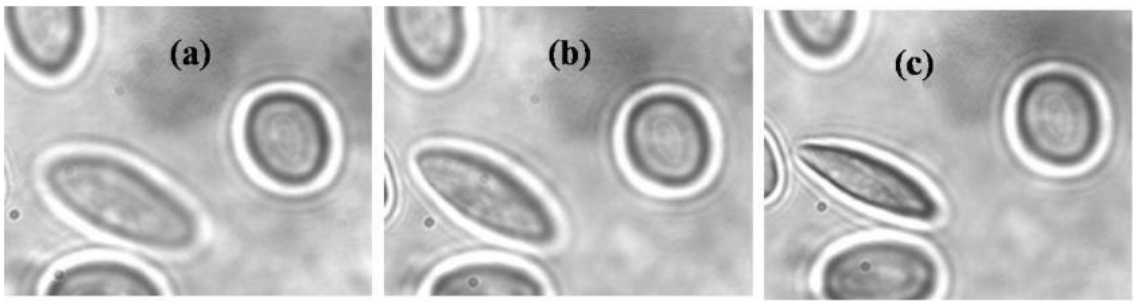

Fig1. An aRBC reorienting about the major axis. Frames (a) and (b) are separated by about 0.56s and (b) and (c) by about 0.49s

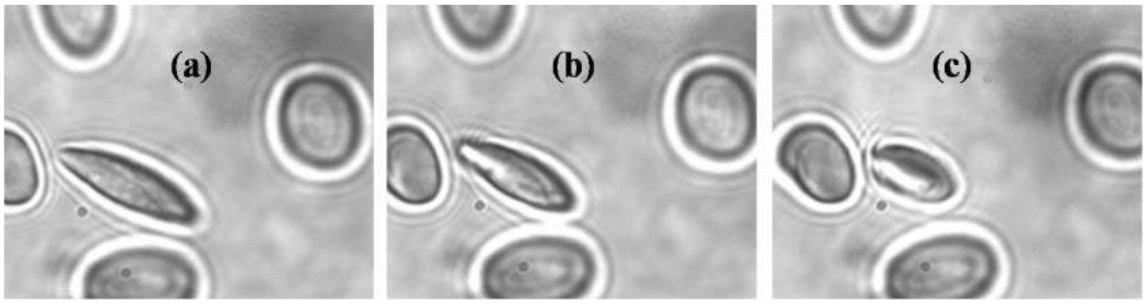

Fig2: aRBC shown in Fig 1 continues to show a further reorientation, this time, about a perpendicular to the plane of the aRBC. Frames (a) and (b) are separated by about 0.84s and (b) and (c) by about 1.47s

In [4], we explain the observed reorientation sequence by means of comparing the work done by the laser torque against the drag experienced by a reorienting cell in each of the possible reorientations of the aRBC.

b) Circularly Polarized Laser

We find that, amongst the trapped cells only 70% show both I and II reorientations and the remainder show only the I reorientation. These results need further exploration with cell populations segregated according to their age so as to take into consideration subtle change in the chemical composition and the consequent changes in refractive index, changes in shape and the consequent changes in the birefringence distribution and furthermore the influence of the shape-dependent drag coefficient.

c) Elliptically Polarized Light

We find that we are able to control the extent of the II reorientation in elliptically polarized OT by controlling the degree of ellipticity of the laser polarization. We are able to infer a II reorientation through an angle $< 90^{\circ}$ by comparing the cross-section of the trapped cell under elliptically polarized light with the case of a cell trapped with linearly polarized light. Similar results were obtained in [4] Understanding these results would require modelling with careful considerations of the cell shape, size and the birefringence distribution across the cell volume and the consequent competition between shape and birefringence induced torques. This work is currently underway.

Acknowledgements

The authors acknowledge the DST Nano-mission for a previous grant under which most of the equipment was bought. PP acknowledges UGC and SSI DST for student grants.

References

1. Z. Cheng, P. M. Chaikin and T. G. Mason, Phys.Rev.Lett., 89, 108303, (2002)
2. Parthasarathi P et.al., J. Biomed. Opt., 18(2), 025001, (2013)
3. Nagesh B V et al., J. Biomed. Opt., 19(11), 115004 (2014)
4. R. C. Gauthier, M. Ashman and C. P. Grover, App. Opt., 38(22), 4861 (1999)

Delay Time Calculations for Digitally Tunable Optical Filter System

Anirudh Banerjee,
Centre of Photonics and Opto-Electronics & Department of Electronics and Communication,
Amity School of Engineering and Technology,
Amity University, Uttar Pradesh, Lucknow, India.
anirudhelectronics@yahoo.com

Abstract: Delay time calculations for the wavelengths of a 12 channel digitally tunable optical filter system are presented. This method of finding delay time can be used to analyse the timing performance of the system and optimising the system performance by decreasing the wavelength routing lengths. The method can be expanded for any number of wavelengths to be filtered.

Keywords: Optical Filter; Digitally Tunable; Delay Time; Routing

1. Introduction

Tunable optical filter system is one of the most important subsystems of any optical communication network. These filters can dynamically choose the wavelengths to be transmitted by using a tuning mechanism or selection system. The selection system routes the desired wavelength to the output while blocks all other wavelengths. One of the most popular selection systems is electrical tuning system which offers high speed and computer compatibility and controllability. Recently, a digitally tunable optical filter system [1] was designed for wavelength selective switching based optical network, in which selection of output wavelengths was done by giving combinations of '0' and '1' at the inputs of SOAs (Semiconductor Optical Amplifiers). The filter system used 2 splitters, 12 two-by-two (2×2) wavelength-selection elements with thin-film filters, 7 SOAs and 1 four-by-one (4×1) combiner. The selected wavelength reached at the combiner output after transmission and/or one or more reflections from the wavelength selection elements. The idea presented in that work [1] used lesser number of SOAs in comparison to other digitally tunable filter systems [2]. This work presents delay time calculations for different wavelengths transmitted through that system. These delay time calculations can be used to analyse the timing performance of the system.

2. Theory and Calculations

By looking into the paths followed by each wavelength between input SOAs and output SOAs in reference [1], the delay time equations can be written as

$$t_{\lambda 1} = t_t + t_f \tag{1}$$

$$t_{\lambda 2} = t_{r\lambda 2\lambda 1} + t_t + t_f \quad (2)$$

$$t_{\lambda 3} = t_{r\lambda 3\lambda 1} + t_{r\lambda 3\lambda 2} + t_t + t_f \quad (3)$$

$$t_{\lambda 4} = t_{r\lambda 4\lambda 1} + t_{r\lambda 4\lambda 2} + t_{r\lambda 4\lambda 3} + t_t + t_f \quad (4)$$

$$t_{\lambda 5} = t_t + t_{r\lambda 5\lambda 1} + t_f \quad (5)$$

$$t_{\lambda 6} = t_{r\lambda 6\lambda 5} + t_t + t_{r\lambda 6\lambda 2} + t_f \quad (6)$$

$$t_{\lambda 7} = t_{r\lambda 7\lambda 5} + t_{r\lambda 7\lambda 6} + t_t + t_{r\lambda 7\lambda 3} + t_f \quad (7)$$

$$t_{\lambda 8} = t_{r\lambda 8\lambda 5} + t_{r\lambda 8\lambda 6} + t_{r\lambda 8\lambda 7} + t_t + t_{r\lambda 8\lambda 4} + t_f \quad (8)$$

$$t_{\lambda 9} = t_t + t_{r\lambda 9\lambda 5} + t_{r\lambda 9\lambda 1} + t_f \quad (9)$$

$$t_{\lambda 10} = t_{r\lambda 10\lambda 9} + t_t + t_{r\lambda 10\lambda 6} + t_{r\lambda 10\lambda 2} + t_f \quad (10)$$

$$t_{\lambda 11} = t_{r\lambda 11\lambda 9} + t_{r\lambda 11\lambda 10} + t_t + t_{r\lambda 11\lambda 7} + t_{r\lambda 11\lambda 3} + t_f \quad (11)$$

$$t_{\lambda 12} = t_{r\lambda 12\lambda 9} + t_{r\lambda 12\lambda 10} + t_{r\lambda 12\lambda 11} + t_t + t_{r\lambda 12\lambda 8} + t_{r\lambda 12\lambda 4} + t_f \quad (12)$$

where $t_{\lambda n}$ is the delay time for the nth wavelength between input and output SOAs; the values of 'n' are [1] $n = 1,2,3.....12$; $t_{r\lambda n\lambda m}$ is the time taken by the nth wavelength to go into the wavelength selection element for λ_m center wavelength, and coming back after reflection; t_t is the time taken by the nth wavelength in passing through the wavelength selection element with λ_n center wavelength; t_f is the time taken by the λ_n wavelength in passing through the fibers.

If $t_{r\lambda n\lambda m} = t_t = t_f = 10ps$ for $n = 1,2,3.....12$ and $m = 1,2,3.....,12$. The calculated delay times are $t_{\lambda 1} = 20ps$, $t_{\lambda 2} = 30ps$, $t_{\lambda 3} = 40ps$, $t_{\lambda 4} = 50ps$, $t_{\lambda 5} = 30ps$, $t_{\lambda 6} = 40ps$, $t_{\lambda 7} = 50ps$, $t_{\lambda 8} = 60ps$, $t_{\lambda 9} = 40ps$, $t_{\lambda 10} = 50ps$, $t_{\lambda 11} = 60ps$ and $t_{\lambda 12} = 70ps$. The average delay time for the system is $45ps$.

3. Conclusion

The delay time calculations for all wavelengths of a recently proposed 12 channel digitally tunable optical filter system are given. This method of calculating delay time can also be used in similar type of systems to analyse the timing performance of the system and to optimise the system performance by decreasing the wavelength routing lengths. The method can be expanded for any number of wavelengths to be filtered.

References

[1] A. Banerjee, S.K. Awasthi, U. Malaviya and S.P. Ojha, J. Opt. Netw. 4, 691 (2005).

[2] X. Li, J. Chen, G. Wu, and A. Ye, Opt. Express 13, 1346 (2005).

Quasi-distributed strain and temperature sensing using four in-line multiplexed Fiber Bragg Gratings.

Koustav Dey, Sourabh Roy, B. Ramesh Kumar, M. Sai Shankar, P. Kishore

Abstract

The ability to serially multiplex Fiber Bragg Grating (FBG) sensors provides advantage for monitoring quasi distributed sensing. With over a decade of development, researchers have devised three main techniques for serial multiplexing of FBG sensors. Of them, wavelength division multiplexing (WDM) is the first form of multiplexing explored for the FBG sensor and most prominent technique in serial multiplexing. Here, we demonstrate the multiplexing of FBG sensors for quasi-distributed monitoring using WDM techniques. We have taken four *in-line FBGs* with different characteristic central wavelength placed in various points of the measurand fields (Strain and temperature). Among the four FBGs, two are used for measuring temperature and remaining two for measuring strain. The experiment has been repeated for different combinations of FBGs for strain and temperature sensing simultaneously. We achieved good linearity of 0.999.

Keywords:

Fiber Bragg Grating; Multiplexing; Distributed sensing; WDM; Optical fiber.

Introduction:

FBGs have been shown to measure an array of various measurands such as temperature, pressure, stress/strain, etc. [1]. FBGs are mostly used for quasi-distributed measurement of strain and temperature. Here, we propose a method of multiplexing FBGs for distributed sensing. The whole area of sensing can be divided in some matrix segments. Hence a wavelength division multiplexing scheme can be opted and signal can be detected with interrogator [2]. For this purpose four in-line FBGs with different characteristic central wavelength have been placed in various points of the measurand fields (strain and temperature). Eventually, the corresponding wavelength shift of four in-line FBGs due to temperature and strain are noted using interrogator.

Experimental Details:

An array of four in-line FBGs of central wavelength of ~1512nm (FBG1), ~1520 nm (FBG2), ~1528 nm (FBG3) and ~1536 nm (FBG4) respectively have been taken for distributed monitoring. Among these four FBGs, at first FBG1 and FBG4 are deployed for temperature sensing while FBG2 and FBG3 for sensing strain. For sensing the temperature, the FBGs are kept on heater plate connected with a dimmer-stat for controlling temperature and for strain sensing the FBGs are pasted on cantilevers, connected with strain gauge circuits. The experiment has been repeated for different combinations of FBGs for strain and temperature sensing simultaneously. The temperature range from 25^0C -90^0C with 5 degree step interval and applied loads from 50gms to 700 gms with 50 gms step interval are considered for this experiment. Initially for measurement temperature of 25^0C and load of 50gms were taken, then temperature raised with 5^0C interval and loads with 50gms interval. For measuring strain a *full bridge* strain gauge circuit was used.

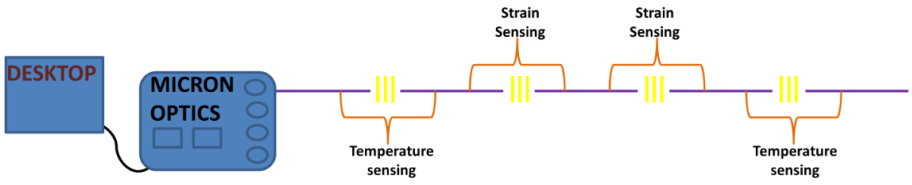

Fig.1 Schematic of experimental setup

Koustav Dey
National Institute of Technology, Warangal
Physicskoustav@gmail.com
Dr. Sourabh Roy
National Institute of Technology, Warangal
sroy.physics@gmail.com

Results:

The graphs between temperatures vs. Wavelength shift and strain vs. Wavelength shift have been drawn. For measuring Strain, loads are converted to strain using the formula $E_0 = (\frac{E}{4}) * K_s * \varepsilon_0$. Where E_0=bridge o/p voltage (mV). E = Excitation Voltage; K_s=sensitivity (~2); ε_0 = Strain ($\mu\varepsilon$). For temperature sensing as the temperature is increased the wavelength shift also increases correspondingly (Fig. 2 (a) & (b)).For strain sensing, as the loads are increased the wavelength shift is also increasing accordingly but with negative slope (Fig. 2 (c) & (d)) Because, as the output voltage of strain gauge circuit decreases with increasing loads. Further the output voltage is proportional to strain. As a result we got negative slope. The experiment has been repeated for different combinations of FBGs for strain and temperature sensing simultaneously

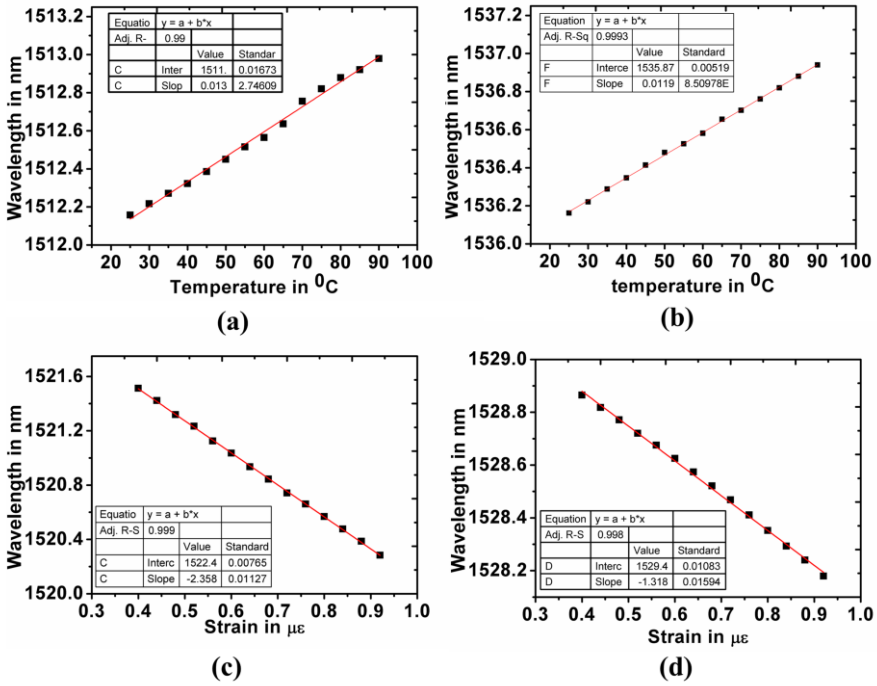

Fig.2 (a) and (b) Wavelength shift with temperature, (c) and (d) Wavelength shift with Strain.

Conclusions:

We achieved very good linearity of 0.999. This scheme of multiplexing is very prominent in simultaneous measurement of strain and temperature for distributed monitoring. The obtained results of strain and temperature measurements from this scheme perform better with respect to existing method.

Acknowledgement:

The authors are highly grateful to BRNS (RS-872-GoI-BRNS (DAE)-SR-PHYSICS (2017-18)), for their Funding**.**

Reference:

[1] Y.J. Rao, Meas. "In-fiber Bragg grating sensors'' Sci. Technol. 8, 355-357 (1997)

[2] A.D. Kersey, T.A. Berkoff , W.W. Morey., "Multiplexed fiber Bragg grating strain-sensor system with a fiber Fabry-perot wavelength filter '' Optics Letter, 18, 16 (1993)

[3] Marcel Fajkus, Isa Navruz et al. "capacity of wavelength and time division multiplexing for quasi distributed measurement using fiber Bragg Gratings'' Optics & optoelectronics, 13,5 (2015)

OSI-ISO 2018 manuscript No.
(33)

Optically induced multipole switching in toroidal metasurface

Manoj Gupta[1,2], and Ranjan Singh[1,2]

[1] Division of Physics and Applied Physics, School of Physical and Mathematical Sciences, 21 Nanyang Link, Singapore 637371
[2]Centre for Disruptive Photonic Technologies, The Photonics Institute, Nanyang Technological University, 21 Nanyang Link, Singapore 637371

E-mail: ranjans@ntu.edu.sg

Abstract

Metasurface consisting of resonator array integrated with active element, could enable switching between various modes of multipole excitations with respect to incoming radiation. Switching toroidal excitation to fundamental electromagnetic excitation provides an innovative approach of implementing multifunctional features in a single device. Toroidal dipole, which is visualized as the currents flowing on the surface of torus along its meridians, offers weak electromagnetic scattering compared to the electric and magnetic dipoles, plays an important role in tailoring the losses by radiative means. Here, we demonstrate an optical metamaterial switch that supports dynamic transition from weakly-radiative *toroidal dipole* excitation to strongly-radiative *electric* or *magnetic dipole* excitations, through optical control of active element in planar hybrid metasurface.

The unit cell design consists of a planar asymmetric resonator pair arranged in the mirrored configuration, which supports a toroidal resonance excitation. Suppressing electromagnetic resonance through silicon patches beneath the gaps of resonators in mirrored configuration, one could dynamically switch toroidal resonance to a magnetic dipole or an electric dipole resonance.

Keywords: toroidal dipole, multipole switching, metasurface

1. Introduction

Frequency dependent electromagnetic properties have facilitated in realization of state-of-the-art techniques, such as enhancing optical activity, stimulating nonlinearity, by exploiting the novel features artificially designed materials.[1, 2] Here, we like to narrow down our discussion to mainly three excitation features, which are electric, magnetic, and toroidal.

Electromagnetic spectrum of the conventional double gap symmetric SRR in the unit cell configuration of planar metasurface usually results in broad line-shaped dipole resonance, which couples strongly to free space. The moment of electric dipole lies in the plane of metasurface and is along the electric field polarization of the incoming radiation. If asymmetry is introduced by shifting one or both the gaps in SRR, then an asymmetric resonance mode with significantly narrower linewidth, known as Fano resonance, appears in addition to electric dipole resonance.[3] At this instant, current distribution in SRR is in magnetic dipole type configuration, which has projection perpendicular to the plane of metasurface. Mirroring asymmetric SRRs leads to further linewidth narrowing of asymmetric resonance due to toroidal dipole excitation, which has moment in the plane of metasurface.[4]

2. Discussion

In this active scheme, silicon layer beneath the split gap of a metallic resonator of metamaterial array acts as a active material that controls the optical properties of the hybrid metamaterial in presence of the optical pump beam. By selectively suppressing electromagnetic resonance of one or both resonators in mirrored configuration, toroidal resonance could be switched to magnetic dipole or an electric dipole resonance. In absence of optical pump, Fig 1a shows toroidal excitation in presence of terahertz pulse, having its electric

field polarization along X direction. In presence of optical pump pulse silicon shorts the gaps of one (Fig 1c) or both (Fig 1b) resonator, leading to switching of toroidal excitation to electric dipole or magnetic dipole type excitation of SRRs in metasurface array.

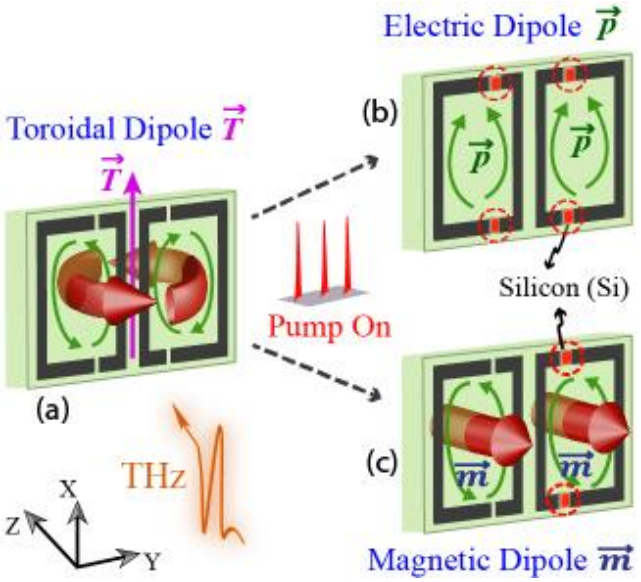

Fig. 1 Switching in the response of unit cell from (a) toroidal dipole to (b) electric or (c) magnetic dipole in presence of optical pump. Here, green arrow represents current along SRR strips, region enclosed in dotted red circle represnts optically excited silicon in split gaps. Conical red arrow shows magnetic flux due to circulating currents in SRR.[5]

Acknowledgements

This work was supported by the Singapore Ministry of Education Grant No. MOE2015-T2-2-103.

References

[1] E. Almeida, O. Bitton, and Y. Prior, Nat. Commun. **7**, 12533 (2016).
[2] B. Lee, H. Kwon, S. Kim, and F. Rotermund, Opt. Mater. Express 6, 993 (2016).
[3] R. Singh, I. Al-Naib, M. Koch, W. Zhang, Opt. Express 19, 6312 (2011).
[4] M. Gupta, R. Singh, Adv. Opt. Mater. 4, 2119 (2016).
[5] M. Gupta, Y.K. Srivastava, R. Singh, Adv. Mater 30, 1704845 (2018).

Ultrafast dual-channel switching and ultrathin superconducting metamaterials

Yogesh Kumar Srivastava[1,2], Ranjan Singh[1,2]

[1]Division of Physics and Applied Physics, School of Physical and Mathematical Sciences, Nanyang Technological University, 21 Nanyang Link, Singapore 637371, Singapore.

[2]Center for Disruptive Photonic Technologies, The Photonics Institute, Nanyang Technological University, 50 Nanyang Avenue, Singapore 639798, Singapore.

E-mail: ranjans@ntu.edu.sg

Abstract: In this work, we demonstrate all-optical dual-channel switching of sharp Fano resonances excited in superconducting asymmetric split ring resonators. Upon irradiation with optical pump, the ultrasensitive Cooper pairs in superconductor undergo dual dissociation-relaxation dynamics within a single superconductivity restoration cycle and lead to dual switching windows in picoseconds timescale. The extreme sensitivity of Cooper pairs to external perturbations enable access to such unique dual switching features, which can be readily engineered by varying the substrate properties.

Moreover, we introduce a thinnest superconducting terahertz metamaterial. We demonstrate that superconducting metamaterials of thickness 25 nm supports excitation of Fano resonances while metallic samples of identical thickness do not show any Fano resonance. Upon irradiation with optical pump, ultrathin superconducting metamaterials show extremely low threshold switching. Our results manifest new ways to realize extremely low threshold ultrafast dual channel switchable devices.

Keywords: Metamaterials, superconductors, terahertz metamaterials, ultrafast switch

1. Ultrafast dual-channel switching

Superconductors are an interesting family of materials that have attracted considerable attraction from both the fundamental and applied physics community. Superconductors possess zero DC electrical resistance and perfect diamagnetism below T_c. The unique and dramatic properties of the superconductors are attributed to the presence of Cooper pairs. Ultrafast response observed in the Cooper pair dynamics upon photoexcitation of the high-T_c cuprate superconductors is widely explored to understand the underlying physics and the mechanism which leads to Cooper pair formation. When irradiated with an optical pulse of energy higher than the binding energy of the Cooper pairs, the Cooper pairs dissociate into quasiparticles.[1] The dissociated quasiparticles reunite to form Cooper pairs again in a very short time scale of the few picoseconds. During this process, there is a large dramatic reduction in the conductivity of the superconductor.[2] The ultrafast switching between macroscopic quantum superconducting phase and the resistive phase of photo-excited cuprate superconductors can be exploited for high-speed quantum-photonic devices. Interestingly, we discovered the existence of dual dissociation-relaxation channels within a single superconductivity restoration cycle. Dual switching channels arise due to primary and secondary dissociation of Cooper pairs, which eventually results in two distinct pathways for the modulation of THz radiation at picoseconds timescale.[3] This peculiar observation leads to the discovery of superconducting dual-channel, ultrafast switchable devices which could be highly advantageous for various application in time division multiplexing, superconducting

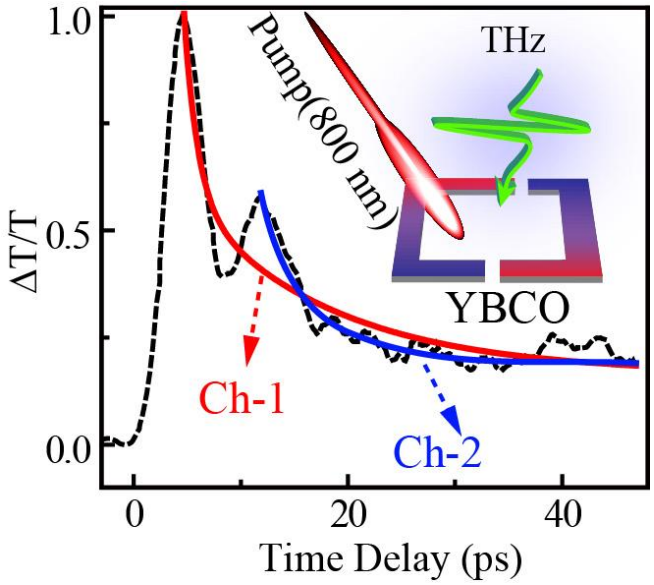

Fig.1 Schematic illustration of the dual-channel switch. Cooper pair dynamics measured using OPTP method at the optical pump fluence of 254.8 μJ/cm^2. The inset depicts the unit cell of the TASR metamaterial and artistic illustration of OPTP measurements.

photodetectors, THz high-speed wireless communication and superconducting radiation sensors.

The artistic illustration of the unit of designed asymmetric split ring metamaterial and OPTP measurement scheme is shown in the Fig. 1.[4] The metamaterials sample was fabricated using wet chemical etching of 50 nm thick YBCO film deposited over the r-cut sapphire substrate. The sample was irradiated with an optical pulse of wavelength 800 nm (1.55 eV) which has energy much larger than the binding energy of the Cooper pairs (20-30 meV) in YBCO.[5] The large change in the conductivity of YBCO metamaterial upon photoexcitation is measured in terms of the differential terahertz transmission as shown in the Fig1. The two switching channels observed in a single superconductivity restoration cycle is shown by red and blue arrows in Fig. 1. The two switching channels arise due to the primary and secondary dissociation of the Cooper pairs by an optical pulse. We also demonstrate that the optical pump fluence required to switch the Fano resonance could be substantially reduced by reducing the thickness of the YBCO metamaterial. The 25 nm thick superconducting metamaterials show strong Fano resonance which could not be achieved by identical metallic structures. The Fano resonance could be switched using extremely low fluence of the optical pump fluence.

References

1 V. V. Kabanov, J. Demsar, B. Podobnik, and D. Mihailovic, Phys. Rev. B 59 (2), 1497 (1999).

2 R. Singh, J. Xiong, K. A. Abul, H. Yang, A. T. Stuart, Q. X. Jia, J. T. Antoinette, and H.-T. Chen, *Nanophotonics* 1, 117 (2012).

3 Y. K. Srivastava, M. Manjappa, L. Cong, H. N. S. Krishnamoorthy, V. Savinov, P. Pitchappa, and R. Singh, Adv. Mater. 30 (29), 1801257 (2018).

4 R. Singh, I. A. I. Al-Naib, M. Koch, and W. Zhang, Opt. Express 19 (7), 6312 (2011).

5 T. Tom and S. Bryan, Rep. Prog. Phys. 62 (1), 61 (1999).

Formatting instructions for abstract/short paper submission by Authors

Plasmonic Cylindrical Nanoshell and Its Sensing Applications

Alexander A. Iskandar
Physics of Magnetism and Photonics Research Division
Institut Teknologi Bandung
Jl. Ganesa 10, Bandung 40132, Indonesia
Email: iskandar@fi.itb.ac.id

Abstract

Stimulated by the discovery of the large field enhancement due to the localized surface plasmon resonance (LSPR) effect of a metal nanoparticle, nanoplasmonic sensing has over the last two decades rapidly evolved into an important subject of major research interest. Metal nano particles and nanostructures have been reported to offer a wide field of applications ranging from refractive index sensing to biomedical applications. For those applications a large variety of nano metallic systems have been introduced, ranging from single metal nano particle (MNP), various configuration of MNPs, to MNP of more complicated shapes. Among the large variety of MNPs proposed in the research literature, the MNPs of core–shell structures have attracted growing research interest. It allows the introduction of an additional parameter of shell thickness invoking the plasmon hybridization (PH) effect between inner and outer surface plasmons, as well as the core size giving rise to the cavity dependent effects. This structure therefore offers increased sensing tunability. Further, a symmetry breaking of the core-shell structure us expected to introduce additional features of the scattered wave characteristics promising among others, the potential of directed wave sensing applications.

Presented in this talk are several of our research results on cylindrical plasmonic system, including a system of metallic nanotube for complementary high-performance sensing of gases and liquids, metallic cylindrical multishell system of highly sensitive responses with large Figure of Merit and non-concentric metallic cylindrical nanoshell and its directed wave sensing performance.

Keywords

Metal Nano Particle, Cylindrical Nanoshell, Plasmonic Sensing

Acknowledgments

This work was supported by Penelitian Dasar Unggulan Perguruan Tinggi DIKTI 2017 (Contract Number 532m/I1.CO1/PL/2018) from Indonesian Ministry of Research, Technology and Higher Education.

Reference list

[1] R. N. S. Suryadharma, A. A. Iskandar and M. O. Tjia, *J. Appl. Phys.* **120** 043105 (2016).

[2] Suhandoko D. Isro, Alexander A. Iskandar and May-On Tjia, *J. Opt.* **19** 115003 (2017).

Characterization of High-sag Micro-lens by Digital Holography Technique using an Index Matching Polymer

Amit K. Agarwal, Om Prakash Naraniya, and Ajay Kumar
Instruments Research and Development Establishment, Dehradun-248008, INDIA

Abstract: Characterization of micro-lenses can be performed by interferometry based digital holography technique. However, Nyquist sampling criteria limits the dynamic range of this technique and so this technique cannot be used for surfaces with high slope, i.e. fast lenses. In this work results are presented on high-sag micro-lens characterization by submerging the micro-lens in a near index-matching polymer which reduces the effective phase slope and improves dynamic range of the digital holography technique.

1. Introduction

Digital Holography (DH) [1,2] is a very versatile technique which has been used in recent times to characterize the surface profile of Micro-optical components [3, 4]. Different geometrical parameters of a micro-lens such as surface profile, focal length, sag, diameter, radius of curvature (ROC), f-number and NA can be measured either directly or indirectly by DH technique. For characterization of high-sag micro-lens the change in phase across the cross-section of the micro-lens is fast enough. To reduce the sampling points to less than the Nyquist sampling criteria which limits applicability of DH technique for high-sag or fast micro-lens. By submerging these micro-lenses in a near index matching polymer, effective focal length of the micro-lens can be increased. This gives lesser effective phase change and therefore sufficient number of sampling points for the given detector for charaterization of fast micro-lens (small f-number).

2. Theory

In comparison to the other techniques, DH gives quantitative phase estimates of the object which can be translated to a surface profile map if the refractive index of the material is known. In DH, the interferogram produced by the object wave and reference wave is recorded by a camera. The angle (θ) between the object wave and reference wave is related to the fringe period (Δ) and wavelength of operation (λ) by the relation

$$2\Delta \sin\left(\frac{\theta}{2}\right) = \lambda \tag{1}$$

The lower limit of the angle (θ) in Eq. (1) is determined by the maximum frequency content of the object. The upper limit of the angle given by Eq. (1) is determined by the Nyquist sampling criterion which states that the sampling frequency should be at least twice as much as the maximum signal frequency. The upper limit due to Nyquist criteria limits the use of this technique for characterization of high-slope phase surfaces like fast microlenses. However, if a suitable near index matching polymer is used to submerge the micro-lens under test, the effective phase slope is reduced and it makes the characterization of the fast micro-lens possible. In this work, an additional layer of poly di-methyl siloxane (PDMS) is introduced, on the top surface of micro-lens. This leads to less refraction of light as shown in Fig. 1 and the effective focal length can be written as

$$f_{eff} = \left(\left(\frac{R_C}{n_s - 1} \right)^{-1} + \left(\frac{R_C}{n_l - 1} \right)^{-1} \right)^{-1} = \frac{R_C}{n_s - n_l} \tag{2}$$

where, R_C, n_s and n_l are ROC, refractive indices of micro-lens and cured polymer, respectively. The effective focal length is increased by the factor of $(n_s - 1)/(n_s - n_l)$ and phase difference between the vertex to edge of the micro-lens is reduced by the same factor.

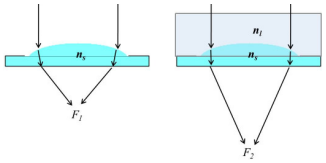

Fig.1: Increase in effective focal length of micro-lens by submerging it in a polymer of near matching refractive index n_l.

3. Experimental Setup

A Mach-Zehnder interferometer setup was used to record digital holograms. As shown in Fig.2, a collimated laser beam is split into two plane waves and recombined through the use of two mirrors and two beam splitters. The object (micro-lens submerged in polymer) is placed in the object arm of the interferometer and it interferes with the

reference arm on second beam splitter. Since, the micro-lenses are small in diameter, a 10X objective is placed in object arm and the same matching 10X objective is placed in reference arm to nullify the phase introduced by this objective. The interference pattern is imaged onto a CMOS camera.

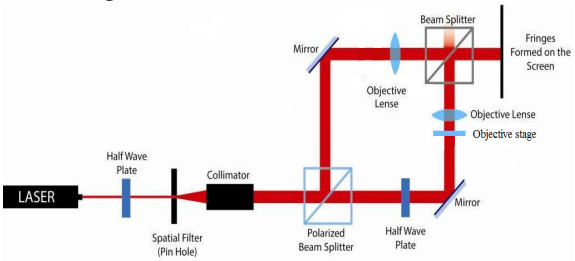

Fig.2: Schematic of the experimental setup used for DH based approach for characterization of high-sag (fast) microlenses.

The sample is a commercial micro-lens with ~ 0.8 mm diameter and ~ 70 µm sag on a 1 mm thick BK7 substrate. PDMS is mixed with its curing agent and poured over micro-lenses. The sample is degassed and cured at 80 deg C for 6 hrs. The refractive index of cured PDMS is 1.45 and it almost matches with the refractive index of BK7. As shown in Fig. 1, this leads to an increase in effective focal length of micro-lenses and so the fringes in the hologram can be sampled easily by the detector.

4. Results and Discussion

The recorded hologram of micro-lenses before and after submerging in PDMS is shown in Fig. 3(a) and 3(b). The phase profile can be reconstructed by Fresnel's reconstruction method. It is not possible to process the hologram in Fig. 3(a) because of sub-sampled fringes due to high slope of micro-lenses. The hologram in Fig. 3(b) can be reconstructed to obtain the phase profile. Fig. 3(c) shows the experimentally measured and calculated phase profile of center micro-lens in Fig. 3(b).The sag and diameter of micro-lens are compared with their known values in Table 1. The results are also compared with simulations using Zemax software and found in good agreement.

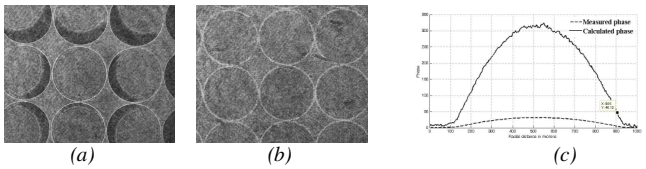

(a) (b) (c)

Fig. 3: Experimental results: (a) Recorded hologram of micro-lens before submerging in PDMS, (b) after submerging in PDMS, (c) dashed curve shows the measured phase profile of one of the micro-lens(submerged in PDMS) solid curve shows the calculated phase profile of micro-lens in air.

	Sag	Diameter
Measured by DH	68 µm	0.76 mm
Actual value	71 µm	0.80 mm

Table 1: Comparison of sag and diameter of micro-lens

5. Conclusions

A method is demonstrated for characterizing micro-lens with high-sag using DH technique. Effective dynamic range of DH was found to be improved by submerging the high-sag micro-lens in a near index matching polymer PDMS. The same experimental setup and reconstruction technique can be used for measuring phase profile of high-sag micro-lens.

6. Acknowledgements

Authors are thankful to Director, IRDE for permitting to publish this work.

7. References

[1]. U. Schnars and W. Juptner, Digital Holography: Digital Hologram Recording, Numerical Reconstruction, and Related Techniques, Springer, Ist Ed. (2004).

[2]. M. Paturzo, V. Pagliarula, V. Bianco, P. Memmolo, L. Miccio, F. Merola, and P. Ferraro, "Digital Holography: A metrological tool for quantitative analysis: Trends and future applications" *Opt. Lasers in Eng.* 104, 32-47, (2018)

[3]. F. Charrire, J. Khn, T. Colomb, F. Montfort, E. Cuche,Y. Emery, K. Weible, P. Marquet, and C. Depeursinge, "Characterization of microlenses by digital holographic microscopy," *Appl. Opt.*, 45 829-835, (2006).

[4]. F. Merola, L. Miccio, S. Coppola, V. Vespini, M. Paturzo, S. Grilli, and P. Ferraro, "Exploring the capabilities of Digital Holography as tool for testing optical microstructures," *3D Res.* 2, 1-8, (2011).

Performance Evaluation of Super-Resolution Algorithms in Multiaperture Imaging Camera

Arun Kumar[a]*, O. P. Naraniya[a], Unnikrishnan G[b], and Ajay Kumar[a]

[a]Instruments Research and Development Establishment, Dehradun-248008, INDIA
[b]Defence Institute of Advanced Technology, Pune, INDIA
**Author e-mail address:arunkumar@irde.drdo.in*

Abstract: In this paper the multiple low resolution images obtained from a Multiaperture camera have been used to reconstruct a scaled up high resolution (HR) image using the Super-resolution algorithm. In a Multiaperture camera each channel provides the degraded image on which a mathematical operation was done to estimate the degradation function to achieve deblurred images, and to fuse them together shift and add operation is used. The experimental results from the implementation of the developed algorithm on a Multiaperture camera are presented and the image quality compared by detecting sharpness in frequency domain with other methods.

1. Introduction

The performance of multiaperture imaging system is limited by either the detector or the optics depending on whether the angular resolution of the optics exceeds the Instantaneous Field of View (IFOV) of the detector or not [1]. For the case when diffraction effects due to the finite aperture of opticslimits the performance of the imaging system, one needs to use larger aperture optics. When detector limits the performance, one needs to use detector with smaller pixel pitch and more number of pixels. Often this leads to increased cost or there are technological limitations. An alternate approach to overcome the limitations of the detector is to use signal processing techniques to generate a scaled up image with enhanced resolution by using multiple images shifted relative to each other by a fraction of the detector pixel pitch which is referred to as Multiframe super resolution technique. The super resolution (SR) image reconstruction is an inverse problem. In multiaperture imaging system the HR image undergoes blur degradations mainly due to limited aperture size of the optics resulting in a loss of information and also due to additive noise. This makes it an ill posed problem.
In this paper, the developed algorithm presented and compared the image quality compared by detecting sharpness in frequency domain in real world situation.

2. Theory

The essential ingredients of any super-resolution image reconstruction mainly are the estimation of the HR image by upsampling onto an HR grid by taking samples from subpixel shifted LR images and correct for imaging channel degradations. Many of the SR algorithms proposed earlier, perform the above two tasks in a single step. In cases where they are performed separately, the LR images are fused together after appropriate shifts (shift estimated beforehand) and the images so obtained is corrected for degradation assumed to be known a priori.

In a departure from the above approaches, here the above two tasks are performed in two separate and independent steps. In the first step that is done separately for each channel, the degradation function (assumed to be unknown) and the images corrected for degradation are estimated simultaneously for each channel using an iterative optimisation technique. In the second step, the estimated image of each channel is fused together to generate a single HR image.
The fusing of the images is done by shifting the images and adding in such a way that the Total Variation of thefinal image is maximised. This approach has the following advantages: 1) since the degradation function estimation and correction is done separately for each channel, there is flexibility to assume a different degradation function for each channel; .2) since the shift and add operation is done as a separate step, any errors in shift estimation is limited only to this step.

3. System description

The Multiapertue imaging camera optics comprises of a 5x5 array of Microlenses. Each microlens has a diameter of 0.8mm and a focal length of 4mm. The lens array is placed at a distance of 4mm from a CMOS sensor with 1024 x1280 pixels and pixel pitch 5.2 µm x 5.2 µm. A window of 950x950 pixels was used on the raw image from the detector as the 5x5 array of images from the Microlens array falls on 1024x1280 pixels of the detector. The entire image of 950x950 pixels was segmented into 5x 5 equal regions which give 25 LR images. The center image is taken as reference image.

4. Experimental results and discussion

The results obtained from the Multiaperture camera are shown in Figs. 1 for the object statue. The object was about 50cm high and about 30cm wide placed at a distance of 2.7m from the camera alongwith a few smaller objects placed in front of the statue at varying distances with the farthest object at about 30cm in front of the statue. Figs. 1(a),1(b) and 1(c) show a frame grabbed by the Multiaperture camera, the LR image that corresponds to the center lens in the array interpolated by a factor of 2 using cubic spline interpolation and the HR image scaled up by a factor of 2 and estimated using the algorithm developed in this paper respectively.

The performance of the developed super-resolution algorithm is compared with two regularised optimisation methods proposed in Ref. [1]. This method referred to as Method I, in which L2 norm is used as data fidelity term and the regularisation term is the Tikhanov regularisation. The results were obtained using codes available in public domain [2]. The parameters used for Method I are: Regularisation factor-0.05, Number of iterations-20, Step size-8, Regularisation kernel 1/16 [1 1 1;1 -8 1;1 1 1], deconvolution kernel-gaussian low pass filter of size 5x5. The results obtained using the Method I are given in Fig. 1(d). A No reference Image quality metric defined in the frequency domain [3] was used to compare the methods.The metric was calculated as follows: The two dimensional Fourier Transform of the image is performed. The Image quality metric in the Fourier domain is determined by finding the number of pixels that has the absolute value of the Fourier Transform greater than a threshold value normalised by the total number of pixels. The threshold is chosen as the 1/1000 of the maximum value of the absolute value of Fourier transform. The Frequency domain Image quality metric effectively determines the spread of the Fourier spectrum. The Fourier spectrum spread will be more if the image has higher spatial frequency content. The thresholding operation makes the metric less sensitive to noise as compared to other spatial domain image quality metric like Variance. Table 1 gives the values of the Fourier domain Image quality metric of the LR image; the HR is image estimated by the method developed here in as well as Method I for statue as object.

The algorithms were tested with real world objects illuminated with white light. The 25 images in the array had different intensity levels and different SNR. The outermost images had poorer SNR as compared to the center image as the outermost lenses in the array received less light as compared to the center lens.

	LR image	Present Method	Method I
Statue	0.0353	0.0509	0.0368

Table 1: Comparison of the developed method with two other methods based on no reference frequency domain image quality Metric

(a) (b) (c) (d)

Fig. 1. (a) A frame grabbed by the Multiaperture camera of size 950x950 pixels (b) LR image that corresponds to the center lens in the array interpolated by a factor of 2 to size 200x320 pixels (c) HR image of size 200X320 pixels reconstructed using the method presented in the paper.(d) Image reconstructed by Method I

5. Conclusion

In conclusion, it may be observed that the proposed method gives better results as compared to the other two methods. This is also reflected in the values of Frequency domain image quality metric given in Table 1. The result shows that the algorithm performs robustly in real world situations.

6. Acknowledgements

Authors are thankful to Director, IRDE for permitting to publish this work.

7. References

[1] . M. Elad, and A. Feuer, "Restoration of single super-resolution image from several blurred noisy and down-sampled measured images,"IEEE Trans. Image Processing, vol. 6, pp. 1646-1658, Dec. 1997.

[2]. https://users.soe.ucsc.edu/ milanfar/software/superresolution.html

[3]. K. De and V. Masilamani, "Image sharpness measure for blurred images in frequency domain", Procedia Eng., vol. 64, pp. 149-158,2013.

Angular Roughness Measurement of Metal Surfaces using optical reflection of TE and TM polarized light

Tania Das[1] and Kallol Bhattacharya[2]

[1]*Department of Electronics and Communication Engineering, Heritage Institute of Technology, Chowbaga, Kolkata 700107, India.*
[2] *Department of Applied Optics and Photonics, University Of Calcutta, JD block-2 , Sector-III, Kolkata 700098,India.*

[1]*taniadas.physics@gmail.com*

Abstract: The present work proposes a non-contact optical polarization based technique for determining surface roughness of metal surface. The sample is mounted on a prism, illuminated by a linearly polarized collimated light beam and two intensity frames are digitally recorded with specific orientations of an analyzer. The pair of intensity data frames captured with this simple setup is combined through an algorithm developed for the purpose, assuming that the refractive index of the sample is known, to find the phase difference between the transverse electric and transverse magnetic components which preserve the information about surface roughness.

Keywords: Surface Roughness, Phase, Polarization, Refractive Index.

1. Introduction

Surface roughness is defined as the repetitive and random deviation from the nominal surface that forms the three dimensional topology of the surface. Roughness measuring techniques can be divided into two broad categories such as (i) a contact type such as mechanical stylus method and (2) a noncontact type such as different optical methods [1, 2].The present work proposes and demonstrates a simple non contact optical two-frame non-interferometric technique for measuring surface roughness. The theory behind this technique is optical reflection from metal surface. Here roughness is measured in terms of phase change associated with the reflected TE and TM polarization states of light from the rough sample. The difference of phase between these orthogonal states of polarization is indicative of the angle at which light is reflected from the sample, and hence leads to measurement of the surface profile.

2. Theory, Equation and Experimental Set Up

The phases φ_s and φ_p for transverse electric (s-polarized) and transverse magnetic (p-polarized) polarized light respectively, due to reflection at the interface of dielectric metal medium having refractive indices n_1 and n_2, (n_2=n+ik) can be expressed as[3]

$$\phi_p = \tan^{-1}\frac{2v\cos\theta_1}{u^2+v^2-\cos^2\theta_1} \tag{1}$$

$$\phi_s = \tan^{-1}\frac{2v\cos\theta_1(n^2-k^2-2u^2)}{u^2+v^2-(n^2+k^2)^2\cos^2\theta_1} \tag{2}$$

Where,

$$u^2 = \frac{1}{2}\left[\left(n^2-k^2-\sin^2\theta_1\right)+\left\{\left(n^2-k^2-\sin^2\theta_1\right)^2+4n^2k^2\right\}^{\frac{1}{2}}\right] \tag{3}$$

$$v^2 = \frac{1}{2}\left[-\left(n^2-k^2-\sin^2\theta_1\right)+\left\{\left(n^2-k^2-\sin^2\theta_1\right)^2+4n^2k^2\right\}^{\frac{1}{2}}\right] \tag{4}$$

The phase difference φ_{diff} between the p-polarized and s-polarized components and can be expressed as

$$\phi_{diff} = \phi_p - \phi_s \tag{5}$$

From Eqns. 1-5 it may be observed that the phase difference between the s and p components is a function of refractive indices n_1 and n_2 as well as incident angle θ_1. So, for a rough metal surface where the surface normal varies continuously, the phase variation occurs due to variation of incident angle assuming that the metal has an uniform refractive index. Fig.1(a) represents the experimental set up. Here USAF target used as a sample where we have attempted to evaluate the surface roughness of the Chromium coating on glass as shown in Fig 1(b). Two intensity data frames are recorded on a CCD with the transmission axis of the output polarizer (LP2) oriented along 45^o and 135^o so that the s and the p components are added in-phase and out-of-phase respectively. From these data frames the phase change associated with the height change due to surface roughness can be determined using an algorithm and can be expressed as [4]

$$\phi_{diff} = \cos^{-1}\left(\frac{I_{45^0}-I_{135^0}}{I_{45^0}+I_{135^0}}\right) \tag{6}$$

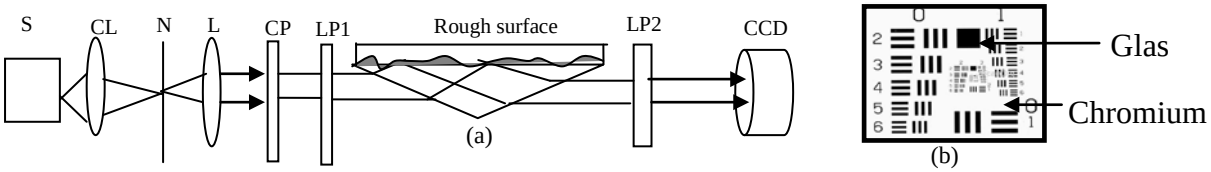

Fig.1.(a).Schematic diagram of the experimental in-line setup. Source= LED, CL=Condenser Lens, N=pin hole, L=Lens, CP=Circular Polarizer, LP1=linear polarizer with 45^0 angle, LP2=Linear Polarizer, CCD=Charge coupled Device. (b) USAF target used as sample.

3. Result and Discussion

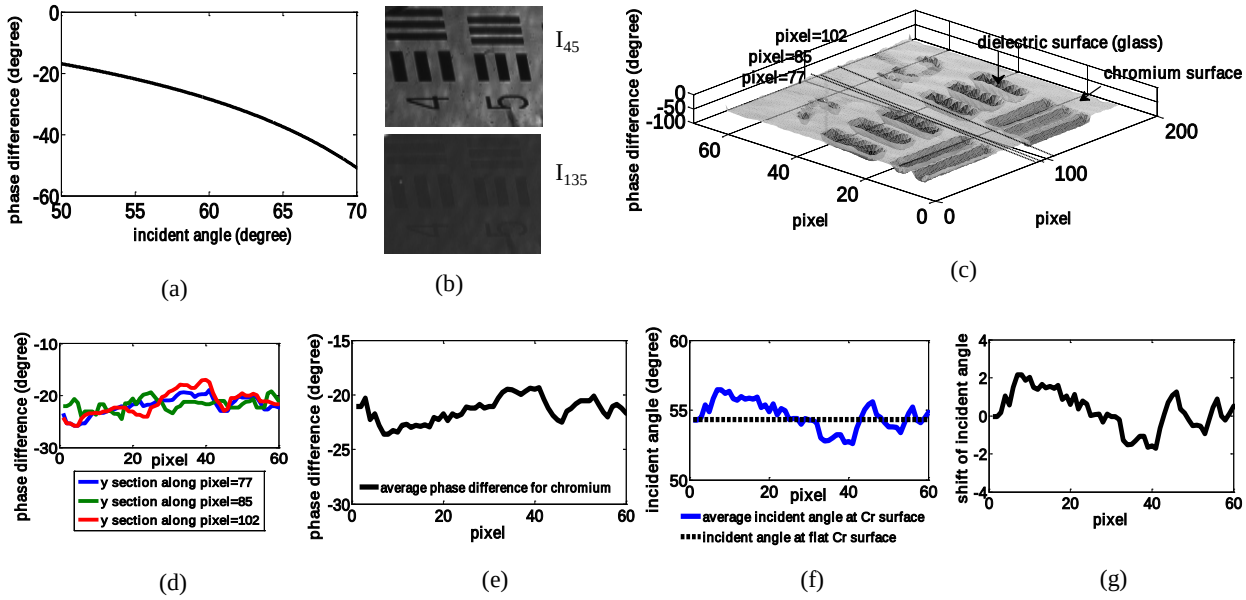

Fig.2. (a) Calibration curve for determining surface roughness for Cr (n=3.1399,k=3.3150). (b) Two intensity data frames I_{45} and I_{135} recorded by CCD (c) 3D phase profile of sample (d)2D phase profile along y section along rows of pixels (e) average phase difference for sample (f) variation of incident angle due to presence of surface roughness (g) Deviation of incident angle due to surface roughness from the nominal surface incident angle.

Two intensity data frames I_{45}^0 and I_{135}^0 are recorded as shown in Fig.2 (b). The 3D phase profile is reconstructed from these intensity data frames is shown in Fig.2(c). Fig 2(d) and 2(e) represent the 2D variation of phase difference along the y section of 3D profile. Assuming that refractive indices are constant for prism (n_0=1.518), oil (n_1=1.721) and metal (n_2=n+ik=3.1399+i3.3150) the only factor responsible for the variation in φ_{diff} is variation of incident angle on the metal surface. Using the calibration curve shown in Fig.2(a), the phase difference change can be converted into variation of incident angle and this is shown in Fig.2(f). Fig.2(g) represents the deviation of incident angle due to surface roughness from the nominal surface incident angle.

Alternatively, for an optically flat metal surface, its complex refractive index may be easily determined.

5. References

1. H.G. Rhee, Y.W. Lee, I.W. Lee, and T.V.Vorburger , *'Roughness Measurement Performance Obtained with Optical Interferometry and Stylus Method'*, Journal of optical society of Korea,Vol. 10(1),pp48-55(2006).
2. Z.Yilbas,M.Hasm,*'Surface roughness measurement using an optical system'*, Journal of Materials Processing Technology,Vol.88(1-3) 88, pp10-22,1999.
3. M.H Chiu, J.Y.Lee, and D.C.Su,*'Complex refractive-index measurement based on Fresnel's equations and the uses of heterodyne interferometry'*, Applied Optics, Vol38 (19), 1999.
4. T. Das, K.Bhattacharya, *"Refractive index profilometry using Total Internally Reflected light field"*, J.Applied Optics, Vol.56 (33), 2017

Investigations on self-healing property of Bessel Gaussian and Gaussian Beam propagation through Pseudo Random Phase Plate mimicking atmospheric turbulence

Mohamed Yaseen[1], PramodPanchal[2] and C S Narayanamurthy[2]

[1]*Department of Physics, National Institute of Technology, Warangal, India*

[2]*Applied and Adaptive Optics Laboratory, Department of Physics, Indian Institute of Space Science and Technology(IIST), Valiamala(PO), Trivandrum – 695547, India*

**Corresponding author: nyaseen14@gmail.com, pramod.panchal25@gmail.com and naamu.s@gmail.com*

Abstract: In this paper we study and investigate the Self-healing tendency of Gaussian and Bessel-Gauss beams when it propagates through Pseudo Random Phase Plate (PRPP) mimicking atmospheric turbulence. We find that atmospheric turbulence distorts Bessel beams to a lesser extent when compared with variations and distortion of Gaussian beam.

Keywords: Bessel-Gaussian Beam, Zernike Polynomial, Pseudo Random Phase Plate, Atmospheric Turbulence.

INTRODUCTION:

The ability of the optical beam to recover its initial amplitude or intensity profile after encountering an obstacle is dubbed as self-reconstructing [1]. Study of such phase fluctuations of the incident beam when it propagates through a turbulent atmosphere has substantial interest in free space optical communication, imaging through optical turbulence and quantum optics [1,2].

The beam from a He-Ne laser source is considered as Gaussian beam. A Gaussian beam is beam of monochromatic electromagnetic radiation whose transverse amplitude distributions are of Gaussian functions. The optical distributions of laser beams and the modal field distributions of optical waveguides with special index profiles may be Gaussian [3]. On the other hand, Bessel beam was originally proposed by Durnin [4] as a solution of scalar Helmholtz equation containing an infinite amount of power. The complex amplitude of Bessel beam is given as,

$$U(r,\phi,z=0) = J_1(k_r,r)\exp\left(-r^2/\omega_0^2\right)\exp(il\phi)$$

Where J_l denotes the lth order Bessel function of the first kind, k_r is the radial component of the wavevector with wavenumber $k = 2\pi/\lambda$ and w_o is the waist of the Gaussian beam [2]. The two fascinating features of Bessel beam are its transverse intensity profile through their entire free space propagation i.e. non-diffracting propagation and self-healing ability. Although ideal Bessel beams with infinite energy cannot be generated experimentally, approximations to Bessel beams are made in practice by focusing a Guassian beam with an axicon lens (Lens with a conical surface which transforms a laser beam to a ring shaped distribution) to generate Bessel-Gauss beams [5].

EXPERIMENTAL PROCEDURE

The schematic of Fig. 1, shows the double passage geometry of the experiment to measure the Self-healing of Bessel – Gaussian (BG) beams. A He-Ne laser source generating a TEM_{00} wave field of wavelength 633nm and 75mW power is attenuated using Neutral density filters as the Shack-Hartmann Wavefront Sensor (SHWFS) and Charge-Coupled Device (CCD) not sensitive to high powers. The TEM_{00} wave field is then allowed to propagate through an axicon lens of physical angle 1 degree. The optical beam coming out of the axicon lens is called as Bessel-Gaussian beam. Then the BG beam is allowed to propagate through a turbulent atmosphere by using PRPP (Pseudo Random Phase Plates) which introduces phase fluctuations by the rotation of glass plate, where the speed of rotation can be controlled by external micro-controller. The beam from PRRP is made to strike on the mirror where the reflected beam again experiences an atmospheric turbulence and directed to the beam splitter. It should be noted here that the source is now considered at the beam splitter, SHWFS and CCD are successively kept at distance (d) ranging from 5cm to 15cm from the beam splitter. The beam view and wave front variation of the beam is captured at various distances from beam splitter using CCD and SHWFS respectively. Instantly the speed of the rotation of PRPP is increased from 0 to 6000 rotations per minute and the variation in beam view is captured using CCD.

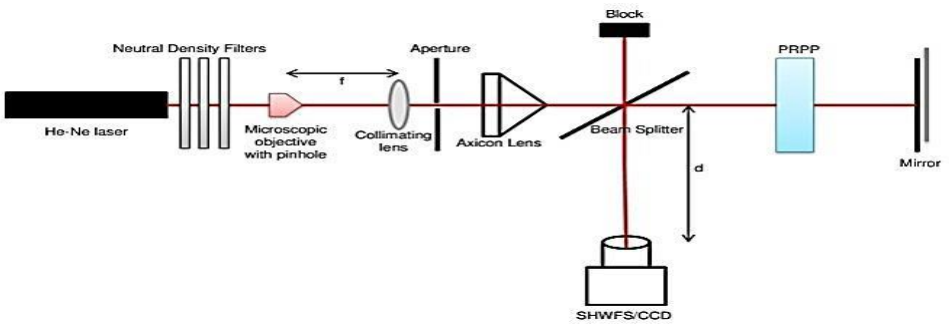

Fig.1 Double Passage geometry of GB beams with turbulence.

Now the PRPP from the experimental setup is slowly removed and BG beam is made to propagate in the free space without any atmospheric turbulence and its variation in wavefront at various distances is captured using SHWFS and CCD. To measure the self-healing tendency of Gaussian beam, axicon lens from the geometry shown in Fig.1 is removed from the setup and same procedure is repeated.

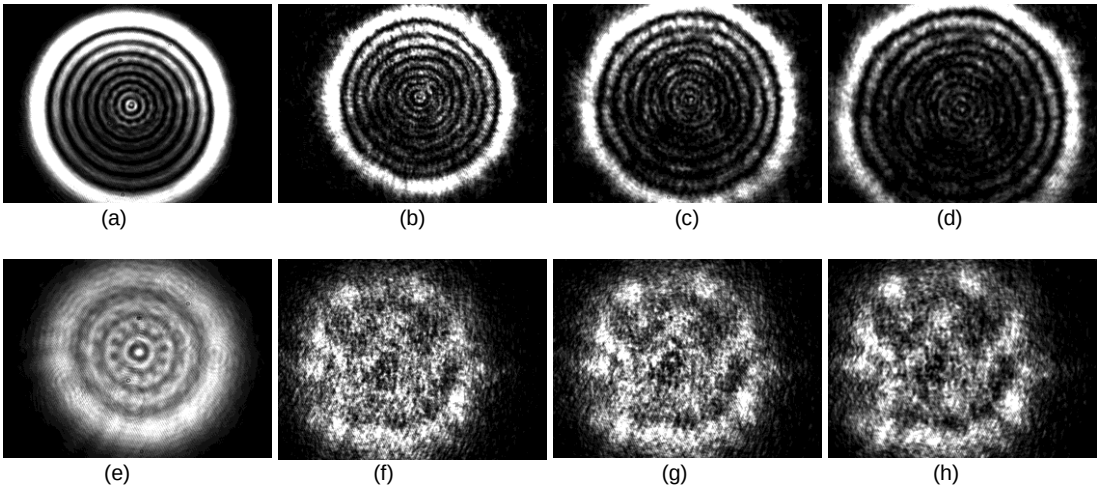

Fig.2 CCD shots of optical beams. (a) and (e) represents BG and Gaussian beams without turbulence respectively. (b),(c),(d) and (f),(g),(h) represents BG and Gaussian beams with turbulence at distances 5cm,10cm,15cm from beam splitter respectively.

RESULTS AND ANALYSIS:

Fig. 2 depicts the propagations of optical beams after encountering atmospheric turbulence at various distances which are instantly captured by CCD. On comparison with undistorted beam it is clearly visible from the results that the BG beams self-heals rapidly and retains its shape almost similar to that of free space propagating beam , whereas the Gaussian beam distorts abruptly as it propagates in a turbulent atmosphere. Figures 3(a) and 3(b) shows the variations of Zernike polynomial with respect to their index profile i.e. type of aberrations; it is clearly evident that variation in optical aberrations of BG beams is comparatively less than Gaussian beams at varying distances.

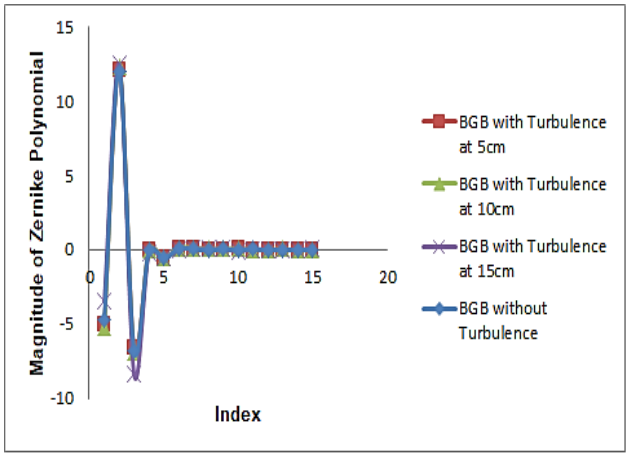

Fig.3 (a) Plot of Zernike polynomial vs aberrations of BG beams

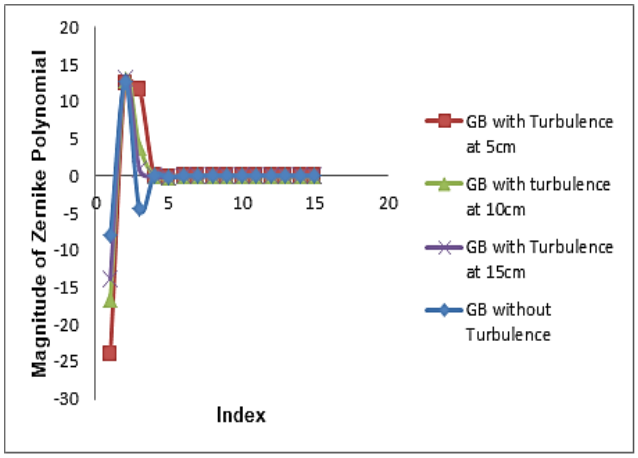

(b) Plot of Zernike polynomial vs aberrations of Gaussian beams

CONCLUSIONS:

As the variation of Zernike polynomial for BG beams remains almost the same for beams with turbulence at varying distances and beam view recorded by CCD distorts to a lesser extent when compared with variations and distortion of Gaussian beam, we could conclude that Bessel beams self-reconstructs itself when it propagates through an atmospheric turbulence. The future scope of our research work is to study the twist parameter of the incident beam while propagating though a turbulent atmosphere using variance matrices, as it is widely used in quantum optics.

REFERENCES:

[1] Andrea Aiello, Girish S. Agarwal (2015) https://arxiv.org/abs/1501.05722
[2] Nokwazi Mphuthi, Roelf Botha and Andrew Forbes, JOSAA, Vol.35, No.6 (2018)
[3] Keqian Zhang, Dejie Li, Electromagnetic Theory for Microwaves and Optoelectronics (Springer-Verlag Berlin Heidelberg , 2008), pp. 577-620
[4] J.Durnin, J.J. Miceli, Jr, J.H. Eberly, Optics Letters, Vol.13, No.2 (1988)
[5] Peng Li, Yi Zhang, Sheng Liu, Huachao Cheng, Lei Han, Dongjing Wu, and Jianlin Zhao, Optics Letters, Vol.25, No.5 (2017)

Antireflection coating simultaneously effective in LRF and CCD systems

Anil Kumar, S. K. Singh, A. S. Upadhyay and Suman Awasthi

Thin Film Division, Instruments Research & Development Establishment (IRDE), Dehradun

Corresponding Author:

Anil Kumar, e-mail: bansal_anil@irde.drdo.in

Abstract

In the present course of work, a high efficiency dual band anti-reflection coating on BK7 optics is reported for CCD (486-656nm) and 1535nm laser range finder (LRF) systems. The two layer design has been developed using HfO_2 and SiO_2 as high and low index materials. The sample was fabricated by physical vapor deposition in a high vacuum coating plant with EBG source. The design was fabricated by simplex method and the developed coating has high transmission and environmental stability as per MIL-C-48497. The coated sample was measured by double beam spectrophotometer (Perkin Elmer, lambda- 950) giving 99.7% and ~96.8% transmission for 1535nm and CCD range, respectively.

Keywords

CCD, anti-reflection coating, spectrophotometer, EBG, refractive index

Experimental Details

BK7 glass is a highly homogeneous optical glass with refractive index 1.51 and is used in large scale in the optical industry for fabricating optical components. In light matter interaction, the incident light splits into reflection, transmission and absorption components depending upon the optical properties of the material. The transmission of polished bare BK7 glass is ~ 91.6%, rest of the optical energy is reflected back as reflection component as there is negligible absorption. Anti - reflection coating is an essential requirement for using any optical glass components in instrumentation applications to minimize the reflection losses.

The general trend in developing anti-reflection coating for a single wavelength is to deposit alternate layers of high and low refractive index materials of $\lambda/4$ optical thickness with λ as the design wavelength. The same is not true if one has to develop an anti-reflection coating for two different wavelength bands or two distinct wavelengths far apart. For developing such a coating, a multilayer coating has to be designed. In this work, a dual band anti-reflection coating has been developed using only *two alternate layers of high and low indices*. SiO_2 and HfO_2 were selected as low and high index materials for developing the AR coating on BK7 substrate for better performance. The film has been designed and the process of optimization was carried out by simplex method with Macleod thin film design software for various different refractive index materials. The optimized design gave a solution with overall layer thicknesses less than half wave optical thickness @ 1535nm for BK7 glass. The transmission of BK7 could further be enhanced by using MgF_2 as low index material instead of SiO_2 at the cost of lower laser damage threshold.

The coating was fabricated using electron beam gun (EBG) evaporation technique on HHV coating unit 300 BC on BK7 substrate. The substrate was fixed in a dome shaped substrate holder which rotates on its axis for ensuring the thickness uniformity of the deposited thin film layers. Initially the chamber was evacuated up to a pressure of 2×10^{-6} mbar. The temperature of the chamber was raised to 250^{o} C (with tolerance of $\pm 5^{o}$ C) before starting deposition. Alternate layers of HfO_2 and SiO_2 were deposited on the substrate in oxygen atmosphere at a pressure of 2.5×10^{-4} mbar. The ambient conditions like temperature and pressure were kept constant while depositing the layers.

Results and Conclusion

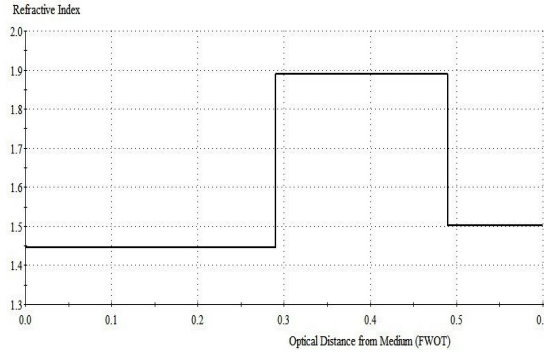

Fig. 1 Refractive index profile of the ARC design

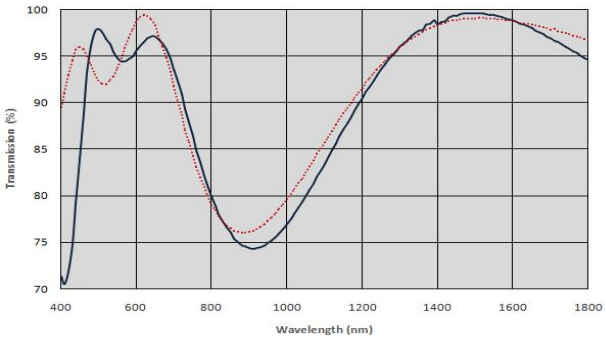

Fig. 2 Designed (dashed) and experimental (solid) transmission curve of dual band ARC BK7 sample

The transmission was measured by Perkin-Elmer, lambda 950 spectrophotometer. A 99.7% transmission @ 1535nm wavelength and an average of ~ 96.8% in CCD region (486-656nm) were obtained for both side coated sample (sample thickness = 3mm). It is also concluded that higher refractive index substrate gave better efficiency in terms of transmission both in CCD and 1535nm range. This optimized thicknesses of layers save time, material and also enhances the durability and coating stability. The deposited films have been tested for stability in accelerated environmental conditions; the coating has been found to pass MIL-C-48497 tests. The achieved optics has a high laser damage threshold estimated to be 500MW/cm^2.

Acknowledgments

Authors are highly grateful to Director, IRDE for his support and motivation for the present course of work.

References

- W H Southwell, App Opt. 24, (1985) 457
- Ronald R. Willey, Practical design of thin films, 4th edn. (Willey optical consultants, Charlevoix, 2014), pp. 375–377
- H. Angus Macleod, Thin film optical filters, 3rd edn. (IOP publication, 2001), pp. 92-101

Optical Design of a Panoramic Lens for SWIR Camera

Vikas Dua*, R P Nautiyal, Manish Uniyal, Ranabir Mandal, P. K. Sharma
Instruments Research & Development Establishment, Dehradun - 248008
Email : vikasdua@irde.drdo.in

Abstract :-

For long range imaging applications in challenging atmospheric conditions, Short Wave Infrared (SWIR) imager has become popular over imagers exploiting visible spectrum. For getting long range performance, the optics focal length for such system will be large, which leads to a narrow field of view optics. So to cover a large area, either an array of sensors or a scanning platform is required. In this paper, the optical design of a panoramic optics is discussed where a top mirror will rotate horizontally to cover large area onto a fixed detector. The effect of image rotation because of top mirror rotation is addressed optically by using Pechan prism. The f#2.5 optics is designed for a 1280x1024 array with 10ε m pitch SWIR detector.

Key Words: Optical Design, Panoramic optics, SWIR lens.

Introduction

At long ranges and under low visibility conditions, the signal-to-noise ratio in the SWIR will be significantly better than in the visible spectrum. This advantage makes SWIR imager popular for long range applications in challenging atmospheric conditions. Though the SWIR spectral band covers 0.9 to 2.5 ε m , the 0.9 to 1.7 μm region became popular due to mature InGaAs detector technology. The wide spectral band necessitates good correction of dispersion which in turn makes the selection of lens materials very difficult. Both optical glasses as well as IR materials transmit in the SWIR spectral band. However, refractive index and dispersion values of optical glasses as well as IR materials for the SWIR band are not readily available. Use of visible optical glasses has the advantages of low density compared to IR material, low cost, high transmission and low reflection loss etc. On the other hand, IR materials have higher refractive index which facilitates better aberration correction with lesser number of lens elements. In this design, a combination of both visible optical glasses as well as IR materials was used to give overall advantage.

For getting long range performance, the optics focal length will be large, which leads to a narrow field of view optics. To cover a large area, an array of sensors can be used or the system needs to be mounted on a scanning platform. In this paper, optical design of a panoramic optics is discussed where a top mirror will rotate horizontally to cover large area onto a fixed detector.

Optical Design and Layout

The designed optics is for InGaAs detector having 1280 × 1024 array with 10μm pixel pitch. The effective focal length is 300 mm which covers a field of view of 2.44° × 1.96°. To enable the optics to work in very low light level conditions, the f number is kept 2.5.

The rotation of top mirror with respect to a fixed detector leads to the rotation of image in the focal plane. A suitable sized Pechan prism is inserted in the optics layout for de-rotation of image. The ray diagram is shown in fig 1. To cater for the chromatic aberration for such a large focal length, a catoptric module consisting of two mirrors are used to reduce the aperture followed by 6 spherical lenses of glass materials NPK51, PSF67, NLAF2, ZnS in the dioptric module.

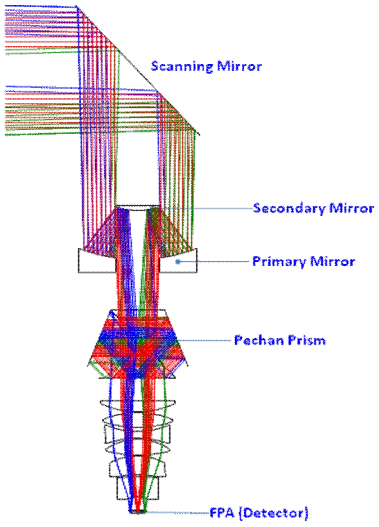

Fig. 1

Performance Evaluation

The performance of the designed system has been evaluated by MTF, Rim Ray and Field Aberration curves. The MTF plot shows that contrast is near 0.6 for on-axis field and greater than 0.3 at all other fields at 30lp/mm (Fig. 2). Despite the large spectral band, the RIM ray curves clearly depict that the transverse aberrations are within 50 µm for the rays coming at all field angles with respect to optical axis of system (Fig. 3). Field aberration curve (Fig. 4) shows that Longitudinal spherical aberration, Field curvature, Astigmatism & Distortion are also well corrected and distortion is less than 1%.

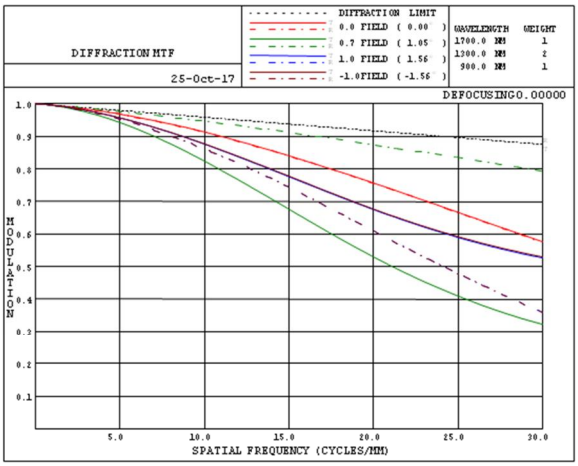

Fig 2

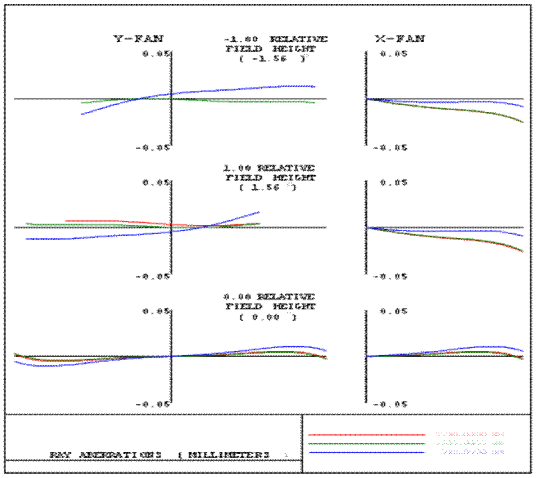

Fig. 3

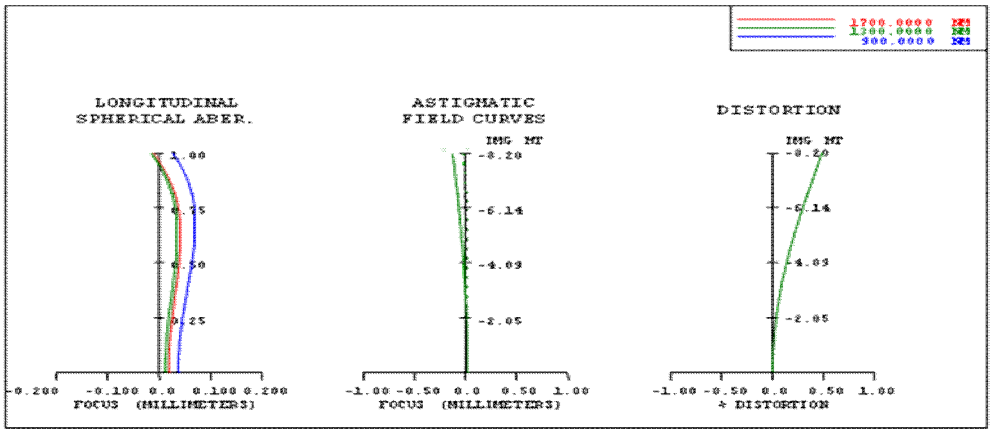

Fig. 4

Acknowledgements

Authors are thankful to the Vision Instrumentation Design Centre of IRDE for their help and valuable inputs of detector. Authors are also grateful to Group Director (Optical Engineering) and Director IRDE for their guidance, inspiration and encouragement.

References

1. Robert E. Fisher, Biljana Tadic-Galeb, ñOptical System Designò, McGraw-Hill, 2008.
2. Military Standardization Handbook, ñOptical Designò, MIL-HDBK-141, 1962
3. Drigana Peric and Branko Livada, ñ Analysis of SWIR Imagers Application in Electro-Optical Systems ñ, ResearchGate, June 2017.
4. M. P. Hansen, D. S. Malchow, "Overview of SWIR detectors, cameras, and aplications", Proc. SPIE Vol. 6939, Thermosense XXX, 2008
5. R. G. Driggers, V. Hodgkin, R. Vollmerhausen, ñWhat Good Is SWIR? Passive Day Comparison of VIS, NIR, and SWIRò, Proc. SPIE Vol. 8706, Infrared Imaging Systems: Design, Analysis, Modeling, and Testing XXIV, 2013
6. Gibbs et al. ñImaging System having a Rotatable Image ï Directing Deviceò, US Patent no. 8072482 B2, Dec. 2011

OSI-ISO 2018 manuscript No.
(42)

Surface treatment of ITO coated PET sheet for coating with optically transparent polymer

Kajal Chaudhary[1,†] · **J. Ramkumar**[1,2] · **S. Anantha Ramakrishna**[3]

Abstract Currently, ITO coated PET sheets are widely used as transparent conductive flexible films. However, the brittle nature of ITO causes it to have poor scratch resistance and hence poor handling capability leads to early failure of the electric device. We protected the ITO surface by coating it with an optically transparent and robust polymer to improve handling and scratch resistance. Before coating, the effect of UV, plasma and chemical surface treatments over ITO surface is compared using contact angle measurements. Among these, plasma surface treatment was found to be the most effective means to increase the hydrophilicity and wettability of substrate without any noticeable degradation in optical properties. Polyvinyl butyral (PVB) was drop cast at ambient temperature over the substrate to obtain a protective film of 10 μm thickness. Optical transparency of ITO-PET (substrate) before and after coating with polyvinyl butyral are compared.

Keywords ITO coated PET sheets · Surface treatment · Transparent protective coating

Conductive films typically grown by the vacuum-sputtering process have found to have numerous application in modern electronic devices including solar cells, metamaterial absorbers, etc [1]. Indium tin oxide (ITO) coated polyethylene terephthalate (PET) is one among the widely used flexible and transparent conductive films. However, due to the brittle nature of ITO, it offers poor mechanical strength, scratch and wear resistance which leads to a decrease in the conductivity with time resulting in an early failure of the devices [2]. In this work, we cast 15 % Polyvinyl butyral (PVB) solution in

1. Material Science Programme, Indian Institute of Technology Kanpur, Kanpur 208016, India
† E-mail: kaajal@iitk.ac.in.
2. Department of Mechanical Engineering, Indian Institute of Technology Kanpur, Kanpur 208016, India
3. Department of Physics, Indian Institute of Technology Kanpur, Kanpur 208016, India

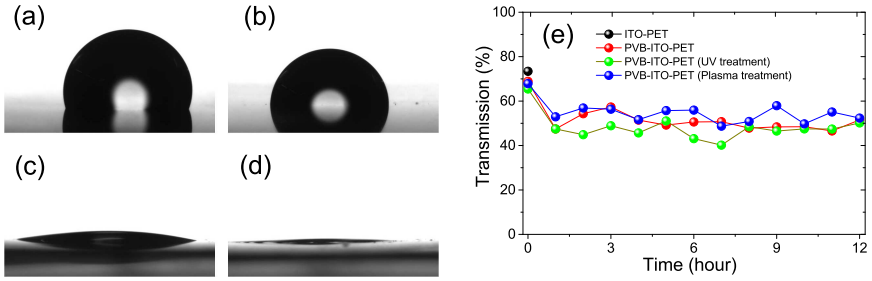

Fig. 1 Contact angle of ITO coated PET surface, (a) without any surface treatment,(b) after UV treatment, (c) after plasma treatment and (d) after chemical treatment. (e) Plot of optical transmission versus time for which the samples were drenched in water.

methanol over the substrate (ITO coated PET) and dried it at ambient temperature which resulted in an optically transparent tough protective films of 10 μm thickness which are further scalable to a large area. Primarily the surface of ITO has been made hydrophilic to increase the adhesion strength of the coating [3].

We explored the effect of broadband UV source, nitrogen plasma and chemical treatment comprised of dipping the substrate in 1 : 1 solution of hydrogen peroxide and ammonia by volume and after washing with water which was further treated with potassium hydroxide solution. Without any surface treatment the contact angle of ITO surface was measured to be 108.3° which drops down to 85°, 11.7° and 4° for UV, plasma and chemical surface treatment respectively as shown in Fig 1 (a, b, c, d) respectively. Although the chemical surface treatment resulted in the lowest contact angle, the film had lost the optical transparency which is our essential requirement hence only UV, and plasma treated substrates were coated and further investigated. The optical transparency of PVB coated substrate has been compared with the bare substrate using a red laser of wavelength 632.8 nm. Average optical transmission of the substrate was found to be 73.4 %, which was slightly reduced to 68.9 % after PVB coating as shown in Fig 1(e). The transmission decreases due to the non uniformity in the coating, which can further be improved by optimizing the drop cast method. We drenched the coated samples in water to note the change in transparency with time, after 12 hours it reduces to 52.3 %. Coating from the substrate without surface treatment got delaminated after 9 days of being soaked in water while it remains attached to the treated substrate for more than 20 days, hence showing increased adhesion.

References

1. Yuang-Tung, et.al, Improvement of organic solar cells by flexible substrate and ITO surface treatments, Applied Surface Science, 256 7606-7611 (2010)
2. K.A. Sierros, N.J. Morris, S.N. Kukureka, D.R. Cairns, Dre and wet sliding wear of ITO-coated PTE components used in flexible optoelectrnic applications , Wear, 267 625-631 (2009)
3. Fulvia Villani, et.al, Inkjet printed polymer layer on flexible substrate for OLED applications, Phy. Chem. C, 113 13398-13402 (2009)

Wavelength interrogated differential resonance parameter measurement for improved performance of ITO based surface plasmon resonance sensor

Jayeta Banerjee[1*], Sukla Rajak[2], Mina Ray[3]
[1,3] *Department of Applied Optics & Photonics, University of Calcutta (Technology Campus)*
Acharya Prafulla Chandra Siksha Prangan, JD-2, Salt Lake, Sec-III, Kolkata – 700 106, India
[2] *Department of Physics, M.U.C. Women's College, Burdwan*
[*] *Corresponding Author e-mail address: j.banerjee87@yahoo.com*

Abstract

In this paper, we have studied plasmonic structure with transparent conducting material in Kretschmann configuration which is found to increase the sensitivity and improve the performance of SPR sensors in wavelength interrogation mode. Indium tin oxide (ITO) is taken as alternative plasmonic material beyond conventional plasmon generating metal. Selection of ITO thickness and incident angle is important for designing an efficient sensor with high figure of merit. We have investigated the wavelength sensitivity for the change of refractive index of the sample in the order of two. Moreover, sensitivity can be increased by using differential reflectance measurement approach. Theoretical simulation based results validate that the proposed sensor can provide higher sensitivity by measuring the differential phase.

Keywords

Surface plasmon resonance, ITO, Sensitivity, Figure of merit

Introduction

SPR sensing technology has enjoyed rapid development in the past two decades and undergone a boom in recent years for the detection of biological and chemical analytes [1]. Surface plasmons (SPs) are free charge oscillations which occur at the metal-dielectric interface depending upon the incident beam properties. Surface plasmon resonance (SPR) occurs under attenuated total reflection (ATR) coupling mode induced by TM polarized light after satisfying phase matching condition. In [2] we have reported sensing of concentration of hemoglobin and temperature of water using Ag-Au bimetallic structure. The reflectance constrained Dynamic range [3] can be increased using the higher wavelength. The performance of plasmonic sensor can be limited by the optical losses in metals in the near infrared regime (NIR). In this respect, Indium tin oxide (ITO) has been found to be a good alternative to noble metals for generation of SPs [4]. V. Maslov et. al. experimentally demonstrated ITO based SPR sensor in the visible region [5]. Earlier, we have experimentally verified plasmonic excitation [6,7] in the prism based structure with Al as plasmon generating metal film. In this paper, we have investigated ITO based Kretschamann configuration in NIR region. ITO thickness is optimized and angle is selected in order to achieve maximum figure of merit (FOM). In this context, incident angle is kept fixed for wavelength interrogation. Reflectance, phase, field enhancement curves have been studied for different samples in gaseous medium and corresponding sensitivity have been calculated. Furthermore, differential resonance parameters have been studied which are found to provide increased sensitivity.

Description of the structure and numerical results

Schematic diagram of the plasmonic structure using transparent conducting oxide (ITO) film is shown in Fig. 1(a). An ITO layer with thickness of 150 nm is coated over BK7 glass prism and is in contact with the sensing medium (air).

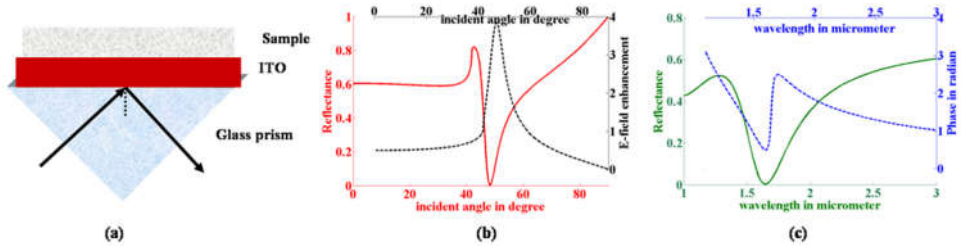

Fig. 1 (a) Schematic diagram of plasmonic structure. Reflectance and field enhancement curves in (b) angular interrogation, and (c) wavelength interrogation.

Acknowledgment

J. Banerjee would like to acknowledge Department of Science & Technology, Government of India for financial support (Ref.No.SR/WOS-A/PM-1015/2015) under Women Scientist Scheme.

The choice of metal thickness has been done by some preliminary optimization technique. Here, as the study has been done in wavelength interrogation mode, wavelength dispersion has been taken into account. The dielectric constant of ITO has been calculated using Drude model. The reflectance and electric field enhancement curves in angular interrogation are shown in Fig 1(b). The reflectance and phase plots are shown in Fig 1(c) as we are interested in studying resonance in wavelength regime.

Fig 2(a) shows the contour plot of reflectance for simultaneous selection of angle and wavelength of ITO based SPR structure. ITO thickness is varied following some optimization technique as shown in Fig 2(b). Thickness-dependent SPP on ITO thin films was reported in [8]. Considering 150nm as optimum ITO thickness, incident angle is varied (Fig 2(c)) in order to get minimum reflectance and minimum full width half maximum (FWHM) which is desirable. Resonance occurs in NIR in all cases. FOM is defined as the inverse of the product of reflectance minimum and FWHM. It is found that 48 deg corresponds to maximum FOM shown in table in Fig 2(d).

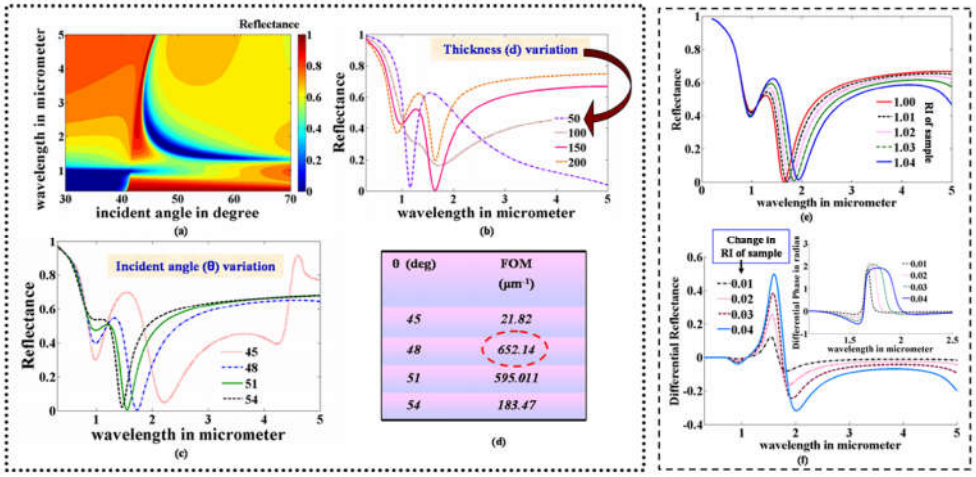

Fig. 2 (a) Simultaneous angular and wavelength interrogation of reflectance in contour plot, (b) ITO thickness optimization and (c) angle selection in wavelength interrogation. (d) Figure of merit is tabulated for the angles shown in (c), (e) sensing of RI of analytes with optimized structure, (f) differential reflectance and differential phase (inset) plot for change of RI of the order of two in wavelength regime.

In addition to this, sensing of gaseous sample has been done in wavelength interrogation as shown in Fig 2(e). Spectral sensitivity for sample with refractive index (RI) n=1.01, 1.02, 1.03 and 1.04 is 5500, 6000, 6500 and 7200 nm/RIU respectively, considering air (n=1) as reference. Our aim is to improve the sensitivity of the designed sensor. It is already reported that phase dependent resonant behavior of SPR measurement technique provides certain improvement over the sensitivity acquired by the conventional angular and wavelength interrogation. Differential reflectance and differential phase (inset) have been plotted for the same samples as shown in Fig 2(f). Differential reflectance/phase is the direct difference of reflectance/phase of the test sample with the reference sample. We achieved maximum sensitivity of 17,799 nm/RIU using differential approach. Differential resonance parameters can be experimentally evaluated using proposed set-up of our earlier report [9].

Conclusions

In this paper, we have studied plasmonic resonance in Kretschmann configuration using ITO as the plasmon generating material instead of noble metals in near infrared region. ITO thickness is optimized and incident angle is selected in order to obtain maximum FOM. It is found that differential reflectance or phase measurement approach is preferable in order to increase the sensitivity. Thus, present cost-effective technique may open up new ventures in nanoplasmonic sensing and imaging.

References

[1] J. Homola, Chem. Rev., 108, 462-493 (2008).
[2] J. Banerjee, M. Bera, M. Ray, Plasmonics, DOI 10.1007/s11468-016-0446-4 (2016).
[3] J. Banerjee, M. Bera and M. Ray, Journal of Appl. Physics, 117, 113102, 1-13 (2015).
[4] C. Rhodes, S. Franzen, J.P. Maria, M. Losego, D. N. Leonard, B. Laughlin, G. Duscher, and S.Weibel, J. Appl. Phys. 100, 054905 1–4 (2006).
[5] V. Maslov, G. Dorozinsky, N. Kachur, American Journal of Optics and Photonics, 4(3), 20-24 (2016).
[6] J. Banerjee, M. Ray, Appl. Phys. Lett., 110 181105-1-5 (2017).
[7] J, Banerjee, M. Bera, M. Ray, J. Opt. Soc. Am. B 33, 1462 -1469 (2016).
[8] S. Rajak and M. Ray, J Opt. 43(3), 231–238 (2014).
[9] J. Banerjee, M. Bera, M. Ray, Optics Communications, 403, 55-61 (2017).

OSI-ISO 2018 manuscript No.
(44)

Optical Design and Analysis of Passively Athermalized Si-Ge Optics in MWIR Band

Ranabir Mandal[1]*, Amitava Ghosh[1], Ajay Ghosh[2]

Abstract
Silicon and Germanium are the most preferred materials for the design of optics in Mid-Wave InfraRed (MWIR) band and Aluminum is used as housing material of the objective lens. Use of these materials suffers from degradation of the image quality due to thermal defocusing. To cater to this problem, active athermalization method is used where a lens module is adjusted for keeping the image focused on detector's Focal Plane Array. In this paper the performance of a Silicon- Germanium combination lens module and the performance with temperature are studied. By using Invar as housing material, feasibility of designing a temperature immune optics is explored. The image quality of the designed MWIR lens for the operating temperature range -20°C to +60°C shows that the design system is passively athermalized.

Keywords Passively athermalized optics, MWIR lens, Optical design, Lens design

Introduction

The material used for the elements of a MWIR thermal imager have large index variation due to temperature change and as a result the image becomes defocused because of environmental temperature change[1]. To cater for this, generally position of one element/ group is adjusted to focus it which is commonly known as active athermalization. To implement this active atheralization additional hardware like motors, temperature sensors and control electronics are required in the system, which increases the complexity in opto-mechanical design. The other way of tackling this thermal defocusing is optical (passive) athermalization, where optics itself takes care of compensating thermal defocus due to thermal expansion of housing as well as variation in refractive index of material[2]. As a result a passively athermalized infrared system requires no moving parts and thus makes the system much simpler.
Silicon and Germanium are the most preferred materials in MWIR optics design[2, 5]. In the paper, Ge-Si lens system and their performance with temperature is investigated. Based on the study, two sample designs are presented which show the feasibility passively athermalized optical system in MWIR spectral band for the temperature range of -20°C to +60°C.

Si-Ge lens properties:

If two thin components of power $\emptyset_1$ and $\emptyset_2$ separated by a finite distance d, having chromatic dispersive power ω_1 and ω_2 with thermal dispersive power θ_1 and θ_2 respectively and y_a and y_b are the paraxial ray heights at the two elements respectively, its power, chromatic focal shift ω and thermal focal shift θ can be expressed as [3,4]

Power of the lens, $\emptyset = y_a\emptyset_1 + y_b\emptyset_2$ (1)
Chromatic focal shift, $\omega = y_a^2\omega_1\emptyset_1 + y_b^2\omega_2\emptyset_2$ (2)
Thermal focal shift $\theta = y_a^2\theta_1\emptyset_1 + y_b^2\theta_2\emptyset_2$ (3)
and relation between y_b and y_a is

$$y_b = y_a(1 - d * \emptyset_1) = y_a(1 - k) \quad (4) \qquad \text{where } k = (d * \emptyset_1)$$

Ranabir Mandal
email : ranabir@irde.drdo.in

[1]*Instruments Research & Development Establishment, Raipur Road, Dehradun*

[2]*Department of Applied Optics and Photonics, University of Calcutta, Kolkata*

Using achromatic condition, (ω=0), the power distribution of the two components with respect to the values of $'k'$ and corresponding thermal defocusing can be computed. The results for a unit power lens (ϕ = 1) are shown in Table 1.

k	0.0	0.05	0.1	0.15	0.2	0.25	0.3	0.35	0.4
$\emptyset_1$	1.737	1.807	1.891	1.996	2.128	2.3017	2.537	2.878	3.412
$\emptyset_2$	-0.737	-0.849	-0.99	-1.172	-1.411	-1.736	-2.197	-2.889	-4.000
y_b/y_a	1.0	.95	0.9	0.85	0.8	0.75	0.7	0.65	0.6
θ	1.54E-05	1.6E-05	1.68E-05	1.77E-05	1.89E-05	2.04E-05	2.25E-05	2.55E-05	3.03E-05

Table 1 Thermal defocus of Si-Ge lens for ω=0

Optical Layout & Performance Evaluation

An InSb cooled detector, sensitive in 3.6 to 4.9μm band, having 320X240 array with 20μm pixel pitch is considered for studying the feasibility to design an optically passive MWIR lens. A non-pupil forming Si-Ge objective having focal length 50mm is designed with Invar as housing material. The layout (Fig 1) and MTF for different fields with respect to temperature (Fig 2) are shown below

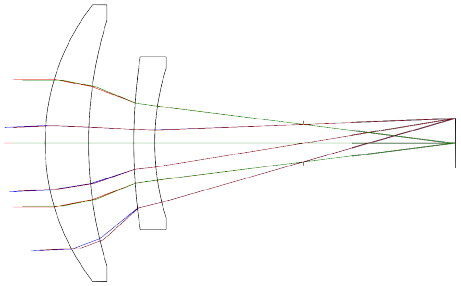

Fig. 1 Non-pupil forming lens

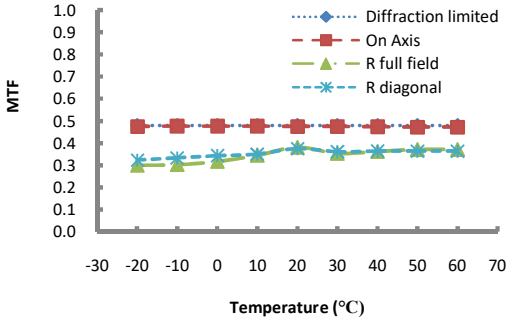

Fig. 2 MTF variation with temperature

Conclusion:

This paper describes the solution space of designing a passively athermalized Si-Ge lens in MWIR band. A non pupil forming type lens is successfully designed demonstrating image quality retention over the temperature range -20°C to +60°C.

Acknowledgement

The author gratefully acknowledges the encouragement from Director, IRDE to carry out this design work as well as permission to publish the results.

Reference

1. H. Jamieson, ‘‘Thermal effects in optical systems" , Opt. Eng.20(2), (1981)
2. P. J. Rogers, “Athermalized FLIR optics,” Proc. SPIE 1354, (1990).
3. Y. Tamagawa, S. Wakabayashi, T. Tajime, and T. Hashimoto, “Multilens system design with an athermal chart,” Appl. Opt. 33, (1994).
4. Y. Tamagawa and T. Tajime, “Expansion of an athermal chart into a multilens system with thick lenses spaced apart,” Opt. Eng. 35, (1996).
5. Chris Bigwood Andrew Wood, Two-element lenses for military application, Optical Engineering 50(12), (2011)

Ultrafast Switching in Single Resonator Based THz Metamaterials

S. Jagan Mohan Rao[1], Gagan Kumar[1] and Dibakar Roy Chowdhury[2]
[1] Department of Physics, Indian Institute of Technology Guwahati, India, 781039
[2]Mahindra Ecole Centrale, Jeedimetla, Hyderabad, India, 500043
Email: sjagan@iitg.ac.in

Abstract

We studied ultrafast switching response of fundamental resonance mode in single gap split ring resonator based terahertz metamaterials through optical excitation of radiation damaged silicon. We have noticed the dynamic transition of the fundamental resonance from ON-to-OFF state on a time scale of 4 picoseconds (ps) and subsequently recovery of the resonance to the ON-state within next 20 ps.

Keywords: Terahertz; Metamaterials; Split Ring Resonators; Ultrafast Switching.

1. Introduction

In the Electromagnetic spectrum, terahertz gap represents a technologically important and comparatively immature field mainly due to the lack of practical devices such as filters, switches, modulators, lenses etc. [1] In this scenario metamaterials can play significant role in designing and improving the performances of such devices. Metamaterials are novel artificial composites with unusual electromagnetic properties emerging from their geometrical structure rather than the composition [2-6]. In this context, controlling electromagnetic properties of terahertz metamaterials at ultrafast time scale is an important study.

2. Brief discussion about work

In this work, we examined the ultrafast switching of fundamental resonant mode in terahertz metamaterials through optical excitation of ion implanted silicon placed in the gap of a single split ring resonator (SRR). Upon optical excitation, we observe the active transition of the fundamental resonance from ON-to-OFF state on a time scale of 4 picoseconds (ps) and then fast recovery of the resonance to the ON-state within next 20 ps. We have done numerical simulations using CST microwave studio and the results are in well agreement with our experimental findings. Further we have simulated electric field distributions in the metamaterials unit cell clearly supporting our experimental observations, showing the intense electric field lines at the resonator gaps at resonance, responsible for inductive-capacitive (LC) resonance, which completely disappears and switches OFF the resonance after being optically excited. The ultrafast switching of the metamaterial resonance is attributed to the relaxation of the photo-carriers through the defect-states of radiation-damaged silicon layer. Our demonstrated scheme allowed us to photo-dope and tune the silicon conductivity at an ultrafast time scale precisely in the gap region of the SRR, in contrast to previous scheme where the properties of the entire substrate were modified because of optical excitation [4]. We have further employed a tri exponential theoretical model to examine the charge carrier relaxation process inside the ion implanted silicon layer. This work has potentials to enable ultrafast terahertz devices by combining the emerging phenomena of metamaterials with well-established silicon technologies.

3. Acknowledgements

The authors are gratefully acknowledged the financial support from the SERB (SB/FTP/PS-051/2014 and EMR/2015/001339). Department of Science &Technology, India.

4. References

1. Tonouchi M, Nature photonics 1(2), 97(2007).
2. J.B. Pendry, A.J. Holden, D.J. Robbins, W. Stewart, IEEE transactions on microwave theory and techniques 47(1), 2075(1999).
3. D. Roy Chowdhury, R. Singh, J.F. OHara, H.T. Chen, A.J. Taylor, A.K. Azad, Applied Physics Letters 99(23), 231101(2011).
4. D.R. Smith, W.J. Padilla, D. Vier, S.C. Nemat-Nasser, S. Schultz, Physical review letters 84(18), 4184 (2000).
5. H.T. Chen, W.J. Padilla, J.M. Zide, S.R. Bank, A.C. Gossard, A.J. Taylor, R.D. Averitt, Optics letters 32(12), 1620 (2007).
6. D. Roy Chowdhury, R. Singh, A.J. Taylor, H.T. Chen, A.K. Azad, Applied Physics Letters 102(1), 011122 (2013).

Temperature-Controlled Soliton Tunneling in Chalcogenide Fiber

Satya Pratap Singh, Keshav Samrat Modi, Jasleen Kaur, Umesh Tiwari, and Ravindra Kumar Sinha

Abstract We have proposed an alternative route to generate tunable supercontinuum in a liquid-filled chalcogenide capillary optical fiber (CCOF) when it is pumped by a hyperbolic secant femtosecond pump pulse in the anomalous dispersion regime. Utilizing the temperature-assisted dispersion tailoring, generation of dispersive wave which is tunable within a broad range of 2500nm is reported with detailed investigations of various predictions of dispersive waves through phase-matching characteristics. We have also observed the temperature-controlled soliton tunneling effect. It is observed that soliton spectral tunneling depends on the width of the normal dispersion region sandwiched between the two anomalous regions if the maximum value of the dispersion in the normal dispersion region is constant. Hence it is possible to switch-on or off soliton spectral tunneling effect by changing the temperature, however, it is not possible by changing the pump power or pulse width of the input soliton.

Keywords Supercontinuum generation, Dispersive wave, Soliton tunneling, Chalcogenide capillary optical fiber.

Introduction

Coherent radiations in mid-IR region from 2-6 μm are of great interest due to their huge applications in spectroscopy, remote sensing, free space communications, non-invasive medical diagnosis and defense related applications such as detection of biological and explosion hazards and enhancing the capability of night vision equipment. Supercontinuum generation is a convenient technique for generating broadband radiation from near- to mid-IR wavelength regimes. The generation of mid-IR radiation by supercontinuum has taken a great interest due to the arrival of the highly nonlinear soft-glass fibers and photonic crystal fibers (PCFs) [1, 2]. The dispersive wave (DW) plays an important role in spectral broadening and blue-shifting of the supercontinuum generation [3]. The phase matching (PM) condition, between the soliton (ω_s) and the dispersive radiation (ω_d) that relies on the matching of the group velocity of the soliton and the dispersive wave, determines the wavelength of the generated DW [4]. The phase matching condition is given as

$$\beta(\omega_d) = \beta(\omega_s) + \beta_1(\omega_s)(\omega - \omega_s) + \frac{\gamma P_s}{2}. \quad (1)$$

Where $\beta(\omega_s)$ and $\beta_1(\omega_s)$ are propagation constant and inverse group velocity of soliton, respectively. P_s is the peak power of the soliton formed after the fission and ω_s is the dispersive wave. By changing the PM characteristics, the wavelength of the DW radiation can be tuned. In this paper, we have proposed an alternative way to generate a temperature-controlled broadband mid-IR supercontinuum radiation in a liquid-filled chalcogenide COF which is tunable within a broad range of 2500nm.

Results and Discussions

The structural parameter of the COOF (R = 2μm, a/R = 0.25) is chosen in such a way that it exhibits an almost flat dispersion profile (Fig.1) with three ZDWs which is very helpful in the tunable parametric amplifier and Supercontinuum generation. The detailed investigations on the dispersion characteristics of CCOF Structure is given in the ref. [5]. The tunability feature in the device appears due to infiltration of thermo-optic liquid into air-capillary of the CCOF. There are many liquids which are transparent in mid-IR wavelengths, e.g., CCl_4 which is transparent upto 6μm with more than 80% transparency [6]. The temperature-dependent refractive index of As_2S_3 is also taken into account. A hyperbolic secant pulse with peak power of 30W and pulse-width of 100fs at a wavelength of 3.0μm is launched in the anomalous dispersion region of the CCOF. Fig. 2(a) and Fig. 2(c) show the phase matching curves of DW and soliton at two different temperatures ΔT = 0 and 40 °C, obtained by solving the phase matching (PM) Eqn. (1). The corresponding spectral evolution of the

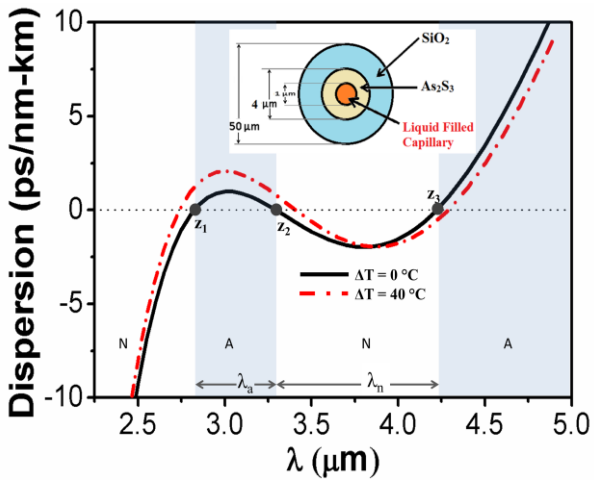

Fig. 1 Dispersion characteristics of the CCOF (R = 2 μm, a/R = 0.25 and n_{liq} =1.45) at various temperatures (ΔT = 0, and 40 °C) above room temperature, $\Delta\lambda_n$ and $\Delta\lambda_a$ are the widths of the normal and anomalous regions which are denoted by N and A. The inset shows typical CCOF schematic cross-section where, R and a denote radius of core and capillary.

❖ Satya Pratap Singh
satya0pratap@gmail.com

CSIR- Central Scientific Instruments Organisation, Sector 30, Chandigarh-160030,

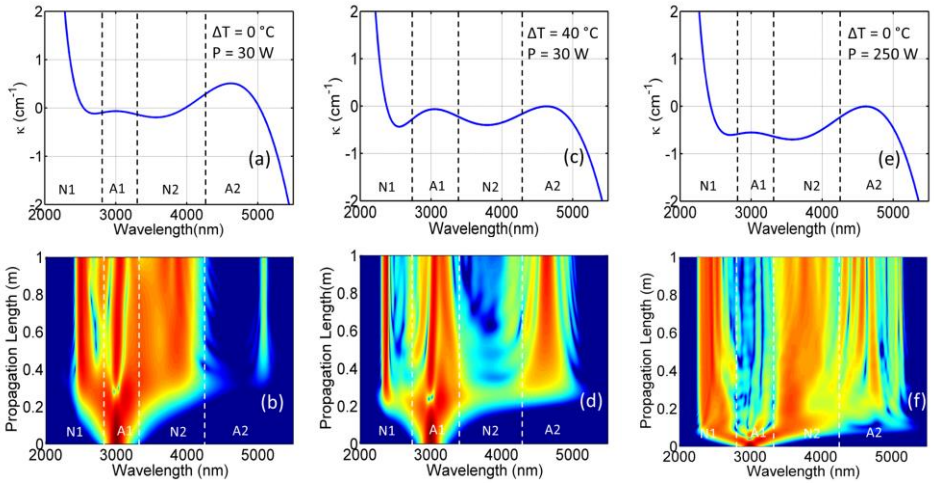

Fig. 2 The phase matching characteristics of DW and the spectral evolution of the soliton across whole fiber length at different temperatures (ΔT = 0 and 40 °C) and input soliton power (P = 250W).

soliton across the fiber length at these temperatures (i.e. ΔT= 0°C and 40°C) are depicted in Fig. 2 (b) and (d). Three vertical black and white dashed lines correspond to three ZDWs of the fiber, N and A represent the normal and anomalous dispersion regions. In case of a dispersion profile having three ZDW point, two regions of anomalous dispersion are separated by a normal dispersion region, when a pulse is launched in one of the anomalous dispersion region (A1), there is a sharp switching of the soliton frequency from anomalous dispersion region (A1) to the second anomalous dispersion region (A2). This behavior of the soliton is referred to as spectral soliton tunneling [4, 7]. The Raman self-frequency shift plays a key role in the soliton propagation dynamics and tunneling to the other anomalous dispersion region. The generated DW at 5050 nm in the anomalous dispersion region does not possess sufficient power to form a stable soliton. When the temperature is varied from ΔT = 0 °C to 40 °C while keeping other parameters fixed, the phase matching curve (Fig. 2(c)) predicts the generation of two dispersive waves. However, the strong spectral peak in the anomalous dispersion region (A2) is not a dispersive wave because the intensity of the generated DW is sufficient to form soliton.
We have also try to obtain the spectral soliton tunneling (SST) effect by varying the input pump power and pulse width while keeping temperature fix at 0 °C. Even if we have made the DW PM characteristics same as in case of the SST at 40 °C and pump power 30 W (Fig. 2 (c)) by increasing the pump power to 250 W while keeping temperature fix at 0 °C, we didn't get the SST effect as evident from the Fig. 2 (e). So, we can say that SST depends on the width of the normal dispersion between the two anomalous regions if the maximum value of the dispersion in the normal dispersion region is constant with the temperature (Fig. 1). Hence.by changing the temperature, the width of the normal dispersion can be controlled and hence the SST which is not possible by varying pump power and pulse width of the input soliton.

Conclusions

In conclusions, an alternative way to generate tunable mid-IR supercontinuum by controlling the phase matching characteristics of the dispersive waves has been investigate along with the temperature-controlled soliton tunneling in a liquid-filled chalcogenide COF when it is pumped by a hyperbolic secant pulse in the anomalous dispersion region. To simulate the soliton pulse dynamics and the generation of dispersive wave nonlinear Schrodinger equation has been used.

Acknowledgements The author, Dr. S. P. Singh is gratefully to the DST- Science and Engineering Research Board, India for providing the financial support through National post-doctoral fellowship (File No: PDF/2016/003647). Authors are also thankful to CSIR-CSIO, Chandigarh for providing research facilities.

References

1. R. R. Gattass, L. Brandon Shaw, V. Q. Q. Nguyen, P. C. C. Pureza, I. D. Aggarwal, and J. S. Sanghera, Opt. Fiber Technol., 18, 2012.
2. C. R. Petersen, U. Møller, I. Kubat, B. Zhou, S. Dupont, J. Ramsay, T. Benson, S. Sujecki, N. Abdel-Moneim, Z. Tang, D. Furniss, A. Seddon, and O. Bang, Nat. Photonics, 8, 2014.
3. D. R. Austin, C. M. de Sterke, B. J. Eggleton, and T. G. Brown, Opt. Express, 14, 2006.
4. J. M. Dudley, S. Coen, and G. Genty, Rev. Mod. Phys., 78, 2006.
5. S. P. Singh, V. Mishra, P. K. Datta, and S. K. Varshney, J. Light. Technol., 33, 2015.
6. A. R. Chraplyvy and T. J. Bridges, Opt. Lett., 6, 1981.
7. E. N. Tsoy and C. M. De Sterke, Phys. Rev. A - At. Mol. Opt. Phys., 76, 2007.

Bandgap Tuning in GaAs based Photonic Crystal Waveguides using Thermo-Optic Effect

Vadapalli Durga Rama Pavan, Koustav Dey, Sourabh Roy*

Department of Physics, National Institute of Technology, Warangal – 506 004 (India)

*sroy.physics@gmail.com

ABSTRACT

Thermal tuning of photonic bandgap using the concept of thermo-optic effect is presented in this paper. GaAs slab with air holes, arranged in a triangular lattice is used as the Photonic Crystal Waveguide (PCW). A micro heater, with plates parallel to the slab is assumed for creating localized heating and varying refractive index of the slab. Temperatures ranging from25 ^{o}C to 75 ^{o}C are assumed for this purpose. The refractive index and the dielectric constant of slab are calculated at these temperature values using thermo-optic equation at wavelengths 1.31 µm, and 1.55 µm. For obtaining wider bandgap, a fraction filling ratio of 0.3 is used throughout the process. The simulations are performed in MIT Photonic Bands (MPB) software. Using the output of the program, band diagrams were obtained and it is observed that the bands were shifting with change in temperature. The applications of the proposed system include on chip integrated networks, switching and routing devices in communication and ultrafast networks.
Keywords: Photonic Crystal Waveguide, photonic bandgap, bandgap tuning, thermo-optic effect, optical switches.

Introduction:

Photonic Crystal Structures (PCS) are gaining the attention of both scientific and commercial fraternities due to their wider light controlling and modulating applications [1]. These are the structures formed by periodic arrangement of refractive index, for achieving specific applications like, transmission or reflection of band of frequencies, slowdown of light due to dispersion mechanism, parametric amplification, optical switching even nonlinear effects such as second harmonic generation, four-wave mixing [1,2,3,4]. The variation in refractive index is achieved by various methods, including creating air holes and placing parallel cylindrical rods in a slab of semiconductor material [1,5]. These structures possess photonic bandgap, which determines the frequency of operation. Photonic Crystal Waveguide (PCW) is formed by eliminating one row of air holes or cylinders [6]. The photonic bandgap of a PCS and PCW depends on the geometry of the structure and the material from which PCS is fabricated [1]. Most common method of altering bandgap and dispersion features is of a PCS and PCW is altering of the geometry [6].

In the present work, refractive index of the slab material is considered as varying by adopting thermo-optic effect [7, 8]. This can be realized by creating localized heating of PCW by a micro-heater. Here, GaAs based PCW with air holes, arranged in triangular lattice are considered as the base structure [9]. Initially the bandgap of the structure is calculated at room temperature. Later, using thermo-optic equation [7, 8], the refractive index of the slab and its dielectric constant are calculated at two wavelengths 1.310 µm and 1.550 µm at temperatures ranging from 25 ^{o}C to 75 ^{o}C. These dielectric constant values are used during the simulation, performed in MIT Photonic Bands (MPB) software. The results reveal that the band gap is increase in temperature.

Theory and Methods:

According J. McCaulley, et al, [7], the refractive index of the gallium arsenide at near infrared regions is given by $n(T) = n(T_{ref})/exp[(T_{ref} - T)\ \beta]$ where 'T' corresponds to temperature of the sample, T_{ref} corresponds to reference temperature, and β represents temperature coefficient or thermo-optic coefficient of the material. For this work, T_{ref} was chosen as 20 ^{o}C. Using this equation, refractive index and therefore dielectric constant of GaAs is calculated at increasing temperatures.

Air holes, arranged in the triangular lattice were considered in the GaAs slab for creating PCW [9]. For localized heating, a micro-heater is considered. The schematic of the proposed system is shown in figure 1.

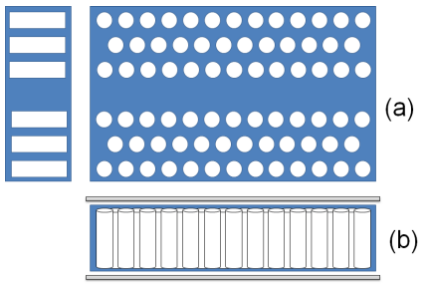

Fig 1: Schematic arrangement of the proposed system with micro heater. (a)Top and side view. (b) Front view of the system.

The simulations were performed in MPB software and the obtained eigen frequencies are plotted against the 'k' index of the structure. The simulations were performed by considering dielectric constant at various temperatures and the band diagrams were plotted for further analysis.

Results and Discussions:

The initial band diagram shows that the photonic bandgap exists between the bands 6 and 7. For a lattice constant of 350 nm it is found to be 0.2393 eV at 20 ^{o}C. The band diagrams of the slab with increasing temperature were obtained by simulation and the position of band 6 and band 7 were plotted against temperature as shown in figure 2. The plots show that the bands are shifting contributing to shift in bandgap.

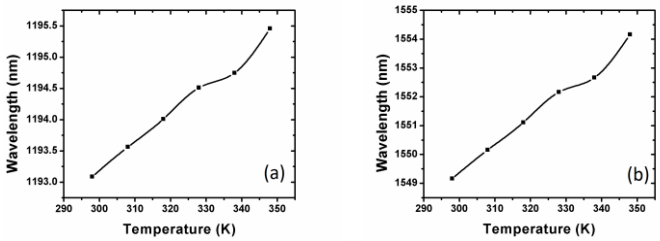

Fig 2: Shift in bands due to increase in temperature (a) shift of band 6 (b) shift of band 7.

Figure 3 shows the band 6 and 7, against k-index at two temperatures 25 ^{o}C and 75 ^{o}C. The plot clearly shows the shift in bands due to rise in temperature.

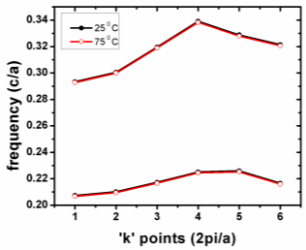

Fig 3: Shift of band positions due to temperature

The shift in band positions was calculated at 75 ^{o}C using the obtained output. The upper band (band 7) is shifting about 4.9991 nm and the lower band (band 6) is shifting about 2.3736 nm, when compared to that of at 20 ^{o}C. The total shift in the bandgap is found to be about 2.625 nm. This shift is sufficient enough for switching applications in communication networks and on-chip applications.

Conclusions:

A theoretical model for tuning the bandgap of a PCW through thermo-optic effect is proposed and the variations in the bandgap are studied. It is found that the bands of the proposed system are shifting with temperature. The variations are even higher at higher values of temperature. The proposed system can have on chip applications for switching of signals, all optical devices, switching and routing devices in communication and ultrafast networks.

Acknowledgements:

Authors sincerely thank Department of Science and Technology (DST), Government of India for funding this work through INSPIRE fellowship.

References:

[1] E Yablonovitch J. Mod. Opt. 41, 2 (1994) https://doi.org/ 10.1080/09500349414550261
[2] T. Baba, Nat. Phot. 2, pp: 465-473 (2008) https://doi.org/10.1038/nphoton.2008.146
[3] S. Roy, A. Willinger, S. Combrie, A. De. Rossi, et al., Opt. Letters 37, 14 (2012)
[4] S.Roy, M.Santagiustina, P Colman, et al., IEEE Phot. 4, 1 (2012) https://doi.org/10.1109/JPHOT.2011.2181942
[5] V.D.R.Pavan., et al., (2014) https://doi.org/10.1364/PHOTONICS.2014.T3A.16
[6] R.M. De La Rue,C. Seassal (2012) https://doi.org/10.1002/lpor.201100044
[7] J. A. McCaulley, et.al., Phys. Rev. B 49, 11 (1994) https://doi.org/10.1103/PhysRevB.49.7408
[8] Jang Pyo Kim and Andrew M. Sarangan Opt. Letters 32, 5 (2007) https://doi.org/10.1364/OL.32.000536
[9] D.N. Chigrin, and A.V. Lavrinenko (2004) https://doi.org/ 10.1109/ICTON.2004.1361984

OSI-ISO 2018 manuscript No.
(51)

Development of latent fingermarks on aluminum surfaces

Anjani Kumar Tiwari[1,†] · **Ismail Mekaaoui-Alaoui**[2] · **Sriram Guddala**[1] · **S. Anantha Ramakrishna**[1]

Abstract We report the enhanced visualization of latent fingermarks that were collected on rough aluminum surfaces having high diffuse reflectivity. We use a vacuum metal deposition technique to detect the fiducial features of the fingermark by depositing a thin layer of gold and zinc sulfide on the fingermark residue. The optical properties like reflectance from the residue and the deposited layers of gold and zinc sulfide are analyzed using the transfer matrix method. The calculation reveals that the best image contrast will emerge for the gold layer thickness of 10 nm and zinc sulfide layer thickness of 170 nm. Implementing these values in the experiment, we succeeded in developing the fiducial feature of the fingermark with 70 % success ratio and also recover the fingermarks for the aged sample stored for 65 days under temperature and pressure conditions.

Keywords Latent fingermarks · Rough aluminum surface · Vacuum metal deposition · Reflectance

Fingermark detection is among the benchmark technology for personal identification purposes. In recent times, the fingermark development techniques have significantly evolved [1]. Often, the detection method depends on the physical and chemical nature of the surfaces on which the fingermarks are located. Many specimens may present several constraints such as surface roughness, high background fluorescence, etc. which can hamper the visualization of the fingermarks [2]. For example, commercial aluminum used for constructing soft partitions, windows, door frames, etc. have the microscopic surface roughness which creates a large background scattering for light making the development of fingermark remarkably challenging. In this work, we show the enhance visualization of latent fingermarks that are collected on the rough aluminum surfaces with a success ratio of 70 %.

To develop the aged fingermarks we used the metal deposition technique in a vacuum chamber at a low pressure of 2×10^{-5} mbar [3]. For the deposition, the material was placed in a tungsten boat, and the fingermark samples were mounted about 20 cm above it. When the electrical heating is applied, the evaporating material flux gets deposited on the fingermark samples. The thickness of

1. Department of Physics, Indian Institute of Technology Kanpur, Kanpur 208016, India
†E-mail: tiwari.tifr@gmail.com
2. Physics Department, Faculty of Sciences Semlalia, Cadi Ayyad University, Marrakech 40000, Morocco

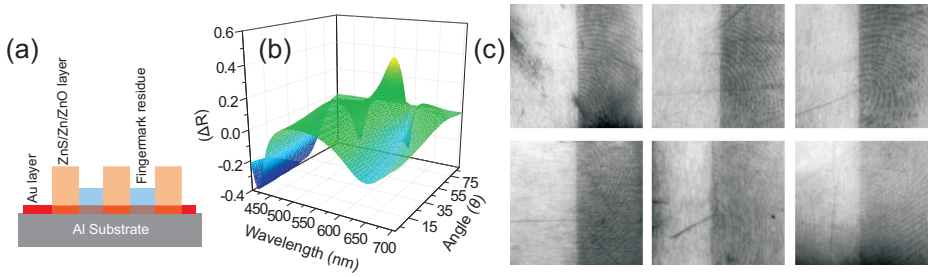

Fig. 1 Schematic representation of the thin layer of gold and one of the zinc-based materials deposited on the fingermark residue. (b) Difference between the reflected light from the fingermark residue region and the Au-ZnS bi-layer region. (c) Images of the fingermark samples collected from six donors aged between 20 to 35 years. The left halves are the virgin region, and the right halves are the developed region using Au-ZnS bi-layer deposition.

the material is precisely monitored using a quartz crystal thickness monitor. The evaporating flux of the first material (Au vapor) penetrates the porous fingermark residue and gets uniformly deposited throughout the aluminum substrate. When the second layer of ZnS is deposited, it only attaches to the nucleating islands of gold in the valley regions and leaves the fingermark residue uncoated. Fig 1 (a) shows the schematic diagram of the fingermark system. The parallel homogeneous layers represent the fingermark residue and deposited materials. On this system, we perform the transfer matrix calculation to obtain the approximate thicknesses of the materials so that the contrast in the reflectivity from different regions of the fingermark maximizes. Fig 1 (b) plots the difference in reflectivity (ΔR) from the fingermark ridge and valley region by having the following parameters. The thickness of fingermark residue = 100 nm, its refractive index = 1.55, gold layer thickness = 10 nm and ZnS layer thickness = 170 nm. For these parameters, the peak in ΔR is observed at 560 nm, near the maximum spectral sensitivity of the human eye. Based on these inputs, we performed the fingermark development using the vacuum metal deposition technique. Fig. 1 (c) shows the fingermarks collected from six donors, one female, and five male donors aged 20 to 35 years. The left halves of the samples are the virgin area with no depositions. In most cases, the fingermarks are not visible. The right halves show the developed fingermarks area. There is a definite enhancement in the visibility of the fingermarks. We observed that for gold and ZnS combination with the above-stated parameters the fingermark visibility improves significantly, and we can recognize the fiducial features in about 70 % of the samples. Using the same procedure, we have also successfully enhanced the visualization of latent fingermarks aged over two months under normal temperature and pressure conditions.

Acknowledgements We acknowledge DST, India through project No. DST/PHY/20130147. AK Tiwari also thanks DST for the INSPIRE Faculty Award (DST/INSPIRE/04/2016/002068).

References

1. H. C. Lee, R. Ramotowski, R. E. Gaensslen, Advances in fingerprint technology, 2nd edn. Boca Raton, FL: CRC Press (2001).
2. C. Lennard, Fingerprint detection: current capabilities. Aust. J. Forensic Sci. 39: 5571 (2007).
3. A. K. Tiwari, I. M. Alaoui, S. Guddala, and S. A. Ramakrishna, Enhanced visualization of latent fingermarks on rough aluminum surfaces using sequential Au and Zn/ZnS/ZnO depositions, J. Forensic Sci. 63: 1275-1281 (2018).

OSI-ISO 2018 manuscript No.
(52)

Establishing the paucity of Thermal Effects for Pulsed versus CW Lasers in Fluids

Tushar Gaur[1], Debabrata Goswami[2,*]

Abstract: A numerical method to understand and analyze the laser-induced heating in various solvents have been described in this paper. We have developed the model comparing heating in continuous wave (CW) laser and pulsed laser for pure water, binary mixtures of water in ethanol and methanol. This comparative study has been done by using numerical simulation through MATLAB©. Interestingly, our results show that thermal effects in pulsed condition are always lesser than the CW case irrespective of the choice of fluid.

Keywords: Thermal Effects, Continuous Wave Laser, Pulsed Laser, Heating, Light-matter interaction.

1. Introduction

Lasers are known for generating heat through absorption while propagating through an absorbing medium. This heating property has been used effectively in in various fields such as biological treatments, laser welding, cutting and melting of metals in machining, etc. The major advantage of using a very tightly focused laser beam is in its precision and accuracy, which is much higher than any other conventional methods used earlier [1]. In this paper, we illustrate how temperature builds up in [1]different fluids (water, water-ethanol mixture and water methanol mixture) using a tightly focused laser heating source. We are also comparing the results obtained with a CW and a pulsed laser. We also show the distinct effect of these two types of lasers on the temperature profile in the absorbing medium over a period of exposure time.

This model has been presently developed only for the longitudinal direction of propagation of laser beam. The present model can be utilized to obtain the temperature profile for materials as long as its material properties, such as, specific heat capacity, heat conduction, density and absorption coefficient are known.

2. Heat Generation Concept and Mathematical Model:

The basic concept behind the generation of heat within a material when irradiated with a tightly focused high intensity laser beam comes from the flow of heat due to conduction of heat within a material [2]. For the sake of simplicity, we have ignored the convective heat flow effects as of now. This conduction of heat follows the parabolic heat equation given as follows [3]:

$$\rho C_\rho \frac{\partial T}{\partial t} - \nabla.(K\nabla T) = q_v \quad (1)$$

Here ρ is density of material, $C_\rho$is specific heat capacity, T is temperature, K is thermal conductivity and q_v is volumetric heat source. In our case K is constant in all the directions and hence equation (1) reduces to:

$$\rho C_\rho \frac{\partial T}{\partial t} - \mathrm{K}\nabla^2 T = q_v \quad (2)$$

This equation is the final form of heat conduction equation in our model. Volumetric heat generated is due to absorption of intensity by the material and is given by:

[1]Tushar Gaur
Center for Lasers and Photonics, Indian Institute of Technology Kanpur, India
E-mail: tgaur@iitk.ac.in

[2]Prof. Debabrata Goswami
Center for Lasers and Photonics & Dept. of Chemistry, Indian Institute of Technology Kanpur, India
*E-mail: dgoswami@iitk.ac.in

$$q_v = \alpha I(r,t) \quad (3)$$

Here α is the absorption coefficient of the material and I(r,t) is the intensity of the laser beam. Laser beam intensity in our case is given as:

$$I(r) = \frac{I_o}{wz^2} e^{-\alpha z} \quad (4a)$$

$$I(r) = \frac{I_o}{wz^2} e^{-\alpha z} e^{\left(-\left(\frac{t}{\tau}\right)^2\right)} \quad (4b)$$

Here, the first equation (4a) is for the CW laser and the second equation (4b) is for the pulsed laser, such that, τ is the pulse width and t is time. I_o is the peak intensity at the center, which comes out to be same in both the cases.

3. Results and Discussion:

Our results show that in the case of pulsed laser due to limited time interaction, the peak temperature attained is smaller as compared to the CW laser. Additionally, it is clearly seen that for the case of CW laser, after a certain time period the temperature becomes constant. The constant data that was used for all simulations are shown in Table 1.

Table 1 This table contains all the constants that were used while simulating the results. Numerical aperture of 1.2 was used.

(Data from Ref. 4)	Water	Water Ethanol Mixture	Water Methanol Mixture
Conductivity ($Kg.m^{-3}$)	0.6	0.586	.581
Specific Heat ($J.Kg^{-1}K^{-1}$)	4186	4120	4090
Density ($kg.m^{-3}$)	997	990	987
Absorption Coeff. (m^{-1})	1100	1094	1090

On the other hand, in the case of pulsed laser, the temperature rises to a peak temperature that is smaller than the CW case and then decreases gradually after the pulse is switched off. This property of pulsed laser can be utilized efficiently in the areas where laser induced damages are to be prevented. All these results are summarized below in figure 1, where our pulse width is fixed at 20 µs.

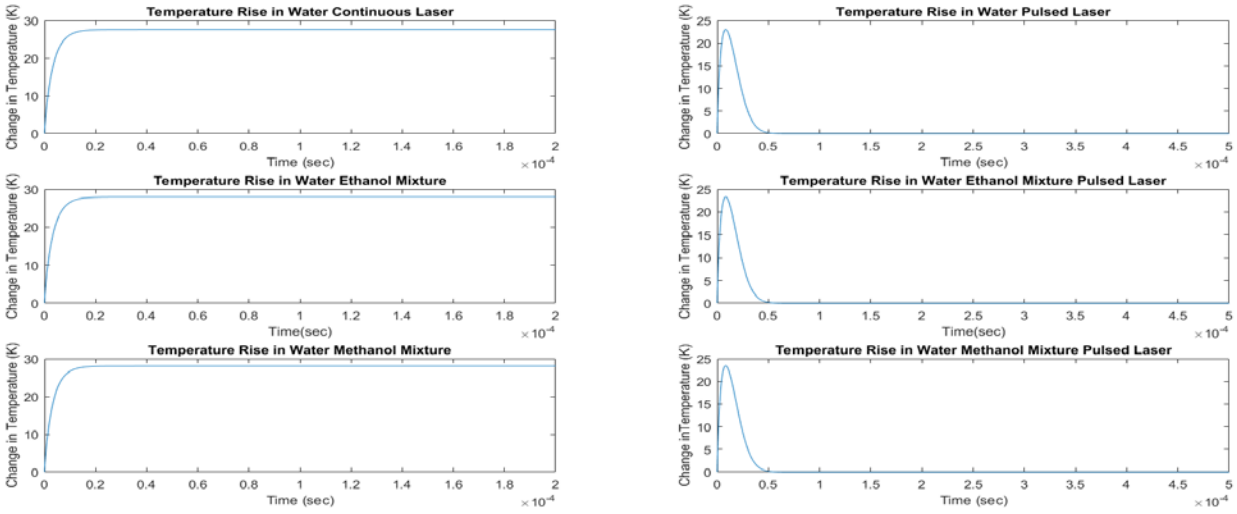

Figure 1 Numerical results have been generated using 10 mW of laser power at the wavelength 1560 nm with a highly focusing numerical aperture lens (1.2) for both pulsed and continuous wave lasers.

4. References

[1] Carslaw H.S. , "Introduction To Mathematical Theory of The Conduction Of Heat," 1-60, London Macmillan and Co. Ltd. (1921).

[2] Alphan Sennaroglu, Attila Askra, Fatihcan M. Atay, "Quantitative Study of Laser Beam Propagation in Thermally Loaded Absorber", Journal of Optical Society of America, Vol 14, 356-363 (February 1997)

[3] Yilbas, Bekir Sami , "Laser Heating Application: Analytical Modelling", 1 – 50 Amsterdam Elsevier (2012)

[4] Pardeep Kumar, "Thermal lens study of strong absorbing samples with femtosecond laser pulse train", PhD Thesis (IIT Kanpur 2014)

Unification of Coherence and Polarization through Phase Shifting Digital Holography

Izabel Thomas, Pramod Panchal and C. S. Narayanamurthy

Applied and Adaptive Optics Laboratory, Department of Physics, Indian Institute of Space Science and Technology,

Valiamala P.O., Thiruvananthapuram 695547, India
Email: izabelth@gmail.com, pramod.pancahl25@gmail.com, naamu.s@gmail.com

Abstract : The relationship between the phenomena of coherence and polarization is demonstrated through phase shifting holography. Phase shifting digital holography is used in which phase of the reference wave is varied stepwise. Effect of path length and hence coherence is studied using dynamic phase shifting where as polarization state is changed in geometric phase shifting holography. The holograms obtained for both the methods are numerically reconstructed and then studied.

Keywords: Digital Holography, Dynamic and Geometric phase shifting, angular Spectrum of waves

1. INTRODUCTION

The phase shifting digital holography was first suggested by *Yamaguchi and Zhang* [1]. This method can reconstruct an arbitrary cross section of a three-dimensional object with higher image quality and a wider viewing angle than from conventional digital holography using an off-axis configuration. They measured the complex amplitude of the object wave at the CCD plane located at finite distance in the in-line setup by using phase shifting interferometry. The phase of the reference waves is changed stepwise. Phase shifting digital holography captures at least three interferograms with mutual phase shift in the reference wave. Each interferograms indicate the phase relationship between the light returned from all points on the object and the controlled reference beam of light. The resulting four interference fringes are processed by a computer to yield the distribution of the complex amplitude of the wave. Then the distribution is Fresnel transformed in the computer to reconstruct images at arbitrary planes.

We take multiple holograms corresponding to different phase shifts. Hologram can be expressed as

$$I = |U+R\exp(-j\,\delta)|^2 \quad (1.1)$$

$$= |U|^2 + |R|^2 + U^*R\exp(j\,\delta) + UR^*\exp(-j\,\delta) \quad (1.2)$$

Where U and R denotes object and reconstruction wave respectively and δ denotes the phase difference [2]
In four-step PSH, four holograms are acquired sequentially. The phase differences for the four holograms are δ= 0, δ = π/2, δ = π, and δ =3π/2.The complex amplitude of object is given by

$$U = \frac{(I0 - I\pi) - j\,(I\pi/2 - I3\pi/2)}{4\,R*} \quad (1.3)$$

2. DYNAMIC AND GEOMETRIC PHASE SHIFTING HOLOGRAPHY

Michelson geometry is employed to create interference pattern at the CCD plane as shown in fig 1.In dynamic PSH method the reference mirror is mounted on *a piezoelectric transducer* (PZT) so that the optical path difference between the object light and the reference light can be adjusted. In geometric phase shifting digital holography,[3] the phase shift can be done with geometric phase only, it does not depends on optical path length or wave length. The rotating wave plates are used for changing the geometric phase. i.e the rotating wave plates are introduced in the reference arm of the Michelson interferometer. The two quarter wave plates are placed in the reference arm. The first QWP is fixed at 45^0 with the polarizer. The second QWP is placed near to QWP 1 which is free to rotate. After passing through QWP1,the light becomes right circularly polarized. The beam then passes through QWP2, which is free to rotate through any angle then it is converted back to linearly polarized light.

If Ex and Ey represents the x and y components of electric field vectors which are mutually orthogonal and are perpendicular to the direction of propagation of the reference beam. Then the intensity can be written as

$$I(\theta, \phi) = Jxx\cos^2\theta + Jyy\sin^2\theta + Jxye^{-i\phi}\cos\theta\sin\theta - Jyxe^{i\phi}\sin\theta\cos\theta\,, \quad (2.1)$$

Where $Jxx = E_xE_x^*$, $Jyy = E_yE_y^*$, $Jxy = E_xE_y^*$, $Jyx = E_yE_x^*$and the corresponding coherency matrix can be written as

$$\frac{1}{2}\begin{bmatrix} 1+cos2\theta & \exp(-i\varphi)\,sin2\theta \\ \exp(i\varphi)\,sin2\theta & \exp(-i\varphi)\,sin2\theta \end{bmatrix} \quad (2.2)$$

Where θ and ϕ represent the polar and azimuthal angles, respectively, on the Poincaré sphere. . If the rotation of QWP2 by an angle of ψ then beam suffers a geometric phase shift equal to 2ψ. This phase (2ψ) is the geometricphase ϕ_G, which does not depend on the optical path length or wavelength, unlike the dynamic phase ϕ_D.

Thus the phase of the reference beam suffers a pure geometric phase shift equal to 2ψ with respect to the object beam.

Holography is performed for a five rupee coin and changing the phase as $0, \frac{\pi}{2}$, π and $\frac{3\pi}{2}$. Since Michelson geometry is used, the beam scattered from the object and the reference wave interferes through the beam splitter and an interference pattern is observed on the camera plane. Good patterns can be obtained by adjusting the position and distance between the object and camera. The holograms are captured and reconstructed using Matlab code using *angular spectrum approach* [4]

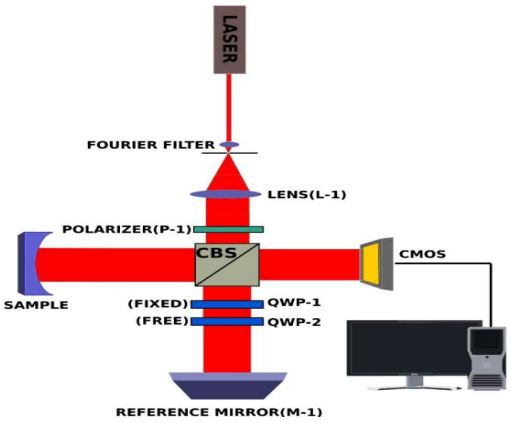

Fig 1 Expeimental Set up

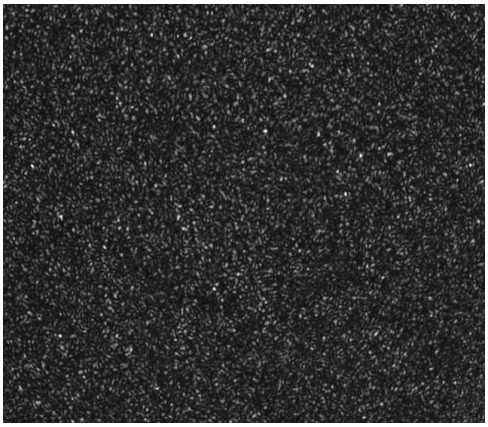

Fig 2 Hologram for $\frac{\pi}{2}$ phase shift in dynamic PSDH

3. RESULTS AND CONCLUSION

A typical digital hologram is shown in fig 2. The hologram is recorded with the geometry of figure 1.The object is placed at d = 45.5 cm from the CCD array of 640 × 480 pixels with pixel size=$9.9\ \mu$m. The wavelength is 632.8 nm. The holograms reconstructed using numerical methods are shown below.

In dynamic phase shifting, phase shift is introduced by changing the length of reference arm. This is done through controlling the positions of piezo mirror. To obtain a stable interference pattern, the path difference of beam traversing two arm of Michelson interferometer should be less than the coherence length. In geometric phase shifting, the quarter wave plates introduce phase shift between two components of light wave, thereby altering its polarization.The images that we reconstructed using dynamic and geometric phase shifting methods are both found to be identical. Hence we conclude that the principles of coherence and polarization are unified through phase shifting holography.

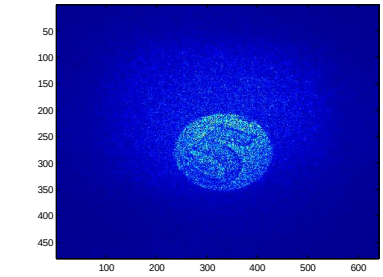

Fig 3 Reconstructed image in dynamic PSDH

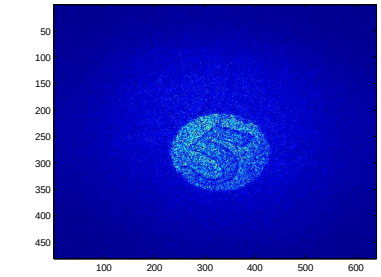

Fig 4 Reconstructed image in geometric PSDH

4. REFERNCES

[1] Yamaguchi I and Zhang T 1997 Phase-shifting digital holography *Opt. Lett.* **22** 1268–70
[2] Introduction to Modern digital holography with MATLAB ,Ting-chung poon Virginia Tech, USA, Jung-Ping liuFeng Chia University, Taiwan
[3] Geometric phase shifting digital holography Boaz Jessie Jackin, C. S. Narayanamurthy, and ToyohikoYatagai , vol. 41, no. 11 / june 1 2016 / optics letters.
[4] Practical algorithms for simulation and reconstruction of digital in-line holograms Tatiana Latychevskaia.

OSI-ISO 2018 manuscript No.
(54)

Macroscopic quantum entanglement in a modulated optomechanical system

Subhadeep Chakraborty · Amarendra K. Sarma

Abstract We propose a scheme to entangle two mechanical oscillators in an optomechanical system, within the current state-of-the art experimental setups, by exploiting the periodic modulation of both the external driving and mechanical coupling strengths. It is found that, depending on the strength of the mechanical coupling, one could observe either a stationary or a dynamical behavior of the mechanical entanglement. The entanglement observed is found to be significantly robust against the oscillator temperature.

Keywords Cavity Optomechanics · Quantum Entanglement · Mathieu's Equation

Cavity optomechanics is arguably one of the most exciting areas of modern quantum optics with a goal to realize the true quantum mechanical behavior of a macroscopic object. It has witnessed tremendous progress in both theoretical and experimental research, and now considered as one of the most potential platforms for the so-called quantum technology. The basic prototype of such an optomechanical system comprises of an optical cavity with one fixed and the other a movable end mirror, where the radiation pressure force is implemented to couple the light field with the mechanical motion. Based on this platform, several studies have already been reported on the ground state cooling of mechanical oscillators, generation of quantum entanglement and squeezinig of nanomechanical oscillators etc.[1,2]. In this work, we have considered an optomechanical system consisting of two identical mechanical oscillators placed

S. Chakraborty
Department of Physics, Indian Institute of Technology Guwahati, Guwahati-781039, Assam, India
E-mail: c.subhadeep@iitg.ac.in

A. K. Sarma
Department of Physics, Indian Institute of Technology Guwahati, Guwahati-781039, Assam, India

within a Fabry-Perot optical cavity. In addition, we have considered a periodic modulation on both the external driving and the mechanical coupling given by $E(t) = E_0 + E_1 \cos(\Omega t)$ and $\lambda(t) = \lambda_0 \cos(\Omega t)$ respectively. The complete Hamiltonian (in the unit of $\hbar = 1$) of the system can be written as [3]: $H = \Delta_0 a^\dagger a + \sum_{j=1}^{2} \frac{\omega_m}{2}(q_j^2 + p_j^2) + g a^\dagger a \sum_{j=1}^{2} q_j + \lambda(t) q_1 q_2 + i\left(E(t)a^\dagger - E^*(t)a\right)$, where a ($a^\dagger$) is the annihilation (creation) operator of the cavity field (with frequency detuning Δ_0), q_j is the dimensionless position operator of the j-th mechanical oscillator (with frequency ω_m), and g is the single-photon optomechanical coupling strength. Moreover, owing to the interaction with the external environment, we have included all the necessary fluctuation-dissipation processes affecting the dynamics of both the cavity field and the mechanical oscillators. As the dynamics of the quantum fluctuations is of our prime concern, we expand each operators around its classical mean values, and derive equation of motion corresponding to the correlation matrix. Fig. 1 depicts the time evolution of the quantum entanglement (as quantified by the so-called logarithmic negativity [2]), for various mechanical coupling strengths for two different oscillator temperatures. One can see that, depending on the strength of the mechanical coupling, the entanglement dynamics could be essentially different. In order to obtain more insight, we have introduced the normal modes of the mechanical oscillators. Our study shows that the dynamical transition occurs only when one of the normal mode becomes unstable. Furthermore, we have shown that this unstable normal mode satisfies an equation analogous to Mathieu's equation, from which one can give an analytical estimation of the critical mechanical strength where the transition occurs. The proposed scheme is based on the current state-of-the art experimental setups and hence it should be very promising and experimentally feasible.

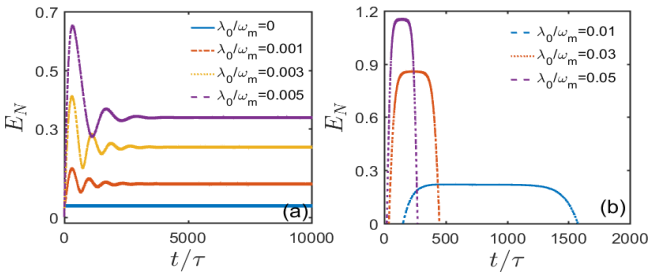

Fig. 1 Entanglement dynamics of the two coupled mechanical oscillators for various coupling strengths.(a) $T/T_0 = 0$ and (b) $T/T_0 = 3$, where $T_0 = \hbar\omega_m/k_B$.

References

1. M. Aspelmeyer, *et al.*, Rev. Mod. Phys. 86, 1391 (2014).
2. D. Vitali, *et al.*, Phys. Rev. Lett. 98, 030405 (2007).
3. S. Chakraborty and A.K. Sarma, Phys. Rev. A, 97, 022336 (2018).

OSI-ISO manuscript No:
(56)

Tripartite entanglement in three-mode optomechanics

Kousik Mukherjee*, Paresh Chandra Jana
Department of Physics and Technophysics, Vidyasagar University, Midnapore, 721102, India
*Corresponding author: kousikmukherjee89@gmail.com

Abstract: We investigate the existence of intermodal entanglement of a weakly driven, damped three-mode optomechanical system containing two optical modes and a mechanical mode. The Hamiltonian of the system solved using short time dynamics by solving corresponding equation of motion for different field modes. Variations of the nonclassical correlation with laser detuning and mechanical resonance frequency are studied under different coupling strength. The system exhibits the higher order nonclassical correlation even in weak coupling regime conditions and this investigation should be useful for quantum information processing.

Keywords: optomechanics, nonclassical, entanglement

Summary of the article:

Entanglement is a nonclassical property, important for different fundamental questions and potentially useful in quantum computation and quantum information processing [1,2]. This property is observed for a multi-particle system. If the wave-function of a multi-particle system can't be factorized into a product of wave functions of the individual particle then the state is called a non-separable or an entangled state. The idea of this nonclassical correlation has been drawn from a novel thought experiment by Einstein, Podolsky and Rosen. Optomechanical systems provide a good platform to study this quantum behaviour at macroscopic scale. The existence of entanglement is already studied theoretically and observed experimentally in different optomechanical system [3,4]. The evidences of the nonclassical behaviour can be revealed by negativity of Wigner functions, homodyne detection etc. In this article, we are interested to study intermodal entanglement of a three mode optomechanical system, in which two cavities are coupled to a single mechanical resonator. This type of system has potential application in gravitational wave detectors [5] etc. Three-mode entanglement is a type of higher order nonclassicality which are much useful from weak or lower order nonclassicality. Higher order nonclassicality have application in cavity magnomechanics, cavity quantum electrodynamics etc. and these effects have drawn attention in recent both theoretically and experimentally [6]. Motivated by these we decided to study higher order entanglement as no effort has been made yet.

The system Hamiltonian of the model is [7]

$$H = \omega_m c^\dagger c - \Delta\, a^\dagger a + g(a\, b^\dagger + a^\dagger\, b)(c + c^\dagger) + i\Omega(\, b^\dagger - b) \qquad (1)$$

where a , b and c are the destruction operator for two optical mode and mechanical mode respectively. ω_m and g represent the frequency of the mechanical mode and coupling strength respectively. The driving strength $\Omega = \sqrt{\kappa P/\hbar\omega_b}$, with P is Laser power, κ cavity line width and ω_b resonance frequency of cavity mode b.

In order to investigate intermodal entanglement we use Li *et al.* moment based criteria [8]. For the state $ab|c$ is entangled if $\langle N_a N_b N_c\rangle < \left|\langle abc^\dagger\rangle\right|^2$ and $\langle N_a\rangle\langle N_b\rangle\langle N_c\rangle < |\langle abc\rangle|^2$. We define these two conditions as

$$E = \langle N_a N_b N_c\rangle - \left|\langle abc^\dagger\rangle\right|^2 \qquad (2)$$

$$\xi = \langle N_a\rangle\langle N_b\rangle\langle N_c\rangle - |\langle abc\rangle|^2 \qquad (3)$$

If $E < 0$ and $\xi < 0$ then tripartite entangled state exists.

To find out E and ξ , we solve numerically the quantum master equation of the system. The master equation is

$$\dot{\rho} = -i[H, \rho] + L_\rho \qquad (4)$$

Where the Lindblad operator $L = L_a + L_b + L_c$, with $L_a\rho = \frac{\kappa}{2}(2a\rho\, a^\dagger - a^\dagger a\rho - \rho\, a^\dagger a)$, $L_b\rho = \frac{\kappa}{2}(2b\rho\, b^\dagger - b^\dagger b\rho - \rho\, b^\dagger b)$ and $L_c\rho = \frac{\gamma}{2}(2c\rho\, c^\dagger - c^\dagger c\rho - \rho\, c^\dagger c)$ where γ is mechanical damping.

For our numerical calculations we choose, weak coupling regime in which coupling strength smaller than cavity decay rate and others are experimentally realistic parameters.

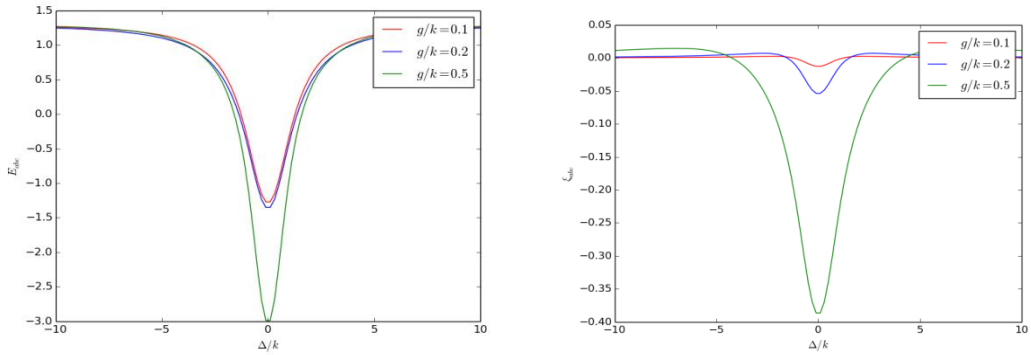

a) b)

Fig. 1. Variation of a) E and b) ξ with normalised cavity detuning for different values of g/k with $\gamma/k = 0.01$ and $E/k = 0.07$.

Fig. 1. a) and b) are shown the variation of the depth of steady state entanglement as a function of cavity detuning. Maximum entanglement observed for zero detuning i.e. resonant excitation of optomechanical frequency for both conditions but depth of entanglement is slightly different. Our study is shown that system exhibit intermodal entanglement between two cavity field modes and mechanical mode in weak coupling regime which should be useful for quantum computation.

References:

1. S. Braunstein and P. van Loock, Rev. Mod. Phys. 77, 513 (2005)
2. M. Hillery, Phys. Rev.A 61, 022309 (2009)
3. Y. D. Wang, S. Chesi and A. A. Clerk, Phys. Rev. A 91, 013807 (2015)
4. K. Mukherjee and P.C. Jana, J. Opt. , 016, 0339 (2016)
5. V. Braginsky, S. Strigin, and S. Vyatchanin, Phys. Lett. A. 287, 331 (2001)
6. A. Allevi *et al.*, Phys. Rev.A 85, 063835 (2012)
7. N. Lorch and K. Hammerer, Phys. Rev.A 91, 061803(R) (2015)
8. Z. G. Li *et al.*, Phys. Rev.A 75, 012311 (2007)

OSI-ISO 2018 manuscript No.
(58)

Plasmon mediated photoluminescence enhancement from Quantum Dot solid

Riya Dutta · Jaydeep K Basu

Abstract We present here the Photoluminescence enhancement of Quantum Dot(QD) solid formed heterostructure for a particular separation between QD and Gold Nano Particle(AuNP). This exciton-plasmon interaction strongly depends on the size, structure and separation of QD and AuNP. It achieves maximum enhancement at separation 3 nm. This tunable enhancement arises from the contention between Plasmon mediated excitonic mode and Non radiative energy transfer.

Keywords QD Solid · LSPR · Exciton

Nanoparticles offer unpredicted optical properties as they are small enough to confine their electrons and produce quantum effects.It has been demonstrated that the spontaneous emission rate of a single emitter depends on the environment.[1] The enhancement of spontaneous emission rates emerged when they are matched in a resonant cavity (the Purcell Effect)[2].These modifications of the spontaneous decay rate can be observed in the presence of metallic surfaces. The optical and photo thermal properties of noble metal nanoparticles arise from localized surface Plasmon resonance (LSPR). To probe this properties, here we have used Gold Nano particle(AuNP)based CdSe Quantum dot(CQD) system where both assembled into monolayer heterostructures.Incorporation of AuNPs leads to generate Surface Plasmon Polariton (SPP). Recently some studies [3-4] have suggested the possibility of obtaining the strong coupling and collective emission (CE) from an ensemble of quantum emitters medi-

Riya Dutta
Indian Institute of Science,Bangalore, India.
E-mail: riya@iisc.ac.in

Jaydeep K Basu
Indian Institute of Science,Bangalore, India.
E-mail: basu@iisc.ac.in

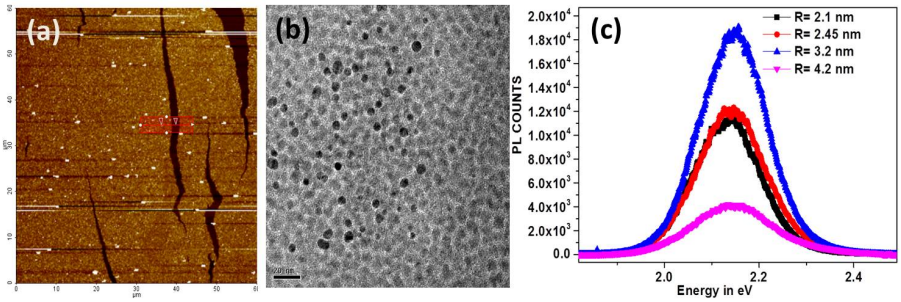

Fig. 1 (a)AFM image shows the compact monolayer film.(b)TEM image of the CQD-AuNP heterostructure film shows the inter-paticle distance between CQD and AuNP.(c)Individual PL emission spectra from the film for different surface separation between AuNP and QDs(R).

ated by Plasmon of Metal Nano Particle.In our previous report[5-6], we have reported how surface plasmon of AuNPs can mediate collective emission in compact CQD monolayers by changing the effective density[7]. Mostly emission of QD is reduced in the presence of MNPs because of energy dissipation in the metal.To study the dependence of this QE on surface separation(R) of AuNP and CQDs, we have studied QD-AuNP based distinct systems which are differed by non-identical R values.Fig 1(c) shows the photoluminescence photon counts from AuNP based QD films. Which indicates the maxima arises around 3 nm. With decreasing R, the QE of the system reaches maximum for a particular regime of R where quenching is expected. The system become less efficient otherwise. The emission of a QD increases in the presence of AuNPs that comes from Plasmon-induced electric field amplification inside a complex. The regime of increased emission can be realized via enhancement of optical absorption or via amplification of the emission process.For a optimum condition of size and separation (R) It can overcome the increment in non-radiative decay rate.

References

1. Bellessa J, Strong Coupling between Surface Plasmons and Excitons in an Organic Semiconductor, J . Phys Rev Lett, 93,36404. (2004)
2. Purcell, Resonance Absorption by Nuclear Magnetic Moments in a Solid, E. M. Phys. Rev., 69, 681 (1946)
3. A.O. Govorov, ExcitonPlasmon Interaction and Hybrid Excitons in SemiconductorMetal Nanoparticle Assemblies, Nano Lett, Vol. 6, No.5, 984-994,(2006)
4. O. Kulakovich,Enhanced Luminescence of CdSe Quantum Dots on Gold Colloids, Nano Lett, Vol. 2, No.12,1449-1452, (2002)
5. L.N.Tripathi, M. Praveena, and J. K. Basu,Plasmonic Tuning of Photoluminescence from Semiconducting Quantum Dot Assemblies,Plasmonics 8,657 (2013).
6. M. Praveena, A. Mukherjee, M. Venkatapathi, J.K. Basu, Plasmon-mediated emergence of collective emission and enhanced quantum efficiency in quantum dot films, Phys. Rev. B, 92, 235403,(2015)
7. F.J. Garcia-Vidal,Quantum Emitters Near a Metal Nanoparticle: Strong Coupling and Quenching,PRL 112, 253601 (2014)

Passively Athermalised and Large Aperture Trans- receiver optics for Eye safe LRF

V.K. Mishra , Arun Sundriyal, P.K. Sharma
Instruments R&D Establishment (DRDO) Dehradun 248008
email: pks@irde.drdo.in

ABSTRACT : In present paper the optics design of a single channel trans- receiver is proposed that will utilize common front optics for collimator and receiver both .Collimated light will use central part while peripheral part of front optics will be utilized for collection of scattered radiation from target. One important factor on which receiver performance depends is aperture of receiving optics. In adverse climatic conditions when there is a large variation in temperature, output divergence of transmitter and spot size of receiver are also affected which can adversely affect the reliability of ranging. In present paper the design , performance and scheme of such an optical system is discussed.

Keywords : *Laser Range Finder, Transmitter, Receiver, Interference Filter, spot diagram, Detector*

Introduction: Laser range finder is a versatile device to calculate the distance of any target of interest. In traditional design ,transmitter and receiver optics form two different channels. To make the system compact now a days single channel Trans- receiver optics is used. Trans- receiver optics is more compact and it eases the packaging of the system. The designed system consists of an afocal module through which laser light will be transmitted and the same optics will be used to collect scattered radiation from the target. The received radiation passes through interference filter and group of focusing lenses that will focus it on the APD detector. A suitable combination of lens material and housing material can reduce the effects of temperature variation on spot size and output beam divergence.

Optical design

The system is designed in such a way that an eye- safe laser beam from the transmitter passes through the a hole in a right angled prism and then incident on the front negative lenses of beam expander, and then it passes through the central part of front optics .In this design input beam divergence was considered as 10 mrad and the output beam divergence of the order of 0.5 mrad was achieved.

The aperture of receiver optics is 145 mm derived after considering factors like reflectivity of target and atmospheric attenuation of signal. The incoming beam has been made parallel before incidence on the interference filter used to block the unwanted radiation from falling onto the detector .Receiver optics has a field of view 0.7 mrad and focal length 285 mm. High index material has been used to control the aberration and length. The performance of receiver optics is analyzed through spot diagram, while performance of beam expander is analyzed through rim ray plot..

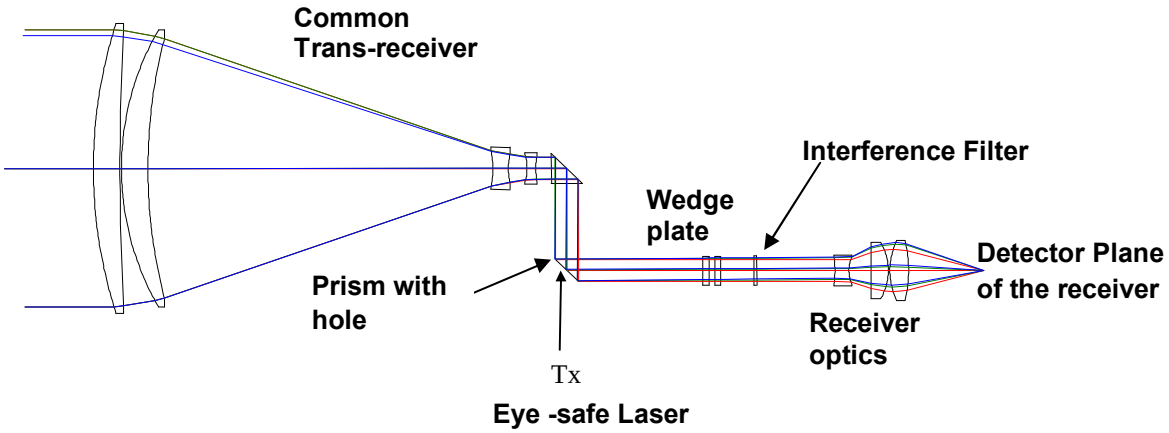

Fig.1 Optical Design Layout

Passivē athermalisation :

Due to variation of operating temperature from -30°C to 55°C, there will be change in spot size on receiver and on output divergence of transmitted beam. To compensate the changes in optical parameters, movement in optical element is required. Compensation can also be achieved without movement of optical component by choosing

suitable housing material. In this case analysis has been done and found that the combined effect (housing material as well as optics) gives excellent results throughout the required range of athermalisation (-30°C to 55°C). The thermal effects can compensated by choosing different housing materials in combination with lens material. Use of stainless steel (Ŭ~99x10^{-7} /°C) or titanium (Ŭ~108x10^{-7} /°C) as housing material in place of aluminum (Ŭ~236x10^{-7} /°C) gives very good result in all temperature range.

Table . 1 Analysis of variation of output divergence with temperature with different housing materials

Temp (°C)	Order of error in output divergence (µrad) with different housing material		
	Aluminum	SS416	Titanium
20°C	23	21	21
-30°C	140	40	53
+55°C	104	27	31

Table .2 Analysis of variation of RMS spot size on receiver with temperature with different housing materials.

Temp (°C)	Order of error in RMS spot size (µ) with different housing material		
	Aluminum	SS416	Titanium
20°C	20	23	23
-30°C	125	40	55
+55°C	99	20	21

Conclusion: With proper selection of housing material along with lens material, reliability of ranging can be ensured for extreme temperature conditions.

Acknowledgement: Authors are grateful to Director Instruments R&D Establishment Dehradun for granting permission to publish this work.

References :

1.Review Laser Range Finder Systems, P. A.Forrester and K. F. Hulme, J. Optical and Quantum Electronics 13 (4) (1981).
2.Forrester ,P A and Hulme,K F, òReview Laser range finder system,Journel of optical and quantum electronic,Vol 13 (4),1981

Optical Design of fast MWIR optics for airborne IRST

Vishal Bhushan, Rakesh Nangia, P K Sharma
Instruments Research & Development Establishment, Raipur Road, Dehradun
E-mail address: vishal@irde.drdo.in

Abstract: Infrared search and track (IRST) systems are required for fighter aircrafts to enable them to passively search, detect, track, classify, and prioritize multiple airborne targets under all aspects, look-up, look-down, and co-altitude conditions and engage them at as long ranges as possible. The system requires a fast f-number optics having large field of regard. In this paper, optical design of a fast f-number optics having three discrete fields of view (FOV) has been presented that will work in mid-wave Infrared (MWIR) spectral region. In case of mirror stabilized system, there will be rotation of the image as the detector orientation remains fixed. The provision for countering this image rotation has also been discussed in the paper.

Keywords: IRST, thermal imaging, FOV, MWIR, Three fields of view, Derotation.

Introduction: IRST systems are becoming more and more important in air defense applications because radars do not meet the requirement of passive surveillance, suffer from jamming, and are vulnerable to anti-radiation missiles. Other reason for preference of IRST systems over radars is a dramatic increase in IR sensor performance, resulting in long-range detection capability. In addition, IRST should be able to provide landing and flying-aid capability during night and bad weather conditions. A three field of view optics design with image derotation and deblurring mechanism has been presented in this paper.

Design Specifications:

Effective Focal Length	:	75mm (Narrow FOV); 38mm (Mid FOV); 19mm (Wide FOV)
F/Number	:	1.5 (All FOVs)
Spectral Band	:	3.6µm – 4.9µm
Detector Type	:	640x512 cooled InSb
Pixel pitch	:	15µm

Optical Design and Description: Optical layout of designed optics has been shown in figure 1.The designed optics consists of different sub modules. Scanning Mirror used to provide 360° azimuth and +40°/-20° elevation degree of freedom. There are three afocal magnification changeover optics (MCO) modules that will come one by one in the optical path with a motorized assembly in order to change the field of view. As the top mirror rotates in azimuth, the image will also be rotated. In order to cater for this image rotation, a dove prism has been introduced that will move in sync with the top scanning mirror. The beam is then focused onto the focal plane of the detector by a base thermal imager optics which is common for all the three fields of view. Moreover, as the top mirror rotation will be very fast, the image will be blurred because of limited integration time of the detector. In order to cater for this image blurring, a fast steering mirror (FSM) has been introduced in the base thermal imager channel which will also be in closed loop with the top scanning mirror. Design optimization has been carried out using CodeV® optical design software.

Acknowledgments: Authors are thankful to the project team from the Vision Instrumentation Design Centre of IRDE for their help and valuable inputs. Authors are also grateful to Group Director, Optical Engineering Division and Director IRDE for their guidance, inspiration and encouragement.

References:

[1] L. Fortunato, G. Colombi, A. Ondini, C. Quaranta, C. Giunti, B. Sozzi, G. Balzarotti, "SKYWARD: the next generation airborne infrared search and track," Proc. SPIE 9819, Infrared Technology and Applications XLII, 98190K (20 May 2016)

[2] Hari Babu Srivastava, Y., B. Limbu, Ram Saran, and Ashok Kumar, "Airborne Infrared Search and Track Systems", Defence Science Journal, Vol. 57, No.5, September 2007, pp.739-753.

[3] Code V® is a product of Optical Research Associates/ Synopsis, Pasadena, CA.

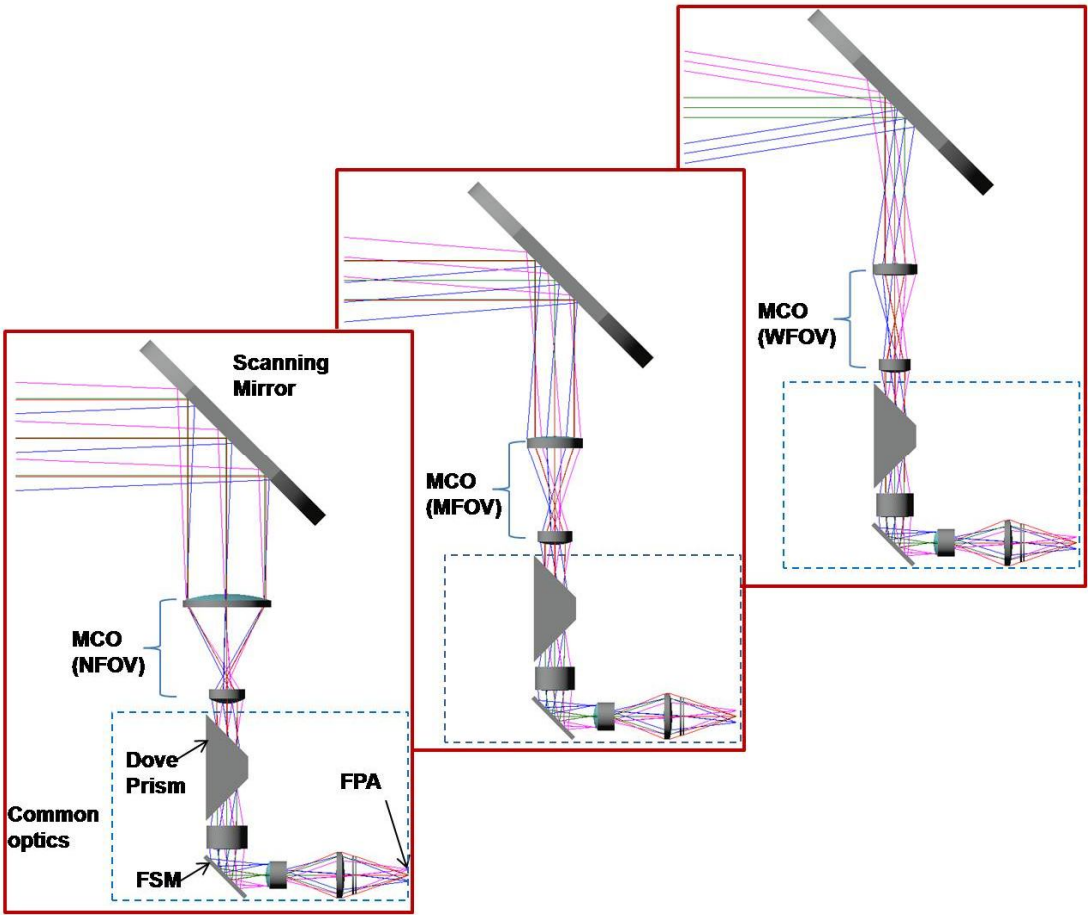

Fig. 1 Optical Layout of three FOV

Tunable selective edge enhancement of Xylem phase sample using fractional spiral phase filtering

Satyajit Maji and Maruthi M. Brundavanam*
Department of Physics, Indian Institute of Technology Kharagpur, Kharagpur-721302, India.
*bmmanoj@phy.iitkgp.ernet.in

Abstract: Transparent phase sample which lacks contrast in bright-field imaging can be imaged at better contrast by attaining edge enhancement which transforms the phase difference at the edges of the sample to intensity contrast. Using a fractional order spiral phase filter in a Fourier filtering setup, selective edge enhancement is achieved where a selective direction of the edge can be more contrast enhanced. The degree of enhancement is controlled by the fractional charge of the spiral phase and direction of the enhancement can be tuned by input wavefront curvature. This is explained by the transformation of the field profile of the point spread function corresponding to optical vortex beams with different fractional charge. Tunable and selective edge enhancement is demonstrated using a transparent Xylem tissue on a glass slide imaged with some fractional order spiral phase filters. Quantitative phase imaging capability of the demonstrated technique is investigated.

Keywords: spiral phase contrast imaging, fractional Hilbert transform, fractional spiral phase filter, selective edge enhancement.

Introduction

Using an integer order spiral phase filter in a 4f configuration Fourier filtering setup, isotropic edge enhancement of a transparent phase sample has been achieved. This action mathematically describes the two-dimensional generalisation of the radial Hilbert transformation [1]. The isotropic edge enhancement is described by the convolution of the object field with the Fourier transformation of the spiral filter function of the form exp(imφ) [2]. Here φ is the azimuthal angle and 'm' is an integer, generally of unit value. As the filter is circularly symmetric for integer values of 'm', the achieved edge enhancement is isotropic. But for some application more contrast at some part of the sample is desired which exhibits a shadow effect [3], visually resembling an oblique incidence of the input light. In that cases, a fractional spiral filter where the 'm' is now a fractional number is found to be very useful. Mathematically, this action can be related to the fractional Hilbert transform [4].

In this study, it is demonstrated that the degree and spread of this selective enhancement can be tuned by the fractional order spiral phase filters. Further the orientation of the enhanced edge can be tuned by the input wavefront curvature. Previously, anisotropic edge enhancement has been achieved using different shifted and anisotropic vortex profiles that has their individual advantages [5]. Here the fractional order spiral phase filter enables advantages of both shifted and anisotropic vortex filter simultaneously. The potential of this technique to make a quantitative phase reconstruction of the sample by numerical post-processing will be discussed.

Experimental details

The schematic experimental setup is shown in figure 1(a). A spatially filtered and collimated beam of a He-Ne laser is focussed using a lens (f =5 cm) on to the Xylem sample on a glass slide. The scattered light from the sample is collected by a microscope objective (MO) lens (10X, 0.25 NA) and then propagated to the phase filter plane using a telescopic system such that the filter plane is the Fourier conjugate plane of the sample plane. Spatial phase filters (shown in figure 1(b)) are displayed on a spatial light modulator (SLM) placed at the Fourier plane.

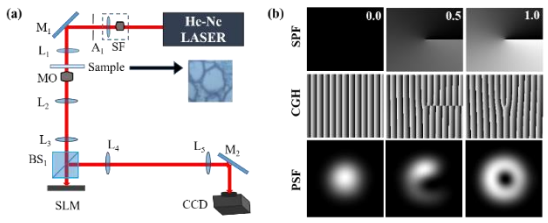

Fig. 1 (a) Schematic setup for achieving selective edge enhancement using fractional spiral phase filters. (b) some on axis (SPF) and off-axis (CGH) spiral phase filters with the corresponding point spread functions (PSF)

As the spiral phase filters, the computer generated on-axis spiral phase function (SPF) and off-axis bifurcation grating holograms (CGH) have been used for the current study. After the Fourier filtering, it is again brought to the Fourier conjugate plane by another lens and is imaged on the CCD camera. The input wavefront curvature on the phase filter can be tuned by translating the SLM along the beam axis within the Rayleigh range and maintaining the collimation by keeping the optical

distance between L_3 and L_4 same. The bottom row of figure 1(b) shows the point spread functions (PSF) of corresponding fractional order spiral phase filters.

Results

The edge-enhanced images after Fourier filtering using different fractional phase filters are shown in figure 2 for both on axis SPF and off-axis CGH. The case when m=0 implies a bright field imaging which illuminates the total field of view but fails to feature out the relevant and important details of the object in terms of local change in thickness or refractive index of different parts of the sample. For m=1 spiral phase filter, an isotropic edge enhancement of all the different orientation of the object is achieved simultaneously. But most interestingly, with a fractional order spiral phase filter a gradual and orientation specific change in the contrast is visible. For SPF of order below 0.5 some anisotropic edge enhancement is achieved but the background illumination is still present. At and beyond 0.5, a clear distinction in contrast of two diametrically opposite direction of the phase sample demonstrate that a selective edge enhancement of different parts of the object is achieved (enhanced edges are shown by red arrow). This is due to the anisotropic PSFs (as shown in 1(b) for 0.5) when using fractional spiral phase filters. Image intensity in former on-axis SPF case is more but it shows high noise across the object. On the other hand, the later using CGH shows slightly reduced intensity but less noisy intensity variation.

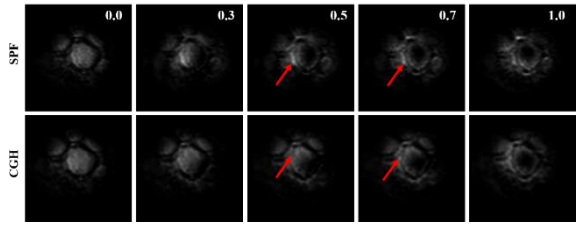

Fig. 2 Selective edge enhanced images filter of a Xylem test sample on a glass slide with different fractional order spiral phase. The red arrow points the direction of enhancement

Conclusion

The edge enhanced images of the Xylem sample using different spiral phase filters demonstrate that by choosing proper fractional order of the spiral filter a specific orientation of the sample within the field of view can be enhanced up to a certain degree. Thus both the advantages of using a shifted anisotropic phase vortex filter in a Fourier filtering setup can be achieved. Moreover, the orientation of the enhanced edge can be further tuned by the input wavefront curvature. The results are explained by the point spread function of the FOV beams [6] and will be discussed in details during the conference.

Acknowledgement

The authors acknowledge support from INSPIRE - DST, India and SRIC, IIT Kharagpur.

References

[1] J. A. Davis, D. E. McNamara, D. M. Cottrell, J. Campos, Opt. Lett. 25, 2 (2000)
[2] G. Situ, M. Warber, G. Pedrini, W. Osten, Opt. Commun. 283, 1273 (2010)
[3] A. Jesacher, S. Furhapter, S. Bernet, M. Ritsch-Marte, Phys. Rev. Lett. 94, 233902, (2005)
[4] J. A. Davis, D. E. McNamara, D. M. Cottrell, Appl. Opt. 37, 29, (1998)
[5] M.K. Sharma, J. Joseph, P. Senthilkumaran, J. Opt (Springer) 42, 1 (2013)
[6] S. Maji, M.M. Brundavanam, J. Opt. 20, 045607 (2018)

OSI-ISO 2018 manuscript No.
(65)

Designing a hyperbolic metamaterial resonator for spontaneous emission rate enhancement from silicon-carbide based quantum emitters

Nadeem Ahmed · Faraz A. Inam

Abstract Here we computationally studied the single photon emission from a silicon carbide (SiC) nanoparticle based vacancy-centre on the top of the hyperbolic metamaterial (HMM) structure. The relevant HMM parameters such as the top dielectric layer thickness and number of HMM periods were optimized to achieve substantial spontaneous emission enhancement in the single photon emission from SiC based quantum emitters.

Keywords Hyperbolic metamaterial · silicon-carbide · single photon sources · spontaneous emission rate

Multilayer metal-dielectric hyperbolic meta-material (HMM) structures are being used to achieve emission enhancement from single photon emitters. These HMM's are known to provide emission enhancement over a broad emission spectrum extending to few hundred nanometers [1]. Recently, bulk SiC has also emerged as a promising host for ultra-bright single quantum emitters with count rate of $2 \times 10^6 cps$ [2]. Here, we computationally studied emission from a single silicon carbide (SiC) nanoparticles based vacancy centre on the top of the HMM structure. The emission peak for these vacancy centres is known to be around 900 nm [3]. We optimized height of the top dielectric layer along with the number of metal-dielectric periods required for getting optimum spontaneous emission rate (SER) enhancement [4] for dipole emission on top of the structure.

Figure 1 shows the schematic of our HMM design. The alternate packing of metal (Au) and dielectric (ZnS) layers provides HMM with hyperbolic

Nadeem Ahmed
Department of Physics, Aligarh Muslim University, Aligarh, Uttar Pradesh, India – 202002
E-mail: khannadeemamu@gmail.com

Faraz A. Inam
Department of Physics, Aligarh Muslim University, Aligarh, Uttar Pradesh, India – 202002

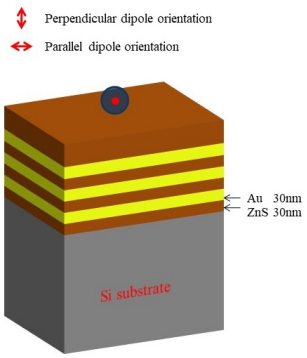

Fig. 1 Schematic of HMM model consisting alternate layers of ZnS and Au of thickness 30 nm with the SiC sphere on the top ZnS layer.

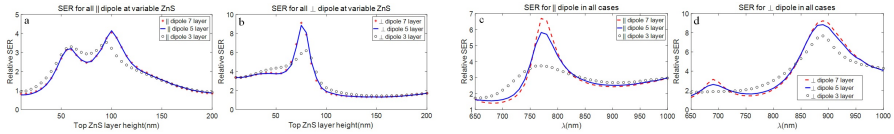

Fig. 2 Relative SER plots. In (a) and (b) emission rate is calculated for the variable height of top ZnS layer in the case of parallel and perpendicular dipole respectively. In fig. (c) and (d) relative SER is calculated at optimum height of top ZnS layer which for parallel and perpendicular dipole

dispersion relation. For, top ZnS layer height of 75 nm we observed the maximum SER enhancement for perpendicular dipole orientation. Figure 2c and 2d shows the SER performance as a function of the number of HMM layers. On the basis of these result we can conclude that the optimum choice for the multi-layered HMM structure is 5 layered HMM structure.

References

1. D. Lu, J. J. Kan, E. E. Fullerton and Z. Liu, Enhancing spontaneous emission rates of molecules using nanopatterned multilayer hyperbolic metamaterials, Nature Nanotechnology 9, 48-53 (2014).
2. S. Castelletto, B. C. Johnson, V. Ivády, N. Stavrias, T. Umeda, A. Gali and T. Ohshima, A silicon carbide room-temperature single-photon source, Nature Materials 13, 151-156 (2014).
3. A. Lohrmann, B. C. Johnson, J. C. McCallum, and S. Castelletto, "A review on single photon sources in silicon carbide," Reports Prog. Phys. 80(3), 034502 (2017).
4. Purcell, E. M. Spontaneous emission probabilities at radio frequencies, Phys. Rev. 69, 681 (1946).

Diaphragm-less Micro-tip Cantilever as Low Frequency Microphone

Sumit Dass and Rajan Jha*

Nanophotonics and Plasmonics Laboratory, School of Basic Sciences, Indian Institute of Technology Bhubaneswar, Khurda, 752050, India

* rajaniitd@gmail.com; rjha@iitbbs.ac.in.

Abstract

We propose a very compact diaphragm free acoustic sensor consisting a tapered SMF micro-tip in cantilever configuration. The change in the light coupling between the micro-tip and the source fiber caused by the acoustic pressure is utilized to detect the external acoustic signal. Experimental results show that the sensitivity and working range of the sensor depends upon the length of cantilever and hence, the performance of the sensor can be easily tuned. The SMF only structure along with intensity-based interrogation makes this acoustic sensor very cost effective. Experimental results show that for a cantilever length of 15.53 mm, the probe has a maximum acoustic sensitivity of 196 mV/KPa, minimum detectable pressure of 1.03 Pa/√Hz and the linear frequency range is 0-250 Hz.

Keywords

Microphone; Optical Cantilever; Single mode fiber; Fiber optics sensor; Micro-tip; Acoustics.

Acoustic sensors or microphones find application in many application from flight path estimation to structural health monitoring of nuclear plants [1,2]. Researchers have successfully demonstrated that microphones can also be utilized for vehicle classification, gas flow measurement, muscle vibration measurement and bioacoustics analysis of insects[3,4]. Recently reported optical fiber microphones (OFMs) exhibit equal or even better performance as compared to traditional piezoelectric based microphones in terms of sensitivity, bandwidth and noise equivalent pressure[5–7]. Furthermore, the OFMs have inherent advantages of multiplexing, remote sensing and immunity to electromagnetic signals. Majority of OFMs utilize thin diaphragm as a part of the sensing element. This category of OFM is dominated by interferometric structures involving very small and thin reflecting diaphragms[8,9]. In order to overcome the complexity involved with diaphragm fabrication and to avoid the requirement of costly phase/wavelength measuring devices, we propose a simple and intensity dependent acoustic sensor. The sensing structure is a cantilever type and it consists of a tapered single-mode fiber (SMF) tip placed in front of an SMF tip.

The proposed setup consists of a tapered microfiber tip placed in front of vertically cleaved SMF, as shown in Fig. 1. To fabricate the tapered micro-tip, firstly a simple SMF taper is fabricated using well-established flame and brush technique[12]. The SMF taper is then carefully cleaved at the waist position where the fiber diameter is smallest. By doing so, we will create two tapered micro-tips. The inset of Fig. 1 shows the micrograph of one such tapered micro-tip with a tip diameter of 17.28 μm and length of tapered tip is 1.24 mm. Now, a SLED source is pigtailed with a standard SMF, its end is vertically cleaved and placed on a computer-controlled stage. The tapered micro-tip is placed on another computer-controlled stage, as shown in the Fig. 1. The other end of the micro-tip fiber is connected to a photodetector system.

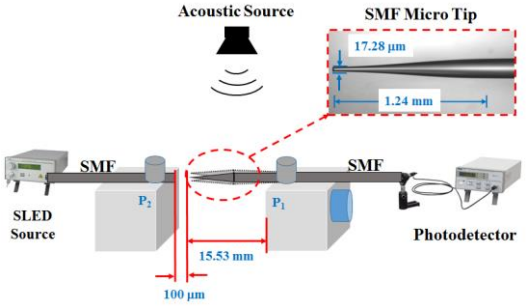

Fig. 1. Schematic of tapered microfiber based optical fiber microphone.

The broadband light generated by the SLED source comes out of the 8 μm core of the SMF tip and gets coupled to the tapered micro-tip placed at a close distance. The output field intensity at the SMF tip follows a Gaussian distribution curve. While keeping the output power of SLED constant, the amount of light which gets coupled to the guided mode of tapered microfiber depends on two parameters; first being the distance between tapered micro-tip and cleaved end of SMF and the second parameter is the axial alignment of tapered micro-tip with respect to the cleaved end of SMF. If we start moving the taper micro-tip further away from the untapered SMF tip then the coupled optical power will start

decreasing. Similarly, maximum power will be coupled to tapered micro-tip if the central axis of micro-tip coincides with that of the untapered SMF tip. Any deviation from this optimum position will result in a decrease of coupled light[13]. Such a small displacement can also be caused by airborne acoustic pressure waves. Hence, given a proper cantilever length, the tapered micro-tip can be used to sense the acoustic waves.

To examine the acoustic performance of such a tapered micro-tip-based cantilever structure, an acoustic source is placed in front of the tapered micro-tip with a cantilever length of 15.53 mm, at 5 meters. For referencing a commercial microphone (B&K) is placed just beside the fiber cantilever setup. The acoustic source is placed in such a way that it is equidistant to both the microphone setups and its central point is in the same place as that of the microphones. Acoustic waves of different frequency and intensity are generated from the acoustic source and this signal deflects the micro-tip of the fiber cantilever structure. This deflection changes the amount of optical power coupled to the tapered micro-tip which is recorded by using a photodetector (Thor Labs). The output of the photodetector of OFM with cantilever length 15.53 mm for an acoustic signal of 200 Hz is shown in Fig. 2(a). Figure 2(b) shows the respective FFT of the photodetector output signal.

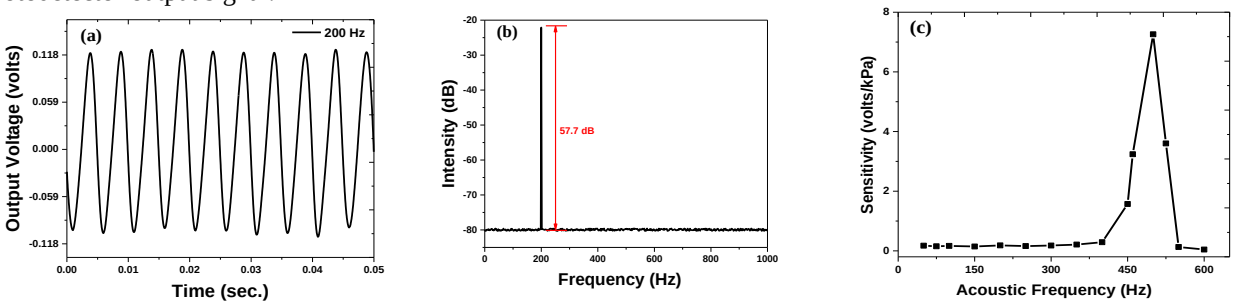

Fig. 2. (a) Time domain and (b) frequency domain response of Sensor-1 at 250 Hz acoustic signal; (c) variation of acoustic sensitivity with frequency.

With the help of the signal recorded by the reference microphone, we can calculate the acoustic sensitivity of the sensing setup. The sensitivity variation with frequency for the OFM is shown in Fig. 2(c). The sensitivity is nearly constant for low acoustic frequencies and then it starts increasing rapidly to reach a maximum value, following which the sensitivity again starts decreasing. The point of maximum sensitivity corresponds to the first order natural frequency (f_{fn}) of the cantilever structure which is 500 Hz, as shown in Fig. 2(c). Considering the linear working frequency range to be half of the natural frequency, we get the linear frequency range as 0-250 Hz for the cantilever length 15.53 mm.

In conclusion, we successfully fabricated and demonstrated a tapered microfiber tip based acoustic sensor. The micro-tip is employed as a cantilever and the change in the light coupling efficiency between the two fiber tips in presence of external force is utilized to detect the applied acoustic pressure. For a cantilever length of 15.53 mm, the acoustic sensitivity at 200 Hz is 0.196 V/KPa.

Acknowledgement

This work is partly supported by DST funded project EMR/2016/003446.

References

[1] K.W. Lo and B.G. Ferguson, Proc. 6th Int. Conf. Inf. Fusion, FUSION 2003 **1**, 62 (2003).

[2] T. Washio and M. Kitamura, J. Nucl. Sci. Technol. **31**, 91 (1994).

[3] A. Courteville, T. Gharbi, and J.Y. Cornu, IEEE Trans. Biomed. Eng. **45**, 145 (1998).

[4] R.W. Mankin *et al.* , J. Econ. Entomol. **93**, 1173 (2000).

[5] C. Jan, W. Jo, M.J.F. Digonnet, and O. Solgaard, Photonics Technol. Lett. IEEE **28**, 123 (2016).

[6] J. Ma, H. Xuan, H.L. Ho, W. Jin, Y. Yang, and S. Fan, IEEE Photonics Technol. Lett. **25**, 932 (2013).

[7] J.A. Bucaro, N. Lagakos, B.H. Houston, J. Jarzynski, and M. Zalalutdinov, J. Acoust. Soc. Am. **118**, 1406 (2005).

[8] W. Wang, N. Wu, Y. Tian, X. Wang, C. Niezrecki, and J. Chen, Opt. Express **17**, 16613 (2009).

[9] F. Xu, J. Shi, K. Gong, H. Li, R. Hui, and B. Yu, Opt. Lett. **39**, 2838 (2014).

[10] J.M. De Freitas, T.A. Birks, and M. Rollings, Opt. Express **23**, 5850 (2015).

[11] G. a Cranch, G. a Miller, and C.K. Kirkendall, J. Acoust. Soc. Am. **132**, 103 (2012).

[12] S. Dass and R. Jha, IEEE Photonics Technol. Lett. **28**, 31 (2015).

[13] S. Dass and R. Jha, Scientific Report, In Press (2018).

OSI-ISO 2018 manuscript No.
(67)

Tamm-plasmon-polaritons in periodic and aperiodic photonic crystals

Mukesh K. Shukla · Ritwick Das
E-mail: ritwick.das@niser.ac.in

Abstract One dimensional (1D) periodic photonic geometries are optical analogues of widely-investigated counterparts in condensed-matter physics. Due to the cyclic evolution, the em-field picks up a quantized geometric phase or alternately 'Zak'-phase while moving between equivalent points within the photonic pass bands. Such investigations have revealed topological photonic insulators and topologically-protected optical surface states. This feature, however, is not apparent in a quasi-periodic or deterministically aperiodic system. In the present work, we discuss and provide a plausible route to define 'Zak'-phase in a 1D quasi-periodic (Fibonacci) lattice.

Keywords Photonic crystals · Tamm-plasmon-polaritons · Bragg diffraction

Tamm-plasmon-polariton (TPP) modes are a variant of optical surface states which are strongly confined at the interface of metal ($-ve$ dielectric constant) and a distributed-Bragg-reflector (DBR). Such modes allow free-space excitation in both the polarizations. They have been widely explored in the periodic configurations such as DBRs and they have been employed for ascertaining the topological (or 'Zak') phase of the pass bands. However, aperiodic geometries such as Fibonacci sequence and Thue-Morse sequence based DBRs, which posses photonic bandgaps (PBGs) by virtue of long-range order, have not been explored from this perspective [2]. In the present work, we have investigated the existence of TPP modes at the interface of 1D quasi-crystals such as *Fibonacci sequence* (FS)-lattice and plasmon-active metal. We further explore the possibility of existence of TPP modes in deterministic aperiodic crystals based on *Thue-Morse sequence* (TMS). We consider two dielectric material for the study namely SiO_2 ('A') and Ta_2O_5 ('B') having thicknesses d_A and d_B. For ascertaining the reflection spectrum, we consider standard transfer matrix

School of Physical Sciences, National Institute of Science Education and Research, HBNI, Jatni - 752050, India

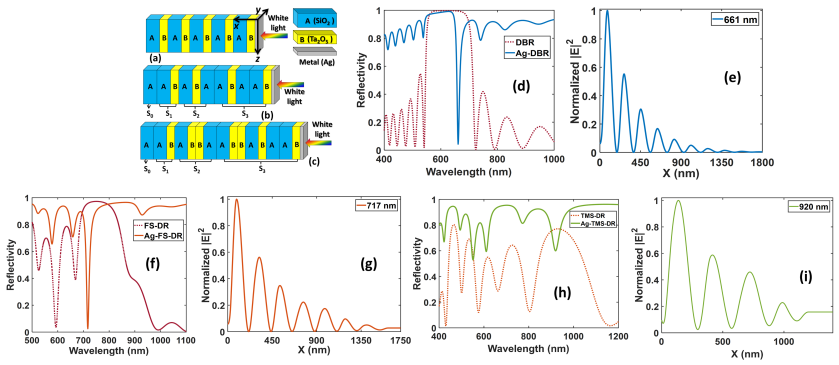

Fig. 1 (a), (b) & (c) Schematic of DBR, FS-DR and TMS-DR. Reflection spectrum and mode-field distribution of DBR in (d) & (e), $\mathbf{C} - Ag$ in (f) & (g) and $\mathbf{F} - Ag$ in (h) & (i) respectively.

method [ref]. As can be seen in the Fig. 1(d), a DBR with 10 unit cells exhibits a PBG ranging from $570 - 720\ nm$. With a thin metal layer (Ag) (30 nm) placed adjacent to DBR, a sharp drop in reflectivity could be observed within the PBG which depicts a TPP mode excitation. This is confirmed from the mode-field distribution at resonance wavelength ($\lambda_r = 661\ nm$) as shown in Fig. 1(e). In a similar manner, we consider a FS defined through $S_n = S_{n-1}S_{n-2}$ for $n \geq 2$ with $S_0 = A$ and $S_1 = B$. A few strings could be written as $S_0 : A; S_1 : B; S_2 : BA; S_3 : BAB; S_4 : BABBA$; and $S_5 : BABBABAB$. In the present case, let us consider a distributed reflector (DR) sequence defined through a linear chain ($\mathbf{C}$) comprised $S_0S_1S_2S_3S_4S_5$. The simulated reflection spectrum for a geometry $\mathbf{C} - Ag$ where $d_{Ag} = 30\ nm$ is shown in Fig. 1(f). The PBG as well as TPP-like excitation at $\lambda_r = 717\ nm$ is evident (Fig. 1(g)). The TPP-like excitation in lowest-order PBG has been employed for ascertaining 'Zak'-phase of the zeroth-order pass band of $\mathbf{C}$ which would be discussed in the symposium. On a similar note, we have considered a TMS based 1D-lattice defined by $S_n = S_{n-1}S_{n-1}^{\dagger}$ and $S_n^{\dagger} = S_{n-1}^{\dagger}S_{n-1}$ for $n \geq 1$ with $S_0 = A$ and $S_0^{\dagger} = B$. Following this chain rule, the reflection spectrum for a lattice $\mathbf{F} \equiv S_0S_1S_2S_3S_4 - Ag$ where $d_{Ag} = 30\ nm$ is shown in Fig. 1(h,i). Multiple discernible PBGs and moderately sharp reflectivity minima within a few PBGs depict TPP-like mode excitation which could be confirmed from the mode-field distribution. Using the TPP-like excitation in $\mathbf{F}$ crystal, we could ascertain reflection phases of backscattered waves from different PBGs. Using this information, we explore the possibility of exciting topologically protected optical modes in TMS lattice based heterostructure configuration during the symposium.

References

1. S. A. Maier, Plasmonics: Fundamentals and Applications, Springer (2007).
2. W. Steurer and D. Sutter-Widmer, J. Phys. D: Appl. Phys., 40 R229 (2007).

Characterising the *gas-drag forces* on various laser-heated interface.

Biswajit Panda[1], Komal Chaudhary, Mehar S. Sidhu, Kamal P. Singh
Department of Physical Sciences, Indian Institute of Science Education and Research, Mohali, Sector 81, SAS Nagar, Manuali, P.O. 140306, India.
Email: 2biswajitpanda@gmail.com[1]

Abstract

We used a simple setup to measure the magnitude of the *gas-drag* force and distinguish it from radiation pressure force which a interface of two medium experiences by a laser beam. We demonstrate the formation of gas-drag forces by Watt-level laser on various interfaces and results are validated using COMSOL simulations. Given its 180 degree directionality and 10 times higher magnitude, compared to the radiation force, one can use these *gas-drag* forces for various applications like smoke remover in case of fire or levitation of lightweight objects.

Keywords : gas-drag forces, radiation pressure force, laser heating, solid-gas interfaces.

Main

When a high power laser hits on a solid-gas interfaces, two forces are generated. One, the radiation pressure force, in the direction of the laser beam. This force is the result of the momentum transfer of the photons to the solid surface. Second, the *gas-drag forces*, opposite to the direction of the laser beam. This force is the result of the air pressure difference created by the diffused heat on the solid/liquid interface due to lasing action. Given the magnitude of the radiation pressure (order of nN), earlier studies used constraint setups and calculations, which ignores these gas-drag forces [1-2].

For a solid gas interface like laser action on an Al mirror, the heat diffuse on a solid surface due to high power laser, creates a temperature difference between top and bottom surfaces. This results into a air turbulence circling inside a bounded system,, creating a lift force (like radiometer). We devised a simple setup to measure this lift force or gas-drag force for various laser power.

The gas-drag force on a mirror was found to, *linearly increases with power* and *10 times that of the magnitude* of the radiation pressure force. These forces gradually decreases to zero as the diffused heat from laser cools down, when laser is switched off.

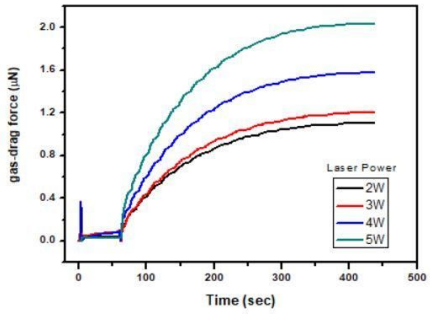

Magnitude of the gas-drag force with time on a light weight mirror.

To validate the theory of the air turbulence generated due to lasing action resulting to the gas-drag force, we used visible smoke (size: 0.1 - 1 micron) on silicon wafer.

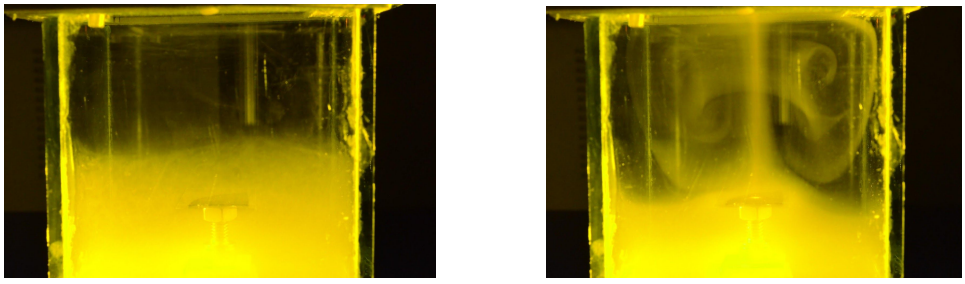

LASER OFF LASER ON

Images showing the air turbulence created by the lasing action on a silicon wafer.

Air flow in the surrounding, because of heat diffusion from silicon wafer, is simulated in COMSOL by solving Navier-Stokes Equation and simulated results are in good agreement with the experimental observations.

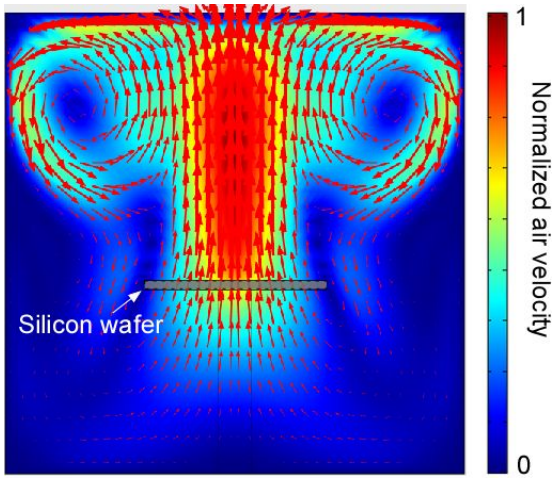

COMSOL simulation image showing the air turbulence created by the lasing action on a silicon wafer.

In conclusion, we have calculated the gas drag force using a simple setup. Given the magnitude of these force, one needn't ignore the effects of these forces for a stimulated lasing action. Due to the nature of these forces, one can build applications like smoke remover, in case of fire and other hazards or levitation of small lightweight objects.

References

1. Liu, Bin, et al. "Radiation pressure and gas drag forces on a melamine-formaldehyde microsphere in a dusty plasma." *Physics of Plasmas* 10.1 (2003): 9-20.
2. Haralson, Zach, and J. Goree. "Temperature dependence of viscosity in a two-dimensional dusty plasma without the effects of shear thinning." *Physics of Plasmas* 23.9 (2016): 093703.

OSI-ISO 2018 manuscript No.
(69)

A hyperbolic metamaterial based design for practical solid-state single photon sources with GHz photon collection rates

Faraz A. Inam · Abhinav Kala · Nadeem Ahmed · Achanta Venu Gopal

Abstract Here we report the design of a 5-layered, planar hyperbolic metamaterial (HMM) resonator-antenna for efficient photon extraction from solid-state single photon sources (SPS). Our resonator-antenna design is composed of a dielectric that is indexed-matched to diamond/silicon-carbide (SiC). We analyzed the performance of this resonator-antenna system for the Purcell enhancement, quantum and collection efficiencies. Our calculations show a large spontaneous emission rate enhancement with Purcell factor in the range of 300, along with the collected photon count rates in the range of few GHz over the broad emission spectrum (650-900 nm). This broadband range covers the emission spectrum of most of the diamond/SiC based SPS. Our design is the first to report GHz range photon count rates from solid-state SPS. Compared to the previous computational designs, our design show a state-of-the art improvement in the antenna-performance for solid-state SPS with properties very close to a practical SPS.

Keywords Single photon sources · quantum optical technologies · hyperbolic metamaterial · resonator-antenna · collected photon rate · Purcell enhancement

Faraz A. Inam
Department of Physics, Aligarh Muslim University, Aligarh, Uttar Pradesh, India 202002
Department of Condensed Matter Physics and Material Science, Tata Institute of Fundamental research, Mumbai, India 400005
E-mail: faraz.inam.phy@amu.ac.in

Abhinav Kala
Department of Condensed Matter Physics and Material Science, Tata Institute of Fundamental research, Mumbai, India 400005

Nadeem Ahmed
Department of Physics, Aligarh Muslim University, Aligarh, Uttar Pradesh, India 202002

Achanta Venu Gopal
Department of Condensed Matter Physics and Material Science, Tata Institute of Fundamental research, Mumbai, India 400005

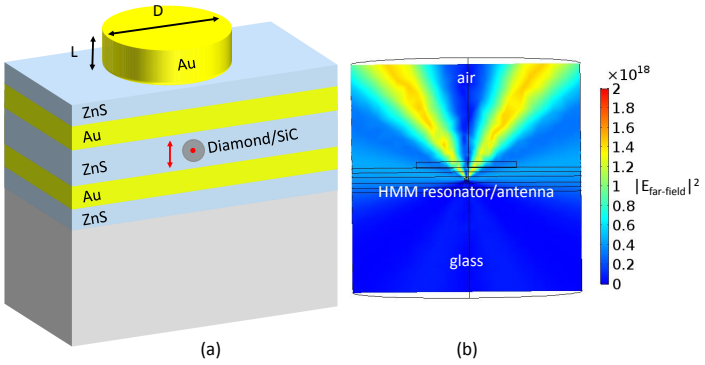

Fig. 1 a) Schematic image of the 5-layered Au-ZnS HMM like resonator with cylindrical Au antenna on top. (b) The in-plane far-field dipole radiation profile of the 5-layered Au-ZnS resonator-antenna. The dipole is considered to be oriented perpendicular to the Au interface

Solid-state single photon sources (SPS) such as quantum dots or color centers in diamonds, silicon-carbide have shown promises for practical deployment in the emerging quantum optical technologies [1]. Many of these technologies including quantum cryptography and quantum communications demand data rates in the GHz range [1]. This thereby limits the use of these SPS, where the maximum observed photon count rates are limited to few MHz with lifetimes of the order of few nanoseconds [2]. These technologies are presently relying of probabilistic SPS based on nano-linear processes for practical applications [1].

Here we report the design of a 5-layered planar hyperbolic metamaterial (HMM) [3] based cavity resonator with metallic antennas that results in collected photon count rates of the order of few GHz from diamond/silicon-carbide based SPS. The design is based on sandwiching the nanodiamond/SiC crystal between a period of metal/dielectric, gold/zinc-sulphide HMM layers [4]. The zinc-sulphide (ZnS) is chosen as a dielectric due to its close refractive index-matching with that of diamond/SiC and helps in the near to far-field out-coupling of emission from diamond/SiC based quantum emitters [4].

References

1. I. Aharonovich, D. Englund, and M. Toth, Solid-state single-photon emitters, Nature Photonics 10, 631641 (2016).
2. N. H. Wan, B. J. Shields, D. Kim, S. Mouradian, B. Lienhard, M. Walsh, H. Bakhru, T. Schrder, and D. Englund, Efficient Extraction of Light from a Nitrogen-Vacancy Center in a Diamond Parabolic Reflector, Nano Letters 18, 27872793 (2018).
3. A. Poddubny, I. Iorsh, P. Belov, and Y. Kivshar, Hyperbolic metamaterials, Nature Photonics 7, 948957 (2013).
4. F. A. Inam, N. Ahmed, M. J. Steel, and S. Castelletto, Hyperbolic Metamaterial Resonator-Antenna Scheme for Large, Broadband Emission Enhancement and Single Photon Collection, Accepted in JOSA B (2018).

OSI-ISO 2018 manuscript No.
(70)

A Comparison of Optical Delay of Light in SBN:60 and SBN:75

Satchi Kumari . Stuti Joshi

Abstract Slowing down of light pulses has been studied theoretically in SBN:60 and SBN:75 via degenerate two-wave mixing technique. The optical delay and the corresponding group velocity were found to vary systematically with the pulse width. Role of response time and electro-optic coefficients of these crystals onto optical delay is studied.

Keywords Slow light. photorefractive crystals. two-wave mixing. group velocity.

Introduction

Strontium barium niobate (SBN) is a well know photorefractive crystal for nonlinear optics (NLO) [1-2]. It has various device applications viz. self-pumped phase conjugation, spatial filtering, spatial solitons and two-wave mixing [3-5]. Two-wave mixing (TWM) phenomenon leads to Optical delay in the SBN crystal [4-5]. In two-wave mixing a continuous strong pump beam and a weak pulsed probe beam are launched onto the crystal. The interference of these beams forms a grating pattern inside the crystal. These gratings diffract the light from pump to probe. The probe beam gets amplified and delayed. This optical delay is measured by comparing two pulses, first travelling in the air and second travelled through the crystal [6]. The role of time is very important in these experiments since grating formation and stabilization governs the optical delay [7]. To study the dynamics of time scale, pluses with various pulse width are launched and its effect on optical delay and nature of output pulse (amplification and broadening) is studied.

Further, SBN has unique open crystal structure containing vacant lattice sites [2]. Therefore, it potentially exhibits a greater flexibility for doping. The electrooptic coefficient is influenced by the doping (Sr/Ba ratio). Hence, in the present study optical delay is compared for two different SBN crystal viz SBN:60 and SBN:75 [8] with different Sr/Ba ratio, as a function of pulse width.

Theory

Let us consider a Gaussian signal pulse launched onto the PR crystal with the form given by equation 1,

$$S(0,t) = S_0 exp\left[\frac{-t^2}{T^2}\right] \quad (1)$$

Satchi Kumari
Centre for Applied Physics, Central University of Jharkhand, Ranchi, India
E-mail: satchikumarisingh@gmail.com

Stuti Joshi
Department of Physics, Indian Institute of Technology, Delhi, India
E-mail: stutijoshi86@gmail.com

$S_\omega(0)$ is the Fourier transform of the input amplitude S(0, t) and T is the input pulse width.

$$S_\omega(0) = \frac{1}{\sqrt{2\pi}}\int_{-\infty}^{\infty} S(0,t)\exp(-i\omega t)\,dt$$

On interaction with the SBN crystal and after travelling a distance d inside the crystal the form of equation will be as follow [9].

$$S_\omega(d) = S_\omega(0) \times exp\left[\left(\Gamma\frac{d}{2}\right)\left(\frac{1}{1-i\omega\tau}\right)\right] \quad (2)$$

In the above Eq. the first exponential term $\left[\left(\Gamma\frac{d}{2}\right)\right]$ represents the signal pulse due to two wave mixing. The second term $exp\left(\frac{1}{1-i\omega\tau}\right)$ represent the frequency dependent delay. On substitution for Eq. (1) in the Eq. (2) we get the following expression [9]

$$S_\omega(d) = S_0 T\frac{1}{\sqrt{2}}exp\left(-\frac{\omega^2T^2}{4}\right) \times exp\left[\left(\Gamma\frac{d}{2}\right)\left(\frac{1}{1-i\omega\tau}\right)\right] \quad (3)$$

In order to compare output signal pulse with input signal pulse we find the inverse Fourier transform of eq (3). The detailed derivation can be seen from reference 9.

$$\frac{S(d,t\ )}{S_0} = \frac{T}{\sqrt{\pi}\tau}\int_0^{\infty} exp\left(-\frac{x^2T^2}{4\tau^2}+\frac{\Gamma\frac{d}{2}}{1+x^2}\right) \times \cos\left\{x\left(\frac{t}{\tau}-\frac{\Gamma\frac{d}{2}}{1+x^2}\right)\right\}dx \quad (4)$$

The normalized output pulse at the exit of PR crystal is represented by Eq. (4). The exponential term in Eq. (4) accounts for PR two wave mixing gain. The cosine term accounts for the optical delay in output pulse.

Numerical simulation and Results

The input and corresponding output pulse is generated by using equations (1) to (4). The fixed parameters used for the numerical simulation are enlisted in table 1. These ferroelectric /electro-optic coefficients of SBN:60 and SBN:75 were estimated at 514.5 nm (1-2) with light intensities 1-10^4 W/cm^2.

Table (1) Electro-optic coefficients of the SBN:60 and SBN:75 crystals.

Parameter	SBN:60	SBN:75
r_{13}	47 pm/V	67 pm/V
r_{33}	235 pm/V	1340 pm/V
n_e	2.33	2.35
n_o	2.36	2.37
t_r	0.03 sec	0.1 sec

The simulated delay and corresponding group velocity of signal pulse at the exit of PR crystal is compared for SBN:60 and SBN:75.

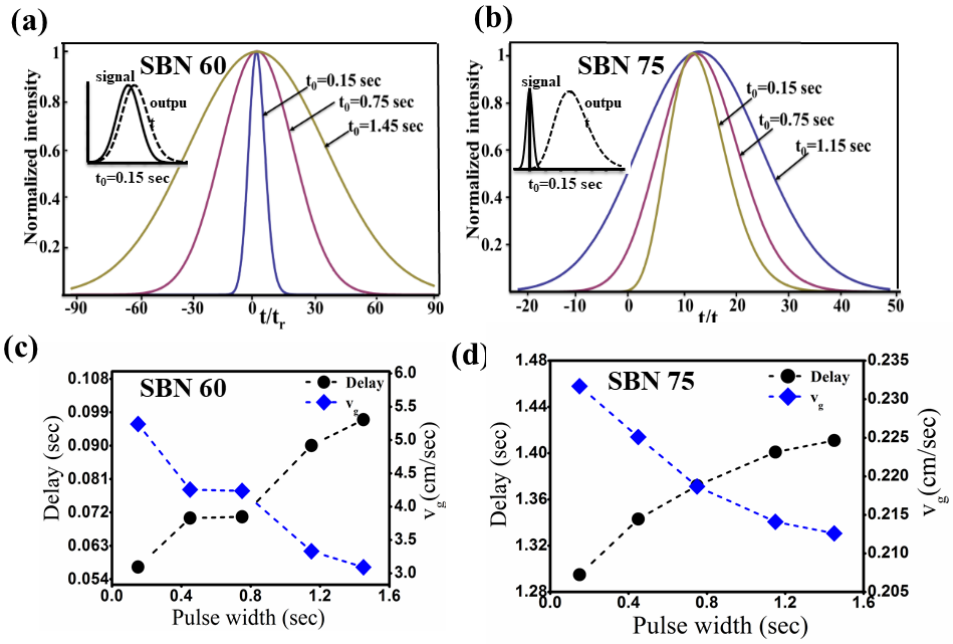

Figure 1. Shape of the output signal for (a) SBN:60 and (b) SBN:75 for different values of input pulse width. Variation of delay and the corresponding change in group velocity as a function of t_0 (c) for SBN:60 (d) for SBN:75.

Figure 1a and 1b, shows the normalized output intensity $|S(d, t)/S_0)|^2$ as a function of normalized time (t/t_r) for three different values of the input pulse width (t_0) 0.15 sec, 0.45 sec and 1.45 sec respectively, at a fixed value of beam crossing angle 2= 40^0 for SBN:60 and SBN:75 respectively. The delay is estimated by comparing the peak of input and output pulse as shown in inset of figure 1a and b. Delay and corresponding group velocity as a function of input pulse width is plotted in figure 1c and 1d for SBN:60 and SBN:75 respectively. It can be seen from Figure 1c and 1d that delay increases with increase in pulse width for both the crystals. The increase in delay with increase in pulse width arises due to PR coupling. On increasing the pulse width, more charge carriers diffuse throughout the crystal and a stable grating is formed. The refractive index change will also be large and thus the output signal will observe more delay with increase in pulse width. However, the estimated delay is two orders of magnitude higher in case of SBN:75 than SBN:60. For SBN:60, we get maximum group velocity of 5 cm/sec for t_0 = 0.15 sec and minimum group velocity of 3 cm/sec for t_0 = 1.15 sec. while for SBN:75, we get maximum group velocity of ~ 0.23 cm/sec for t_0 = 0.15 and minimum group velocity of ~ 0.21 cm/sec for t_0 = 1.15 sec. The higher delay in SBN:75 as compared to SBN:60 can be attributed to large response time of 0.1 sec in case of former as compared to 0.03 sec in the later. The grating formation time will reduce by one order of magnitude in SBN:75 as compared to SBN:60. Thus for a given pulse width more stable grating will be formed in SBN:75 crystal than that of SBN:60, resulting in higher delay. Further, the detailed mechanism of amplification and broadening shall be compared and presented in the conference.

Conclusion

In summary, large optical delay has been obtained for SBN:75 than SBN:60 under similar experimental conditions. With the increase in pulse width delay has been found to increase. SBN:75 is showing order of magnitude higher delay as compared to SBN:60.

Acknowledgment

This work was supported in part by Department of science and technology Govt. of India IFA12-PH-48 (INSPIRE).

References

1. P. V. Lenzo, E. C. Spencer and A. A. Ballman, Electro-optic coefficient of strontium noinbate, Appl. Phys. Lett. **11,** 23 (1967).
2. M. D. Ewbank, R. R. Neurgaonkar, W. K. Cory, and Jack Feinberg, Photorefractive properties of strontium barium niobate, J. Appl. Phys. **62**, 374 (1987).
3. T. Lukasiewicz, M. A. Swirkowicz, J. Dec, W. Hofman and W. Szyrski, Strontium barium niobate single crystals, growth and ferroelectric properties, Journal of Crystal Growth **310,** 1464 – 1469 (2008).
4. Wolfgang Horn, Jan v Bassewitz and Cornelia Denz, Slow and fast light in photorefractive SBN:60, J. Opt **12** 104011(2010).
5. H. N. Yum, M. Salit, G. S. Pati, S. Teng, P.R. Hemmer and M. S. Shahriar, Fast light in a photorefractive crystal for gravitational wave detection, Opt. Exp. **16** 20448 (2008).
6. M. Chi, J. P. Huignard and P. M. Petttersen, A general theory of two wave mixing in non-linear media, J. Opt. Soc. Am. B **26** 1578 – 1584 (2009).
7. Satchi Kumari and Alika Khare, Effect of pump-probe polarization and crystal orientation on pulse propagation in Ce:$BaTiO_3$ via degenerate two wave mixing, IEEE J. Q. E. **48** 1036 (2012).
8. Mary J. Miller, Edward J. Sharp, Gary L. Wood, and William W. Clark Ill, G. J. Salamo and Ratnakar R. Neurgaonkar, Time response of a cerium-doped Sr0.75Ba0.25Nb206 self-pumped phase-conjugate mirror, Optics Letter, **12**, 340-342 (1987).
9. Satchi Kumari and Rina Kumari, Optical delay in photorefractive SBN:61 and SBN:61:Ce via two-wave mixing: A theoretical study, Optik **168**, 714-720 (2018).

Thin Film Sensing with Terahertz Metamaterials

Sabyasachi Banerjee[1], Maidul Islam[2], Ch. Sai Amith[1], Jagan Mohan Suraboina[2], Gagan Kumar[2], Dibakar Roy Chowdhury[1]

[1]Mahindra Ecole Centrale, Hyderabad, Telangana, India, 500043

[2] Department of Physics, IIT Guwahati, Assam, India, 781039

*email: dibakar.roychowdhury@mechyd.ac.in

Abstract

We investigate thin film sensing capabilities of various terahertz (THz) metamaterial structures, one comprising of an array of asymmetric double split gap ring resonators (SRR) and the other having simple rectangular SRRs. The sensitivity and corresponding figure of merit (FoM) of the odd and even resonant modes are analyzed with respect to different thicknesses of the coated analyte film. Such studies should be very useful for the development of metamaterial based sensing devices in near future.

Keywords: *thin film; metamaterials; sensors; figure of merit*

Introduction

Nowadays metamaterials are an area of avid research owing to the unusual properties they display, which are not observed in naturally occurring materials. Metamaterials have found promising applications in diverse areas viz. medical diagnostics, food quality control, sensing, detection of noxious gases, development of ultra-high speed communication devices etc.

The concept of metamaterials was first demonstrated in the microwave region[1], but it was soon extrapolated to other regions of the electromagnetic spectrum including terahertz. Operational THz frequencies occupy a very narrow band (0.1–5 THz) in the electromagnetic spectrum and can result in several interesting phenomenon and applications in terms of light matter interactions. Due to the longer wavelengths, it is relatively easier to fabricate metamaterials for THz since its basic building blocks split ring resonators (SRRs) have dimensions of typically few tens of microns[2]. Because of the ease of fabrication and planar nature of metamaterial (known as 'meta' surface), it forms a convenient platform for thin film sensing.

Discussions

Here, we examine two different THz metamaterial structures with potentials in thin film sensing. Fig.1 shows the unit cell of an asymmetric resonator based MM which displays sharp resonance peaks [3] due to the excitation of dark eigen modes having high Q factor. Such high Q asymmetric SRRs can be used to design highly efficient THz sensing devices. In order to examine the sensing abilities of this planar metamaterial, analyte layer is applied on top of the metamaterial, hence sensitivity and FoM values are calculated.

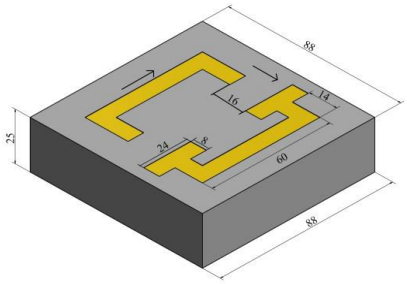

Fig1. Schematic of a unit cell of the asymmetric resonator (units in μm).

In another example, we examine the sensing capabilities of fundamental and higher resonance modes supported by single split gap ring resonators based metamaterials [4] [5]. We have used loss-less analyte of different thicknesses over the metamaterial structures. The refractive index of the coated thin film is varied in order to calculate the sensitivity and figure of merit of few of the lowest resonance modes. Our study shows that the lowest order or fundamental resonance exhibits the highest FoM values making it ideal for thin film sensing.

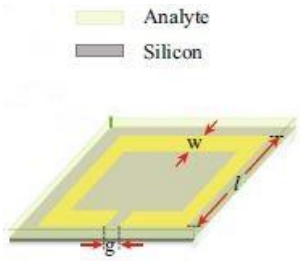

Fig.2 Schematic of planar Terahertz metamaterial geometry consisting of gold SRRs on a silicon substrate

Conclusion

In summary we have analyzed thin film sensing potentials for single and double split gap ring resonator based terahertz metamaterials. The sensing capabilities in terms of sensitivities and figure of merits (FoMs) are calculated for both the structures. It was found that dark mode (double gap ring resonator) based MM with high Q factor resonances demonstrate higher sensitivity compared to typical single gap ring resonators based MM.

References

[1]Pendry, J. B. et al. Magnetism from conductors and enhanced nonlinear phenomena. IEEE Transaction on microwave theory and technique 47,2075–2084 (1999)

[2] S Jagan Mohan Rao, Deepak Kumar, Gagan Kumar, Dibakar Roy Chowdhury, "Modulating the near field coupling through resonator displacement in planar terahertz metamaterials", Journal of Infrared, Millimeter, and Terahertz Waves, Vol 38, Issue 1, Pages 124-134 (2017)

[3]V. G. Vaselago, "The electrodynamics of substances with simultaneously negative values of epsilon and mu," Sov.Phys. Usp.10, 509–514 (1968)

[4] Maidul Islam, S. Jagan Mohan Rao, Gagan Kumar, Bishnu P. Pal & Dibakar RoyChowdhury, "Role of Resonance Modes onTerahertz Metamaterials basedThin Film Sensors", Scientific Reports, 7, 7355 (2017)

[5]Wiltshire, M. C. K. et al. Microstructured magnetic materials for RF flux guides in magnetic resonance imaging. Science 291,849–851 (2001).

Utilizing Shape Adaptive Grinding (SAG) process for fabrication of aspheres in optical glass

Sandeep Mishra, Brijesh Kumar Yadav, Amitava Ghosh
Instruments Research and Development Establishment, Raipur Road, Dehradun
Corresponding author's e-mail: sandeepmishra@irde.drdo.in

Abstract

Shape Adaptive Grinding (SAG) is an emerging process for fabrication of aspheric optical components. Process mechanism has been studied mostly on chemical vapour deposited Silicon carbide substrates. Here we have shown that this process can also be utilized for generation of aspheric profiles in glass substrates. Using SAG process an aspheric surface in BK7 glass was generated from a grinded spherical surface and average surface roughness was controlled below 300nm.

Keywords

Grinding, Polishing, Sub-aperture polishing

1. Introduction: In recent years, Shape Adaptive Grinding (SAG) has emerged as a cost effective alternative for machining of very hard materials such as CVD-SiC [1, 2].Aspheric and freeform surfaces can be generated using SAG process. In SAG process flexible diamond sheets are used for making tools. In these sheets diamond particles are deposited in the form of circular or polygon pellets on a metallic mesh. This metallic mesh is backed on a canvas sheet. SAG tools are made by gluing this sheet on an air-inflated spherical membrane (bonnet). The characteristic semi elastic nature of SAG tool is achieved by combining the flexibility of the air-inflated bonnet with rigid contact formed between diamond pellets and optics. The SAG tool presses against the optics to form a small spot on the optics. Diameter of this spot is governed by equation 1 and can be changed by altering the offset (Δz).

$$d = 2\sqrt{2R\,\Delta z} \quad \ldots\ldots\ldots\ldots\ldots\ldots\ldots\ldots\ldots\ldots\ldots\ldots \quad (1)$$

where d is the diameter of the spot, R is the radius of the bonnet and z is the offset.

Due to semi-elastic nature of SAG tool this process can be implemented even on low stiffness machines and high surface accuracy and low surface roughness can be achieved.

2. Fabrication of glass aspherics using SAG: To investigate effectiveness of this process for fabrication of glass aspherics on a 7 axes machine platform, Intelligent Robotic Polishing System (IRP 400, M/s Zeeko Ltd. make) was used. Spherical bonnet of 40mm radius was used to make SAG tool. Metal bonded flexible diamond sheet with a particle size of 9 µm was glued on the bonnet. Final radius of SAG tool was found to be 41.89mm. A parabolic surface on BK7 glass was fabricated to investigate effectiveness of the SAG process on glass substrate. The parameters for parabolic surface and SAG tool are given below

S.No.	Description	Parameters
1	Parabolic surface	Material: BK7 R=422.98mm (Cave), K=-1 Diameter=160mm
2	SAG tool	Radius= 41.89 mm Pressure= 1bar, offset=0.2mm Diamond pellet size= 9 µm

Table1. Parameters for parabolic surface and SAG tool

To generate this parabolic surface with SAG tool, first a concave curvature of 429.762 mm was generated over a 160mm aperture of a BK7 glass plate. The diameter and thickness of glass blank were 165.0mm and 20.5mm, respectively. A manual curve generator (Make Adcock Shipley) with diamond bonded tool was used for curve generation. After curve generation the part was measured on a stylus profilometer (Mahrsurf LD260). A diamond stylus with 2 µm tip radius was used for surface form measurement. This measurement result was fitted against the designed parameters of parabolic surface to derive tool path for corrective polishing. Fabricated spherical surface had a form error of 29.37µm (Peak to Valley) with respect to parabolic profile of the surface. In the next step the part was mounted on a 7 axes CNC polishing machine (IRP 400). Corrective polishing tool path was derived from the 2D profile error generated in the previous step. In the corrective

polishing method, machine feed rates were moderated according to the input error. Material removal rates (MRR) were derived from a removal test experiment on a flat BK7 glass substrate. Only 50% error was targeted for correction. Instead of cerium oxide slurry, re-circulating water was used for cooling and removing the fine glass chips generated during shape adaptive grinding process. Surface profile measurement before the start of SAG process is shown in figure 1. Flexible diamond sheet and SAG tools are shown in figure 2 & 3, respectively.

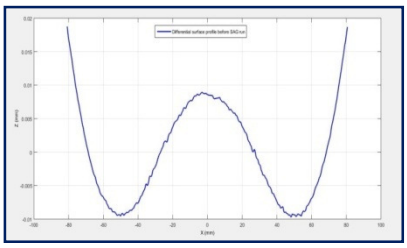

Fig.1 Surface profile before SAG process (PV=29.37 µm)

Fig.2 Diamond Sheet

Fig.3 SAG tool

As only 50% error was targeted in this step, measurement results (Figure 4) shows good conformance to the material removal test data. Differential profile obtained in this step was used to derive the corrective polishing feed rates for the next SAG run. At the end of this step surface profile error was reduced to 5.14 µm. Surface profile measurement after 1st and 2nd SAG runs are shown in figure 4 &5, respectively. For surface roughness characterization, measurement data was taken at various locations of optics with a sampling length of 10mm. After 2 runs of SAG process, the average surface roughness was reduced to 250nm. Results achieved in this SAG process are comparable to those achieved in conventional grinding. As the profile error was reduced to only 5.14 µm (PV) from 29.37 µm (PV) and average surface roughness of 250 nm was obtained, polishing process was resumed after this. Effectiveness of SAG process is shown in figure 6. Here surface profiles were averaged and the lowest point on profile was chosen to lie on x axis.

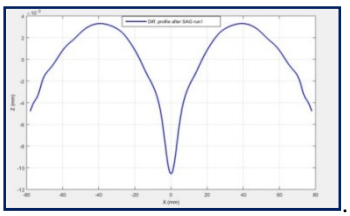

Fig.4 Surface profile after SAG run1(PV=14.38 µm)

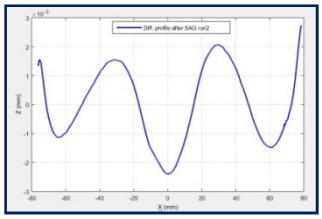

Fig.5 Surface profile after SAG run1(PV=5.14 µm)

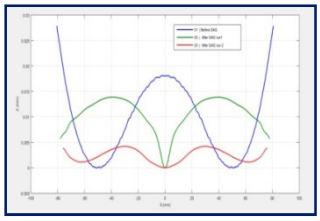

Fig.6 Comparison of surface profile before and after SAG runs

3. Conclusion: Figure 6 shows the effectiveness of SAG process. With this process surface form error and surface roughness can be quickly reduced. SAG is an emerging process and its effectiveness on CVD-SiC has already been established. Here we have utilized this process on glass substrate. This process provides a very cost effective method for aspheric surface grinding. SAG process can be easily implemented on low stiffness polishing machines. Different SAG tools can be easily made according to the requirement. This process eliminates the need of expensive diamond bonded cup tools or wheels. Surface form and surface roughness achieved in this process are comparable to aspheric grinding process. Using SAG process freeform surfaces can be generated on glass or other optical materials as tool paths can be generated in raster mode.

4. Acknowledgement: Authors are thankful to Sh. Benjamin Lionel, OS & Director IRDE for his support and encouragement.

5. References

[1]A. Beaucamp et al. / CIRP Annals - Manufacturing Technology 64 (2015) 305–308306, http://dx.doi.org/10.1016/j.cirp.2015.04.096

[2]A. Beaucamp et al. / CIRP Annals - Manufacturing Technology, Dec (2014) DOI: 10.1016/ j.cirp.2014.03.019

Phase retrieval using liquid crystal variable retarder based on reference-less non-interferometric technique

Alok Kumar Gupta and Naveen K. Nishchal*
Department of Physics, Indian Institute of Technology Patna, Bihta, Patna, Bihar-801106, INDIA
*nkn@iitp.ac.in

Abstract: Non-interferometric phase retrieval techniques are useful for three-dimensional (3D) imaging of a pure phase object. Phase objects usually do not alter the intensity of light wave but it does make a significant change in the phase. Exploiting the phase delay information is helpful to visualize several biological objects, processes, and their movements, which are nearly transparent in bright field microscopy. In this paper, a non-interferometric and non-iterative phase retrieval method has been demonstrated using a commercially available liquid crystal variable retarder. The method is based on conventional transport-of-intensity (TIE), which does not require any physical displacement of the recording camera. Instead, intensity images are recorded at different refractive indices. The liquid crystal retarder introduces required change in the refractive index of the input beam by changing the applied voltage. Phase image has been retrieved numerically in MATLAB with the help of modified TIE expression. The 3D surface plot of the retrieved phase has been realized.

Keywords: Phase retrieval, Transport-of-intensity, Non-interferometric method, Liquid crystal variable retarder

1. Introduction

Phase objects have surface unevenness or difference in its refractive index with respect to its surroundings. A phase object can be imaged using phase retrieval techniques [1]. There are several phase retrieval techniques in the literature which include phase contrast [2] interferometric [3,4], iterative [5,6] and non-interferometric non-iterative techniques [7]. The transport of intensity (TIE) based phase retrieval method comes under non-interferometric non-iterative techniques. Being a non-interferometric method, TIE has advantages over the conventional interferometric techniques [7].

In this paper, a modified TIE based technique has been utilized for phase retrieval. The conventional TIE method uses two intensity images at different displacements which need recording camera to be shifted. That physical shift may involve mechanical instability error. This mechanical instability error can be avoided using the modified TIE based technique. In this case, two intensity images are recorded at different refractive indices. Liquid crystal variable retarder (make: Thorlabs Inc.) is inserted in the path to change the required refractive index. 4*f* imaging setup has been utilized to record the intensity images. Transparent ultraviolet (UV) glue drops on glass side is used as a pure phase object. Numerical analysis to retrieve phase image is done on MATLAB. Theoretical analysis and experimental results are discussed in the following sections.

2. Theoretical analysis

The monochromatic beam propagating along the *z*-axis passes through an object and tunable refractive index medium with a thickness *L*. Under the paraxial approximation, the complex field $u(x,y,z)$ after passing the object,

$$u(x,y,z) = u_0(x,y,z)e^{-i\varphi(x,y)} \tag{1}$$

where $u_0(x,y,z)$ is the amplitude and $\varphi(x,y)$ carries the phase information of the object. After solving the propagation with angular spectrum method and taking derivative with *n*, we obtain the differential equation [8]

$$\frac{\partial u(x,y)}{\partial n} = \frac{-iL}{2k_0 n^2}\nabla^2 u(x,y) - ik_0 L u(x,y) \tag{2}$$

It can be seen that Eq. (2) is similar to the paraxial wave equation. So, TIE like equation can be derived to show the intensity-phase relation with the variation of refractive index in the medium. The modified TIE equation is,

$$\frac{\partial I(x,y,n)}{\partial n} = \frac{L}{k_0 n^2}\nabla.(I\nabla\varphi) \tag{3}$$

Eq. (3) shows that phase information can be retrieved if the intensity variation is calculated with respect to the change of the refractive index.

3. Experimental results

As shown in Figure 1, a collimated monochromatic beam of laser (wavelength 633 nm) is incident on the object. Drops of UV glue on glass slide is used as phase object. Diffracted beam from object is passed through 4*f* imaging processor and liquid crystal variable retarder. Finally, the intensity images stacks are taken on a CCD camera (make: Imaging Source) and stored on computer. Images are taken at different refractive indices introduced through controlling the applied voltage on liquid crystal retarder. Datasheet of retarder (available on Thorlabs website [9]) has been used for measurement of refractive index at a particular voltage.

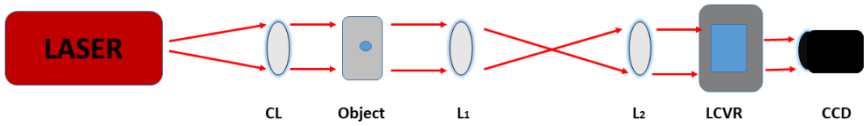

Fig. 1 Schematic diagram of experimental setup (CL: collimating lens, L: lens, LCVR: Liquid crystal variable retarder, CCD: charge-coupled device camera)

The recorded intensity image (Fig. 2(a)) is used to calculate the derivative. Then using FFT solver of conventional TIE on MATLAB, phase image (Fig. 2(b)) of the object is retrieved and its surface (Fig. 2(c)) has been plotted.

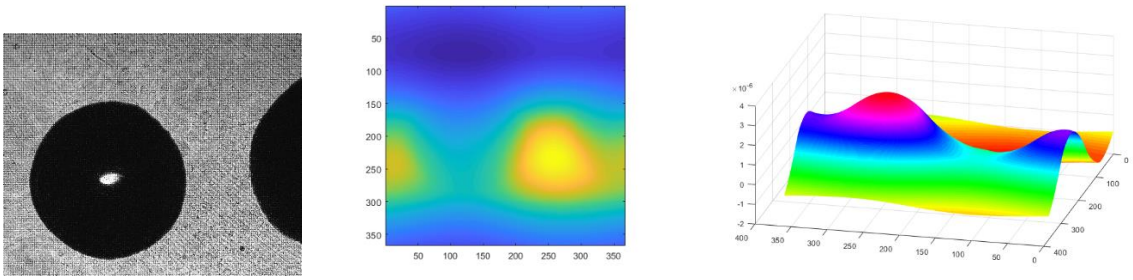

(a) (b) (c)

Fig. 2(a) Intensity image of glue drop, **(b)** retrieved phase image, and **(c)** 3D surface profile

4. Conclusion

As seen from results, the quadrature surface profile of glue drops has been retrieved. Actual shape of glue looks like semi-spherical which is verified by the retrieved result.

Acknowledgment

The authors acknowledge the funding from the Council of Scientific and Industrial Research (CSIR), Govt. of India, under Grant No. 03/ (1351)/16/EMR-II.

References

[1] K. A. Nugent, D. Paganin, and T. E. Gureyev, Phys. Today 54, 27-32 (2001).
[2] F. Zernike, Physica 9, 686-698 (1942).
[3] G. Nehmetallah and P. P. Banerjee, Adv. Opt. Photon. 4, 472-553 (2012).
[4] K. Khare, P. T. S. Ali, and J. Joseph, Opt. Express 21, 2581-2591 (2013).
[5] J. R. Fienup, Appl. Opt. 52, 45-56 (2013).
[6] R. W. Gerchberg and W. O. Saxton, Optik 34, 275-284 (1971).
[7] M. R. Teague, J. Opt. Soc. Am. 73, 1434-1441 (1983).
[8] C.-H. Chen, H.-F. Hsu, H.-R. Chen, and W.-F. Hsieh, Sci. Rep. 7, 46223 (2017).
[9] Thorlabs. Inc. Full-Wave Liquid Crystal Variable Retarders. from *https://www.thorlabs.com/*

Wave propagation analysis through pseudo random phase plate (mimicking atmospheric turbulence) for imaging

Christi Jose, J Sreelakshmi, Pramod Panchal and ***C S Narayanamurthy****,*

Applied and Adaptive Optics Laboratory, Department of Physics, IIST, Valiamala(PO), Trivandrum - 695547

Abstract

Imaging through atmospheric turbulence is challenging due to the temporal fluctuations of refractive index spoiling quality image of distant object. In this paper we report some of our experimental investigations by propagating different class of beams through a Pseudo Random Phase Plate (PRPP) mimicking Kolmogorov type atmospheric turbulence and its influence on imaging.

Introduction The turbulence[1,2] in the atmosphere can spoil optical communication and can distort images for ground-based astronomy. The phase and amplitude profiles of a distant object get distorted according to the characteristics of the medium. This optical effect that decreases with altitude is mainly due to temperature fluctuations that results in refractive index variations. The advent of the adaptive optics (AO) technique helps to identify the image distortions and retrieve the unperturbed light from the source. In astronomy, AO functions between a celestial object and an imaging device in order to remove aberrations. The quality of image is restored by the application of this technique. In this paper we report experimental investigations of wave propagation through PRPP as well as phase screen with different Fried Parameters (characteristic length known as Coherence length, which limits the detectors' aperture size) represented by r_0 values.

2. Higher order aberration measurements of Laguerre-Gaussian Beam Propagating through Pseudo Random Phase Plate(PRPP)

Our experimental arrangement is illustrated in the Fig. 1.The He-Ne laser beam of 632.8 nm is passed through a polarizer and a spatial filter so as to get a linearly polarized smooth intensity profile of the Gaussian beam. The filtered beam is collimated using a lens of focal length 75 mm. Using a polarizing beam splitter, the light is X-polarized in the transmitted direction and Y-polarized in the reflected direction. Here the transmitted beam is allowed to fall on the spatial light modulator in which the phase profile of Laguerre-Gaussian light beam of different modes is loaded. The information is loaded by the computer.

1.

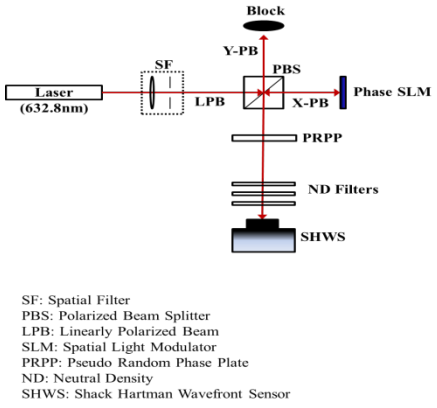

SF: Spatial Filter
PBS: Polarized Beam Splitter
LPB: Linearly Polarized Beam
SLM: Spatial Light Modulator
PRPP: Pseudo Random Phase Plate
ND: Neutral Density
SHWS: Shack Hartman Wavefront Sensor

2.

Fig.1

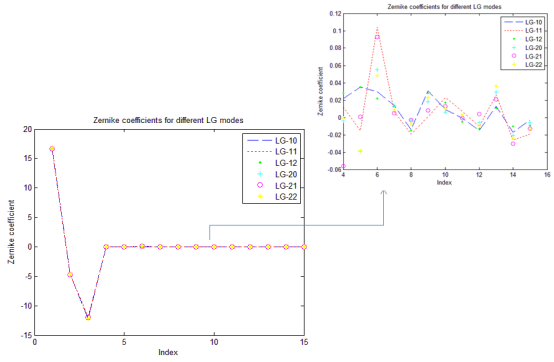

Fig.2

controlled phase hologram generated using MATLAB programming. The reflected beam from SLM is captured using a Shack-Hartmann wavefront sensor and the Zernike coefficients are analyzed to find the wavefront aberrations. This is repeated by placing pseudo random phase plate (PRPP) which is designed to provide atmospheric turbulence like conditions in laboratory [1]. The results are plotted for analyzing the wavefront aberrations in the presence of turbulence.

2.1 Results and Discussions

The Zernike coefficients for different Laguerre-Gaussian modes obtained when the experiment is performed without turbulence and with turbulence introducing PRPP respectively. The Zernike coefficient for different LG modes in the presence of turbulence is shown in Fig.2. The variation in aberrations between different modes is in the decimal range so that it is difficult to distinguish between different modes. These small random variations between different modes are due to unpredictable characteristics of turbulent medium.

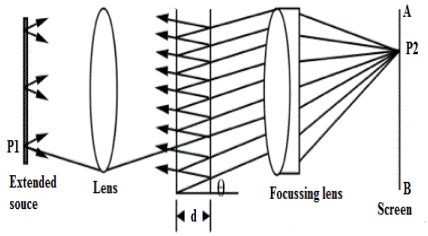

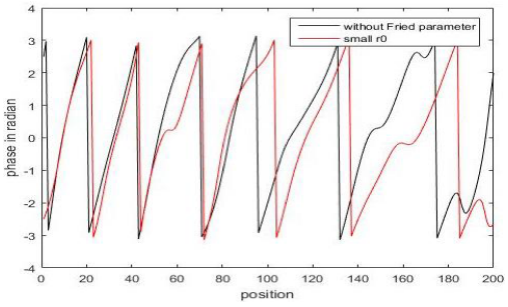

Fig.3 **Fig.4**

3.Wave propagation through phase screen with various Fried Parameter Values

3.1 Introduction

Most of the interference phenomena are due to the superposition of two coherent beams but Fabry-Perot interferometer(Fig.3) uses amplitude splitting and multiple beam interference phenomena. It consists of two plane parallel highly reflecting surfaces separated by a distance d. These reflecting surfaces are generally two semi silvered mirrors. The separation distance 'd' is usually large of the order of 0.1 to 10cms. It uses the transmitted light from the interferometer to produce fringes. Light gets reflected back and forth inside the air film between the plane plates, which are thinly silvered on the inner surfaces. The observation of interference pattern is made near the normal direction. Hence the fringes obtained from this device come under the 'fringes of equal inclination'. Using such an interferometer and by inserting phase screens with different Fried parameter values we investigate the behavior of least fluctuating beams by analyzing the interferograms. We have used Mercury and laser beam for this analysis.

3.2 Results and discussion

The light from the source directly fell on the Fabry Perot etalon and the interference pattern formed is recorded. Since the fringes are circular and the presence of unlimited rays in the fringe formation due to multiple reflection, the phase unwrapping is little bit difficult. So, the obtained fringes are cropped into half the portion. Then, by using the commonly used Fourier transform method, the phase is unwrapped. Due to the focusing of the fringes of equal inclination the fringe system is a concentric rings system. Fig.4 shows the variation of phase information of different sources with the introduction of Fried's parameter and it is found that the fluctuations in phase happen more randomly for mercury where as only small variations occur in its phase for laser beams as expected.

3. References

1. John W. Strohbehn, III Optical Propagation through the Turbulent Atmosphere, Progress in Optics, Vol.9 (1971), 73-122

2. R K Tyson, Principles of Adaptive optics, CRC Press(Taylor and Francis), 2011

Wave propagation analysis of Laguerre–Gaussian beam through PRPP

Rekshma J [1], Pramod Panchal [2], Richa Sharma [3], Rakesh Kumar Singh[4] and C. S. Narayanamurthy [2]

[1]*Department of Optoelectronics, University Of Kerala, Kariavattom Campus, Thiruvananthapuram 695581 Kerala, India*
[2]*Applied and Adaptive Optics Laboratory, Department of Physics, Indian Institute of Space Science and Technology, Valiamala P.O., Thiruvananthapuram 695547, India*
[3]*Space Application Centre, Jodhpur Tekra, Ambawadi Vistar P.O., Ahmedabad 380015 Gujarat, India*
[4]*Department of Physics, Indian Institute of Technology (BHU), Varanasi, Uttar Pradesh, India*
**Corresponding author: rekshmajb773@gmail.com and naamu.s@gmail.com*

Abstract: Laguerre–Gaussian (LG) beams are generated using vortex phase plate and analysed the propagation of this Laguerre-Gaussian beam through a pseudo-random phase plate. One of the quantities of physical interest such as the twist parameter is estimated from the variance matrix generated from Shack–Hartmann wave front sensor data. Fluctuations of twist at various distances are also estimated. The estimated quantities are then used to compare the distorted Laguerre-Gaussian beam with its undistorted counterpart.

INTRODUCTION:

Laguerre–Gaussian (LG) beams are optical beams having doughnut-shaped intensity distribution and a singularity in its phase distribution. These type of beams gained increasing attention, especially after Allen et al. [1] demonstrated that these modes carry orbital angular momentum (OAM) of light. LG modes can be obtained as a solution of a scalar wave equation in the paraxial approximation and can be expressed in cylindrical coordinates which is given by [2]

$$LG_l^n(r,\varphi,z)=\left(\frac{2}{\pi|n|!}\right)^{\frac{1}{2}}.\frac{1}{w(z)}\left(\frac{r\sqrt{2}}{w(z)}\right)^{|n|}.\exp\left(\frac{-r^2}{w(z)^2}\right).\exp(-in\varphi).\exp(i[kz-kr^2/2R]).\exp(i\theta) \quad (1)$$

Where $w(z)=w_0\sqrt{(1+\left(\frac{z}{z_r}\right)^2)}$, $R_s=z[1+\left(\frac{z}{z_R}\right)^2]$

$$z_R=\frac{\pi w_0^2}{\lambda} \quad , \quad \theta=(|n|+1)\tan^{-1}\left(\frac{z}{z_R}\right) \quad (2)$$

In eq. (1) and (2), r, φ, and z represent the cylindrical coordinate parameters, w(z) denotes the transverse beam size with w_0 being the waist radius at z =0, k is the wave number, ZR represents the Rayleigh range of the Gaussian envelope, R_s is the wavefront radius of curvature , and φ denotes the Gouy phase, which changes with the propagation distance from the waist position. The azimuthal index *n*, corresponding to the topological charge of the embedded singularity, indicates the number of twists of the helical wavefront within a wavelength and represents the amount of OAM, in units of *ħ*, carried by each single photon. The index *l* represents the number of radial nodes on a plane perpendicular to the direction of propagation and is thus related to the distribution of the intensity pattern in *l*+ 1 concentric rings around the central dark zone of the phase singularity (where |n|≥1).

A given wave-field can be characterised by computing the expectation value of the observable operators (position and momentum). For an LG beam this can be done by evaluating its second moments which forms the so called Variance matrix (V) [4]. In this work when an LG beam propagates through a turbulence mimicking medium such as a Pseudo-random phase plate (PRPP), its phase and amplitude tends to change thus getting distorted, which is captured through the Variance matrix (V). The variance matrix can be calculated at a particular distance, using Shack-Hartmann wavefront sensor (SHWS). Then V corresponding to the distorted and the undistorted LG beam can be. Data for intensity and beam centroid position extracted from the SHWS is used for evaluating the variance matrix. This does not involve any inbuilt wavefront reconstruction algorithm [4]. In addition to the estimation of variance matrix, we also determines certain parameter which can be derived from the variance matrix such as Twist parameter, τ at various distances for LG beams for both i.e., with and without propagation through PRPP.

LG BEAM CHARACTERIZATION USING VARIANCE MATRIX:

The variance matrix of a paraxial light-field is defined as a 4 × 4 matrix. The variance matrix, stated as V [3], is defined as

$$V=\begin{pmatrix}V_{11} & V_{12}\\ V_{12}^T & V_{22}\end{pmatrix} \text{ where, } V_{11}=\begin{pmatrix}<x> & \frac{1}{2}<\{\Delta x,\Delta p_x\}>\\ \frac{1}{2}<\{\Delta x,\Delta p_x\}> & <\Delta p_x^2>\end{pmatrix} \quad V_{12}=V_{21}^T=\begin{pmatrix}<\Delta x\Delta y> & <\{\Delta x\Delta p_y\}>\\ <\{\Delta p_x\Delta y\}> & <\Delta p_x\Delta p_y>\end{pmatrix}$$

$$V_{22}=\begin{pmatrix}<\Delta y^2> & \frac{1}{2}<\{\Delta y,\Delta p_y\}>\\ \frac{1}{2}<\{\Delta y,\Delta p_y\}> & <\Delta p_y^2>\end{pmatrix}$$

It obeys the uncertainty principle which is stated as:

$$V + \frac{i\hat{\lambda}}{2}\alpha \geq 0 \ ; \text{where} \quad \alpha = \sigma \oplus \sigma;$$

where $\sigma = \begin{pmatrix} 0 & 1 \\ -1 & 0 \end{pmatrix}$, σ is the Pauli matrix.

The twist parameter τ, extracted from V can be given by

$$\tau = \frac{1}{\hat{\lambda}}(< x p_y > - < y p_x >)$$

which gives the measure of how much a wave-field twists as it propagates along z axis.

EXPERIMENTAL PROCEDURE:

At the beginning, TEM_{00} wave-field of wavelength 633 nm and 12 mW power from a He–Ne laser source is allowed to pass through a spatial filter to remove random fluctuations from the intensity profile of the laser wave-field. The wave-field is then collimated to align the wave-field in a specific direction. The output wave-field from the collimating lens is subjected to pass through a vortex phase plate (VPP) which generates a LG beam. Our experiment is performed in two procedures. In the first procedure, this beam is allowed to propagate a distance d before being detected by the SHWS. The distance d is varied to 20 different positions at an interval of 2.5 cm and the variance matrix is estimated for about 250 wave-field samples of this LG beam at each distance. Fig. 1 shows the schematic diagram for second procedure where the PRPP is introduced at a distance of 10 cm from VPP and the SHWS is placed at various distances from PRPP and the variance matrices of the wave-field samples are estimated at each distance.

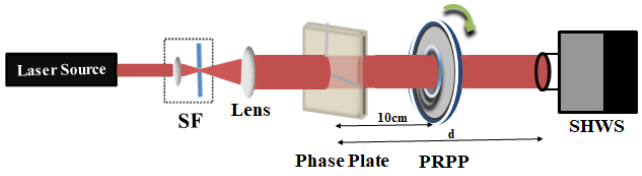

Fig1: LG beam propagation through PRPP

RESULTS:

In Fig. 2 (i), the values of the twist parameter measured at a distance of 12.5 cm from VPP for 250 samples are shown. Fig. 2 (i), shows the measured values of the twist parameter for the experimental procedure, in which the PRPP was not inserted in the wave-field path, in black colour, and the PRPP was inserted, in red colour. Clearly, there is noticeable enhancement in the values of twist when PRPP was inserted i.e. on an average the twist parameter value for the LG beam propagating through free space is approximately zero but on the other hand, the average twist parameter value for the LG beam propagating through PRPP is found to be -1.2 where the negative sign shows the direction of twist. Fig. 2 (ii), shows the plot of twist as a function of distance and Fig. 2(iii) shows the fluctuation of twist as a function of distance. From both the frames (i) and frame (ii), it is clearly seen that, on an average there is an increase in the values of twist for the wave-field passing through PRPP than the wave-field propagating through free space.

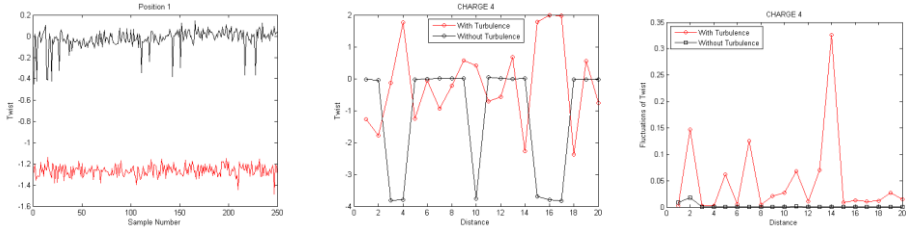

(i) (ii) (iii)

Fig 2: (i) Corresponds to the measured values of twist, for both the cases, i.e., with (black) and without (red) the insertion of a PRPP. (ii) Plot shows measured twist values at 20 different positions as a function of distance for both with and without the insertion of the PRPP. (iii) The fluctuation of twist as a function of distance for with and without the insertion of the PRPP.

CONCLUSION:

We have studied Laguerre-Gaussian beam of different modes propagated through a PRPP (mimicking atmospheric turbulence). The uncertainty principle has been used as a tool in discriminating the data. We have studied one of the quantities of physical interest such as the twist parameter and its fluctuations at different distances for both i.e., with and without PRPP. We have found that there is enhancement in twist parameter and its fluctuations upon the insertion of the PRPP.

REFERENCES:

[1] L. Allen, M. W. Beijersbergen, R. J. C. Spreeuw, and J. P.Woerdman, Phys.Rev. A **45**, 8185–8189 (1992).
[2] G. Ruffato, 1, M. Massari, and F. Romanato, Opt. Lett. 39,5094-5097 (2014).
[3] J. Solomon Ivan and Kaumudibikash Goswami, J. Opt. Soc. Am. A **32**, 1118-1125 (2015).
[4] Richa Sharma, J. Solomon Ivan, and C. S. Narayanamurthy, J. Opt. Soc. Am.A **31,** 2185-2191 (2014).

Generation of orbital angular momentum of light using liquid crystal spatial light modulator

Praveen Kumar and Naveen K. Nishchal*
Department of Physics, Indian Institute of Technology Patna, Bihta, Patna, Bihar-801 106
**nkn@iitp.ac.in*

Abstract: The orbital angular momentum (OAM) is an intrinsic property of light that has attracted much attention in many research fields for its special phase and intensity distribution. Twisted light carrying OAM is a special kind of structured light that has helical wavefront and a phase singularity point on the propagation axis that results in ring-shaped transverse amplitude profile. The OAM is proportional to the number of intertwined helices constituting the wavefront, represented by topological charge (TC). These orthogonal OAM modes can be employed to encode information onto a laser beam. The TC carried by the OAM beams are determined by the fork-like interferograms. In this paper, vortex beams with integral topological charges have been generated. This has been achieved through displaying the computer generated holograms on the liquid crystal spatial light modulator. The fringe pattern resulting from the interference of vortex beam with plane wavefront gives the visualization of phase pattern encoded on the spatial light modulator. Mach-Zehnder interferometer is implemented to obtain these fringes for confirmation.

Keywords: Vortex beam, Orbital angular momentum, Mach-Zehnder interferometer, Computer generated holograms.

1. Introduction

Optical vortex light beam with helical phase structure has phase singularity in its beam axis [1]. Phase of such beam is mathematically represented by $\exp(\pm il\phi)$, where $\phi(x,y)$ is the azimuthal angle and l is the topological charge (TC). Each photon of such vortex beam carries orbital angular momentum (OAM) whose magnitude depends on the TC as $\pm l\hbar$. Some of the potential applications of OAM are lasers communications, optical manipulations and imaging [1-5]. The beam carrying OAM can be experimentally produced using various methods [6-9]. Azimuthal phase mask converts a Gaussian beam into a helical mode whose wavefront resemble an l-fold corkscrew [1-2]. Simply a spiral phase plate can be used for this purpose [7]. For generating OAM with higher TC, diffraction based techniques are preferred [8]. Computer generated holograms (CGHs) displayed on spatial light modulator (SLM) are most convenient tool for variable diffractive optical elements.

2. Principle

Confirmation of TC can be done using various interferometric techniques, such as self-referenced or Michelson interferometry [9-10]. We have used a Mach-Zehnder based interferometer. This method is simple and stable. Moreover, same setup can be utilized, if SLM is replaced by holograms [9]. Observed interference pattern gives the visualization of encoded phase pattern onto the SLM [10].

$$T = T_o + T_1 \exp[\pm il\phi + 2\pi Ax + 2\pi Ay] \tag{1}$$

Eq. (1) is the phase-only transmission function of electric field after being diffracted from CGH, produced by adding linear phase grating to the desired phase function $\phi(x,y)$ [14]. 1/A is the spatial period of added linear phase grating and T_o *and* T_1 are coefficients corresponding to zeroth and first order term, respectively. Eq. (1) shows that zero-order term does not contain phase information.

$$I(x,y) = T_o^{\,2} + T_1^{\,2} + 2T_oT_1\{\cos(\phi + 2\pi Ax + 2\pi Ay)\} \tag{2}$$

The same transmission function given by Eq. (1) is obtained for two beams. The zeroth order diffracted light from beam 2 and first order from beam 1 are made to interfere with each other. The output intensity is given by Eq. (2). The desired phase variation is observed in the interference pattern.

3. Experimental results and discussion

The experimental arrangement for generating the OAM using Holoeye 2002 SLM is shown in Figure 1. Laser beam of wavelength 532 nm is expanded and collimated. Beam splitter, BS1 splits collimated beam into beam 1 and beam 2 (showed by solid and dashed lines, respectively). Mach-Zehnder interferometer setup is used to make both beams travel along same direction. They are allowed to diffract from the CGH displayed on the SLM. Zeroth order diffraction component of beam 2 and first order component of beam 1 are simultaneously allowed to pass

through pin hole with beam. Rest components are filtered out. Resulting beam 1 has helical phase and the beam 2 has plane wavefront. The CCD (make: Imaging Source) has been used for recording intensity of interference pattern of beam 1 and 2. For the recording intensity of OAM beam, beam 2 is blocked. CGHs for different TCs (l = 1 to 5) are displayed one by one for generating different modes of OAM.

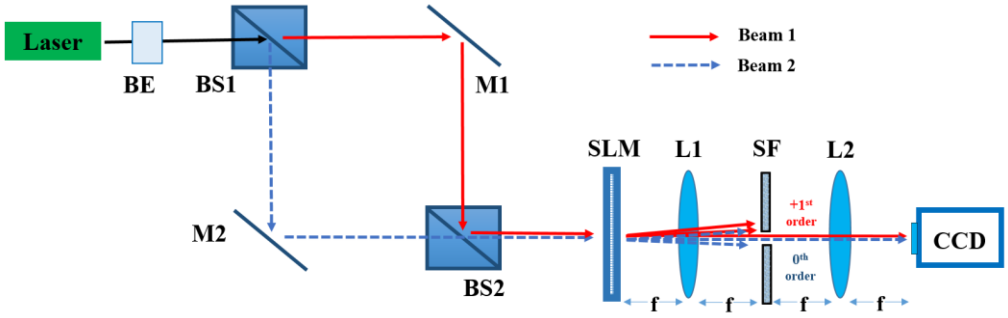

Fig. 1 Schematic of the experimental set-up. BS: beam splitter, M: mirror, HG: holographic grating, L: lens, f: focal length, SF: spatial filter, CCD: charge-coupled device camera.

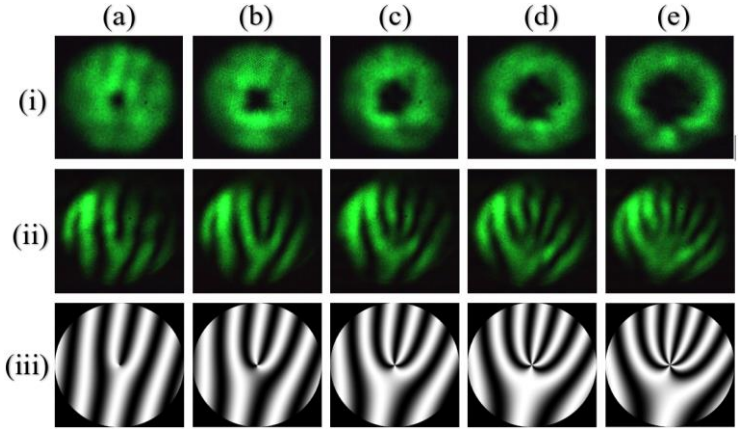

Fig. 2 (i) Generated OAM beams. Interference patterns of vortex beam and plane wavefront: **(ii)** experimentally observed, and **(iii)** obtained theoretically. Different orders of topological charges (TC) from l = 1 to 5, respectively are shown in **Fig. (a - e).**

4. Conclusion

The vortex beams carrying OAM with (l = 1 to 5) are generated using the CGHs. The fork type structure observed experimentally in the interference pattern confirms the presence of vortex beam.

Acknowledgment

The authors acknowledge the funding from the CSIR, Govt. of India, under Grant No. 03/ (1351)/16/EMR-II.

References

[1] M. Padgett, Opt. Express 25, 11265 (2017)
[2] L. Allen, M. W. Beijersbergen, R. J. C. Spreeuw, J. P. Woerdman, Phys. Rev. A 45, 8185 (1992)
[3] G. Gibson *et al*., Opt. Express 2, 5448 (2004)
[4] H. He, M. E. J. Friese, N. R. Heckenberg, H. Rubinsztein-Dunlop, Phys. Rev. Lett. 75, 826 (1995)
[5] C. Maurer, A. Jesacher, S. Bernet, M. Ritsch-Marte, Laser Photon. Rev. 5, 81 (2010)
[6] A.V. Carpentier, H. Michinel, J. R. Salgueiro, D. Olivieri, Am. J. Phys.76, 916 (2008)
[7] M. W. Beijersbergen, R. P. C. Coerwinkel, M. Kristensen, J. P. Woerdman, Opt. Commun. 112, 321 (1994)
[8] V. Y. Bazhenov, M. S. Soskin, M. V. Vasnetsov, J. Exp. Theor. Phys. Lett 52, 429 (1990)
[9] D. Kumar, A. Das, B. R. Boruah, Rev. Sci. Instrum. 84, 026103 (2013)
[10] J. B. Bentley, J. A. Davis, J. Albero, I. Moreno, Appl. Opt. 45, 7791 (2006)

OSI-ISO 2018 manuscript No.
(79)

Scatter distribution over the FOV of VELC on Aditya-L1 mission

Suresh Venkata · B. Raghavendra Prasad

Abstract Visible Emission Line Coronagraph (VELC) on board ADITYA-L1 mission is an internally occulted reflective coronagraph. To achieve proposed science goals of the mission, total instrument background should be minimum. Major contributor to the instrument background in VELC is scattered light of solar disk due to the RMS microroughness and contamination over the Primary Mirror (M1). VELC being an internally occulting system, scatter generated at the primary mirror interface due to all source points (Sun is an extended source with an angular size of 32 arcmin) do not contribute the scatter over the field of view. VELC covers a wide band of wavelength ranging from 5000 Å-10750 Å. Hence, the scatter over the FOV at different wavelengths is not the same. Another important factor to be considered is the surface topography of M1 at different spatial scales / frequencies. In this paper we describe in detail about the effect of source size, wavelength and surface topography of M1 at different spatial scales / frequencies on scatter distribution over the FOV of VELC with the help of simulations. All the simulations are carried out using Advanced System Analysis Program (ASAP).

Keywords VELC · Aditya -L1 mission · scatter · microroughness · wavelength · spatial scales / frequencies

1 Introduction

Visible Emission Line Coronagraph (VELC) [1] is the prime payload on Aditya-L1 mission. VELC is designed [2] to perform simultaneous observations of solar corona in imaging, spectroscopy and spectro-polarimetry modes. Primary mirror of VELC collects the solar disk and coronal light over the Field of View

Suresh Venkata · B. Raghavendra Prasad
Indian Institute of Astrophysics, II Block, Koramangala, Bangalore-560034
E-mail: venkata@iiap.res.in, brp@iiap.res.in

of 3 Ro. Secondary mirror with central elliptical hole at the prime focus of VELC ejects the solar disk and coronal light upto 1.05 Ro and reflects the coronal light over the FOV 1.05 - 3 Ro towards different channels. The solar corona is million times fainter than the solar disk, scatterd disk light from the primary mirror (M1) of VELC can over shawdow the actual coronal signal. Thus, compramize the targetted science goals. In order to meet the science goals of the misson, total instrument background should be less than 5 ppm (parts per million) with respect to the disk brightness. RMS microughness and contamination over the M1 surface will result in scattering of disk light, which is the main source of instrument background. In order to control the scatter, M1 surface should be super polished and with minimum contamination.

2 Effect of wavelength, source size and spatial sclaes / frequencies

Theoretical studies carried out to determine the scatter distribution over the continuum channel of VELC. With the help of these studies microroughness and contamination limits on M1 surface are specified [3]. In addition to the continumm channel, VELC performs observations in spectroscopic and spectropolarimetric modes at 5303 Å, 7892 Åand 10747 Å. Harvey BRDF parameters for different wavelengths of interest are calculated to determine the scatter over the FOV. These parameters are used for simulating the scatter distribution over the FOV for different wavelengths. In order to determine the source angles the contributes maximum scatter over the FOV, simulations are carried out considereing different angular sizes of the source (maximum 32 arcmin). From the simulations it is evident that the source points toward the limb of the solar disk contrbutes to maximum scatter over the FOV. Based on the scatter angles and their contibutions towards the total instrument background, critical scattered light paths are identified. These scatter angles are converted into spatial scales / frequencies by using Bragg's law. With the help of simulations, scatter over the FOV due to surface microroughness over different spatial scales / frequencies of M1 is estimated.

References

1. B. Raghavendra Prasad et.al., Visible Emission Line Coronagraph on Aditya-L1, Current Science, Vol. 113, No. 4, 613-615 (2017)
2. N. Rajkumar et.al., Optical design of visible emission line coronagraph on Indian space solar mission Aditya-L1, Experimental Astronomy, Vol. 45, No. 2, 219-229 (2018)
3. Suresh N Venkata et.al., Scatter studies for visible emission line coronagraph on board ADITYA-L1 mission, J. Astron. Telesc. Instrum. Syst. 3(1) 014002 (2017)

Dual tunable multicavity resonator based photonic bandgap structure as hybrid optical filter

Subrata Karmakar[1*], Rajorshi Bandyopadhyay[1, 2], Rajib Chakraborty[1]
1 Department of Applied Optics and Photonics, University of Calcutta, Kolkata, INDIA
2 Regent Education and Research Foundation, Barrackpore, Kolkata, INDIA
subratak1610@gmail.com,rajorshi.aop@gmail.com,rcaop@caluniv.ac.in

Abstract: A photonic bandgap structure is proposed here for designing mode independent optical filters. The structure is basically hybrid in nature, which is constructed by stacking low refractive index material and high refractive index material.For this design, sputtered Titanium dioxide (TiO_2) and Electro-optic (EO) polymer SEO125 are taken as high and low refractive index material.The length of high refractive index material as well as low refractive index material is pre-calculated and adjusted to provide both flat-top and narrow band transmission spectra with a sharp peak. To design the filter, the concept of electro-optic as well as angle tuning is also utilized. The designed narrowband optical filter can have a bandwidth as low as 2 nm and is insensitive of the modes of light. We have shown different results by changing different parameters of electro-optic and angle tuning mechanism. This type of optical filters is very useful in Wavelength Division Multiplexing (WDM) systems used in optical communications.

Keywords: Photonic bandgap structure, Cavity resonator, Wavelength division multiplexing, Electro-optic tuning

1. Introduction

Photonic Band Gap (PBG) structure is a periodic structure with spatial distribution of materials having suitable refractive index (RI) contrast. This type of structure is essentially characterized by the existence of photonic band gap that forbids propagation of a certain frequency range of light [1]. Optical PBG structures, such as fiber Bragg gratings [2], multilayer thin-film filters [3, 4], sensors, low power lasers [5] have been used as photonic devices.

The proposed PBG structure is basically a three cavity resonators consists of periodic layers of high and low r.i. dielectric with a low index material sandwiched between each of these three resonators. The structure will act as a transmission band pass filter having a flat top response, centered at 1550 nm. It is shown here that the bandwidth and position of the spectral output can be changed by controlling the r.i. of the EO polymer (low index material) and the angle of incidence of the light the structure can be made to act as flat-top bandpass and narrowband transmission filter useful for multiplexing applications. Thus the structure acts as hybrid optical filter.

2. Results and discussion

Phase shifted narrowband transmission filter using high (nH) and low (nL) refractive index (RI) material working in Fabry-Perot resonator principle have already been proposed in [1]. Three such resonators are made to overlap with each other here to design the proposed flat-top bandpass filter and the resulted structure looks like$(HL)^{N1}2H(LH)^{N1}L(HL)^{N2}2H\ (LH)^{N2}\ L\ (HL)^{N3}2H(LH)^{N3}$, where H and L represent the high and low index layer respectively.N1,N2,N3 represent the number of bilayers in the first, second and in the third resonator respectively. It is seen that when the structure is excited with a source of central wavelength 1550 nm, a flat-top transmittance spectra is obtained at the output ,if a relation among the bilayers like N1=N3 and N2=N1+1 is maintained. The flat-top nature of the spectrum can be improved if the structure is modified as$L\ 1.587\ H\ \ L\ (HL)^{N1}\ 2H\ (LH)^{N1}\ L\ (HL)^{N2}\ 2H\ (LH)^{N2}\ L\ (HL)^{N3}2H(LH)^{N3}L\ 1.587\ H$ and the transmittance spectrum (FWHM bandwidth 8nm) of such structure is shown in Fig.1a for N1=N3=3 and N2=4. For this design, sputtered Titanium dioxide (TiO_2) and Electro-optic (EO) polymer SEO125 are taken as high and low refractive index material. The refractive indices (r.i.) of TiO_2 and EO polymer are taken as 2.567 and 1.621 at 1550 nm respectively [2]. The width of the high and low index material are considered as 260.3 nm and 733.7 nm respectively. The FWHM bandwidth of the spectra can be made narrower if the number of bilayers is increased. Fig.1b depicts the same.

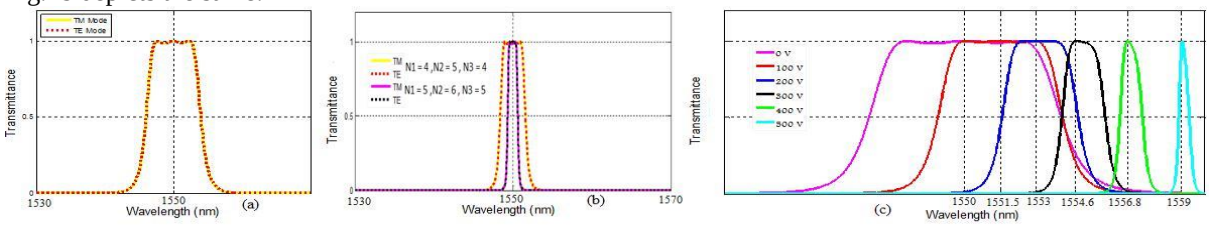

Figure 1 (a) Spectral response of the proposed PBG structure for flat-top bandpass filter. (b) Effect of increasing the number of bilayers (c) Electro–optic tuning for converting the flat-top bandpass spectrum to narrowband spectrum.

Electro-optic property of the EO polymer can be utilized to change the r.i. of it by applying an electric field across crystal axis of the EO polymer to select r_{33}electro-optic coefficient. The change in the refractive index of EO polymer due to applied electric field [3] can be calculated by the equation

$$\Delta n_{EO} = \frac{1}{2}(n_{EO})^3 r_{33}\frac{V}{d} \quad \text{.....(1)}$$

where, V is the applied voltage , d is the interelectrode gap, n_{EO} is the r.i. of EO polymer at the wavelength under consideration and Δn_{EO} is the change in r.i. Electro-optic coefficient of EO polymer is considered as 100pm/V [3]. Designing the structure as mentioned in [1], it is possible to apply the voltage across the EO polymer layers and thereby the r.i. of EO polymer can be changed. For normal incidence of light, if the applied voltage across the EO polymer is increased, it is found that the FWHM bandwidth of the pass band got narrower. However this bandwidth narrowing is associated with a shift of the transmittance peak from 1550 nm which is shown in Fig.1c. This shifting of the transmitted peak from the working wavelength (here 1550 nm) can be once again tuned to the desired position by angle tuning which is shown in Fig. 2a. From this figure, it is clear that a rotation of 6.7 degree of the light source or the device results a narrow band transmission peak having bandwidth 2 nm at 1550 nm. It is also clear from the figure if only TE or TM mode of light is considered angle tuning can be done for wider range of wavelength. But if an output is required which will be TE, TM insensitive, a restriction is automatically imposed on this angle tuning. From this figure it is also evident that to get a transmission band with 2 nm bandwidth insensitive to TE, TM mode of light, the light source can maximum be rotated by 9 degree.

If the central wave length of the transmitted band is plotted against the applied voltage, Fig. 2b is obtained. The curve remains linear as long as the structure provides a flat top response and once aging becomes linear as the structure starts providing narrow band transmission with a sharp central peak.

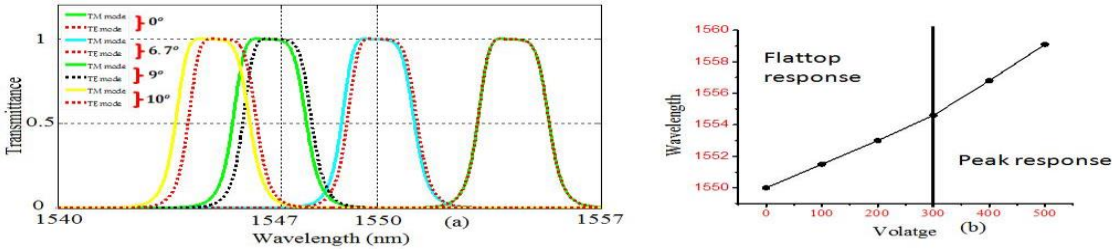

Figure 2: (a) Effect of angle tuning (b)Wavelength voltage plot showing linearity for both flat-top and peak response region.

3. Conclusion

In this paper a structure is proposed which provides hybrid outputs. Initially a PBG structure is designed which works as a bandpass filter with almost flat top response. Applied electric field is used to control the bandwidth of the spectral output. Then angle tuning is suggested to tune the peak at the desired position. The limits of rotation of the incident ray for which the output spectra will remain insensitive to TE, TM mode of light are also shown here. It is found here that the incident ray is required to be rotated by a maximum angle of 6.7 degree to get the output at the desired position with 2nm bandwidth. At last the linearity nature of plot for wavelength versus applied voltage is also discussed. Thus, a double tunable PBG structure design is proposed which can work as optical modulator to provide a flat-top band pass response having a central wavelength at 1550 nm and at the same time a narrowband tunable transmission filter which can provide a TE, TM insensitive output transmittance spectra.

4. References

[1] S. John, ‘‘Strong localization of photons in certain disordered dielectric superlattices,’’ Phys. Rev. Lett. 58, 2486– 2489 (1987).

[2] H. Wen, M. Terrel, S. Fan and Michel Digonnet, “Sensing With Slow Light in Fiber Bragg Gratings”,IEEESensors J. , Vol. 12, No. 1, January 2012

[3] M. Gerken and D. A. B. Miller “Multilayer Thin-Film Stacks With Steplike Spatial Beam Shifting”, J.Lightwave Technol., Vol. 22, No. 2, February 2004

[4] R. Bandyopadhyay and R. Chakraborty , “Design of tunable transmission filter using one dimentional defective photonic crystal containing electro optic material”, Opt.Engg, vol. 54 (11),2015.

[5] L. Florescu , K. Busch , S. John ,"Semi-classical Theory of Lasing in Photonic Crystals", J. Optical Society of America B19, 2215 (2002).

Assessment of retardance and polarizance through time resolved Mueller matrix in Early Detection of Cervical Cancer

Mohammad Zaffar[1], Gyana Ranjan Sahoo[1], Asima Pradhan[1,2]
[1]Department of Physics, Indian Institute of Technology Kanpur, Kanpur, UP, 208016, India,
[2]Centre for Lasers & Photonics, Indian Institute of Technology Kanpur, Kanpur, UP, 208016, India
Author e-mail address: asima@iitk.ac.in

Abstract

We report here time dependent retardance and polarizance properties, accessed through time resolved Mueller matrix, from stromal region of cervical tissue. As the disease evolves, time dependent circular degree of polarization is more preserved as compared to time dependent linear degree of polarization. The exponentially increasing retardance in healthy collagen changes to an almost constant variation in the precancerous case. Interestingly, the chirality of collagen network that rotates the plane of polarized light in either direction in normal sample get limited to only clockwise direction during the progression of the disease. These results show potential in the early detection and understanding mechanisms of morphological changes in cervical cancer development.

Keywords

Time resolved Mueller matrix, polarizance, retardance, chirality, cervical cancer

Introduction

Cervical cancer is one of the major causes of female mortality around the world. Early diagnosis is the key to survival with the optical techniques aiming towards this through various approaches [1-4]. Time resolved Mueller matrix in backscattered geometry has shown its capability to address turbid media with picosecond resolution [5]. Weakly scattered photons carry direct information about histological characteristics of tissue. It has been reported in [6] that time-resolved Stokes vectors of transmitted optical signals differentiate normal and stunned myocardium tissues. Optical characterization based on time-resolved Stokes-Mueller measurements is a diagnostic tool of immense potential, which can be of assistance to the management of cardiovascular diseases [6]. The full 4 x 4 time-gated Mueller matrix can reflect altered structures in cervical tissues. Time-gated signals will be helpful in reducing the depolarization effect of random scattering in biological tissues. The transmission measurements are used for the first-step characterization of such tissues because they are supposed to provide more information than the reflection measurements. Because of the highly birefringent and chiral nature of stromal region, its complete characterization in terms of optical properties like retardance (birefringent and chirality) and polarizance (degree of polarization effect) through polar decomposition becomes crucial in early detection of cervical cancer. Here, we investigate time dependent retardance and polarizance properties of stromal region of cervical tissues extracted through polar decomposition of time resolved Mueller matrices for early detection of cervical cancer.

Experimental Methods and Materials

Figure 1(a) shows the schematic diagram of the experimental set up in transmission mode. It consists of a PicoQuant picosecond pulsed diode laser (PDL) (440 nm with pulse width 56 ps and average power 1.5 mW) to illuminate the sample and a LaVision Intensified charge coupled device (ICCD) to record images. A PSG unit consists of a quarter wave plate followed by a linear polarizer while PSA unit consists of the same optical element as PSG placed in reverse order. Images at 16 different elliptical polarization states of laser light are used to construct time gated Mueller matrix of stromal region of normal and precancerous cervical tissue sections in a transmission mode [2,4]. A polar decomposition has been applied on time gated MM of healthy and precancerous cervical tissues to extract different optical properties.

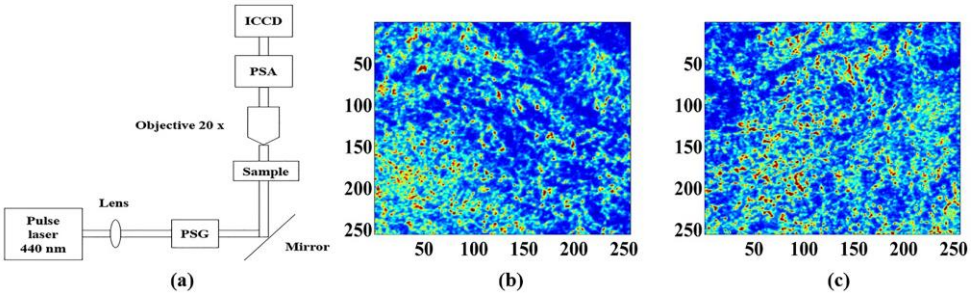

Fig. 1 (a) Schematic diagram of the experimental set-up to record images for different polarization states for constructing the time gated Mueller matrix and typical co-polarized microscopic images of stromal region of normal (b) and precancerous (c) respectively

Results and Discussions

Time gated linear polarizance (LP), linear 45 polarizance (LP-45) and circular polarizance (CP) extracted from time gated MM on applying polar decomposition are shown in figure 2(a), 2(b) and 2 (c) respectively. It is clear from figure 2 that degree of linear polarization decreases and degree of circular polarization increases with time evolution during the progression of the disease as circular polarization suffers less depolarization compared to linear polarization. The time gated circular retardance and retardance are shown in figure 3(a) and 3(b) respectively.

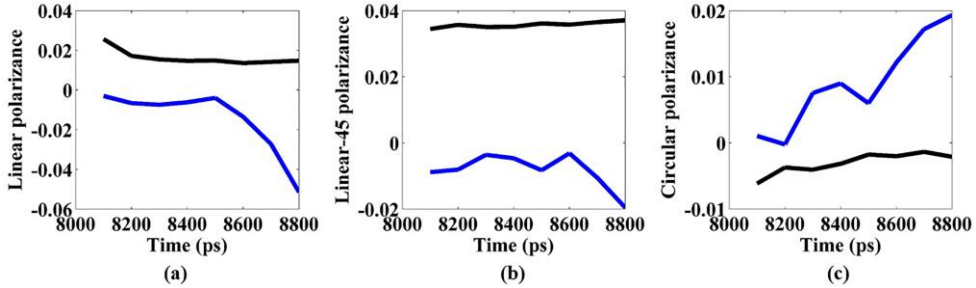

Fig. 2 (a) Linear polarizance for normal (black) and precancerous (blue) and (b) linear 45 polarizance for normal (black) and precancerous (blue) and (c) circular polarizance for normal (black) and precancerous cervical tissue sections (blue)

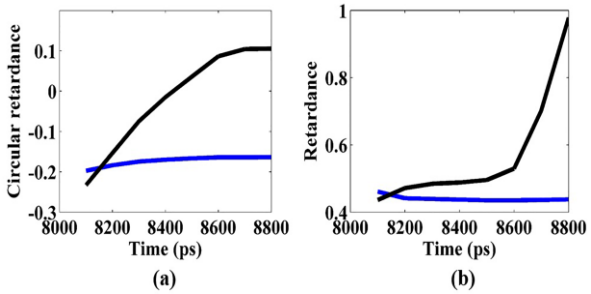

Fig. 3 (a) Circular retardance for normal (black) and precancerous (blue) and (b) retardance for normal (black) and precancerous cervical tissue sections (blue)

The time dependent retardance property of collagen network increasing exponentially for normal samples decreases and is almost constant in the precancerous case as shown in figure 3(b). The decrease in the time dependent retardance may be attributed to the loss of linear retardance as collagen cross links get broken during the progression of the disease. Collagen network is highly birefringent and chiral in nature. Initially, chirality of collagen network that rotates the plane of polarised light in clockwise direction ($n_L < n_R$) and afterwards in anticlockwise direction ($n_L > n_R$) in healthy collagen gets limited to only clockwise direction ($n_L < n_R$) in the precancerous case where n_L and n_R are refractive indices experienced by left and right circular polarization of light respectively. This behaviour of stromal region may be attributed to the loss of chiral nature as the disease evolves.

Conclusion

Polar decomposition has been applied on time resolved Mueller matrices of normal and precancerous cervical tissue sections to extract time dependent polarizance and retardance properties of stromal region. Time dependent circular degree of polarization suffers less depolarization as compared to linear degree of polarization as disease progresses. Time resolved retardance, increasing exponentially in healthy collagen, degrades. Chirality of collagen network that rotates the plane of polarized light in either direction gets limited to only clockwise direction in precancerous case implying loss of chiral nature during the progression of the disease. These results show potential in the early detection and understanding mechanisms of morphological changes in cervical cancer development.

References

1. J. Rehbinder and H. Haddad, J. Biomed. Opt., 21(7), (2016).
2. P. Shukla and A. Pradhan, Opt. Express, 17(3), (2009).
3. N. Ghosh, J. Appl. Phys., 105(10), 102023, (2009).
4. M. Zaffar and A. Pradhan," in 13th International Conference on Fiber Optics and Photonics, W2B.3, (2016).
5. I. Berezhnyy and A. Dogariu, Opt. Express 12, (2004).
6. C.W. Sun, L.S. Lu, C.C. Yang, Y.W. Kiang, and M.J. Su, Opt. Express 10, (2002).

OSI-ISO 2018 manuscript No.
(82)

2-colour pump-probe setup and carrier dynamics study

Banoj Kumar Nayak · Shriganesh Prabhu · Venu Gopal Achanta

Abstract We developed an ultrafast time-resolved pump-probe setup with 35fsec time resolution to study the carrier dynamics in semiconductors as well as plasmon dynamics in metamaterials. The setup is unique that we can do either collinear or non-collinear degenerate or non-degenerate time-resolved measurements. The time-dependent nonlinear phenomena can be well understood in ultrafast timescales in this setup. We have demonstrated the carrier dynamics of GaAs by exciting carriers to energy levels much higher than its conduction band-edge.

Keywords ultrafast · time-resolved · carrier · GaAs · dynamics

Time resolved pump-probe spectroscopy is an important technique to study ultrafast carriers dynamics of a wide range of materials such as semiconductors, metals, organics as well as nanostructures with short carrier lifetimes [1, 2]. The optical response of a material for a particular probe wavelength varies with different pump wavelength of excitation as both carrier energy and carrier density are strongly dependent on the excitation wavelength. So, a 2-colour pump-probe method will give a broader and detailed insight of carrier dynamics of a material and corresponding change in optical properties in picosecond timescales [3].

We have setup a time-resolved 2-colour pump-probe setup with 35fs temporal resolution. The high power amplifier laser operates at 800nm wavelength with 25fs pulse duration. It has a secondary laser output generated through op-

Banoj Kumar Nayak
DCMPMS, Tata Institute of Fundamental Research, Mumbai-400005, India
banoj.nayak@tifr.res.in

Shriganesh Prabhu
DCMPMS, Tata Institute of Fundamental Research, Mumbai-400005, India

Venu Gopal Achanta
DCMPMS, Tata Institute of Fundamental Research, Mumbai-400005, India

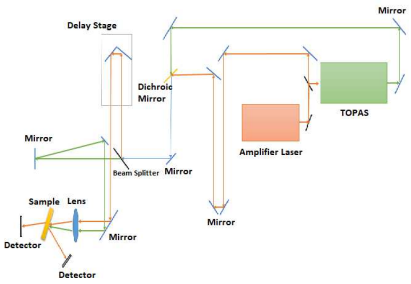

Fig. 1 2-colour Pump-Probe Setup

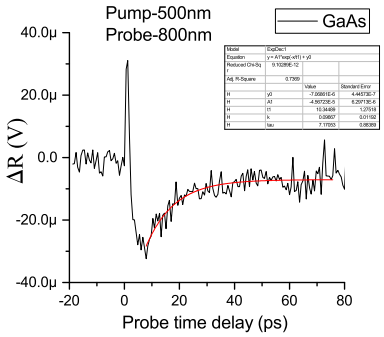

Fig. 2 Pump-probe measurement of transient reflectance change for GaAs

tical parametric amplifier(OPA) which can operate from 275nm upto 1600nm wavelength. The 800nm-amplifier laser is used as probe and output from OPA is used as pump. We made sure that both the laser beams are travelling almost equal optical path before reaching the sample so that the center of the delay stage corresponds to zero time delay between pump and probe pulses. Then, the collinear pump and probe beam were focused by a lens and spatially overlapped at the focal plane. Then, the sample was kept at overlap region. Differential reflection and differential transmission of the sample were measured by lock-in technique.

We have demonstrated the ultrafast carrier dynamics of GaAs with probe wavelength of 800nm, little above the band-edge wavelength. Pump wavelength of 500nm was used to excite the carriers in GaAs to energy levels much higher than its conduction band-edge. Fig.2 shows differential reflection vs time delay of probe for GaAs at given pump and probe wavelength with 1mW pump power. The data can be divided into three components i.e. fast rise, a fast decay and a slow decay component. The slow decay lifetime of carriers is around 10ps at 500nm excitation wavelength. This setup is also being used for ultrafast surface plasmon polariton dynamics as well as hot carrier dynamics in plasmonic structures.

Acknowledgements We are thankful to Gajendra Mulay for providing technical support.

References

1. Sheng–Fu Horng , Shi-Hsiang Lu et al., Comparison of optical pump-probe characterization of low-temperature-grown GaAs at well-above bandgap and near-bandedge wavelengths, Optical and Quantum Electronics, 32, 573-584 (2000)
2. Sanjeev Singh, Zeev Valy Vardeny, Ultrafast Transient Spectroscopy of Polymer/Fullerene Blends for Organic Photovoltaic Applications, Materials, 6, 897-910 (2013)
3. Yu Tokizane, Katsuhiro Shimatake et al., Global evaluation of closed-loop electron dynamics in quasi-one-dimensional conductors using polarization vortices, Optics Express, 17, 24198-24207 (2009)

OSI-ISO 2018 manuscript No.
(83)

Estimating OAM of light using partial Fourier transform

P. A. Ameen Yasir · J. Solomon Ivan

Abstract An algorithm to extract phases with dislocations from intensity measurements is proposed, and demonstrated on paraxial wave fields. The proposed algorithm makes use of the partial Fourier transformation which does not conserve the longitudinal orbital angular momentum and hence can create or destroy phase dislocations naturally, and can distinguish between their orientation. A method to realize the partial Fourier transformation using thin cylindrical lenses is outlined. Unambiguous phase retrieval is numerically demonstrated on random complex superpositions of Laguerre-Gaussian modes with both integer and fractional orbital angular momentum.

Keywords Phase retrieval · Fourier optics · Wave optics

PACS 42.30.Rx · 42.30.Kq · 42.25.-p

Wave-fields whose phases have dislocations have been well-explored in the literature [1]. Such wave-fields occur naturally in several contexts such as in optics, electron beams, x-ray beams, atom interferometry, Bose-Einstein condensates, etc. A well-known example in paraxial wave optics are the Laguerre-Gaussian (LG) modes which are the stable solutions of the paraxial wave equation, and these are readily realized in experiments. In fact, the LG modes and their superpositions are known to possess well-defined orbital angular momentum (OAM), which is intrinsically linked to the dislocations in their phase [2]. An important problem in regard of LG modes and their superpositions is the detection of dislocations in their phase (also their orientation), estimation of such a phase through intensity measurements, and estimation of

P. A. Ameen Yasir
Department of Physics, IIST, Valiamala P.O., Thiruvananthapuram 695 547, India
E-mail: ameenyasir.p.a@gmail.com

J. Solomon Ivan
Department of Physics, IIST, Valiamala P.O., Thiruvananthapuram 695 547, India

OAM possessed by such wave-fields [1]. While amplitude is readily available through intensity measurements, phase is in principle retrieved.

In this work [3, 4], we propose and demonstrate an algorithm to retrieve phases with dislocations (and consequently the OAM) through transverse plane intensity measurements. The algorithm is inspired by the well-known Gerchberg-Saxton (GS) algorithm [5], albeit with one fundamental difference in that: while the GS algorithm is based on two dimensional Fourier transform which conserves the longitudinal OAM of the wave-field, the proposed algorithm uses partial Fourier transform (i.e., Fourier transformation in one transverse coordinate and identity transformation on the other; see Fig. 1) [4], which does not typically conserve the same, and can distinguish between the orientation of the dislocations. In our opinion, the present technique is not only relevant to optics, but to a wider context, where phases with dislocations occur naturally.

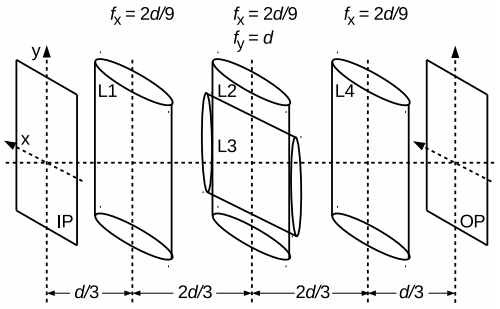

Fig. 1 Realization of partial Fourier transformation using thin cylindrical lenses L1, L2, L3, and L4. Here, IP (OP) stands for input (output) plane.

References

1. G. Gbur, *Singular optics* (CRC Press, 2017).
2. L. Allen, M. W. Beijersbergen, R. J. C. Spreeuw, and J. P. Woerdman, "Orbital angular momentum of light and the transformation of Laguerre-Gaussian laser modes," Phys. Rev. A **45**, 8185 (1992).
3. P. A. A. Yasir and J. S. Ivan, "Estimation of phases with dislocations in paraxial wave fields from intensity measurements," Phys. Rev. A **97**, 023817 (2018).
4. P. A. A. Yasir and J. S. Ivan, "Realization of first-order optical systems using thin lenses of positive focal length," J. Opt. Soc. Am. A **34**, 2007 (2017).
5. R. W. Gerchberg and W. O. Saxton, "A Practical Algorithm for the Determination of Phase from Image and Diffraction Plane Pictures," Optik **35**, 237 (1972).

Diffuse reflectance spectroscopy on human oral tissue and saliva for detection of oral cancer

Pavan Kumar[1], Surendra Kumar Kanaujia[2], Asima Pradhan[1, 3]

[1]Department of Physics, Indian Institute of Technology Kanpur (IITK), Kanpur 208016, India
[2]Department of ENT, Ganesh Shankar Vidyarthi Memorial College (GSVM), Kanpur 208002, India
[3]Center for Lasers and Photonics (CELP), IIT Kanpur, Kanpur 208016, India
E-mail address: asima@iitk.ac.in

Abstract

A comparative study has been performed on human oral tissue and saliva samples for oral cancer detection on three groups: oral squamous cell carcinoma (OSCC), dysplastic, and normal by using diffuse reflectance (DR) spectroscopy. DR spectra obtained from tissue consists of blood valleys as well water absorption dips while human saliva only consists of the water absorption dip. Classification has been performed by employing principal component analysis (PCA), Mahalanobis distance model, and receiver operating characteristic (ROC) analysis. DR spectroscopy for oral tissue is able to differentiate OSCC to normal, dysplasia to normal, and OSCC to dysplasia with the accuracy of 95 %, 83 % and 77 %. For saliva, it differentiates respective groups with the accuracy of 85 %, 81 %, and 77 %. Obtained results with human saliva are significantly good for discrimination of OSCC to normal and dysplasia to normal. Thus it may be supplementary tool for detection of oral cancer.

Keywords

Oral cancer, tissue & saliva, diffuse reflectance spectroscopy, Mahalanobis distance

Introduction

Incidence rate of oral cancer are increasing progressively due to late diagnosis and lack of early symptoms. If diagnosed at an early stage, there is higher chance of cure. Worldwide it is the 6th most common cancer and in India it is ranked number one among males and third most in females. [1].

In the conventional techniques, tissue biopsy with histopathologic examination is gold standard for the clinicians but it is an invasive process for diagnostic purpose. Cancer detection has been performed by research groups by using non-invasive techniques such fluorescence spectroscopy, diffuse reflectance spectroscopy etc. and significant good results have been obtained [2 - 4].

During the evolution of cancer various changes occur in the tissue of oral cavity, such as nuclear size distribution, blood concentration, fluorophore concentration etc. Unlike the change in human oral tissue, obvious changes are not seen in human saliva, however biochemical changes do occur and are reflected in it during development of oral cancer. Human oral tissue and saliva both consist of many fluorophores such as amino acids (tryptophan, tyrosin etc.), coenzymes (NADH, FAD etc.), collagen, porphyrins, proteins, amylase, deoxyribonucleic acids (DNA), ribonucleic acids (RNA), etc. In a previous study, we have shown that fluorescence from saliva detects precancer with significantly high sensitivity and specificity [5].

Materials and Methods

Measurements were performed on 86 oral tissue samples and 86 saliva samples of oral squamous cell carcinoma (OSCC), dysplastic, and normal groups. Sample collection was done in Hallet hospital affiliated to GSVM medical college, Kanpur. Ethical clearance was obtained with IEC communication number IITK/IEC/2015-16/2/10. Histopathology reports were later obtained and compared with optical results.

Diffuse reflectance (DR) measurements were taken on spectrofluorimeter (Fluorolog 3, Model FL3-22). For DR measurements, slit width was fixed at .5 nm for both monochromators (excitation and emission) and spectra acquisition were taken in 0.1s integration time in the interval of 1 nm. Signals were recorded in the scan range of 300 to 650 nm.

Experimental results and discussion

Averaged diffuse reflectance (DR) spectra of OSCC, dysplastic, and normal oral tissue and saliva samples in the scan range of 300 – 650 nm are shown in the Fig. 1(a) & (b). DR spectra of tissue samples of all the three groups (OSCC, dysplastic & normal) show valleys near 410, 537 and 577 nm which are due to blood absorption and a kink near 397 nm may be Raman band of water. A dip near 505 nm is also present in the spectra of all groups which is attributed to absorption by water. Averaged spectra of saliva samples shown in Fig. 1(b) show significant difference in intensity between OSCC to normal. DR spectra of saliva only show a valley near 513 nm which is due to water absorption and a kink near 397 nm which may be the Raman band of water. Overall contribution to the tissue and saliva spectra are attributed due to presence of scatters (cells, nucleus, mitochondria, etc.) and absorbers (hemoglobin, water, etc.).

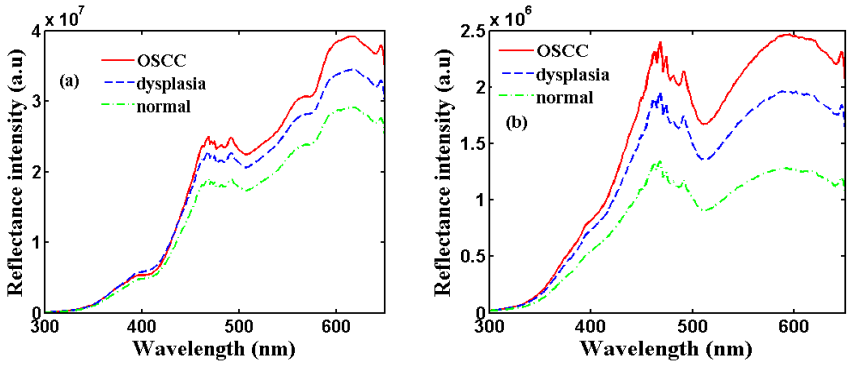

Fig. 1 Averaged diffuse reflectance spectra (DR) spectra of OSCC, dysplastic and normal (a) oral tissue (b) saliva

Data Analysis

Principal component analysis (PCA) has been applied on the DR spectra of oral tissue and saliva samples in scan range 300 to 700 nm. Data sets of DR spectra have dimension of 351 and are reduced to 7 dimensional data set by computing principle components (PCs). From the computed PCs, Mahalanobis distances are calculated and receiver operating characteristic (ROC) analysis are performed on these distances. ROC on the Mahalanobis distances obtained from PC scores of DR spectra of tissue are able to differentiate OSCC to normal, dysplasia to normal, and OSCC to dysplasia with sensitivities 97 %, 78 %, 74 % and specificities 92 %, 88 %, 81 % respectively while ROC on the Mahalanobis distance obtained from PC scores of DR spectra of saliva is able to differentiate respective groups with sensitivities 88 %, 74 %, 68 % and specificities 80 %, 88 %, 89 % respectively. ROC curves are shown in Fig. 2(a) & (b) respectively.

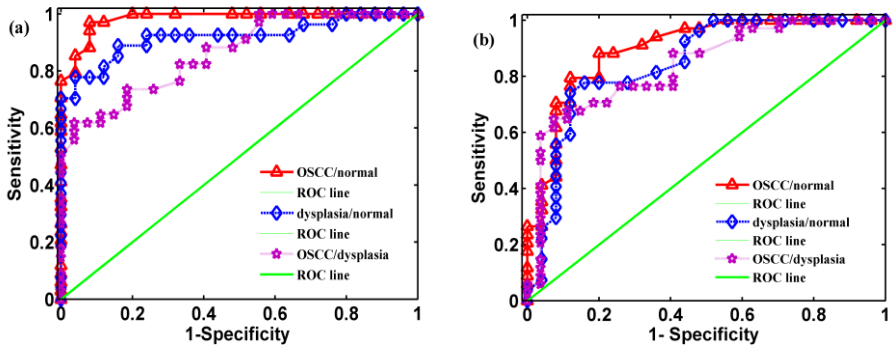

Fig.2 Receiver operating characteristic (ROC) curves for OSCC to normal, dysplasia to normal, and OSCC to dysplasia for (a) human oral tissue samples (b) human saliva samples

Conclusion

Results with human saliva appears to be as good as oral tissue especially for discrimination of OSCC to normal and dysplasia to normal. It shows that human saliva may be useful supplementary diagnostic medium for oral cancer detection since its collection is non-invasive.

References

[1] R. Dikshit, P. C. Gupta, C. Ramasundarahettige et al., Cancer mortality in India: a nationally representative survey. Lancet 379:1807-16 (2012)

[2] Y.N. Mirabal et.al, Reflectance spectroscopy for in vivo detection of cervical precancer. J. biomed. Opt 7 (4), 587-594 (2002).

[3] D. C De Veld, M. J. Witjes, H. J. Sterenborg and J. L. Roodenburg, "The status of in vivo autofluorescence spectroscopy and imaging for oral oncology," Oral Oncol 41:117-131 (2005)

[4] J. L. Jayanthi, N. Subhas, M. Stephen, E. K. Philip & V. T. Beena, Comparative evaluation of the diagnostic performance of autofluorescence and diffuse reflectance in oral cancer detection: a clinical study. J Biophotonic 4(10), 696-706 (2011)

[5] P. Kumar, A. Singh, S. K. Kanaujia and A. Pradhan, Human saliva for oral precancer detection: a comparison of fluorescence and Stoke shift spectroscopy. J Fluoresc 28(1) 419-426, (2018).

Development of Metal Organic Framework-integrated Optical Fiber for Gas Sensing Application

Shwinky[1], Aditi Chopra[1,2], Girish C. Mohanta[1,2] and Sudipta Sarkar Pal[1,2]
[1]CSIR- Central Scientific Instruments Organization (CSIR-CSIO), Chandigarh-160030, India
[2]Academy of Scientific and Innovative Research (AcSIR-CSIO), Chandigarh-160030, India
e-mail address: sudipta@csio.res.in

Abstract: Deposition of metal organic framework (MOF) on optical fiber surface has been studied experimentally in order to develop a MOF integrated fiber optics gas sensor. HKUST-1 MOF thin film was grown over optical fiber surface through layer-by-layer (LBL) method and simultaneous variation in the transmission spectra of the fiber was investigated. The MOF thin film grown for five cycles resulted into 40% transmission loss and broad absorption peak around 700 nm. Parallelly, fiber optics surface plasmon resonance (SPR) response was generated through metallic (Au) film deposition over the fiber and change in SPR response due to MOF film growth was also studied. The overall wavelength shift was found to be 30 nm for five cycles of MOF grown. The high porosity and surface area of MOF could act as pre-concentrator for gas molecules and thus could result into highly sensitive fiber optics gas sensor.

Keywords: *Optical Fiber, Surface Plasmon Resonance (SPR), Metal-organic frameworks (MOFs), Gas Sensor*

1. Introduction

The property of optical fibers to guide light to a remote location makes them an ideal platform to perform remote sensing at precise locations that are often hard to reach. Integration of optical fiber with suitable materials for biological and chemical sensing has given birth to a new technological vision – Lab on Fiber [1]. Optical fiber-based gas and vapour sensing is comparatively less explored. For trace gas analysis, less number of molecules within the interaction volume and difficulty in adsorbing them on the fiber surface become serious obstacles and lead to poor sensitivity. Integration of a porous film with high surface area on optical fiber surface can help to pre-concentrate gas molecules on the fiber surface resulting in effective increase in interaction volume. Metal organic frameworks (MOFs), in which metal ions are coordinated to organic linkers, are three-dimensional crystalline hybrid structures with high surface area and porosity [2]. They can provide pre-concentrating effects, host guest interaction and molecular sieving properties. Moreover, suitable functionalization of MOFs can result in controlled host-guest interaction leading to the selectivity of the sensor. Among optical fiber sensors, surface plasmon resonance (SPR) based sensing mechanism provides an ultrasensitive detection platform by monitoring the RI change of the medium, but the same principle makes it highly non-specific, and therefore an additional functionalization step with recognizing elements is obligatory [3,4].

In this work we are integrating MOF thin film on optical fiber surface so that gas molecules can be pre-concentrated around the sensing area resulting in an enhancement in sensitivity. We are also developing metal coated optical fiber surface functionalized with MOFs which would provide chemical recognition for gases/vapours necessary to introduce specificity in SPR based sensing.

2. Experimental Methods

For the deposition of MOF, multimode optical fiber (core diameter 400μm) was used and the cladding of the central portion of fiber was removed (approx. 1-1.5cm) to expose the core to the air. HKUST-1 is chosen as the MOF which has an open framework topology. Besides high pore volume and surface area, HKUST-1 contains an open metal site which makes it highly preferable and capable for selective adsorption and separation of various gases [5,6]. For deposition of MOF thin films on optical fiber surface, layer-by-layer method was used with freshly prepared ethanolic solutions of copper (II) acetate and trimesic acid linker. Different number of cycles of MOF can be deposited according to desired application. The fiber was connected between the visible light source (Halogen light source, Ocean Optics) and the spectrometer (Avantes) as shown in the schematic in figure1.

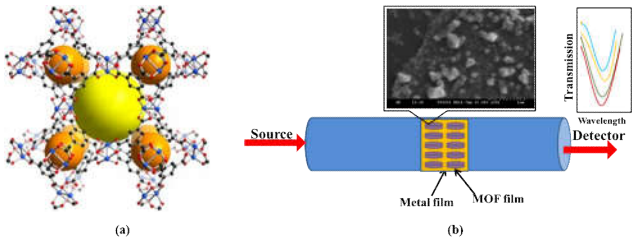

Fig. 1.Schematic of (a) HKUST-1 framework and (b) Experimental configuration along with SEM image of HKUST-1 deposited fiber surface.

3. Results and Discussion

The crystalline structure of deposited HKUST-1 film is confirmed by FESEM and XRD. The optical response of HKUST-1 thin films on bare and gold coated optical fiber is shown in figure 2. In case of bare fiber, with every cycle of MOF deposition, loss in transmission is observed as change in intensity (figure 2a). It indicates more absorption of light with the growth of thin film of MOF.

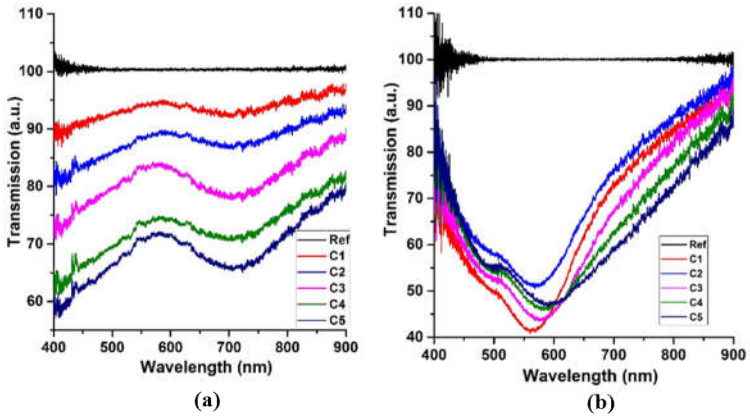

Fig. 2. (a) for 5 cycles of HKUST-1 on bare fiber (b) Transmission spectra for 5 cycles of HKUST-1 on Gold coated fiber.

In case of sputter coated gold fiber, the position of plasmonic dip in the transmission spectrum shifts towards higher wavelength with increase in number of MOF cycles. This is due to the fact that effective refractive index of MOF layer changes with the increase in number of cycles which affects the plasmonic response of Au film as shown in the figure 2b. Both the films are then used for ammonia sensing. It is also observed that with heating or with vacuum activation the MOF films can be recovered for re-use.

4. Conclusion

The MOF deposition on uncladded part of bare as well as gold coated optical fiber have been experimentally investigated. The change in transmission spectrum with every cycle signifies the growth of MOF on the optical fiber. This MOF coated optical fiber could act as the probe for the detection of gas molecules even at the lower concentrations.

Acknowledgement

Authors acknowledge the Director, CSIR-CSIO for financial support and Dr. Udaybir Singh for his help in gold coating of the fiber.

References

1. A. Ricciardi, A. Crescitelli, P. Vaiano et al. Analyst 140**,** 8068 (2015).
2. S. Osama. Materials 3, 1302 (2010).
3. L. Guo, J. A. Jackman, H -H. Yang et al., Nano Today 10, 213 (2015).
4. S. Unser, I. Bruzas et al., Sensors 15, 15684 (2015).
5. T. Toyao, K Liang, Kenji Okada et al. Inorganic Chemistry Frontiers, 2, 434 **(**2015),
6. Lin, Kuen-Song, et al. International journal of hydrogen energy, 37 13865 (2012)

OSI-ISO 2018 manuscript No.
(86)

Structured illumination using low cost diffractive optical element (DOE) for super-resolution microscopy

Shilpa Tayal[1], Veena Singh[1], Rakesh Joshi[1], Dalip Singh Mehta[1]

Received: date / Accepted: date

Abstract Structured illumination is a technique to improve resolution beyond the diffraction limit of an optical microscope. It increases the effective numerical aperture of the microscopic system. Generally, spatial light modulators (SLM) has been used for generating structured beams for illumination but SLMs are bulky and costly. Here, we report the use of off-the-shelf, low-cost diffractive optical element (DOE) for structured illumination microscopy. DOE is like a 2-D grating that will create 2-dimensional diffraction pattern in the Fourier plane. The mechanical movement in the system reduces the stability of the system and creates error. This could be overcome to some extent with the use of DOE as compared to grating. DOE can be used to create multiple beam interference and different fringe density interference pattern can also be obtained by rotating it. Simulation and experimental results will be presented.

Keywords：structured illumination, super resolution, resolution, microscopy

1. Introduction

Structured illumination microscopy is a technique to improve the spatial resolution of the image by collecting information from frequency space that is outside the diffraction limit of the optical system. This can be done by illuminating a sample with the structured pattern. Abbe stated that the microscope cannot give the resolution beyond the diffraction limit of the system which was governed by the numerical aperture (NA) of the objective and condenser lens. The resolution of the image depends on the wavelength and the numerical aperture of the system. The maximum NA for the oil immersion is 1.4 which limits the axial and lateral resolution by 500nm and 200nm respectively [1]. Structured illumination is the super-resolution microscopy in which the resolution can be doubled thus we can achieve the axial and lateral resolution up to 250nm and 100nm respectively. The applications include the study of membrane nanostructure, protein aggregation, nuclear machinery, molecular architecture of cell-cell interface and synaptic transmission [2].SLM and grating are usually used for illuminating the sample with the structured pattern but SLM is a very costly device and grating requires a lot of mechanical movement. It has been reported that grating requires rotation for taking a different set of images at each angle [2]. Here, we are proposing a technique that is low cost and requires less mechanical movement, we have used laser machine to make hole on cardboard such that it will pass only those angular illumination that is required at a time and sequentially open the holes in Fourier plane of the DOE so that we can get the required 2-beam interference pattern. To take phase shifted images at an angle, we are using a translation-stage with micro-stepper motor which reduces the cost further as compared to PZT. Micro-stepping controller has been designed using a TB6560 motor controller which has 1/16 micro-stepping but a controller that can give resolution in nanometer scale having 1/64 micro-stepping can also be designed. The proposed system design offers high efficiency for high-resolution imaging in a very cost-effective manner.

Shilpa Tayal
Department of Physics, Indian Institute of Technology Delhi
E-mail: tia.tayal@gmail.com

2. Experimental setup

The schematic view of the experimental set-up is shown in fig1. The sample (S) is illuminated by the structured pattern created by DOE. The green diode laser 532nm has been spatially filtered (SF) and then collimated beam from lens (L1) falls on DOE. The 2-D diffraction pattern is observed in the Fourier plane (FP) of the DOE. Here, in the FP of the DOE only two point sources are shown but actually many point sources will form. In the FP of DOE, the mount is placed such that at a time only 2 -beams are passing through it, keeping the other holes closed. In this way, rotation of diffracting element is not required, only translation motion is required to record phase-shifted pattern at a particular angle that is given by micro-stepping motorized translational stage. Lens (L3) combines the beams and sample is illuminated by interference pattern. Microscopic objective (MO) will collect information beyond diffraction limit due to the illumination of the sample with this modulated pattern and L4 is the tube lens that will collimate the beam and then it will fall on camera. Here, we recorded 12 images, 3 each at 0^0,45^0,90^0 and 135^0 angles so that more filling in frequency space can give rise to better results

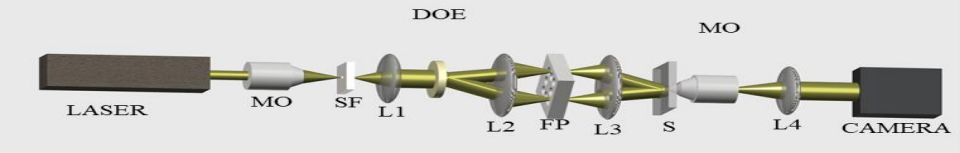

Fig.1 Experimental set-up of structured illumination microscopy for high-resolution imaging

3. Results and Discussion

The simulation result are shown in fig 2(a), (b), (c) and (d), the size of the object was taken to be 1µm, the PSF generated using diffraction limited frequency of the system was 0.25µm^{-1} and the frequency of the modulation pattern was similar to diffraction limited frequency. The obtained improvement in resolution of the image was almost double [3]. Fig 2(a) and (c) were obtained without illuminating the object with the modulation pattern and fig 2(b) and (d) were obtained by illuminating the object with modulation pattern. Hence, we propose that DOE can also be used to illuminate the sample with multiple beams such that single shot structured illumination with multiple beam interference can be achieved.

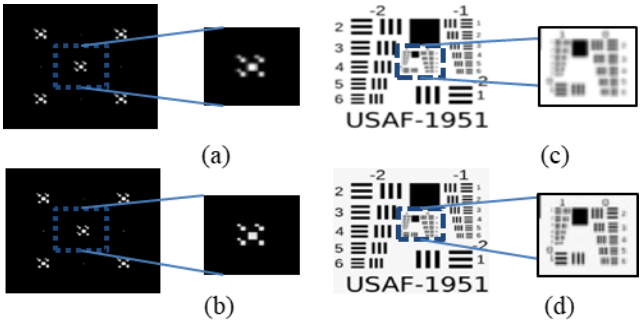

Fig.2 (a) and (c) showing images without structured illumination , (b) and (d) showing images with structured illumination.

Reference

[1].M. G. Gustafsson, "Surpassing the lateral resolution limit by a factor of two using structured illumination microscopy," J. Microsc. , 198, 82–87 (2000).
[2].S. Chowdhury and J. Izatt, "Structured illumination quantitative phase microscopy for enhanced resolution amplitude and phase imaging,"Biomed. Opt. Express 4, 1795–1805 (2013).
[3] Kedar Khare, Fourier Optics and Computational Imaging, 279-283.Wiley Publication(2015)

Refractive Index Sensor based on Fano Resonance for all Dielectric Metasurfaces

Keshav Samrat Modi, Jasleen Kaur, Satya Pratap Singh, Umesh Tiwari, Ravindra Kumar Sinha

Abstract In this paper, we have numerically studied the Fano resonance arising from the interaction of bright and dark mode in all dielectric two-dimensional periodic metasurfaces. Two arc-shaped nanostructures made up of silicon are placed back to back on a silica substrate with unequal geometrical parameters. The simulation has been carried out using Finite difference time domain method. Fano resonance arises at 1109 nm wavelength due to the asymmetric shape. We have proposed a refractive index sensor utilizing the Fano characteristics arising from the asymmetric geometry. The redshift in the resonance curve is observed when the refractive index (n) of the surrounding environment of Si arc varies from 1.0 to 1.3 and 1.4. The achieved sensitivity of the sensor is 180 nm/RIU and the figure of merit is 30.

Keywords Metasurfaces, Fano resonance, All-dielectric metasurfaces, RI Sensor

Introduction

Electromagnetic metamaterials and metasurfaces are gaining huge interest due to their ability to manipulate the direction and orientation of electromagnetic waves in the desired manner. The metasurface is usually made up from metallic components which bring ohmic losses [1] and to resolve this issue all dielectric metasurfaces made up from high index materials such as Silicon, Germanium and Tellurium were proposed as they result in less dissipation of energy. When light with a frequency below or near the bandgap frequency hits the dielectric medium both the electric and magnetic resonances are excited. Two Mie resonances are there where the first Mie resonance behaves as a magnetic dipole whose behaviour is similar to split ring resonator and second Mie resonance correspond to electric dipole [2]. The beauty of using dielectric materials in addition to less dissipation of energy is that the resonances are achieved at optical frequencies whereas metallic split-ring resonators work better at low frequencies. Metamaterials show various functionalities including negative refractive index, perfect absorption, transmission etc. These functionalities result in many potential applications such as cloaking, perfect lens, sensing etc. Few papers have been reported on Fano resonance-based sensing of refractive index using all dielectric metasurface with difference designs [3-5]. In this paper, we have designed a refractive index sensor based on Fano resonance. Fano resonance is a sharp curve in the absorption or transmission spectrum when the bright and dark mode overlap [4]. When there is an asymmetry in the Nanoresonators which is achieved with a simple bent or asymmetric gap between the resonators there arises an interference between the dipolar and quadruple modes and that produces a Fano feature [2]. Since Fano resonances are very sensitive to the outside dielectric environment and due to the sharp line width of Fano curve it is designed to be used as a refractive index sensor.

Ravindra Kumar Sinha
dr_rk_sinha@yahoo.com

CSIR- Central Scientific Instruments Organisation, Chandigarh-160030, India

Design of Metasurface

The schematic of the proposed metasurface is depicted in Figure 1. The unit cell of all dielectric metasurface composed of Si arcs of uneven lengths over Silica substrate as shown in Figure 2. The sweep angle made by the major arc is 2.79 radians and that of the minor arc is 2.09 radians. The inner and outer radius of the arcs is 150 and 300 nm respectively. The Si arcs have a thickness 110 nm and the period (P) of the unit cell is 700 nm. Results are obtained by Finite element method (FEM) (in COMSOL Multiphysics) where the periodic metasurface is illuminated by an x-polarized normally incident plane wave. The response of the metasurface was observed for the air (n=1) and refractive indices of 1.3 and 1.4.

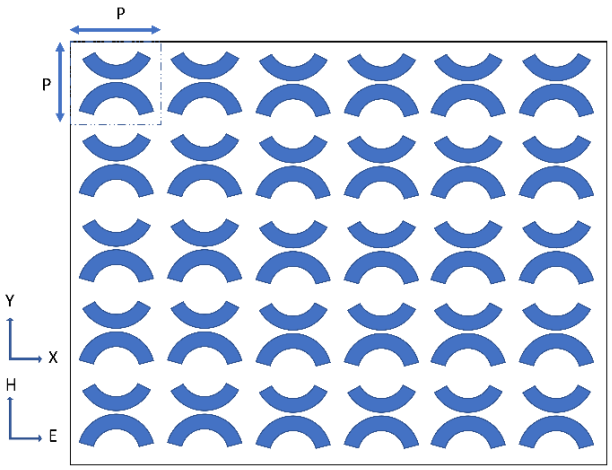

Fig. 1 The schematic of periodical array of all dielectric metasurface of Si arcs over Silica substrate.

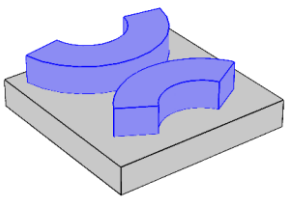

Fig. 2 Three-dimensional schematic of all dielectric metasurface (unit cell) composed of Si arcs (blue) of different lengths placed back to back on a Silica substrate (grey).

Results

A Fano transmittance curve of the proposed structure has a quality factor (Q) 184.83 and spectral contrast 99.95% as shown in Figure 3. A sharp Fano peak is observed at 1109 nm. The asymmetric field distribution at the Fano-resonance is due to the uneven arc length. The graphical representation of electric field distribution in the xy plane

at z=5 nm above the metasurface is shown in Figure 4. The redshift in the resonance peak of transmission spectra is observed when the refractive index of the surrounding environment of Si arc varies from 1.0 to 1.3 and 1.4 as shown in Figure 5. It can be observed from the transmittance spectrum that the resonant peak is red-shifted to 1162 and 1180 nm as the refractive index increases to 1.3 and 1.4, respectively. The sensor is showing sensitivity around 180 nm/RIU and figure of merit (FOM) is 30.

Conclusions

The numerical study of Fano resonance based all dielectric metasurface for refractive index sensing is presented. Due to the asymmetry in the design of proposed metasurface, the Fano resonance peak wavelength is observed at 1109 nm with high Q-factor of 184.83 and spectral contrast of 99.95%. The dependency of Fano resonance peak on the refractive index of the surrounding environment is utilized for the refractive index sensing application. The Fano resonance based all dielectric metasurface refractive index sensor have a sensitivity of 180nm/RIU and FOM of 30.

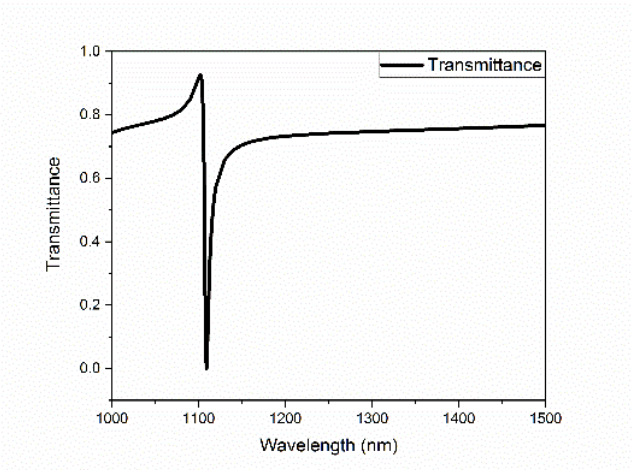

Fig. 3 Transmittance spectra of all dielectric metasurface showing Fano resonance peak at 1109 nm wavelength for n=1 (air).

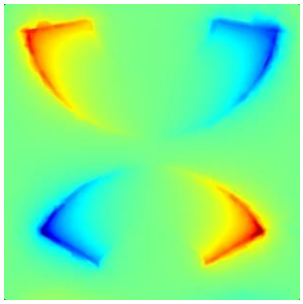

Fig. 4 The Electric field (E_z) distribution at the Fano resonance (anti-peak of transmission spectrum), calculated in x-y plane, 5 nm above the top surface of the arcs.

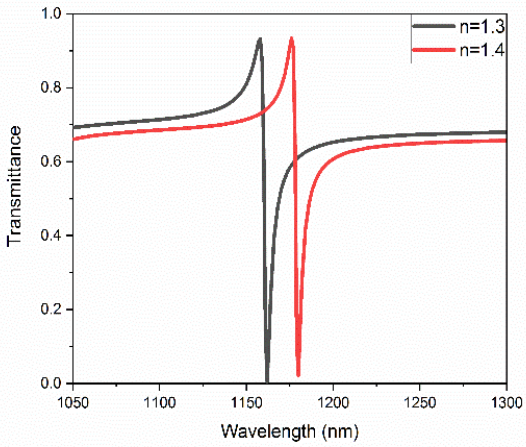

Fig. 5 Transmittance curve of all dielectric metasurface when the refractive index (n) of the dielectric environment is 1.3 (black) and 1.4 (red).

Acknowledgements The authors are gratefully acknowledged the financial support from Department of Science and Technology, India for funding GAP 0344 "*All Dielectric, plasmonic and hybrid photonic nanostructure*" project. Authors are also thankful to CSIR-CSIO, Chandigarh for providing research facilities.

References

1. T. Ao, X. Xu, Y. Gu, Y. Jiang, X. Li, Y. Lian, F. Wang, Opt. Commun. 414, 160-165 (2018).
2. S. Jahani, Z. Jacob, Nat. Nanotechnol. 11, 23-36 (2016).
3. Y. Lee, S. Kim, H. Park, B. Lee, Sensors. 17, 1726 (2017).
4. G. Liu, X. Zhai, L. Qi Lin, S. Xia, X. Luo, C. Zhao, Plasmonics. 13, 15-19 (2016).
5. J. Zhang, W. Liu, Z. Zhu, X. Yuan, S. Qin, Opt. Express 22, 30889-30898 (2014)

OSI-ISO 2018 manuscript No.
(89)

Design of a near-infrared astronomical photometer optimized for use at low altitude astronomical sites

Anwesh Kumar Mishra · U. S. Kamath

Abstract Due to the presence of high water vapour concentration, low altitude astronomical sites are generally considered as sub-optimal for near infrared astronomical observations. However with the availability of newer type of detectors as well as filter sets, it might be possible to fully utilize such sites in this wavelength range. In regards to this we discuss of possible optical designs for a single pixel photometer to be used on the 1 meter Carl Zeiss telescope at the VBO(Vainu Bappu Observatory), Kavalur. We present simulations on the variability of sky transmission for this site as well as estimation of SNR (signal to noise ratio) for the designed instrument.

Keywords Astronomical photometry · Near infrared · Optical design · Optical filters

1 The problem of variable atmospheric transmission:

In the near infrared wavelength range, Earth's atmosphere is characterized by certain windows of good transmission followed by regions of very low transmission. The major culprit for absorption in these wavelengths are rotational and vibrational transitions in molecules such as CO_2 and H_2O. Hence atmospheric transmission is a strong function of the concentration of these molecules.In particular water vapour concentration can change in very short timescales. Variability of water vapour causes a variable extinction of the sky throughout the night. This issue is more prominent at low altitude astronomical sites where there is an inherently large concentration of water vapour. We compare the results of such variability in figure(1) between a high altitude site(Hanle) and a low altitude site(Kavalur). It can be seen that there is a significant amount of variability present within the traditional-extended Johnson- Y(1.02 microns), J(1.22 microns) and H(1.63 microns) photometric filters.

2 Design goals for a photometer suitable for low altitude sites

In order to avoid the issue of variable transmission it is essential that both the target star as well as the standard star are observed within a small time scale- possibly of the order of a few minutes. In order to achieve high signal to noise ratio within a small integration time,the photometer should consist of high throughput optics as well as a detector with small NEP(Noise Equivalent Power). The responsive spectral range of the instrument needs to be such that at least three photometric bands are covered while blocking out the high intensity thermal radiation present in longer(greater than 3.5 microns) wavelengths. The field of view of the instrument needs to be slightly bigger than the seeing limited stellar disk so as to reject additional sky background.Following this argument, we have fixed a field of view of 8 arc-seconds for the instrument.

Anwesh Kumar Mishra
IIA Bangalore,
E-mail: anwesh@iiap.res.in
Ph. 8895439668

U. S. Kamath
IIA Bangalore,
E-mail: uskamath@iiap.res.in

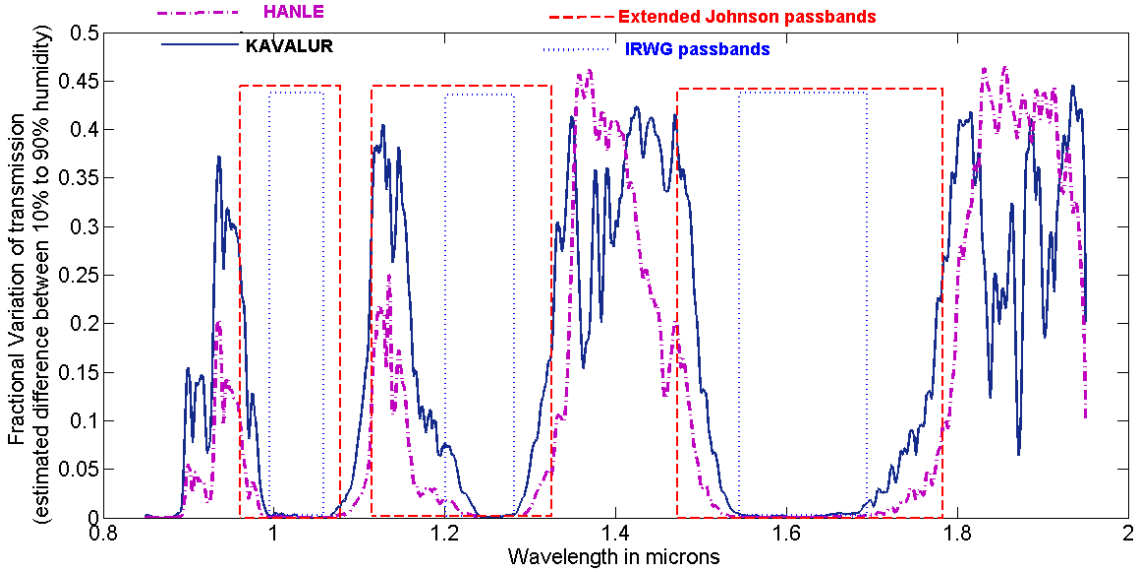

Fig. 1 A plot of variability of sky transmission in the near infrared. We have used site parameters such as latitude,altitude and a global model of atmosphere using the software ATRAN to calculate atmospheric transmission as a function of wavelength.For both the sites of Kavalur and Hanle,transmission at 10 % and 90% water vapour concentration is calculated. The difference of transmission for low and high water vapour content is given in this figure. As seen from the figure, the IRWG(Infrared working Group)[1] recommended filters block out most of the highly affected regions.

Table 1 List of optical designs and estimated SNR, The SNR is calculated for a 1 second integration period

Sl. No.	Design type	No. lens elements	Expected throughput	J_{SNR} (6th magnitude star)	iJ_{SNR}[IRWG] (6th magnitude star)
1	Focal reducer	1 (CaF2)	38 %	35	15
2	Collimator-Camera	2 (Caf2)	34 %	31	13
3	Collimator-Camera	4 (BK7 and Fs9)	28 %	26	11
4	Collimator-Camera	4 (Off the shelf achromatic doublet)	25 %	23	10

Detector selection: Among various available detector materials in the near infrared we have shortlisted InGaAs type detectors for our purpose. These detectors typically have spectral response from 0.9 to 1.85 microns. This satisfies the requirement as stated in section 2. We have chosen the model G12181-203k from Hamamatsu as the specific detector for our purpose. This is a single pixel detector having a low NEP of $9 \times 10^{-15}(W/Hz^{1/2})$ and a small size of 0.3 mm (diameter). Additionally this particular detector operates using a two-stage thermo-electric cooler which eliminates the need of liquid nitrogen cooling.

3 Summary of various optical designs

Since the instrument is meant to be single pixel based,the focus of our optical design is to minimize on axis chromatic and spherical aberrations. A summary of the possible optical designs is presented in table (1). We also estimate the expected SNR of these various designs and list them out.All designs manage a SNR of better than 10 even in the narrower IRWG bandpass filters,with an integration of one second only. The design using off the shelf achromats is chosen as the final design for the best compromise between complexity and performance.

References

1. Milone, E.F. and Young,A.t. Infrared Passbands for Precise Photometry of variable stars by Amateur and professional astronomers , JAAVSO , Volume 36, (2008)
2. Milone, E.F. and Young,A.t. Infrared Passbands for accurate IR photometry: the IRWG set, Bulletin of the American Astronomical society,Volume 34, p.1316 (2002)

OSI-ISO 2018 manuscript No.
(90)

Plasmonic quasicrystals

Shilpa Samdani · Aman Agrawal · Vijay Mocherla · Amogh Naik · Ajith Ravishankar · Venu Gopal Achanta

Abstract Plasmonic Quasicrystals (PlQC) have a broadband plasmonic response. In this work we have studied the origin and dependence from the broadband response of the PlQC. For this purpose we fabricated the PlQC by varying the hole sizes, period of the base lattice and thickness of the plasmonic metal. We see that the enhancement in normalized transmission is dependent on the hole size.

Keywords Plasmonic Quasicrystals · Broadband Plasmonics · Collective response of hole array · Surface Plasmon Polaritons

Plasmonics is a sub-field of nanophotonics that studies interaction of free electrons in metals with electromagnetic field. The hybrid light-matter states formed as a result are called Surface Plasmon Polaritons (SPPs). However, SPP generation at metal-dielectric interface requires momentum matching of the incident EM radiation and the surface plasmons which can be achieved through sub-wavelength gratings. By solving Maxwells equations at the metal-dielectric interface it is known that only TM polarized incident light can excite surface plasmons at metal-dielectric interface.
Plasmonic Quasicrystals (PlQC) are subwavelength air-hole structures in a metal film that support SPPs regardless of the incident EM field polarization and launch angle over broadband. PlQCs have long-range ordering and rotational symmetry but no translational symmetry [1].

Shilpa Samdani
Tata Institute of Fundamental Research, Mumbai
E-mail: shilpahsamdani@gmail.com@gmail.com

Aman Agrawal · Vijay Mocherla · Amogh Naik · Venu Gopal Achanta
Tata Institute of Fundamental Research, Mumbai

Ajith Ravishankar
KTH Royal Institute of Technology, Sweden

Following is the SEM image of PlQC pattern with 600nm base lattice and five-fold rotational symmetry fabricated in 100nm thick Gold film.

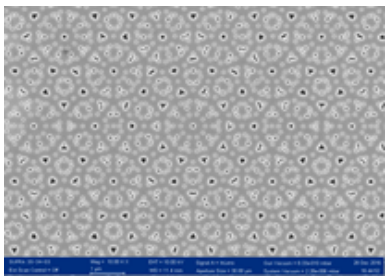

Fig. 1 SEM image of PlQC with 600nm base lattice and five-fold rotational symmetry.

Upon changing period of base lattice to 1000nm the plasmonic response is red-shifted. The hole diameter also affects the nature of the spectrum due to the collective response of the hole array. We have also studied the effect of metal film thickness on the response of the PlQC. The patterns were fabricated on Gold sputtered metal films using e-beam lithography and Reactive Ion Etching.

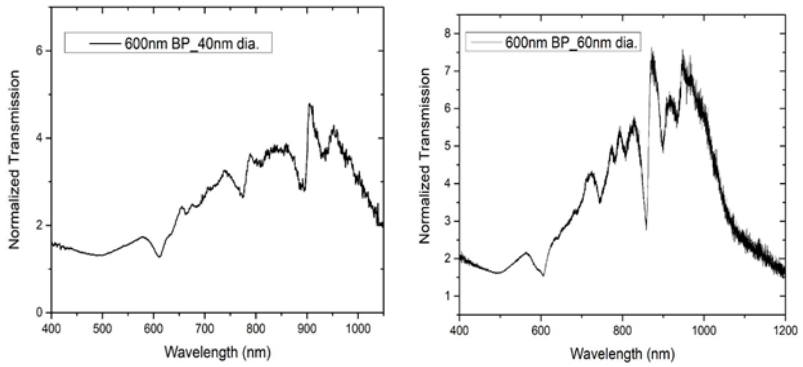

Fig. 2 600nm Base period Quasiperiodic pattern with 40nm hole diameter and 60nm hole diameter in 100nm Au film. (Plotted using OriginPro 2015)

As can be expected we observe higher transmission enhancement for larger hole diameters in the PlQC.

References

1. Kasture, S., Ravishankar, A. P., Yallapragada, V. J., Patil, R., Valappil, N. V., Mulay, G., Achanta, V. G. (2014). Plasmonic quasicrystals with broadband transmission enhance-ment. Scientific reports,4,5257 .

Control transfer of optical energy in the Ince-Gaussian higher order modes

Brijesh Kumar Singh
Department of Physics, School of Physical Sciences, Central University of Rajasthan, Ajmer-305817, India
brijeshsingh@curaj.ac.in

Abstract

Ince-Gaussian optical beams are known to be the third complete family of exact and orthogonal solutions of the paraxial wave equation. Their elliptically symmetrical transverse intensity profiles are described by the Ince polynomials. The higher order modes constitute of different lobes varies from each other in terms of size and optical energy distribution. Here, we present a generic method to transfer the optical energy from the lobes having maximum optical energy to the lobes having minimum or lesser optical energy of the higher order Ince-Gaussian beam, in a control manner. The proposed method also equalizes the maximum optical energy in each lobes present in the particular higher order modes of the beams. Such transformation of optical energy among the lobes of the Ince-Gaussian beams makes them available simultaneously for equal participation in most of the applications like particle manipulation, optical lithography and propagation through turbulent media.

Keywords

Ince-Gaussian beam, elliptical beams, laser modes, beam shaping, structured beams, optical energy

Introduction

Recently, much attention has been paid to explore the characteristics of the Ince-Gaussian (IG) beams. The exact solutions of the free-space paraxial wave equation in Cartesian and circular cylindrical coordinates systems are the Hermite-Gaussian (HG), and Laguerre-Gaussian (LG) beams, respectively. Similarly, Ince-Gaussian beams constitute the third complete family of exact and orthogonal solutions of the paraxial wave equation in the elliptic cylindrical coordinate system[1]. Mathematically, it is described by Ince polynomials which form the transverse field distribution with elliptical symmetry. By changing the value of the ellipticity parameter of IG beams such as for zero and infinity values, it can be transformed into HG and LG beams, respectively. Therefore, HG and LG beams are correspond to the special limiting cases of the IG beams. Like the HG and LG beams, IG beams also show the shape invariant feature and its width is periodic function of the propagation distance. The higher orders modes of IG beams consist of numbers of lobes having different shape and size with unequal optical energy distribution given by following expressions[1]

$$IG^{e}_{p,m,\varepsilon}\left(r\right)=AC^{m}_{p}\left(i\xi,\varepsilon\right)C^{m}_{p}\left(\eta,\varepsilon\right)\exp\left(-r^{2}/{w_o}^{2}\right),\quad IG^{o}_{p,m,\varepsilon}\left(r\right)=BS^{m}_{p}\left(i\xi,\varepsilon\right)S^{m}_{p}\left(\eta,\varepsilon\right)\exp\left(-r^{2}/{w_o}^{2}\right), \tag{1}$$

where, the super indices ***e*** and ***o*** refer to even and odd IG beams, respectively, and *A* and *B* are normalization constants. Equation (1) is valid for the waist plane at $z=0$, where the transverse field distributions are described by the even and odd Ince polynomials, C^{m}_{p} and S^{m}_{p}, respectively, of order *p* and degree *m*, while ξ and η are radial and angular elliptic coordinates given by $x=w_o\left(\varepsilon/2\right)^{1/2}\cosh\xi\cos\eta$, $y=w_o\left(\varepsilon/2\right)^{1/2}\sinh\xi\sin\eta$. w_o and ε are the beam waist and elliptic parameters of the Ince polynomials. As we can see from the above expressions, three main parameters order *p*, degree *m*, and ellipticity ε shape the transverse intensity profiles of IG beams. Since, all the lobes of higher order IG beams are not equally intense; they cannot be utilized simultaneously with equal efficiency in applications. Therefore, here, we present a systemic method to equalize the optical energy of each lobe as well as control transfer of optical energy from high energy lobes to the low energy lobes in the different modes of Ince-Gaussian beams by using an appropriate mask.

Methods

The computer generated hologram we used is an annular phase mask consists of two regions with opposite phase and is given by following expression [2-5]

$$\Psi\left(r\right)\propto\begin{cases}-1 & r\le r_{\pi}\\ 1 & r_{\pi}\le r\le r_{\max}\end{cases} \tag{2},$$

where, $0<r_{\pi}<r_{\max}$, and $r_{\max}=d/2$, *d* is the diameter of the mask aperture at the pupil plane and *r* is the radial co-ordinate. When the binary phase mask given by Eq. (2) is illuminated with the input plane wave, output beam generated at the focal plane of the lens is the Fourier transform FT$\left\{\Psi\left(r\right)\right\}$ of the mask. By changing the value of r_{π} optical energy is transferred from one lobe to other lobes in a control manner of higher order IG beams. The phase mask

corresponds to the even Ince Gaussian beam from Eq. 1 is modulated by the proposed phase mask produced from Eq. (2) at the pupil plane of the Fourier transforming lens. By taking the Fourier transform of the modulated resultant phase mask at the pupil plane, we observed the modulation in the intensity profiles of the IG beams at the Fourier plane.

Results and discussion

The phase map and corresponding transverse intensity distribution of the even IG_{22} mode are shown in the first column of Fig.1 (a & g, respectively). The optical energy is not uniformly distributed in the horizontally oriented lobes of the mode as it is consist of two high energy side lobes with one low energy lobe at the centre. At the pupil plane of the lens, phase map 1(a) is modulated by the phase mask of Eq.(2). The modulated phase maps for $r_\pi = 0.3$ & 0.52 are shown in the first row of Fig.1 (b & c, respectively). Corresponding to these phase maps, the transverse intensity profiles are generated at the Fourier plane of the lens as shown in the second row of Fig.1 (h & i, respectively). We observed that when we continuously increases the r_π value optical energy are constantly transferred from two side lobes to the central lobe and for $r_\pi = 0.3$ all the three lobes of IG_{22} modes become equally intense (Fig.1h). Further, for $r_\pi = 0.52$, central lobe is more intense in comparison to that of the two side lobes (Fig.1i) i.e. the optical energy distribution in this intensity profile is reversed to the original intensity distribution of IG_{22} mode (Fig.1g). At this value of r_π additional low intensity side lobes are also appeared. All the intensity profiles are normalized from 0 (black) to 1(white) and phase maps vary from 0 (black) to π (white). Similarly, we applied the mask to modulate the even IG_{20} mode, consists of three vertically oriented lobes where central lobe is more intense than the two side lobes. Optical energy distributions in all the three lobes of IG_{20} are opposite to that of the IG_{22} mode with different orientations. The phase map and corresponding transverse intensity distribution of the even IG_{20} mode are shown in the fourth column of Fig.1 (d & j, respectively). It is observed that for $r_\pi = 0.12$ the optical energy is transferred from central lobe to the outer side lobes which make the entire three lobes equally intense (Fig.1k). For $r_\pi = 0.01$, the two outer side lobes become more intense in comparison to that of the central lobe as shown in Fig. 1(l).

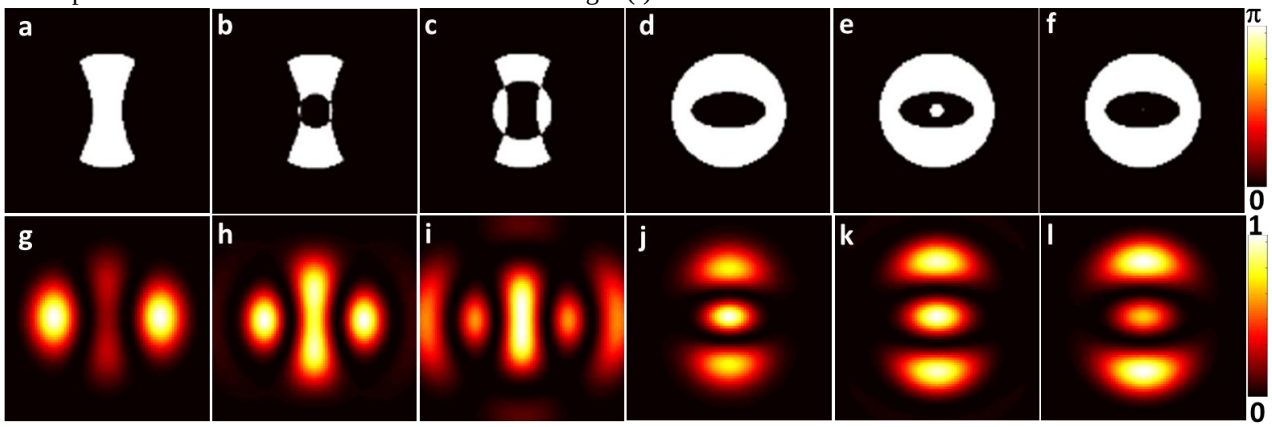

Fig.1 First row corresponds to the phase maps of even Ince Gaussian beam; IG_{22} mode (a-c) and IG_{20} mode (d-f); (a, d) normal phase maps, while (b, c, e, f) with mask for $r_\pi = 0.3, 0.52, 0.12, 0.01$, respectively. Transverse intensity profiles in second row (g-l) are corresponded to the Fourier transform of the phase maps (a-f), respectively.

Conclusions

In conclusion, here, we present a systematic method to modulate the optical energy distribution among the different lobes of the higher order Ince-Gaussian beams. Using this method, the optical energy is being transferred from high intense lobes to the low intense lobes in a control manner. In this process, all the lobes become equally intense as well as low intense lobes are converted into the high intense lobes. This control modulation of optical energy makes all the lobes simultaneously available with equal efficiency for many applications especially for particle manipulation. Also, the different lobes can be converted into more intense or less intense based on the desired applications.

Acknowledgments

Author thankfully acknowledges the financial support from UGC start up grant, India.

References

1. M. A. Bandres, J. C. Gutierrez-Vega, Opt. Lett. 29, 144 (2004).
2. M. P. Cagigal, J. E. Oti, V. F. Canales, P. J. Valle, Opt. Comm. 241, 249 2004).
3. B. K. Singh, R. Remez. Y. Tsur, A. Arie, Opt. Lett. 40, 4703 (2015).
4. B. K. Singh, H. Nagar, Y. Roichman, A. Arie, Light Sci. Appl. 6, e17050 (2017).
5. Y. Eliezer, B. K. Singh, L. Hareli, A. Bahbad, A. Arie, Opt. Express, 26, 4933 (2018).

Measurement of Precise Bending Angle with Optical Fiber Goniometer

Arpit Rawankar, Vinaya Redkar*
Department of Electronics & Telecommunication Engineering, University of Mumbai, Mumbai, India

*vinayaredkar@gmail.com

Abstract: Fiber bending attracts various applications of optical sensing, even though optical signal gets attenuated while undergoing external bending. The fiber bending losses depends on bend radii, bending angles, wrapping turns and wavelength of light. The attenuation due to macro bending occurs in optical fiber when radius of bend is very large as compare to fiber core radius. Goniometers are widely used in industries for measurement of contact angle, bend angle and surface tension. The proposed research is implemented on the concept of using fiber optic sensor to measure bending angles between two planes of contact. A single mode fiber coupled laser source with wavelength 850 nm is used for this setup. The three paddle fiber polarizer is used to control the polarization of beam which occurs during various bends. The measurement of loss of optical power is investigated for different bend angles and bend radii. The precise measurement of bending angle is completed by fitting the bending attenuation data with fiber bend parameters.

Keywords: *Goniometer, Bending Angle, Paddle fiber polarizer, Bending loss.*

System Setup: The principle of proposed concept is to measure output power and bending loss with respect to different angles this carried out using an optical fiber goniometer. Optical fiber goniometer that make use of intensity modulation of a laser beam propagating in single mode optical fiber [1]. Fiber polarizer controller is used to maintain the polarization status of fiber which is changed by rotation or bend of fiber.

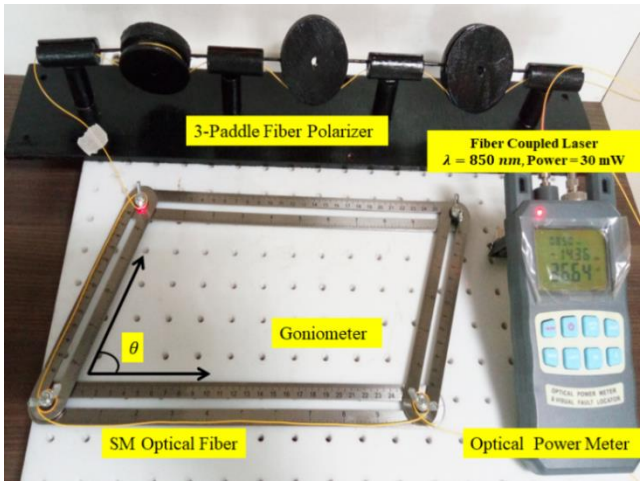

Fig1 Optical fiber goniometer system setup

Fiber polarization controller consists of three endlessly rotatable wave plates, including two quarter-wave plates and one half-wave plate. The polarization paddle was coupled with single mode fiber (core size 5μm) using a 1-1-1 loop configuration. Typically initial power measured 30 mW at no bending of fiber. Various bending angle configuration is achieved by varying arc of fiber bends and fiber radii. When fiber is bend at any arbitrary angle, the complete bending arc of fiber exhibits optical loss mechanism. The output was monitored using a power meter and corresponding power was obtained for each bending angle. The bending attenuation due to wavelength is neglected in this experiment as laser source of fixed wavelength (850 nm) is used for measurement of all bending losses. The output power P_0 exponentially increases with angle of bend [2] and is given as

$$P_0 = A * Exp(B\theta) \quad (1)$$

The attenuation (L_φ) is measured as function of bending angle (θ)

$$L_\varphi = A_\varphi + B_\varphi \theta + C_\varphi \theta^2 \quad (2)$$

Where, A_φ, B_φ & C_φ are fitting parameters dependent on bending angle

The fiber bending attenuation (L_R) with respect to bending radii is given as

$$L_R = A_R \, Exp\,(-B_R R) \quad (3)$$

where A_R and B_R are radius dependent fitting parameters. The total bending attenuation is calculated as [3]

$$L_{total} = L_\varphi + L_R \quad (4)$$

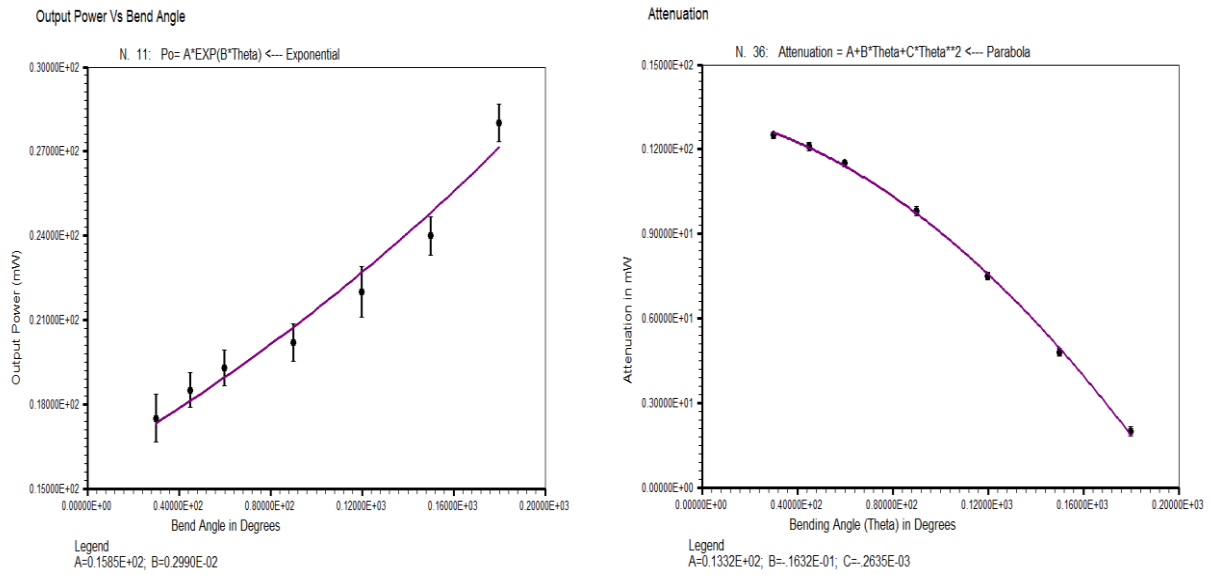

Fig2(a) **Fig2(b)**

Fig2 Measurement of output power Fig2(a) and Power loss Fig2(b) with various bending angles

Analysis: As it is shown in Fig2(a) and Fig2(b), the bending angle variation with output power and overall attenuation is observed. The large bending angles with small radius of bend exhibit low attenuation, while the small bending angles with large bend radius exhibit high attenuation. The angle measurement for each fiber bend is demonstrated with precision accuracy of $\pm 1°$.

References

1. Honglei Guo et.al, Sensors 2011, 11, 3687-3705.
2. Seon Geun Kim, Optical Review Vol. 21, No. 5 (2014) 694–697.
3. Jingxian Cui, Optics Express 18197,Vol. 25, No. 15, 24 Jul 2017.

OSI-ISO 2018 manuscript No.
(93)

Tailoring polarization singularity lattices by phase engineering of three beam interference

Saba N. Khan, Sushanta K. Pal, and P. Senthilkumaran

Abstract Structured optical lattices obtained from interference of three radially polarized waves arranged in umbrella geometry possesses interlaced polarization singularity structures. These lattices are known to be populated with both positive and negative index C- and V-point singularities as a consequence of index conservation. In this article, we focused on tailoring these polarization lattices by perturbing the interfering beams with a relative encoded phase. We have shown that a spatial lateral-shifting of the ellipse- and vector fields by an *order of lattice parameter* can be achieved through an appropriate phase engineered design.
Keywords Singular optics; Interference; Polarization; Optical lattice.

1. Introduction

Our group has recently demonstrated that the superposition of three non-coplanar, axially symmetric, radially polarized beams can generate novel optical lattice structures embedded with interlaced C-point and V-point polarization singularities [1]. A next step ahead would be to look for tailoring these embedded polarization singularities. Motivated with this fact, in this article, the idea is to use appropriately designed set of relative-phase encoded radially-polarized waves whose interference attains the targeted tailorability.

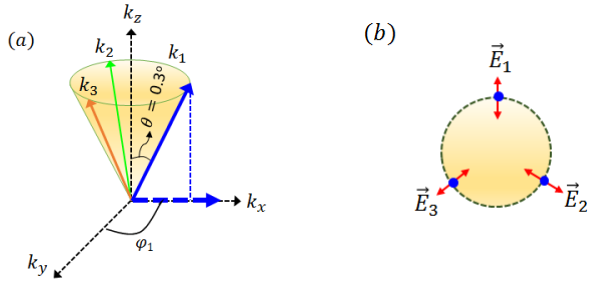

Fig. 1. (*a*) Schematic of the three radially wave beams arranged in an umbrella geometry. (*b*) Transverse plane projection of k_m onto a circle is shown by blue dots for *three* radially polarized waves. Red arrows show plane of polarization of individual beam.

2. Generation of polarization singularity lattices

We consider the superposition of three radially polarized plane waves arranged in an umbrella geometry as shown in Fig. 1. The wave vectors corresponding to these interfering beams can be expressed as [2] ,

$$k_m = k_0\{\sin\theta_m \,.\cos\varphi_m\,, \cos\theta_m \,.\cos\varphi_m\,, \cos\varphi_m\} \qquad (1)$$

where, m {= 1, 2, 3} is the designation given to the respective beam, θ_m is the angle subtended by the axially symmetric wave vectors to the central z-axis, φ_m is the angle between the projection of a wave vector on the transverse plane ($k_x k_y$) and the k_x axis. In our case, θ_m is fixed to 0.3° to abide by paraxial approximation and the φ_m's are chosen to be π/2, 7π/6, and 11π/6 respectively for the three interfering beams. Subsequently, the electric field of the m^{th} wave in the transverse plane can be expressed as,

$$\vec{E}_m = \left(E_{mx}\hat{x} + E_{my}\hat{y}\right).exp^{i(\vec{k}_m.\vec{r}+\emptyset_m)} \qquad (2)$$

where, $\emptyset_m$ is the initial phase offset imparted to the respective beams. The polarization distribution of the superposed fields can be completely described by the generalized Stokes

Saba N. Khan
Department of Physics, Indian Institute of Technology Delhi, Hauz Khas, New Delhi-110016, India.
E-mail: saba04star@gmail.com

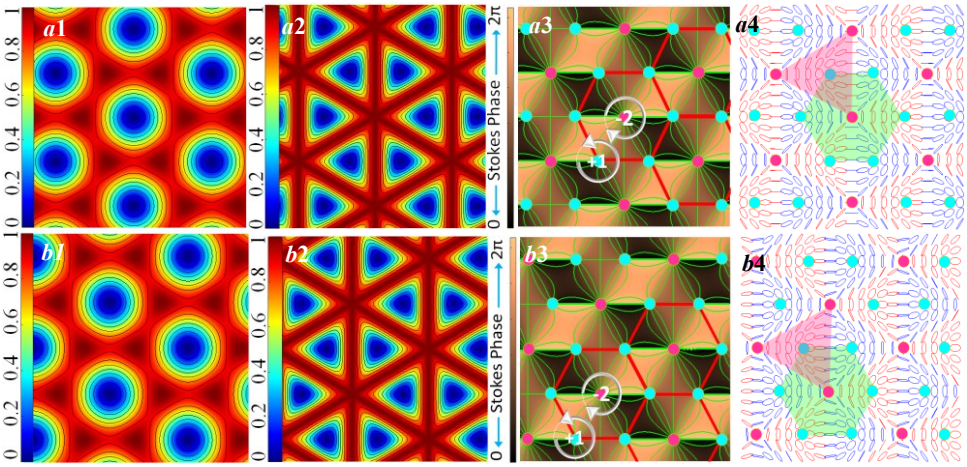

Fig. 2. Simulated three beam interference (a1-a4) without phase engineering (b1-b4) with phase engineering: (a1, b1) transverse intensity distribution of the resultant field; (a2, b2) Stokes intensity (S_{12}); (a3, b3) phase variation of the Stokes field; (a4, b4) polarization distribution.

parameters $\{S_0, S_1, S_2, S_3\}$ whose mathematical description in terms of constituent fields is readily available in several books and literature [3]. For a completely polarized light, C-points are circular polarization points at which $S_3 = \pm 1$ and $S_1 = S_2 = 0$. Similarly, in terms of Stokes parameter, V-points are the intensity nulls where each of the Stokes parameter vanishes. An effective way to probe such polarization singularities embedded in the ellipse fields and vector fields is through complex Stokes field (S_{12}) constructed from the Stokes parameters ($S_{12} = S_1 + iS_2$); since, here the polarization singularities appear as phase singularities. In Fig.2 (a1-a4), we show the simulated transverse intensity distribution of the superposed beams, Stokes field intensity, corresponding Stokes phase variations and the polarization distributions for the case when there is no relative phase imparted to the interfering beams ($i.e.\ \emptyset_m = 0$). The phase variation of S_{12} infers that the vortices with topological charge +1 represents the C-point (lemon) and with -2 depicts V-points (disclinations). The flower patterned phase contour lines plotted over the phase-maps further depicts nodes with three and six petals as C- and V-points respectively. The phase contour lines in this case are the azimuth lines (a-line) of the polarization distribution.

3. Phase engineered polarization singularity lattices: *tailorability*

It is perceived from the simulation that a lateral shifting of the polarization singularities can be achieved by encoding each of the radially polarized beam with an appropriate initial phase offset. In our case, a relative phase of $\emptyset_m = 2\pi m/3$ among the superposing beams yielded a spatial shifting of the embedded polarization singularities by an *order of lattice parameter* as depicted in Fig.2 (b1-b4). The presence of this initial perturbation is well controlled and can be realized experimentally by impinging an accurately designed phase mask to the spatial light modulator of the experimental configuration reported in [1]. The *experiments to demonstrate this are underway and the detailed computational analysis and experimental investigation* will be presented in the conference.

4. Conclusion

We propose a technique for generating and tailoring interlaced polarization singularities lattices (combination of lemon and disclinations) in the three beam interference by a phase engineered superposition of three radially polarized plane beams. The spatially shifted polarization lattices are realized by perturbing the participating beams with a relative phase-encoded. By an appropriate tuning of the input polarization state of the interfering beams, one can obtain the other degenerate set of C-point (star) and V-point (+) singularities.

References

[1] S. K. Pal, Ruchi, and P. Senthilkumaran, "C-point and V-point singularity lattice formation and index sign conversion methods," *Optics Communications* 393, 156–168, 2017.

[2] Robert W. Schoonover, "Creating polarization singularities with an N-pinhole interferometer," *Physical Review* A 79, 043809: 1-7, 2009.

[3] D. H. Goldstein, "*Polarized Light*," CRC Press, 2011.

OSI-ISO 2018 manuscript No.
(94)

C Points Ring from Orthogonally Polarized Vortex Beams

Gauri Arora, Sushanta Kumar Pal and P. Senthilkumaran

Received: date / Accepted: date

Abstract Polarization singularities are points in an inhomogeneously polarized beam where some of the parameters that define state of polarization of light become undefined. Polarization singularities can be described as superposition of right circularly polarized (RCP) and left circularly polarized (LCP) scalar vortices. We present a method to produce C point polarization singularities in a symmetric ring by using superposition of orthogonally linearly polarized vortex beams of topological charges l_1 and l_2 where $l_1 \neq l_2$. It is found that number of C points in a ring depend upon the difference $(l_1 - l_2)$ and it is independent of the absolute value of l_1 and l_2. Varying topological charges in orthogonally polarized beam will lead to net change in OAM content of the beam which give rise to change in number of C points. C point being more stable against small perturbation might open new ideas to use this beam in application related to particle trapping, optical communication and many more**.**

Keywords Singular optics, Interference, Polarization, C points

1. Introduction: Light beams with inhomogeneous polarization distribution have tremendous growing applications in the field of photonics, microscopy, quantum science etc. These inhomogeneously polarized beams may contain polarization singularities which are divided into two broad categories: ellipse field singularities and vector field singularities. C points and V points are polarization singularities in ellipse field and vector field respectively. At V point, the polarization direction of electric field of the beam is indeterminate whereas C points are points of circular polarization in inhomogeneously polarized ellipse field where orientation of polarization ellipse is undefined [1]. Lattice of C points and V points can be generated experimentally using multiple beam interference [2]. C points can be described as superposition of homogenously polarized vortex (Right circularly polarized) and non-vortex beam (Left circularly polarized). In this article, we introduce a method to generate C point polarization singularities in a symmetric ring by using interference of orthogonally (linearly) polarized vortex beams of topological charges l_1 and l_2 where $l_1 \neq l_2$. It is found that number of C points in a ring is equal to $2(l_1 - l_2)$ and hence depends on the net content of OAM (orbital angular momentum) in resultant beam. Reversing l_1 and l_2 will give rise to both sign inversion and handedness change for each C point in the ring. Results shown in this article can be realized experimentally using simple interferometric set up. This structured beam of polarization singularities may find application in optics communication due to its robust nature in atmospheric turbulence medium [3].

2. Mathematical description: Components of orthogonally polarized vortex beam in linear basis can be written as:

$$E_x = r^{l_1} \exp(il_1\phi)\,\hat{x} \qquad E_y = r^{l_2} \exp(il_2\phi)\hat{y}$$

Where E_x is horizontally polarized vortex beam of topological charge l_1 and E_y is vertically polarized vortex beam of topological charge l_2. Due to spatially varying amplitude and phase distribution of interfering beams, the resultant beam will have spatially varying polarization distribution

Gauri Arora
Department of Physics, Indian Institute of Technology Delhi, Hauz Khas, New Delhi-110016
E-mail: gauriarora02@gmail.com

3. Simulation Results and Discussion: Simulation results for interference of linearly polarized OAM beams with different topological charges are shown in Fig1 and Fig2. Fig1 shows the stokes phase (a-d) and corresponding stokes intensity (e-f) for resultant beam with topological charge difference 1,2,3,4 respectively. In each case topological charge of C points alternate in sign along the ring and hence net C point index of the resultant beam is zero but net orbital angular momentum carried by the beam is non zero due to the non-zero value of $(l_1 - l_2)$. Phase distribution for $l_1 = 1$and $l_2 = 5$ are shown in fig. 2(a) and (b) respectively. Polarization distribution corresponding to the resultant field is shown in Fig2(c). It can be easily seen from Fig2(d-f) that on reversing value of l_1 and l_2, both sign and handedness of C point polarization singularity changes in the ring. It can be easily observed from fig2(c and f) polarization distribution that number of stars and lemons are same and their handedness also varies alternatively in a ring. Blue and red color in fig2 correspond to regions of left and right handed beam and black color corresponds to linear polarization state. Green dots in polarization pattern show the position of C points in the ring. Detailed explanation of the idea and mathematical description would be presented in the conference.

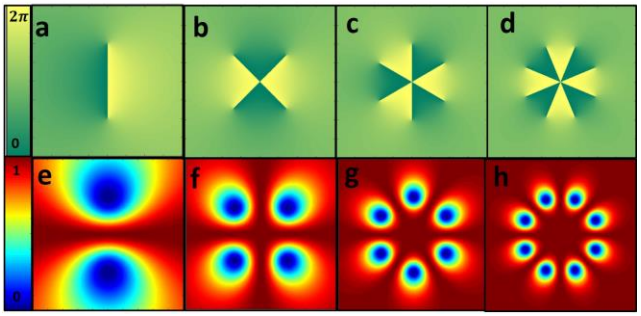

Fig. 1: Stokes Phase (a-d) and Stokes intensity (e-h) for resultant field obtained using interference of orthogonally(linearly) polarized OAM beams with $\boldsymbol{l_1 = 2, 3, 4, 5}$ and $\boldsymbol{l_2 = 1}$ respectively

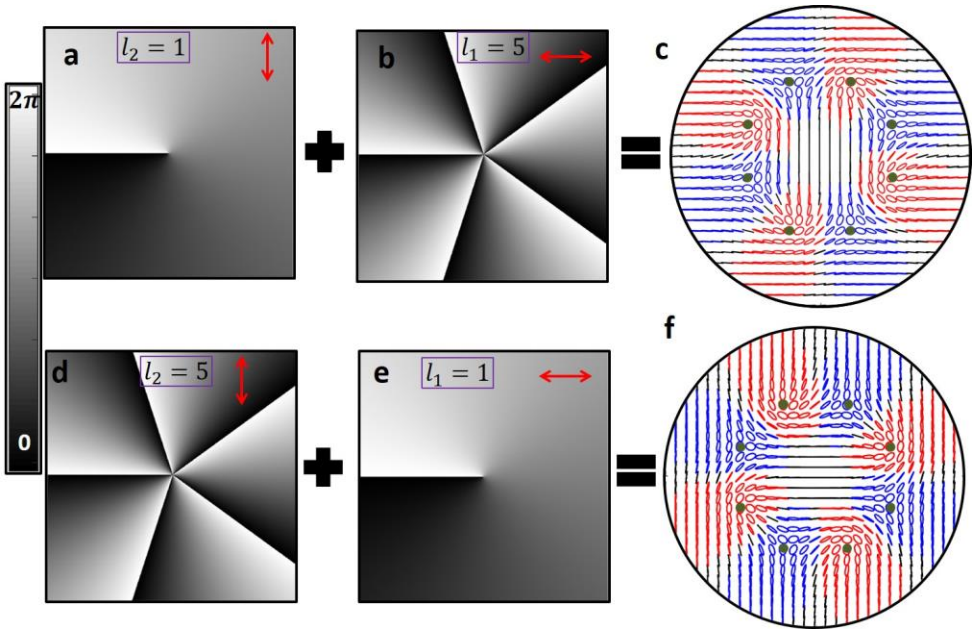

Fig. 2: Optical phase of interfering vortex beams and the resultant polarization pattern consisting of C points in a ring

4. References

[1] I. Freund., "Polarization singularity indices in Gaussian laser beams, Opt. Commun.", 201,251-270(2002)

[2] Sushant a Kumar Pal and P. Senthilkumaran, "Cultivation of Lemon Fields" ,Opt. Express, 24,28008-28013,(2016)

[3] Priyanka Lochab, P. Senthilkumaran, and Kedar Khare,"Robust laser beam engineering using polarization and angular momentum diversity.", Opt.Express, 25, 17524-17529, (2017)

OSI-ISO 2018 manuscript No.
(95)

Optical Design of a Binocular Eyepiece for HD OLED

S S Dhoni, Manish Uniyal, Ranabir Mandal, P K Sharma

Abstract

For comfortable viewing of an opto-electronic sight, it is better to view through a binocular eyepiece than a monocular eyepiece. In binocular eyepiece a single micro-display is used as input to the eyepiece and the scene is projected to both the eyepieces by splitting the input light. In this paper the design of such an eyepiece is discussed. The input is 1280X1024 format, 12μm pitch OLED. Optical design addresses the dioptric adjustment of ± 4D and Intra Pupil Distance from 55 to 75 mm.

Keywords: eyepiece, optics for micro-display, magnifier design, optical design

Introduction:

An eyepiece is used to view the real image formed by the objective of an optical system. In modern imaging systems, sensors like CCD, CMOS or infrared focal plane array are used to capture the image formed by objective lens. The final image is generally displayed through a bigger sized LCD display. For many handheld applications, it is convenient to view the image through eyepiece like a telescopic system. For that a very small display, known as micro display is used. A magnifier with suitable magnification factor is used to view the micro display. Binocular display increases the comfort of the viewer as both eyes can be used to view the image. This calls for two separate micro-display devices with their own magnifiers coupled to both eyes and this requires a high degree of alignment between the two micro-displays, which should be retained for a long time. The other solution is a binocular eyepiece where the micro-display image is collimated and then split into two channels and projected on both the eyes, to view through the respective eyepiece module. In this paper design and analysis of a binocular eyepiece with magnification 11X for viewing a micro display is discussed.

Layout:

The designed binocular optics contains three modules. The first module collimates the micro-display image followed by a splitter (two mirrors having 90° angle between them), then image forming module and last one is eyepiece module. By varying the distance between splitting mirror and image forming module, the Intra Pupil Distance (IPD) can be varied from 55mm to 75 mm.

S S Dhoni
E-mail: ssdhoni@irde.drdo.in

Instruments Research and Development Establishment,
Raipur Road, Dehradun-248008

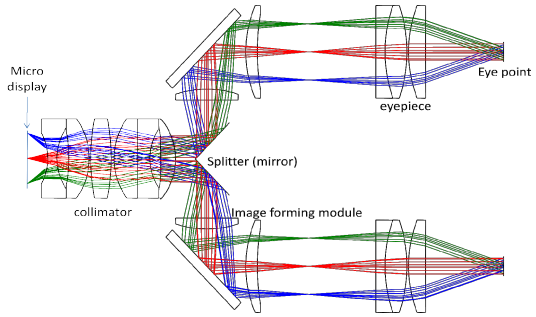

Fig 1 Layout of binocular eyepiece

The three modules are designed separately, then combined together and optimised to ensure the performance with pupil matching of the three modules.

Acknowledgement:
Authors gratefully acknowledge the encouragement from Shri Amitava Ghosh, Group Director, Optical Engineering group and Director, IRDE for permission to publish this work.

References:

[1] Daniel Malacara, Zacarias Malacara "Hand Book Of Optical Design (2nd Edition)", *Marcel Dekker, Inc.* New *York* (2004).
[2] Robbert E. Shannon, "The Art and Science of Optical Design" Cambrige University Press, USA (1997).
[3] W.J. Smith, "Modern optical engineering" SPIE publication 2010.
[4] Robert E. Ficher, BiljanaTadic-Galeb, Paul R. Yoder, "Optical System Design", SPIE publication.

Optical Interferometry Technique for Measurement of Heart Rate Variability

*Jyoti Gondane, M.S. Panse, Arpit Rawankar

Department of Electrical Engineering, Veermata Jeejabai Technological Institute (VJTI), Mumbai, India

* jagondane@el.vjti.ac.in

Abstract: The advantages of optical measurement methods in biomedical diagnostics like heart rate variability (HRV) is that many vital functions can be measured noninvasively and more precisely. The aim of sensing methods proposed here is to observe the activity of heart with approach based on a low-cost self-mixing laser interferometer based technique to measure vibrations on human skin with very high accuracy and temporal resolution. In this technique, the information is carried in the electromagnetic field, which is a superposition of two wave fronts which have travelled along different routes. One of these wave fronts has undergone a frequency shift due to interaction with a moving target or particles. This frequency shift is called the Doppler shift. After coherent mixing of these two waves at a photo detector, information about the velocity of the target can be obtained from the frequency of the superposition signal. When visible or near infrared wavelengths (600-1500nm) can be used, it is possible to achieve a resolution of 300-750 nm if only one detector is used and the difference of constructive and destructive interference is considered. It works on the basis of optical interference, requiring two coherent light beams, with their respective light intensities I1 and I2, to overlap. The resulting intensity is not just the sum of the single intensities, but is modulated intensity. The interference term relates to the path length difference between both beams.

Keywords: Interferometry, Doppler shift, HRV, AOM

Principle of Operation: The laser beam is first split into two beams (reference and measurement). The measurement beam with frequency is focused onto the measurement point on the test surface. The reflected beam, experiencing a frequency shift (heart rate frequency) proportional to the velocity of the test surface, is re-combined with the reference beam at an optical detector. Figure 1 shows an example of the basic concept used in this approach.

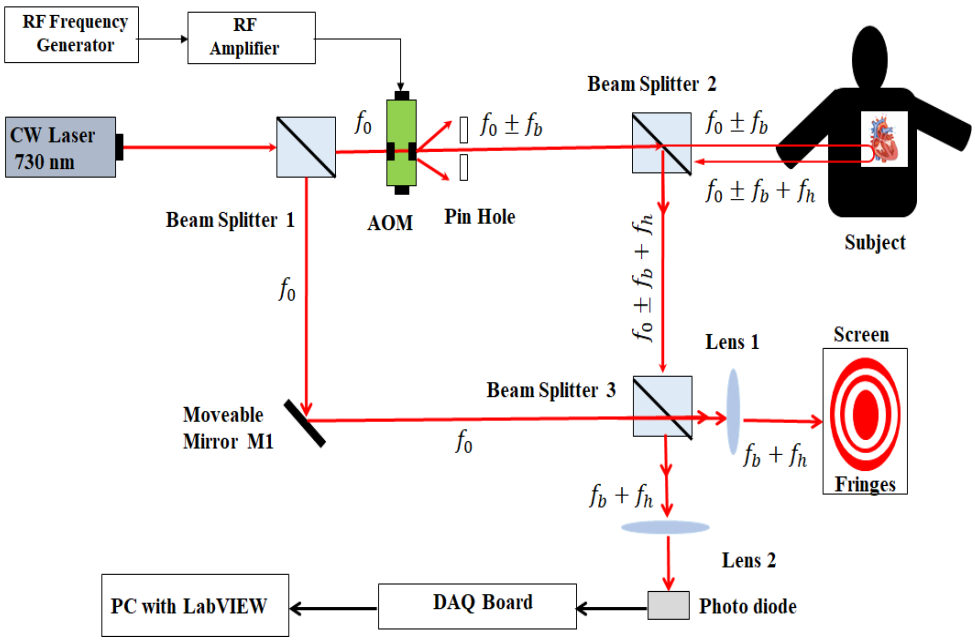

Fig. 1 Optical Heterodyne Detection Technique for HRV Measurement

An Acousto-Optic Modulator (AOM) which contains Bragg cell is used to shift the frequency of the reference laser by f_b (typically 60 KHz). Without a Bragg Cell, the system would not be able to distinguish whether the detected movement is towards or away from the laser. This 60 KHz signal $\pm f_b$ is demodulated electronically to provide a voltage output proportional to instantaneous velocity. A voltage proportional to displacement can also be provided by decoding the relative phase between the carrier signal driving the Bragg cell and the photo-detector signal. The laser oscillator produces a beam with reference frequency f_0. The scattered or reflected light has a

frequency equal to $f_0 + f_b + f_h$. This scattered light is combined with the reference beam at the photo-detector. The initial frequency f_0 of the laser is very high. The resulted beat frequency between the two beams, which is at $f_b + f_h$ (typically in the tens of MHz range). The output of the photo detector is a standard Frequency Modulated (FM) signal, with the Bragg Cell frequency as the carrier frequency, and the Doppler shift as the modulation frequency [1]. This signal can be demodulated by demodulator in the instrument controller to derive the velocity vs. time of the vibrating target. The Brag's cell is available in free space type AOMs as well as in the form of fiber grating inside fiber core, so both type of systems can achieve frequency shift which is principle of optical heterodyne detection. The frequency shift is detected at photo diode which will be read to an interfacing board. The graphical user interface is provided by NI-LabVIEW. The basic idea of heterodyne detection is to introduce a small frequency shift between two interfering beams. One acts as the reference beam, the other is the object beam. Their frequencies are shifted with difference of ω_b by using acousto-optic modulator (AOM), The electric fields of the reference and the object arms can be described as

$$E_{ref}(t) = A_{ref}\, exp\left[i\{(\omega_0)t + \varphi_{ref}\}\right] \quad (1)$$

$$E_{obj}(t) = A_{obj}\, exp\left[i\{(\omega_0 + \omega_b)t + \varphi_{obj}\}\right] \quad (2)$$

$$I\,(x,y,t) \propto \left|E_{ref}(t) + E_{obj}(t)\right|^2 \quad (3)$$

$$I\,(x,y,t) = A_{obj}^2 + A_{ref}^2 + 2A_{obj}A_{ref}\cos[\Delta\omega t + \varphi(x,y)] \quad (4)$$

where $\Delta\omega = \omega_0 - (\omega_0 - \omega_b)$ and $\Delta\varphi(x,y) = \varphi_{ref} - \varphi_{obj}$. The frequency of the beat signal, Δω, is sufficiently low within the bandwidths of the detector. Demodulate I(x,y,t) with a reference sinusoidal signal Δω, the first two items in the equation (4) are the DC components and will disappear after demodulation, phase and frequency information are extracted. The Bragg's modulation frequency (ω_b) can be detected by using optical heterodyne setup which uses self-phase interferometry technique as shown in Fig. 2. The heart rate variability measurement is completed by introducing subject's heart rate frequency (ω_h) vibration to one of the beam splitter of Mach-Zehnder interferometer [2]. In this case frequency shift is given by

$$\Delta\omega = \omega_0 - [\omega_0 - (\omega_b + \omega_h)] \quad (5)$$

Equation (5) represents output at photo detector which consists of $(\omega_b + \omega_h)$. Thus by demodulating the output with Bragg's frequency, the heart rate vibration frequency can be determined [3].

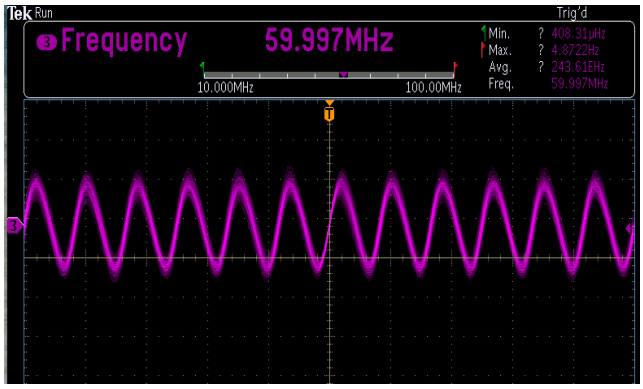

Fig. 2 Optical beating signal

Analysis: The self-phase interferometry technique provides precision accuracy for vibration measurement which includes various application in detection of biomedical signal and structural vibrations. Heterodyne setup involves use of Bragg's cell for modulation of optical signal which improves the detection of beat frequency as compare to homodyne detection technique.

References

1. T. Bosch, Opt. Eng. 40, 20–27 (2001).
2. Donati S, Laser Photonics Rev. 6, 393–417 (2011)
3. Julien Perchoux, MDPI Sensors, 16, 694,1-26 (2016)

Experimental comparison of performance parameters of Fourier and Fresnel holograms in digital holography using space-bandwidth product

Lavlesh Pensia[1, 2], Gaurav Dwivedi[1, 2], Raj Kumar[1, 2,*]

[1]CSIR-Central Scientific Instruments Organisation, Chandigarh-160030, India
[2]Academy of Scientific and Innovative Research (AcSIR), CSIR-CSIO, Chandigarh-160030, India
[*]Corresponding author: Email: raj.optics@csio.res.in, Phone: +91-172-2672308

Abstract: The space-bandwidth product is a measure of the performance of an optical system. In this paper, the space-bandwidth products of Fourier and Fresnel holograms in off-axis digital holography are compared and both methods are experimentally analyzed in terms of speed, size, accuracy, resolution and root mean square error. Further it is also verified that the Fourier hologram gives information about a rotation of space and frequency coordinates and Fresnel hologram introduces a shear in the space coordinate.

Keyword: Space-bandwidth product, digital holography, root mean square error.

Experimental Results: The space-bandwidth product (SBP) signifies the field of view of an optical system and the amount of data transferred from an object to the recording plane. The space-bandwidth product of an object is given by the product of object size X and the spatial frequency bandwidth $\Delta\nu$[1].

$$SBP = X\Delta\nu \tag{1}$$

In case of Fresnel off-axis setup, the space bandwidth product is represented as[1]

$$SBP^{'} = 2(SBP + N_F^{-1}) \tag{2}$$

In case of Fourier off-axis setup, the space-bandwidth product is represented as[1]

$$SBP^{'} = 2(N_F^{-1}) \tag{3}$$

Where N_F is the Fresnel number. Requirement of space-bandwidth product in Fourier hologram is less than Fresnel hologram which is shown in Fig. (1) and (2) and explained in equations (2) and (3) respectively.

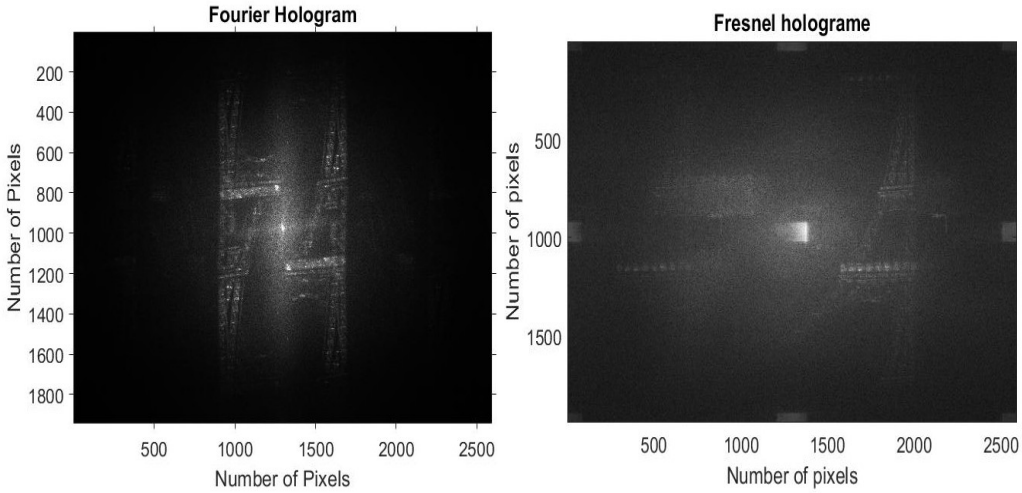

Fig. 1 (a) Reconstructed image from a recorded digital Fourier hologram and (b) reconstructed from a recorded digital Fresnel hologram

References:

1. Daniel Claus, Daciana Iliescu and Peter Bryanston-Cross, Appl Optics, vol. 50, No. 34 (2011).
2. U.Schnars and W. P. O. Juptner,Measurement Science and Technology 13, R85-R-101 (2002).
3. Adolf W. Lohmann, Rainer G.Dorsch, David Mendlovic, Zeev Zalevsky and Carlos Ferreira, J. Opt. Soc. Am. A, 13, 3 (1996).
4. Mark A. Neifeld, Optics Letters / Vol. 23, No. 18 (1998).

Time resolved response of fish cornea exposed to single femtosecond laser pulse

Mehra S. Sidhu and Kamal P. Singh*
Department of Physical Sciences, Indian Institute of Science Education and Research, Mohali, Sector 81, SAS Nagar, Manuali, P.O. 140306, India.
*Email: sidhums@iisermohali.ac.in**

Abstract

Nonlinear interaction of fs-laser and soft tissues like cornea and elastomers like PMMA (Contact lens) and PDMS is a dynamic process where the biomechanical properties might be perturbed by the laser beam during the time-course of the processing. Here we demonstrate the time-resolved response of focused single fs-laser pulse on soft-tissues like Cornea, elastomers like PDMS and PMMA (Contact lens) near ablation threshold where the energy is nonlinearly absorbed by the target. Using high speed photography and single shot selection from the pulse train, we observe long exponential relaxation dynamics of crater diameter.

Keywords: Cornea, femtosecond laser, PDMS, PMMA

Main

Femtosecond laser pulses have been used in the field of eye surgery, particularly corneal flapping procedure namely LASIK, providing the advantages of combined high precision and minimized collateral tissue damage [1]. While prominent side-effects after LASIK are relatively rare, fs-laser flap-creation results in creation abnormal roughened corneal surfaces, vision defects such as irregular astigmatism, interface haze, and transient light sensitivity syndrome caused by increased light scattering [2]. The challenge in femtosecond laser dissection is to optimize clinical operating conditions for maximal precision and minimal damage to surrounding corneal tissues. Thus, it is vital to understand the single pulse response of soft materials. Since, when the surgery systems are operating at several MHz repetition rates, the interaction time of pulses with material plays a significant role in increasing or decreasing the surface roughness [3].

The CEP amplified femtosecond laser system (FEMTOLASER, AUSTRIA) with 2 mJ energy at the wavelength of 800 nm with a repetition rate of 1 kHz was used to modify the soft surfaces. The pulse duration of the laser is about 25 fs. The laser energy could be attenuated with variable neutral density filter (Thorlabs). The laser beams are focused on the sample surface by using an objective lens (10X). The laser beam spot size at sample surface was determined to be about 2.5 μm in diameter. The laser polarization is set to be perpendicular to the processing direction. The two high speed mechanical shutters was synchronized with input pulse and the high-speed charge-coupled device (CCD, FASTCAM, Photron, Japan) to capture the time resolved video after exposing to a single femtosecond pulse[4]. The video was converted to time resolved optical images using home built LABVIEW software to analyze the change in crater diameter of ablated surface as a function of time.

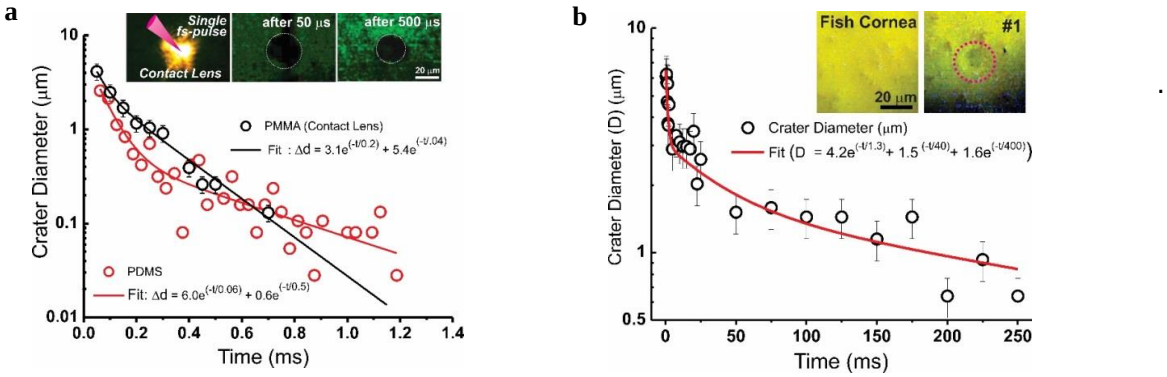

Fig. 1 Time resolved response of soft materials towards single fs-pulse, change on crater diameter as a function of time (a) PMMA & PDMS (b) Fish Cornea

The surface optical image trains were extracted from the fast CCD camera video captured during laser irradiation. Inset of Figure 1(a) shows a set of crater images as a function of time delay after single-shot laser pulse with energy of 50 μJ on PMMA surface. The crater diameter has reached to its maximum value of about 26 μm within less than 0.1 ms. After 1 ms, the crater size is eventually invariant of about 22.2 μm in diameter. In case of PDMS, The crater diameter has reached to its maximum value of about 15 μm within less than 0.1 ms. After 1 ms, the crater size is eventually invariant of about 11.3 μm in diameter. In both materials, we observe the 4 μm change in crated diameter with the time span of 1 ms. If the pulse repetition rate change from 1 kHz to 2 kHz, viz. two pulses in 1 ms time scale, perhaps make a chance of two pulses interacting with the materials without an elastic relaxation, this may increase the roughness in focal volume. Fig. 1 b shows the time resolved relaxation of fish cornea (*in vitro* conditions) where the surface was exposed to single fs- pulse with 10 uJ energy. The crater diameter has reached to its maximum value of about 20 μm within less than 0.1 ms. After 250 ms, the crater size is eventually invariant of about 5.5 μm in diameter. We observe a significant change in crater diameter as a function of time. Thus, in order to achieve better performance in fs-laser cornea cutting/dissecting operation, it is quite necessary to carefully design inter-pulse interval considering the material relaxation time with respect to the exposure of a single fs- pulse.

References

1. Vogel, J. Noack, G. Huttman, and G. Paltauf, Appl. Phys. B-Lasers Opt. 81, 1015 (2005).
2. G. D. Kymionis, et al., Br. J. Ophthalmol. 98, 133 (2014).
3. H.Y. Moon, M. S. Sidhu, H. S. Lee and S.C. Jeoung, Optics Express, 23, 19854 (2015)
4. M. S. Sidhu and K. P. Singh, 13th Intern. Conf. on Fiber Optics and Photonics, IIT Kanpur Th3A.90, (2017)

Detection of surface defects in Silicon during ultra-precision machining

Neha Khatri [1,2*], Suman Tewary [1], Harry Garg [1,2], Vinod Karar [1,2]
[1]*CSIR - Central Scientific Instruments Organisation, Chandigarh, 160030, India*
[2]*Academy of Scientific & Innovative Research (AcSIR), CSIR-CSIO, Chandigarh*
*Corresponding author Email: nehakhatri@csio.res.in, nehakhatriuiet@gmail.com

Abstract
The surface defects and sub surface damages induced during ultraprecision machining of hard and brittle materials influence the physical and mechanical properties of the optical components. These defects are attributed to various factors and are required to be examined & eliminated. The experimental evaluation of these defects is very time consuming as well as expensive, whereas the theoretical exploration lacks accuracy due to various assumptions involved. The aim of this research is to identify the optimum machining conditions during diamond turning of silicon to achieve a defect free surface and further to identify the depth of defect encountered during various machining combinations using image processing technique.

Keywords: Silicon, Diamond Turning, Surface Defects.

Introduction

Silicon is a widely used material and has significant attention due to its use in high precision devices. The focusing mirrors for x-rays are built on silicon material having a high degree of crystalline perfection [1]. The nano-scale material removal by diamond turning is one of the popular method with which it is feasible to produce deterministic finish on brittle materials for such applications [2,3]. The development of silicon mirrors without causing surface and subsurface defects is exceedingly challenging due to its high hardness and brittleness. In recent years, emphasis has been laid to the consequences of surface and subsurface damage in brittle materials. These defects severely limit the life of the components by failure of critical optical properties as well as catastrophic fracture. Hence it is of great importance to perform a comprehensive study to analyze surface defects in diamond turning of silicon. There are many factors which cause sub surface damage stresses and affect the surface quality [4]. In view of this, it is important to quantify the defects so that further decision making could be done. In this work, image processing based approach is used for evaluating the surface defect in silicon is presented.

Experimental Setup

All the experiments were performed in a single point diamond turning machine Nanoform-250. A single crystal diamond tool with nose radius of 1.5 mm and rake angle of -25° degrees is used for machining silicon. The process parameters considered in this research are: depth of cut, tool feed rate and spindle speed. The parameters were varied in three levels as shown in Table 1. The experiments were performed based on Response Surface Methodology design. The 20 set of possible combinations of process parameters and their levels were investigated.

Table 1. Coded level & actual values of Cutting Parameters

Parameters	Units	Coded Levels				
		-1	-α	0	+α	+1
Spindle Speed (SS)	rpm	500	702	1000	1297	1500
Tool Feed Rate (TFR)	µm/rev	1	1.3	1.5	2.2	2.5
Depth of Cut (DOC)	µm	0.5	0.7	1	1.3	1.5

The machined surface was further investigated to evaluate the defects and valleys induced in silicon by Coherence Correlation Interferometer for the best and worst combinations. Image processing is used for further quantification.

Methodology

Quantification from non-contact surface profile is a difficult job and requires high accuracy. The surface profilometer software has limitations to provide the volumetric information of defects at different locations. It is essential to quantify the volumetric information such as crack dimensions at different locations. Hence, it becomes a two-step

problem, first to quantify the locations of such defects and second to quantify the volumetric information. In the proposed approach, the defect locations are quantified from the surface profile using image processing algorithms, where the intensity of the image pixels corresponds to peaks and valleys of the surface. The input image is segmented and the morphological properties such as area, perimeter and centroid are calculated to quantify and localize the defects. Once, the locations are obtained, the neighbourhood surface profile is extracted and the approximate volume of the region is calculated based on the 3D surface profile. A design of experiment is performed to generate 20 set of experiments and the three cases are considered for the study – best and worst surface profile based on average surface roughness. From the results, it is estimated that the calculated defect locations could be validated from the actual surface profile and it is expected that the quantification will have high significance in justifying the usage of the machined silicon surfaces for further product development.

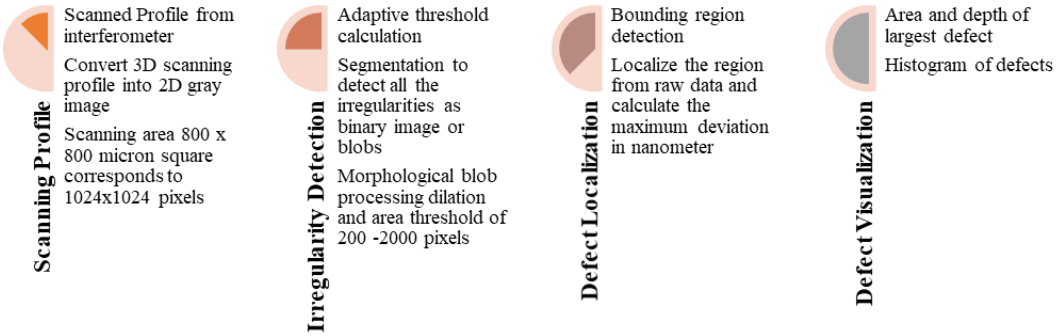

Fig. 1 Schematics of proposed approach: Interferometry data analysis using Image Processing

The step by step output from the approach is shown in Figure2. It can be observed from Figure 2 that the surface profile in the first row has less depth of defect compared to the surface profile in the second row.

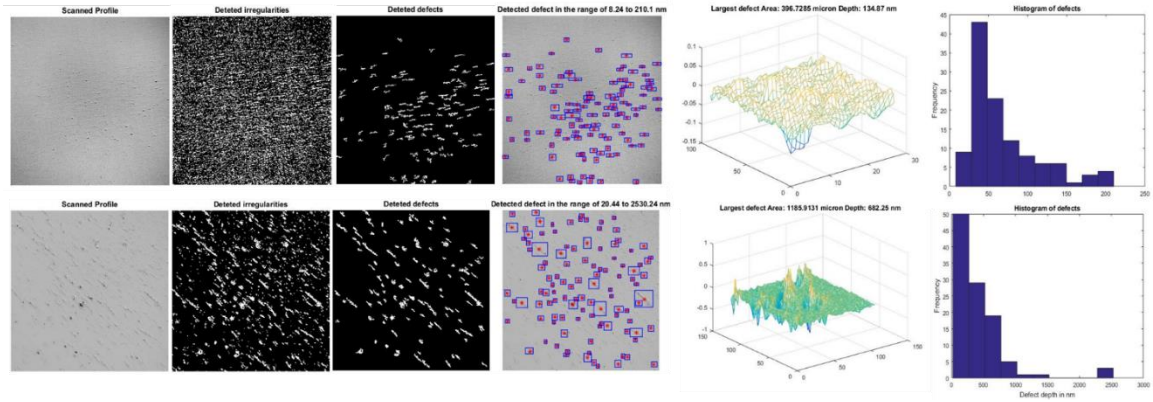

Fig. 2 Scanned profile, irregularities, defects after postprocessing, detected defects, 3D profile & histogram of defects

Conclusion

The surface defects during worst & best combinations were analyzed by 3D reconstruction approach, whose outcome give more accurate and comprehensive analysis about the severity of the defect by determining the average depth of the crack. The proposed research will have high significance in justifying the usage of the machined silicon surfaces for further product development.

References

1. S. Goel, X. Luo, A. Agrawal, and R. L. Reuben, International Journal of Machine Tools and Manufacture, (2015), pp. 131-164
2. N. Khatri, R. Sharma, V. Mishra, M. Kumar, V. Karar, and R.V. Sarepaka, International Conference on Optics & Photonics, 96540M, (2015)
3. FZ Fang, and VC Venkatesh *CIRP Annals-Manufacturing Technology* 47(1) 45-9 (1998)
4. Y. Jiwang, T. Asami, H. Harada, and T. Kuriyagawa. Precision Engineering 33, (2009)

Error Analysis of the Novel Polarization Phase shifting Interferometric Technique.

Pretheesh Kumar V C, A R Ganesan
Indian institute of technolog, Madras Chennai, India.
Author e-mail address: pretheeshvc@gmail.com

Abstract:
Compared to a Michelson interferometer, a cyclic interferometer is very stable to environmental turbulences and vibrations. But it is not very much used in metrological applications as it is difficult to introduce phase changes in one of the beams alone. However it was shown by us that a cyclic interferometer can be used to measure tilt angles up to 2 nrad. This was done employing polarization phase shifting interferometry and a new method polarization phase shifting interferometry (PPSI) was developed for the same. The method is elegant compared to other methods described in literature, as it uses less optical components. In any phase shifting measurements, the variations in the induced phase can be a major source of error. In a Michelson interferometer, these variations are formed due to errors in the movement of the mirrors. But in the case of PPSI, it is due to the in accuracies in the rotation of the half wave plate. Here we quantify the errors in our measurement using the new technique due the flaws in the phase shifts.

Key words: Cyclic Interferometer, Polarization Phase Shifting, Angle Measurement, Phase Unwrapping.

1. Introduction

Interferometry had always been an excellent tool in various metrological applications [1]. It was shown by us that a cyclic interferometer can be used as an excellent tool for precise angle measurement and tilt angles as low as 2 nrad was measured using this technique. Also, a novel method of PPSI was developed for this [2].

2. Tilt measurement using the newly developed PPSI

Figure 1 shows the diagram of a multiple reflection cyclic interferometer with PPSI, designed for precise tilt angle measurement. Any tilt in M_3 will be amplified by the number of reflections between the mirror and can accurately

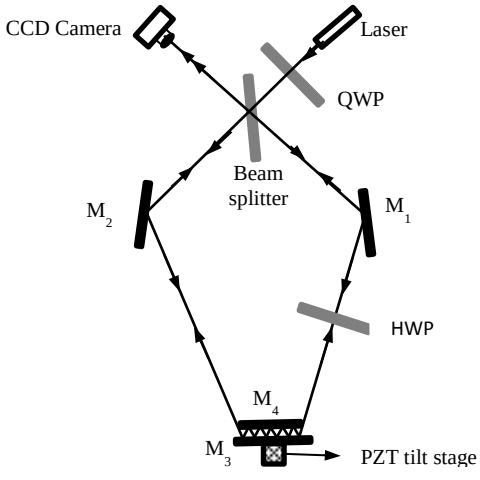

Fig. 1 A multiple reflection cyclic interferometer with polarization phase shifting.

measured by analyzing the interferogram using PPSI. The rotation of the HWP by θ, creates a phase shift of 4θ in the interferogram. The new methods has the advantage that it requires a polarizing beam splitter and a polarizer less, compared to the simplest PPSI method that can be found in the literature.

3. Error Analysis

The major source of error in the PPSI methods is the misalignment of the wave plates. The change in visibility due to the misalignment of the quarter wave plate has already been studied numerically and published [3]. Here we numerically estimate the errors induced in the tilt measurement due to the inaccuracies in phase shifts ,ie the errors in the rotation of the HWP. The polarization optics can be mathematically described using the Jones calculus. Using the same The PPSI method can be simulated and required phase shifts can be given to evaluate the tilt precisely. Initially correct phase shifts were given to verify the code and the erroneous phase shifts were given to quantify the errors in the tilt measurement.

4. Results

Figure 2 shows the tilt measurement done with the above mentioned technique. It can be seen that the introduced tilt and measured tilt are in good agreement up to 2 nrad. Figure 3 shows the deviation in the measurement due to the erroneous phase shifts given, for a tilt of 50 nrad. It can be seen that for small deviation in the rotation of the HWP, the errors in tilt measurement are negligible. But after 5 degrees it can be seen that the measurement becomes very erroneous. The Actual errors in a real experiment may be bigger when coupled with other errors.

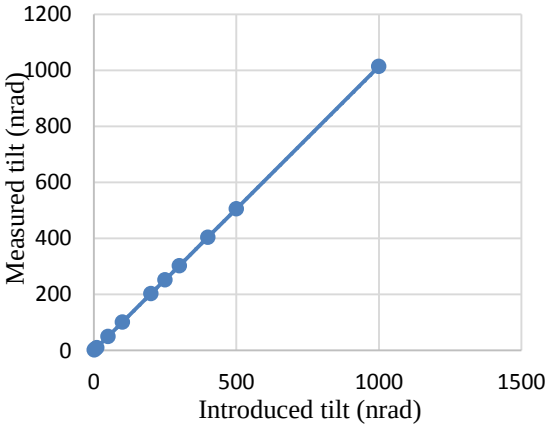

Fig. 2. Tilt measurement using the newly developed PPSI method in cyclic configuration

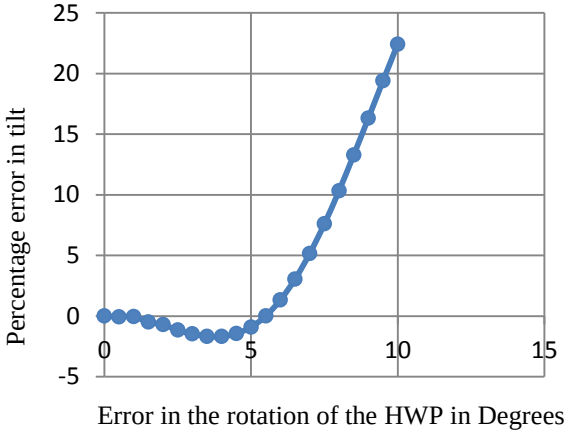

Fig. 3. Deviations in the measurement due to the erroneous phase shifts

5.Conclusions

The newly developed method is an excellent tool for polarization phase shifting and it renders precise measurement unto 2 nrad. The small errors in the phase shifting alone do not affect the measurement significantly. However the deviations above 5 degrees produce significant errors in the measurent.

4. References

[1] D. Malacara, Optical Shop Testing (Wiley, New York, 1991)

[2] Joenathan, C. et al. Nanoscale tilt measurement using a cyclic interferometer with polarization phase stepping and multiple reflections. Appl. Opt. 57, B52 (2018).

OSI-ISO 2018 manuscript No.
(101)

Extra-ordinary transmission from nanosized *opaque* plasmonic gratings in near infra-red region for highly sensitive refractive index sensing

Sachin K. Srivastava[1,*] • Amandeep Kaur[2] • Udaybir Singh[1]

Abstract Polymeric nano-gratings coated with subwavelength plasmonic coatings were examined both theoretically and experimentally. Extra-ordinary transmission (EOT) in NIR region was observed from these *opaque* plasmonic films. The reason for EOT was attributed to transfer to extra-momenta from plasmons to rough grating structure to emit back light at the other end of the grating. Control experiments with s-polarized light were performed to confirm purely plasmonic character of the transmission phenomenon. Further, these structures were used for refractive index (RI) sensing. A sensitivity of about 2250 nm/RIU was achieved experimentally.

Keywords Extra-ordinary transmission • plasmonics • sensors • near-infrared • gratings

Introduction

Extra-ordinary transmission from subwavelength plasmonic structures has attracted researchers from all around the globe due to interesting Physics involved and intriguing potential new applications. EOT was first reported by Ebessen et.al., in 1998, where about 6 % transmission from perforated plasmonic films of 200 nm holes in a 150 nm thick film with about 900 nm periodicity was observed [1]. The reason behind such an enhancement was attributed to surface plasmons which could funnel the incident light to the other end of the subwavelength plasmonic film. The investigations on thicker plasmonic films of around 1μm also reported such phenomena [2], where the light of any polarizations could be passed through [3]. Also, such films did not require any plasmonic materials. The transmission through such thick films was attributed to cavity mode resonances which are similar to Fabry-Perot cavities. Because of the inherent property of shift of resonance wavelength of plasmons due to change in the in the refractive index of the adjacent material, the wavelength of the light transmitted through such films can be tailored to desired value. Such investigations lead to optical filters [4]. Further, the same property of plasmons has been utilized for sensing applications [5]. A self-referenced EOT sensor in NIR communication window using metal-nano-slit arrays was reported for water detection in ethanol [6]. Most of these studies were performed on perforated plasmonic films and the incident light was explained to funnel through the holes via plasmons [7]. In recent times, it was theoretically predicted by Abutoama and Abdulhalim that a non-plasmonic slit array with a sandwiched thin plasmonic layer between the slit array and the substrate showed enhanced transmission in NIR region [8].

In this work, EOT from *opaque* plasmonic nanograting in NIR spectral range has been reported. A polymer grating of about 800 nm period was coated with a 50 nm thick gold layer. The scanning electron microscope (SEM) image of the aforementioned grating is shown in Fig.1 (a).

* sksrivastava@csio.res.in
1 Advanced Materials & Sensors Division, CSIR-Central Scientific Instruments Organization, Chandigarh-160030
2 Department of Physics, Punjabi University, Patiala-147002

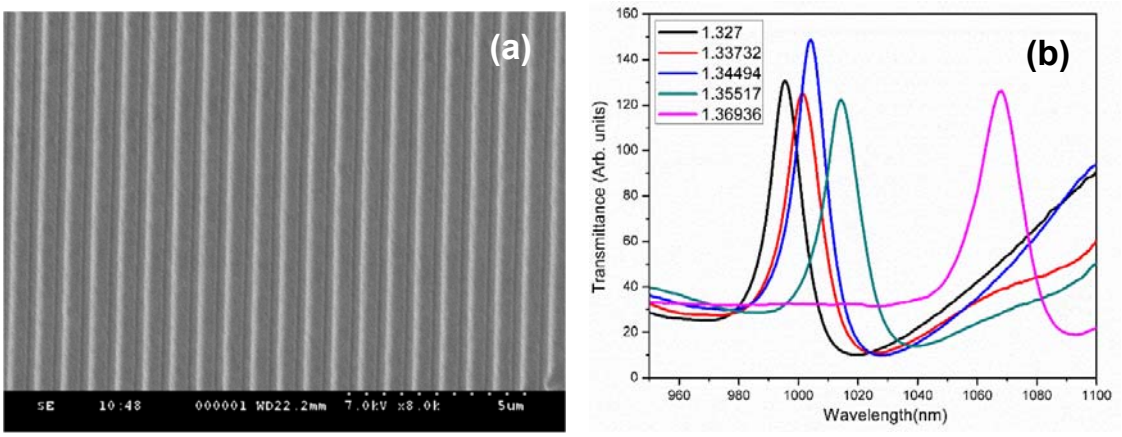

Fig.1. **(a)** SEM image of the plasmonic nano-grating structure; **(b)** Transmission spectra for varying refractive indices of the analyte over the plasmonic nanograting

Results and discussion

The transmission spectra both for TE and TM polarized light were recorded. No transmission peaks for TE polarization were observed. Fig.1 (b) shows the transmission spectra of the nanograting for varying refractive indices of the analyte over it for TM polarization. The samples of varying refractive indices were prepared dissolving different amounts of sucrose solutions in distilled water. The refractive indices of thus prepared sample solutions were measured using a high precision refractometer. It can be observed that for each sample solution, a peak in the transmission spectrum is observed. The wavelength corresponding to the maximum transmission is termed as resonance wavelength. It is further observed that every sample solution of different refractive index has a characteristic resonance wavelength which, further shows a red shift with an increase in the refractive index of the analyte medium. The refractive index sensitivity was estimated to be 2250 nm/RIU. The transmission though such opaque films can be understood as follows. Gratings can be used for the excitation of surface plasmons because they impart the additional required phase to the incident light. So, a light beam, whenever finds a corrugated metallic film, can couple to surface plasmons. On a similar note, similarly, under favorable conditions, surface plasmons travelling on a corrugated surface may radiate light back. This is what exactly happens in this case. Since the plasmonic film is only 50 nm thick, the incident light at one side excites surface plasmon super modes on both the interfaces, which leads to emission of light on the other side of the film. A detailed study, including simulations using RCWA is still undergoing.

Conclusions

Extra-ordinary transmission through nanostructured gratings is possible for opaque thin plasmonic films. Refractive index sensitivity of 2250nm/RIU was estimated for such structures.

Acknowledgements This work was partially supported by DST-INSPIRE Faculty Award no. DST/INSPIRE/04/2015/002800. Amandeep thanks Director CSIR-CSIO to grant permission and provide all support to carry out her M.Sc. thesis work at CSIR-CSIO, Chandigarh.

References

[1] T.W. Ebbesen, H.J. Lezec, H.F. Ghaemi, T. Thio, P.A. Wolff, Nature 391, 667 (1998).
[2] M. Luo, Q.H. Liu, J. Opt. Soc. Amer. B, 28, 629 (2011).
[3] T. Bian, B. Dong, Y. Zhang, Opt. Commun. 285, 1523 (2012).
[4] Y. Qiu, L. Zhan, X. Hu, S. Luo, Y. Xia, Displays, 32, 308 (2011).
[5] R. Gordon, D. Sinton, K.L. Kavanagh, A.G. Brolo, Acc. Chem. Res.8, 1049 (2008).
[6] S.K. Srivastava, I. Abdulhalim, Opt. Lett. 40, 2425 (2015).
[7] H. Liu and P. Lalanne, Nature, 452, 728 (2008).
[8] M. Abutoama and I. Abdulhalim, Opt. Exp., 23, 28667 (2015).

Spectral shaping using polarization control in nematic liquid crystals

Gyaprasad* and Bhaskar Kanseri

Experimental Quantum Interferometry and Polarization (EQUIP), Department of Physics,
Indian Institute of Technology Delhi, Hauz Khas, New Delhi-110012, India.
Email*: gyaprasad@physics.iitd.ac.in.

Abstract

We demonstrate both theoretically and experimentally that the nematic liquid crystal (LC) can be used to manipulate the broadband source spectra. By placing the LC cell between a polarizer and an analyzer, one can use the combined device as a spectral filter. We also demonstrate that the source spectrum also gets manipulated by changing the LC cell thickness and by tuning the voltage applied across the LC cell. Such spectral manipulating device is expected to find applications in spectral shaping, data communication and application.

Keywords

Spectral manipulation, Polarization, birefringence, spectral filter.

Introduction

Spectral shaping is an active area of research in optics. Spectral changes can be introduced by various methods e.g. by polarization induces [1, 2], propagation induces [3], scattering induces [4], etc. We use a nematic liquid crystal for spectral shaping by using its birefringence property. The retardance depends on the wavelength of light and thickness of retarder (LC).

$$\Phi = \frac{2\pi}{\lambda}.\Delta n(\lambda).d$$

Where Φ, Δn and d, are the retardance, the birefringence and the thickness of retarder respectively. The birefringence itself depends on the wavelength of incident light. Each wavelength of input broadband spectrum feels different retardation and hence persist different polarization state.

Experimental details

Experimental set-up consists of a white light LED source, a spectral filter (400-1100nm) of band width 70nm, a polarizer, and an analyzer as shown in Fig.1 (a). A Lens L1, is used to focus the light in fibre coupled with the spectrometer. The output spectra can be recorded using spectrometer. The liquid crystal cell is inserted between the polarizer and analyzer with its director making 45 degree angle to the input polarization and the analyzer is rotated w.r.t. reference axis of input polarization. First we have used an aperture of 1 mm diameter just after the LED source to make point source output then use the lens to make it collimated. Spectral filter (central wavelength 550nm, FWHM 70nm) is used to filter the Gaussian input from LED light. The lens L2, is used to focus the light on the detector.

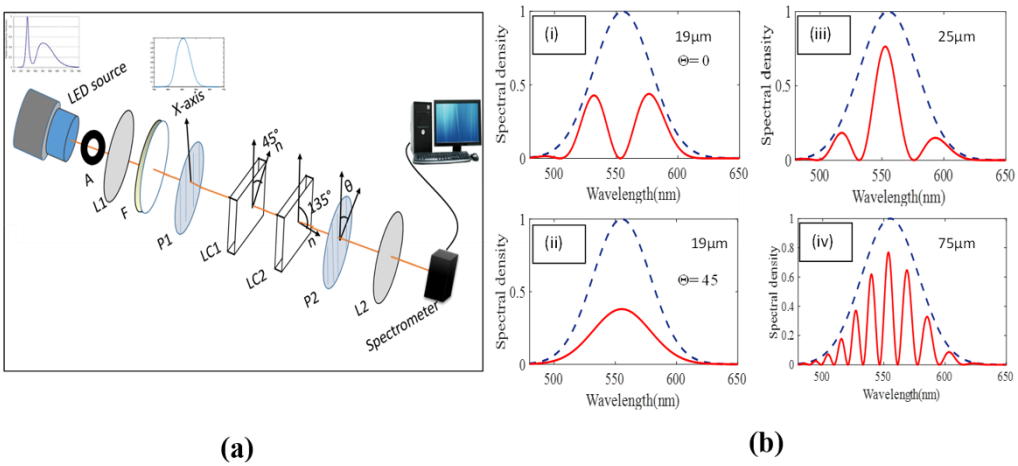

Fig.1. (a) Experimental scheme of spectral manipulation. L1 and L2: convex lenses, F: spectral filter, P1 and P2: polarizer and analyzer, LC: liquid crystal cell. Figure (i) and (ii) shows spectral density vs wavelength plot for different analyzer angle and Figure (iii) and (iv) shows spectral density vs wavelength for different cell thickness.

Results and Discussion

We have theoretically and experimentally studied the spectral manipulation using nematic liquid crystal. Nematic liquid crystal cells of different thicknesses are used along with a polarizer and an analyzer to manipulate the spectra. First, we have fixed the LC cell thickness and varied the analyzer angle. We have also studied the effect of LC cell thickness on the spectra. Theoretical analysis of output spectra is carried out by writing the Jones matrices of various components used in the experiment. Figure.1. (b) (i-ii) show the experimental results of the spectral change for the different analyzer angle. When the analyzer angle is 0^0, the spectrum splits into two peaks Figure.1. (b) (iii-iv). On changing the analyzer angle to 45^0, it changed to a single peak spectra. On further increasing the thickness of LC cell keeping analyzer angle fixed, the number of peaks increases. Also we have studied the spectral changes on varying the thickness of LC cell.

Acknowledgments

Authors are thankful to the financial support received from the funding agencies, SERB for grant YSS/2015/000367, YSS/2015/000743 and UGC for Junior Research Fellowship.

References

1. B. Kanseri, J. of Opt. **15,** 055407 (2013).

2. Han P, Spectral shifts with polarization control. J. Opt. **15,** 105710 (2013).

3. J. Pu, O. Korotkova and E. Wolf, **31**, 2097 (2006).

4. T. Shirai and T. Asakura, J. Opt. Soc. Am. A **12**, 1354 (1995).

Coherent coupling of fluctuations in optomechanics

Devender Garg[1], Anil k. Chauhan[2], Asoka Biswas[3]
Department of Physics, Indian Institute of Technology Ropar[1,2,3]
Rupnagar, Punjab 140001, India
devender@iitrpr.ac.in

Abstract

The interaction between a quantum and a mesoscopic system has always been intriguing in understanding the quantum-classical interface [1,2]. For example, in the optomechanical system, coherent coupling between the cavity mode and the mesoscopic oscillator leads to several nontrivial quantum effects, namely quantum state transfer, cooling, squeezing, and nonlinear effects [3,4]. In this paper, we show how the energy fluctuations in two membranes suspended inside a cavity can be adiabatically exchanged by using pulses that drive the cavity modes [5]. The adiabatic transfer of fluctuations from one membrane to the other is attained through a "dark" mode, which is robust against the decay of the mediating cavity mode.

Keywords: quantum optics, optomechanics, adiabatic transfer, quantum information

Method

We first consider two membranes suspended inside the cavity, dividing the cavity into three segments [see **Fig:1**]. We obtain the equations of fluctuation of the relevant operators and a zero-eigenvalue solution of the corresponding evolution matrix. This shows that a suitable sequence of pulses that drive the cavity modes can lead to a deterministic adiabatic transfer of energy fluctuations from one membrane to the other, in a way akin to stimulated Raman adiabatic passage.

The Hamiltonian of the system can be written as follows

$$H = Ho + H_J + H_I + H_P \qquad [1]$$

H_O, H_I, H_J, H_P are the unperturbed, optomechanical coupling, transmission and the pulse Hamiltonian respectively. Dark state corresponding to zero Eigenvalue is

$$\Psi_D = \left(2g_1 g_2 \alpha_L \alpha_R\right)\delta\hat{a}_M + \left(g_2\alpha_R\right)\delta\hat{b}_1 - \left(g_1\alpha_L\right)\delta\hat{b}_2$$

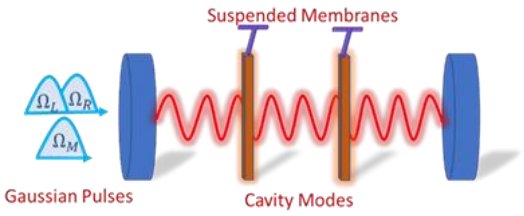

Fig 1: Setup of cavity optomechanical system

Results

We find that it is possible to coherently couple the fluctuations of the two membranes [see **Fig:2**], even if the mirrors are highly reflecting. The cavity mode in the middle remains unpopulated in such adiabatic transfer. This opens up an avenue of quantum communication between two truly mesoscopic systems.

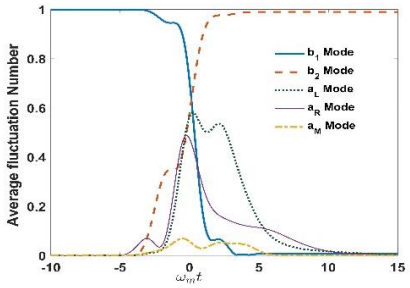

Fig:2 Phonons population transfer between the membranes

Acknowledgements:
Department of Science and Technology for fellowship.

References:

[1] M. Aspelmeyer, T. J. Kippenberg, and F. Marquardt, Rev. Mod.Phys. 86, 1391 (2014).
[2] F. Marquardt, J. P. Chen, A. A. Clerk, and S.M. Girvin, Phys.Rev. Lett. 99, 093902 (2007).
[3] L. Tian, Phys. Rev. Lett. 108, 153604 (2012).
[4] Y.-D. Wang and A. A. Clerk, Phys. Rev. Lett. 108, 153603 (2012).
[5] Devender Garg, Anil Kumar Chauhan and Asoka Biswas, Phys. Rev. A 96, 023837 (2017).

Double Shot Interferometric Polarimetry to calculate Jones Matrix of Spatial Light Modulator

Surya Kumar Gautam[1], Vipin Tiwari[2], Nandan Bisht[2], Dinesh N Naik[1], Rakesh Kumar Singh[3] *

[1] *Applied and Adaptive Optics lab, Department of Physics, Indian Institute of Space Science and Technology, Trivandrum, India*
[2]*Physics Department, Kumaun University SSJ Campus Almora (UK), India*
[3]*Department of Physics, Indian Institute of Technology (BHU), Varanasi, Uttar Pradesh, India*
**Corresponding author: krakeshsingh@gmail.com*
Acknowledgment: The authors acknowledge support from the Science and Engineering Research Board (SERB) (EMR/2015/001613).

Abstract: We present double shot interferometric polarimetry to accurately measure the Jones matrix of a spatial light modulator (SLM) as a function of input gray levels for SLM display. The light modulated by a reflective type liquid crystal SLM is made to interfere with two orthogonally polarized (X and Y) reference waves at the camera which enable us to capture the vector amplitude and phase leading to resultant polarization information of the modulated light (Jones vector). By measuring and combining the Jones vectors of the modulated light from the SLM for two incident light having the linear states of polarization $+45^0$ and other -45^0 respectively, the Jones matrix of the SLM device is calculated. This method is efficient compared to the existing one which requires four shots to calculate the Jones matrix elements.

Introduction

Liquid Crystal (LC) Spatial Light Modulator (SLM) is a device capable of spatially modulating the amplitude and phase of light by virtue of 2-D array of discretely addressed the (LC) cells through the application of voltage proportional to the gray level displayed through a digital controller / computer. They are so versatile that they became indispensable part in innumerable applications such as Digital Holography [1], Wavefront Shaping [2], Computational Ghost Imaging and Phase Conjugation etc require the use of the SLM. However, before one can use the SLM in any of these applications, one need to characterize its properties and calibrate it.

Many methods are available to characterize the SLM [2]. Here we propose double shot interferometric polarimetry to find out the Jones matrix of the SLM. If we know the Jones matrix of SLM corresponding to every gray level that we display for modulation, we can predict the behavior of the SLM very accurately. Therefore, this method is essential and it gives us complete information about the SLM.

At one gray level, to measure the corresponding Jones matrix, the proposed method requires two recordings of interference of modulated light with the vector reference beams, by illuminating the device with input light having linear states of polarization of $+45^0$ and -45^0 respectively. In each recorded interference image, a mesh-like carrier frequency modulated pattern formed by the interference of the two orthogonal reference waves (X and Y) with their corresponding field components in the light modulated by the SLM. To record such interference patterns we used the experimental setup shown in Fig. 1.

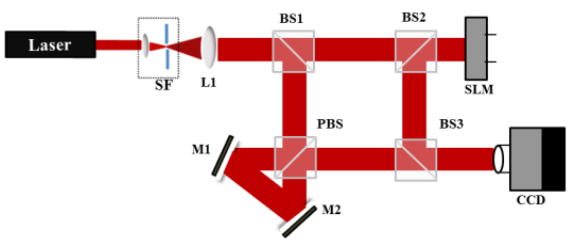

Fig 1 Experimental setup

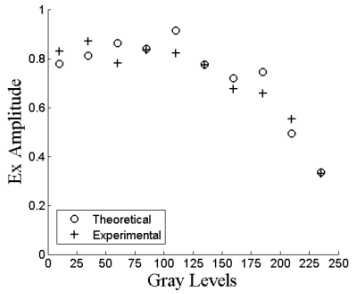

Fig 2 Variations of Electric Field with respect to the gray levels

Theory

Let us assume Jones vector with components along X and Y directions, for the incident coherent light to be $U = \begin{bmatrix} U_x \\ U_y \end{bmatrix}$, where U_x and U_y are complex phasors. The modulation of the light using SLM device under particular gray level is described by a 2×2 Jones matrix J , such that the output Jones vector E is related to the input Jones vector through the matrix equation $E = JU$[3-5]

$$\begin{bmatrix} E_x \\ E_y \end{bmatrix} = \begin{bmatrix} J_{xx} & J_{xy} \\ J_{yx} & J_{yy} \end{bmatrix} \begin{bmatrix} U_x \\ U_y \end{bmatrix}$$

If we can characterize a given device by specifying its Jones matrix, we will then be able to understand completely the effect of that device on an incident wave with a specific state of polarization.

For $+45^0$ input polarized light $U = \begin{bmatrix} 1 \\ 1 \end{bmatrix}$, the output vector components can be written as Eq. (1-2)

$$E_x^+ = J_{xx} + J_{xy} \qquad (1) \qquad\qquad E_x^- = J_{xx} - J_{xy} \qquad (3)$$

$$E_y^+ = J_{yx} + J_{yy} \qquad (2) \qquad\qquad E_y^- = J_{yx} - J_{yy} \qquad (4)$$

Similarly for -45^0 input polarized light, the corresponding output vector components can be written as Eq. (3-4).

The Jones matrix elements for SLM corresponding to the particular gray level are derived using above four equations

$$J_{xx} = \frac{1}{2}(E_x^+ + E_x^-) \qquad\qquad J_{xy} = \frac{1}{2}(E_x^+ - E_x^-)$$

$$J_{yx} = \frac{1}{2}(E_y^+ + E_y^-) \qquad\qquad J_{yy} = \frac{1}{2}(E_y^+ - E_y^-)$$

The four field components given in Eq. (1)-(4) are retrieved through Fourier transform method of fringe analysis [6] of two recorded interferograms. In a similar fashion, Jones matrix components can be retrieved in two shots for each gray level to completely calibrate the SLM.

Results and Conclusion

We are able to record all four elements of the Jones matrix at one gray level using this two shots method. And by changing the gray level digitally and by repeating this method we found the Jones matrices for all the gray levels. Once we know the Jones matrices of the SLM at all gray levels, it is possible to predict the output electric fields by illuminating SLM with known input polarized light. Fig. 2 shows the X component of output electric field vector E_x variations predicted from the recorded Jones matrices by illuminating SLM with X polarized light and also it showed the good match with the experimentally recorded ones.

Reference

[1] Kohler, C., Schwab, X., Osten, W, Appl. Opt. 45, 960-967 (2006).
[2] Eng, S. H., Cai, D., Wang, Z., Alameh, K., & Jiang, W., (Proceedings of Conference on Optoelectronic and Microelectronic materials and Devices. (pp. 105-108) (2007)
[3] M. M. Sreelal, R. V. Vinu, and Rakesh Kumar Singh, Opt. Lett. 42, 5194-5197 (2017).
[4] Zhuo Wang, Larry J. Millet, Martha U. Gillette, and Gabriel Popescu, Opt. Lett.33, 1270-1272 (2008).
[5] V. Aparna, N. K. Soni, R. V. Vinu, and R. K. Singh, Proc. SPIE 10074,100741P (2017).
[6] Takeda, M., Ina, H. and Kobayashi, S, J. Opt. Soc. Am., 72, 156 (1982).

Hybrid Silicon Photonic Devices for Switching and Memory Applications

Rajesh Kumar*, Shubham Singh, Nadir Ali and Aditi Sharma

Indian Institute of Technology Roorkee, Roorkee-247667, India
**rajeshfph@iitr.ac.in*

Abstract- Silicon photonics is on the forefront to lead photonics technology for short and long reach optical communication. Multi-and fully-functional optical chips require integration of active and passive photonic components and devices on a single chip. Many photonic components and devices with extremely high performance have been demonstrated that can be integrated on a single chip and many are either missing or have poor performance. Photonic memories, buffers and switches that are non-volatile in nature and consume lesser power while having ultra-low footprint are in the category of later. The talk will focus on novel solutions potentially useful for chip to chip and long reach communication using non-volatile phase change material $Ge_2Sb_2Te_5$ integrated on silicon photonic platform. Such devices can be realized at current optical communication wavelength of 1.55 μm as well as emerging window of optical communication around 2 μm.

Keywords- Silicon photonics, phase change material, non-volatile memory, optical switches

1. Introduction

Photonics integrated circuits are envisioned to bring paradigm shift in short and long reach optical communication. Silicon photonics is the leading platform for integration of optical devices on a single chip because of its low fabrication cost, electronic–photonic integration, and compatibility with the Si microelectronics manufacturing process (CMOS). Optical devices have several advantages over the conventional electronic devices in terms of latency, power consumption and the bandwidth. However, so far, silicon is unable to deliver all the functionalities required for fully functional optical circuits. One of the possible solutions is to use hybrid combinations of different materials for the functionalities that silicon is unable to provide [1].

Here, we present a hybrid approach that can be used to realize non-volatile reconfigurable electro-optic/all optical devices such as memories, switches, couplers and routers, integrated on silicon-on-insulator (SOI) platform for Near and Mid-IR spectral region. Chalcogenide phase change material $Ge_2Sb_2Te_5$ (GST) is used as an active material to hybridize the Si waveguide. This material exists in two stable phases i.e. amorphous (a-GST) and crystalline (c-GST), and exhibits high optical contrast when switched between these phases (with switching time of sub-nanoseconds) using electrical/optical pulses. Due to non-volatile nature of GST no bias is required to sustain a particular state in reconfigurable optical devices [2].

2. Proposed Devices

By taking the hybrid approach various devices can be realized using GST as an active material on silicon platform. Here, we present the specimen optical devices namely an all-optical memory, and 1 × 2 directional coupler switch. A non-volatile all-optical phase change photonic memory device is designed by utilizing coupling between GST and Si waveguide at 1.55 μm wavelength [3]. Fig 1(a) shows the schematic view of memory device where Si waveguide is hybridized by placing GST on top of Si waveguide. GST dimensions are optimized in order to achieve maximum coupling of light between Si waveguide and GST layer. The field profiles for a-GST and c-GST with SOI waveguide are shown in Fig 1(b). The phase transformation of GST from a-GST to c-GST and vice-versa can be achieved by applying a pump laser source through input waveguide. The binary states ‘1’ (a-GST) and ‘0’ (c-GST) of memory are interchanged with the help of purely optical input. Due to high crystallization temperature (140℃) of GST, the data saved in the amorphous form remains stable for a long time and thus the non-volatile nature of memory is retained. The obtained contrast between the ‘0’ and ‘1’ memory states for the device is 7.5 dB. The dimensions of this device are very compact compared to the reported devices [4] which leads to ultralow power consumption. The idea of phase change is further exploited to obtain a memory with higher contrast. In this case, Si waveguide is etched and a 50 nm thick film of GST is embedded in the slot as shown in Fig 1(c).

Acknowledgement

We acknowledge the funding received from Faculty Initiation Grant-Indian Institute of Technology Roorkee and Science and Engineering Research Board – Department of Science and Technology, Govt. of India (File no.-ECR/2016/001350).

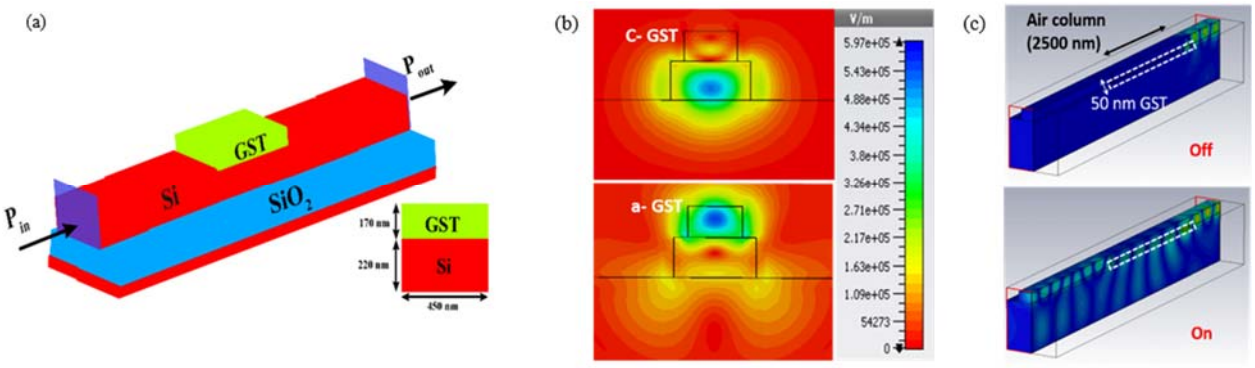

Fig. 1 (a) Schematic of GST on top of SOI waveguide, **(b)** field profile in two phases, and **(c)** hybrid air-GST SOI photonic memory

As an another example, we propose and present design and simulation analysis of a 1 × 2 directional coupler switch by enabling coupling between the Si and hybrid Si-GST waveguide at 2.1 µm wavelength [5]. As shown is Fig 2 (a), a 20 nm thick GST layer is embedded with partially etched Si waveguide. The normalized power transmission and power flow for the a-GST (cross state) and c-GST (bar state) phases are shown in Fig 2 (b) and (c), respectively.

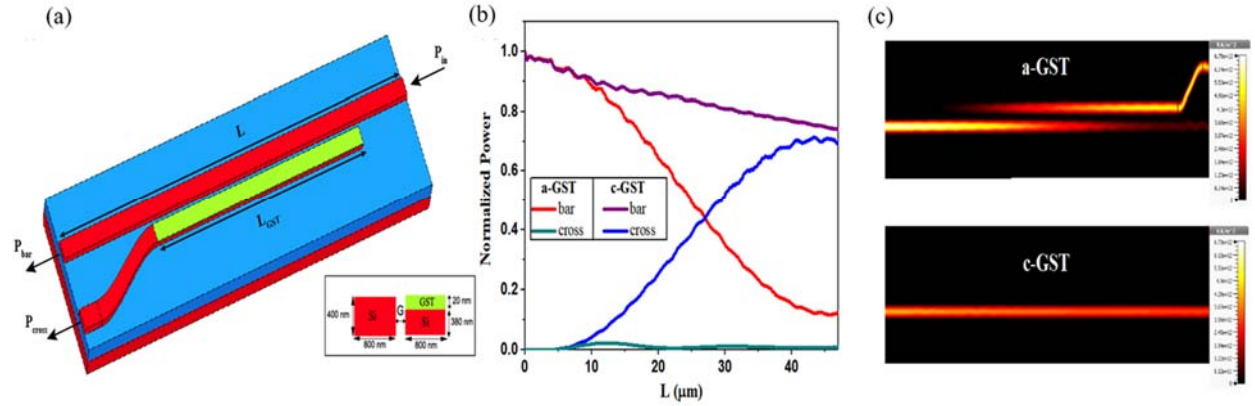

Fig. 2 (a) Schematic view of GST based 1 × 2 directional coupler switch, **(b)** calculated normalized transmission for a-GST and c-GST phases, and **(c)** simulated power flow for bar and cross state of the switch

3. Conclusion

We simulated and analyzed the photonic devices for memory and switching application by hybridizing SOI waveguide for currently used communication band at 1.55 µm and the emerging spectral band around 2.0 µm.

References

[1] G. T. Reed, G. Mashanovich, F. Y. Gardes and D. J. Thomson, Nat. Photon., 4 (2010).

[2] M. Wuttig, H. Bhaskaran, and T. Taubner, Nat. Photon., 11 (2017)

[3] S. Singh, N. Ali and R. Kumar, in the proceedings of PIERS, Singapore (2017)

[4] C. Rios et al., Nat. Photon., 9 (2015)

[5] N. Ali and R. Kumar, in Frontiers in Optics and Laser Sciences, Washington DC 2018 (Accepted)

OSI-ISO 2018 manuscript No.
(107)

Study of Photon Blockade Effect in Double Quantum Dot in a Semiconductor Microcavity

M. Singh · P. Jha · A. B. Bhattacherjee

Abstract We propose a scheme to implement a strong photon blockade with two interacting quantum dots, optically coupled to a semiconductor microcavity. The photon blockade effect is enhanced by simultaneously driving the microcavity and one of the two quantum dots with two classical laser fields. The mechanism associated with strong photon blockade is the quantum interference effect with different transition paths.This system has been found to be a tunable source of single or two-photon with applications in solid state quantum computation and quantum information processing.

Keywords Semiconductor microcavity · Quantum dot · Photon blockade

PACS 42.50.-p · 78.67.Hc · 78.67.-n

1 Introduction

The technological development of classical computing reaching the fundamental limit imposed by device miniaturization is one of the obstacles of Moor's Law [1].Over the past few years, quantum dots (QDs) have emerged as perfect candidates to overcome this limitation due to their narrow linewidths and their capability of implementing tunable optoelectronic devices. QDs optically

M. Singh
Department of Physics and Astrophysics, University of Delhi, Delhi-110007, India
E-mail: madhavkrsingh89@gmail.com

P. Jha
Department of Physics, DDU College, University of Delhi, New Delhi

A. B. Bhattacherjee
Department of Physics, Birla Institute of Technology and Science Pilani, Hyderabad Campus, India

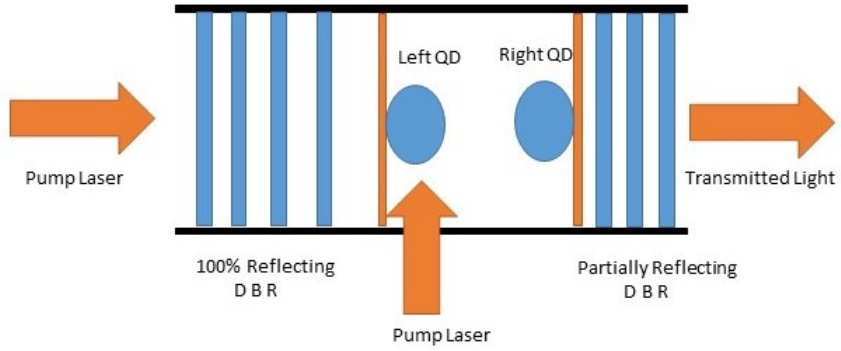

Fig. 1 Schematic picture of the system studied which comprises of two quantum dots embedded inside the semiconductor microcavity fabricated using Distributed Bragg reflectors (DBR).The microcavity and one of the quantum dots are simultaneously driven by external laser fields.

coupled to semiconductor microcavities provide an ideal system to study the field of cavity quantum electrodynamics. Recent studies have observed the strong coupling regime of cavity quantum electrodynamics in which the photonic mode of cavity and exciton modes of QD mix together to produce quasiparticles called polaritons [2,3,4]. Such strong interactions between QDs and microcavitities allow us to generate non-linear optics near the single photon level [5,6,7] and have plausible applications in the field of quantum networking and quantum information plateforms [8,9,10,11,12,13,14].

An important aspect for single photon manipulation is to achieve photon blockade. Photon blockade occur when one photon blocks the other photon transmission induced by quantum anharmonicity ladder of energy spectrum with strong nonlinear interaction between single photons corresponding to orderly output of photons leading to strong antibunching[15].

Multiple quantum dots (QDs) in a cavity is an important next step for various quantum information techniques[16,9,17]. Double QDs in a semiconductor microcavity provides a more complex system to analyze the physics useful in quantum application. In this paper by combining the tools of cavity electrodynamics with those of quantum dots, a novel scheme for generating strong photon blockade with a double QD coupled to a microcavity is proposed. The photon blockade mechanism is realized through multi-photon level.

2 Model and Hamiltonian

We consider here a system consisting of two quantum dots optically coupled to a semiconductor microcavity supporting a single field mode. The two quantum

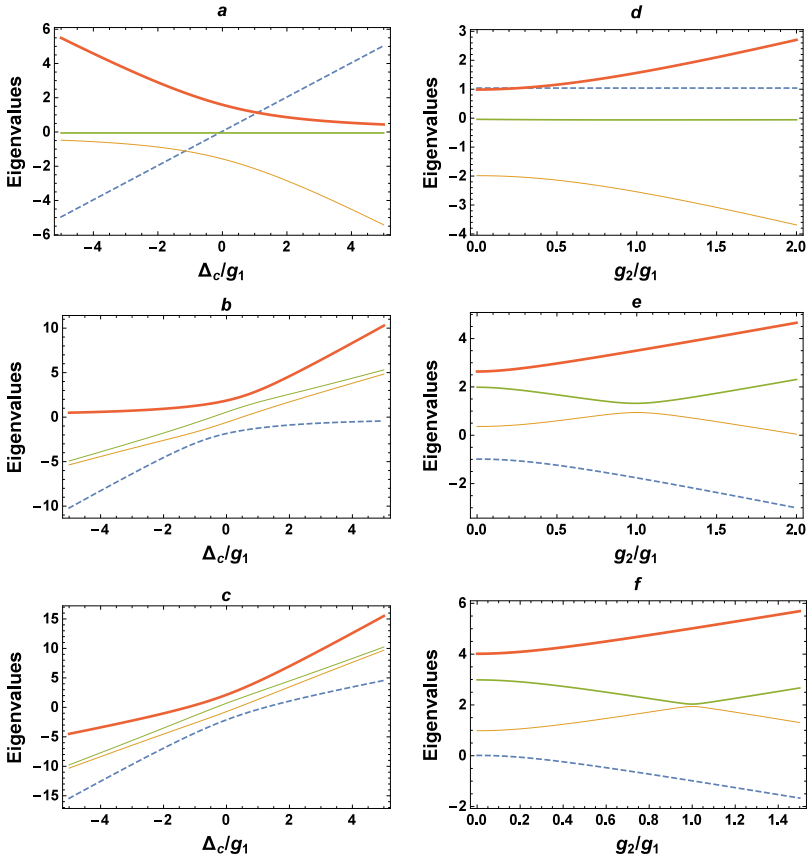

Fig. 2 Eigenvalues of Hamiltonian (2) as a function of $\frac{\Delta_c}{g_1}$ (a,b,c) for parameters $g_1 = 20GHz$,$\Delta_c = \Delta_{d1} = \Delta_{d2}$,$g_2 = 0.5g_1$,$J_z = 0.02g_1$ and $w_D = 0.02g_1$, one photon (a), two photons (b) and three photons (c). Eigenvalues as a function of $\frac{g_2}{g_1}$ (d,e,f) one photon (d), two photons (e) and three photons (f).

dots are also interacting with each other where each quantum dot is considered as an excitonic two - level system. The semiconductor microcavity can be fabricated with the help of a set of distributed Bragg reflectors (DBR). Light confinement is achieved by the combined action of DBR along the x-direction and air guiding dielectric which provides confinement in the y-z plane [18]. DBR mirror consists of quarter-wavelength thick high and low refractive index layers. The reflectance of DBR is proportional to the number of pairs and the difference between high and low index pairs [19]. The first and the last layers are AlGaAs. This enhances the coupling of light in/out of the structure since the refractive index of AlGaAs lies between those of GaAs and air [19].InAs quantum dots can be embedded inside the array of GaAs layers according to known techniques.

The Hamiltonian describing the coupled system is given by

$$H = \omega_c a^\dagger a + \frac{\omega_{d1}}{2}\sigma_z^{(1)} + \frac{\omega_{d2}}{2}\sigma_z^{(2)} + g_1(a^\dagger\sigma_-^{(1)} + a\sigma_+^{(1)}) + g_{(2)}(a^\dagger\sigma_-^{(2)} + a\sigma_+^{(2)}) + \eta(e^{-i\omega_p t}a^\dagger + e^{i\omega_p t}a^\dagger) + 2J_z\sigma_z^{(1)}\sigma_z^{(2)} + w_D[\sigma_+^{(1)}\sigma_-^{(2)} + \sigma_-^{(1)}\sigma_+^{(2)}] + \Omega_1(e^{i\omega_L t + i\theta_1}\sigma_-^{(1)} + e^{-i\omega_L t - i\theta_1}\sigma_+^{(1)}), \quad (1)$$

where $a^\dagger$ and a are the creation and annihilation operators of the cavity mode. Also $\sigma_+^k = \sigma_{ij}^k$ and $\sigma_-^k = \sigma_{ji}^k$ with $\sigma_{ij} = |i\rangle\langle j|$(k=1,2) are the QD spin projection operators with i, j labeling the two involved levels for the two quantum dots identified by the index $k = 1, 2$. $\sigma_z^k = |i\rangle\langle i| - |j\rangle\langle j|$ represent the population difference of the two levels in the two QDs. In the above Hamiltonian (with $\hbar = 1$), the first term represent the energy of the cavity having a frequency ω_c. The second term and the third term describes exciton energy in the first and second quantum dot having frequency ω_{d1} and ω_{d2} respectively. The fourth and the fifth term describes the QD optical cavity mode coupling where g_1 and g_2 are coupling strengths corresponding to the two QDs ($k = 1, 2$) with the semiconductor microcavity. The sixth term describes the optical pumping by a laser field with frequency ω_p and strength η. The seventh term describes the coloumb interaction that determine the static exciton-exciton dipole interaction energy and the eighth term explains the Föster interaction. Finally the ninth term accounts for additional pump field applied to the QD with index $k = 1$ with a frequency ω_L and provides a Rabi coupling strength Ω_1. Here θ_1 is the relative phase between the QD pumping field and the cavity driven field.

The Hamiltonian of the system in a frame rotating at driving laser frequency ω_p can be written as

$$H_{rot} = \Delta_c a^\dagger a + \Delta_{d1}\sigma_z^1 + \Delta_{d2}\sigma_z^2 + g_1(a^\dagger\sigma_-^1 + a\sigma_+^1) + g_2(a^\dagger\sigma_-^2 + a\sigma_+^2) + \eta(a^\dagger + a) + 2J_z\sigma_z^1\sigma_z^2 + w_D\sigma_+^1\sigma_-^2 + w_D\sigma_-^1\sigma_+^2 + \Omega_1(e^{i\theta_1}\sigma_-^1 + e^{-i\theta_1}\sigma_+^1), \quad (2)$$

where $\Delta_c = \omega_c - \omega_p$, $\Delta_{d1} = \frac{\omega_{d1}}{2} - \omega_p$, $\Delta_{d2} = \frac{\omega_{d2}}{2} - \omega_p$.
The above hamiltonian in absence of external pump and cavity driven field can be solved in closed subspace with eigenstate basis $|n, g^1, g^2\rangle$, $|n-1, e^1, g^2\rangle$, $|n-1, g^1, e^2\rangle$ and $|n-2, e^1, e^2\rangle$. Where n is the number of photon excitation, g^k and e^k are the ground and excited levels of the two QDs labelled as $k = 1, 2$.

3 Energy Eigenvalues and Photon Blockade

Eigenvalues of Hamiltonian (2) without external fields are plotted in Fig.2 as a function of $\frac{\Delta_c}{g_1}$ (a,b,c) and $\frac{g_2}{g_1}$ (d,e,f) for different photon numbers. Fig.2 shows

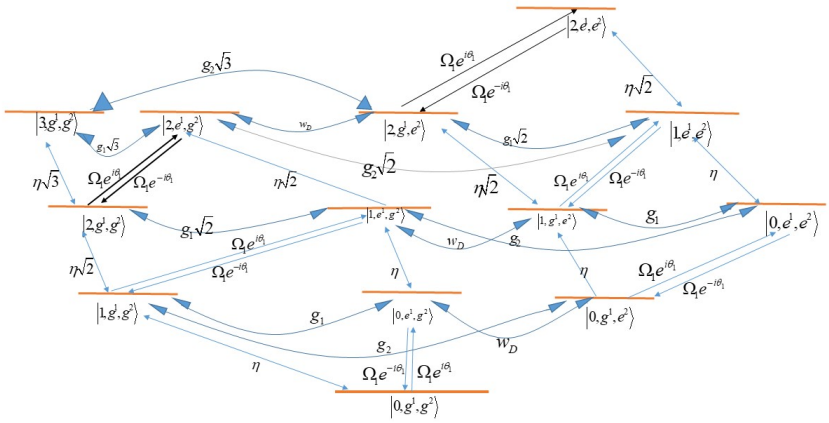

Fig. 3 Energy Level diagram of the dressed states in the coupled double quantum dot-cavity system and the transition paths for the Quantum Interference for photon blockade.

absence of avoided crossings (plots "a" and "d") for photon number $n = 1$. The eigenvalue plots as a function of $\frac{\Delta_c}{g_1}$ displays that avoided crossings appear at $\Delta_c = 0$ for $n = 2$ and $n = 3$. The eigenvalue plots as a fucntion of $\frac{g_2}{g_1}$ shows that avoided crossings appear at $\frac{g_2}{g_1} = 1$ for photon numbers $n = 2$ and $n = 3$.

In order to analyze the photon blockade effect, we will consider the statistical properties of photons in the microcavity, which can be obtained by zero-time second-order correlation function as

$$g^{(2)}(0) = \frac{\langle a^\dagger a^\dagger a a \rangle}{\langle a^\dagger a \rangle^2} \tag{3}$$

The second-order correlation function $g^{(2)}(0) < 1$ corresponds to the sub-Poissonian statistics, which signifies photon anti-bunching and hence photon blockade occurs.

The Hamiltonian described in equation(2) can not be diagonalized in closed subspace. The photon blockade phenomena in the system can be studied with the wavefunction

$$|\Psi\rangle = \sum_{n=0}^{\infty} C_{n,g^1,g^2} + \sum_{n=1}^{\infty} C_{n-1,e^1,g^2} + \sum_{n=1}^{\infty} C_{n-1,g^1,e^2} + \sum_{n=2}^{\infty} C_{n-2,e^1,e^2}, \tag{4}$$

where C_{n,g^1,g^2}, C_{n-1,e^1,g^2}, C_{n-1,g^1,e^2} and C_{n-2,e^1,e^2} are probability coefficients. Taking into account the phenomena of photon blockade effect we need to curtail the photons so all higher photon excitation with $n \geq 3$ are removed. With a condition $C_{3,g^1,g^2} = 0$ the three photon excitations are suppressed

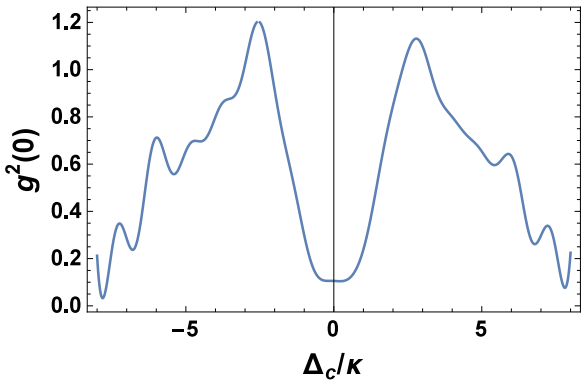

Fig. 4 The zero-time delay second order correlation function $g^{(2)}(0)$ as a function of cavity light detuning Δ_c/κ for parameters $g_1 = 4\kappa$, $g_2 = 1.5\kappa$, $J_z = 0.02\kappa$, $w_D = 0.02\kappa$, $\Omega_1 = 1.41\kappa$, $Cos(\theta_1) = 0.9891$,$\Delta_c = \Delta_{d1} = \Delta_{d2}$

resulting in only one or two excited photon in the nanocavity. So the wavefunction for the system can be expanded as

$$\begin{aligned}|\Psi\rangle = & C_{0,g^1,g^2}|0,g^1,g^2\rangle + C_{0,g^1,e^2}|0,g^1,e^2\rangle + C_{0,e^1,g^2}|0,e^1,g^2\rangle \\ & + C_{0,e^1,e^2}|0,e^1,e^2\rangle + C_{1,g^1,e^2}|1,g^1,e^2\rangle + C_{1,e^1,e^2}|1,e^1,e^2\rangle \\ & + C_{1,e^1,g^2}|1,e^1,g^2\rangle + C_{1,g^1,g^2}|1,g^1,g^2\rangle + C_{2,e^1,g^2}|2,e^1,g^2\rangle \\ & + C_{2,g^1,e^2}|2,g^1,e^2\rangle + C_{2,e^1,e^2}|2,e^1,e^2\rangle + C_{2,g^1,g^2}|2,g^1,g^2\rangle \\ & + C_{3,g^1,g^2}|3,g^1,g^2\rangle \end{aligned} \tag{5}$$

From the the wave function we obtain equations of motion for the probability coefficients from which we obtain their corresponding steady state solutions numerically. From the steady state solutions, we obtain the relative phase $(\theta_1)_{optimum}$ and Rabi coupling strength $(\Omega_1)_{optimum}$. The zero-time delay second order correlation function $g^{(2)}(0)$ as a function of cavity light detuning Δ_c/κ is shown in Fig. 4. It is noticed that $g^{(2)}(0)$ is asymmetric for red and blue detuning and shows strong photon blockade effect at $\Delta_c = 0$. The mechanism associated with strong photon blockade is the quantum interference effect with different transition paths as shown in Fig.3. For large value of detuning $g^{(2)}(0)$ drops to almost zero which cannot be attibuted to photon blockade mechanism. At large detunings, higher photon excitations are far off-resonant due to the anharmonicity of energy spectrum.

4 Full quantum model - master equation

The time dynamics of second order correlation function $g^{(2)}(\tau)$ as a function of time delay τ can be evaluated numerically in frame of master equations in Lindblad form using the quantum toolbox in PYTHON (QuTip, Release

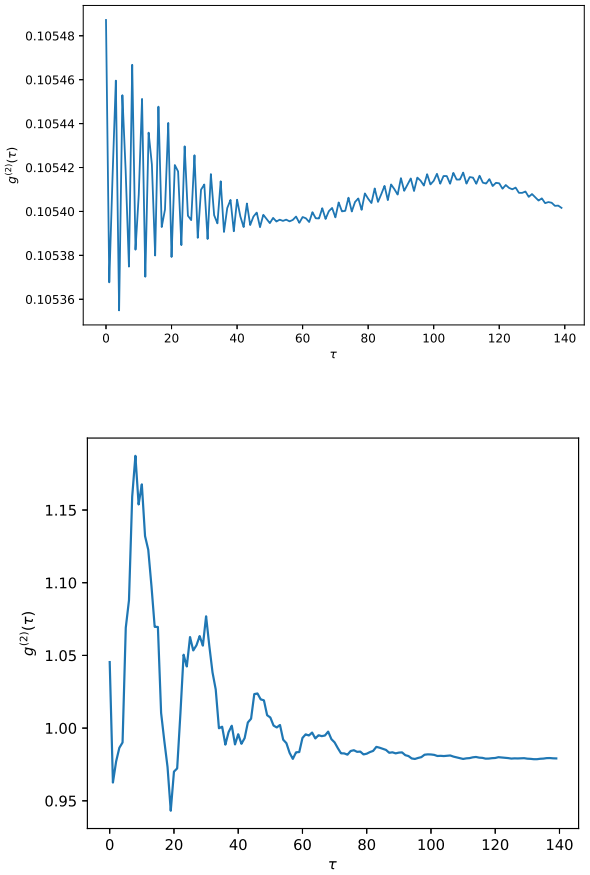

Fig. 5 Top plot: Second order correlation function $g^{(2)}(\tau)$ as a function of time delay τ at the point $\Delta_c = 0$ for $g_1 = 4\kappa; g_2 = 1.5\kappa; Cos(\theta_1) = 0.9891; \Omega_1 = 1.41\kappa; \gamma_{\parallel} = 0.05\kappa; \gamma_1 = \gamma_2 = 0.3\kappa; J_z = 0.02\kappa; w_D = 0.02\kappa$ and $\Delta_c = \Delta_{d1} = \Delta_{d2} = 0$. Bottom plot: Second order correlation function $g^{(2)}(\tau)$ as a function of time delay τ at the point $\Delta_c = 2.76\kappa$ for $\Delta_c = \Delta_{d1} = \Delta_{d2} = 2.764\kappa$ and other parameters same as that for top plot.

4.2.0) [20]. Since analytical solution of the master equation is very difficult, QuTiP provides a numerical solution of the density matrix $\rho(t)$.The master equation in the Lindblad form is written as

$$\frac{d\rho}{dt} = -i[H, \rho] + L(\rho), \tag{6}$$

where

$$L(\rho) = \frac{\kappa}{2}[2a\rho a^\dagger - a^\dagger a\rho - \rho a^\dagger a] + \sum_i \frac{\gamma_\parallel^i}{2}[\sigma_z^i \rho \sigma_z^i - \rho] + \sum_i \frac{\gamma_i}{2}[2\sigma_-^i \rho \sigma_+^i - \sigma_+^i \sigma_-^i \rho - \rho \sigma_+^i \sigma_-^i]. \quad (7)$$

Here, $\frac{\kappa}{2}$ is the cavity field decay rate. $\frac{\gamma_1}{2}$ and $\frac{\gamma_2}{2}$ are the total QD dipole decay rate including the spontaneous rate $\frac{\gamma_\parallel^1}{2}$ and $\frac{\gamma_\parallel^2}{2}$ into leaky modes and the pure dephasing rate γ^{1*} and γ^{2*} i.e $\frac{\gamma}{2} = \frac{\gamma_\parallel}{2} + \gamma^*$. .

Fig.5 displays the second order correlation function $g^{(2)}(\tau)$ as a function of time delay τ at the points $\Delta_c = 0$ (top plot) and $\Delta_c = 2.76\kappa$ (bottom plot) corresponding to the anti-bunching and bunching points of Fig.4 respectively. Anti-bunching effect with $g^{(2)}(0) < 1$ and $g^{(2)}(0) < g^{(2)}(\tau)$ indicates that the transmitted light is sub-Poissonian and antibunched. At $\Delta_c = 0$ (top plot) it is clear that the output light stay antibunched at all times. On the other hand at $\Delta_c = 2.76\kappa$ (bottom plot), $g^{(2)}(0) \approx 1.05$ and at later times does not satisfy the antibunching criterion $g^{(2)}(0) < 1$ and $g^{(2)}(0) < g^{(2)}(\tau)$.

5 Conclusions

In conclusion, we have proposed a new setup comprising of a double quantum dot in a semiconductor microcavity with simultaneously driving the cavity field and one of the quantum dots and realized strong tunable photon blockade. Photon statistics with strong antibunching effect have been observed by optimizing the relative phase θ_1 and coupling strength Ω_1. Specifically this system can be tuned to be a source of single or double photon with applications in various cavity quantum electrodynamics system.

Acknowledgements P.K Jha is thankful to DST for the financial support. A.B.B is grateful to BITS Pilani, Hyderabad campus for the facilities to carry out this research.

References

1. G.E.Moore, Progress in Digital Integrated Electronics, International Electron Devices Meeting, IEEE, pp.11-13 , (1975).
2. J.P.Reithmaier, G.Sek, A.Loffler, C. Hofmann, S.Kuhn, S. Reitzenstein, L.V.Keldysh, V.D.Kulakovskii, T.L.Reinecke, and A.Forchel, Strong coupling in a single quantum dot-semiconductor microcavity system, Nature **432**, 197 (2004).
3. T.Yoshie, A.Scherer, J.Hendrickson, G.Khitrova, H.M.Gibbs, G.Rupper, C.Ell, O.B.Shchekin, and D.G.Deppe, Vacuum Rabi splitting with a single quantum dot in a photonic crystal nanocavity, Nature **432**, 200 (2004).
4. E.Peter, P.Senellart, D.Martrou, A.Lemaitre, J.Hours, J.M.Gerard, and J.Bloch, Exciton-Photon Strong-Coupling Regime for a Single Quantum Dot Embedded in a Microcavity, Phys. Rev. Lett. **95**, 067401 (2005).
5. E.Waks and J.Vuckovic, Dipole Induced Transparency in Drop-Filter Cavity-Waveguide Systems, Phys. Rev. Lett. **96**, 153601 (2006).

6. D.Englund, A.Faraon, I.Fushman, N.Stoltz, P.Petroff, and J.Vuckovic, Controlling cavity reflectivity with a single quantum dot, Nature **450**, 857 (2007).
7. I.Fushman, D.Englund, A.Faraon, N.Stoltz, P.Petroff, and J.Vuckovic, Controlled Phase Shifts with a Single Quantum Dot, Science **320**, 769 (2008).
8. D.Bouwmeester, A.Ekert and A.Zeilinger, The Physics of Quantum Information (Springer, 2000).
9. A.Imamoglu, D.D.Awschalom, G.Burkard, D.P.DiVincenzo, D.Loss, M.Sherwin, and A.Small, Quantum Information Processing Using Quantum Dot Spins and Cavity QED, Phys. Rev. Lett. **83**, 4204 (1999).
10. A.Ekert, R.Jozsa, Quantum computation and shors factoring algorithm. Rev. Mod. Phys. **68**, 733 (1996).
11. E.Knill, R.Laflamme, G.J.Milburn, A scheme for efficient quantum computation with linear optics. Nature **409**, 46 (2001).
12. L.-M.Duan, M.D.Lukin, J.I.Cirac, and P.Zoller, Long-distance quantum communication with atomic ensembles and linear optics. Nature **414**, 413 (2001).
13. V.Scarani, The security of practical quantum key distribution. Rev. Mod. Phys. **81**, 1301 (2009).
14. J.L.O'Brien , A.Furusawa, J.Vučković, Photonic quantum technologies. Nat. Photon. **3**, 687 (2009).
15. J.Tang, W.Geng, and X.Xu, Quantum Interference Induced Photon Blockade in a Coupled Single Quantum Dot-Cavity System, Sci. Rep. **5**, 9252 (2015).
16. D.Bouwmeester, A.Ekert and A.Zeilinger, The Physics of Quantum Information (Springer, 2000).
17. S.-B.Zheng and G.-C.Guo, Efficient Scheme for Two-Atom Entanglement and Quantum Information Processing in Cavity QED, Phys. Rev. Lett. **85**, 2392 (2000).
18. J.Gudat, "Cavity Quantum Electrodynamics with quantum dots in microcavities", Phd. Thesis, University of Leiden (2012).
19. H.K.H. Choy, "Design and fabrication of distributed Bragg reflectors for vertical-cavity surface-emitting lasers", M.Sc. Thesis, Mc Master University (1996).
20. QuTip: Quantum Toolbox in Python, Version 4.2.0, (2017).

Analysis of Fiber Bragg Gratings

Ramesh Kumar[1], Anurag Sharma[1]
[1]*Department of Physics, Indian Institute of Technology Delhi*
E-mail address: asharma@physics.iitd.ac.in

Abstract: In this paper we discuss a new method for the analysis of fiber Bragg gratings (FBGs). This method is based on the collocation framework, and being a bidirectional method, it is inherently capable of dealing with reflections in multiple reflecting structures such as FBGs. In this method, the structure is assumed to be azimuthally symmetric and therefore, although the FBG is a 3D structure, the computational effort required is only for a 2D propagation problem in radial and longitudinal coordinates. The present method can treat the reflections in the uniform, chirped and the apodized FBGs. The azimuthal symmetry, however, precludes its use for tilted gratings or blazed FBGs.

Keywords: Fiber Bragg grating, reflections, transmission, optical fiber, collocation method.

1. Introduction

An FBG is a periodic perturbation written in the core of an optical fiber and it has further added a feature in an optical fiber for several new applications. It was first experimentally observed by KO Hill [1] that by exposing the core of an optical fiber by UV-light results in the perturbations of refractive index in the core of an optical fiber. FBGs offer a wide range of applications such as wavelength filters, mirrors and wavelength division multiplexers for communications. One of the most promising features of FBGs is the tunability of spectral characteristics. The narrow band reflection encouraged researchers for the applications such as strain and temperature sensing [2,3]. The undesirable spectral peaks, e.g., in fiber amplifiers, can be suppressed by using an FBG with a suitable apodization profile [4]. The tuning of the full width at half maxima (FWHM) is possible using a chirping profile [5]. It is possible to achieve a desired spectral characteristic by the designing the grating profile.

2. Results and Discussion

The analysis of FBGs is important to make a proper design. The transfer matrix method and the coupled mode theory (CMT) are often in use for the analysis of the FBGs [6]. However, in cases where the index contrast is high the CMT is no longer an appropriate choice for analysing FBGs.

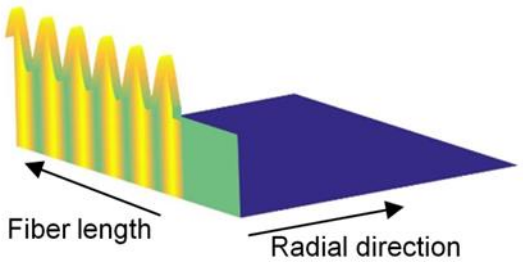

Fig.1: 2D Schematic of the fiber Bragg grating showing period variation of refractive index in the fiber length direction

We propose a new method for the analysis of the FBGs using the collocation formulation. The collocation method is bidirectional in nature and is capable of handling reflections in FBGs [7]. The collocation method for the planar structure is already reported in the literature [7,8]. The structure of the FBGs is assumed to be azimuthally symmetric and therefore, the wave equation for the azimuthally fileds involves only two variables, the radial and the longitudinal, making is an effective 2D propagation equation. This symmetry speeds up the computations for structures such as uniform, apodized, chirped FBGs. The method, therefore, can be for modelling FBGs for applications such as strain and the temperature sensing. As a test example, we have tuned the perturbation index and obtained the spectral response. Figure 1 shows the schematic of the FBG and Fig.2 shows the spectral response

for different index perturbation amplitudes. The response using the CMT is also included. The small difference in the results indicates the approximation made in the CMT. More results for apofized and chirped FBGs will be presented at the conference.

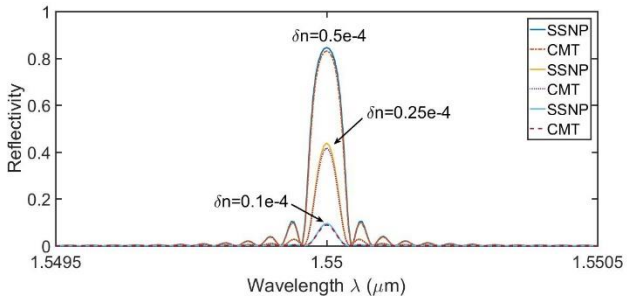

Fig-2 Spectral response of the fiber Bragg grating for three different amplitudes of the perturbation index in the fiber.

References

[1]. K. O. Hill, B. Malo, F. Bilodeau, and D. C. Johnson, Annu. Rev. Mater. Sci. 125, (1993).
[2]. S. Melle, K. Liu, and R. Measures, Appl. Opt. 32, 3601 (1993).
[3]. M. G. Xu, L. Reekie, Y. T. Chow, and J. P. Dakin, Electron. Lett., 29, 4 (1993).
[4].P. S. Cross and H. Kolgenik, Opt. Lett., vol. 1, pp. 43–45 (1977).
[5].F. Ouellette, Opt. Lett., vol. 12, no. 10, pp. 847–849(1987).
[6]. J. Chen, B. Liu, H. Zhang, Front. Optoelectron. China, vol. 4, pp. 204-212 (2011).
[7]. A.K. Taneja and Anurag Sharma, Opt. Quant. Electron. vol. 32, pp. 1033-1046 (2000).
[8]. Manmohan Singh Shishodia and Anurag Sharma, Opt. Commun. vol. 276, pp. 246-250 (2007).

OSI-ISO 2018 manuscript No.
(110)

Propagation Studies in Photonic Lantern Devices using Adiabaticity

Sugeet Sunder and Anurag Sharma

Received: date / Accepted: date

Abstract Adiabatic taper transitions tend to have very large device lengths. Beam Propagation Methods (BPM) have been employed to study propagation in such devices. Owing to large device lengths and stringent meshing requirements, these methods are computationally very intensive. We present an intuitive and computationally economical approach based on exploiting adiabaticity to deal with propagation in Photonic Lanterns. We compare our results with those reported using BPM.

Keywords Space Division Multiplexing, Photonic Lanterns, Single Mode Fibres, Adiabaticity

1. Introduction

Space Division Multiplexing (SDM) needs devices to couple light from spatially separated input sources (usually single mode fibers (SMFs)) to specific modes of a common output, like Few Mode Fibers (FMF) [1]. Several mode multiplexer devices have been reported in the recent years to satisfy this demand [2,3]. Photonic Lantern devices also used as mode-multiplexers, can be realized experimentally by considering an adiabatically tapered bunches of *n*-SMFs, such that the output of the bunch supports the *n*-modes of an *n*-moded FMF. These devices, owing to the stringent requirements of adiabaticity have very large device lengths, which scale quadratically with the number of cores. In this article we outline a fast, efficient and intuitive alternative to BPM to study propagation in such devices.

2. Propagation Algorithm

Let us consider a Photonic Lantern device with *n*-SMF inputs leading onto an *n*-moded FMF. Exciting an individual SMF core, implies exciting a superposition of the super-modes of the structure. Mathematically,

$$|l_m\rangle_z = a_{mn}|s_n\rangle_z \tag{1}$$

where, $|l_m\rangle_z$ represents the mode of the m^{th} SMF and $|s_n\rangle_z$ represents the supermodes of the combined structure at a certain point along the propagation direction 'z', while the matrix 'a' contains the expansion coefficients. The above equation assumes the Einstein summation convention. The adiabatic theorem asserts that these coefficients remain constant. In [4], the authors have shown a similar analysis for the case of efficient taper transitions in Photonic Crystals. This assertion can be exploited to find the field at any arbitrary position along the direction of propagation, simply by calculating the super-modes at that position and a prior knowledge of 'a'. Therefore, if we can calculate 'a' at $z = z_1$, then at any point $z = z_k$, the field propagating from the m^{th} SMF, can be calculated as,

$$|\psi\rangle_z = \sum_n a_{mn}|s_n\rangle_{z_k} e^{-\int_{z_0}^{z_k} i\beta_n(z)dz} \tag{2}$$

The propagation constants $\beta_n(z)$ are well behaved in adiabatic taper, they are calculated for different taper values and are interpolated based on the variation of the taper transition along the propagation direction. This is particularly useful in applying Shortcuts To Adiabaticity protocols (STA) [5], that could decrease the device length while preserving adiabaticity by considering non-linear taper transitions.

Sugeet Sunder
Indian Institute of Technology Delhi
sugeet@physics.iitd.ac.in,

Anurag Sharma
Indian Institute of Technology Delhi
asharma@physics.iitd.ac.in

3. Results and Discussions

Two different Photonic Lantern structures differentiated based on the functionality of mode-selectivity have been studied using the reported method and compared with the traditional Alternating Direction Implicit Finite Difference Beam Propagation Method (ADIFDBPM), implemented using MATLAB. The Photonic Lantern device parameters are detailed in Fig.1. The fields propagated for different adiabatic transitions yield same results in both the case using both the methods as shown in Fig.2.

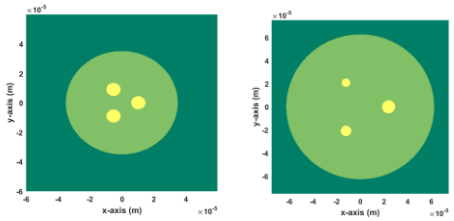

Fig.1 (a)(left) and (b)(right) are the cross-sectional refractive index profile at the input untampered end for the conventional lantern and the Highly mode-selective Photonic Lantern respectively. The structure in Fig.1a has three cores arranged on the vertices of an equilateral triangle, having equal cores with diameters of 8.75µm and refractive indices satisfying an NA of 0.12, for both the layers. It is tapered from 70µm to 14µm [2]. The Highly mode-selective structure shown in Fig.1b has dissimilar cores of diameters 11µm, 7µm and 8.8µm respectively. The NA for this case is 0.11 and it is tapered from 125µm to 14µm [3].

The reported method has many advantages compared to traditional BPM. It is flexible in the choice of meshing and grid size for different values of taper as opposed to BPM, thus reducing the error due to staircase approximation, which in BPM, increases monotonically. Further, to calculate the I/O characteristics for different taper transitions, we need to run the BPM simulation for every step all over again, while in the reported method, a new function for $\beta_n(z)$ in (2) would suffice. The computational time is reduced by over a factor of 10 with a four times higher resolution of the mesh.

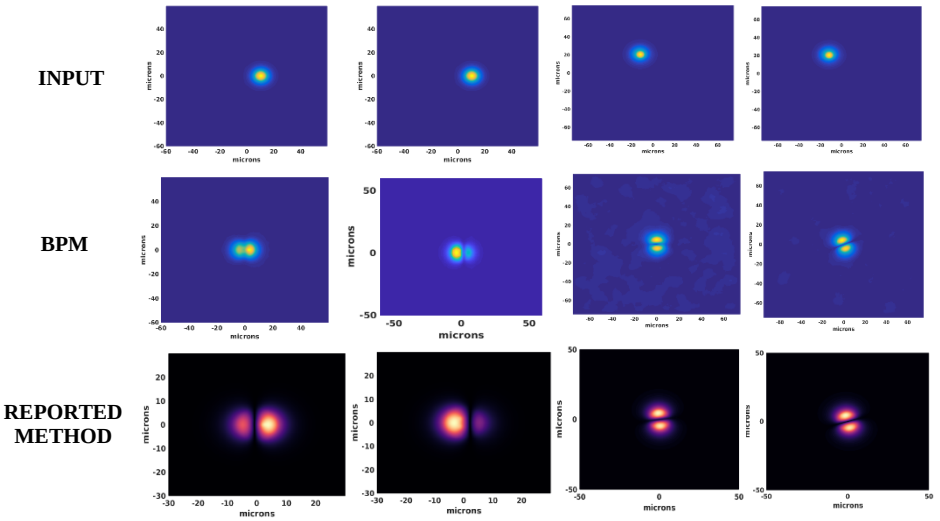

Fig.2 The figure shows a comparison between fields obtained from BPM and the reported method for various cases. Col.1 represents a linear taper and Col.2 represents a quadratic taper in the case of the conventional Photonic Lantern. The next two columns depict I/O characteristics of the highly mode selective Photonic Lantern under linear taper. In the third column the field is propagated up to 20mm while the fourth column up to 30mm. The grid sizes vary in the plots of the two methods. The axis units are in microns.

References

[1] Birks, T. A., S. Yerolatsitis, and K. Harrington. "Adiabatic mode multiplexers." (IEEE-OFC), (2017)

[2] Fontaine, Nicolas K., et al. "Geometric requirements for photonic lanterns in space division multiplexing." Optics express 20, 27123-27132, (2012)

[3] Shen, Li, et al. "Highly Mode Selective 3-Mode Photonic Lantern through Geometric Optimization." 2018 Optical Fiber Communications Conference and Exposition (OFC). IEEE (2018)

[4] Johnson, Steven G., et al. "Adiabatic theorem and continuous coupled-mode theory for efficient taper transitions in photonic crystals.", Physical review E, 66.6, 066608 (2002)

[5] Martínez-Garaot, Sofía, Juan Gonzalo Muga, and Shuo-Yen Tseng. "Shortcuts to adiabaticity in optical waveguides using fast quasiadiabatic dynamics." Optics express 25.1, 159-167 (2017)

OSI-ISO 2018 manuscript No.
(111)

Optical millimeter wave signal generation employing cascaded Polarization modulators

Baskaran Mahalingam . Santhoshi Gayathri T

Abstract Millimeter wave frequencies are becoming vital as they bolster a large number of applications requiring higher data rates. In this paper, we have demonstrated an external modulation based frequency multiplication technique for the generation of a 160 GHz millimeter wave signal. The proposed scheme which uses a 4 stage cascaded structure of Polarization modulators proves to be a lucrative solution since the chosen modulation index of 2.826 is phenomenally low. A precise choice of phase shifts between the cascaded stages, ensures 2 eighth order peaks spaced 160 GHz apart. This technique renders an Optical Sideband Suppression Ratio (OSSR) and Radio Frequency Spurious Suppression Ratio (RFSSR) of 65 and 45 dB respectively. Simulation results are verified from a mathematical standpoint. A higher Frequency Multiplication Factor (FMF) eliminates the requirement of a high frequency Radio Frequency Local Oscillator (RF LO).

Keywords Millimeter wave signal . Polarization modulators . OSSR . RFSSR

1 Introduction

Complexities at the lowest level, cost effectiveness and operational stability are the key factors that buttress the fact that frequency multiplication based external modulation techniques have been gaining a large attention in the recent years. Mach-Zhender modulators are most commonly utilized in photonic based microwave source generation approaches. An FMF of 16 was achieved through dual stage cascaded MZMs with the electrical and optical side harmonic suppression ratios of around 61 and 48 dB respectively [1]. One of our earlier proposed works on 16 tupling involving cascaded MZMs rendered an OSSR of around 54 dB [2].However all the MZM based techniques share the common shortcomings of practical values of Extinction Ratio and bias drifts. These effects of these drawbacks on the system performance is clearly explained in [3].

Polarization modulation schemes involving phase modulators can overcome these setbacks as they offer a higher independence to the effects of Extinction Ratio and bias drifts. Works involving phase modulators are very few in number. An MZI architecture with four linear phase modulators in parallel was suggested [4], to implement frequency octupling. The electrical phase shifts tend to deviate from the desired values due to the variable lengths of the interconnects from RF source to the modulators. All existing techniques based on phase modulators have only been able to achieve frequency octupling. In this paper, we have proposed a novel scheme to implement 16-tupling using phase modulators. A polarization modulator comprises of two phase modulators with their phase modulation indices being complimentary. The proposed work makes use of 4 polarization modulators in a cascade architecture. Since the optical path of the signal modulated by the laser source is the same, our scheme exhibits a cutting edge advantage over the dual arm architectures that suffer from power imbalances between the two arms.

Baskaran Mahalingam
St Joseph's Institute of Technology
E-mail: baski.maha@gmail.com

2 Methods involved and Results

Fig.1 depicts the block schematic of the proposed scheme.
Output after polarizer 1 is given by

$$E_1 = E_c e^{j\omega_c t}\{J_0(m) - 2J_2(m)\cos 2\omega_{rf}t + 2J_4(m)\cos 4\omega_{rf}t - 2J_6(m)\cos 6\omega_{rf}t + 2J_8(m)\cos 8\omega_{rf}t\} \quad [1]$$

$J_8(m)$ in the above equation has a negligible amplitude due to the choice of modulation index.
A phase shift of 45° is introduced between every successive stage. Output at the second stage is

$$E_2 = 2E_c e^{j\omega_c t}\{\frac{J_0(m)^2}{2} - [J_0(m)J_2(m) - J_2(m)J_4(m) + J_6(m)J_4(m) - J_6(m)J_8(m)]\big(\sin 2\omega_{rf}t - \cos 2\omega_{rf}t\big) - J_4(m)^2\cos 4\omega_{rf}t + [J_2(m)J_6(m) - J_2(m)^2]\sin 4\omega_{rf}t - [J_2(m)J_8(m) - J_0(m)J_6(m)]\cos 6\omega_{rf}t + [J_2(m)J_4(m) - J_0(m)J_6(m) - J_2(m)J_8(m)]\sin 6\omega_{rf}t + [J_0(m)J_8(m) + J_8^2(m)]\cos 8\omega_{rf}t - J_2(m)J_8(m)\cos 10\omega_{rf}t - J_4(m)J_6(m)\sin 10\omega_{rf}t\} \quad [2]$$

Fig.3 depicts the output spectrum at this stage suggesting us the presence of carrier, 2nd, 4th, 6th, 8th and 10th order harmonics.

$$E_3 = E_c e^{j\omega_c t}\{J_0^2(m) + [J_0^2(m)J_2(m) + J_2^2(m)J_0(m) - J_2^2(m)J_4(m) + J_4^2(m)J_6(m)]\sin 2\omega_{rf}t + [2J_6^2(m)J_4(m) - J_4^2(m)J_8(m) + J_0^2(m)J_6(m)]\cos 4\omega_{rf}t + [J_4^2(m)J_2(m) + J_2^2(m)J_0(m) + J_2^2(m)J_0(m) - J_2^2(m)J_8(m)]\sin 6\omega_{rf}t + [J_8^2(m)J_0(m) + J_0^2(m)J_8(m) + J_6^2(m)J_4(m) + J_2^2(m)J_4(m)]\cos 8\omega_{rf}t + [J_4^2(m)J_6(m) - J_4^2(m)J_2(m)]\sin 10\omega_{rf}t + J_4^2(m)J_8(m)\cos 12\omega_{rf}t + [J_8^2(m) + 2J_6^2(m)J_4(m)]\cos 16\omega_{rf}t\} \quad [3]$$

E_3 serves as the carrier to the final PolM. Proceeding in a similar fashion we obtain,

$$E_4 = E_c e^{j\omega_c t}\{[J_6^2(m)J_4(m) + J_2^2(m)J_4(m)]\cos 8\omega_{rf}t + [J_8^2(m) + 2J_6^2(m)J_4(m)]\cos 16\omega_{rf}t\} \quad [4]$$

Equations [1] [2] [3] and [4] are in great accordance with figures 2, 3, 4 and 5 respectively suggesting that mathematical derivations validate simulation results.
Fig. 5 depicts 2 strong 8th order sidebands with a frequency spacing of 160 GHz.

$$\text{OSSR} \approx 10\log_{10}[\frac{J_6^2(m)J_4(m) + J_2^2(m)J_4(m)}{J_8^2(m) + 2J_6^2(m)J_4(m)}]^2 \approx 64.8\text{dB}$$

$$\text{RFSSR} \approx 10\log_{10}[\frac{J_6^4(m)J_4^2(m) + J_2^4(m)J_4^2(m)}{2J_8^2(m) + 4J_6^4(m)J_4^2(m)}]^2 \approx 62\text{dB}$$

It is evident from Fig.5 that mathematically derived OSSR agrees well with the obtained simulation result. Fig.6 shows the obtained RF spectrum after photo detection. Sidebands having power levels below -60 dB do not need to be considered and hence the discrepancy between RFSSR obtained through simulation and through derivation can be ignored.

3 Conclusion

A 16 tupling technique for the generation of MM wave signals using polarization property has been proposed. The inherent drawbacks associated with MZM based schemes have been alleviated. The frequency tunability attribute of this scheme enables it to be extended in 60 GHz wireless applications. Optical and electrical side harmonic suppression ratios achieved are very high indicating that slight deviations under non ideal conditions would not undermine the quality of the generated signal. Advantages of lower RF LO frequency and an extremely low modulation index, makes the practical implementation of this technique feasible.

Acknowledgement The authors thankfully acknowledge Dr. K. Esakki Muthu, Assistant Professor of ECE, University VOC. College of Engineering, Tuticorin, for his useful suggestions and discussions.

References

1.K.Esaki Muthu,Frequency 16-tupled optical millimeter wave generation using dual cascaded MZMs and 2.5 Gbps RoF transmission, Optik, 140,338-346(2017)
2. M.Baskaran,Optical millimeter wave signal generation with frequency 16-tupling using cascaded MZMs and no optical filtering for radio over fiber system, Journal of European Optical Society, 14(2018), https://doi.org/10.1186/s41476-018-0080-1
3. Xiaogang Chen,Generalized study of microwave frequency multiplication based on two cascaded MZMs,Optik,127, 4061- 4067(2016)
4. Mehadi Hasan., "A photonic frequency octo-tupler with reduced RF drive power and extended spurious sideband suppression," Optics Laser Technology, 81, 115-121(2016)

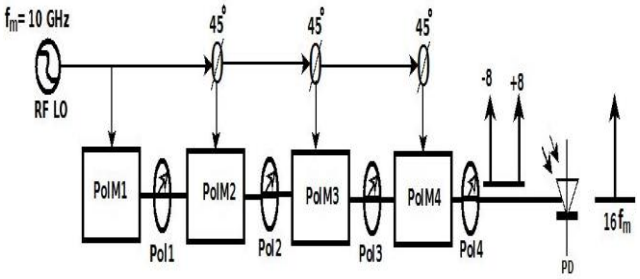

Fig.1 Block schematic of the proposed scheme

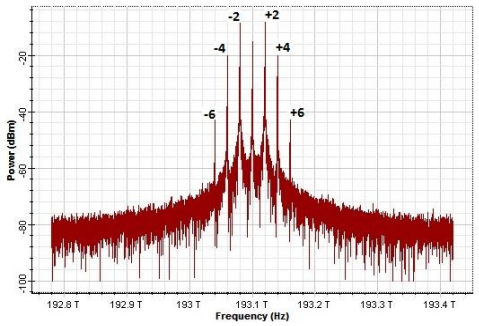

Fig.2 Output Spectrum of Polarizer 1

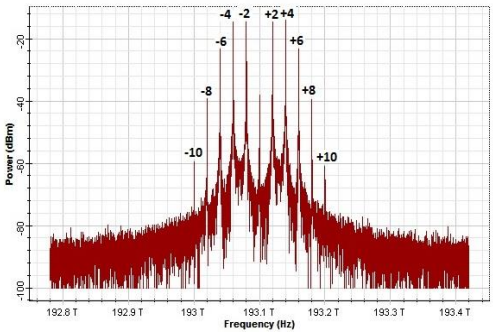

Fig.3 Output Spectrum of Polarizer 2

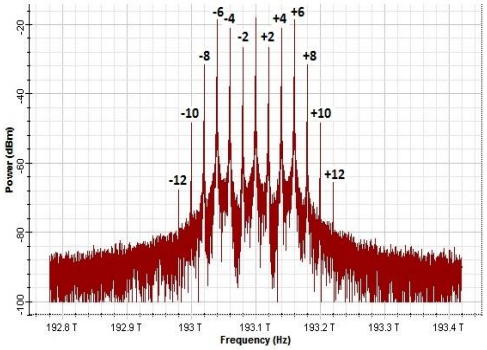

Fig.4 Output Spectrum of Polarizer 3

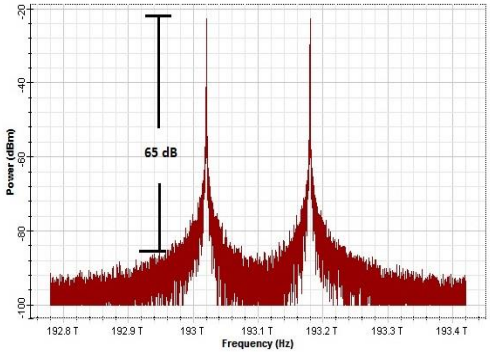

Fig.5 Output Spectrum of Polarizer 4

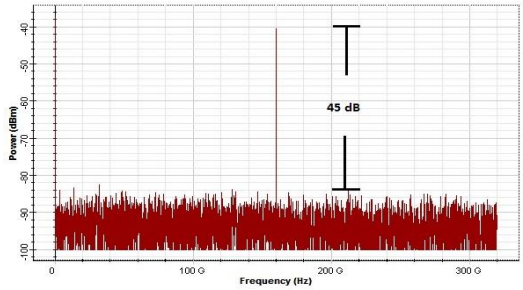

Fig.6 RF spectrum after photo detection

High Reflectivity Protective Silver Coating

Rouchin Mahendra[1,2], Ramesh Chandra[2]
[1]*Instruments Research & Development Establishment, Dehradun– 248 008, India*
[2]*Institute Instrumentation Center, Indian Institute of Technology, Roorkee-India*
Email: rmahendra@irde.drdo.in

Abstract

High reflectivity protective silver coating is desirable for military and space applications such as telescopes[1-2], opto-electronics systems like laser target designator, laser range finder etc. Bare silver based optics possess a very high reflectivity for wavelengths greater than 400nm, however bare silver gets tarnished in atmosphere. The paper reports the design and development of protective silver coating with an average reflectivity R>95% in the visible region, 97.5% @ 1064nm and 97.8% @1550nm. Adhesion test (MIL-C14806) was performed to validate the integrity of coated sample. The sample was placed in deionized water for 24hrs and no peeling of coating was observed.

Keywords: Silver coating, high reflectivity, optical coating

Experiment and Results

The silver coating was done on fused silica wafer using TFDS-462B e-beam coating system. The fused silica substrate was cleaned using ultrasonic cleaner in soap solution, acetone, isopropanol and deionized water and was dried using dry nitrogen. After the cleaning process the sample was prepared for coating. Most of the metals like gold, silver and aluminium have poor adhesion with the fused silica or glass substrates; therefore a buffer layer has to be added before the metal layer to improve adhesion. After depositing the buffer layer of nichrome, 100-200nm thickness of Ag layer was coated followed by protective oxide layers. The chromium acts as an adhesive for the silver thin film and nickel gives mechanical strength to the silver layer. A protective layer of AlN is coated followed by stack of SiO_2/HfO_2.The coated sample was tested with a UV-VIS spectrophotometer and found to have an average reflectivity of 95% in the visible region as shown in Fig1. The average reflectivity at 1064nm and 1550nm measured using Integrating sphere were 97.5% and 97.8% respectively. The design and development of the coating is done at an incidence angle of 45°. The deposition of metallic layers was done at a temperature of 50-60°C and at a vacuum of 10^{-6}torr, while during the deposition cycle of oxide layers the temperature was raised to 250°C and vacuum maintained at 2.5×10^{-4}torr.

The adhesion test[3] (tape test) of the protective silver substrate was done, and no peeling of coating was observed on the tape as shown in Fig 2.

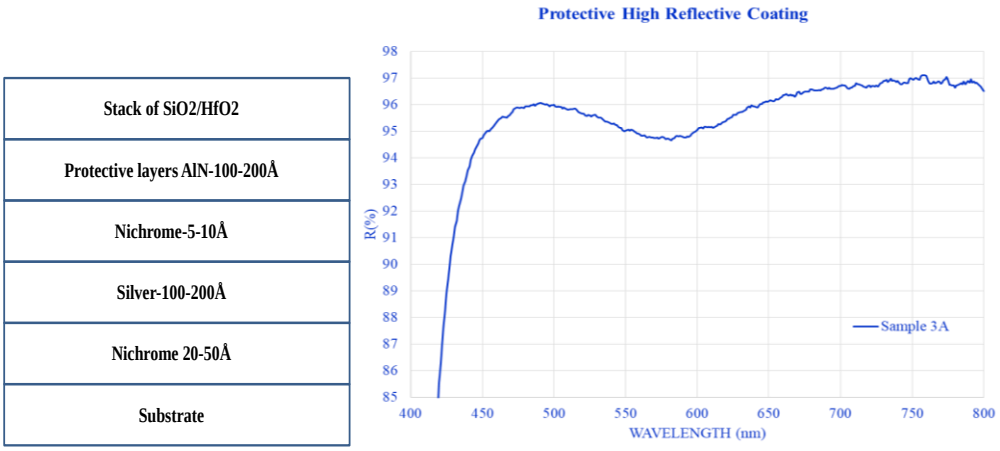

Fig 1: Schematic of durable silver coating and Reflection Vs Wavelength curve for protective silver in the visible region

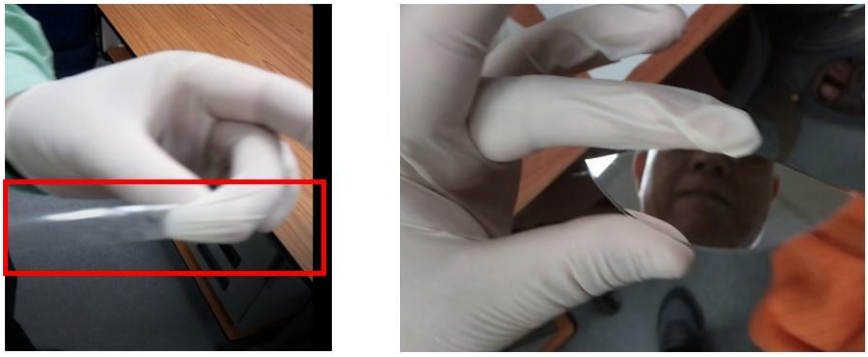

a b

Fig 2: Adhesion test of the silver coated sample: **a)** No coating traces on the tape **b)** Silver coated sample after adhesion test

Fig 3: Silver Coated sample dipped in DI water for 24hrs

The silver coated sample was dipped for 24hrs in de-ionized water and there was no peeling of the Ag coating from the test sample.

Conclusion

The reflectivity result of the silver coated samples is very encouraging. The adhesion of the silver was tested using a tape test. The sample was dipped for 24hrs and there was no peeling of the silver coating observed. The silver coating results are promising and will be useful for various optical components used in defence applications

Acknowledgement

The authors wish to acknowledge Director, IRDE for encouragement and grant of permission to submit this paper.

Reference

1.Chung-Tse Chu, Peter D. Fuqua, and James D. Barrie, "Corrosion characterization of durable silver coatings by electrochemical impedance spectroscopy and accelerated environmental testing", OSA, Vol 45, No.7,pp 1583-1593, 2006.

2. D Y Song, "Progress in the development of a durable silver based high reflectance coating for astronomical telescopes", Applied Optics, 24, 8, 1164-1170, 1985.

3. J.D. Rancourt, "Optical Thin films", SPIE optical engineering, pp 158-162, 1996.

Spectral Domain Optical Coherence Tomography for Diagnosis of Suspicious Oral Lesions –A Case Series

Prashanth Panta, Ambekar Yogeshwari Sanjay, Pawan Kumar, Renu John*

Indian Institute of Technology, Hyderabad

* Corresponding author: renujohn@iith.ac.in

Abstract

Optical Coherence Tomography (OCT) is a label-free imaging technique which provides volumetric information of tissues comparable to histology images. In this study, six different oral tissues were examined following incisional biopsy using Spectral Domain-OCT (SD-OCT) and the images were further reconstructed using in-house developed algorithm. The micro-anatomical structures like blood vessels, and the different layers of the oral mucosa (keratin layer, epithelium, epithelium-connective tissue interface (rete-peg outline) and underlying lamina propria) are clearly delineated. Our results highlight the potential of OCT as a quick screening tool for oral malignancies, particularly for screening oral potentially malignant disorders, which have a high risk of oral cancer development.

Keywords: SD-OCT, oral cancer, oral potentially malignant disorders, optical diagnosis, early detection

OCIS Code: (110.0110) Imaging systems; (110.4500) optical coherence tomography.

Introduction

Optical Coherence Tomography (OCT) is a clinically adaptable, high-resolution, non-invasive, non-contact imaging modality that gives cross-sectional images of sample based on the intensity of backscattered light. It can be used in the early detection of various diseases including cancer. The backscattered light contains vital information about the subtle morphological changes within the tissue of interest. Oral cancer is among the most prevalent cancers globally, and India alone contributes to 1/3rd of the world oral cancer burden. Oral cancers are often diagnosed during late stage (III-IV), and identification at early stages (I-II) can improve patient survival remarkably. Early diagnosis of oral cancer is possible with OCT as oral cancers are primarily 'epithelial malignancies'. The subtle morphological changes in the epithelium that occur in the early stages of oral cancer, cannot be detected through visual examination, but can be easily picked up through OCT imaging, which has a depth of penetration of 2-3 mm. Moreover, OCT is the label-free approach. It can easily identify the micro-anatomical details within the suspected oral lesion with precise delineation of keratin layer, epithelium, basement membrane, and the supporting lamina propia.

Methods

Study were conducted on six different oral lesions, ranging from oral submucous fibrosis to oral cancers, using SD-OCT. Standard protocols were followed while handling the biopsy specimen. The clinical samples were transported in normal saline for imaging, and immediately after imaging they were transferred into 10% formalin and processed for histology. The respective OCT images were reconstructed from the interferograms using the in-house developed algorithm on a Matlab^{TM} platform, and are shown in the results section.

Results

The reconstructed OCT images clearly indicate highly scattering regions, angiogenesis and morphological changes in the tissues suspected for oral cancers. The results correlated with histological diagnosis by a pathologist. The clinico-pathological findings and corresponding OCT observations will be presented in this study.

Conclusion

The oral tissues that were included in this study consisted of a representative sample of oral lesions ranging from oral submucous fibrosis to oral cancers. The reconstructed SD-OCT images correlated well with histology. Our results indicate the potential of OCT in the early diagnosis of oral cancer, through screening of suspected oral lesions.

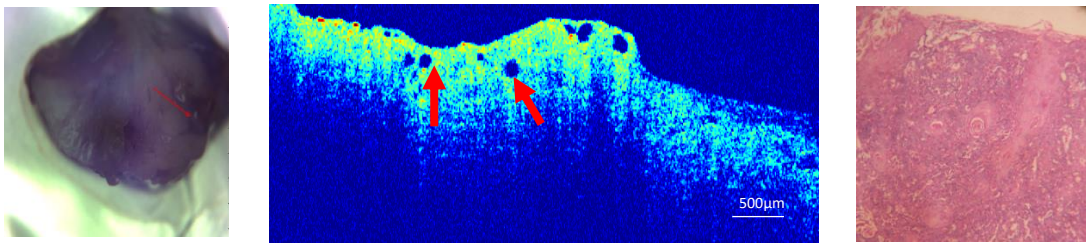

(a) (b) (c)

Fig.1 Oral Tissue Case I study, (a) Camera image of oral tissue (b) Reconstructed SD-OCT image using the developed algorithm (c) Histology image of sample. The SD-OCT image or oral cancer shows evidence of tumor-angiogenesis at different locations, a strong marker for cancer.

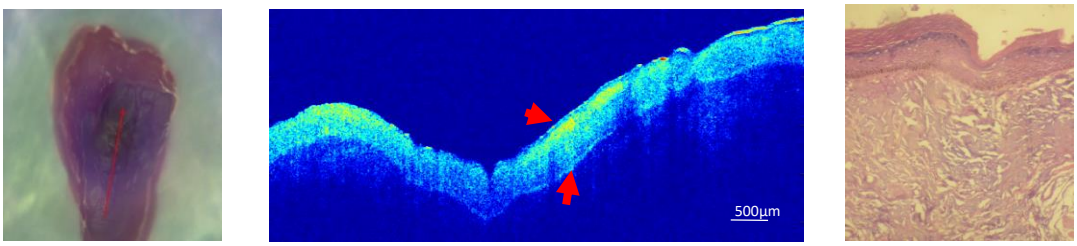

(a) (b) (c)

Fig.2 Oral Tissue Case V study, (a) Camera image of oral tissue (b) Reconstructed SD-OCT image using the developed algorithm (c) Histology image of sample. The SD-OCT image of oral submucous fibrosis specimen shows a flattening of rete-pegs, which correlated to histology images.

References

[1] Wilder-Smith P, Jung WG, Brenner M, Osann K, Beydoun H, Messadi D et al. In vivo optical coherence tomography for the diagnosis of oral malignancy. Lasers Surg Med. 2004; 35(4):269-75.

[2] Ali, M. and R. Parlapalli, Signal processing overview of optical coherence tomography systems for medical imaging. Texas Instruments, SPRABB9–June, 2010.

[3] Shield KD, Ferlay J, Jemal A, Sankaranarayanan R, Chaturvedi AK, Bray F et al. The globalincidence of lip, oralcavity, and pharyngealcancers by subsite in 2012.CA Cancer J Clin.2017; 67:51-64.

Spectroscopic Optical Coherence Tomography on Clinical Samples

Ambekar Yogeshwari Sanjay*, Pawan Kumar*, S. Anuradha Sekaran**, R. Pradeep**, Nageshwar Reddy**, Renu John*†

*Indian Institute of Technology Hyderabad

**Asian Institute of Gastroenterology, Hyderabad

† Corresponding author: renujohn@iith.ac.in

Abstract: Optical Coherence Tomography is a clinically adapted, high resolution, non-invasive, non-contact imaging modality that enables volumetric imaging of samples from the backscattered light. The reconstructed image of SD-OCT shown in this study gives the morphological information that lacks the biochemical property of tissue. To overcome this, Spectroscopic OCT is performed by post-processing the backscattered OCT data without any additional requirement of experimental set-up. An algorithm has been developed for time frequency analysis and spectroscopic metric mapping on the intensity OCT images using HSV mapping. In this study, we have shown the improvement in contrast by implementing the spectroscopic OCT algorithm on clinical samples. Different types of tissues have different properties, which can be differentiated using spectroscopic OCT. This could serve as a potential diagnostic tool for differentiating the tissue type and for detecting malignancies in tissues.

Keywords: Spectroscopic Optical Coherence Tomography, Spectral-domain Optical Coherence Tomography, OCT Clinical Application, Spectral-domain OCT data post processing

OCIS Code: (110.0110) Imaging systems; (110.4500) optical coherence tomography.

Introduction:

Optical Coherence Tomography is a label-free interferometric imaging modality that gives the depth-resolved structural information from backscattered light at different depths of the sample. Along with the morphological information (from typical OCT reconstruction method), functional information can also be extracted using Spectroscopic OCT method. The spectroscopic property of the sample can be extracted using the wavelength dependent absorption and scattering of the sample, present in the backscattered OCT raw data. In Spectroscopic OCT, the raw OCT data is post-processed using a different algorithm to extract the spectroscopic signature of the tissues. system. It doesn't require any extra hardware setup.

Methods

Spectral Domain OCT with central wavelength 930 nm and bandwidth of 100 nm is used for the stomach tissue analysis. The post-processing on the raw interferogram giving Spectroscopic OCT is achieved using the developed code in MATLAB. The Short Time Fourier Transform (STFT) with Gaussian window of size 80 pixels is applied on the normalized raw data to get the time frequency transformation. Spectral Centroid is calculated for every depth of A-scan and mapped it on the intensity OCT images to get the depth-resolved spectroscopic OCT images.

Results:

The spectral centroid metric is mapped on the intensity OCT image of the stomach tissue to give the spectroscopic property of the tissue. The wavelength coming from different depth depends on the property of tissue at that particular depth. In figure 1, there is structural loss (that may be malignant) the cyan color is visualized (figure 1d). The top layer of OCT image contains maximum reflection so it is visualized as the magenta color and the tissues where the structures are easily visualized gives the wavelength corresponding to the violet color (figure 1c). So this algorithm can be used

to detect the type of tissue, distinguish the cancerous part and non-cancerous part of tissue. The results from OCT are co-validated from histology data.

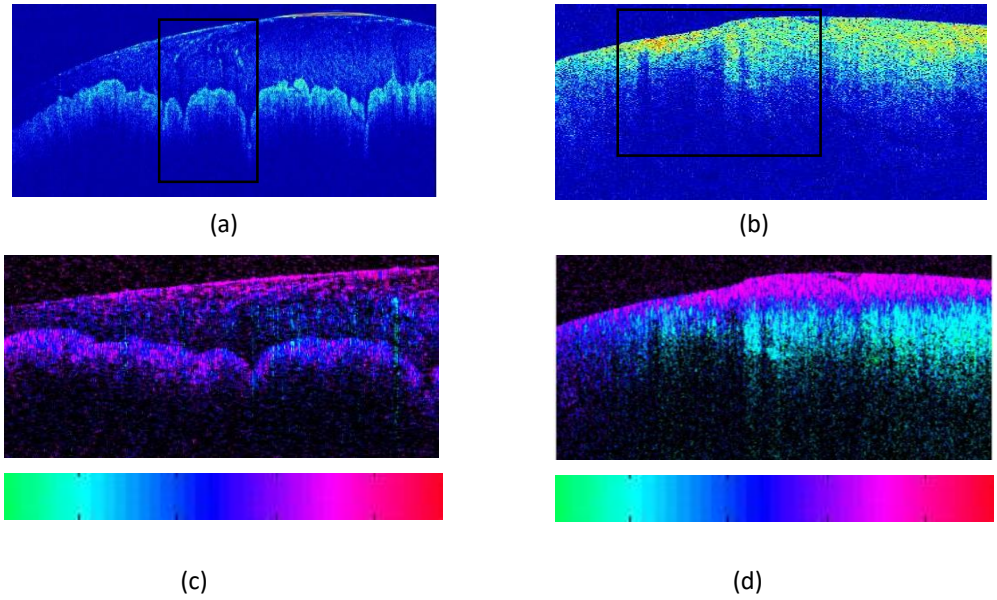

Fig. 1 (a) & (b) Intensity OCT images reconstructed from raw interferogram of normal part and the suspected part of stomach tissue (c) & (d) Spectroscopic OCT image corresponding to the data (shown in box) by spectral centroid mapping

Conclusion:

Spectroscopic OCT enhances the contrast of the OCT images. Advancement in this technique could be used to distinguish the normal and the suspected malignant tissues and margins.

References:

[1] Huang, D., et al., Optical coherence tomography. science, 1991. 254(5035): p. 1178-1181.

[2] Morgner, U., et al., Spectroscopic optical coherence tomography. Optics letters, 2000. 25(2): p.111-113.

[3] Jaedicke, V., et al., Comparison of different metrics for analysis and visualization in spectroscopic optical coherence tomography. Biomedical optics express, 2013. 4(12): p. 2945-2961.

[4] Amy L. Oldenburg et al., Spectroscopic Optical Coherence Tomography and Microscopy. IEEE Journal of selected topic in Quantum Electronics, VOL. 13, NO. 6, November /December 2007

[5] Hyeong Soo Nam & Hongki Yoo, Spectroscopic Optical Coherence Tomography: A review of Concepts and Biomedical Applications. Applied Spectroscopy Reviews (2017) http://dx.doi.org/10.1080/05704928.2017.1324876

Design and fabrication of modified double half wave band pass filter using alternately stacked TiO_2/SiO_2 multilayer

Mukesh Kumar [1, 2*], Neelam Kumari [1], Amit L Sharma [1], Vinod Karar [1,2]
[1]*CSIR - Central Scientific Instruments Organisation, Chandigarh, 160030, India*
[2]*Academy of Scientific & Innovative Research (AcSIR), CSIR-CSIO, Chandigarh*
*Corresponding author e-mail: mukeshk@csio.res.in

Abstract
Optical narrow band pass filters are widely used as wavelength division multiplexing components in fiber optic communications as well as for deriving a monochrome light source from a white light source in many optical instruments. In the present study, a multilayer band pass filter using 11 layers of alternate TiO_2 and SiO_2 were fabricated on a BK7 substrate using ion assisted electron-beam deposition technique. The filter was designed to have maximum transmission at 545 nm (Green) with adequate bandwidth to allow maximum energy transmission in the green wavelength band. The films were deposited in an oxygenated reactive environment at a vacuum level of 10^{-6} mbar. The fabricated filter was characterized using UV-Vis-NIR spectrophotometer to assess their suitability in wavelength specific filtering of light. The fabricated filter was found to have a bandwidth of 45 nm with a peak transmission of 91.5% at 545 nm.

Keywords: Vacuum Deposition, Band pass Filter, Spectrophotometer, Optical Coating

Introduction

Optical band pass filters have immense application in fiber optic based communication systems where multiple signals are encoded as specific wavelengths of light and then transmitted and decoded into the constituent signals at the destination [1]. Band pass filters are equally useful in monochromator, spectrophotometers and other optical characterization tools where wavelength selective filtering of white light source is required to derive a specific band of light signals. Optical thin film filters work on the principle of interference of light and usually consists of a stack of materials having alternately high and low refractive index [2]. Depending on the thickness and the refractive index of the constituent material, light waves emanating out of each interface of the multilayer stack can either interfere constructively or destructively giving rise to either reflective or anti-reflective properties respectively. TiO2 and SiO2 are the two most widely used material combination to fabricate optical interference filters owing to their excellent absorption-free film properties and complimentary residual stress patterns [3, 4]. For a band pass filter, usually the multilayer stack consists of quarter wave reflector stacks separated by a half wave spacer layer. In the present study, an 11 layer double half wave band pass filter has been designed and fabricated using ion assisted e-beam deposition technique.

Design of the Bandpass Filter

The bandpass filter was designed to pass 545 nm wavelength with a full width at half maximum (FWHM) bandwidth of 45 nm. The bandwidth and pass band wavelength was decided as per the requirement of an optical lighting system which derives different wavelengths from a white light source.

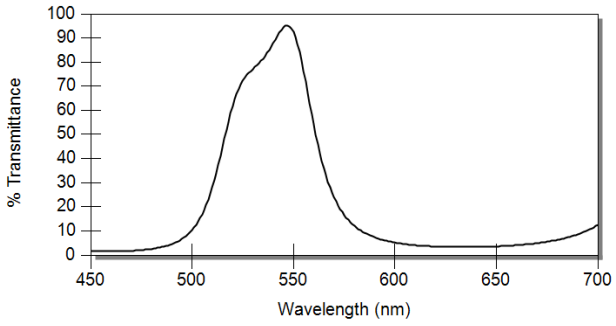

Fig. 1 Target optical spectrum of the band pass filter

The target optical spectrum of the bandpass filter as required by the user is as given in Fig.1. The structure of a basic double half wave band pass filter was considered as the starting design for this study. A double half wave band pass filter usually has following arrangements of constituents [1]:

Reflector | Half Wave | Reflector | Half Wave | Reflector

For a 11 layer design, the above arrangement was further expanded as given below where H indicates TiO_2 and L indicates SiO_2 layer:

(1H 1L 1H) | 2L | (1H 1L 1H 1L 1H) | 2L | 1H

Considering the target optical spectrum as shown in Fig. 1 as the optimization targets, the above design was optimized further to achieve the target spectra. Damped least square algorithm was used for this optimization process. After optimization, the following layer arrangement was achieved:

1.13H 1.00L .97H 1.97L .97H .98L .88H .78L .93H 1.98L .98H

Deposition of the Multilayer Structure

The material used for deposition was vacuum-grade 99.9% pure granulates of SiO_2 and tablets of TiO_2 (procured from Umicore Thin film Products). The fabrication of the multilayer was carried out using Ion Assisted dual e-beam Deposition (IAD) technique where two separate electron beam guns were used for evaporating SiO_2 and TiO_2 sequentially. During deposition, the substrate temperature was maintained at 150 ˚C by using a front quartz heater inside the chamber to achieve higher mechanical strength and absorption-free thin film structure.

Results

After deposition of the 11-layer structure on BK7, the sample was characterized using UV-Vis-NIR spectrophotometer (Cary 7000, Make: Agilent) and the optical spectrum as observed is given in Fig. 2.

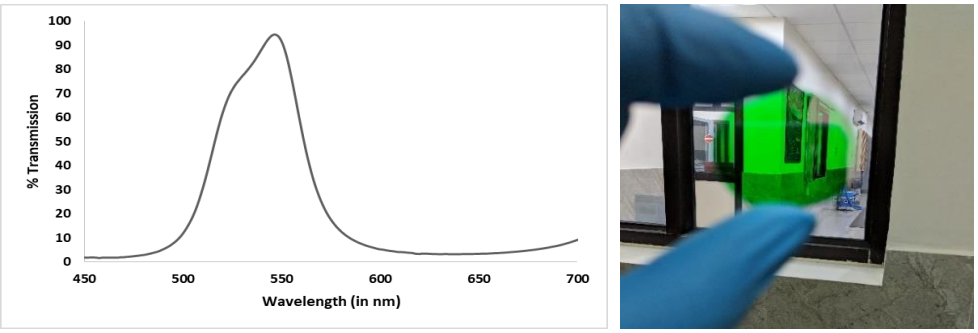

Fig. 2 Measured optical transmission spectrum of the fabricated filter (with the photograph of the filter)

Conclusion

It was observed that the measured optical spectrum is in agreement with the simulated data as well as the target spectrum showing excellent reproducibility of the simulated data on to the actual filter. The fabricated filter has multiple applications in the areas of astronomy, biomedical imaging and optical instrumentation.

References

1. H. A. Macleod, *Thin-film optical filters* (CRC press, 2001).
2. P. W. Baumeister, "Optical coating technology," Lecture notes for the five-day short course engineering **823**, 7-4 (2004).
3. M. Kumar, N. Kumari, P. K. Rao, V. Karar, S. Ramagopal, and A. L. Sharma, "Multi-layer dielectric thin-film optical filters for beam folding applications," in *International Conference on Optics and Photonics 2015* (International Society for Optics and Photonics2015), p. 96540F.
4. M. Kumar, N. Kumari, A. L. Sharma, and V. Karar, "Ion assisted deposition of silica-titania multilayer optical filter for beam steering of nd:Yag laser," Vacuum **155**, 142-146 (2018)

OSI-ISO 2018 manuscript No.
(116)

Tamm-plasmon-polaritons in period doubling sequence based 1D photonic crystals

Mukesh Kumar Shukla · Anupa Kumari · Ritwick Das

Abstract We explore the possibility of existence for Tamm-plasmon-polariton (TPP) modes in period-doubling sequence (PDS) based one dimensional photonic crystal. Certain photonic bandgaps (PBGs) allows TPP-like modes to exist which are primarily dependent on reflection phase. The study also draws a comparison between the propagation characteristics of TPP-like modes in a PDS and that in a conventional periodic photonic crystal.

Keywords Bragg reflectors · Surface waves · Tamm-plasmon-polaritons

Photonic crystals, which exhibit photonic bandgaps (PBGs) by virtue of periodic modulation of refractive index, is now been utilised for various applications. Amongst them, the most important one is the high reflecting broadband dielectric mirrors [1]. Interestingly, periodic multilayers such as distributed-Bragg-reflectors (DBRs) support Tamm-plasmon-polariton (TPP) modes when they share an interface with a thin plasmon-active metal film. In this work, we show that the TPP modes could exist at the interface of an aperiodic sequence such as period doubling sequence (PDS) and a metal.
We have considered two dielectric materials namely SiO_2 (A) and Ta_2O_5 (B) with thickness d_A and d_B respectively. The material dispersion is taken from [1]. In order to obtain the reflection spectrum, we employed the standard transfer matrix approach. We have considered a plane electromagnetic wave which is assumed to satisfy the condition $k_A d_A = k_B d_B = \pi/2$ where $k_A = \frac{\omega}{c} n_A$ and $k_B = \frac{\omega}{c} n_B$ are the wave-vectors in A and B respectively. It could be seen in Fig. 1(c) that conventional DBR with unit cells $N = 10$ exhibits a PBG in the visible ($580 - 720\ nm$) wavelength region with $d_A = 125\ nm$ and $d_B = 60\ nm$. A 30 nm thick Ag layer placed adjacent to the DBR gives rise to a sharp drop in reflectivity within the PBG at $\lambda_r = 661\ nm$ which could be observed in Fig. 1(c)(solid line). In Fig. 1(d), we plotted the intensity of

School of Physical Sciences, National Institute of Science Education and Research, HBNI, Jatni - 752050, India. E-mail: mukesh.s@niser.ac.in

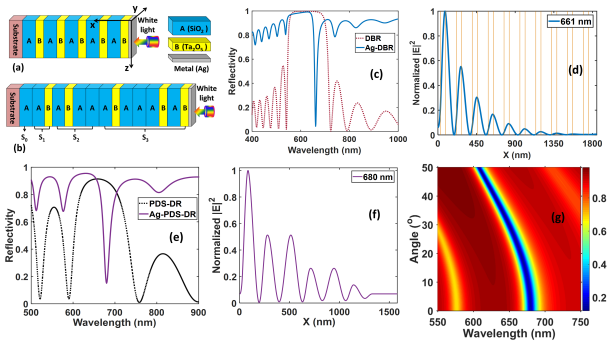

Fig. 1 Schematic and reflection spectra of Ag-DBR as well as Ag-PDS-DR are shown in the (a), (c) and (b), (e) whereas (d) and (e) represents the field variation of the corresponding TPPs respectively. (g) represents the angle dependence of the TPP mode in PDPhC-Ag.

the normalised mode-field distribution which depicts a decaying envelope as one moves away from 'Ag-DBR' interface. In a similar manner, we analyse a period-doubling sequence (PDS) based 1D photonic lattice which could be generated with the formula $S_{n+1} = S_n S_n^\dagger$ and $S_{n+1}^\dagger = S_n S_n$ having $S_0 = A$ and $S_0^\dagger = B$ [2]. The inflation rule for this sequence is $A \rightarrow AB, B \rightarrow AA$. After n iterations, the total sequence length would be 2^n. A few strings could be expressed as $S_0 = A; S_1 = AB; S_2 = ABAA; S_3 = ABAAABAB$. We construct a PDS based 1D-photonic crystal (PDS-DR) which appears as $S_0S_1S_2S_3$ or $AABABAAABAAABAB$. The corresponding reflection spectrum is shown the Fig. 1(e). Interestingly, the PDS exhibits a PBG extending from $\approx\ 600 - 760\ nm$. Its origin could be traced to long range correlations which coherently add the backscattered waves. The strength of coherent addition defines the sharpness of band-edges encompassing the PBG. With a 30 nm Ag film placed adjacent to PDS-DR, the reflection spectrum shows a discernible reflectivity drop at $\lambda_r = 680\ nm$ within the PBG which is a distinct signature of TPP-like mode excitation. In order to confirm, we plotted the mode-field distribution at $\lambda_r = 680\ nm$ (in Fig. 1(f)) which exhibits a maxima at the metal and PDS-DR interface and decaying envelope as one moves away from the interface. It is interesting to observe that the oscillatory field (with a decaying envelope) has *period* which is twice that for a conventional DBR. This could be attributed to double-period sequence of PDPhC. The TPP-like excitation in Ag-PDS-DR configuration exhibits similar (but non-identical) angular dispersion in comparison with conventional TPP mode [3]. This is depicted in Fig. 1(g) which exhibits a blue-shift at wider angles of incidence . The TPP-like resonance in Ag-PDS-DR geometry is, however, appreciably broad as compared conventional TPP resonance owing to smaller micro-cavity finesse.

References

1. S. A. Maier, Plasmonics: Fundamentals and Applications, Springer (2007).
2. W. Steurer and D. Sutter-Widmer, J. Phys. D: Appl. Phys., 40 R229 (2007).
3. M. K. Shukla and R. Das, Opt. Lett. 43, 362-365 (2018).

Investigation of polarization structure of vector vortex beams upon scattering

Srinivas Pachava[1,2], Nijil Lal[2,3], Nirmal K Viswanathan[4], RP Singh[2], Balaji Srinivasan[1,*]
[1]*Department of Electrical Engineering, IIT Madras, Chennai 600036, India*
[2]*Physical Research Laboratory, Ahmedabad, Gujarat 380009, India*
[3]*Indian Institute of Technology Gandhinagar, Palaj, Gandhinagar 382355, India*
[4]*School of Physics, University of Hyderabad, Hyderabad 500046, India*
**E-mail: balajis@ee.iitm.ac.in*

Abstract: We generate optical vector vortex beams with definite polarization structure using a Sagnac interferometer and propagate them through a ground glass diffuser. The scattered radiation observed at the Fourier plane is found to retain its intensity profile as well as the polarization structure.
Key words: Vector vortex beams, scattering, polarization.

1. Introduction:

Vector vortex beams possessing a spatially variant polarization state are used in various applications such as measuring the chirality of a medium [1], free-space optical communications [2], and study of the molecular orientations [3]. One of the common optical phenomenon we encounter in such applications is scattering. Properties of vector vortex beams including degree of polarization (DOP), speckle size, scintillation index have been studied when propagated through scattering medium [4] as well as a turbulent atmosphere [5] with the primary focus of mitigating the scattering effects and enabling robust transmission of light beams through the medium. However, the observations in such work were carried out in the normal spatial plane and not the Fourier plane. Gangi et al [6] reported the recovery of the vorticity of a light beam at the Fourier plane after scattering.

In this article, we have experimentally generated the vector vortex beam using a Sagnac interferometer-based setup and studied its scattering as it is transmitted through a ground glass diffuser (GGD). Upon imaging the scattered vector vortex beam in the Fourier plane, we find that the beam has recovered not only its intensity profile but also its polarization structure. Similar results are observed for a rotating GGD as well.

Experiment:

For our experiments, we used a modified polarizing Sagnac interferometer to generate vector vortex beam because of the inherent immunity of the common-path configuration to external perturbations [7]. The schematic of the experimental setup used is shown in Fig. 1(a), where a spiral phase plate (SPP) is used in the Sagnac loop to generate the vortex beam. The output of polarizing beam splitter (PBS) is a superposition of two linearly polarized vortex beams. The beam is then passed through a quarter wave plate (QWP_1) to convert linear polarization states to circular polarization states. The relative phase shift between the two circularly polarized components obtained because of PBS and QWP_1 is compensated using a half wave plate (HWP_2). The vector vortex beam represented in Equ. 1. is thus experimentally generated with SPP of topological charge 2 and QWP at an angle of 135^0 and the obtained intensity profile is shown in Fig. 1 (b).

$$E \propto e^{i2\emptyset}(\hat{x} - i\hat{y}) + e^{-i2\emptyset}(\hat{x} + i\hat{y}) \qquad (1)$$

The polarization structure of the vector vortex beam is experimentally verified using Stokes polarimetry [8]. The polarization map overlapped on the intensity structure is shown in Fig. 1(b), wherein the red, green and blue colours indicate right elliptical, left elliptical and linear polarization states respectively. The generated vector vortex beam is passed through the 600 grit GGD (Thorlabs Inc.). The scattered light from GGD is further analysed using Stokes Polarimetry.

We performed the experiment in two scenarios, one without rotating the GGD and one with rotating the GGD. In the former case, the polarization map which is overlapped on the intensity structure is captured at 22 cm away from GGD and is shown in Fig. 1(c). The beam exhibits speckled intensity and polarization patterns. If the scattered beam is imaged with a convex lens (f = 20 cm) in the Fourier plane, we observe that the intensity as well as polarization structure of the beam are recovered (Fig. 1(d)). Such an observation indicates that the scattered radiation preserves both the intensity as well as the polarization structures.

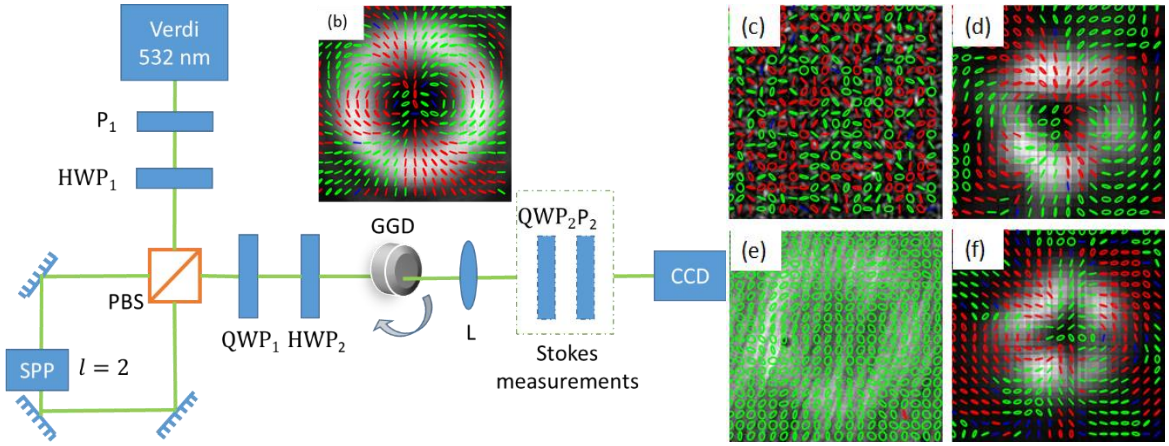

Fig. 1. (a) Sagnac interferometer to generate vector vortex beams, $P_{1,2}$: Polarizer, SPP: Spiral phase plate, $HWP_{1,2}$: Half wave plate, $QWP_{1,2}$: Quarter wave plate, PBS: Polarizing beam splitter, GGD: Ground glass diffuser, L: convex lens (f=20 cm). (b) Polarization map overlapped on the corresponding intensity profile of vector vortex beam, red, green and blue colours indicate right elliptical, left elliptical and linear polarization states respectively. Polarization map at 22 cm after GGD and at the focal plane of lens, (c) & (d) when GGD is not rotating, (e) & (f) when GGD is rotating.

We repeated the above experiment by rotating the GGD with some angular velocity so that the scattering profile is sampled across multiple locations. The output beam polarization map and intensity structure captured without the lens are shown in Fig. 1(e). In this case, the speckles got averaged out because of the non-zero speed of the GGD which resulted in ring intensity pattern with background intensity speckles. However, the polarization map is left elliptical in nature (perhaps due to a residual phase retardation) and does not resemble the input polarization map. On the other hand, when the scattered beam is imaged at the focal plane we observe that the intensity as well as polarization structure are preserved (Fig. 1(f)).

Based on the above studies, we conclude that the polarization structure of a scattered vector vortex beam is preserved along with the intensity structure. Such a result is consistent with the notion that the spin and orbit angular momentum for a vector vortex beam is coupled with respect to each other.

Acknowledgements:

The authors would like to thank Dr. GK Samantha from the Physical Research Laboratory for lending necessary components. Srinivas would like to acknowledge the Ministry of Human Resources Development (MHRD), Government of India for his PhD research assistantship.

References:

1. C. T. Samlan, R. R. Suna, D. N. Naik, and N. K. Viswanathan, Appl. Phys. Lett. **112**, 31101 (2018).
2. J. Wang, Photonics Res. **4**, B14 (2016).
3. L. Novotny, M. R. Beversluis, K. S. Youngworth, and T. G. Brown, Phys. Rev. Lett. **86**, 5251–5254 (2001).
4. S. G. Reddy, V. Kumar, R. P. Singh, and Y. Miyamoto, Opt. InfoBase Conf. Pap. 4–6 (2014).
5. W. Cheng, J. W. Haus, and Q. Zhan, Opt. Express **17**, 17829–17836 (2009).
6. G. R. Salla, C. Perumangattu, S. Prabhakar, A. Anwar, and R. P. Singh, Appl. Phys. Lett. **107**, (2015).
7. P. Srinivas, P. Chithrabhanu, N. Lal, R. P. Singh, and B. Srinivasan, Opt. Lett. **43**, 2579–2582 (2018).
8. D. H. Goldstein, *Polarized Light* (2010).

Stomach Cancer Detection Using Spectral Domain Optical Coherence Tomography

Pawan Kumar*, Mohamed Nijas*, Ambekar Yogeshwari Sanjay*, S. Anuradha Sekaran**, R. Pradeep**,

Nageshwar Reddy**, Renu John*†

* Indian Institute of Technology Hyderabad

**Asian Institute of Gastroenterology, Hyderabad

† Corresponding author: renujohn@iith.ac.in

Abstract: Optical coherence tomography (OCT) is a well-adapted imaging technique with applications in biology, medicine, and material investigation. OCT is capable volumetric imaging of tissues close to cellular resolutions. In this study we investigate the feasibility of OCT in tissue classification. We have carried out intra-operative imaging of surgically resected stomach tissues and report our results with correlated histology. OCT is able to differentiate normal and abnormal tissues present in the stomach lining. The scattering and morphological changes evident in OCT images are in agreement with histological reports. Results evidently prove the feasibility of optical biopsy using this technology to distinguish normal and abnormal mucosa of the stomach. The studies show the potential of OCT in surgical guidance, demarcation of cancer margins, and early diagnosis of oesophageal cancers in gastrointestinal endoscopic imaging.

Keywords: Spectral Domain Optical Coherence Tomography, OCT image reconstruction, OCT clinical application, GI endoscopy imaging, Stomach Cancer diagnosis.

OCIS Code: (110.0110) Imaging systems; (110.4500) optical coherence tomography.

Introduction:
Optical coherence tomography is an interferometric technique based on interference of the backscattered light from each layer of the sample to reconstruct depth resolved data. The key features of OCT in the medical field are real-time imaging, high acquisition rates, cellular-level resolution, spectroscopic feature extraction and a compact, non-invasive instrumentation. The variation in the morphology of the tissue can be used to determine the abnormality in the tissue.

Methods:
Stomach tissue study is carried out using Spectral Domain OCT (SD-OCT) with central wavelength 930 nm and bandwidth of 100 nm. The required protocol has been followed for tissue handling. The sample was kept in normal saline before imaging. The images were taken at the different cross-sections of the sample. After imaging, the sample was transferred to the formalin and sent for histology. The raw OCT interferograms obtained from the SD-OCT system are used to reconstruct the cross-sectional images using the in-house developed reconstruction code in MATLAB.

Results:
The reconstructed SD-OCT images from the raw data at different position of biopsy sample are shown in the figure 1. Figure (b),(c) and (d) show are the normal, marginal and tumorous region corresponding to the camera image shown in figure 1 (a) of the tissue sample. The morphological changes in the tissue at different region can be easily identified by the SD-OCT images. In normal region, typical mucosal epithelial structure can be observed with the gastric pits, gastric glands openings and other layers of cells below. The structural organization which is very clear in normal tissue starts disappearing in the marginal regions. In fully tumorous part there is a total structural loss with highly scattering tissue due to the presence of multinucleated cells and high nuclear to cytoplasmic ratios and angiogenesis. These structural variations can be effectively used in diagnosis of stomach cancer.

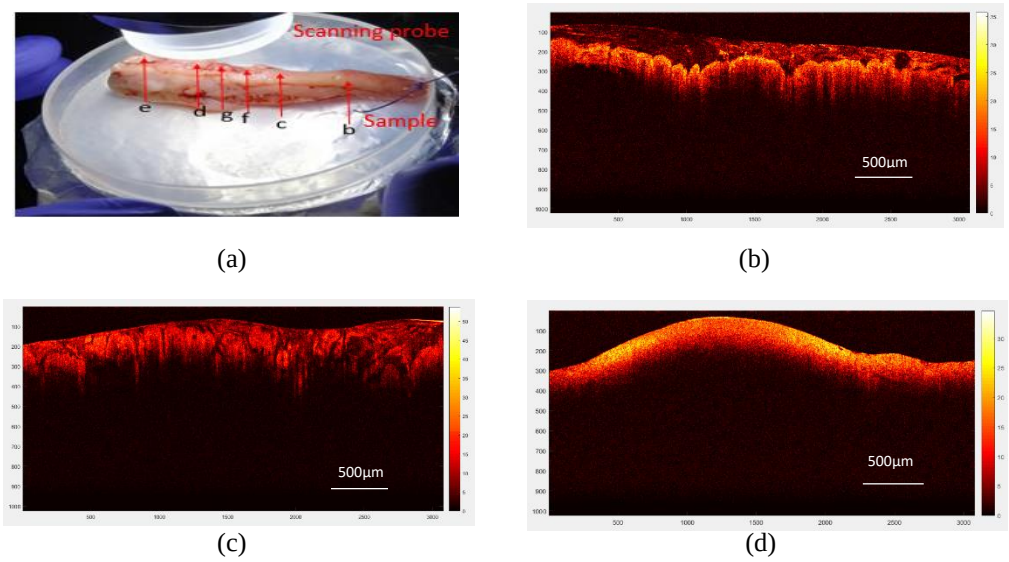

(a) (b)

(c) (d)

Fig. 1 (a) Shows the sample cross-section where OCT is performed (b) Normal tissue. (c) Transition stage, (d) Tumorous tissue

Conclusion:

Spectral domain OCT can be effectively used in demarcation of different types of tissues. The structural changes observed in this study can be used for identifying tumor margins and for early diagnosis of esophageal cancer. Results evidently prove the feasibility of optical biopsy using this technology to distinguish normal and abnormal mucosa of the stomach. The studies show the potential of OCT in surgical guidance in identifying clean tumor margins, and early diagnosis of oesophageal cancers in gastrointestinal endoscopic imaging.

References:

[1] Huang, D., et al., Optical coherence tomography. Science 254(5035): p. 1178-1181 (1991)
[2] Zahid Yaqoob, et al., Spectral domain optical coherence tomography: a better OCT imaging strategy, Bio Techniques (2005), https://doi.org/10.2144/000112090
[3] Wojtkowski M., High-speed optical coherence tomography: basics and applications, Applied Optics 49: D30-D61, (2010)
[4] Benjamin J. Vakoc, et al., Cancer Imaging by Optical Coherence Tomography: Preclinical Progress and Clinical Potential, Nature Reviews Cancer 12.5: 363–368 (2012)

OSI-ISO 2018 manuscript No.
(119)

Particle fallout measurements on optical surfaces in cleanrooms using non contact profilometer

Annie Varghese · Suresh Venkata · S Kathiravan · Shalabh Mishra · Raghavendra Prasad B

Received: date / Accepted: date

Abstract Particulate contamination on optical surfaces degrades the performance of space optical payloads. MIL-STD-1246C provides a theoretical estimate of particulate contamination on surfaces under different cleanroom conditions. It assumes spherical geometry of the particles to calculate the obscuration area. However, in a given cleanroom environment particles with different sizes and geometries do exist. Thus, the actual obscuration area of the particles on surfaces is different from that predicted by the theoretical models. Most of the devices that are used to measure the particulate contamination on optical surfaces can detect the particles of size greater than 5 μm only. Particles as small as 0.5 μm can affect the performance of the UV-VIS optical payloads with super polished optics due to their contribution towards Mie scattering. A new technique is adopted to measure the shape and size of the particles precisely. For these measurements non contact optical profiler Zygo NewView 8200 is used. Current work provides the details about the measurements carried out to determine the size of the particles deposited on surfaces in ISO- 4 to 8 (ISO 14644-1) class cleanrooms.

Keywords Particulate contamination · Space payloads · Cleanroom · MIL-STD-1246C · ISO 14644-1 · Mie scattering

1 Introduction

Cleanrooms are classified as ISO-1 to ISO-8 based on ISO-14644-1 standard [1]. Particulate deposition on surfaces in cleanroom mainly depends on classification, airflow type, exposure time and surface orientation. Area obscured

Annie Varghese · Suresh Venkata · S Kathiravan · Shalabh Mishra · Raghavendra Prasad B
Indian Institute of Astrophysics, II Block, Koramangala, Bangalore-560034
E-mail: venkata@iiap.res.in, brp@iiap.res.in

by the particulate contamination on surfaces can be estimated by using Particle Fall Out (PFO) plates and PFO photometer [2].PFO photometers that are operational at present can detect the particles of sizes greater than 4 - 5 μm only. But in cleanrooms small size particles are more in comparison to the large size. With help of PFO photometers and MIL-STD-1246C [3], obscuration area of the particulate contamination on active surfaces can be estimated. But, major problems in this estimation is the smallest particle size detected by the photometer and the geomtry of the particles considered by MIL-STD-1246C. These two factors can lead to inappropriate estimation of the obscuration area. A new measurement technique is required to determine the exact size, geometry and number of particles deposited on surfaces in cleanroom environments.

2 Measurements

In order to determine the exact shape and size of the particles Zygo NewView 8200 non contact optical profilometer is used. This can resolve the particle of size 0.18 μm with 50X magnification and field of view of 80 x 80 μm. The sampling area for particle size measurements can be increased with the help of stitching algorithm. Measurements are carried out by using the profilometer with 5.5X, 10X and 50X magnification. Obscuration area measured using profilometer, PFO photometer and estimated using MIL-STD-1246C are compared for different particle sizes.

3 Results

Measured area of obscuration due to particulate contamination on surfaces in cleanrooms is given in Table 1.

Table 1 Fractional area of obscuration (in ppm) due to particulate contamination on surfaces

Cleanroom class	Profilometer measurements	PFO photometer
ISO-4	92.067	84
ISO-6	1070	1206
ISO-7	2391.54	1617
ISO-8	3134.06	2272

References

1. IEST, ISO 14644 Standards and IEST technical guides to the ISO standards (1999).
2. PFO, Particle Fall Out Photometer Mk5..
3. MIL-STD-1246C, Military standard: Product cleanliness levels contamination control program (1994).

Bragg fibers: A modern approach towards Sensing and Optoelectronic applications

Ritesh Kumar Chourasia*, Vivek Singh
**Department of Physics, Institute of Science, Banaras Hindu University, Varanasi-221005.*
**Department of Physics, Maharani Kalyani College, Darbhanga.*
Author e-mail address: riteshphyzics@gmail.com

Abstract: Performance study of sensing parameters of Bragg fiber based biosensor has been analyzed in presence of defect layer. In addition, Bragg fiber with PMMA defect cavity and PMN-PT piezoelectric voltage sensitive thin layer has shown potential optoelectronic application as inline narrow band optical filter. Both applications of Bragg fibers are best in its class and show improved sensing parameters, major spectral shift with applied DC voltage and narrower bandwidth.
Keywords: Bragg fibers, Transfer matrix method, Henkel formalism, Defect mode, Biosensors, Inline narrow optical filter.

1. Introduction

Recently, Bragg fiber waveguides have attracted the attention of researchers due to their potential as a promising candidate for a variety of applications such as bio-sensing [1-3], surface emitting lasers [4-5], Boolean olfaction [6], simultaneous humidity-strain monitor [7] and many more modern applications. Bragg fiber has overcome the shortcomings of conventional optical fiber based devices due to the presence of high index solid core for total internal reflection based wave guiding mechanism. It is known that light propagates in usual fibers in an optical dense core due to TIR from its boundary. Therefore fiber properties (dispersion, optical loss, nonlinear parameters) are determined by the properties of core materials. However, there also exist other mechanism providing the localization of light and its directional propagation in a fiber with a hallow core and multilayer claddings over it. The mirror properties of such claddings are determined by Fresnel reflections from many interfaces of a multilayer structure with alternating values of the permittivity and the subsequent constructive interference of reflected waves through Bragg reflection. Fibers with multilayer periodic claddings and a core made of an optically less dense material are called Bragg fibers. A specific feature of these fibers is that radiation only in some spectral ranges can propagate in the core of a Bragg fiber i.e. these fibers also shows photonic bandgap (PBG) and these PBG shifted with the variation in core refractive index. People have encountered this property and utilize it in Biosensors [1-3]. But, the sensing parameters found by using PBG as sensing signal has poor values it can be enhanced by using a defect cavity or layer in Bragg fiber multilayer structure. This defect layer or cavity act as Febry-Perot resonator due to which a very sharp pass band (defect peak) is observed in PBG. Thus this defect peak open possibilities to improve sensing performance as well as explore the way for modeling optoelectronic devices as inline optical filters, MUX/DMUX/WDM, couplers, isolators etc.

2. Figures

The schematic sketches which revel the structure and working principle of Bragg fiber as sensors and voltage controlled inline narrow band optical filter are shown here.

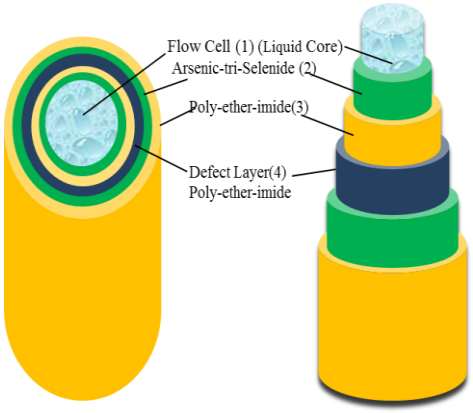

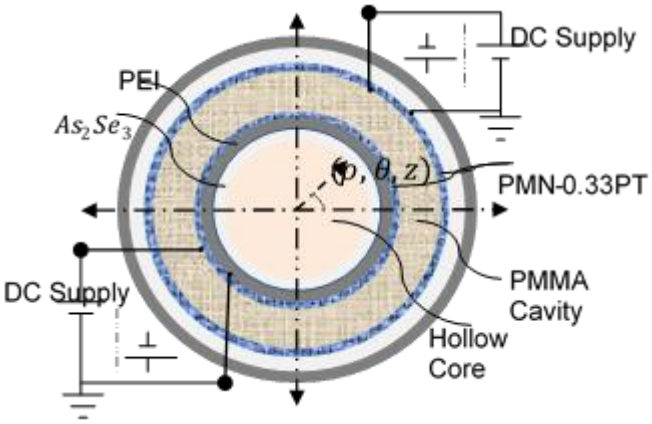

Fig. 1 Schematic structure of BFW with liquid core for bio sensing. Fig. 2 Schematic structure of BFW with hollow core for voltage tunable inline narrow band optical filter.

3. Equations

The well-known Transfer matrix method and Henkel formalism is used to model the multilayer cylindrical structure by solving Helmholtz equations in cylindrical coordinates. The reflection and transmission coefficient obtained using the complete transfer matrix is as follow:

$$r_{\mathrm{d}} = \frac{(T_{21}^{'} + jp_0 C_{\mathrm{m0}}^{(2)} T_{11}^{'}) - jp_f C_{\mathrm{mf}}^{(2)} (T_{22}^{'} + jp_0 C_{\mathrm{m0}}^{(2)} T_{12}^{'})}{(-jp_0 C_{\mathrm{m0}}^{(1)} T_{11}^{'} - T_{21}^{'}) - jp_{\mathrm{f}} C_{\mathrm{mf}}^{(2)} (-jp_0 C_{\mathrm{m0}}^{(1)} T_{12}^{'} - T_{22}^{'})} \tag{1}$$

$$t_{\mathrm{d}} = \frac{4\sqrt{\varepsilon_0/\mu_0}}{\pi K r_0 H_{\mathrm{m}}^{(2)}(k_0 r_0) H_{\mathrm{m}}^{(1)}(k_0 r_0)[(-jp_0 C_{\mathrm{m0}}^{(1)} T_{11}^{'} - T_{21}^{'}) - jp_{\mathrm{f}} C_{\mathrm{mf}}^{(2)} (-jp_0 C_{\mathrm{m0}}^{(1)} T_{12}^{'} - T_{22}^{'})]}, \tag{2}$$

where $p_0 = \sqrt{\varepsilon_0/\mu_0}$ and $p_{\mathrm{f}} = \sqrt{\varepsilon_{\mathrm{f}}/\mu_{\mathrm{f}}}$ are the admittance of core and final media, $T_{11}^{'}, T_{12}^{'}, T_{21}^{'}$ and $T_{22}^{'}$ are the matrix element of the inverse matrix of $\hat{T}$, $K = \omega\sqrt{\varepsilon_0\mu_0}$ is the free-space wave number and $C_{\mathrm{ml}}^{(1,2)} = \frac{H_{\mathrm{m}}^{(1,2)'}(k_1 r_1)}{H_{\mathrm{m}}^{(1,2)}(k_1 r_1)}$, $l = 0, f$.

4. Results and Discussion

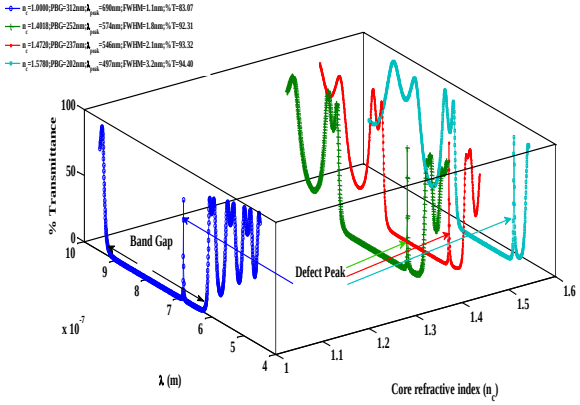

Fig. 3 PBG representation of Bragg fiber waveguide biosensor at different core refractive index and their respective spectral shift in transmission peak.

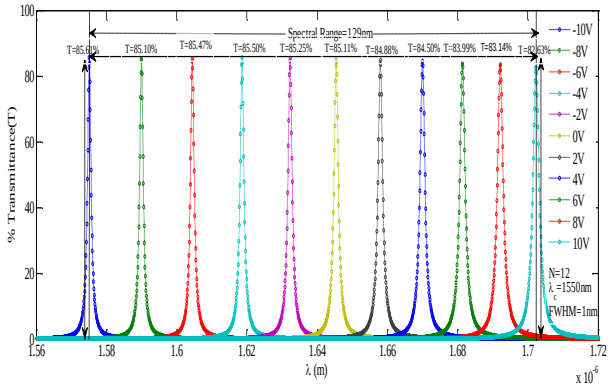

Fig 4 The variation in Defect peak position in the band gap regime with positive and negative DC bias voltage applied on PMN-0.33PT.

In order to see the performance of proposed waveguide based sensor, a *15 cm* length of the cylindrical multilayer structure having hallow core diameter $r_c = 165\mu m$ is chosen. The core is surrounded by periodic concentric claddings layers of high refractive index material Arsenic tri-selenide $n_H = 2.82$ and low refractive index material Poly-ether-Imide $n_L = 1.66$ with their respective thicknesses $d_H = 76(\mu m)$ and $d_L = 124(\mu m)$ [3]. In this structure a defect layer of low index material (Poly-ether-Imide) having refractive index $n_D = 1.66$ and quarter wave stack thickness $d_D = \lambda_c / 4n_d$ is introduced after the 5^{th} unit cell of (H/L) bilayers by breaking the symmetry. Also, the liquid used to fill the core of waveguide have refractive indices *1.4019*, *1.4620* and *1.5780* (all standardized at a center wavelength $\lambda_c = 589.3nm$ at a temperature of $25^0 C$. The maximum sensitivity through our proposed structure is obtained $S \approx 334nm/RIU$ which is approximately same $S \approx 330nm/RIU$ as reported by Rowland et al. [3] through experiment. But the detection accuracy and overall performance (Quality parameter) of our proposed structure are improved considerably due to very small FWHM of transmission peak.

5. Conclusions

Sensing performance of a novel liquid filled cored cylindrical multilayer sensor having defect mode is compared with a similar cylindrical multilayer sensor. Although the obtained sensitivity in our proposed case is similar to those obtained in [3] but the overall performance of our proposed sensor is much better that those reported in [3]. Also the Bragg fiber waveguide has shown potential candidature for the voltage tunable inline narrow optical filter.

6. References

H. Qu, M. Skorobogatiy, Sensors and Actuators B 161, 261–268 (2012).
H.J. Watts, C.R. lowe, D.V. Pollard-Knight, Anal. Chem. 66, 2465-70 (1994).
K. J. Rowland, S. Afshar V., A. Stolyarov,Y. Fink , T. M. Monro, Opt. Express 20, 48-62 (2012).
J. Li, H. Qu, M. Skorobogatiy, Opt. Express 24, 15687-15701 (2016).
J. Li, K. Nallappan, K. Guerboukha, M. Skorobogatiy, Opt. Express 25, 4126-4144 (2017).
M. Yaman, A. Yildiim, M. Kanik, T.C. Cinkara, M. Bayindir, Anal. Chem. 84, 83-90 (2012).

OSI-ISO 2018 manuscript No.
(121)

Study of spatial light modulators as turbulence phase screen and wavefront sensor and its limitations in astronomical adaptive optics systems

Suresh Venkata · Sreekanth Reddy V · Raghavendra Prasad B

Abstract Spatial light modulators (SLM) are widely used in applications involved for phase and amplitude modulation. A variable voltage can be applied to liquid crystal molecules of SLM to change their tilt angles. This causes change in refractive index and so the optical path length of the beam propagated through it. We used HOLOEYE LC-R 720 SLM to simulate atmospheric phase screen in laboratory. The SLM with a pixel pitch of 20 μm could give input frame rate of 60 Hz. Effect of Earth's atmospheric turbulence is created in laboratory using the SLM. It is also used as wavefront sensor and corrector. Known aberrations in the form of zernike coefficients are fed as input to the SLM and its response is measured using a Shack-Hartman wavefront sensor. This analysis shows that SLM could generate the high frequency wavefront distortions (it could also correct it), as compared to deformable mirror (DM) which is preferably used in astronomical adaptive optics systems. But the SLMs have slow response time and slow frame rate, unlike DM which can be used in high frequency correction. Thus, SLMs can provide high spatial frequency but its temporal frequency is poor. In this paper, the feasibility of using SLM in astronomical adaptive optics system is discussed and its limitations are examined.

Keywords Spatial light modulator · atmospheric turbulence · adaptive optics

1 Introduction

The liquid crystal (LC) molecules in SLM has property of optical and electrical anisotropy. This phenomenon induces variable tilts in molecules for an input

Suresh Venkata · Sreekanth Reddy V · Raghavendra Prasad B
Indian Institute of Astrophysics, Bangalore, India
E-mail: venkata@iiap.res.in, brp@iiap.res.in

voltage. Due to optical anisotropy in LC molecules, its refractive index changes with applied voltage. This induces random path lengths to the wavefronts intercepted with it. Thus SLM can be used as light modulator, either in its phase or amplitude [1–5].

A layout of laboratory set up is shown in Figure 1. An atmospheric phase screen based on Von-Kormann model is generated for coherence length (r_0) of range 6-15 cm [4]. The response of the SLM is sensed using a Shack-Hartman wavefront sensor. The power spectral density of Von Karmann model is given by equation(1).

$$\Phi(K) = 0.023(r_0)^{-5/3}(K^2 + K_0^2)^{-11/6} exp^{-K^2/{K_m}^2}, \tag{1}$$

where, $K_m = 2\pi/l_m$, $K_0 = 2\pi/l_0$ and l_m, l_0 are inner and outer scales of atmospheric turbulence. Typically, the inner scale will be few millimeters and the outer scale will be in the order of few tens of meters.

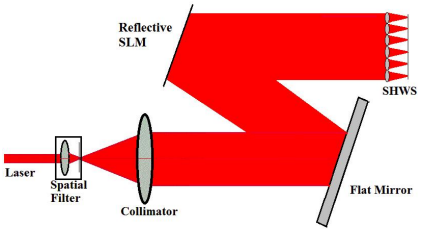

Fig. 1 Experimental layout for testing the spatial light modulator

In real time, the atmosphere has coherence length (ro) in the range of 6 - 15 cm at 650 nm. The SLM is used to generate these turbulance conditions in laboratory and its response is evaluated. Performance of SLM as Shack Hartmann sensor with different microlens diameters and focal lengths is verified. Functioning of SLM as DM is tested for a set of stroke resolutions and stroke lengths. These experiments are helpful in determining the response of SLM and its usage in astronomical adaptive optics systems.

References

1. Richard W Bowman et al, Article title, An SLM-based ShackHartmann wavefront sensor for aberration correction in optical tweezers, Journal of Optics, 12, (2010)
2. Carolina Rickenstorf et al, Programmable simulator for beam propagation in turbulent atmosphere. Optical Society of America, 24 (2016)
3. Gordon D. Love, Wave-front correction and production of Zernike modes with a liquid-crystal spatial light modulator, Optical Society of America, 36 (1997)
4. J. Houzet et al, Ultrafast laser spatial beam shaping based on Zernike polynomials for surface processing, Optical Society of America, 24 (2016)
5. Akondi Vyas et al, Spatial Light Modulator for Wave-Front Correction, ICOllTOP 2009, Department of Applied Opt.ics and Photonics, University of Calcutta (2009).

OSI-ISO 2018 manuscript No.
(122)

Nonlinear transmission measurement to study field dependent ionization process in dielectric medium

Anubhab Sahoo, P. P. Rajeev, Sivarama Krishnan

Received: 07/08/2018 / Accepted: date

Abstract: Dielectric media are transparent to low intensity near infrared (NIR) light due to their inherently large band gap. However, at sufficiently higher intensities, nonlinear absorption takes place by multi-photon processes and field assisted collisional ionization [1]. For relatively long pulse durations (t_p), typically above $t_p > 100$ fs, laser driven electrons can gain large kinetic energies by mechanisms such as inverse bremsstrahlung [2]. This leads to further ionization by electron impact and a subsequent avalanche. In short pulses, $t_p < 100$ fs, these electrons are excited to the conduction band by multiphoton absorption [1]. On this time scale, the energy transfer from electrons to the lattice is negligible compared to collisional heating. The nonlinear ionization observed in these cases is due to field dependent avalanche [3]. In order to study field dependent ionization processes, we carried out single-shot nonlinear transmission measurements to determine the breakdown threshold in fused silica. Single-shot nonlinear optical transmittance was measured with varying the incident pulse power. In order to enable this, control electronics with a boxcar averager and LabVIEW programs to vary experimental parameters were built in our lab. The results of these measurements and interpretation of the physics involved in these processes will be presented herein

Keywords Multiphoton ionization, avalanche, femtosecond laser pulse, dielectric breakdown, fused Silica

Anubhab Sahoo
Indian Institute of Technology Madras, Chennai 600036, India
E-mail: anubhabphy@gmail.com

P. P. Rajeev
Central Laser Facility, STFC Rutherford Appleton Laboratory, Didcot OX11 0QX, United Kingdom
E-mail: pprajeev@gmail.com

Sivarama Krishnan
Indian Institute of Technology Madras, Chennai 600036, India
E-mail: srkrishnan@iitm.ac.in

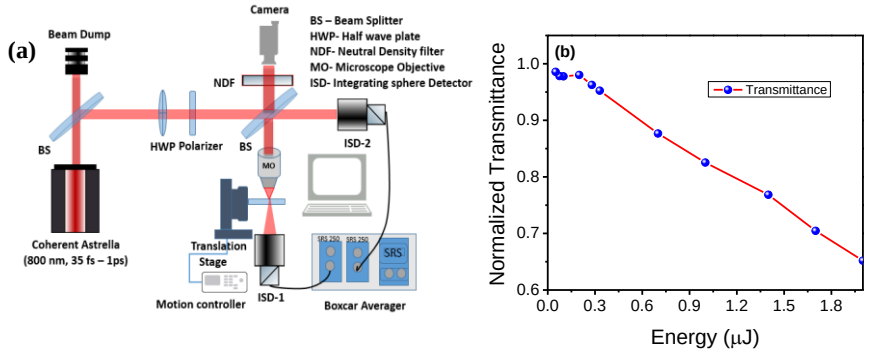

Fig. 1 (a) The experimental set up for the transmission measurement through a transparent dielectric medium. Figure 1 (b) shows the normalized transmittance curve as function of incident energy for 100 fs pulse duration.

Ultrashort laser pulses centred at a wavelength of 800 nm with repetition rates of 1 kHz are tightly focused using 0.25 NA microscope objective to 250 μm inside the fused silica. The pulse duration can be varied from 35 fs to 1 ps using pulse compressor and stretcher motor assembled with Coherent's Astrella fs-laser. For each pulse duration, the input laser intensity was controlled using a combination of half-wave plate and a polarizer. The single shot pulse interaction with the sample was studied by translating the sample with a velocity greater than the repetition rate of the pulse. This kind of single shot measurement can avoid memory effects [4] on transmission. To measure the incident and the transmitted power in parallel, the input beam is split into two perpendicular components using a 50:50 beam splitter. The experiment should be carried out at peak power below the critical power (P_{cr}) , in order to avoid the self-focusing and self-phase modulation in pulse propagation [5] in the medium. In order to measure such low energy pulses integrating sphere detectors was used in the incident and the transmitted part. Using the experimental setup as shown figure-1(a), the transmission through fused silica was studied as a function of intensity for the pulses of duration varying from 50 fs to 1 ps. The transmittance for 100 fs pulse duration as shown in the figure 1(b). The transmittance remains constant for lower energy and above a threshold point there is a sharp inflection in the transmittance due to nonlinear absorption. This experiment was carried out for the different pulse durations to study the pulse width dependence of breakdown threshold for the sample.

Reference

1. P. P. Rajeev, M. Gertsvolf, P. B. Corkum, and D. M. Rayner, Phys. Rev. Lett. **102**, 1 (2009).

2. D. Du, X. Liu, G. Korn, J. Squier, and G. Mourou, Appl. Phys. Lett. **64**, 3071 (1994).

3. B. C. Stuart, M. D. Feit, S. Herman, A. M. Rubenchik, B. W. Shore, and M. D. Perry, Phys. Rev. B **53**, 1749 (1996).

4. P. P. Rajeev, M. Gertsvolf, E. Simova, C. Hnatovsky, R. S. Taylor, V. R. Bhardwaj, D. M. Rayner, and P. B. Corkum, Phys. Rev. Lett. **97**, 253001 (2006).

5. R. W. Boyd, Nonlinear Optics, 3rd ed. Reed Elsevier India Pvt. Ltd, Delhi (2015).

Generation of non-classical states in Quantum Emitter-Surface plasmon set up

Karun Mehta* and Shubhrangshu Dasgupta
Department of Physics, Indian Institute of Technology, Ropar
*karun.mehta@iitrpr.ac.in

Abstract

The coupling of the electromagnetic fields to the conductor's electron plasma oscillations at the interface gives rise to surface-bound electromagnetic wave. The intensity-intensity correlation of photons emitted by two interacting Quantum dots (placed near to the metal-dielectric interface) into the surface plasmon mode is examined. The interaction of this confined surface plasmon field leads to the nonclassical state of the photons, thanks to their indistinguishability.

Keywords

Surface Plasmon (SP), Quantum dot (QD), Metal-dielectric interface, non-classicality

Introduction

The surface plasmon is a coupled mode of electromagnetic wave and electron density oscillation on the planar metal-dielectric interface. It is a surface electromagnetic wave that propagates along the interface and decays exponentially with distance into each medium. Surface plasmon wave can only be excited in the TM mode [1]. A Quantum emitter gets strongly coupled to the surface plasmon mode by emitting radiation that propagates along the interface and scatters out as photons in free space at the end of the interface [2].

We find that photons are prepared in N00N-like non-classical states[3]. Our technique of obtaining non-classical states is unique as compared to those proposed in the system with nano-fiber and atomic gas [4].

Model

Our model consists of two identical quantum emitters (say quantum dots) placed near to metal-dielectric interface at a fixed distance. These QDs interact with each other via dipole-dipole interaction. Each QD can be considered as a two-level system $(|g>,|e>)$ and has a transition frequency ω_o with dipole moment μ. Two detectors D1 and D2 are placed in the far-field region at the end of the interface which detect the scattered photons in free space (see **Fig1**).

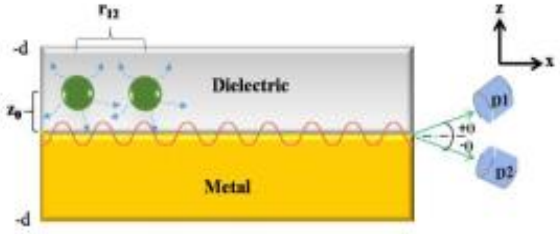

Fig 1: Radiative coupling of QDs to the SP mode

The Hamiltonian describing the dynamics of QDs is

$$H = \frac{\hbar}{2}\omega_o \sum_{i=1}^{2}(S_i^+ S_i^- - S_i^- S_i^+) + \hbar\Omega_{12}(S_1^+ S_2^- + S_2^+ S_1^-) + \frac{\hbar}{2}\sum_{i=1}^{2}\Omega_i S_i^+ e^{-i\omega t} + h.c$$

where S_i^+ and S_i^- are the atomic raising and lowering operators, Ω_{12} denotes dipole-dipole interaction and Ω_i represents the driving Rabi frequency of i^{th} QD.

These dots situated at a distance r emit photons in surface plasmon mode at a rate larger than free space decay rate. SP wave propagates along the interface in +x direction as a plane wave. There is a finite probability of transmission as photons in free space at the end of interface. The transmission probability depends on the permittivities and permeabilities of the two media [5].

The non-classical properties of the emitted photons have been analyzed by the second order correlation function, which denotes the probability of joint detection of the two photons at the detectors D1 and D2 and is calculated using quantum regression theorem [6].

Results

A high degree of correlation between photons is observed at the detectors. Second order correlation function ($g^{(2)}(\tau)$) has been plotted for different distances between quantum dots such that dipole-dipole interaction between them is different (**Fig 2)**. We observed that both detectors D1 and D2 do not click simultaneously, referring to a dip at τ = 0 and as τ increases, $g^{(2)}(\tau)$ also increases such that $g^{(2)}(\tau) > g^{(2)}(0)$. It shows that photons are anti-bunched. The results can be attributed to indistinguishability of the photons in the SP mode.

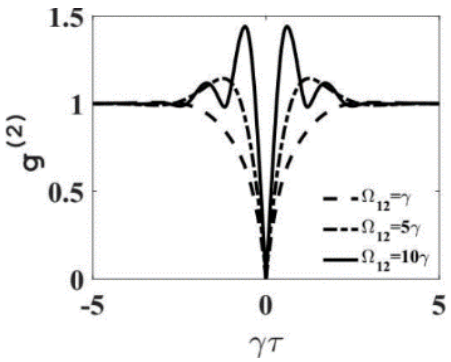

Fig 2: Second order correlation function for different interaction energy between QDs

Further zero coincidence between photons reaching detectors D1 and D2 leads to $\frac{1}{\sqrt{2}}(|2,0> \pm |0,2>)$ states of the photons in Fock state basis. Since the photons are completely identical in the SP mode, therefore it is not possible to distinguish between photons reaching at detectors, hence leads to non-classicality. In our proposal considering N-QDs placed within $r<\lambda_{SP}$ (wavelength of surface plasmon wave) emitting N-photons one could prepare general N00N like state $\frac{1}{\sqrt{2}}(|N,0> \pm |0,N>)$

References

[1] S.A Maier, Plasmonics: Fundamental and Applications (Springer, USA, 2010), pp. 21-27
[2] A.V Akimov, et al. Generation of single optical plasmons in metallic nanowires coupled to quantum dots. Nature 450, 402-406 (2007)
[3] Boto, J.P. Doeling et al. Quantum Interferometric Optical Lithography: Exploiting Entanglement to beat the diffraction Limit 85, (2000)
[4] Fam Le Kien, K. Hakuta. Correlations between photons emitted by multiatom fluorescence into a nano-fiber. Phys. Rev. A 77, 033826 (2008)
[5] A. Maradudin, et al. The optics of surface and guided wave polaritons. Progress in Surface Science 33.3, 171-257 (1990)
[6] H. J. Carmichael, Statistical Methods in Quantum Optics 1. (Springer, New York, 1999)

OSI-ISO 2018 manuscript No.
(124)

Study of internal energy flows in lattice of polarization singularities

Ruchi and P. Senthilkumaran

Abstract The total transverse energy flow (TEF) of light is determined both by the spin angular momentum (SAM) and the orbital angular momentum (OAM) part of light. The spin angular momentum of light is associated with the polarization of the beam, whereas orbital angular momentum is associated with optical vortices or the spatial inhomogeneity in the beam. Here we analyze the patterns of the internal flows in array of polarization singularities embeddded with both C-points and V-points. The circulations of the flow lines reveal the presence of C-points in the lattice. The direction of the flow of the spin flow density vectors is found to be opposite to the handedness of the C-point.

Keywords Singular Optics · Optical Vortices · Polarization singularities

1 Introduction

Standard approaches for characterization of light beams are not sufficient to understand the internal processes that constitute inner life of light beam especially for the beams that carry angular momentum (AM). Study of internal energy flows [1,2] provide a natural and efficient way for peering into the light fields and studying their most intimate and deep features. Importantly, the energy flows represent immediately observable quantities with explicit and unambiguous physical meaning.

Ruchi
Indian Institute of Technology Delhi, Hauz Khas Delhi-110016
E-mail: ruchirajput19@gmail.com

P.Senthilkumaran
Indian Institute of Technology Delhi, Hauz Khas Delhi-110016
E-mail: psenthil@physics.iitd.ac.in

Spatially varying polarization distributions can possess various singular points like C-points, V-points and L-lines [3–5]. C-points are points of circular polarization states surrounded by ellipses whose azimuths are arranged in specific manner. On the contrary, V-points are found to occur in vector fields. Generally, these polarization structures are identified in any field from their morphological parameters- ellipticity and azimuth. In this paper, we study the total transverse energy flow in an array of polarization singularities embedded with both C-points and V-points. The circulation of the flow lines mark the presence of C-points and the handedness of the C-point can be determined from the direction of the flow of the spin flow density vectors. V-points, on the other hand are located at the saddle point of S_3 distribution where, S_3 is the third Stokes parameter.

2 Energy Flow in Lattices

An array of polarization singularities can be generated from the interference of three or more planes waves with their state of polarization (SOP) arranged in specific manner [6–8]. The resultant field E_R of the superposition can be written as

$$E_R = E_X\hat{x} + E_Y\hat{y} \tag{1}$$

where E_X and E_Y are orthogonal and transverse components of resultant field E_R. The complex amplitudes E_X and E_Y satisfy the parabolic equation of paraxial optics which in case of free propagation has the form

$$i\frac{\partial E_m}{\partial z} = -\frac{1}{2k}\nabla^2 E_m \tag{2}$$

where $\nabla \equiv \left(\frac{\partial}{\partial x}, \frac{\partial}{\partial y}\right)$ is the transverse gradient, k is the propagation vector and $m = \{X, Y\}$. The total transverse energy flow density, $S_\perp$ (TFD) of the distribution can be described as the sum of spin flow density, S_S (SFD) and orbital flow density, S_O (OFD) which can be written as $S_\perp = S_S + S_O$. The SFD produce pure transverse contribution to the energy flow and can be expressed as

$$-\frac{1}{2k}\left[\hat{z} \times \nabla S_3\right] \tag{3}$$

where S_3 is the third Stokes parameter that characterizes the presence of circular polarization. Orbital flow density consists of separable summands S_X and S_Y owing to each linear polarization component. These separable summands are called partial OFDs and are given as

$$S_m = \frac{ic}{16\pi k}\left(E_m \nabla E_m^* - E_m^* \nabla E_m\right) \tag{4}$$

for $m = \{X, Y\}$.

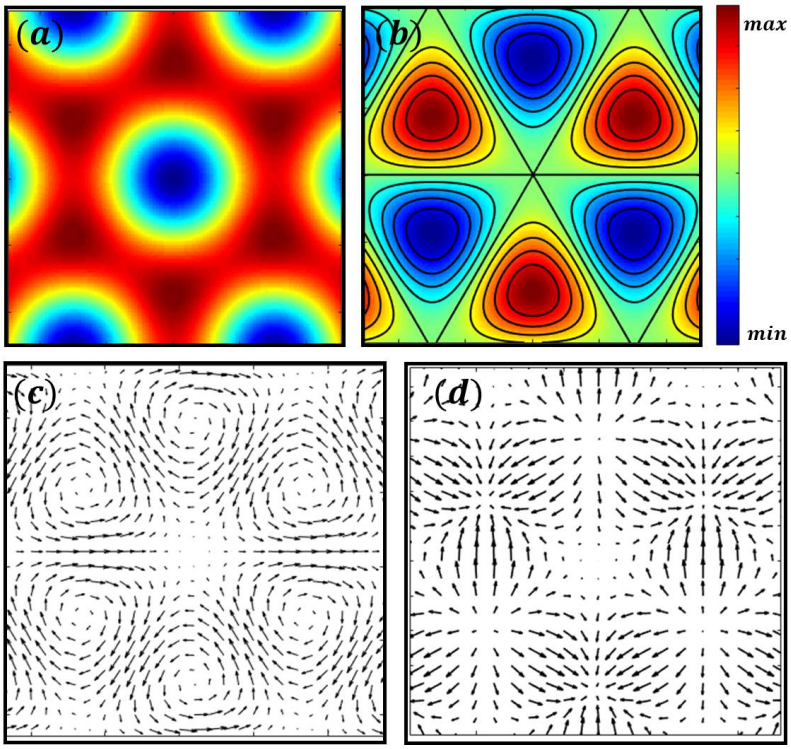

Fig. 1 (a) Transverse intensity distribution of the resultant field; (b) Distribution of the third Stokes parameter S_3 along with constant level- lines of S_3; (c) Spin flow density vector distribution of the resultant field; Note the circulating (vortex) character of the SFD near extrema of S_3 distribution. (d) Vector distribution representing the gradient of the third Stokes parameter S_3.

Figure 1 (a) depict the transverse intensity of the resultant field. The distribution of the third Stokes parameter S_3 along with its contours is shown in Fig. 1(b). Due to eqn. 3, SFD vectors shown in Fig. 1(c) are orthogonal to the gradient of S_3 shown in Fig. 1(d). Consequently, the vectors of the spin flow density are always oriented along the constant-level lines (contours) of S_3. When moving along contours of S_3 in the SFD distribution, area of high S_3 values remains to the left. This means that near extrema of S_3, the SFD field has a vortex character as can be clearly seen in Fig. 1(c). The circulation of the SFD vectors marks the presence of C-points in the distribution. It can be seen that the SFD circulates positively (counter-clockwise) around the maxima of the S_3 distribution, whereas it rotates clockwise around the minima of S_3.

The partial orbital flow density (OFD) corresponding to the resultant field of the interference of three plane waves is given by eqn. 4. In contrast to the spin part, the OFD has contribution from both the polarization component. Figure 2(a) and 2(b) depict partial OFD distribution corresponding to X and

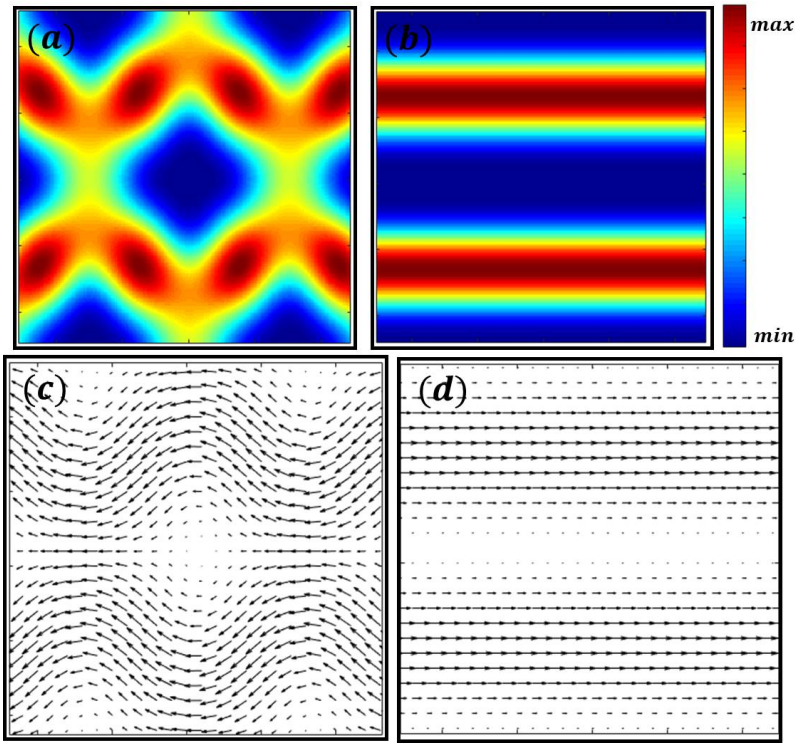

Fig. 2 (a) and (c) Orbital flow density distribution and its vector distribution corresponding to the partial orbital flow density S_X. (b) and (d) Orbital flow density distribution and its vector distribution corresponding to the partial orbital flow density S_Y.

Y component respectively. The orbital flow density vectors corresponding to S_X and S_Y are shown in Fig. 2 (c) and (d).

3 Conclusion

In this work, we have presented an attempt of describing resultant field due to superposition of three plane waves through the analysis of transverse energy flow patters. The energy flow patterns show circulating behavior around the C-points and contain information that have one to one correspondence with the morphological parameters of C-points.

References

1. A.Ya. Bekshaev and M.S. Soskin, "Transverse energy flows in vectorial fields of paraxial beams with singularities," Opt.Commun., vol.271, pp.332–348, (2007).
2. Aleksandr Bekshaev, Konstantin Y Bliokh and Marat Soskin, "Internal flows and energy circulation light beams," J.Opt., vol.13, 053001, (2011).

3. MR Dennis, "Polarization Singularities in paraxial vector fields:morphology and statisics," Opt.Commun., vol.213, pp.201–221, (2002).
4. I Freund, "Polarization singularity indices in Gaussian laser beams," Opt.Commun., vol.201, pp.251–270, (2002).
5. I Freund and M Soskin and AI Mokhun, "Elliptic critical points in paraxial optical fields," Opt.Commun, vol.208, pp.223–253, (2002).
6. SK Pal and P Senthilkumaran, "Cultivation of lemon fields," Opt. Express, vol.24, pp.28008–28013, (2016).
7. SK Pal, Ruchi and P Senthilkumaran, "C-point and V-point singularity lattice formation and index sign conversion methods," Opt, Commun., vol.393, pp.156–168, (2017).
8. Ruchi, SK Pal and P Senthilkumaran, "Generation of V-point Polarization Singularity Lattices," Opt. Express, vol.25, pp.19326–19331, (2017).

Investigation of spectral broadening induced by Self-phase modulation employing a tanhyperbolic-Gaussian pulse in non-linear media

Rimlee Saikia*, Aditya Baishya, Utpal Talukdar and Nitu Borgohain
Department of Physics, University of Science and Technology Meghalaya
Techno City Baridua, 9th mile, Ri Bhoi, Meghalaya-793101, India
*e-mail: rsaikia424@gmail.com

Abstract:-

This paper is a theoretical analysis of efficient spectral broadening induced by Self-phase modulation in non-linear optical media employing a tanhyperbolic-Gaussian pulse neglecting the effect of dispersion and fiber loss. We found that with increase of Ω_0 the pulse undergoes a frequent phase shift and the spectral distribution of this tanhyperbolic -Gaussian pulses revealed that the spectrum broadens assymmetrically with the increase of Ω_0 . Therefore, the results of this investigation expose that tanh-Gaussian pulse may have potential applicability in supercontinuum generation.

Keyword:- *Self-phase modulation, Kerr effect, tanhyperbolic Gaussian pulse, tanh-parameter*.

I. Introduction

Self-phase modulation(SPM) refers to the phenomenon in which laser beam propagating in a medium interacts with the medium and imposes a phase modulation on itself which leads to spectral broadening of optical pulse. The physical origin of the phenomenon lies in the fact that due to Kerr effect, the refractive index of the material of the medium experienced by the pulse varies depending on the point within the pulse. So there is a difference between the refractive indices at the the leading edge, at the trailing edge and in the middle. This results in a frequency chirp which eventually leads to the broadening of the frequency spectrum of the pulse.

In a landmark paper published in 2004, Konar and Jana reported much efficient self-phase modulation dominated pulse broadening generated by “sine hyperbolic Gaussian” pulse [1]. Also a couple of years back, Borgohain, Sharma and Konar also predicted the efficient SPM dominated supercontinuum generation in photonic crystal fibers, via cosh-Gaussian pulses[2]. Since, it is predicted that optical pulses other than Gaussian or sech-Gaussian may also offer efficient results. Therefore, it would be worth investigating pulse propagation effects of tanhyperbolic Gaussian pulses in optical media.

II. General formalism

The spectral broadening that we observe is due to self-phase modulation is due to the optical Kerr effect which gives refractive index as,

$$n(I) = n_0 + n_2 . I \qquad \ldots(1)$$

n_0 is the linear refractive index of the material, n_2 is the change in refractive index due to the light source, which is nonlinear. Considering a *tanh-Gaussian pulse* propagating through a medium of the form;

$$Q(\Omega, t) = A_0 \exp[-\frac{t^2}{2T_0^2}\{1 - \tanh(\Omega t)\}] \qquad \ldots(2)$$

Figure (1) shows the tanh-Gaussian pulse for different values of Ω_0. The tanh-Gaussian pulse with normalized power is given by figure (2). The evolution of the tanh-Gaussian pulse is given by the non-linear Schrodinger equation;

$$i\frac{\delta A}{\delta z} = -\frac{i\alpha}{2} A + \frac{\beta_2}{2}\frac{\delta^2 A}{\delta T^2} - \gamma |A|^2 A \qquad \ldots(3)$$

where A is the slowly varying amplitude of the pulse envelope and the three terms on the R.H.S. of the equation respectively govern the effects of fiber loss, dispersion and non-linearity on pulse propagation. In absence of dispersion and fiber loss, equation (3) becomes;

$$i\frac{\delta A}{\delta z} + \gamma |A|^2 A = 0 \qquad \ldots(4)$$

The solution to the above equation is of the form;

$$Q(z,\tau) = Q(0,\tau)\, e^{i\phi_{nl}(z,\tau)} \quad \ldots(5)$$

$\phi_{nl}(z,\tau) = |Q(0,\tau)|^2\, \delta$, is the non-linear phase shift due to the intensity dependent change in the refractive index.

The phase shift gives the frequency shift of the pulse as;

$$\delta\omega = \frac{-\delta\phi_{nl}}{\delta\tau} \quad \ldots(6)$$

$$= \delta\frac{\partial}{\partial\tau}(|Q(0,\tau)|^2) \quad \ldots(7)$$

the variation of non-linear frequency shift (δω) of Gaussian and tanh-Gaussian pulse is shown in figure (3). The time dependence of δω leads to a frequency chirp and the intensity spectrum of the pulse I(ω) can be obtained by using;

$$I(\omega) = \left| Q(z,\omega) \right|^2$$

where $Q(z,\omega) = \frac{1}{2\pi}\int_{-\infty}^{\infty} Q(z,T)\exp[i(\omega-\omega_0)T]dT$ …(8)

Due to complicated structure of the cosh-Gaussian pulses, it is not possible to evaluate above equation in closed form. Therefore we resort to numerical evaluation.

III. Results and Discusssions:-

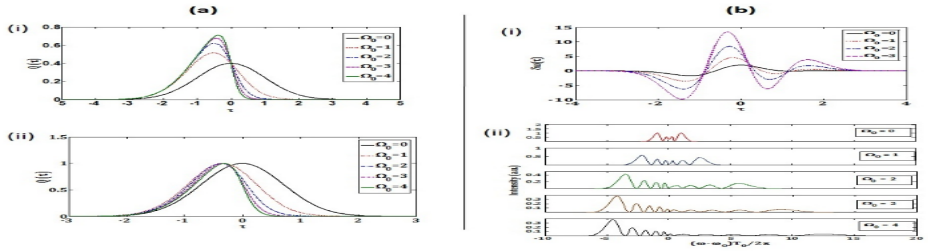

Fig(a)i. *Profile of tanh-Gaussian pulse for different tanh-parameter* Ω_0 *,* $\Omega_0 = 0$ *corresponds to Gaussian pulse.* **Fig(a)ii.** *Profile of tanh-Gaussian pulses for different tanh-parameter* Ω_0 *at normalised power.* **Fig(b)i.** *Variation of non linear frequency shift (δω) of Gaussian and tanh-Gaussian Pulses.***Fig(b)ii.** ***SPM*** *broadened spectra of tanh-Gaussian pulse for different tanh-parameter* Ω_0 *.*

Results shows that with higher values of tanh-parameter, the pulse steepens towards the trailing edge (fig.1). For comparison with the Gaussian pulse, we normalize the input power, the resulting pulse forms are as shown in fig.2. The tanh pulse undergo both blueshift and redshift at the trailing and leading edge simultaneous which is not the case for Gaussian pulse (fig.3).

IV. Conclusion:-

In conclusion, in this paper we have theoretical found that the broadened spectra of the tanh-Gaussian pulses are associated with considerable internal structure. With the increase in the value of Ω_0, most dominant peaks move towards spectral boundaries. The number of peaks in the spectra increases with the increase in the value of Ω_0 but the peak intensities are found to be gradually decreasing. So spectral broadening of tanh-Gaussian pulse increases with the increase of pulse parameter Ω_0.

Acknowledgement:- Authors acknowledge the moral and financial support of Shri M. Hoque, Chancellor, University of Science and Technology Meghalaya.

.

Reference:-

[1]. Konar and Jana 2004 J.optcom

[2]. Nitu Borgohain and Swapan Konar 2015 Journal of Nanophotonics

Multiple Bragg Wavelengths in DBR integrated with multimode SOI waveguide and their Iterative Computation

Parimal Sah
Department of Electronics and Communication Engineering, BCE, Bhagalpur - 813210, India
parimalsah04@gmail.com

Abstract

Multiple Bragg wavelength were realized by integrating DBR in a multimode SOI waveguide theoretically. An iterative computation of the Bragg wavelengths were adopted showing wavelength and waveguide parameter dependency of effective refractive indices of the guided modes. Theoretically obtained results were verified with 3D FDTD simulation results.

Keywords: Bragg grating, Optical Filter, SOI waveguide, DBR, Multimode

Introduction

Silicon photonics has opened a great opportunity in the area of research in optics regarding on-chip optical signal processing, providing with high integration density, higher data transmission speed and cost effective [1] in silicon-on insulator (SOI) platform. Wavelength filter devices based on distributed Bragg reflectors (DBR) are widely applicable in optical communication, sensing and spectroscopy. Recently, we reported multiple Bragg wavelength devices to demonstrate rectangular-edge filter [2] and photonic passband filter [3]. However, the generalized Bragg equation in these papers do not consider wavelength dependency of effective refractive indices of the guided modes. In this article, we propose an iterative method to compute the multiple Bragg wavelengths which depends not only on the waveguide dimensions but also on the wavelength dependent effective refractive indices of the waveguide.

Theory, Simulation and Results

A 3D scheme of the proposed device is shown in Fig. 1a. It is comprised of input/output single-mode access waveguides (width W_1) and an asymmetrically positioned multimode waveguide (width W_2) with a periodic perturbation (period), supporting two lower order guided modes TE_{00} and TE_{01} with effective indices $n^{00}{}_{eff}$ and $n^{01}{}_{eff}$. For a given

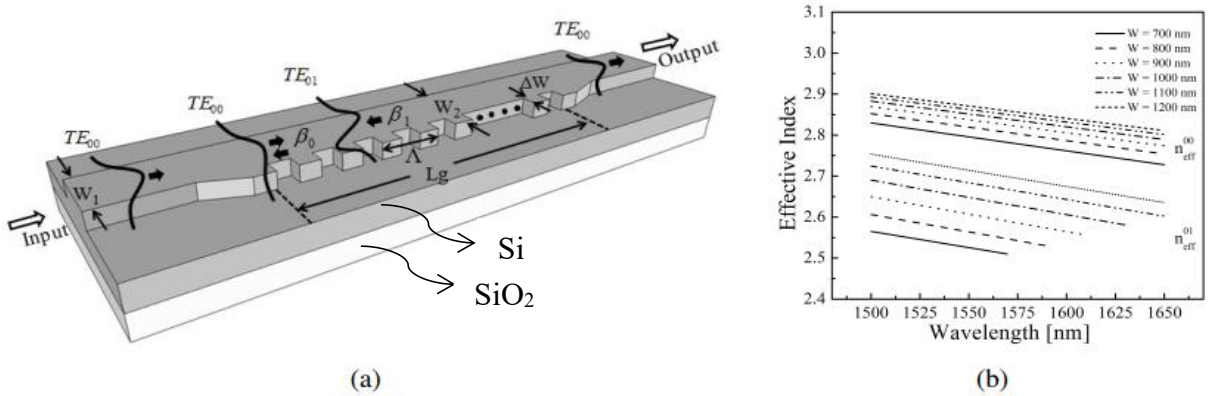

Fig. 1(a) 3D scheme of the DBR integrated with multimode SOI waveguide, (b) Effective indices versus wavelength of the waveguide with width as parameter.

period Λ, the phase matched Bragg wavelengths in the multimode waveguide region are given by $\lambda_B{}^{00} = 2\Lambda n^{00}{}_{eff}$ and $\lambda_B{}^{01} = \Lambda(n^{00}{}_{eff} + n^{01}{}_{eff})$. But, to incorporate wavelength dependency of effective indices, $n^{00}{}_{eff}$ and $n^{01}{}_{eff}$ should be computed at $\lambda_B{}^{00}$ and $\lambda_B{}^{01}$ respectively. Thus, the corrected Bragg wavelengths can be given as:

$$\lambda_B^{00}(updated) = 2\,\Lambda\, n_{eff}^{00}(\lambda_B^{00}) \quad (1)$$

$$\lambda_B^{01}(updated) = 2\Lambda\left[n_{eff}^{00}(\lambda_B^{01}) + n_{eff}^{01}(\lambda_B^{01})\right] \quad (2)$$

where $n^{00}{}_{eff}(\lambda_B{}^{00})$ and $n^{00}{}_{eff}(\lambda_B{}^{01})$ are the effective refractive indices of the fundamental guided mode at the

wavelengths λ_B^{00} and λ_B^{01}, respectively; and $n^{01}{}_{eff}(\lambda_B^{01})$ is the effective index of the first order guided mode at wavelength λ_B^{01}. These Bragg wavelengths and corresponding refractive indices were computed iteratively for a given waveguide using the following steps (**S1** to **S7**):

S1: Select the waveguide dimension such as it allows two lower order modes.
S2: Compute effective indices $n^{00}{}_{eff}$ and $n^{01}{}_{eff}$ at some reference wavelength using Eigen mode solver.
S3: Compute Bragg wavelengths λ_B^{00} and λ_B^{01} using Eq. 1 and 2 with effective indices as in S2.
S4: Compute updated effective indices $n^{00}{}_{eff}(\lambda_B^{00})$, $n^{00}{}_{eff}(\lambda_B^{01})$ and $n^{01}{}_{eff}(\lambda_B^{01})$ at wavelengths computed in S3.
S5 Check whether these effective indices are same as computed in previous step.
S6: If it it not so, go to step S3.
S7: If it is so, store the values of Bragg wavelengths and effective indices obtained in S3 and S4 respectively.

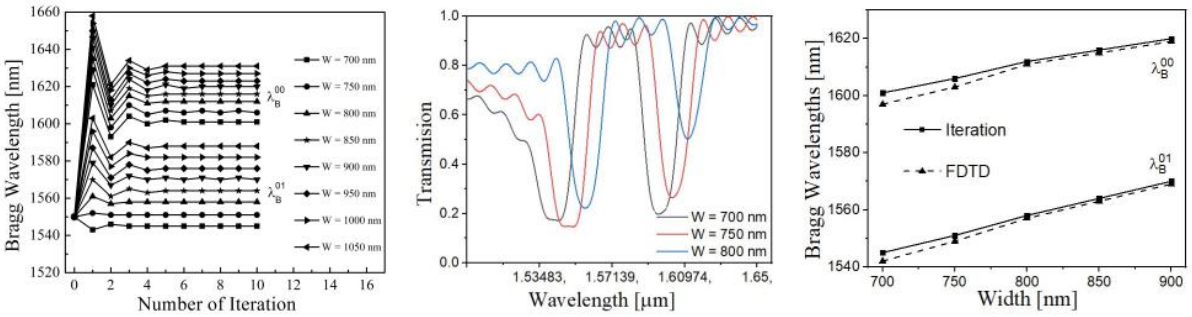

(a) (b) (c)

Fig. 2: (a) Bragg wavelength versus iteration number, (b) 3D FDTD simulated transmission characteristics for three waveguide widths and (c) Comparison of Bragg wavelengths obtained in FDTD and in iterations as a function of waveguide width.

Effective indices (with H = 250 nm, h = 150 nm, W_2-W_1 = 200 nm and Λ = 290 nm) at different wavelength computed using Lumerical mode solver is shown in Fig. 1b to help compute the above steps. After each iteration, updated λ_B^{0m} (m = 0, 1) were noted and plotted (see Fig. 2a) with W_1 as parameter. An equivalent FDTD simulation results of the device are shown in Fig. 2b for grating length 25 nm. The updated λ_B^{00} and λ_B^{01} obtained in iteration and extracted from FDTD results are shown in Fig. 2c. Small deviation of the iteration from FDTD is due to the fact that the average waveguide width were considered for effective indices computation which is only approximation for a waveguide with non-zero slab height. Thus for the given device dimension (waveguide and grating dimensions) one can predict the values of Bragg wavelengths.

3. Conclusion

Multiple Bragg wavelengths in DBR integrated with multimode SOI waveguide were computed using a semi-analytical iterative method. The same were compared with 3D FDTD simulation results. Small deviation between the results can be solved by suggesting some proper modeling of average effective indices for DBR devices.

References

1. Y. A. Vlasov, "Silicon CMOS-integrated nano-photonics for computer and data communications beyond 100G," *IEEE Communications Magazine*, vol. 50, no. 2, pp. s67–s72, 2012.
2. P. Sah and B. K. Das, "Integrated optical rectangular-edge filter devices in SOI," *Journal of Lightwave Technology*, vol. 35, no. 2, pp. 128–135, 2017.
3. ——, "Photonic bandpass filter characteristics of multimode SOI waveguides integrated with submicron gratings," *Applied optics*, vol. 57, no. 9, pp. 2277–2281, 201.

OSI-ISO 2018 manuscript No.
(128)

Measurement of Surface force using Optical tweezers

Avijit Kundu · Shuvojit paul · Soumitro Banerjee · Ayan Banerjee

Abstract Colloidal mesoscopic particles are often used as a probe to study Brownian motion and the interactions between the surrounding medium as well as surfaces. Optical tweezers facilitate such measurements by applying controlled forces on trapped Brownian particles. For example, recently, hindered diffusion has been observed near a surface of a trapped particle by modulating the displacement sensitivity of the tweezers. In this paper, we employ oscillating optical tweezers as a probe to measure surface forces between polystyrene and silica. We modulate a trapped polystyrene particle with an external force in the close proximity (few nm) of a silica surface. Thus, the particle motion is influenced by several factors which include an increased drag force according to Faxen's correction, a spurious force that comes into play due to the diffusion coefficient of the medium becoming position dependent, and finally, the Van der Waals (VdW) force which becomes substantial when the particle approaches the surface. By accounting for the other forces from analytically known results, we are able to directly quantify the Van der Waals force by determining the Hamaker constant H (which qualifies the London-VdW force) from the experimentally measured amplitude of the oscillating particle, which we compare to the amplitude evaluated theoretically. We obtain very good agreement in our measurement of H with the value reported in literature between polystyrene and silica surfaces.

Keywords Optical tweezers · Surface force · Van der Waals force · Hamaker constant · Faxen's correction · Chi-square fitting

Avijit Kundu
Indian Institute of Science Education and Research Kolkata
E-mail: ak15rs035@iiserkol.ac.in

Ayan Banerjee
Indian Institute of Science Education and Research Kolkata
E-mail: ayan@iiserkol.ac.in

1 Introduction

Adhesive forces arise due to the interaction between small particles when the separation between them is small. This force is known as the London-Van der Waals (LVDW) force [1], which acts between two particles as a function of their radii, the distance separating them, as well as on the properties of the surrounding medium. The latter is accounted into the Hamaker constant [2] based on the Lifshitz theory. According to Faxen's correction [3] when a particle comes near to a surface the drag coefficient will get increased. Thus, it is important to characterize these forces in order to estimate their influence in several entities such as bio-molecules or to study intracellular environment.

Several measurement techniques have been developed for measurement of Van der Waals forces such as Total Internal Reflection Microscopy (TIRM) and optical tweezers - both of which measure the force from its effect on the Brownian motion of a particle. Thus, studies exist on measurement of the Van der Waals force between a polystyrene Brownian sphere and a glass sphere [4], and a glass surface [5]. However, both measurements are with localized particles, whose distance with the surface of interest is varied, but the signal to noise is rather less considering that it is only the modified Brownian fluctuations of the particles being measured in order to determine the Van der Waals force.

In contrast, we trap a polystyrene particle and move it close to a surface of a comparatively large silica particle using oscillating optical tweezers. We proceed to measure the amplitude of the particle in the presence of the second, and thus determine the effect of the Van der Waals force with a greater signal-to-noise ratio compared to the measurements from Brownian fluctuations. The effect of the Van der Waals force is pronounced in the motion of the particle when it moves towards the surface, resulting in a general reduction in its response with respect to the amplitude of the drive. We match our experimental results with numerical simulations, and thereafter use a chi-square fitting to determine the Hamaker constant H - which quantifies the VdW force.

2 Theory

We consider a spherical Brownian particle of mass m confined in a harmonic potential close to a flat, rigid surface in a viscous fluid. The Langevin equation describing the trajectory of the particle is given by

$$m\ddot{x} = -\gamma(x)\dot{x} - k(x - x_0) + \gamma(x)\frac{dD(x)}{dx} - \frac{Ha_0}{6\left(d - x\right)^2} + \gamma(x)\sqrt{2D(x)}\xi\left(t\right) \quad (1)$$

where, x is the instantaneous position of the particle, x_0 is the position of the potential minimum, k is the stiffness of the harmonic potential. $\gamma(x)$ is the position dependent friction coefficient which is defined as Faxen's correction

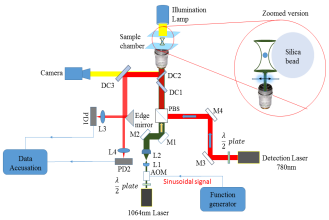

Fig. 1 Schematic diagram of our system (drawn not to scale). Here DC: Dichroic, M: Mirror, L: Lens, PD: Photodiode, PBS: Polarising Beam splitter, AOM: Acousto optic modulator. In the zoomed version: Interaction between two particles of radii a_0(PS) and R(silica) separated by a distance. As $R >> a_0$, the bigger particle surface is approximated as a flat surface.

which is expressed as

$$\gamma(x) = \frac{\gamma_0}{1 - \frac{9a_0}{8h} + \frac{a_0^3}{2h^3} - \frac{57a_0^4}{100h^4} + \frac{a_0^5}{5h^5} + \frac{7a_0^{11}}{200h^{11}} - \frac{a_0^{12}}{25h^{12}}} \tag{2}$$

The third term in RHS of Eq. 1 is associated with spurious force due to position dependent diffusion coefficient of $D(x)$. The radius of the small particle is 1.5μm (a_0), while that of the large particle is 40μm (R).

The noise $\xi(t)$ is the zero mean Gaussian random variable whose variance is defined by fluctuation-dissipation relation $< \xi(t)\xi(t') >= 2k_BT\gamma\delta(t-t')$. As the particle is confined in a harmonic potential in the vicinity of a flat surface, the Van der Waals force arises (also known as London-VdW force). It originates from the interaction between two spherical bodies close to each other, and is further approximated for the case of a flat surface which is used in Eq. 1. H is the Hamaker constant calculated on the basis of the Lifshitz theorem for a spherical body approaches to a surface as given in [2]. Here d is the surface to surface separation between two particles.

We modulate the harmonic potential sinusoidally with an amplitude A and angular frequency ω_0. The forced overdamped Langevin equation can then be written substituting $x_0 = Asin(\omega_0 t)$ in Eq. 1 as,

$$\gamma(x)\dot{x} = -kx + kAsin(\omega_0 t) + \gamma(x)\frac{dD(x)}{dx} - \frac{A_H}{(d-x)^2} + \gamma(x)\sqrt{2D(x)}\xi\,(t) \tag{3}$$

where, $A_H = Ha_0/6$.

3 Result and discussion

Trapping the particle, we move it near the wall until it is at a surface to surface separation of 200nm, after which we apply a sinusoidal force to it. This modulation is essentially used to measure the amplitude response of the particle. Fig[2] shows the measured amplitude response of the trapped particle for each separation that we used in the experiment. Here we observe that as the separation is increased, the amplitude of the particle also increased, with the

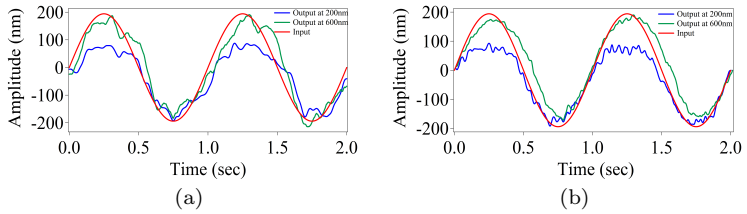

Fig. 2 (a) and (b) show the numerically and experimentally measured amplitude responses with varieng the surface to surface separation between two particles at $200nm$, $600nm$.

least amplitude being obtained for a separation of 200 nm. This is clearly due to the influence of the VdW force, and to measure this force we have taken 8 data points with a surface to surface separation between 200 - 1400 nm, which are then compared to data obtained for without the wall. By comparing the measured amplitudes with that obtained from numerical simulations, and employing a chi-square fit to the differences between the values - we determine the Hamaker constant A_h which corresponds to the minimum of the chi-square. factor to measure the VDW force. Thus, we obtain $A_h = 2.55 \times 10^{-}27$ J-m, which is quite close to the literature value of $2.29 \times 10^{-}27$ J-m for a polystyrene-silica system.

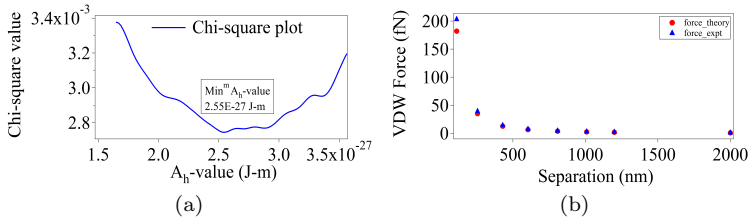

Fig. 3 (a) and (b) show the numerically and experimentally measured amplitude responses with varieng the surface to surface separation between two particles at 200nm, 400nm, 600nm.

4 Conclusions

Thus, we have utilized optical tweezers to directly measure the surface force between two polystyrene and silica spheres. Our method has the significant advantage of large signal to noise, owing to the large amplitude with which the optically trapped polystyrene particle (which acts as a probe) is driven, in comparison to methods reported in earlier which entirely based on the measurement of Brownian fluctuations of the probe. We intend to extend our work to viscoelastic media in the future.

Acknowledgements This work was supported by the IISER Kolkata and DST INSPIRE, Govt. of India.

References

1. H. Hamaker, physica **4**, 1058 (1937).
2. J. N. Israelachvili, *Intermolecular and surface forces* (Academic press, 2011).
3. H. Brenner, Chemical engineering science **16**, 242 (1961).
4. M. A. Bevan and D. C. Prieve, Langmuir **15**, 7925 (1999).
5. E. Schäffer, S. F. Nørrelykke, and J. Howard, Langmuir **23**, 3654 (2007).

OSI-ISO 2018 manuscript No.
(129)

Matter-wave phase operators for quantum atom optics: On the possibility of experimental verification

Kingshuk Adhikary[*1] · **Subhanka Mal**[*1] · **Abhik Kr. Saha**[1] · **Bimalendu Deb**[1]

Abstract In early 90's Mandel and coworkers performed an experiment [1] to examine the significance of quantum phase operators by measuring the phase between two optical fields. We show that this type of quantum mechanical phase measurement is possible for matter-waves of ultracold atoms in a double well. In the limit of low number of atoms quantum and classical phases are drastically different. However, in the large particle number limit, they are quite similar. We assert that the matter-wave counterpart of the experiment [1] is realizable with the evolving technology of atom optics .

Keywords Phase operators · Matter-wave interferometry · double well

K. Adhikary
School of Physical Sciences, Indian Association for the Cultivation of Science, Jadavpur, Kolkata 700032.
E-mail: mska@iacs.res.in

S. Mal
School of Physical Sciences, Indian Association for the Cultivation of Science, Jadavpur, Kolkata 700032.
E-mail: mssm9@iacs.res.in

A. K. Saha
School of Physical Sciences, Indian Association for the Cultivation of Science, Jadavpur, Kolkata 700032.
E-mail: msaks2@iacs.res.in

B. Deb
School of Physical Sciences, Indian Association for the Cultivation of Science, Jadavpur, Kolkata 700032.
E-mail: msbd@iacs.res.in

1 Introduction

In quantum optics, unitary phase operators were introduced in the 1980's by Barnett and Pegg [2] to describe the phase measurement and quantum phase-dependent effects. In the definition of two-mode unitary phase-difference operators [3], it is assumed that the total number of photons is conserved. This assumption can not be valid always except in closed quantum optical systems such as two-mode Raman type processes in high-Q cavities [3]. However, for matter-waves of ultracold atoms in a double-well (DW) trap, the total number of atoms is conserved during the trap lifetime or duration of any experimental measurement on the trapped atoms. It is then necessary to formulate the quantum phase of matter-waves with a fixed number of particles. So, it is important to study quantum atom optics under the influence of unitary phase operators in matter-waves [4,5].

Ketterle's group [6] has first experimentally observed the atom interferometry of two-component Bose-Einstein Condensates (BECs) in a DW trap. They have observed the relative phase between two condensates with matter-wave interference [7]. In this case the DW is analogous to a coherent beam splitter. Their group [8] has demonstrated another experimental technique to determine the relative phase of two condensates by scattering of light. The advantage of this technique is that neither coherent splitting of BECs is required nor is recombination of the matter-waves. Matter-wave interferometry has also been developed using magnetically generated DW traps on an atom chip [9]. Their has been several experiments to determine the spatial phase of the matter wave interference by releasing two condensates from spatially separated potential wells [6]. In those experiments the phase is measured classically. Gross *et al.* first demonstrated experimentally quantum mechanical homodyne detection of matter-wave phase [10]. Recently there are some experiments showing that a few numbers of particles (atomic bosons and fermions) can also be trapped using optical fields [11,12].

Here we discuss the possibility of quantum phase measurement with matter-wave interferometry with small number of bosonic atoms in DW. In the experiment performed by Mandel's group in 1991 [1] two modes of laser were employed in a interferometric homodyne detection scheme. One of the modes was treated classically with large number of photons, and the other quantum mechanically with variable average photon number. They measured the sine and cosine of quantum phase-difference operator and plotted the results as a function of average photon number in the second mode. Their results show that when the average photon numbers in both the modes are small, classical and quantum mechanical phases differ significantly. However, if the average photon number in the second mode is increased, classical and average quantum phases tend to match. Here we discuss the possibility of a matter-wave counterpart of Mandel's experiment using ultracold bosonic atoms in a quasi-1D DW.

2 Phase-operators: A brief review

Here we consider Barnett-Pegg [2] type quantum phase operators for matter-wave of few bosons or fermions. Matter-wave phase operators were first introduced in 2013 [4]. It is shown that [4,5], for a low number of bosons or fermions, unitary nature of the phase-difference operators is important. For large number of photons or quanta, the non-unitary Carruthers-Nieto [13] phase-difference operators yield almost similar results as those due to Barnett-Pegg type unitary operator. Since, in the unitary regime, phase operators are formulated by coupling the vacuum state with the highest number state in a finite-dimensional Fock space, the effects of the vacuum state becomes significant for low number of particles. In early 90's, Mandel's group [1] experimentally determined the phase-difference between two optical fields in both semi-classical and quantum cases. They made use of the sine and cosine of phase-difference operators of Carruthers and Nieto [13] as well as unitary operational phase-difference operators as they defined.

For the material particles, quantum phase operators associated with bosons and fermions have different character. Unitary quantum phase operators for bosons are introduced by the analogy of quantum phase operator formalism of photons. It is difficult to define quantum phase operator for fermions because more than one fermion can not occupy a single quantum state simultaneously. A quantum state for fermions can be either filled (by one fermion) or empty (vacuum state). Therefore, quantum phase-difference between two fermionic modes becomes well defined when single-particle quantum states of fermions are half-filled.

To clarify the canonically conjugate nature of number- and phase-difference operators, one can introduce two commuting operators corresponding to cosine and sine of the phase-difference. Both of them are canonically conjugate to the number-difference operator. These two phase operators plus the number-difference operator forms a closed algebra [4].

To define an appropriate quantum phase operator, a complication arises from the number operator of a harmonic oscillator which has a lower bound state. Dirac [14] first postulated the existence of a hermitian phase operator in his description of quantized electromagnetic fields. Susskind and Glogower [15] first showed that Dirac's phase operator was neither unitary nor hermitian. If someone seeks to construct a unitary operator U by following Dirac's postulate then $UU^{\dagger} = \hat{I} \neq U^{\dagger}U$, hence U is not unitary. Thus Susskind and Glogower [15] concluded that there does not exist any hermitian phase operator. Louisell [16] first introduced the periodic operator function corresponding to a phase variable which is conjugate to the angular momentum. Carruthers and Nieto [13] introduced two-mode phase difference operators of a two-mode radiation field by using two non-unitary hermitian phase operators C and S, measure the cosine and sine of the fields. The two-mode phase-difference operators as defined by Carruthers and Nieto [13] are given by

$$\hat{C}_{12}^{CN} = \hat{C}_1\hat{C}_2 + \hat{S}_1\hat{S}_2$$

$$\hat{S}_{12}^{CN} = \hat{S}_1\hat{C}_2 - \hat{S}_2\hat{C}_1 \tag{1}$$

where

$$\hat{C}_i = \frac{1}{2}[(\hat{N}_i+1)^{-\frac{1}{2}}\hat{a}_i + \hat{a}_i^\dagger(\hat{N}_i+1)^{-\frac{1}{2}}]$$

$$\hat{S}_i = \frac{1}{2i}[(\hat{N}_i+1)^{-\frac{1}{2}}\hat{a}_i - \hat{a}_i^\dagger(\hat{N}_i+1)^{-\frac{1}{2}}]$$

are the phase operators corresponding to the cosine and sine respectively, of i-th mode, where $\hat{a}_i^\dagger(\hat{a}_i)$ denotes the creation(annihilation) operator for a boson and $\hat{N}_i = \hat{a}_i^\dagger\hat{a}_i$. The explicit form of phase-difference operators can be written (with i=1 or 2) as

$$\hat{C}_{12}^{CN} = \frac{1}{2}[(\hat{N}_1+1)^{-\frac{1}{2}}\hat{a}_1\hat{a}_2^\dagger(\hat{N}_2+1)^{-\frac{1}{2}} + \hat{a}_1^\dagger(\hat{N}_1+1)^{-\frac{1}{2}}(\hat{N}_2+1)^{-\frac{1}{2}}\hat{a}_2] \tag{2}$$

$$\hat{S}_{12}^{CN} = \frac{1}{2i}[(\hat{N}_1+1)^{-\frac{1}{2}}\hat{a}_1\hat{a}_2^\dagger(\hat{N}_2+1)^{-\frac{1}{2}} - \hat{a}_1^\dagger(\hat{N}_1+1)^{-\frac{1}{2}}(\hat{N}_2+1)^{-\frac{1}{2}}\hat{a}_2] \tag{3}$$

In interferometric experiments, only the phase difference between two fields matters and not the absolute phase of a field. According to Barnett-Pegg formalism, hermitian and unitarity of phase-difference operators corresponding to cosine and sine of phase have following explicit form

$$\hat{C}_{12} = \hat{C}_{12}^{CN} + \hat{C}_{12}^{(0)} \tag{4}$$

$$\hat{S}_{12} = \hat{S}_{12}^{CN} + \hat{S}_{12}^{(0)} \tag{5}$$

where

$$\hat{C}_{12}^{(0)} = \frac{1}{2}[|N,0\rangle\langle 0,N| + |0,N\rangle\langle N,0|]$$

$$\hat{S}_{12}^{(0)} = \frac{1}{2i}[|N,0\rangle\langle 0,N| - |0,N\rangle\langle N,0|]$$

are the operators which are constructed by coupling the vacuum state of one mode with the highest Fock state of the other mode. $N = \langle\hat{N}_1\rangle + \langle\hat{N}_2\rangle$ is total number of bosons which is conserved. $|N_1, N-N_1\rangle$ represents a two-mode Fock state with N_1 and $(N-N_1)$ being the atom numbers in modes 1 and 2, respectively. The difference of the number or the population imbalance between the two wells is $\hat{W} = \hat{N}_1 - \hat{N}_2$. The commutation relations of the given operators $\hat{C}_{12}, \hat{S}_{12}$ and $\hat{W}$ are as follows

$$[\hat{C_{12}}, \hat{W}] = 2i(\hat{S}_{12} - (N+1)\hat{S}_{12}^{(0)}) \tag{6}$$

$$[\hat{S_{12}}, \hat{W}] = -2i(\hat{C}_{12} - (N+1)\hat{C}_{12}^{(0)}) \tag{7}$$

$$[\hat{C}_{12}, \hat{S}_{12}] = 0 \tag{8}$$

The first two of the above equations imply

$$\Delta C_{12}\Delta W \geq \left|S_{12} - (N+1)S_{12}^{(0)}\right| \tag{9}$$

$$\Delta S_{12}\Delta W \geq \left|C_{12} - (N+1)C_{12}^{(0)}\right| \tag{10}$$

Now, the standard quantum limit of fluctuation Δ_{SQL} in number-difference or phase-difference quantity is given by [5]

$$\Delta_{\mathrm{SQL}} = \frac{1}{N}\sqrt{[S_{12} - (N+1)S_{12}^{(0)}]^2 + [C_{12} - (N+1)C_{12}^{(0)}]^2} \tag{11}$$

and the normalized squeezing parameters for both phase- and number-difference operators, respectively, by

$$\Sigma_p = {\Delta E_\phi}^2 - \Delta_{\mathrm{SQL}} \tag{12}$$

and

$$\Sigma_w = {\Delta W_n}^2 - \Delta_{\mathrm{SQL}} \tag{13}$$

where $\Delta E_\phi = \sqrt{(\Delta C_{12})^2 + (\Delta S_{12})^2}$ is an average phase fluctuation and $\hat{W}_n = \frac{\hat{W}}{N}$, normalized number-difference operator. The system will be squeezed in number or phase variables when Σ_w or Σ_p becomes negative.

3 The Model

To build up the model, we consider a quasi-1D DW trap potential in which bosonic atoms are confined in the two sites of the DW. The DW has two quasi degenerate energy eigenfunction in which the ground band is occupied by the bosons. The idea is to initialize a certain number of bosons in one of the either site of the DW and let them evolve (tunnel) with time. So, the particle number in the other well (N_2) which was initially empty oscillates with time. We have taken the quantum mechanical average of $\hat{N}_2$ and $\hat{S}_{12}$ throughout the time upto which $N_1(t) = N_2(t) = N/2$.

To detect the phase, we propose a scheme of using the DW as double slit of interference experiment. By switching off the optical field, the bosons interfere as they all under the influence of gravity. From that one can detect the phase by absorption imaging the interference pattern on screen and analyzing the density profiles in the pattern.

4 Results and discussions

As the total number of bosons in our case is conserved, we calculate the quantum mechanical average of sine phase-difference operator as a function of number of bosons in the second well for different total number of particles. We consider symmetric trap for non-interacting bosons. Although non-interacting bosons are idealized, we assume the interaction to be very small and our case

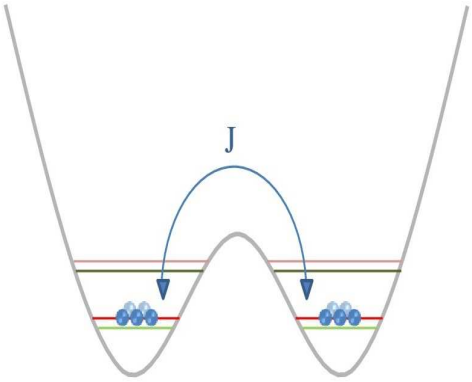

Fig. 1 Schematic of bosons in a quasi-1D DW trap with J being tunneling coefficient.

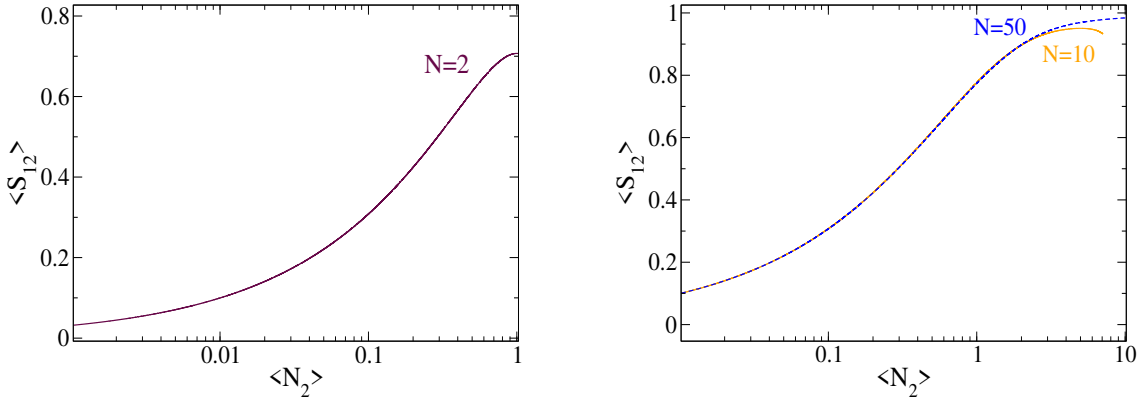

Fig. 2 Calculated values of $\langle S_{12} \rangle$ as a function of average number of bosons for different total number of bosons.

closely resembles to that. To begin with, we initialize the system with all bosons in one well and then the number in the other well (N_2) evolves with time. Throughout the evolution of N_2 up to half of the total population we take quantum mechanical average. Then we have plotted $\langle \hat{S}_{12} \rangle$ with $\langle \hat{N}_2 \rangle$. Our results are similar to that obtained by Mandel's group. For their case they have changed the photon numbers in both the modes treating one mode classically and other mode quantum mechanically. They have also changed the ratio of average photon numbers of two different modes in their experiment. Whereas, in our case we have only changed the total number of particles to mimic their experimental finding.

5 Conclusions

We have studied the sine of quantum phase difference between two sites of a DW for non-interacting bosons. The cosine operator can also be studied in the similar way. We have shown that when the total number of bosons is increased the result has a good agreement with the Mandel's experimental results. It is worth noticing how the results modify in presence of interactions and slight asymmetry of the trap. One can also calculate the fluctuations of sine and cosine phase operators. Recently, phase fluctuation below the shot-noise has been demonstrated experimentally with two components BEC's [17]. The results we obtained suggest that when the particle number is small in either side of the well unitary phase operators become important. This can be attributed to the effect of vacuum term in unitary phase operators. In case of Josephson oscillations in BEC's the unitary quantum phase has not been studied so far. It may be possible to measure the quantum phase of these type of systems by using homodyne detection method.

References

1. Noh J W, Fougères A and Mandel L, Measurement of Quantum Phase by Photon Counting, Phys. Rev. Lett., 67, 11 (1991)
2. Barnett S M and Pegg D T, Phase in quantum optics, J. Phys. A: Math. Gen., 19, 3849 (1986)
3. Deb B, Gangopadhyay G and Ray D S, Population trapping in a Raman-coupled model interacting with a two-mode quantized cavity field, Phys. Rev. A, 48, 2 (1993)
4. Das B, Ghosal B, Dutta Gupta S, and Deb B, Unitary quantum phase operators for bosons and fermions: a model study on the quantum phase of interacting particles in a symmetric double-well potential, J. Phys. B: At. Mol. Opt. Phys, 46, 035501 (2013)
5. Adhikary K, Mal S, Deb B, Das B, Dastidar K R and Dutta Gupta S, Number-phase uncertainty and quantum dynamics of bosons and fermions interacting with a finite range and large scattering length in a double-well potential, J. Phys. B: At. Mol. Opt. Phys., 51, 045302 (2018)
6. Shin Y, Saba M, Pasquini T A, Ketterle W, Pritchard D E, and Leanhardt A E, Atom Interferometry with Bose-Einstein Condensates in a Double-Well Potential, Phys. Rev. Lett., 92, 050405 (2004)
7. Cronin A D, Schmiedmayer J, and Pritchard D E, Optics and interferometry with atoms and molecules, Rev. Mod. Phys., 81, 1051 (2009)
8. Saba M, Pasquini T A, Sanner C, Shin Y, Ketterle W, and Pritchard D E, Light Scattering to Determine the Relative Phase of Two Bose-Einstein Condensates, Science, 307, 1945 (2005)
9. Schumm T et al., Matter-wave interferometry in a double well on an atom chip, Nat. Phys., 1 57 (2005)
10. Gross C, Strobel H, Nicklas E , Zibold T, Bar-Gill N, Kurzki G, and Oberthaler M K, Atomic homodyne detection of continuous-variable entangle twin-atom states, Nat. Lett. 480, 219 (2011)
11. Fölling S, Trotzky S, Cheinet P, Feld M, Saers R, Widera A, Nüller T, and Bloch I, Nature 448, 1029-1033 (2007)
12. Murmann S, Bergschneider A, Klinkhamer M V, Zürn G, Lompe T, and Jochim S, Phys. Rev. Lett. 114, 080402 (2015)
13. Carruthers P and Nieto M M, Phase and Angle Variables in Quantum Mechanics, Rev. Mod. Phys., 40, 411 (1968)
14. Dirac P A M, The quantum theory of the emission and absorption of radiation, Proc. R. Soc. A, 114, 243 (1927)

15. Susskind L and Glogower J, Quantum mechanical phase and time operator, Physics, 1, 49 (1964)
16. Louisell W H, Amplitude and phase uncertainty relations, Phys. Lett., 7, 60 (1963)
17. Burton W C, Kennedy C J, Chung W C, Vadia S, Chen W, and Ketterle W, Coherence Times of Bose-Einstein Condensates beyond the Shot-Noise Limit via Superfluid Shielding, Phys. Rev. Lett., 117, 275301 (2016)

OSI-ISO 2018 manuscript No.
(131)

High Birefringent Photonic Crystal Fibers for THz Guidance

Varun Arora, Vikas Kumar and R. K. Varshney

Abstract We have proposed a new and simple design for a photonic crystal index guided fiber (PCIGBF) providing same order of birefringence as conventional elliptical holes in the PCIGFs, which are difficult to fabricate and maintain its shape. We have considered photonic crystal index guided THz birefringent fiber made of low density polyethylene and hexagonal lattice of unit cell of circular air holes in it. In the proposed fiber, elliptical holes are replaced by two appropriate circular holes. The birefringence can be increased further with the proper optimization.

Keywords Photonic crystal fibers, Terahertz, Birefringence, Polarization mode dispersion

1. Introduction

A considerable amount of interest is shown for Terahertz wave guidance with suitable dispersion in Optical fibers during recent years due to many applications like spectroscopy, communication, imaging etc. Photonic crystal fibers (PCFs) have also generated lot of interest due to their special characteristics like endlessly single mode, high nonlinearity, more dispersion tailoring, supercontinuum generation etc. [1]. PCFs with high birefringence can be used as polarization maintaining fibers required for many fiber devices applications. Such high birefringent fibers can have elliptical air holes, but fabrication of appropriate elliptical holes and to maintain their shape is difficult [2-4]. Moreover fitting them in hexagonal fashion is also a problem and such fibers have relatively higher loss due to poor confinement. To overcome above mentioned problems related to elliptical air hole PCFs, we have proposed a new alternative design, in which elliptical holes are replaced by appropriate circular holes, and hence, easy to fabricate. We have shown that its birefringent characteristics are almost same as reported earlier. Moreover confinement of the modal filed in the proposed fiber is also relatively tight, and hence, having a low loss.

2. Proposed structure and analysis

Schematic diagram of the conventional PCF with elliptical holes and the corresponding proposed structure with their modal field distributions are shown in Figs. 1(a) and 1(b), respectively. Here, the elliptical air hole is replaced by a combination of two appropriate circular holes having same air fractional area to decide the dimension of the circular holes. These holes are made in the background material of low density polyethylene (n=1.53). Enlarged view of dimensions of the elliptical hole and the corresponding two circular holes is shown in Fig. 2(a). Characteristics of the proposed PCF structure are studied by using full vector beam propagation method.

3. Results and Discussions

To study modal characteristics of the proposed structure shown in Fig.1, we have chosen the pitch parameter Λ = 200μm. A comparison of the modal field distributions shown in Fig.1 (a) and (b) clearly illustrates that confinement is relatively low for elliptical hole configuration. Variation of the modal birefringence corresponding to both structures with frequency is shown in Fig. 2 (b); blue and red curves correspond to conventional and proposed structures, respectively. This figure clearly indicates that the modal birefringences of both the structures are nearly same. The corresponding Polarization mode dispersion (PMD) for both the structures is shown in Fig. 3. This figure shows that behavior and magnitude of PMD for both the structures are almost same. More results related to it will be presented in the conference.

Vikas Kumar
Department of Physics, Indian Institute of Technology Delhi, India-110016
E-mail: kumarvikas1027*@gmail.com*

4. Conclusions

A new and simple design for a photonic crystal index guided birefringent fiber (PCIGBF) for THz guidance has been reported. In the proposed fiber design, an elliptical hole present in the conventional PCIGBF is replaced by two circular holes. Our proposed fiber provides almost similar birefringence characteristics as that of conventional elliptical holes in the PCIGBF. However the proposed fiber is easy to fabricate with larger yield and its loss is relatively low due to tighter modal field confinement.

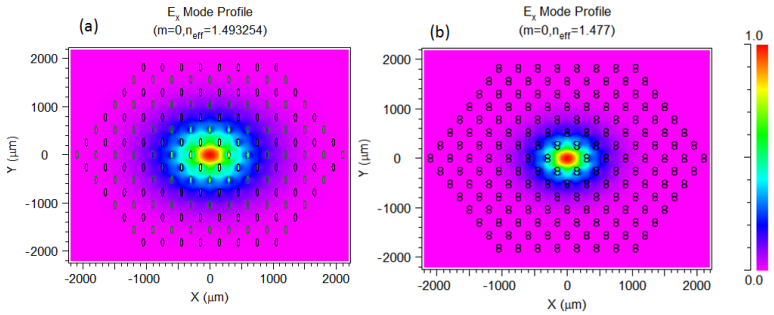

Fig.1. Schematic diagram of the index guiding PCF with modal field distributions at 1THz **(a)** conventional structure with elliptical holes in the cladding, **(b)** proposed structure with two adjacent circles

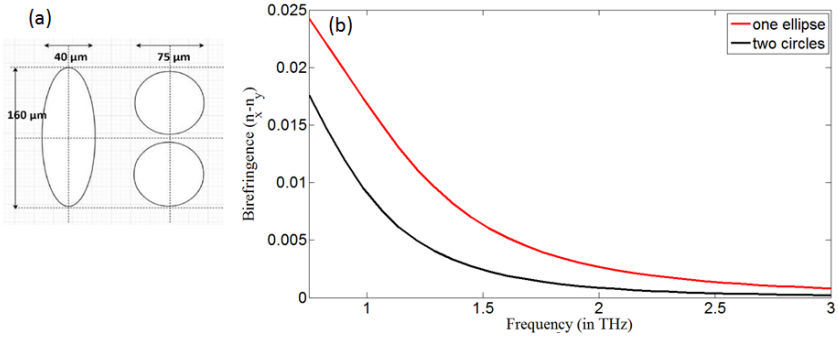

Fig.2. (a) Dimensions of holes in the proposed index guided PCF **(b)** spectral dependence of the modal birefringence of both structures shown in Fig.1

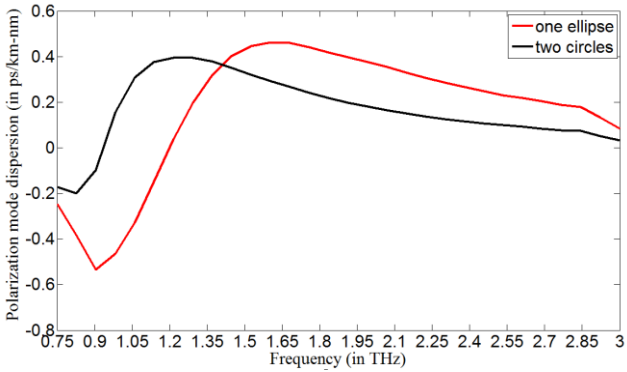

Fig.3. Polarization mode dispersion for the structures with elliptical holes and two circles.

References

[1] A. Barh, B. P. Pal, G. P. Agrawal, R. K. Varshney and B. M. A. Rahman, "Specialty Fibers for Terahertz Generation and Transmission: A Review," in IEEE Journal of Selected Topics in Quantum Electronics, 22, 2, 365-379, (2016).

[2] Y. Yue, G. Kai, Z. Wang, T. Sun, L. Jin, Y. Lu, C. Zhang, J. Liu, Y. Li, Y. Liu, S. Yuan, and X. Dong, "Highly birefringent elliptical-hole photonic crystal fiber with squeezed hexagonal lattice," Optics Letters, 32, 469-471, (2007).

[3] K. Ahmad, S. Chowdhury, B. K. Paul, M. S. Islam, S. Shen, M. I. Islam, S. Asaduzzaman, "Ultrahigh birefringence, ultralow material loss porous core single-mode fiber for terahertz wave guidance," Applied Optics, 56, 12, 3477-3483, (2007).

[4] R. Buczynski, I. Kuzawa, D Pysz, R. Stepien, "Highly birefringent soft glass rectangular photonic crystal fibers with elliptical holes," Applied Physics B., 99, 1, 13-17 , (2010).

OSI-ISO 2018 manuscript No.
(133)

Determination of surface binding properties using rotational optical tweezers

Rahul Vaipully, Dhanush Bhatt, Anand Dev Ranjan, Dillip Satapathy and Basudev Roy

Abstract Rotational optical tweezers uses circularly polarized light to rotate birefringent microparticles. Normally, if the particle is trapped far away from a surface, the rotation rate only goes to zero when the tweezers laser power is turned to zero. However, we find that if one traps close to a surface, the rotation rate goes to zero even at finite tweezers laser powers for some type of substrates. We suspect this to be due to binding between the substrate and the birefringent particle, keeping in mind that the hydrodynamic drag for this mode of rotation cannot increase beyond 1.2 times the drag away from the surface. We use this to probe some surfaces and find that there is no binding for hydrophilic ones but hydrophilic ones particularly tend to show a power threshold beyond which the birefringent particle starts rotating. We also place the particle on the threshold and observe "stick-slip" kind of rotational behaviour.

Keywords Optical tweezers · surface binding energy · birefringent microspheres · colloids

Optical tweezers is a very versatile tool for micromanipulation. The rotational degree of freedom in a birefringent microsphere has been well exploited to rotate a variety of particles using circularly polarized light. However it is generally believed that the rotation rate goes to zero if the particle is trapped too close to surface on account of infinite drag. We find that this statement is incorrect [1] because the drag in this mode of rotation is bound to 1.2 times the value far away from surface. Yet when we place our rotating particle close to some types of surfaces, it ceases to rotate at finite laser powers. We suspect that this is because of binding to the surface and explore the behaviour for many different types of surfaces. For hydrophoblic surface like a PDMS surface coated on glass, there is no sticking especially when the liquid crystalline birefringent microspheres are used. Hydrophilic surfaces, on the other hand, tend to show a sticking behaviour at finite laser powers. We also observe stick-

Indian Institute of Technology, Madras Chennai 600036 E-mail: basudev@iitm.ac.in

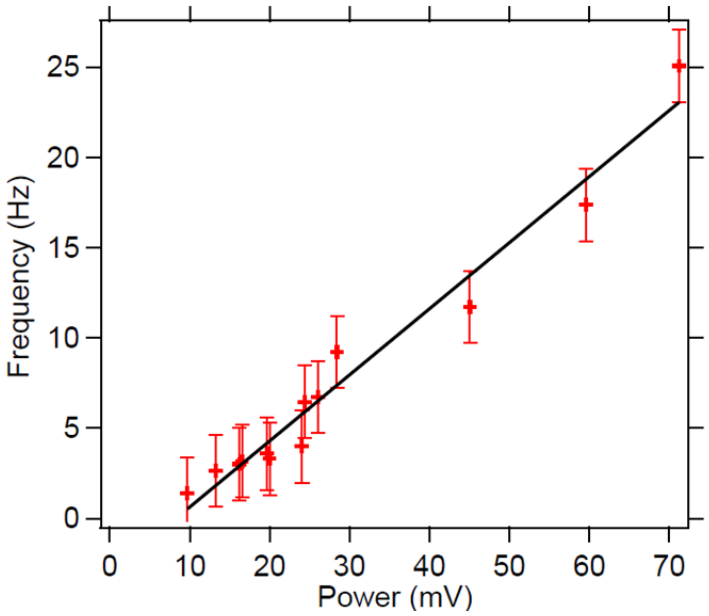

Fig. 1 The rotation rate of the birefringent particle goes to zero close to a surface at non-zero laser powers due to binding with surface.

slip behaviour just above the surface threshold. This can be used to quantify various types of surfaces and the leading order binding mechanisms. We find a regular glass surface mildly hydrophilic and has a low threshold, but when Chitosan substrate was used, the threshold increased significantly, inspite of the fact that chitosan is less hydrophilic than glass. We suspect that this happens because chitosan has adhesive properties particularly in the presence of water.

we study the stick-slip and find that the waiting time distribution can be used to ascertain the potential barrier of the washboard that the particle sees while rotating. We find a value of 0.78 k_BT which is slightly higher than 0.5 k_BT obtained from the equipartition theorem. The threshold shows that hydrophilic binding energy is about 40 k_BT.

Thus we show that the rotation of a particle in optical tweezers stops at finite laser power due to surface binding and show an application of the effect to ascertain surface properties.

References

1. Q. Liu and A. Prosperetti , Wall effects on a rotating sphere, J. Fluid Mech., 657, 1-21 (2010)

Poincare sphere representation for modes of a few-mode fiber

C. Hari Krishna, Koustav Dey and Sourabh Roy*
Department of Physics, National Institute of Technology Warangal, Telangana, India-506 004.
*sroy@nitw.ac.in

Abstract

We have demonstrated the various possible combinations of first order linearly polarized modes of a few-mode optical fiber that generate inhomogeneously polarized vector vortex modes. A set of degenerate linearly polarized modes with tilted polarization vector are shown to be responsible for the generation of a new class of vortex modes apart from well-known zeroth order vector modes. All these modes are positioned on the Poincare sphere according to their spatial polarization. A pair of higher order Poincare spheres is assumed to accommodate the inhomogeneously polarized vector vortex modes.

Keywords: Few-mode optical fiber, vector vortex modes, Polarization, Poincare sphere.

Introduction

Optical beams with inhomogeneous spatial polarization and azimuthally varying phase are drawing much attention owing to their unique features and wide spectrum of applications in scientific and industrial fields. Wide variety of methods have been proposed to generate and manipulate such optical fields using special optical elements including optical fibers [1,2]. The main reason for choosing fibers for this purpose is that these beams are the waveguide modes of the fiber and can be easily excited by controlling launching conditions. In fibers, these modes are derived from combination of scalar modes i.e., first order linearly polarized modes [3]. Additionally, the geometrical representation of such inhomogeneously polarized vector vortex modes (VVMs) is of fundamental scientific interest which is essential in understanding the geometric phase of light beams [4]. It is well known that any arbitrary state of polarization can be accommodated on the surface of a Poincare sphere (PS). This is valid only if the light beam is homogeneously polarized. In otherwise cases, a higher order PS (HOPS) is essential to represent the inhomogeneously polarized modes. A few Poincare sphere representations were proposed in literature that deal with the light beams having finite spin and orbital angular momenta [5, 6].

In view of this, here we have presented a geometrical representation exclusively for the VVMs of few-mode optical fiber (FMF) and also discussed their origin of generation by exploiting fiber mode degeneracy and mode mixing phenomena. All possible orthogonal LP_{11} modes of FMF are located onto a standard PS with respect to their spatial polarization distribution. The linear combinations of these LP_{11} modes, which results in the generation of various possible VVMs, are mapped onto a pair of HOPS. The evolution of new class of VVMs such as spiral and hybridly polarized modes is manifested as the linear combination of a new set of LP_{11} modes with tilted polarization vector.

VVM generation from orthogonal LP_{11} modes

In addition to the conventional LP_{11} modes with orthogonal $\hat{x}$ and $\hat{y}$ polarizations, the modes with polarization vector in the resultant direction, $\hat{u}$ and $\hat{v}$ also exist in an optical fiber, which stands responsible for the generation of spiral and hybrid vector modes. All generated VVMs are identical in spatial intensity but are different in the spatial polarization distribution. The on axis null intensity, resulting from the absence of field leads to the phase singularity which is a significance of helical phase and hence well-defined integral orbital angular momentum of ±1 [7]. Additionally, at the same region, the state of polarization is undefined too which leads to V-type polarization singularity [8]. Hence, these VVMs are phase and polarization singular and both singularities coincide with each other on the axis of VVMs. It is noteworthy to state that the linear combination of LP_{11} modes with orthogonal polarization $\hat{u}$ and $\hat{v}$ leads to the generation of vector modes with clockwise and anti-clockwise spiral polarization which have strong focusing properties next to radial and azimuthal vector modes [9,10].

Poincare sphere representation

In general, any arbitrary state of polarization on the surface of PS can be described using the four stokes parameters (s_0, s_1, s_2 and s_3), which gives the information about linear, elliptical and circular polarization content of the light beam and satisfies $s_1^2 + s_2^2 + s_3^2 = 1$. The coordinates (2ψ, 2χ), on the surface of PS represent the latitude and longitude of any arbitrary point which have their own physical significance in the sense that they represent the ellipse orientation angle (ψ) and the ellipticity (χ) of the polarization ellipse respectively. It is well known that any arbitrary polarization can be represented using any one of the three orthonormal basis $\{\hat{e}_H, \hat{e}_V\}$, $\{\hat{e}_D, \hat{e}_A\}$ and $\{\hat{e}_R, \hat{e}_L\}$ where $\hat{e}$ represents the base vector and H (horizontal), V (vertical), D (diagonal), A (anti-diagonal), R (right circular) and L (left circular) denote their

respective positions on the PS. The location of VVMs on HOPS is justified by the positions of orthogonal LP_{11} modes on PS, which combine to generate respective VVMs.

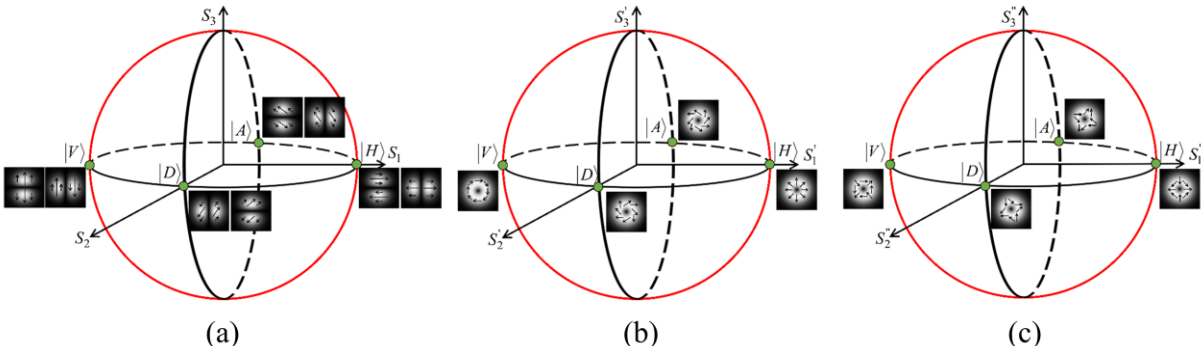

Fig. 1 (a) Allocation of LP_{11} onto PS, Higher order Poincare sphere (HOPS); (b) vector modes with regular polarization distribution (c) vector modes with hybrid polarization distribution

Fig. 1(a) shows the standard PS with conventional and tilted polarized LP_{11} modes located at their respective positions on the equator, according to their spatial polarization. It is clear that the conventional modes with orthogonal $\hat{x}$ and $\hat{y}$ polarizations occupy $|H\rangle$ and $|V\rangle$ positions whereas tilted polarized LP_{11} modes with orthogonal $\hat{u}$ and $\hat{v}$ polarizations occupy $|D\rangle$ and $|A\rangle$ positions respectively. The VVMs generated from the combination of $|H\rangle \pm |V\rangle$ LP_{11} modes occupy $|H\rangle$ and $|V\rangle$ positions, whereas the VVMs from the combination of $|D\rangle \pm |A\rangle$ LP_{11} modes occupy $|D\rangle$ and $|A\rangle$ positions, respectively on HOPS with new coordinate axes S_1', S_2' and S_3' as shown in Fig. 1(b). This HOPS contains vector modes with regular spatial polarization such as radial, azimuthal, spiral and counter spiral. The other linear combinations of LP_{11} modes results in generation of vector modes with irregular or hybrid polarization. These modes can't be accommodated on the same HOPS due to hybrid polarization. Hence, another HOPS is needed so as to accommodate these new hybrid VVMs. The accommodation of these hybrid VVMs on the HOPS with new set of Stokes axes S_1'', S_2'' and S_3'', is made according to previous case and shown in Fig 1(c). These two HOPS, as a pair, serve the need for representation of all possible VVMs of a step index FMF. It is observed that the linear translation along the equator of HOPS can result in new VVMs. Interestingly, a single half wave plate works as an efficient tool for transformation among these vector modes on both HOPS by rotating the local state of polarization. Moreover, all VVMs are phase singular with helicity of order one and it is anticipated that the vector modes that lie diametrically opposite on HOPS may have opposite helicity [7]. This reveals that the translation of vector modes along the equator of HOPS not only changes the orientation of polarization vector but also affects the azimuthal phase profile of the vector mode which shows a strong correlation between polarization and phase of light beams.

Conclusion

The generation of VVMs from the linear combination of first order linearly polarized modes of a few-mode fiber is presented. Poincare sphere approach is presented for the LP_{11} modes as well as the VVMs generated from their linear combination. The location of regular and hybrid VVMs on the HOPS is justified by the positions of orthogonal LP_{11} modes on PS, which combine to generate respective VVMs. This novel approach is efficient and much useful in representation of vector modes of a FMF. The VVMs with spiral and counter spiral spatial polarization which have sharper focusing properties next to radial and azimuthal vector modes are suitable for fields such as particle trapping and optical micro manipulation. The other VVMs with hybrid polarization may also have considerable contribution towards polarization based data encryption by providing addition degree of freedom.

References

[1] Q. Zhan, Adv. Opt. Phot. 1 (2009).
[2] A.M. Yao, M.J. Padgett, Adv. Opt. Phot. 3 (2011).
[3] A.W. Snyder, W.R. Young, J. Opt. Soc. A. 68 (1978).
[4] Giovanni Milione, S. Evans, D. A. Nolan, and R. R. Alfano, Phys. Rev. Lett. 108, (2012).
[5] Z.-C. Ren, L.-J. Kong, S.-M. Li, S.-X. Qian, Y. Li, C. Tu, H.-T. Wang, Opt. Exp. 23 (2015).
[6] W. Shu, X. Ling, X. Fu, Y. Liu, Y. Ke, H. Luo, Phot. Res. 5 (2017).
[7] V.V.G.K. Inavalli, N.K. Viswanathan, Opt. Comm. 283 (2010).
[8] S.K. Pal, Ruchi, P. Senthilkumaran, Appl. Opt. 56 (2017).
[9] R. Borghi, M. Santarsiero, M.A. Alonso, J. Opt. Soc. America. A, 22 (2005).
[10] C. Hari Krishna, S. Roy, Appl. Opt. **57** (2018).

OSI-ISO 2018 manuscript No.
(135)

Micro Photoluminescence Setup for Studies on Single Photon Emitters

Abhinav Kala · Venu Gopal Achanta

Abstract Single photon emitters are essential part of optics-based quantum information technologies. Quantum dots, nitrogen-vacancy centers in nano-diamonds etc. are few of the most widely used solid state single photon emitters [1]. Verification of the presence of a nano-emitter single photon source in a sample is a two-step process – first the spectrum of the light emitted from the sample has to be observed to check the presence of the characteristic photoluminescence of the nano-emitter and then second order time coherence ($g^{(2)}$) function for the emitted light has to be measured [2]. We use a micro photoluminescence setup (Fig. 1) for this purpose.

Keywords Single photon emitters · Hanbury-Brown-Twiss interferometer · Photoluminescence · $g^{(2)}$ function

1 Description of the Setup

Light from a laser is focused on the sample using an objective lens which excites the nano-emitters in the sample. The same objective is used to collect the light emitted from the sample. This light passes through a dichroic mirror to remove the laser light and goes into a spectrometer. The monochromator inside the spectrometer is used to spatially separate the photoluminescence from the light of other wavelengths. The photoluminescence is then provided as a input to a Hanbury-Brown-Twiss interferometer (boxed in green in Fig. 1)

Abhinav Kala
Tata Institute of Fundamental Research, Mumbai
E-mail: abhinav.kala@tifr.res.in

Venu Gopal Achanta
Tata Institute of Fundamental Research, Mumbai

[2]. Coincidence in the triggering of the two avalanche photodiodes is measured using coincidence measuring electronics as a function of time delay between triggering. This measured function is proportional to the $g^{(2)}$ function of the emitted light.

In case of an ideal single photon source at zero time delay $g^{(2)}$ function has the value 0. A value of $g^{(2)}(0)$ less than 1 signals quantum behavior. It's called photon-antibunching, while a value of $g^{(2)}(0)$ greater than 1 is called photon bunching [2]. We try to study nano-emitters coupled to photonic and plasmonic nanostructures using this setup. In Fig. 2 the spectrum observed using this setup shows the cavity enhanced emission of InGaAs quantum dot photoluminescence inside a GaAs photonic crystal cavity.

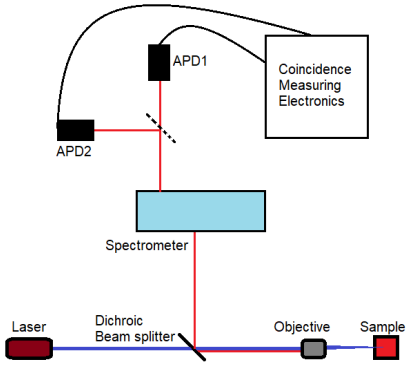

Fig. 1 Schematic of the setup. APD1 and APD2 are two avalanche photodiodes (Figure drawn using MS Paint)

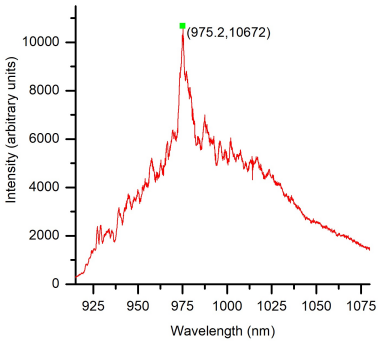

Fig. 2 Emission spectrum of InGaAs quantum dots inside a GaAs photonic crystal cavity. The sharp peak at 975.2 nm is due to the matching of the quantum dot emission wavelength with cavity resonance (Plotted using OriginPro 2015)

References

1. Igor Aharonovich, Dirk Englund, Milos Toth, Solid-state single-photon emitters, Nature Photonics, 10, 631-641 (2016)
2. A. M. Fox,Quantum Optics: An Introduction, 73-123. Oxford University Press, New York (2006)

OSI-ISO 2018 manuscript No.
(136)

Measurement of weak spin-Hall shift using Laguerre-Gaussian beams

Chandravati Prajapati[1] and Nirmal K Viswanathan[2]
[1]*Department of Physics, Koneru Lakshmaiah Education Foundation Hyderabad, Aziz Nagar, Hyderabad*
[2]*Department of Physics, University of Hyderabad, Gachibowli, Hyderabad*
Author e-mail address: chandra9.iitd@gmail.com

Abstract: We exploit quantum weak measurement to measure weak value of spin-Hall (SH) shift for higher-order Laguerre-Gaussian (LG) beams by pre-selecting the LG beam followed by weak interaction via external reflection through a prism surface and post-selection in nearly orthogonal polarization state. It was observed that the resultant SH shift for LG beams have three contributions- the usual spatial SH shift due to Gaussian profile, the angular SH shift due Gaussian profile and the spatial SH shift as a result of coupling of spatial profile of LG beam and angular in-plane of incidence, Goos-Hänchen shift. Further, the Jones polarization calculation for the proposed weak measurement shows that the angular contribution of SH shift was amplified while the spatial SH shift remains unamplified. The SH shift was studied with varying the angle of incidence from 26^0 to 70^0 for l=0 to l=3 mode TM and TE polarized LG beams and the shift is found to be proportional to order of the LG beam.
OCIS codes: Laguerre-Gaussian beam, Polarization, spin-Hall shift, weak measurement

1. Introduction

Spin-Hall (SH) shift of light beam arises when a light beam interacts with dielectric interface. After reflection or refraction, light beam is shifted in the plane of incidence known as Goos-Hänchen (GH) shift and perpendicular to the plane of incidence known as SH shift. These shifts are angular and spatial in nature and very small in magnitude (order of micro to mili radians and micro meters respectively) and therefore are difficult to measure using position sensitive detector or quadrant detector. Quantum weak measurement is an implication of quantum measurement of a system when the interaction between system and measuring device is relatively weak. It is very promising and well known experimental technique to measure the small effects in optical sciences by amplifying them. Laguerre-Gaussian (LG) light beams have phase singularity at the center of beam and associated to have charge which is related to an additional degree of freedom given by orbital angular momentum (OAM).

Theoretically, it has been proved that SH shift for higher-order LG beams increase and proportional to the OAM number but experimental detection of beam shift for LG beams is very limited and is mostly performed by quadrant detector which is very demanding, as these beams are prone to huge intensity deformation and cause large error. On the other hand, weak measurement which is more suitable and successful for measurement of beam shift remained unexplored for LG beams till date and can be used for the same. In this work we have used weak measurement to measure the SH shift of higher-order LG beams after external reflection from the prism surface by varying the angle of incidence. LG beam pre-selected in a specified polarization state undergoes weak interaction via external reflection from the prism surface. The reflected beam is post-selected in a polarization state nearly orthogonal to the pre-selected state and SH shift was extracted from these measurements.

2. Measurement and theory

The experimental setup is shown in the Figure 1. A vertically polarized Gaussian light beam from He-Ne laser of wavelength 632.8 nm and beam size 470 μm passed through a Spiral Phase Plate (SPP) to transform to a higher-order Laguerre-Gaussian (LG) beam. The LG beam is then pre-selected in a definite polarization state using a half-wave plate (HWP) and a Polarizer P_1 and further focused using a convex lens of focal length 50 mm to a beam size of 30 μm onto the BK7 right angle glass prism of refractive index n = 1.51. The prism is mounted on a rotation stage which is rotated during the experiment to change the angle of incidence. The beam after reflection from the prism is collimated using a lens of focal length 75 mm and then post-selected in an orthogonal polarization state using a polarizer P_2. When the polarizer P_2 is positioned orthogonal with respect to P_1, the intensity distribution is two lobe Hermite-Gaussian, oriented vertically in the beam cross-section, which are two orthogonal polarized RCP and LCP components separated due to amplified SH shift. When P_2 is rotated away from the crossed position, the intensity of one of the polarized components is separated.

The SH shift is extracted from the images recorded at crossed position and away from crossed position and plotted as a function of angle of incidence for LG beams of order $l = 0$ to $l = 3$ as shown in figure (lower section) for TM and TE polarized beams. It is observed that the SH shift increases with increasing order of the LG beams. For TM polarized beam, the SH shift is positive and increases with angle of incidence till the Brewster angle 56.5°, and then jumps from high positive value to high negative value and then decreases further with increasing angle of incidence. The SH shift for TE polarized beam increases with angle of incidence up to 46° and then decreases. The experimental result is plotted with the theoretical result. To calculate amplified SH shift theoretically using weak measurement, we have calculated expectation value of transverse y-coordinate between the pre-selected and post-selected states $|\Psi_1\rangle$ and $|\Psi_2\rangle$ for LG beam given by $E(r,\phi)$ using

$$Y_{SH}^{w} = \frac{\langle \Psi_2 | E^{*r}(r,\phi) y E(r,\phi) | \Psi_1 \rangle}{E^{*r}(r,\phi) E(r,\phi) \langle \Psi_2 \| \Psi_1 \rangle}.$$

Theoretical result shows that there is coupling between angular GH shift and complex spatial profile of beam that leads to additional spatial SH shift. Furthermore, Jones polarization calculation of weak measurement shows that there is amplification of only angular SH shift, the spatial SH shift remains unamplified. The theoretical equation of amplified SH shift as a result of weak measurement is written as

$$Y_{SH}^{w} = \frac{1}{k_0}\Re\left[i\left(1+\frac{r_{s,p}}{r_{p,s}}\right)\cot\theta\right] - l\frac{1}{k_0}\Im\left(\frac{\partial r_{s,p}}{\partial\theta}\right) + \frac{Z}{\Delta L}\frac{(1+|l|)}{k_0}\Im\left[i\left(1+\frac{r_{s,p}}{r_{p,s}}\right)\cot\theta\right].$$

3. Figures and tables

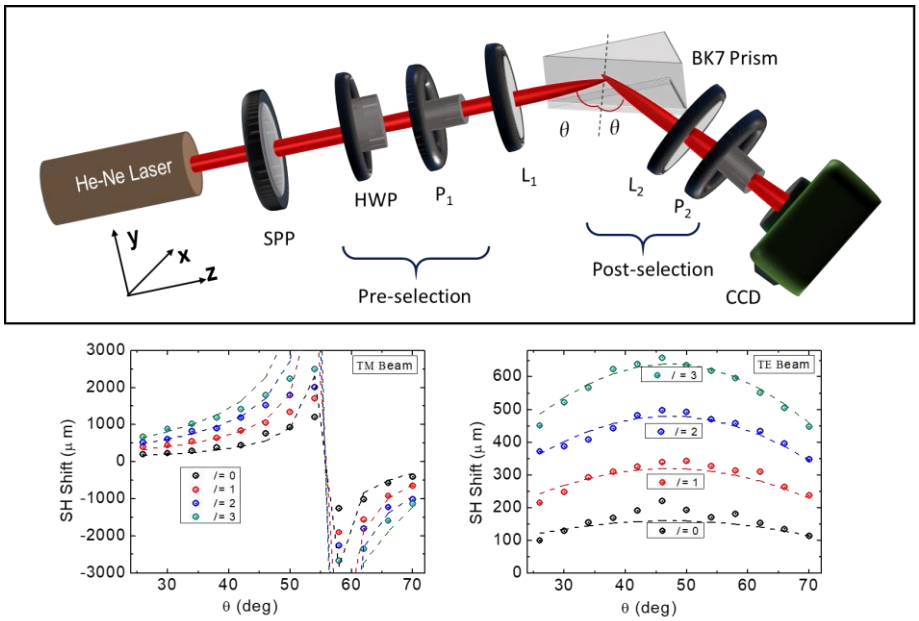

Figure 1: Experimental setup to measure the SH shift of higher-order LG beams using weak measurement. SPP (Spiral Phase Plate) is used to generate LG beams; P_1 and P_2 are Glan Thompson Polarizers used to pre-select and post-select the states; L_1 and L_2 are lenses of focal length 5 and 7.5 cm respectively; HWP, a Half-Wave Plate; CCD, a camera. Lower figure is plot of SH shift for TM and TE polarized beams plotted for various orders of LG beams, l=0 (black), l=1 (red), l=2 (blue) and l=3 (green).

Acknowledgement

The authors acknowledge financial support from Department of Science and Technology-Science and Engineering Research Board.

5. References

[1] K. Y. Bliokh and A. Aiello, "Goos-Hänchen and Imbert-Fedorov beam shifts: an overview," J. opt. 15, 014001 (2013).
[2] O. Hoston and P. Kwait, "Observation of the spin Hall effect of light via weak measurements," Science 319, 787-790 (2008).
[3] Y. Qin, Y. Li, H. He and Q. Gong, "Measurement of spin Hall effect of reflected light," Opt. Lett. 34, 2551 (2009).
[4] Y. Aharonov, D. Z. Albert and L. Vaidman, "How the result of a measurement of a component of the spin of a spin-1/2 particle can turn out to be 100," Phys. Rev. Lett. 60, 1351-54 (1988).
[5] N. W. M. Ritchie, J. G. Story and R. G. Hulet, "Realization of a measurement of a weak value," Phys. Rev. Lett. 66, 1107 (1991).

Birefringence analysis of twist-induced endlessly single-mode microstructure optical fiber

Rakhi Bhattacharya[1] and Nirmal K. Viswanathan[2]
[1]Department of Physics, School of Humanities and Sciences, Koneru Lakshmaiah Educational Foundation, Aziz Nagar, Hyderabad-500075, Telangana, India
[2]School of Physics, University of Hyderabad, Gachibowli, Hyderabad-500046, Telangana, India
Email: rakhi_bhattacharya@yahoo.co.in

Abstract

Birefringence analysis of twist-induced commercially available endlessly single mode microstructure optical fiber (MOF) is presented here and the results are compared with the behavior of standard single mode fiber. The evolution of output Stokes parameters as a function of applied torsion, varied from 0^o to 1440^o, leads to the observation of significant change in birefringence characteristics and twist-induced circular birefringence of the fiber, measured via the polarization ellipse behavior. Enormous change in output state of polarization under same torsion for MOF ESM-12B and conventional SMF has been realized from experimental observation. The mode-field diameter shrinks as the twist rate increases and the plane of polarization rotates in the direction of twist. For an isotropic single-mode fiber, twist induced changes have been studied as a perturbation. All the measurements lead to the potential application of twisted MOFs as polarization rotator.

Keywords: Microstructure optical fiber, Birefringence, stokes polarimetry, polarization ellipse.

Introduction:

Endlessly single-mode microstructure optical fibers (MOF) promise to find applications not only in delivery of broadband radiation in a single spatial mode, but also in current monitoring, short wavelength applications (visible and ultra violet), rotation sensing and other interferometric devices [1-2]. In this paper we discuss the influence of twist on the evolution of the polarization along endlessly single mode MOF, because twist is one of the imperfections usually present on any real or installed fibers [3-4]. Moreover, useful polarization optical devices can be constructed in a fiber by applying controlled twists to it. The influence of twist is intimately linked with the influence of the linear birefringence that exists in any real fiber due to deviations from a circular shape of its core or due to internal stress. We present an experimental study on change in state of polarization for a commercially available endlessly single mode (ESM-12, 87cm length) MOF with no intentional birefringence when a variable twist is applied. Instead of investigating the evolution of the state of polarization (SOP) along the fiber [1, 5] on the Poincare sphere, we investigated the evolution of output Stokes parameters as the applied torsion varied from 0^0 to 1440^0. The polarization state variation of emerging signals has been compared with data obtained for standard single mode fiber (SMF-630, 87cm length). In both cases, the same measurement procedure and polarimetric set up were used.

Experimental Setup:

To measure the input and output state of polarization an experimental setup has established by Stokes polarimetry technique shown in figure 1. The Gaussian beam from an unpolarized, 5 mW, 632.8 nm He-Ne laser is first polarized using a polarizer. The linearly polarized light then passes through a half-wave plate mounted onto a rotation stage to enable adjustment of the polarization direction of the input beam launched into the PCF.

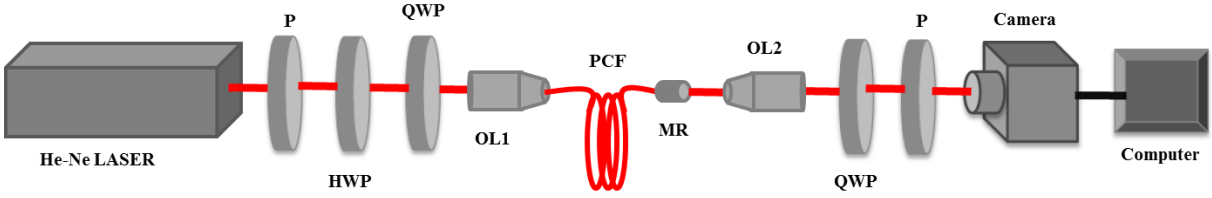

Figure1. Schematic of the experimental setup used for the measurement of birefringence due to twist. P- polarizer; HWP- half-wave plate; OL1, OL2- objective lenses; MOF- microstructure optical fiber; MR- mechanical rotator.

The beam after passing through the polarization components is focused using a 0.25 NA 10 microscope objective lens L1 onto the cleaved end of the ESM-12 PCF, positioned using a three-axis stage. The PCFs used here are about 87 cm long and are kept horizontal with one end fixed and other end mounted with a mechanical rotator to produce twist. At the output end another microscopic lens L2 with 0.40 NA numerical apertures is used to collimate the beam. Quarter wave plate with combination of polarizer is placed at output end to measure stokes parameters.

Results and Discussion:

1.1 Twist Induced PCF

In the present case input state of polarization is fixed, a linearly polarized horizontal beam is launched into the PCF with an objective lens. At the output end Stokes polarimetry setup is used to measure Stokes parameter, normalized stokes

parameter are calculated and shown in figure 2 for various twist angle. The measurement has performed for five different twist angles from 0^0 to 1440^0 with an interval of 360^0.

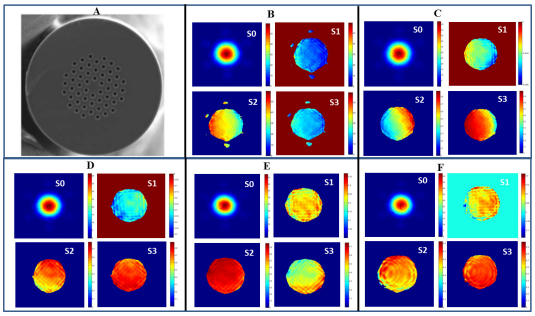

Figure.2 A. Cross sectional view of ESM-12; normalized stokes parameters are shown in different twist angle (B) 0^0, (C) 360^0, (D) 720^0, (E) 1080^0 and (F) 1440^0 at horizontal input polarization.

Initially when no twist is applied i.e. twist angle is 0^0, the normalized Stokes parameters are depicted in figure 2(a). An algorithm is developed to extract the normalized stokes parameters from the experimentally measured data. Total intensity S_0, horizontal and vertical components S_1, diagonal and anti-diagonal components S_2, right circularly polarized (RCP) and left circularly polarized (LCP) component S_3 is calculated and plotted for each twist angle varied from 0^0 to 14400. (θ, δ) intensity of the light variation in the direction which makes an angle θ with the x- axis direction after the phase retardation δ. Ellipticity $\chi = \frac{1}{2} sin^{-1}(S_3/S_0)$ and ellipse orientation $\alpha = \frac{1}{2} tan^{-1}(S_2/S_1)$ are calculated by measured data and ellipse orientations are shown in figure 3(a) for each rotation angle of ESM-12B PCF and figure 3(b) for SM-630 conventional single mode fiber.

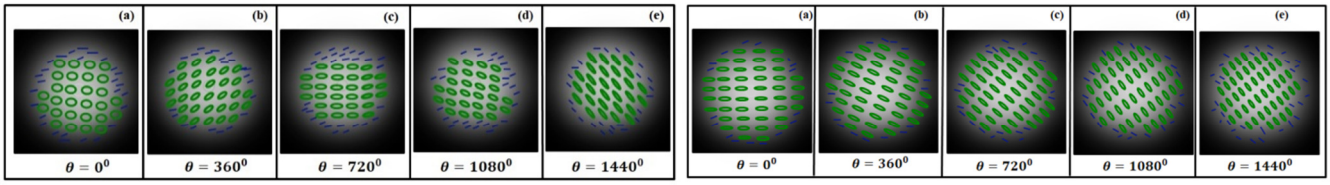

(A) (B)

Figure.3(A) Ellipse orientation of ESM-12B PCF at twist angle (a) 0^0 , (b) 360^0, (c) 720^0, (d) 1080^0 and (e) 1440^0 for horizontal input polarization. Figure.3(B) Ellipse orientation of SM-630 conventional single mode fiber at twist angle (a) 0^0 , (b) 360^0, (c) 720^0, (d) 1080^0 and (e) 1440^0 for horizontal input polarization.

From figure 3(A) it is clear that direction of polarization ellipse and ellipticity changes clockwise as the twist angle is increased. Input state of polarization is fixed for the evolution of the output state of polarization measured for the endlessly single mode fiber (ESM-12B) and the standard single-mode fiber (SMF-630).

Conclusion:

We have studied the evolution of output Stokes parameter as the applied torsion varied from 0^0 to 1440^0. Polarization measurement executed by Stokes polarimetry techniques and significant birefringence properties are observed from polarization ellipse of twist induced MOF and results are compared with standard SMF-28. Enormous change in output state of polarization under same torsion for MOF ESM-12B and conventional SMF has been realized from experimental observation.

Acknowledgement:

This work is supported by the Science and Engineering Research Board (SERB), Government of India through the R&D grant no. YSS/2015/001631. The author would like to thank Science and Engineering Research Board (SERB), Government of India, for providing Young Scientist Award to carry out this research work.

References:

[1] R. Ulrich and A. Simon, "Polarization optics of twisted single-mode fibers," *Appl. Opt.*, vol. 18, pp. 2241–2251, 1979.

[2] S. C. Rashleigh, "Origins and control of polarization effect in single-mode fibers," *J. Lightwave Technol.*, vol. T-1, pp. 312–331, 1983.

[3] F. P. Kapron, N. B. Borelli, and D. B. Keck, IEEE J. Quantum Electron. QE-8, 222 (1972); W. A. Gambling, D. N. Payne, and H. Matsumara, in Digest of Topical Meeting on Optical Fiber Transmission II, (Optical Society of America, Washington, D.C., 1977), p. TuD5.

[4] H. Papp and H. Harms, Appl. Opt. 14, 2406 (1975).

[5] Tentori D., Ayala-Díaz C., Ledezma-Sillas E., Treviño-Martínez F., García-Weidner A., Opt. Commun. 282(5), 830-834 (2009).

Silicon Nano-Waveguide Designs for Broadband Photon Pair Generation at Telecom Wavelengths

Pravin Rawat[1], Shivani Sharma[1], Vivek Kumar[1], V. Venkataraman[1], J. Ghosh[1*]
[1]*Department of Physics, Indian Institute of Technology Delhi-110016, India*
[*]*email: joyee@physics.iitd.ac.in*

Abstract: *Nonlinear photonics in SOI (silicon-on-insulator) waveguides has emerged as a promising technology for quantum light sources at telecom wavelengths (~1.5 μm). Here we explore dispersion engineering through numerical mode simulations in order to design optimal waveguide dimensions for photon pair generation across the entire telecom spectrum (~1.3 – 1.8 μm). Both silica-clad embedded waveguides and air-clad strip waveguides are shown to yield broad phase-matching bandwidths.*
Keywords: Four Wave Mixing, Dispersion, Photon Pair Generation, Kerr Non linearity

1. Introduction

As part of quantum photonic technologies, generation of efficient broadband and photon pairs, especially at telecommunication wavelengths (around 1550 nm), is critical for applications such as long distance quantum communication [1]. Four wave mixing (FWM) in Kerr nonlinear media such as silicon is a way to generate photon pairs symmetrically detuned from a central pump wavelength [2]. Silicon-on-insulator (SOI) nano-waveguides can greatly enhance the efficiency of such nonlinear processes, due to the tight light confinement afforded by high refractive index contrast *($n_{silicon}$ - n_{SiO2} = 2.0007 at 1550 nm)* in addition to the large Kerr nonlinearity *($4-9 \times 10^{-18}\ m^2/W$)* of silicon [3, 4]. The objective of our work is to design optimal SOI waveguides for the generation of broadband photon pairs across the entire telecommunication spectrum (~ 1.3-1.8 μm) pumping at the C-band wavelength of 1550 nm. As waveguide dispersion can compensate for the material dispersion [3], the dimensions of the waveguide are optimized to yield a negligible phase mismatch between the input pump and the generated signal and idler photons.

Fig.1 shows the optimal structure that we obtained (a) for the silica-clad embedded and (b) air-clad strip waveguide designs. Fig. 2 shows the TE (transverse-electric) mode profiles of the respective waveguides. Figure 3 shows the total phase mismatch for the two waveguides, given by [4]

$$\Delta\beta = 2\gamma_{\circ} p_p - \Delta\beta_{linear}$$

Where $\Delta\beta_{linear} = 2\beta_p - \beta_s - \beta_i$ is the linear phase-mismatch ($\beta_p, \beta_s, \beta_i$ are the propagation constants of the pump, signal and idler modes, respectively), and $2\gamma_{\circ} P_p$ is the non-linear phase-mismatch, $\gamma_{\circ}$ and P_p are the effective nonlinearity and pump power respectively. For photon-pair generation through spontaneous FWM, $\Delta\beta_{linear} >> 2\gamma_{\circ} P_p$ for typical pump powers of P_p ~ 1-10 mW. If we include the dispersion term up to fourth-order, the linear phase-mismatch [5] is given by

$$\Delta\beta_{linear} = -\beta_2(\Delta\omega)^2 - \frac{1}{12}\beta_4(\Delta\omega)^4$$

Where $\beta_2 = \frac{\partial^2 \beta}{\partial\omega^2}$ and $\beta_4 = \frac{\partial^4 \beta}{\partial\omega^4}$ is the group velocity dispersion (GVD) parameter and fourth order dispersion (FOD) parameter at the pump wavelength respectively, $\Delta\boldsymbol{\omega}$ is the angular frequency difference between the pump and the signal/idler. For generation of correlated photon pairs, the phase matching condition should be satisfied i.e. $\Delta\beta \sim 0$ or $-\frac{\pi}{2L} < \Delta\beta < \frac{\pi}{2L}$, where L is the length of waveguide (1 cm in our case).

We use both RSOFT and COMSOL FEMSIM packages to find the optical modes, effective indices and dispersion of waveguides with various dimensions, taking into account material dispersion of both silicon and silica [6].

2. Structure and analysis

We analysed two types of SOI waveguides for generation of broadband photon pairs:

1) Embedded (Silica clad)
2) Strip (Air clad)

Embedded Waveguide: As shown in Fig. 1(a), the rectangular embedded waveguide has a core of silicon (blue) and cladding of silica (silicon dioxide, black). Since the most commonly used commercially available SOI wafer has a silicon layer thickness of 220 nm, we kept the height of the rectangular waveguide constant at 220 nm and vary the width. The optimum dimension obtained is 220 nm × 420 nm, yielding the broadest phase-matching bandwidth of ~180nm (see Fig. 3a).

Strip Waveguide: As shown in Fig. 1(b), for the rectangular strip waveguide, the top cladding of silica is not deposited resulting in an air-clad structure. Again, the height of the rectangular waveguide is kept constant at 220 nm and the width varied. The optimum dimension obtained is 220 nm × 758 nm, yielding the broadest phase-matching bandwidth of ~450nmin this case (see Fig. 3b).

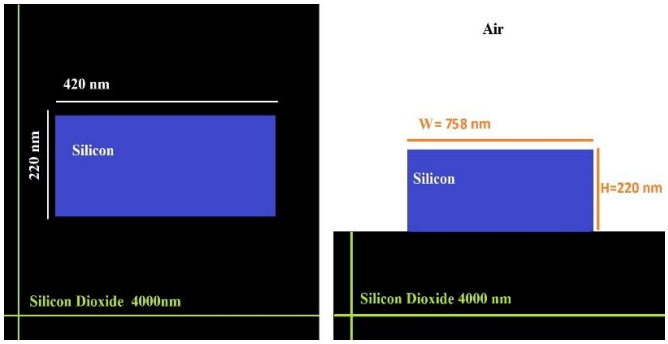

Fig. 1 (a).Embedded Rectangular Waveguide and (b) Strip Waveguide.

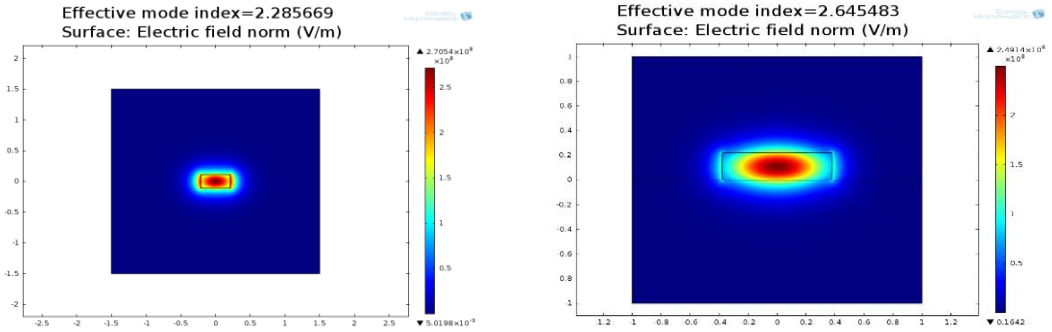

Fig. 2 (a) TE mode profile Embedded Waveguide (b) for Strip waveguide

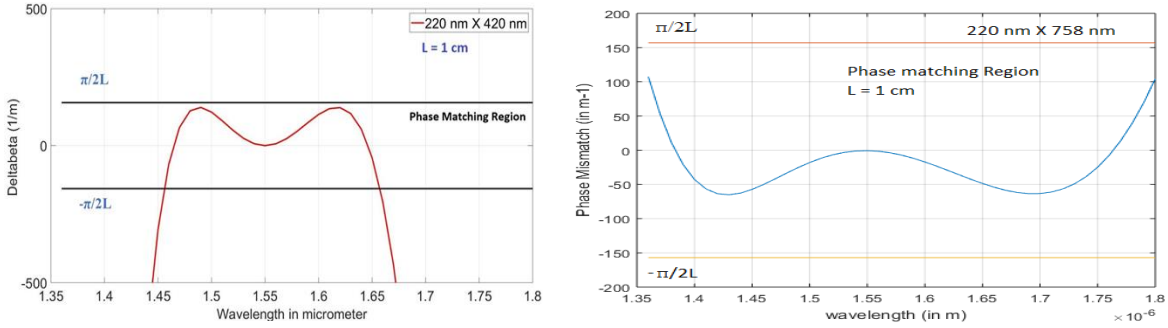

Fig. 3 (a) Phase mismatch (Δβ) for Embedded waveguide (b) Phase mismatch (Δβ) for Strip waveguide

3. Results and Conclusions

A rectangular embedded (silica clad) and strip (air clad) SOI waveguide has been studied and proposed for generation of broadband photon pairs at telecom wavelengths, yielding phase-matching bandwidths of ~200 nm and ~450 nm respectively. Both these types of SOI waveguides with such dimensions are routinely fabricated with existing technology.

4. Application

The proposed waveguides can be used as sources for Wavelength Division Multiplexing (WDM) systems in quantum communication, where single photons at many different channels spaced in frequency/wavelength can be simultaneously used to carry information to boost data rates and/or number of users.

References

[1] Tretyakov, D.B., Kolyako, A.V., Pleshkov, A.S. et al. Optoelectron Instrument Proc. (2016) 52: 453.
[2] Q. Lin and Govind P. Agrawal, "Silicon waveguides for creating quantum-correlated photon pairs," Opt. Lett. 31, 3140-3142 (2006).
[3] Dinu, M., Quochi, F. & Garcia, H. Third-order nonlinearities in silicon at telecom wavelengths. Appl. Phys. Lett. 82, 2954–-2956 (2003).
[4] Mark A.Foster, "Broad-band optical parametric gain on a silicon photonic chip," Nature 441, 960 (2006).
[5] Jonas Hansard, "Fiber-based optical parametric amplifiers and their application," Vol. 8, No. 3, (2002).
[6] https://refractiveindex.info

Analysis of zinc oxide based grating structure over silicon waveguide

Srinjoy Maiti (Research Scholar)†*Dr. (Prof.) Rajib Chakraborty†
† Department of Applied Optics & Photonics, University of Calcutta, JD – 2 (Sector - III), Salt Lake City, Kolkata – 700106, West Bengal
✉srinj.max@gmail.com*, rchakrab@gmail.com

Abstract

A zinc oxide (ZnO) grating structure on top of silicon (Si) waveguide in a silicon-on-insulator (SOI) substrate has been proposed. Gratings of ZnO on top of silicon is a new concept. The proposed structure has been designed to act as an input coupler as well as a sensor in photonic integrated circuits. The structure is made to operate at 1310 nm wavelength in TE mode for first diffraction order. Theoretical analysis using Finite Element Method (FEM) has been done for optimizing the structural dimension and to evaluate as well as to enhance the optical performance of the proposed device. Two cover materials namely air and SiO_2 has been used for the simulation. To optimize the grating coupler, the duty cycle of the grating structure has been varied from 20%-90%. The effect of the variation on the transmitted beam diffracted by the ZnO gratings and guided out by the Si waveguide layer has been studied and the diffraction efficiency has been calculated for each duty cycle value. The variation of the diffraction pattern with the incident angle and the dependency of the diffraction efficiency on the operating wavelength (1300-1320) nm for both the cover materials has been calculated and studied respectively.

Keywords

ZnO, Diffraction grating coupler, Sensor, Photonic device

Introduction

Silicon-on-insulator (SOI) based grating couplers have established itself emphatically as excellent photonic device in both due to its easy productivity, nano-order scalability and high refractive index (r.i.) contrast in between the guiding and the substrate layer thereby exhibiting perfect transmission in IR region of the electromagnetic spectrum [1, 2]. Among different semiconductor oxides, ZnO is gallantly advancing nowadays, in the arena of nano-photonic devices, for grating and sensing applications by the virtue of its high optical transmissivity and high conductivity characteristics [3-5]. The growth of ZnO films on Si films/substrate has already been experimentally validated [6, 7] and their combination is needed to be studied in the field of photonics which is the motivation of this work.

Results and Discussions

The schematic structure of the proposed device has been shown in Fig. 1. In order to ensure negligible light leakage toward the substrate and the buried-oxide (BOX) layers, the widths have been taken as 1.2 µm and 0.8 µm for the substrate and BOX layer respectively. The device comprising of 20 grating elements is designed to operate at 1310 nm in TE mode and the pitch of the grating has been confined to 400 nm to capture only the diffracted pattern of m=1 order. Due to the zero dispersion behaviour, 1310 nm has been chosen as the operating wavelength for the proposed structure. For simulation purpose the r.i. of the Si, BOX and the ZnO material has been taken as 3.505, 1.45 and 1.5715 respectively [8, 9]. Two cover materials namely air (r.i.=1) and silicon di-oxide (SiO_2, r.i.=1.45) has been used throughout the simulation.

Fig. 2 shows the dependency of the diffraction efficiency on the duty cycle of the grating. The duty cycle has been varied from 20%-90% of the grating constant. The maximum value of the efficiency is≈79.1% at 50% duty cycle when the cover material is air and ≈62% at 40% duty cycle when the cover material is SiO_2.Fig. 3 exhibits the diffraction pattern for different incident angles (0^o-90^o) on the grating. The pattern shows the peak value at 17.8^o and 55.7^oincident angle for air and SiO_2 respectively. Though the peak transmittance value is falling by a value of ≈0.17 yet the sharp diffraction pattern of SiO_2 is noticeable and promises to be a good cover material for the proposed structure. Fig. 4 shows the variation of the transmitted power of the grating upon slight variation of the value of the operating wavelength on both plus-minus order. The wavelength that corresponds to the maximum value of the transmittance for both the cover materials is 1310 nm, which is the wavelength aimed at in the design of this grating structure. The drop in the efficiency or the transmittance value with change in the refractive index of the cover material is evident in all the simulated results, which definitely infers to the fact that this structure can also be used as a sensor in photonic integrated circuits.

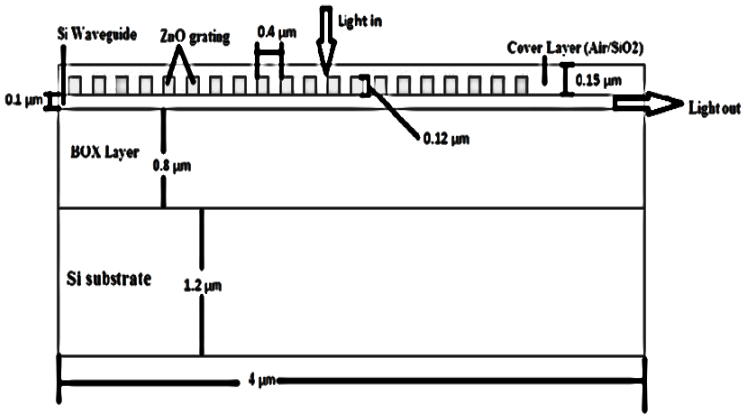

Fig. 1 Schematic diagram of the simulated structure

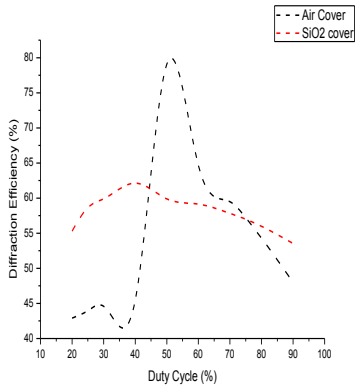

Fig. 2 Diffraction efficiency (m=1) vs Duty Cycle

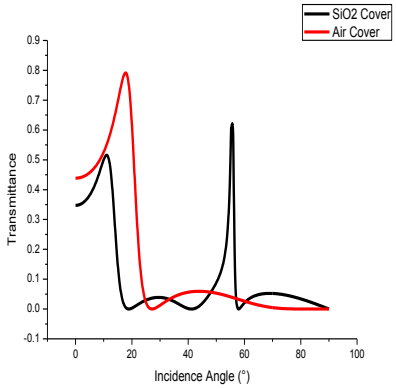

Fig. 3 Diffraction pattern (m=1) vs Incident Angle

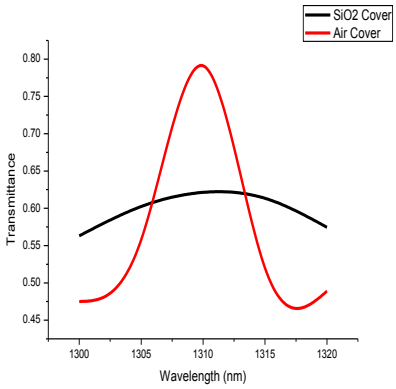

Fig. 4 Transmittance (m=1) vs Wavelength

Conclusions

A ZnO based grating structure on SOI waveguide has been proposed and analysed using FEM method. From the simulated results we can infer that the proposed structure can find its application in the field of photonic devices both as a grating coupler as well as a sensor to track down the variation in refractive index. Optimization of parameters like the BOX layer or the guiding layer height, the grating height etc. may increase the diffraction efficiency of the proposed structure to a higher value with respect to the current value.

References

[1] B. Wei, H. Liu, G. Ren, Y. Yang, S. Ye, L. Pei, S. Jian, Phys. Lett. A 381, 3 (2017)

[2] J. Wang, I. Glesk, L.R. Chen, Sci. Bulletin 61, 11 (2016)

[3] L. Zhu, W. Zeng, Sens. Actuators A 267, (2017)

[4] A. Hastir, N. Kohli, R.C. Singh, J. Phys. Chem. Solids 105, (2017)

[5] P. Struk, T. Pustelny, K. Gołaszewsk, E. Kamińska, M.A. Borysiewicz,M. Ekielski, A. Piotrowska, Opto Electron. Rev. 21, 4 (2013)

[6] M. Zerdali, S. Hamzaoui, F.H. Teherani, D. Rogers, Mater. Lett. 60, 4 (2006)

[7] G.A. Kumar, M.V. Reddy, K.N. Reddy, IOP Conf. Series: Mater. Sci. Eng. (2015) https://doi.org/10.1088/1757-899X/73/1/012133

[8] L. Vivien, D. Pascal, S. Lardenois, D.M. Morrini, E. Cassan, F. Grillot, S. Laval, J.M. Fédéli, L.E. Melhaoui, J. Lightwave Technol. 24, 33 (2006)

[9] C. Stelling, C.R. Singh, M. Karg, T.A.F. König, M. Thelakkat, M. Retsch. Sci. Rep. 7, 42530 (2017)

OSI-ISO 2018 manuscript No.
(140)

Performance Evaluation of bidirectional Distributed Raman Amplifier with equal number of forward and backward pumps

Shameem Saifuddin · **Arunagiri Sivasubramanian**

Abstract In this paper, bidirectional pumped Raman Amplifiers with forward and backward pumps are analysed for the performance in terms of gain and noise figure. Equal number of pumps are used in both directions with multiple wavelengths as it helps to attain a flat gain for the amplifier. The effect of pump powers on the gain and noise figure for a constant pump power ratio is investigated through simulations.

Keywords Distributed Raman Amplifier · Bidirectional pumping · Gain · Noise figure

1 Introduction

Recently Raman fiber amplifiers have gained very much attention in Dense and Ultra Dense WDM system due to their wide bandwidth [1]. Unlike the Erbium doped fiber amplifier, these Raman amplifiers do not need any doped media and the installed fiber itself act as the gain media [2]. Different pumping methods have been reported for different applications as each pumping gives specific gain as well as noise figure. Backward pumping helps in improving noise figure and while forward pumping helps to attain higher gain [3]. Hence, multiple bidirectional pumping is found to be the optimum pumping method in most of Raman Amplifier demonstrations. In this work, we investigate the dependence of gain and noise figure on the pump powers for an amplifier configuration with equal number of forward and backward pumps.

2 Simulation setup

The simulation setup done in Rsoft Optsim software consists of 40 Gbps, 40 channel DWDM link with an inter channel spacing of 50 GHz at a bit rate of 1 Gbps as shown in Fig. 1. The bandwidth considered is 70 nm and a 70 km distributed Raman Fiber Amplifier with zero dispersion is used in the setup. Five pumps are used in the forward and backward direction as indicated in Fig. 1 which are combined using appropriate MUX. Two different sets of pump wavelength were used for simulation. The first set consists of CW laser pumps with optimal wavelengths 1420 nm, 1435 nm, 1450 nm, 1465 nm and 1495 nm as pump wavelengths and the second set consist of pump wavelengths 1445 nm, 1450 nm, 1465 nm, 1480 nm and 1490 nm. The signal wavelength is assumed to be around 1550 nm in both cases. The pump power ratio is maintained at 20% in all cases as all the pumps are fed with the same power [4].

3 Results and Discussion

Bidirectional multiple pumping is analysed with equal number of forward and backward pumps with optimal pump power so that the pump power ratio is fixed at 20%. The backward absolute gain was found to -1000dBm/GHz and forward absolute gain was found for the wavelength range of 1535-1555nm around 2.77 dB. Forward gain for the wavelength 1553-1554 nm is found to be 23.61 dB which is a moderate gain for working as an in-line amplifier. But from the setup, the forward effective noise figure

School of Electronics Engineering
Vellore Institute of Technology
Chennai, India
E-mail: shameem.s2015@vit.ac.in ·

for the wavelength range of 1538-1553 nm is 10.93 dB, which is very high in case of fiber amplifiers and forward SNR for the range of wavelength is 43.01 dB. The backward and forward gain as a function of pump power is plotted in Fig. 2 (a). It may be observed that as the pump power increases, the gain decreases. This is consistent for both the sets of pump wavelengths used for the simulation.

The output signal distortion increases with increase in pump power even when the pump power ratio was fixed at 20%. Though the gain is high, the noise figure increases for higher values of pump. The main advantage of using multiple pumping methods for Raman Amplifiers is a flat gain and it is achieved when the pump power is kept at a low value than high pump power values. As illustrated in Fig. 2 (b), the noise figure for set 1 wavelength is found to be maximum for 1435 nm, whereas it is linear in the case of second set of wavelength.

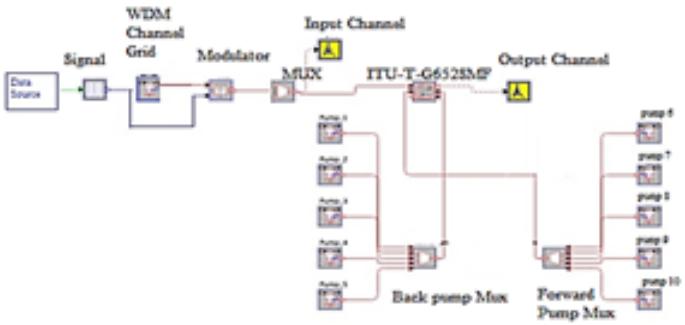

Fig. 1 Simulation setup showing bidirectional pumping with equal number of forward and backward pumps.

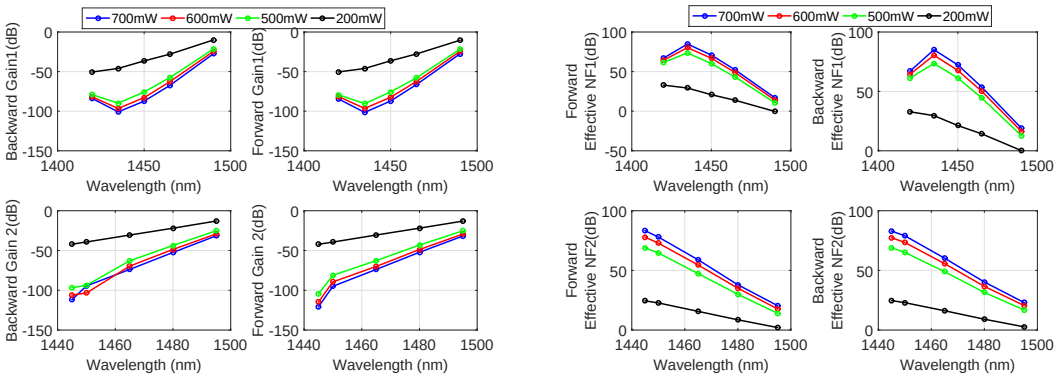

Fig. 2 (a) Forward and backward gain as a function of pump wavelength (b) Forward and backward effective noise figure as a function of wavelength. 1 and 2 indicate the first and second set of pump wavelengths.

4 Conclusion

In this study, the performance of bidirectional pumped Raman fiber amplifier with equal number of forward and backward pumps is analysed in terms of amplifier gain and noise figure. For a fixed pump power ratio, the gain is found to decrease with increase in pump power. The output signal distortion is also found to increase as the noise figure increases with higher pump powers.

References

1. J. Bromage, Raman amplification for fiber communications systems, Journal of Lightwave Technology, vol. 22, no. 1, pp. 79-93, (2004).
2. S. Namiki and Y. Emori, Ultrabroad-band Raman amplifiers pumped and gain-equalized by wavelength-division-multiplexed high-power laser diodes, IEEE Journal of Selected Topics in Quantum Electronics, vol. 7, no. 1, pp. 3-16, (2001).
3. S. Kado, Y. Emori, S. Namiki, N. Tsukiji, J. Yoshida and T. Kimura, Broadband flat-noise Raman amplifier using low-noise bidirectionally pumping sources, Proceedings 27th European Conference on Optical Communication, vol.6, pp. 38-39 (2001).
4. I. Syuaib, M. Asvial and E. T. Rahardjo, Ultra-long span optical transmission using bidirectional Raman amplification, 2015 International Conference on Quality in Research (QiR), pp. 86-89 (2015).

OSI-ISO 2018 manuscript No.
(141)

Localized Magnetic Field Enhancement in Fano Resonance based Active Metamaterial

Subhajit Karmakar[1*], Ravendra K. Varshney[1], and Dibakar Roy Chowdhury[2]

Abstract We study magnetic field enhancement and the creation of near field hotspot in a variable capacitor loaded active Fano metamaterial. Our design consists of dual gap rectangular split ring resonator with external capacitor loaded in the split gaps which supports asymmetric Fano resonance depending upon its structural asymmetry. Fano resonance, due to its indirect excitation, is free from radiation loss and it largely enhances magnetic field by displacement current mechanism. Interaction of incident radiation with metamaterial structure causes manipulation of electromagnetic field near the surface, depending upon structural geometry and design parameters of our metamaterial structure. We report more than six order of magnitude enhancement of magnetic field at resonance frequency in our designed structure. Moreover, the enhancement factor can also be tuned to various values and different frequency range by changing the value of external capacitor and degree of asymmetry. Our study can be used in variable device applications in topological and nonlinear optics.

Keywords Metamaterial, Terahertz, Fano resonance, Magnetic hotspot.

1. Introduction

Interaction of incident electromagnetic wave with any material causes the force applied by the electric field, which is *'c/v'* times higher than that of by the magnetic field [1]. In atomic systems and natural materials, magnetic field and magnetic susceptibility is 4^{th} order of magnitude lower than the corresponding electric field. However, high magnetic field coupling is very important in atmospheric science to detect unwanted radio communication blockage, nonlinear optics, enhanced surface Plasmon generation, spin rectification, optically controlled etching, magnetic optical Kerr effect, memory design, and sensor applications [2-3]. Due to lack of natural magnetic materials, several attempts have been made to localize and confine magnetic field with artificially engineered structures like Metamaterials, which have gained tremendous interest due to numerous applications [4]. One of the limitations of typical metal-dielectric based metamaterial is huge ohmic and radiative loss. Recently, people have demonstrated Fano resonance in asymmetric metamaterial structure to minimize such losses. Fano resonance can be used for various applications like solar energy harvesting, molding of light, highly sensitive sensors etc. [5].

In this paper, we have shown the creation of magnetic hotspot in Fano-resonance based active metamaterial in THz domain through simulations. The degree of magnetic field enhancement and magnetic field spectra have been tuned by changing external capacitor in the lower gap (C_1 in Fig. 1(a)) and asymmetry parameter *'d'*. Such tunable hotspot can be very effective for different applications with varying frequency range.

Subhajit Karmakar
E-mail: *subhajit.k1995@gmail.com
[1] Department of Physics, Indian Institute of Technology, Delhi, India 110016
[2] Department of Physics, Mahindra Ecole Centrale, Jeedimetla, Hyderabad, India 500043

2. Proposed design and simulation results

The structure of the unit cell of our proposed metamaterial has been shown in Fig. 1(a). Substrate (in brown) and resonator (in yellow) consist of silicon (Si) and aluminum (Al), respectively. These structures are stimulated by frequency domain solver in CST microwave studio software with varying 'd' and C_1. Incident field directions are shown in Fig. 1(a).

Magnetic field behavior for d = 20 μm with the presence of capacitor C_1 (= 0.5 fF) and with the absence of C_1 has been shown in Figs. 1(b) and 1(c) respectively. Due to introduction of external capacitor in lower gap, a large displacement current has been induced in the lower gap of the structure, which eventually causes large magnetic field (H) near the resonator surface [6]. The maximum value of magnetic field in the present configuration has been found to be 5.23×10^5 A/m (as shown in Fig. 2(a)) which can be tuned further by varying *'d'* and C_1. In order to show this tunability, we have plotted variation of magnetic field enhancement factor (H/H_0, where, H_0 is the incident Magnetic field) with *'d'* and C_1 as shown in Figs. 2(b) and 2(c) respectively. A maximum of 4.7×10^6 times enhancement has been obtained for C_1=1 fF.

3. Conclusion

In this work, magnetic field enhancement in capacitor loaded active Fano-metamaterial has been studied. It is shown that magnetic field enhancement as high as 4.7×10^6 times is obtained by using C_1 of 1 fF. The enhancement factor has also varied with varying asymmetry and capacitor value in the structure. Such property in plasmonic Fano metamaterial structure can be utilized to make advance nonlinear Fano devices.

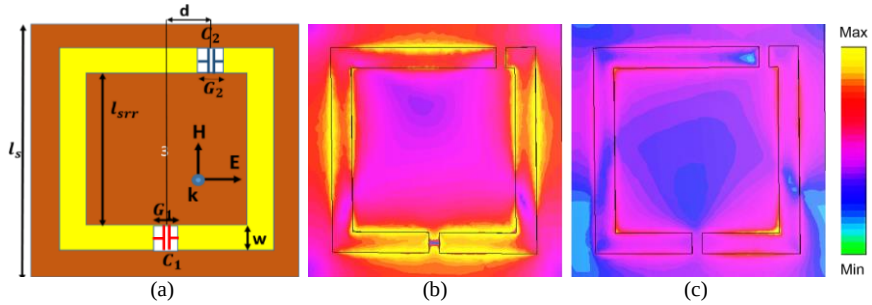

(a) (b) (c)

Fig. 1 (a) Schematic of the proposed Metamaterial structure [l_s=75 μm, l_{srr}=60 μm, w=6 μm, G_1 = G_2 = 3 μm] **(b)** Magnetic field distribution at Fano dip of frequency f=1.167 THz (C_1 in the lower gap) **(c)** Magnetic field distribution at Fano dip of frequency f=1.27 THz (no capacitor)

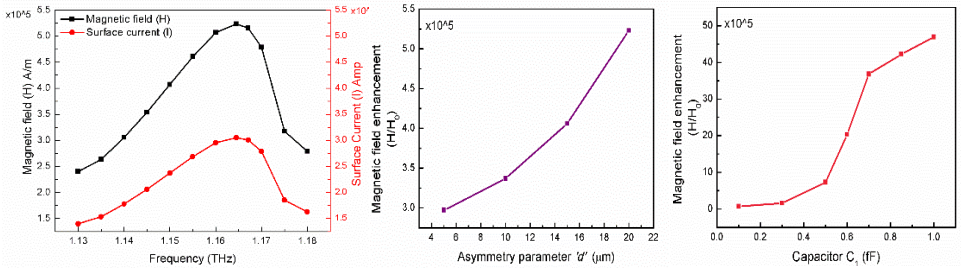

(a) (b) (c)

Fig. 2 (a) Spectral response of magnetic field (H) and surface current (I) at Fano dip (1.167 THz) **(b)** Variation of magnetic field enhancement Factor (H/H_0) for C_1 = 0.5 fF **(c)** Variation of magnetic field enhancement Factor (H/H_0) for d = 20 μm.

References

[1] M. Burresi1 *et al.* Science, 326, 5952 (2009).
[2] Jingbo Sun *et al.* Scientific Reports, 5, 16154 (2015).
[3] Maidul Islam *et al.* Scientific Reports, 7, 7355 (2017).
[4] Min Chen *et al.* Opt. Express, 25, 14089-14097 (2017).
[5] Mikhail F. Limonov *et al.* Nature Photonics, 11, 543–554 (2017).
[6] A. Nazir *et al.* Nano Lett., 14, 6 (2014).

Design and Analysis of Beam Propagation Model for Coherent Combining of High Power Laser Beams

Awakash Dixit, Deepa Venkitesh, and Balaji Srinivasan
Department of Electrical Engineering, Indian Institute of Technology Madras, Chennai-600036, India
**Email: balajis@ee.iitm.ac.in*

Abstract

In the present communication, a beam propagation model based on a diffractive optical element is conceptualised and demonstrated to study the coherent combining of the laser beams in free space. The effect of actual wavefront aberration on the beam combining is also examined quantitively, through the estimation of the Ensquared energy and M^2 parameter.

Keywords: Coherent Beam Combining, High Power Lasers, Diffractive Optical Element, Ensquared Energy, M^2 Parameter

1. Introduction

High power lasers with several kiloWatt output power levels are a critical requirement for direct energy weapon applications. Fiber lasers are an attractive choice for such laser sources since they have high wall-plug efficiency, relative ease of thermal management and near-perfect beam quality (M2 < 1.1). Due to nonlinear effects and thermally-induced mode instabilities, power scaling of a single fiber laser module is limited to around 1 kW. These difficulties limit the operation of individual lasing modules at their optimum power levels [1]. Combining multiple fiber lasing modules, each operating at its optimum power level, is a promising approach to power scaling of single-mode fiber lasers. The coherent beam combining (CBC) technique is an attractive choice due to its scalability and a relatively simple Master Oscillator Power Amplifier (MOPA) configuration. The coherent combining configuration can be classified into two groups - depending on whether the combination occurs in the near-field or the far-field. Most of the combining techniques operate in the far-field, and the interference pattern is generated far away from the laser beam output [2]. Two widely used configurations for CBC are tiled-aperture and beam-splitter overlapped beams. An alternative scheme is to generate the overlap of individual emitters in the near-field, close to the fiber laser outputs, using a specially-designed diffractive optical element.

In this paper, a diffractive optical element based coherent beam combing methodology is considered to scale up the fiber laser power far above the limitation of single fiber laser by manipulating the wavefronts of the multiple beams altogether. Detailed analysis of the beam combination is carried out using a beam propagation model based on the Huygen's Fresnel diffraction.

2. Beam Propagation Model for Coherent Beam Combining

The beam propagation model is conceived to demonstrate the coherent beam combining at 1064 nm wavelength using a diffractive optical element in MATLAB as depicted in Fig. 1(a). Two independent laser sources are considered and are propagated up to the diffractive beam combining element (DBCE); the geometry of which is shown in Fig. 1(b). The DBCE is a bidirectional element, which works as a splitter/combiner depending on the direction of propagation [3].

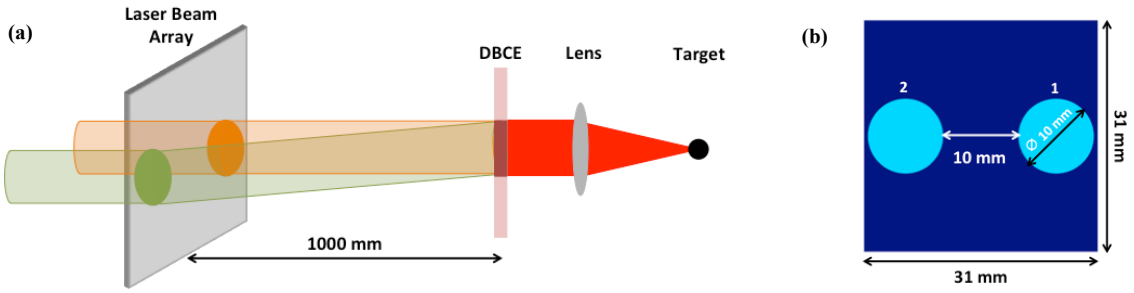

Fig. 1. (a) Beam propagation simulation model and (b) Geometry of the two laser sources

In the simulation model, we consider the two laser beams (diameter: 10 mm, resolution: 2000×2000, λ: 1064 nm) kept at a distance, *d*=20mm, from each other whose spatial profile is described by *U(x,y)*. The two beams are propagated up to 1000mm and are allowed to incident on to the DBCE with an angle (θ_s) of 1.15°. The tilting of the two beams is controlled by mixing the suitable blazed grating with the incoming field in the simulation. Beam propagation at various observation planes is simulated by using the Huygens's Fresnel diffraction integral as in Eqn.1 below.

$$P_n = \frac{e^{ikf}}{i\lambda f}\iint_A U(x,y)e^{\frac{ik}{2f}\left((u-x)^2+(v-y)^2\right)}\,dx\,dy \qquad (1)$$

where, $U(x,y)=\sum_1^n U_0 e^{i\left[\varphi_n(x,y)+\{2\pi\alpha_n r\cos(\theta_n-\beta_n)\}\right]}$ is the profile combined field of the two laser beams in a single window.

The design of DBCE is simulated by the function $O_{DBCE}\left(O_{DBCE}=e^{(i\Phi(x,y)}\right)$. Now the resultant field U_{op1} $\left(U_{op1}=P_n\times O_{DBCE}\right)$ is again propagated up to a lens using a Fresnel diffraction operator; a lens function $\left(\exp\left(-\frac{ik}{2f}\left(u^2+v^2\right)\right)\right)$ is multiplied with field U_{op1} to simulate the focused laser spot at the target plane.

Along the combining of the beams, the effect of wavefront aberration on the final combined beam has also been

studied. The wavefront aberration is defined by the combination of Zernike polynomials, here on-axis aberrations (defocus and spherical) are considered only, using the equation $\left(\exp\left(-ikW(x,y)\right)\right)$ [4]. Now, the resultant field U_{op2} at DBCE is given by $U_{op2} = P_n \times O_{DBCE} \times \exp\left(-ikW(x,y)\right)$. The field U_{op2} is focused by using a lens to get the laser spot.

The beam quality of the combined beam in the presence/absence of wavefront aberration is analysed by estimating the Ensqaured energy (*EsE*) and M^2 parameter. Standard formulations are used to evaluate these parameters [5, 6].

3. Results and Discussion

Simulated profiles of the propagated beams at a different location are illustrated in Fig. 2. Simulation results clearly reveal that if the designed DBSE is used in reverse direction, it will combine the beams. For faithful beam combining, it is prerequisite that the polarization and intensity in the two arm should be the same and uniform.

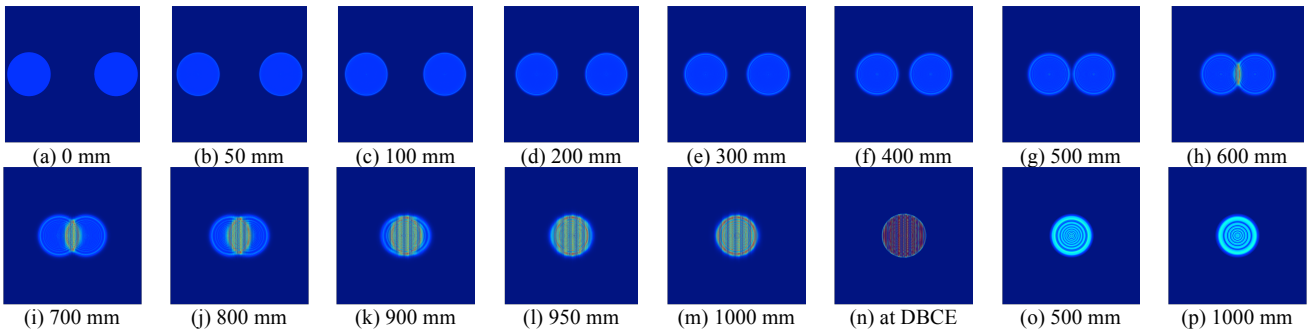

Fig. 2. Propagation of laser beams before and after combining

The design of the experimental setup for DBCE based CBC of the two collimated lasers is conceptualised to estimate the actual beam quality parameters. Collimated high power laser beams are allowed to fall on the DBCE with a precise angle of 1.15° using the tilting mirrors. The actual angles and distances between all the components are estimated. When a collimated laser beam is propagated in any experimental setup through various optical components, each optical component adds the specific amount of wavefront errors in the laser beam depending on its surface roughness (standard roughness for each component from the product catalogue is considered). The transmitted wavefront error (TWE-rms) is estimated for the proposed experimental testbed, and it is found that all optics will combinedly add the approximated wavefront error of the order of λ/8. The effect of this strength of wavefront aberration on the beam combining is also estimated to find out the exact value of the M^2 parameter.

The values *EsE* and M^2 have been estimated using the process as explained in Section 2. It is found that, on increasing the strength of aberration, the size of laser spot increases and energy is spread over a much larger area (Fig. 3(a)), the value of M^2 is also increased due to increase in size (Fig. 3(b)).

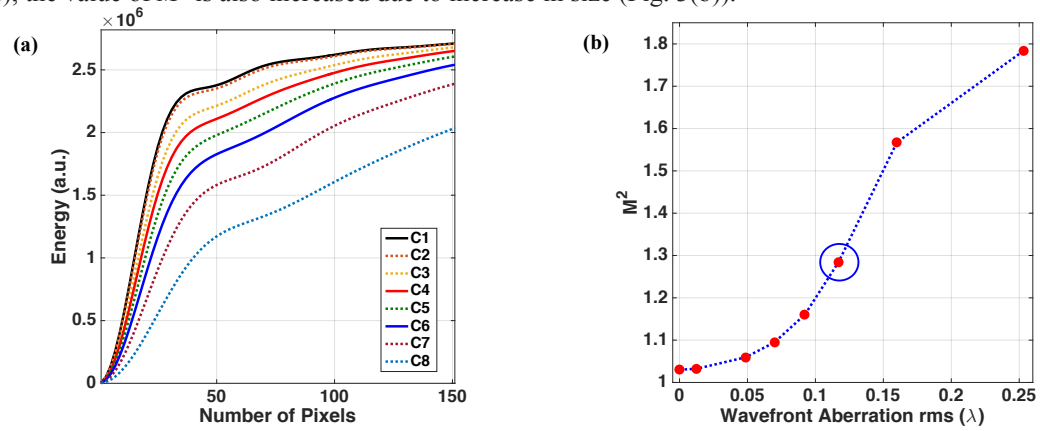

Fig. 3. (a) Estimated graph of Ensquared energy and (b) M^2 in the presence of wavefront aberration of various strengths from the focused laser spots

In conclusion, the design of DBCE element has been finalised and the element is under fabrication using an appropriate lithographic technique. TWE of the testbed has also been estimated which is used to calculate M^2 parameter after combining the beam. The estimated M^2 parameter of the combined beam has been found to lie in between 1.2–1.3.

4. Acknowledgement

The work is supported by DRDO, India (Grant No. ERIP/ER/RIC/2015/10/10/M/01/2025/D(R&D)/1635). Authors are also grateful to Mr Rahul Bhatt, LASTEC, DRDO, India, for technical inputs and discussion.

5. References

1. C. Jauregui, T. Eidam, H. J. Otto, F. Stutzki, F. Jansen, J. Limpert, and A. Tünnermann, Opt. Exp., 20(12), pp. 12912-12925, (2012).
2. P. Bourdon, L. Lombard, A. Durécu, J. Le Gouët, D. Goular, and C. Planchat, SPIE 10254, p. 1025402, (2017).
3. F. Prevost, L. Lombard, J. Primot, L. P. Ramirez, L. Bigot, G. Bouwmans, and M. Hanna, Opt. Exp., 25(9), 9528-9534, (2017).
4. A. Dixit, S. K. Mishra, V. Porwal, and A. K. Gupta, Proc. of Int.Conf. on Opt. & Optelc., p 14, (2014). doi:10.13140/RG.2.1.3961.6967/1
5. A. Dixit, S. K. Mishra, and A. K. Gupta, Opt. & Las. in Eng., 71, pp. 74-84, (2015). doi: 10.1016/j.optlaseng.2015.03.021
6. ISO Standard 11146, 11146-2,(2005). https://www.iso.org/obp/ui/#iso:std:iso:11146:-1:ed-1:v1:en

OSI-ISO 2018 manuscript No.
(144)

Direct measurements of black body like thermal-emission from VO_2 thin films using FTIR spectroscopy

J. K. Pradhan,[1,*] **Bharathi Rajeswaran,**[2]
A. M. Umarji,[2] **S. A. Ramakrishna**[1]

Abstract We experimentally demonstrate that a thin film (nearly 250 nm thickness) of a thermochromic material, vanadium dioxide (VO_2) deposited on top of a plasmonic substrate, indium doped tin oxide (ITO), exhibits switchable black-body-like thermal emission in the wavelength range spanning 3 μm to 5 μm. The thin film emits less infrared radiation when the sample surface is heated to temperatures higher than the phase transition temperature of VO_2, i.e. 68°C. The films were prepared by chemical vapor deposition (CVD) and the thermal emissivity of VO_2 is dynamically controlled by temperature. This wavelength-selective, switchable thermal source can be a potential candidate use for various field applications such as radiative coolers, thermophotovoltaics, infrared imaging, and infrared tagging, etc.

Keywords VO_2, thermal emissivity, phase change material

Tailoring the emissivity ($\varepsilon(\lambda)$) of an object can be useful for several energy harvesting applications such as thermal light sources, thermophotovoltaics, thermal imaging, and thermal tagging, etc. Particularly, mid-infrared (MIR) thermal sources with switchable thermal emissivity have potential use in active camouflage. MIR thermal sources with materials such as VO_2, and $Ge_2Sb_2Te_5$ with dynamic control over their emissivity have been used recently for thermal camouflage [1,2].

In this paper, a highly switchable thermal source with a phase change material VO_2 is demonstrated. The bi-layered design consists of a 250 nm thick VO_2 film on top of a 150 nm ITO coated on a glass substrate, and the VO_2

[1]Department of Physics, Indian Institute of Technology, Kanpur-208016, India
E-mail: *jitendra@iitk.ac.in

[2] Materials Research Centre, Indian Institute of Science, Bangalore-560012, India

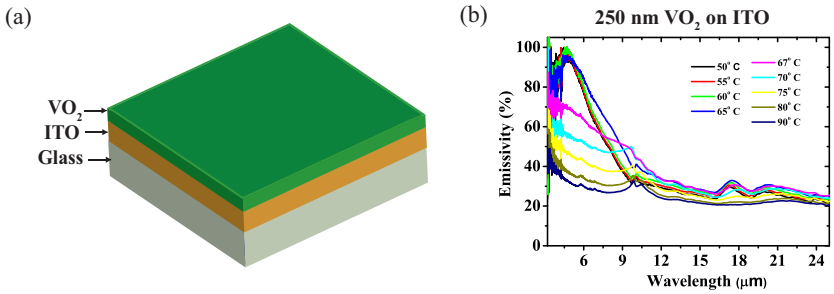

Fig. 1 (a) Schematic diagram of the VO_2/ITO thermal source. The thickness of the bottom ITO and VO_2 films are 150 nm, and 250 nm respectively. (b) The normalized emission spectra of the switchable thermal source measured at different temperatures.

is deposited using CVD. The room temperature emissivity at a peak wavelength (4.9 μm) switches to a low value at high temperature. The high value of emissivity at room temperature arises because of the strong interference effect inside of light in VO_2 [3].

The emission spectra was measured using a FTIR spectrometer with a room temperature cooled deuterated triglycine sulfate (DTGS) detector attached to it. The sample and the reference were placed on a temperature controlled pad (Harrick, Model ATC-024-4) and the sample surface was heated to temperatures varying from 50°C to 90°C. Black soot is considered as the reference because of its high thermal emissivity. The black soot is prepared on a glass substrate using a candle and the soot-coated glass substrate is baked at 120 °C for 30 min to remove the excess parafin from the candle. We measured the spectral radiance of the black soot and the samle by passing the emission coming from these to the DTGS detector. The VO_2 thickness is 250 nm here with the thickness of ITO as 150 nm (see Fig. 1(a)). At room temperature, the sample shows high emissivity peaked at 4.9 μm and it gradually switches to a low value of 30 % at high temperature, i. e. 90 °C. The normalized emissivities ($\varepsilon_{sample}(\lambda, T)$) of VO_2/ITO samples are shown in Fig. 1(b).

In conclusion, a highly switchable thermal source with VO_2 as an active component is demonstrated based on strong interference inside a asymmetric Fabry-Perot cavity . The phase change of VO_2 is induced by temperature and can be controlled dynamically.

References

1. Y. Qu, Q. Li, L. Cai, M. Pan, P. Ghosh, K. Du, and M. Qiu, "Thermal camouflage based on the phase-changing material GST," Light Sci. Apl., **7**, 26(2018).
2. M. A. Kats, R. Blanchard, S. Y. Zhang, P. Genevet, C. H. Ko, S. Ramanathan, and F. Capasso "Vanadium dioxide as a natural disordered metamaterial: perfect thermal emission and large broadband negative differential thermal emittance," Phys. Rev. X **3**(4), 041004 (2013).
3. B. Rajeswaran, J. K. Pradhan, S. A. Ramakrishna, and A. M. Umarji, "Thermochromic VO_2 thin films on ITO-coated glass substrates for broadband high absorption at infra-red frequencies," J. Appl. Phys. **122**, 163107(2017).

OSI-ISO 2018 manuscript No.
(145)

Localization of Energy by Metamaterial Cylindrical Waveguide

Abhinav Bhardwaj * · **Dheeraj Pratap**† · **Kumar Vaibhav Srivastava***

Abstract Recently, inhomogeneous as well as anisotropic cylindrical waveguide is realized by nanoporous alumina microtubes with the radially emanating nanopores. The nanopores of this waveguide can be filled with suitable materials like plasmonic metals, dielectrics, etc. The electromagnetic modes of a circular waveguide filled with a cylindrically anisotropic metamaterial are described by Bessel and Neumann functions of imaginary orders. Even modes with very large angular momentum in such waveguides have a large modal volume and localize near the center of the waveguide. Our calculations show that inhomogeneity plays a relatively significant role in the localization of modes by comparing with an anisotropic homogeneous waveguide with the same fill-fraction. In this waveguide, we can control the localization of fields by different filling materials and fill fractions.

Keywords Inhomogeneous · Anisotropic · Imaginary order modes · Fill-fraction

Nanoporous alumina microwires with the radially emanating pores filled with dielectric or plasmonics metals like silver have been showcased as examples of anisotropic metamaterial fibers [1] and [2]. In this article, we have compared the localization of fields in the homogeneous and inhomogeneous fibers. It is found that the field is highly localized when pores are filled inhomogeneously with air as shown in Fig. 1 and control the position of localization of field by filled inhomogeneously with CdS as shown in Fig. 2. It is also found that the higher electric field intensity is coupled in an inhomogeneously filled fiber as shown in Figs. 1,2.

* Department of Electrical Engineering, Indian Institute of Technology Kanpur, Kanpur 208016, India
E-mail: abhinavb@iitk.ac.in ·
† Department of Physics, Indian Institute of Technology Kanpur, Kanpur 208016, India

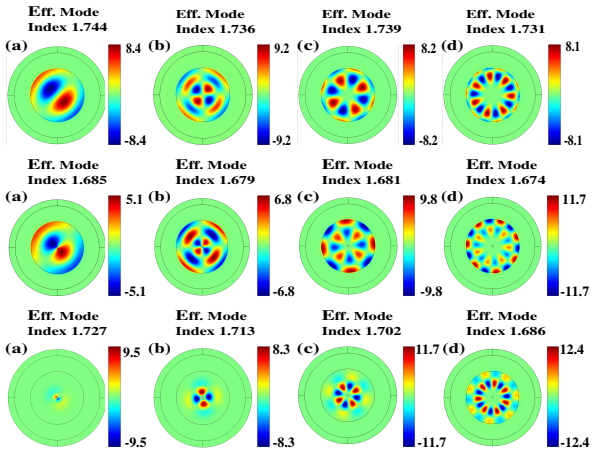

Fig. 1 The distribution electric field component (E_z) for modes (a) $EH_{1,2}$ (b) $HE_{2,3}$ (c) $EH_{4,2}$ and (d) $EH_{7,2}$. The first row, second row and third row are coresponding to isotropic, anisotropic homogeneous and inhomogeneous fiber respectively. The inner and outer radii are 0.5 μm and 12.5 μm and also outer surface is open to air. The fill-fraction for homogeneous and the outer surface of the inhomogeneous fiber is 0.1. Here the field plots are at frequency of 200 THz and nanopores are empty.

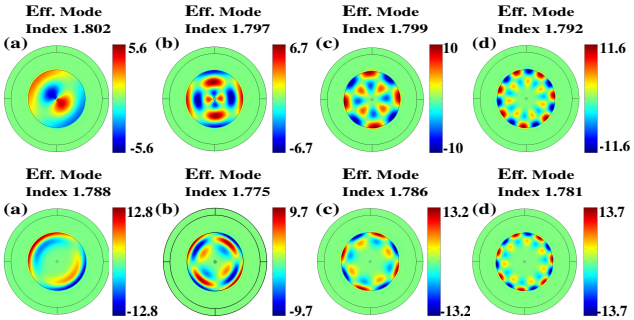

Fig. 2 The distribution electric field component (E_z) for modes (a) $EH_{1,2}$ (b) $HE_{2,3}$ (c) $EH_{4,2}$ and (d) $EH_{7,2}$. The first row and second row are coresponding to anisotropic homogeneous and inhomogeneous fiber respectively. The inner and outer radius are 0.5 μm and 12.5 μm and also outer surface is open to air. The fill-fraction for homogeneous and the outer surface of the inhomogeneously filled fiber is 0.1. Here the field plots are at frequency of 200 THz and nanopores are filled with material CdS.

Acknowledgements The authors acknowledge Prof. S. Anantha Ramakrishna for his suggestions.

References

1. D. Pratap, S. A. Ramakrishna, J. G. Pollock, and A. K. Iyer, "Anisotropic metamaterial optical fibers," Optics Express, Vol. 23(4), pp. 90749085, 2015.
2. D. Pratap, A. Bhardwaj, and S. A. Ramakrishna," Inhomogeneously filled, cylindrically anisotropic metamaterial optical fiber," J. Nanophoton. Vol. 12(3), pp. 033002-033009, (2018).

OSI-ISO 2018 manuscript No.
(146)

Probing inelastic and elastic scattering from Nanowire-nanoparticle (nw-np) junction

Chetna Taneja, Deepak K. Sharma, Danveer Singh, Arindam Dasgupta, Ravi P. N. Tripathi, and G. V. Pavan Kumar

Department of Physics, Indian Institute of Science Education and Research, Pune- 411008

The large local electric field associated with localized and propagating surface plasmons polaritons at metal-dielectric interface, helps us to go beyond the diffraction limit of light. Nanowire-nanoparticle system has both the localized and propagating plasmons excited at the metal dielectric interface. We show that the propagating SPP's excited at one end of the nanowire out couples directionally at the nanowire-nanoparticle junction and influence the molecular emission near the vicinity of the junction [1]. We further show that, when exciting both the end of the nanowires, the counter propagating plasmons significantly increases the SERS signal from the molecules at the junction compared to the emission from the single end excitation of the wire [2]. Elastic scattering from the junction also shows interesting signature in the Fourier space.

Keywords Localized and propagating Plamons, Fourier plane imaging.

References

1. Danveer Singh, Arindam Dasgupta, V. G. Aswathy, Ravi P. N. Tripathi, and G. V. Pavan Kumar, Directional out-coupling of light from a plasmonic nanowire-nanoparticle junction; Optics Letters, Vol. 40, No. 6 (2015).
2. Arindam Dasgupta Danveer Singh Shreyash Tandon Ravi P. N. Tripathi G. V. Pavan Kumar, Remote-excitation surface-enhanced Raman scattering with counterpropagating plasmons: silver nanowire-nanoparticle system; Journal of Nanophotonics, 083899-8 Vol. 8 (2014).

Investigation of exceptional point in a non-Hermitian system

Nirmal K. Viswanathan
School of Physics, University of Hyderabad, Hyderabad 500046, India
nirmalsp@uohyd.ac.in

Abstract

Exceptional points (EPs), the singularities of *non-Hermitian* systems, where both the eigenvalue and eigenvector coalesce, have been under intense investigation due to the unusual topology of its eigenmodes. Following an intense theoretical scrutiny that started more than a decade ago, the EPs have been demonstrated and characterized in a variety of physical systems with coupled characteristics including gain–loss, exciton-polariton, atom-cavity etc., leading to applications including unidirectional light propagation, PT symmetry breaking, selective optical amplification, and spectral dispersion effects.

Historically, Voigt was the first to identify and study singular axes in absorbing biaxial crystal which was subsequently understood and explained by Pancharatnam in terms of birefringence and dichroism and in the recent times has become one of the finest examples of system with non-Hermitian degeneracies or EPs. The recent article by Berry and Dennis [1] brought together the underlying physics of EPs in biaxial crystals under different conditions. The singular axes occur along directions where the birefringence and dichroism are equal in magnitude, and their principal planes make 45° angle with each other. Identifying that the C-point singularities in the crystal, where the polarization is purely circular, coincides with the EPs in the presence of absorption, we characterize the EPs through conoscopic Stokes polarimetry [2]. The two optic axes of the biaxial crystal split into two pairs of singular axes due to dichroism, which coalesce following helical trajectory and disappear upon externally inducing symmetry breaking effect in the system. The complex dynamics of the EPs is studied carefully, which leads to a fine control of the EPs and the associated chiral dynamics. Our results on using the birefringence—dichroism pair, instead of the usual gain—loss pair to realize EPs is expected to generate several intricate features to further the emerging interest in topological optics and photonics involving EPs and their manipulation.

Key Words: Exception point, non-Hermitian system, Biaxial crystal, Polarization

Acknowledgments
The author acknowledges financial support from Science and Engineering Research Board (SERB), India and Dr. Samlan, a co-author in this work.

Reference list

1. M. V. Berry and M. R. Dennis, Proc. R. Soc. London A 459, 1261 (2003).
2. C.T. Samlan and N.K. Viswanathan, “Chiral dynamics of exceptional points in weakly absorbing biaxial crystal,” Opt. Lett., **43**, 3538 (2018).

OSI-ISO 2018 manuscript No.
(148)

High-resolution absorption imaging in a saturated absorption medium

Onkar N. Verma · Sourabh Roy

Abstract We propose an efficient way of diffraction-free imaging of multi-mode transverse profiles in a saturated absorption medium composed of two-level atoms. We find that the diffraction-limited Gaussian modes imprinted on pump beam is efficiently transfered to probe beam with feature size reduced by a factor four. This method of information transfer may find potential applications in all-optical imaging and lithography technologies.

Keywords Paraxial diffraction · saturated absorption · all-optical imaging · lithography techniques.

Paraxial diffraction of laser beams poses a great challenge in image processing, wave-guiding and lithography techniques[1]. Divergence of a laser beam due to diffraction determines its size and shape during its propagation in free space as well as in a medium. The smaller is waist of a laser beam, the quicker it diverges. The divergence of a laser beam can be reduce or even reverse using a nonlinear optical effect known as Kerr effect[2]. Spatial solitons of distinct shape are generated on the same principle of self-focusing due to a strong Kerr effect[3]. However, the Kerr effect is limited due to high intensity light beams propagating through conventional nonlinear media[4]. Therefore, it is very important to search a new class of optical medium that can produce optical solitons at very low light intensities[5].

Here, we propose a method to reverse the paraxial diffraction of multi-mode transverse light fields exploiting a saturated absorption medium composed of two-level gas atoms[6]. In a such medium, two counter-propagating laser beams (a strong pump and a weak probe beam) are generated from a single laser beam. Both the beams are driving the same transition of two-level

Onkar N. Verma
National Institute of Technology Warangal, Warangal-506004, Telangana, India
E-mail: onkarnath15verma@gmail.com

Sourabh Roy
National Institute of Technology Warangal, Warangal-506004, Telangana, India

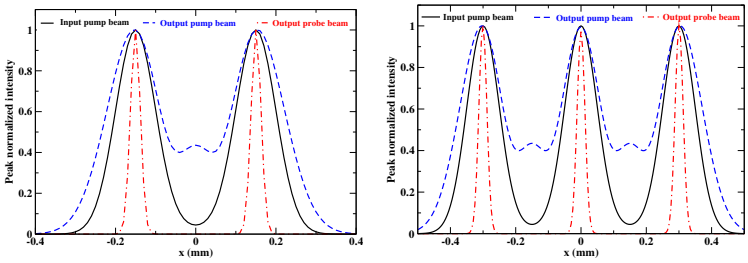

Fig. 1 Comparison between peak normalized intensity distribution of the transmitted probe beam and diffraction-limited pump beam. (a) Two Gaussian-shaped profiles (b) Three Gaussian-shaped profiles. Probe beam is chosen initially a plane wave.

atoms in a vapor cell. Previous theories or experiments in saturation absorption spectroscopy are focused for slow light propagation in temporal domain[7]. However, the spatial profile of strong pump beam may alter the size of weak probe beam during interaction inside the medium. It is, therefore, essential to take into account the spatial effects of laser beams in a such medium.

Fig. 1 illustrates the imaging of two and three Gaussian-shaped profile of pump beam by a plane wave probe beam. The input waist radius of each Gaussian mode is same and equal to 100 μm at the entry facet of vapor cell. The peak normalized intensities of both input and propagated pump beam is plotted with the transmitted probe beam after traversing a 4-cm-long medium. The size of individual peaks of transmitted probe beam profile is measured to be 25 μm. Thus, the feature size of the transmitted probe profile is 4 times smaller than the input pump intensity profile. It is interesting to note that the pump profile is distorted severely after propagating 4-cm-long medium.

Acknowledgements Authors gratefully acknowledge funding from SERB-DST, Government of India (File No. PDF/2016/002679).

References

1. B. A. A. Saleh and M. C. Teich, *Fundamentals of Photonics* (John Wiley & Sons, New York, 1991).
2. R. Y. Chiao, E. Garmire, and C. H. Townes, "Self-Trapping of Optical Beams," Phys. Rev. Lett. **13**, 479 (1964).
3. J. E. Bjorkholm and A. A. Ashkin, "cw Self-Focusing and Self-Trapping of Light in Sodium Vapor," Phys. Rev. Lett. **32**, 129 (1974).
4. T. Hong, "Spatial Weak-Light Solitons in an Electromagnetically Induced Nonlinear Waveguide," Phys. Rev. Lett. **90**, 183901 (2003).
5. H. Kang and Y. Zhu, "Observation of Large Kerr Nonlinearity at Low Light Intensities," Phys. Rev. Lett. **91**, 093601 (2003).
6. M. Sargent III, "SPECTROSCOPIC TECHNIQUES BASED ON LAMBS LASER THEORY," Phys. Rep. C **43**, 223 (1978).
7. R. N. Shakhmuratov, A. Rebane, P. Mgret, and J. Odeurs, "Slow light with persistent hole burning," Phys. Rev. A 71, 053811 (2005).

OSI-ISO 2018 manuscript No.
(149)

Fabrication and Characterization of Sol-Gel Derived TiO_2 Grating Structure for Photonic Applications

Sarad Subhra Bhakat[1*], Payel Ghosh[1], Soham Lodh[2], Rajib Chakraborty[1*]
1. Department of Applied Optics & Photonics, University of Calcutta, JD-2, Sector-III, Salt Lake, Kolkata-700106, INDIA
2. MCKV College of Engineering, Howrah, West Bengal, INDIA
** Corresponding author's email:sarad.subhra@hotmail.com,, rcaop@caluniv.ac.in*

Abstract

Optical properties of titanium-dioxide thin films prepared by the sol–gel technique are presented. The layers were deposited on glass slides by spin coating process. The grating structure was developed by photolithography. The transmission of grating structure so obtained is measured using spectrophotometer. It is seen that the grating structure can be used to improve light output of light emitting diodes or light absorption in solar cells.

Keywords

Sol–gel technique, TiO_2, Diffraction grating, Transmission spectra

1. Introduction

For quite a long time, diffraction grating is being used as a tool to analyze the spectrum of light. Apart from spectroscopic applications, grating based couplers are used in optical interconnects, integrated optical devices, optical communications as well as in sensing [1–3].

In this work we have developed the sol-gel technique to fabricate TiO_2 thin film and then use it to fabricate gratings with this thin film. Although there are several techniques for TiO_2 thin film deposition, but sol-gel technique is a low-cost process which can form uniform coating over a fairly large area. It can be seen that the fabricated gratings can find application in improving the output efficiency of light emitting diodes (LEDs) [4]. It can also be used in increasing the light capturing capacity for solar cell [5].

2. Experimental work

Titanium Isopropoxide (TIP), Acetic and Ethanol, these are three components which were used for TiO_2 sol-gel preparation. All chemicals were supplied by Aldrich Chemicals Ltd. TiO_2 thin films are prepared by Sol-Gel spin- coating method. At first 50 ml of Ethanol and 5 ml of acetic acid was mixed by using a magnetic stirrer for 5 min and then 6.3 ml of TIP was added to the mixture of glacial acetic acid and ethanol. The mixture was continually stirred by using a magnetic stirrer for another 2 hrs, and then cleaned glass substrate was spin coated by TiO_2 precursor sol with the rotation speed of 4000 rpm for 30s. Then, the coating was dried at room temperature for 10 min followed by annealing at 550°C for 1 hr.

The grating pattern is developed on the spin coated TiO_2 layer by means of photolithography. The process involves spin coating of the sample with a photo resist solution (Shipley 1818) followed by pre-baking at 90^0 C for 10 minutes. Then the sample is exposed to UV light through a grating mask for 20s and the grating pattern is obtained by dipping the sample in diluted developer solution (1:3) followed by DI water. Once the pattern is developed the sample is post baked for about 35minutes for proper adhesion of photo resist pattern on the TiO_2 layer. The portions of the TiO_2 layer that is not covered by photo resist (on development of the grating pattern) is etched by dipping the sample in a dilute solution of HF (1:25) for about 8s followed by thoroughly washing in DI water. After properly drying the sample the photo resist is stripped off using the stripper solution. Consequently the glass substrate is left with the grating pattern of TiO_2 on it.

3. Results and discussions

Fig 1. shows the fabricated TiO_2 grating structures where Fig 1(a) shows the grating with the photoresist coating while Fig 1 (b) shows the TiO_2 gratings. The images were taken by Carl Zeiss Axio Observer A1 microscope. The mask used is a diffraction grating having 5 lines/mm.

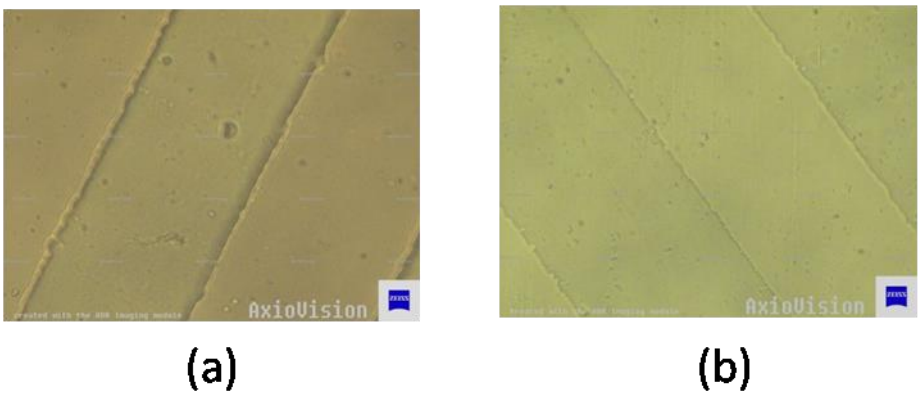

Fig 1. Microscope image of the grating structure (a) with photoresist cover (b) after removal of photoresist

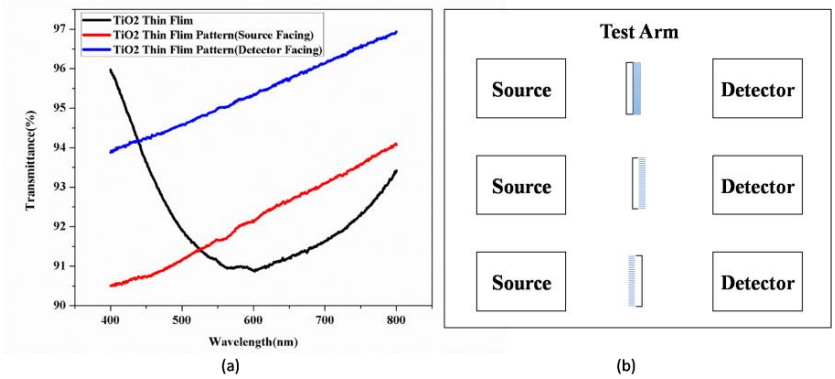

Fig 2. (a) Transmission of the TiO_2 thin film and the TiO_2 gratings for different wavelengths. (b) The orientation of the samples in the test arm

The transmission through the sample in the visible region is observed using PerkinElmer Lambda 45 UV-VIS spectrophotometer. Fig 2(a) gives a plot of the transmission data of a TiO_2 coated glass substrate, TiO_2 grating facing the detector and the grating facing the source. It is seen that in the 2nd case (given in Fig 2(b)) when light is passing through the glass substrate towards the grating, the transmission increases compared to that of the TiO_2 coated substrate. So it can be concluded that if these types of gratings are fabricated on top of LED, it can increase the light output. Usually outputs from LEDs are restricted due to total internal reflection at the high index contrast interface of the LED with air. Undulation, roughening or patterning on the top usually increases the light output efficiency [4]. Our structure also shows the same, although not over the entire visible range. When the fabricated grating structure is facing the light, it is seen that the 400-500 nm wavelength region the transmission is less than that of TiO_2 thin film alone. It means that light in this wavelength region is absorbed. Increase in absorbance of light is advantageous for solar cell applications. So the TiO_2 grating can find applications in enhancement of efficiency of solar cells.

4. Conclusions

In this work we have developed a technique for thin film deposition of TiO_2 using sol-gel technique and have successfully fabricated gratings with this thin film. The fabrication process is given in details. The transmission data shows that fabricated grating can find application in improving the efficiency of LEDs as well as it can be used to enhance the light capturing capacity of solar cells. Although the results shown here are very preliminary but detail study will lead to more promising results in future.

References

[1] W. Shi, V. Veerasubramanian, D.V. Plant, N.A.F. Jaeger, L. Chrostowsk , Proc. SPIE, 9010, 90100F (2014).

[2] C.J. Oton, IEEE Photon J. 8, 2700208, (2016)

[3] S. Ghosh, R. Chakraborty, Optik, 148, 201-208, (2017)

[4] A. Haldar, S. Bera, S. Jana, K. Bhattacharya, R. Chakraborty, Jour. of Applied Physics, 115, 193108 (2014)

[5] N Ahmad, J Stokes and M J Cryan, Journal of Optics (IOP), 16, 125003 (2014)

IN-LINE PHASE SHIFTING INTERFERANCE MICROSCOPE WITH WIRE GRID POLARIZER

Chandan Sengupta[1], Sanjukta Sarkar[1,2*], K.Bhattacharya[1]

[1]Department of Applied Optics and Photonics, University of Calcutta, Kolkata
[2] Department of Electronics and Communication Engineering, Techno India, Kolkata
*Email:sanjuktasarkar1@gmail.com

Abstract: We describe an in-line and common path interference microscope based on Mireau configuration for generating the three dimensional phase profile of a reflecting sample. It is shown that by using suitably converging laser illumination, a wire grid polarizer placed between the objective and the sample is capable of converting a conventional microscope objective into an interference microscope objective. Experimental results are presented and a possibility of polarization phase shifting interferometry is discussed.

I. INTRODUCTION

Standard interferometric set-ups such as Michelson, Twynman-Green, Mach-Zehnderand , Linnikand , Mireau configurations have been developed for quantitative phase measurement. The Mireau configuration [1] stands out among the rest because of its simplicity and elegance. Phase shifting Mireau objectives typically use a piezo translator to shift the objective away or towards the sample so that a phase shift is introduced between the reference and sample beams. In the present study it will be shown that with a suitably placed wire-grid polarizer polarization phase shifting can be conveniently effected without the use of any piezo device. Using this configuration, 3D reconstructions has been demonstrated for reflective objects.

II. EXPERIMENTAL SETUP

Fig. 1 shows the schematic of the experimental setup. The spatially filtered beam of light is made to converge so that after reflection from the cube beam splitter (CBS) and its subsequent passage through the microscope objective, the beam is focused at the point A as shown in Fig.1 (b). The reflected wave front from the interfacing layer of the CBS goes through the microscopic objective and is amplitude divided by the wire grid polarizer (WGP) which is an array of microscopic wires on a glass substrate. The transmitted beam travels to the test surface and is reflected from it. The beam reflected from the sample, is re-transmitted by the WGP as shown in the figure. The reflected *s*-polarized beam from WGP is the reference beam. The two partially orthogonally polarized reflected beams return through the same objective, cube beam splitter and a tube lens on the CCD. Use of Quarter wave plate (QWP) ensures that the two interfering beams are circularly polarized in the opposite sense and phase shifting is achieved simply by rotation of a linear polarizer LP placed before the recording plane.

III.THEORY

Ideally the WGP selectively transmits *p*-polarized light while reflecting *s*-polarized light. However, a small fraction ξ of the transmitted light from the WGP is *s*-polarized. In the Jones formulation, the reference beam E_o and the sample beam E_r may be espressed as,

$$E_0 = O e^{i\delta}\begin{pmatrix}1\\0\end{pmatrix} + \xi O(x,y) e^{i\delta}\begin{pmatrix}0\\1\end{pmatrix} \quad \text{and} \quad E_r = r\begin{pmatrix}0\\1\end{pmatrix} \tag{1}$$

Where, O and δ indicates the amplitude and phase of the sample area under test, r is the amplitude of reference beam ,the Jones vector $\begin{pmatrix}1\\0\end{pmatrix}$ and $\begin{pmatrix}0\\1\end{pmatrix}$ denotes the p and the s polarization components of object beam and reference beam respectively. After its passage through the QWP and LP, the beam emerging from the output polarizer is given by :

$$E = P(\theta)\left[O e^{i\delta}\begin{pmatrix}1\\i\end{pmatrix} + \xi O e^{i\delta}\begin{pmatrix}1\\-i\end{pmatrix} + r\begin{pmatrix}1\\-i\end{pmatrix}\right] \tag{2}$$

where P(θ) is the Jones matrix of a polarizer with its transmission axis along θ and the intensity distribution I on the plane of the CCD is:

$$I = O^2 + \xi^2 O^2 + r^2 + 2O^2\xi\cos 2\theta + 2Or\cos(\varphi + 2\theta) + 2\xi Or\cos\varphi \tag{3}$$

To achieve the polarization phase shifting the angle of transmission axis of the output polarizer is set to 0^0, 45^0, 90^0, and 135^0 to obtain four phase shifted interferogram I_1, I_2, I_3, I_4 respectively at image plane. The phase distribution over the sample, $\delta(x_i, y_i)$, is given by the four-step phase-shifting algorithm

$$\delta = \tan^{-1}\left[\frac{I_4 - I_2}{I_3 - I_1 - 4O^2\xi}\right] \quad (4)$$

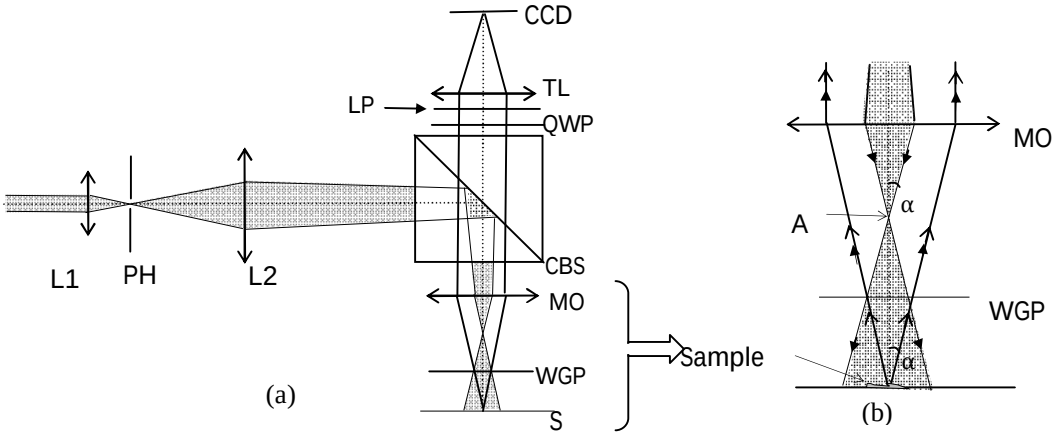

Fig.1 (a)Schematic of the proposed in-line laser interference microscope. (b) The path of rays between the Objective and the Sample shown in detail

IV.EXPERIMENTAL RESULT

To validate this technique a 5X long working distance (LWD) microscope objective and a tube lens(200mm)was used to image the flat surface (mirror).Fig. 2 shows four phase- shifted intrferograms. Reconstructed phase profile of the object is shown in Fig. 3. Fig.4 shows the interferogram and phase reconstruction using Fourier Transform technique from a single frame.

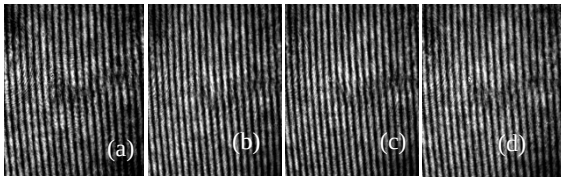

Fig.2 Four phase shifted interferograms

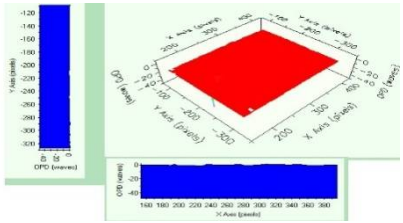

Fig 3. Reconstructed phase profile of the sample

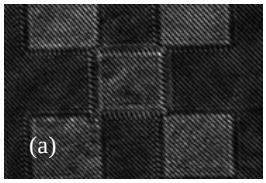

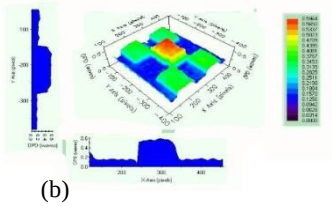

Fig.4. (a) The interferogram and (b) phase reconstruction for a portion of a unpackaged CMOS chip.

V.CONCLUSION

A simple modification of the Mireau objective is proposed for polarization phase shifting interference microscopy. As phase shifting is achieved through polarization means, the proposed technique is suitable for non-birefringent sample.

VI. REFERENCE

1. B. Bhushan, J. C. Wyant, and C. L. Koliopoulos, "Measurement of surface topography of magnetic tapes by Mirau interferometry,"*Appl. Opt.* 24, 1489–1497 (1985).

Observation of temperature dependent Strong coupling between Quantum Dot and metamaterial

Ravindra Kumar Yadav*, Harshavardhan R.K.* and Jaydeep Kumar Basu[1]*

*Indian Institute of Science, Bangalore, India

[1]basu@iisc.ac.in

Abstract: Strong coupling between quantum emitter (QE) and matter is result of reversible exchange of energy between QE and matter which results formation of hybrid energy level of QE and matter. Strong coupling phenomena emerges, when gain mechanism in the system dominates over the loss mechanism which is one of the challenges in plasmonic system. Hyperbolic metamaterial (HMM) is well known for providing large photonic density of states which enhances the decay rate of QE, near the HMM surface **[1].** To reach in strong coupling regime, there are limitations yet, because of the lossy nature of HMM.

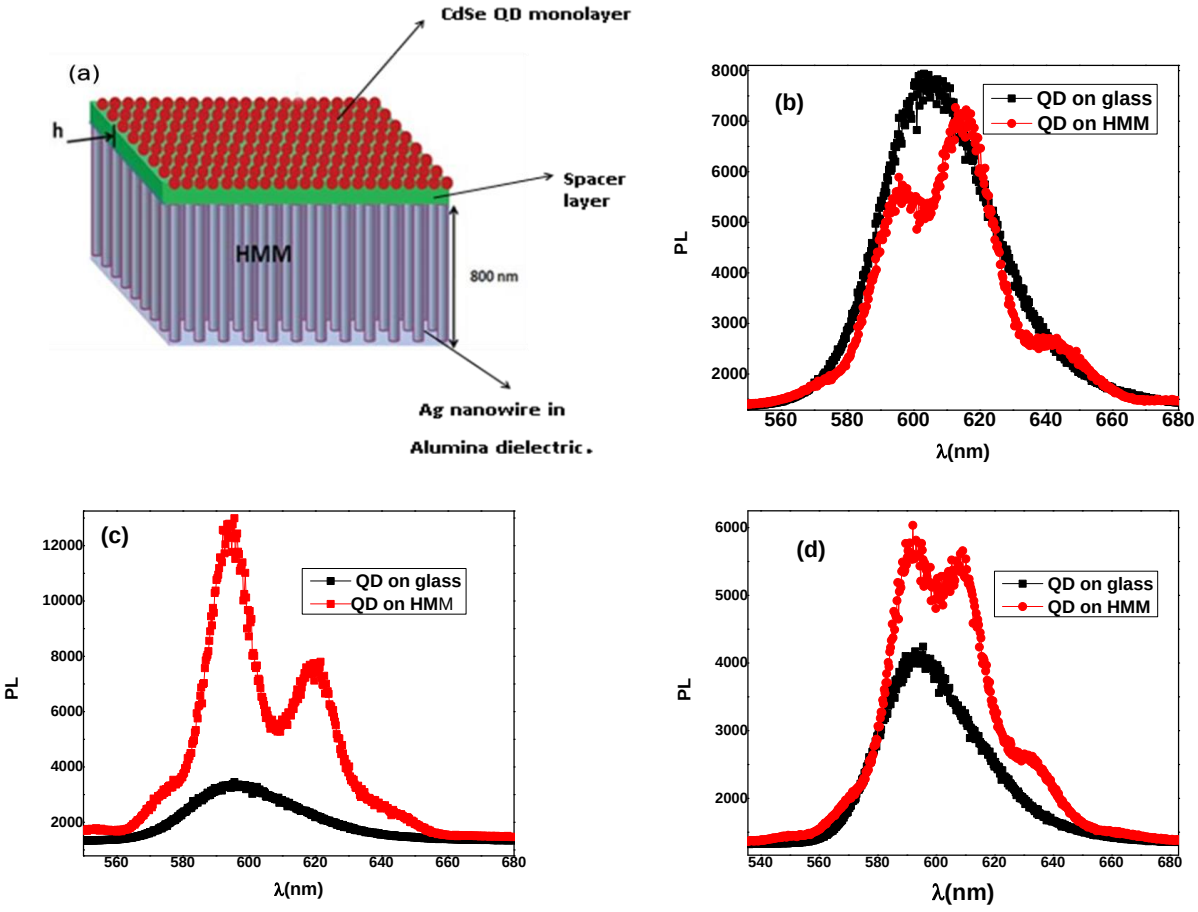

fig.1 (a) Schematic of Hybrid system of CdSe QD monolayer and HMM [2], (b) shows the Photoluminescence (PL) spectra of QD on HMM and QD on glass at room temperature (300K), (c) PL spectra at 140K , (d) PL spectra at 77K.

As we have already reported a way to overcome this losses, by using large Photonic Density of States (PDOS) of HMM and cooperative emission of Quantum Dots (QDs) in form of a monolayer **[2]** as shown in **fig.1(a).** We have observed strong coupling at room temperature using compact monolayer of QDs on HMM **[2].** To avoid the plasmonic losses near the HMM, we have separated HMM and QDs monolayer using polymer spacer. The observed strong coupling is

highly dependent on PDOS dispersion of HMM and number density of QDs **[2].** Quenching in QDs PL near the HMM because of non-radiative losses is still a challenge. To suppress temperature dependent non-radiative losses, we are exploring the temperature dependent study of the same system and we have observed change in magnitude of splitting as well as a change in QDs PL signal, from quenching to enhancement as shown in **fig.1**. We have measured the QDs PL on HMM up to liquid Nitrogen temperature (77K) as shown in **fig.1**.

As we can see in fig.1 splitting magnitude is maximum at 140K and we have also observed quenching at room temperature which is expected result for HMM but at lower temperature, we have observed enhancement**.**

(Prefer oral presentation)

Keywords

Strong Coupling, Hyperbolic metamaterial, Cooperative emission, Quantum Dot.

Acknowledgments

The authors acknowledge DST, Nanomission, India for financial support. The authors also acknowledge SERB, DST, India.

Reference list:

[1] N.S. H. Krishnamoorthy, Z. Jacob, E. Narimanov, I. Kretzschmar and V. M. Menon, **Science**, 336, 205,(2012).

[2] Chaitanya Indukuri, Ravindra Kumar Yadav and J. K. Basu, **Nanoscale,** 9, 11418–11423 (2017).

Excited State Energy Transfer and Third Order Nonlinearity in Plasmon Coupled Fluorophore

Kaweri Gambhir[1,2], Parag Sharma[1,2] and Ranjana Mehrotra[1,2]

[1] Academy of Scientific & Innovative Research (AcSIR) at CSIR-National Physical Laboratory campus, New Delhi - 110012, India
[2] CSIR-National Physical Laboratory, Dr. K.S. Krishnan Marg, New Delhi-11012, India
Email : kawerigambhir@gmail.com

Abstract

Photoinduced gold nanostructures coupled with fluorophes hold great importance as channels for the transfer of energy and information in future all-optical devices. Although, plasmon coupled fluorophores are known to substantiate third-order optical nonlinearity but, the deconvolution of the complex mechanisms involved and their quantification has not been established so far. In this work, we have experimentally realized morphology directed energy transfer between an Eosin yellow (EY) dye and three distinct gold nanoshapes. Raman spectroscopy has been conducted to assert mutual interaction within the hybrid. The relationship between the observed quenching of the dye's fluorescence and the geometrical factors of the gold nanoshapes has been used to comprehend the influence of energy transfers on their enhanced third order nonlinearity. This study may act as a basis for the design of nanocomposites for active photonic applications based on their efficient energy transfer interactions.

Keywords : Z-Scan; Energy Transfer; Plasmons; Flurophore.

Introduction

Nonlinear Optics offers exciting new capabilities for efficient manipulation of photonic signals. As this field continues to evolve, it has lead to the emergence of many promising technologies such as optical communication and computing, dynamic image processing, optical processors, optical switches, wavelength filters and modulators[1]. Whereas, a major application, all-optical switching, has still not been realized because of the lack of a suitable material with a high nonlinear figure of merit. The major requirements of such materials, in addition to large nonlinear optical (NLO) response, are low losses at the wavelength(s) of interest, good optical quality, and mechanical stability, together with easy preparation procedures and low cost [2].
In order to delineate of energy transfer mechanism responsible for the variation in the third order nonlinear optical (NLO) coefficients in plasmonic organic hybrids we synthesized three distinct plasmonic structures namely gold nanoflowers (GNF) and gold nanopebbles (GNP) and gold nanospheres (GNS)[3]. All three different nanoshapes of nearly same size and LSPR (Local Surface Plasmon Resonance) are synthesized, by changing the reaction solvent under the same experimental procedure. Further a dye Eosin Yellow was adsorbed on these nanoparticles. The NLO investigations are conducted using 20 picoseconds laser pulses of wavelength 532 nm as an excitation source in single beam Z-scan setup. UV-visible spectroscopy is employed for monitoring changes in linear absorbance. Photouminance study has been conducted for the emission spectra.

Results and Discussion

EY when hybridized with GNP, GNF and GNS in fixed ratio 1:1 (v/v) illustrated a significant enhancement in the third order nonlinear coeffecients accompanied with a drastic quenching effect in the emission spectra of the dye. The observed quenching in the emission spectra is extremely sensitive to the morphology directed plasmon coupling effect, which originated from the space interaction between the free electrons of metal nanoparticles and dipoles of the dye molecules

The Third order nonlinearity has been evaluated using the following equations:

$$T_{OA(2PA)} = 1 - \frac{\beta I_0 L_{eff}}{2^{3/2}\left(1 + \frac{Z^2}{Z_O^2}\right)} \;\&\; T_{(X)} = 1 - \frac{4X\Delta\phi_0}{(X^2+9)(X^2+1)}$$

where, Z is the sample position; $Z_0 = \left(\pi\omega_0 / \lambda\right)$ is the Rayleigh range, ω_0 is the beam waist at focus, λ is wavelength, I_0 is the peak intensity and β denotes the nonlinear absorption coefficient.

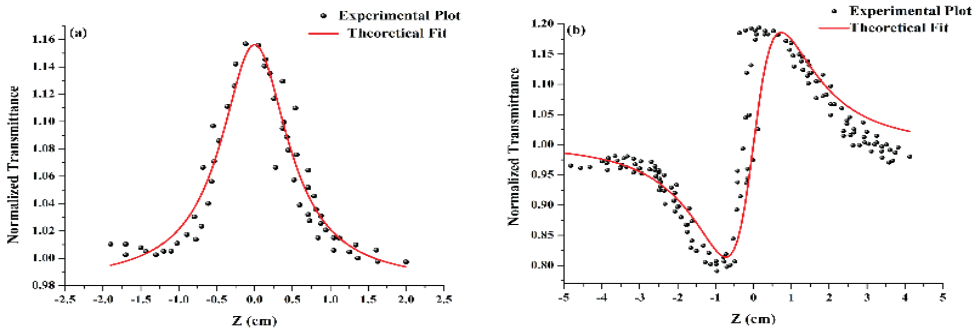

Fig. 1. Z-scan representation of Eosin Yellow (EY) (300μM) (a) open aperture (b) closed aperture.

While, the energy transfer efficiency (Φ_{ET}) from dye to gold nanoshapes is calculated using equation:

$$\Phi_{ET} = \frac{1}{1+(d/R_0)^{n*}};$$

Where, R_0 is the Förster distance, while, n* is the fitting factor and d is the between the donor and acceptor molecules .

Conclusion

In this work, we have focused on the energy transfer mechanism responsible for the variation in the morphology dependent two photon absorption coefficients of EY-gold nanoparticles hybrids. The plasmonic resonances, linear extinction spectra, photoluminance spectra, two photon absorption coefficient and two photon refractive indices of two distinct plasmonic shapes, namely EY-gold nanoflowers and EY-gold nanopebbles, in comparison with conventional EY-gold nanospheres, have been studied. The experimental outcomes infer that the third order nonlinear coeffecients of the hybrids with an organic fluorophore (Eosin Yellow) are in the order nanoflowers > nanopebbles > nanospheres. Further, the study confirmed that the energy transfer within the of EY-GNF hybrid, was NSET while in conjugation with GNS and GNP, FRET dominated the interaction. The results indicate an interesting relationship between the efficiency of the energy transfer mechanism and the enhancement in the third order nonlinear coefficients.

Acknowledgment

The authors are thankful to the Director and the Divisional Review Committee, CSIR-National Physical Laboratory, New Delhi-110012, for granting permission to publish this work. Kaweri Gambhir acknowledges financial support from the Council of Scientific & Industrial Research, India.

References

[1]Andres D Neira, Nicolas Olivier, Mazhar E Nasir, Wayne Dickson, Gregory A Wurtz, and Anatoly V Zayats, *Nature communications* **6**, 7757 (2015).
[2]Gregory A Wurtz, Robert Pollard, Willam Hendren, GP Wiederrecht, DJ Gosztola, VA Podolskiy, and Anatoly V Zayats, *Nature nanotechnology* **6** (2), 107 (2011).
[3]Kaweri Gambhir, Bhumika Ray, Ranjana Mehrotra, and Parag Sharma, *Optics & Laser Technology* **90**, 201 (2017).

OSI-ISO 2018 manuscript No.
(153)

Creating C-point array by diffraction of a C-point through two ring aperture

S. Deepa, Sushanta Kumar Pal, and P. Senthilkumaran

Abstract The ellipse field polarization singularities, commonly known as C-points, are of interest in recent times. We have studied the propagation characteristics of C-point through two ring aperture. The study has revealed some interesting results. On diffraction, the C-point is found to form an array of C-points, around a central C-point. The other C-points are found to be arranged in the form of a circle. The interesting fact is that all the C-points are found to be of same handedness and same C-point index as the central C-point. The far field Stokes phase distribution and the resulting polarization distribution have been presented in this article. This study has been extended to dark C-point too and the corresponding results are presented.

Keywords Singular Optics, Polarization singularities, Diffraction, Apertures.

Polarization singularities, a constituent field of singular optics, are one in which some of the parameters representing the state of polarization (SOP) of a beam become indeterminate. Elliptic point singularities are isolated, stationary points in a plane at which some of the parameters that define polarization ellipse become undefined. The two types of planar elliptic point singularities are points of linear polarization (L-points) at which the handedness of the ellipse becomes undefined, and points of circular polarization (C-points) at which the orientation of the major/minor axis of the ellipse is undefined. Elliptic point singularities in a plane are characterized by singularity index I_C that describes the orientations of surrounding polarization ellipses in the ellipse field. I_C is given by $\frac{1}{2\pi}\oint \nabla\gamma \cdot dl$, where '$\gamma$' is the azimuth.

Generally, a brightC-point can be understood as the superposition of Gaussian beam in left/right circular polarization state and a vortex beam with charge 'm' in right/left state. The non-vortexbeam polarization state decides the handedness of the C-point whereas it is the charge of the vortex beam which decides the index of the C-point. Hence, a C-point can be mathematically represented as,

$$E_{C_{pt}} = \psi_m^{\pm}\sigma^{\pm} + exp\left(\frac{-r^2}{w^2}\right)\sigma^{\mp}$$

where, $\psi_m^{\pm} = \exp(\mathrm{im}\phi)$ denotes an optical vortex of charge 'm' and $\sigma^{\pm}$ denotes the left/right circular polarization state. The lower order C-points can be classified as lemon, monstar and star based on the orientation of the polarization ellipses around the C-point. These generic polarization singularities can be realized when polarized light traverses through inhomogeneous and birefringent media. Different methods for generating lemons and stars have been reported. But not much work has been done on diffraction of C-points. Recently applications of C-points are being reported. C-points have been used to controll emission from quantum emitters[1] and to extract Chern number of the band structure [2], which extends C-point application to the field of topology too.

Here we create bright C-points by superposition of orthogonally circularly polarized Gaussian and vortex beam and then diffract it through a two ring aperture to study the far-

S. Deepa

Department of Physics, Indian Institute of Technology Delhi, Hauz Khas, New Delhi-110016, India.
E-mail: deepa_sankar@yahoo.com

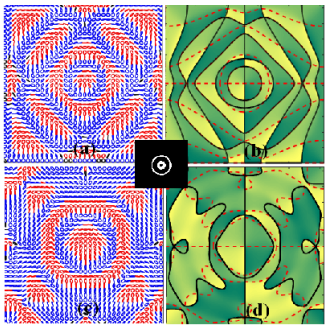

Fig.1. Two ring aperture diffraction (r_1 =0.05mm; r_2=0.1mm; r_3 =0.3mm r_4=0.35mm): (a) and (c) correspond to far field polarization distributions of bright and dark C-point and (b) and (c)their corresponding Stoke's phase distributions.

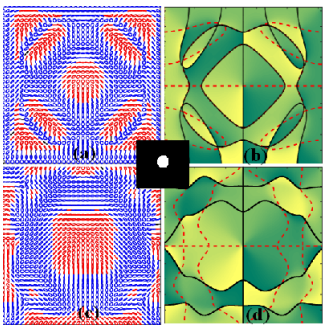

Fig.2. (a) and (c) correspond to polarization distribution of bright and dark C-point on diffraction through a circular aperture (r=0.05mm);(c) and (d) correspond to their Stokes phase distribution, respectively.

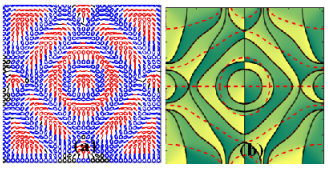

Fig.3: (a) and (b) correspond to polarization distribution andStoke's phase distribution of bright C-point on diffraction through a two ring aperture (r_1 =0.05mm; r_2=0.1mm; r_3 =0.15mm r_4=0.2mm).

field polarization distribution. The beam waist is taken to be $0.5x10^{-4}$ m and $1x10^{-4}$m fordifferent studies. The inner ring of the aperture has r_1=0.05mm with other ring diameters being r_2=0.1mm, r_3=0.3mm and r_4=0.35mm. The Stokes parameters are calculated from the far field electric field components.The polarization patterns and the Stokes phase distributions are computed using Stoke's parameters S_0, S_1, S_2 and S_3. Fig. 1a and 1b show the presence of a central C-point (here, a lemon) surrounded by many lemons which are symmetrically arranged around the central lemon and all are found to have same handedness (here red represents right handedness). L-lines separate regions of left handedness from regions of right handedness.

The same has been done for dark C-point too. A dark C-point is generally generated by the superposition of two orthogonally polarized vortex beams with unequal topological charge. The corresponding polarization distribution and Stokes phase distribution are shown in Fig. 1c and 1d, respectively. They also show additional lemons around them but the polarization distribution around the central C-point is different in both the cases which is evident in Fig.1. The polarization and Stokes phase distributions corresponding to the diffraction of bright and darkC-points from the normal circular aperture with r=0.05 mm, are shown in Fig.2. The apertures considered have been shown at the centre of Fig. 1 and 2. The diffraction of bright C-point through another radii combination of two ring aperture is also studied. The corresponding polarization and Stokes phase distribution are shown in Fig. 3a and 3b respectively. In all the figures the zero contour lines of S_1 and S_2 are marked by red (dotted) and black (solid) respectively. The intersection of these two lines indicates the position of C-points. Thus we have realised generating array of C-point from a single C-point.

In conclusion, we have studied the characteristics of C-points when they are diffracted through normal circular aperture and two ring aperture. On diffraction, the C-points are found to form an array of C-points of same handedness, around a central C-point. The study has been extended to dark C-point too.

We gratefully acknowledge grant from DST Women Scientist Fellowship (SR/WOS-A/PM-66/2017).

References

1. Evgeny Ostrovsky, Kobi Cohen, Shai Tsesses, Bergin Gjonaj and Guy Bartal, "Nanoscale control over optical singularities", Optica 5, 283,(2018).

2. Thomas Fosel, Vittorio Peano and Florian Marquardt, “L lines, C points and Chern numbers: understanding band structure topology using polarization fields”, New J. Phys. 19, 115013 (2017).

OSI-ISO 2018 manuscript No.
(154)

Wavefront sensing by using Michelson interferometer for adaptive optics

Sarvesh Pravin Satpute · Suresh Venkata · Sreekanth Reddy V · Raghavendra Prasad B · Narayanamurthy C S

Abstract Resolution of a ground based telescopes is limited by the atmospheric turbulence irrespective of its aperture size. Adaptive optics (AO) system is a best possible solution to minimize the effect of turbulence and to restore the performance of the telescope near to diffraction limited. The performance of an AO system depends on accuracy of sensing, reconstruction and correction of wavefront. The frequency at which the AO system operates plays a vital role in achieving the desired performance requirements. Shack Hartmann wavefront sensor (SHWS) is the most commonly used tool for wavefront sensing. SHWS can sense the distortions over the spatial scales equivalent to twice the diameter of microlens. This is not suficient to estimate high frequency distortions in the wavefront. To overcome this difficulty, we used interferometric techniques for wavefront sensing. This will help in estimating the high frequency distortions and their contribution towards the total wavefront error. Thus, helps in identifying the frequencies over which the distortions effect the performance. In this paper we discuss the details about the experiments carried out, results obtained from them and comparison with SHWS.

Keywords Wavefront sensing · atmospheric turbulence · adaptive optics and interferometry

Sarvesh Pravin Satpute · Narayanamurthy C S
Indian Institute of Space Science and Technology, Trivandrum, India

Suresh Venkata · Sreekanth Reddy V · Raghavendra Prasad B Indian Institute of Astrophysics, Bangalore, India
E-mail: venkata@iiap.res.in, brp@iiap.re.in

1 Introduction

Wavefront of light passing thorough the atmosphere gets distracted due to random temperature and density fluctuations in the atmosphere. The distorted wavefront results in loss of telescope resolution. Resolution of a ground based telescopes is limited by the atmospheric turbulence [1] irrespective of its aperture size. Adaptive optics (AO) [2] system helps in restoring the performance of the telescope by correcting the distorted wavefront.The functioning of AO system [3] involves sensing the distortions in the wavefront, reconstruction and correcting the wavefront. AO systems can not eliminate the distortions in the wavefront completely, but they minimize the distortion to a great extent.

First step in AO system is sensing the distortions in wavefront. This is typically performed by using a Shack-Hartmann Wavefront Sensor (SHWS). Wave- front sensing capability of the SHWS is limited by the diameter of micro lens that focuses the wavefront. Distortions in the wavefront can be sensed down to the spatial scales equal to twice of the diameter of micro lens array. This may not be sufficient to estimate the high frequency distortions/aberrations in the wavefront.

Interferometry is known for accurate sensing of high frequency distortions in the wavefront. This gives the information that is missing from the SHWS and helps in identifying the limits of the frequencies that induces significant distortions to the wavefront. Hence, a better wavefront sensing that leads to more precise reconstruction and correction.

2 Methodology

In laboratory, atmospheric turbulence is created using a pseudo random phase plate. Light propagating through this plate gets distorted. The distortions in the wavefront are sensed using a Michelson interferometer. The sensed wave- front will be reconstructed using a software module developed in MATLAB Simulink for this purpose. This gives distortions in the wavefront over different frequency spectrum. This information is used in correcting the wavefront and simulating the expected performance of telescopes with different aperture size.

References

1. V I Tatarskii, The effects of the turbulent atmosphere on wave propagation, Israel pro- gram for scientific translations, Jerusalem, ISBN 07065-0680-4
2. R K Tyson, Principles of adaptive optics, 3rd Edition, CRC press (2011)
3. J M Beckers, Adaptive optics for astronomy-principles, performance and applications, Annual review of astronomy and astrophysics, 31 (2011)

Wavefront sensing with modified Mach-Zehnder Interferometer

Ipsita Chakraborty[1] , Payel Ghosh[1*], Sarad Subhra Bhakat[1], Kallol Bhattacharya[1*]

[1]Department of Applied Optics and Photonics, University of Calcutta, JD-2, Sector 3, Salt Lake City, Kolkata 700106

[*]Corresponding author: ghosh.payel77@gmail.com, khattacharya@gmail.com

Abstract

Self-referencing interferometry has been widely used in wavefront sensing. In this paper, we report on a simple method to determine the phase information of an incoming wavefront. For this purpose a modified Mach-Zehnder interferometer is developed. Although the aberrated wavefront enter both the interferometer arms, it is spatially filtered and collimated in the reference arm so as to generate a plane reference beam. The phase information of the wavefront under test can be obtained from the fringe patterns directly with the help of Fourier transform. Experimental results are presented.

Keywords

Wavefront, Self-referencing, Phase, Interferometer

Introduction

Self-referencing interferometry has been widely used for distorted wavefront measurement[1], laser beam diagnostics[2], and adaptive optics wavefront sensing[3]. Compared with the traditional double-beam interference measurement technology, the reference wavefront is generated by the wavefront under test in self-referencing interferometry. The advantages of the self-referencing interferometry are insensivity to the disturbance in environment, strong stability, high spatial resolution and high measurement precision. The most common self-referencing interferometry includes point diffraction interferometry and shearing interferometry. In either of the cases the interference between the sample wavefront and its sheared version or a derived plane wavefront is recorded[4]. The reference wavefront of point diffraction interferometer is an ideal spherical wavefront generated by the diffraction of a pinhole and the phase information of wavefront under test can be obtained from the fringe patterns directly without any special wavefront reconstruction algorithm. The reference wavefront of shearing interferometer is generated by the deformation of wavefront under test and the resultant interference pattern leads to the derivative of the wavefront phase with respect to the direction of shear. The wavefront reconstruction algorithms typically carries out a digital integration procedure to retrieve the wavefront phase[5]. In the present work we report a self-referencing Mach-Zehnder interferometer where self-referencing plane beam is generated by spatial filtering the incoming aberrated wavefront in one of the arms of the interferometer.

Experimental Set-Up

As shown in Fig.1, the incoming aberrated wavefront is amplitude divided by the Cube Beam Splitter (CBS_1) and is directed along the two arms of the interferometer. In one of the arms the aberrated beam is focussed by a 10X microscope objective (MO). It may be observed that the focal spot thus formed is the Fourier Transform of the incoming aberrated wavefront with the higher spatial frequency terms caused by the non-planeness of the wavefront located away from the centre. The pinhole (P) of 10 micrometer diameter placed at the centre of the focal spot acts as an ideal low pass filter. The collimating lens L generates a plane beam of light which is directed towards CBS_2. The neutral density filter is required to adjust the intensity of the interfering beams so as to maximize the fringe contrast. The interference pattern is recorded on a CCD.

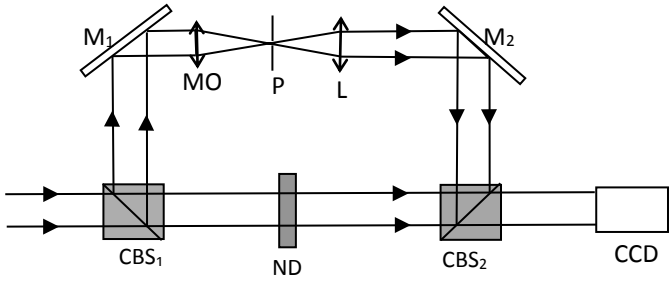

Fig 1: Schematic Experimental Set-up

Experimental Results

The Fourier transform of the captured frame is obtained, a mask is applied so that only one order of the Fourier spectra is allowed the inverse Fourier Transform of which yields the wavefront phase. This is repeated for a plane wavefront and a distorted wavefront and the phase obtained from the latter is subtracted from the former so as to eliminate system errors if any. The recorded interference pattern for the plane wavefront and a distorted wavefront are shown in Figs. 2(a) and (b) respectively. The reconstructed phase over the wavefront for the plane wavefront and the distorted wavefront is shown in Figs. 3(a) and (b) respectively. Fig. 3(c) shows the actual wavefront phase obtained by subtraction of the latter from the former.

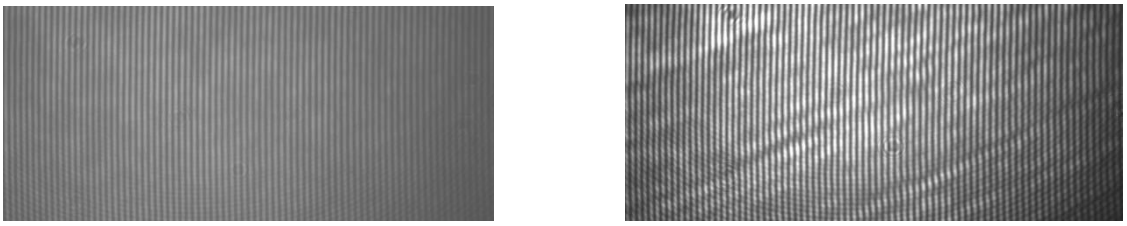

(a) **(b)**

Fig2 (a): Fringe pattern for original wavefront (b) Fringe pattern for distorted wavefront.

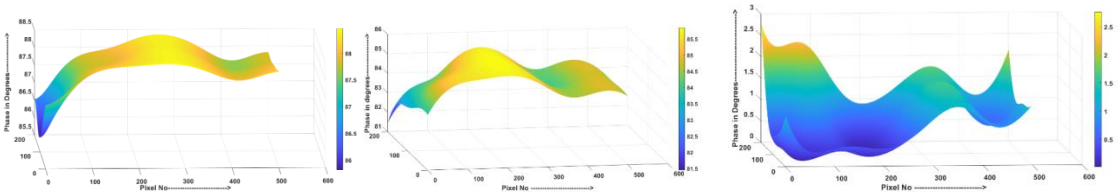

(a) **(b)** **(c)**

Fig 3(a): Undistorted wavefront (b): Distorted wavefront (c) Distortion in the incoming wavefront

References

[1] D. Liu,Y. Yang, and Y.Shen, "System optimization of radial shearing interferometer for aspheric testing," Proc. of SPIE 6834, 68340U (2007).

[2] D.Liu, Y.Yang, and J.Weng, "Measurement of transient near-infrared laser pulse wavefront with high precision by radial shearing interferometer," Opt.Commun. 275(5), 173-178 (2007).

[3] T.Shirai, "Liquid-crystal adaptive optics based on feedback interferometry for high-resolution retinal imaging," Appl. Opt. 41(19), 4013-4023 (2002).

[4] M. B.North-Morris, J.UanDelden, and J. C. Wyant, "Phase-shifting birefringent scatter plate interferometer," Applied Optics 41(4), 668-677 (2002).

[5] J. B.Saunders, "Measurement of wave fronts without a reference standard. Part 1. The wave-front-shearing interferometer," J. Res. Natl. Bur. Stand. Sect.B65, 239-244 (1961).

Solvent dependent Fluorescence Sensing of 5-aminoqionoline by Silver ion based on ICT

NupurPandey*, Nisha Fatma, Sanjay Pant

Photophysics Laboratory, Department of Physics, DSB Campus, Kumaun University, Nainital 263002, Uttarakhand, India

email*mahipndey@gmail.com

Abstract

Metal ions play significant role in various industrial and biochemical processes. However, some metal ions are toxic and hence cause serious health and environmental problems. Because of these features, the detection of metal ions is of great importance. This work describes the fluorescence enhancement and fluorescence quenching of 5 aminoquinoline in different solvents upon binding with silver ions. Very feeble emission of 5AQ is observed in water (polar solvent) which gets enhanced upto ~46 folds in presence of Ag^+ ions. However, in acetonitrile (polar aprotic solvent), the addition of different concentrations of Ag^+ ions results in quenching of 5 AQ (~17 folds). Also a red shift in emission spectrum of 5-AQ is observed upon addition of Ag^+ ions in both solvents. Thus present system appears to be quite interesting in the sensing/recognition of Ag^+ ion in various protic as well as aprotic environments.

Keywords:

5 Aminoquinoline, Silver ions, red shift, ICT.

Acknowledgment

Authors are thankful to Prof. A.B. Melkani, Department of Chemistry, Kumaun University for providing a facility for absorption measurements and Dr. M.S. Mehata, Department of Applied Physics, Delhi Technical University for providing TCSPC facility. Author NP is thankful to UGC New Delhi India for providing research fellowships under the scheme for the meritorious students in sciences (RFSMS).

Introduction

Substituted quinolines constitute a broad class of fluorophores with both technological and academic interest. Amino-quinolines (AQ) belong to the class of molecule that can exist both in enol and keto forms and can interconvert through tautomerization by excited state proton transfer (ESPT) [2-3]. There is a growing interest to sense heavy metal ions selectively for both chemical and biological reasons. Many analytical methods have been applied in that respect, and much attention has been made to fluorometry because of its low cost, selectivity, sensitivity, and response time. [4]. As one of the most commonly encountered HTM elements, silver and silver compounds have been widely utilized in chemistry, pharmacy, the electrical industry, and the photographic and imaging industry [4]. In particular, Ag^+ has received considerable attention because of its bioaccumulation and toxicity.Furthermore, the mechanism of antimicrobial activities of Ag^+ has not been well established because of a lack of suitable detection and imaging methodologies.So far, many of fluorescence sensors based on metal-ligand coordination or chemical reactions for HTM ions detection, especially Zn^+, Cu^{2+}, Pb^{2+}, Fe^{2+} have been reported [4].

Experimental Section

5-aminoquinoline (obtained from Sigma Aldrich), Silver nitrate and other metal salts (obtained from Loba-Chemie) are of 98-99% purity and used without further purification. Steady state absorption spectra, at room temperature, were recorded by UV–Visible Double beam Systronics Model No: 2203 Spectrophotometer. The excitation and emission spectra were recorded by using ISA Jobin Yvon Fluorolog FL3-22 Spectrofluorometer and data were analyzed by related software. Time-correlated single photon counting (TCSPC) system (DeltaFlex-01-DD, Horiba Jobin Yvon IBH Ltd) coupled with Delta Diode (340 nm) and PMT (PPD 850) was used for fluorescence decay measurements

Results and discussion

The absorption maximum of 5-AQ in water is observed at 335nm while for acetonitrile (ACN) it is observed at 345nm.The excitation spectrum of 5-ASA in both aprotic and protic solvent was found to be independent of monitored emission wavelength and exhibits a single peak at ~338nm and 347 in water and ACN (which resembles to its absorption spectrum). On successive addition of Ag^+ ions the optical density is increased and a new peak is developed at 305nm in aqueous solution. In contrast to this, decrease in optical density is noticed on adding the increased concentrations of Ag^+ ions in 5AQ ACN solution. These changes in absorption maximum with addition of Ag^+ ions indicate that there is ground state complex formation between Ag^+ and 5-AQ. Upon adding various concentrations of Ag^+ ions, the fluorescence intensity of 5AQ in water gets enhanced upto 19 folds and also the fluorescence spectrum is shifted towards red side (~23nm). In ACN, the fluorescence intensity of 5-AQ is quenched upto 17 folds which is also accompanied by a red shift of ~46nm upon successive addition of Ag^+ ion (4µm-60mM). Time resolved studies have been performed further understand the nature of quenching of 5AQ with Ag^+ which confirms the nature of quenching to be dynamic. The shift in the FL spectrum may probably be ascribed to the different ICT states formed by the interaction of 5AQ with Ag+ ions. With the help of BH plot the binding constant calculated to be 1.4×10^4 M^{-1} for 5AQ:Ag^+ in ACN. Also 1:1 binding is suggested for both the cases. In addition to this bimolecular quenching constant (k_q) and Stern Volmer constant (K_{SV}) have been calculated.

Conclusion

The present system appears to be quite interesting in the sensing/recognition of Ag^+ ion in various protic an aprotic environments in a concentration range of ion (4µm-60mM). A large Stokes shift is observed which is also beneficial in fluorescence sensing technology to avoid self-absorption and interference from light source.

References:

[1] J.R. Lakowicz, Principles of Fluorescence Spectroscopy, third ed. Springer, 2006. doi:10.1007/978-0-387-46312-4.

[2] J.P. Bridhkoti, H.C. Joshi, S. Pant, Fluorescence characteristics of 5-aminoquinoline in acetonitrile:Water,J. Mol. Liq. 164 (2011) 197–200. doi:10.1016/j.molliq.2011.09.014.

[3] J.P. Bridhkoti, H. Mishra, H.C. Joshi, S. Pant, Photochemistry of 5-aminoquinoline in protic and aprotic solvents, Spectrochim. Acta - Part A Mol. Biomol. Spectrosc. 79 (2011) 412–417. doi:10.1016/j.saa.2011.02.044.

[4] Y. bao Jiang, C. Gao, X. Zhang, J. shui Yao, Q. ze Liu, X. xia Cai, A highly selective and sensitive fluorescence probe with A-π-D-π-A structure for detection of Ag+, J. Mol.Struct. 1163 (2018) 33–40. doi:10.1016/j.molstruc.2018.01.058.

[5] A.C. Gonçalves, J.L. Capelo, C. Lodeiro, A.A. Dos Santos, A selective green emissive chromogenic and fluorogenic seleno-coumarin probe for Cu2+ detection in aprotic media, Photochem. Photobiol. Sci., 16 (2017) 1174-1181. doi:10.1039/C7PP00036G.

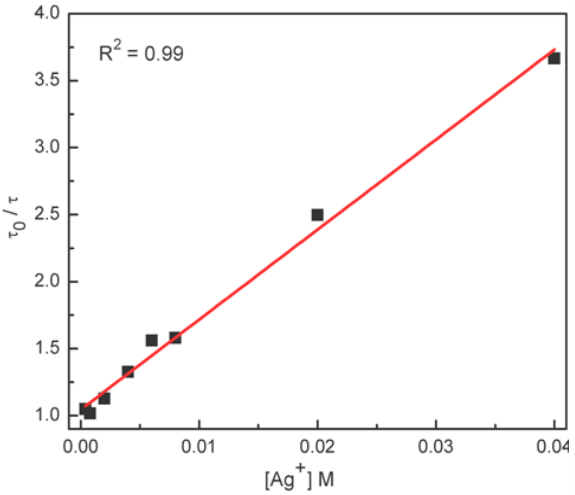

Fig1. SV plot of 5AQ in presence of Ag^+ ions in ACN

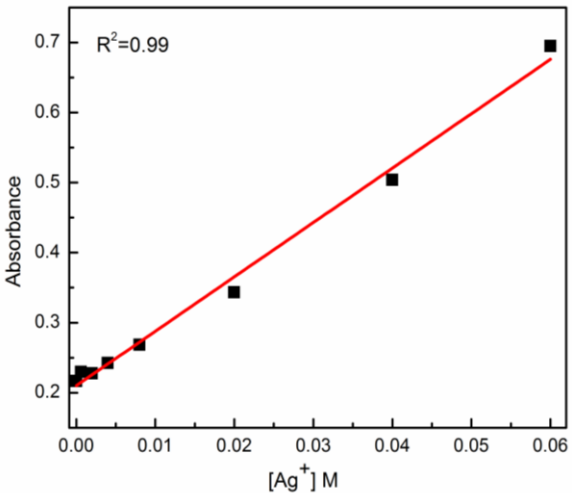

Fig2. Absorption verses concentration graph that suggest 1:1 binding in aqueous solution.

OSI-ISO 2018 manuscript No.
(157)

Binding of Alkaloid, Nobiletin to Double Stranded DNA-Spectroscopic Insights into Nature of Interaction and Anticancer Potential

Bhumika Ray[1,2] and Ranjana Mehrotra[1,2]

[1]*Academy of Scientific & Innovative Research (AcSIR), CSIR-NPL Campus, New Delhi 110012, India*
[2]*Optical Radiation Metrology Section, CSIR-National Physical Laboratory, New Delhi 110012, India*
E-mail: ray.bhumika24@gmail.com

ABSTRACT

Spectroscopy has been proficient in providing molecular signatures related to composition and biochemistry of biological molecules (or tissues), which has propounded methods based on spectroscopy for label-free investigation of biomolecular interactions and *in vivo*/*in vitro* imaging and medical diagnostics. Nobiletin is a natural alkaloid having propitious anticancer activity, however, the cellular targets and underlying action mechanism is not well-defined. Hence, the present work focuses on determining the spectral characteristics of binding between nobiletin and nucleic acid at molecular level. Results concluded here, contribute in realizing the cytotoxic action of this alkaloid inside the cell and also pave the way in developing alkaloid based new chemotherapeutics.

KEYWORDS Vibrational spectroscopy; Anticancer alkaloid; Nucleic acid; Circular dichroism

1. INTRODUCTION

Nobiletin (5,6,7,8,3′,4′-hexamethoxyflavone) is a polymethoxylated natural alkaloid derived from citrus fruit peels, C*itrus nobilis*. This molecule has shown substantial anticancer activity against various types of *in vitro* and *in vivo* tumors cell lines and animal models, respectively. However, its specificity for biomolecules and inhibition mechanism inside the cell is still under investigation. Deoxyribonucleic acid (DNA), the genetic material, has been considered as one of the main cellular target for anticancer small molecules. With this possibility, we have investigated *in vitro* molecular interaction between nobiletin and nucleic acid to unveil the rationale behind its (nobiletin) cellular action (graphical representation, Fig. 1). Spectroscopic methods have been preferred to probe the interaction as these provide structural and conformational information on biological molecules. Besides this, alteration in the biomolecule structure and sub-conformational states owing to its complexation with small molecules (ligands) or any other external factor (such as disruption in the ideal physiological condition) can be clearly assessed.

2. EXPERIMENTAL SECTION

2.1 Stock Solution Preparation

Nobiletin and calf thymus DNA were purchased from Sigma Aldrich Chemicals, USA. The stock solutions of DNA were prepared in tris-HCl buffer (10 mM, pH 7.4) and placed at 8 ºC for 24 h. Similarly, stock solution of alkaloid (nobiletin) and its different dilutions were prepared in deionized water. Alkaloid/DNA molar ratios (r) were prepared by drop wise addition of different concentration of nobiletin into constant concentration of DNA. This was followed by vortexing and incubation at room temperature for 3 h to ensure complexation.

2.2 Methods

Vibrational spectroscopy, circular dichroism and absorption spectroscopy have been employed to determine the binding mode, structural-conformational stability and binding strength of nobiletin complexed with DNA in aqueous solution under physiological conditions.

3. RESULTS

The results suggest that nobiletin directly interacts with DNA double-helix through nitrogenous base residues and possibly intercalates through sugar-phosphate backbone. Conformationally, nobiletin-DNA adductation alters the native B-conformation of biopolymer (DNA), thereby attains an intermediate state, where its native activity is disrupted. The binding strength estimated for the complexation indicate moderate to strong binding affinity of alkaloid for nucleic acid.

4. CONCLUSION

The findings drawn from the study recognize DNA as molecular target of nobiletin and also describe the mechanism of DNA damage exerted by this natural alkaloid that can be the basis for further exploration in demarcating its anticancer potency.

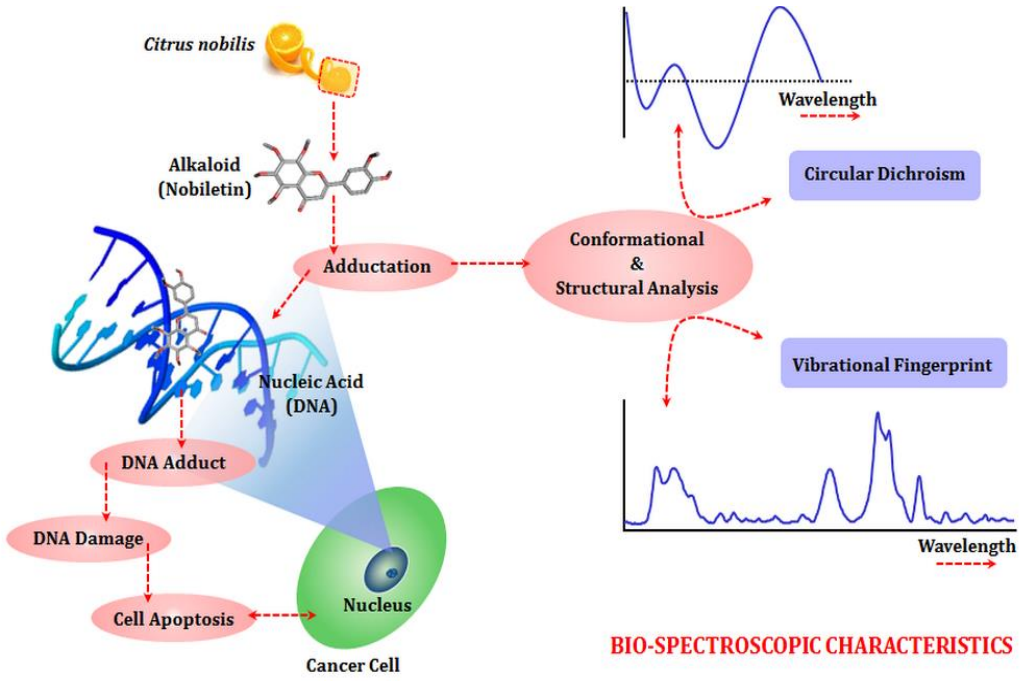

Fig. 1 Bio-spectroscopic (structural-conformational) characteristics of alkaloid (nobiletin) binding with nucleic acid (DNA) and its cellular significance.

ACKNOWLEDGEMENT

The authors are thankful to the Director, CSIR-National Physical Laboratory, New Delhi 110012, India for permitting the presentation of this study. Bhumika Ray is thankful to Department of Science and Technology (IF150181), Govt. of India, New Delhi 110012, India for providing financial support.

REFERENCES

1. S.L. Feng, X.J. Yao, Z.W. Yuan, L. Liu, Y. Xie, U.S. Patent Application, 15/415, 883 (2017)
2. K. Kato, T. Yamazaki, M. Honma, Cancer Research, 1054 (2017)
3. H.-L. Cheng, M.-J. Hsieh, J.-S. Yang, C.-W. Lin, K.-H. Lue, K.-H. Lu, S.-F. Yang, Oncotarget, 35208 (2016)
4. L.K. Morley, J.P. Ferguson, J. Koropatnick, Cancer Letters, 251, 168 (2007)
5. C. Kendall, M. Isabelle, F.B. Hegemark, J. Hutchings, L. Orr, J. Babrah, R. Baker, N. Stone, Analyst, 134, 1029 (2009).

OSI-ISO 2018 manuscript No.
(158)

Off-core long period fiber grating based highly sensitive refractive index sensor

Krishnendu Dandapat, Indrajeet Kumar, Saurabh Mani Tripathi

Abstract A grating structure in the cladding region (off-core) of an optical fiber has been proposed in order to increase its sensitivity for refractive index measurement. For off-core long period fiber grating (LPFG), the sensitivity of ~ 4390 nm per refractive index unit is achieved for a refractive index range of 1.33-1.36 which is 1.4 times higher than that of conventional (in-core) LPFG. Theoretical study suggests that the primary reason for the increase in sensitivity is the modulation in refractive index in the off-core region which leads to existence of resonance wavelengths close to the turn-around point.

Keywords Fiber optics; Fiber optics sensors; Remote sensing and sensors; Fiber Bragg grating

1. Introduction

Accurate refractive index (RI) measurement is most important in scientific and industrial research as it is very important parameter for the measurement of quality of a number of food products, chemicals, and its precise measurement is also very important in medical industrial sectors. Several highly sensitive schemes for RI measurement based on Surface Plasmon Resonance (SPR) [1], long period fiber gratings (LPFGs) [2, 3], metal clad waveguides [4] and reverse symmetry waveguides [5] have been reported. The LPFG based RI sensors have numerous advantages over other sensing schemes as they are very compact in size, highly accurate, spectrally selective, easy to use, inexpensive, and support remote sensing. The resonance wavelength of the LPFG is influenced by an ambient refractive index (ARI) change and because of this the LPFGs can be used as RI sensors. For most of the LPFG sensors, the gratings are inscribed inside the core region and sensitivity is generally low expect etched LPFG and dual resonance LPFG. In this paper, we propose an ultra-high sensitive RI sensor, based on off-core long period gratings. We show that the sensitivity of the off-core grating sensor is much higher, ~ 4390 nm per refractive index unit (RIU), than the conventional LPFGs (~ 2500 nm / RIU) for biological/chemical samples [2].

2. Theoretical Analysis

The schematic of the proposed sensor is shown in Fig. 1. We consider an optical fiber whose core and cladding regions are made of 3.1 mol. % GeO_2 doped SiO_2 with a radius of 4.1 μm and 1 mol. % Fluorine doped SiO_2 with a radius of 62.5 μm, respectively. Sellmeier relation is used to incorporate the wavelength dependency of refractive index [2]. We first choose an appropriate cladding mode that exhibits turn around behavior at desired wavelength and then calculate the grating period (Λ). The total field in the grating region will be the linear combination of core mode and cladding mode fields. The effective indices of the participating core (LP_{01}) and cladding mode (LP_{010}) are 1.441208 and 1.434639, respectively, at the low loss telecommunication wavelength 1.55 μm.

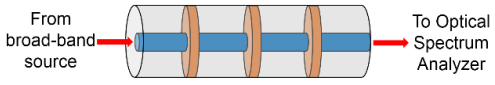

Fig. 1: Schematic diagram of the proposed RI sensor.

The transmission power is calculated using coupled mode theory (CMT). The relationship between the core and cladding field at $z = L$ (output) can be written in terms of their value at $z = 0$ (input) using the matrix equation (1) [2, 6]:

Department of Physics, Indian Institute of Technology Kanpur, Kanpur-208016, U.P., India
E-mail: krishnd@iitk.ac.in

$$\begin{bmatrix} A_{co}(z=L) \\ A_{cl}(z=L) \end{bmatrix} = T_{LPFG} \times \begin{bmatrix} A_{co}(z=0) \\ A_{cl}(z=0) \end{bmatrix}, T_{LPFG} = \begin{pmatrix} \cos(\gamma L) - i\frac{\delta}{\gamma}\sin(\gamma L) & -i\frac{\kappa}{\gamma}\sin(\gamma L) \\ -i\frac{\kappa}{\gamma}\sin(\gamma L) & \cos(\gamma L) + i\frac{\delta}{\gamma}\sin(\gamma L) \end{pmatrix} \quad (1)$$

where, T_{LPFG} is the transfer matrix of LPFG having a grating length L, κ is the cross coupling coefficient between the core and cladding field and can be written as:

$$\kappa = \frac{\omega \varepsilon_0 n_{co}}{2} \int_{r_{co}}^{r_{cl}} \int_0^{2\pi} \Delta n \phi_{co} \phi_{cl} r dr d\psi, \quad \gamma = \sqrt{\kappa^2 + \delta^2} \quad (2)$$

Here, ε_0 is the free space permittivity, r_{co} and r_{cl} are the core and cladding radius, respectively, Δn is the RI modulation in core having a refractive index n_{co} and δ is the detuning parameter. We have considered an initial condition that the light is launched entirely in the core region, so we can write $A_{co}(z=0) = 1$ and $A_{cl}(z=0) = 0$. Substituting the value of the amplitude of core and cladding field, we calculate $A_{co}(z=L)$, using which transmission power is calculated**.**

2. Results and Discussion

The phase matching curve between the core mode (LP_{01}) and cladding mode (LP_{010}) is plotted in Fig. 2(a) for two different ARI. There are two resonance wavelengths for a particular grating period and the resonance wavelengths are shifting opposite to each other when ARI is changed. The phase matching curve is showing maximum shift of the resonance wavelengths at the turn around point (TAP) wavelength.

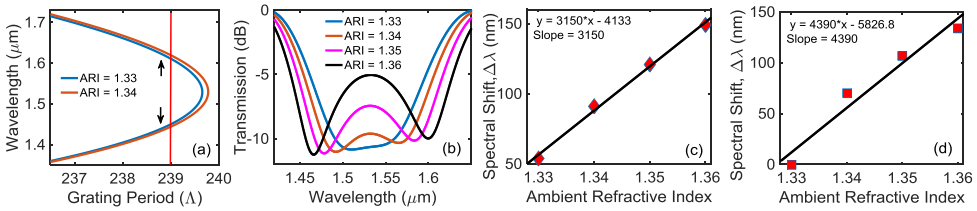

Fig. 2: (a) Phase matching curve between core and cladding mods. (b)Transmission spectra corresponding to four different ambient refractive index. (c) Variation of wavelength shift with respect to the ambient refractive index (ARI) of in-core LPFG.(d) Variation of wavelength shift with respect to ARI of off-core LPFG.

We observe that with increasing ARI, the resonance wavelengths move opposite to each other, shown in Fig. 2(b), which effectively doubles the sensitivity. To compare the performance of our proposed sensor, we also carried out simulations for LP_{01}-LP_{010} mode power coupling using an in-core LPFG. The corresponding sensitivity curve is shown in Fig. 2(c). In Fig. 2(d) the sensitivity curve of our proposed sensor has been plotted. We observe that the proposed scheme is about 1.4 times more sensitive than the in-core LPFG. The proposed sensor can be easily fabricated using Femto-second or CO_2 lasers.

Acknowledgments

Krishnendu Dandapat would like to thank MHRD, Govt. of India. Indrajeet (SERB/PDF/2017/002679) Kumar and Saurabh M. Tripathi (SERB/F/10933/2017) acknowledge Science & Engineering Research Board for financial support.

References

1. J. Homola, "Surface Plasmon Resonance Based Sensors," Springer Series on Chemical Sensors and Biosensors, Springer, 2006.
2. R. Garg, S. M. Tripathi, K. Thyagarajan, and W. J. Bock, "Long period fiber grating based temperature-compensated high performance sensor for bio-chemical sensing applications" Sensors and Actuators B **176,** 1121-1127 (2013).
3. S. M. Tripathi, W. J. Bock, and P. Mikulic, "A wide-range temperature immune refractive-index sensor using concatenated long period fiber gratings" Sensors and Actuators B **243,** 1109-1114 (2017).
4. N. Skivensen, R. Horvath *et. al*, "Deep-probe metal-clad waveguide biosensors" Biosensors and Bioelectronics **22,** 1282-1288 (2007).
5. R. Horvath, L. R. Lindvold, and N. B. Larsen, "Reverse-symmetry waveguides: theory and fabrication" Applied Physics B: Lasers and Optics **74,** 383-393 (2002).
6. Raman Kashyap, Fiber Bragg Gratings, Academic Press.

Holographic spatial filter : An optical design consideration

Abhijit Ghosh[1,*] and A.K. Nirala[2]
[1]Department of Physics, Bhagalpur College of Engineering, Bhagalpur 813210, Bihar, India
[2]Biomedical Optics Lab, Department of Applied Physics, Indian Institute of Technology (Indian School of Mines), Dhanbad 826004, Jharkhand, India
*Corresponding Author : abhi.photonics@gmail.com

Abstract

The present study proposes a novel way for designing a spatial filter using holographic technique. Detailed design consideration and experimental results have been presented.

Keywords

Holographic lens, Spatial Filter, Microscopic Objective, Coherent optics

Introduction

Coherent optics enables the optical systems to perform many sophisticated information processing operations, such as Fourier transform [1], holography [2] and spatial filtering [3]. A spatial filter is a beam converging device coupled with a pinhole. The pinhole, is used to remove interference patterns in a laser beam caused by diffraction from dust, lint, lens imperfections etc. The configuration of the spatial filtering arrangement using conventional lens (Microscopic Objective) is straight forward and is well known but due to the increasing interest towards the holographic optical elements (HOEs) [4] and their monochromatic aberration free performance [5,6], we have developed a new and simple method for designing holographic spatial filter using off-axis holographic lens (hololens).

Optical Design Consideration

Optical assembly for designing holographic spatial filtering arrangement is shown in Fig.1 and Fig.2. Fig.1 describes multiple focal length operation whereas Fig.2 maximum efficiency operation of the hololens in the arrangement. Conventional lens used as a microscopic objective is replaced here by a hololens, details of hololens recording geometry is described in our previous communication [7].

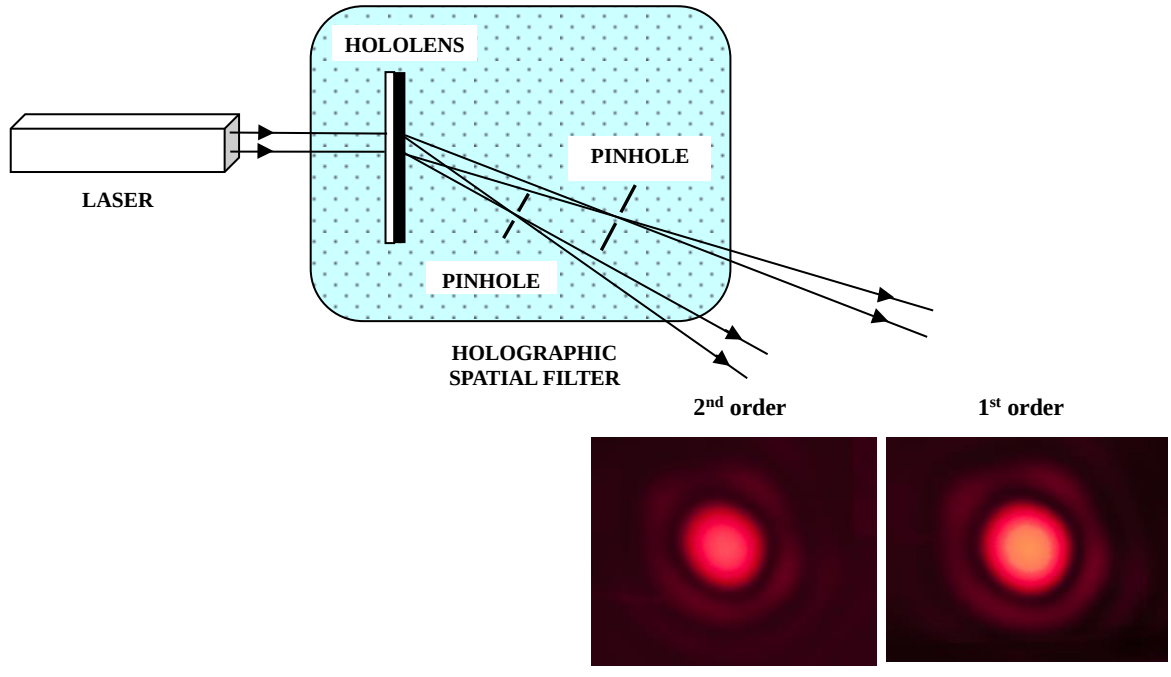

Fig. 1. Holographic spatial filter having multiple focal length operation.

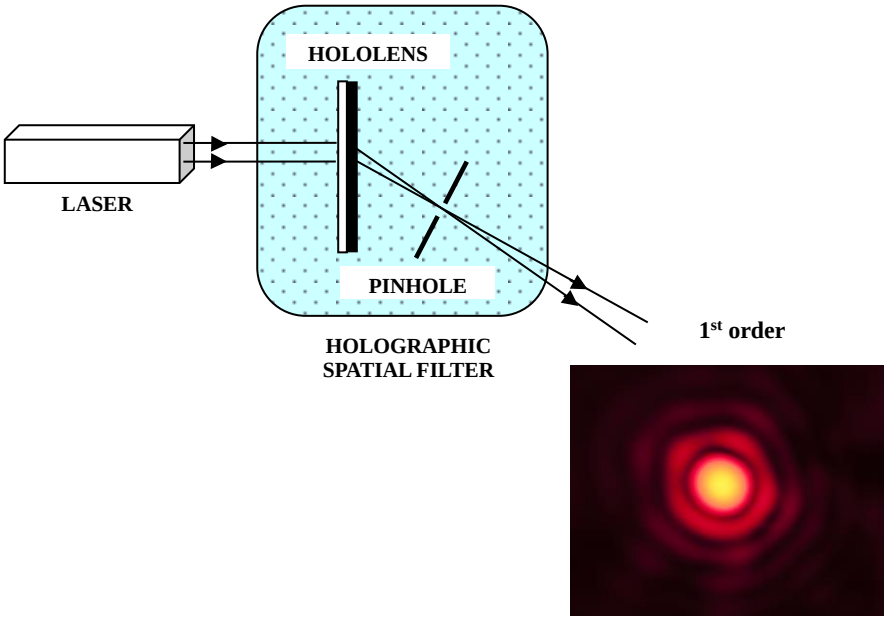

Fig. 2. Holographic spatial filter having maximum efficiency operation.

Here two hololenses have been recorded in present work, having different inter beam recording angles 17° and 45° in free space (corresponding central fringe spacing are 2.14μm and 0.826μm respectively). Lower inter beam recording angle (i.e. 17°) is for obtaining higher order foci (42%, 24% and 5% diffraction efficiency at 1st, 2nd, and 3rd order focal points respectively) and optimum recording angle (i.e. 45°) is for obtaining maximum diffraction efficiency (68%) at 1st order and almost negligible efficiency for the rest of the orders. In multiple focal length operation, an unexpanded laser beam is allowed to pass through the hololens and different higher order foci are retrieved in addition to the principal focus off-axially at positions $f/2, f/3, f/4, f/5, \ldots,$ etc. A pinhole, aperture of diameter 15μm is placed one by one over all the higher order focal points but due to low intensity of higher order foci we have restricted to 2nd order only. In maximum efficiency operation, the same pinhole is placed over 1st order focal point.

Results and Discussion

The design consideration described in this paper is used to evaluate the performance of the holographic spatial filter. Some of the test results are produced in Fig.1 and Fig.2 to substantiate our claim. Airy pattern formed in both 1st and 2nd order, in case of multiple focal length operation is shown in Fig.1 whereas Airy pattern formed in 1st order in case of maximum efficiency operation is shown in Fig.2.

Conclusion

In conclusion it has been experimentally demonstrated that a spatial filtering arrangement can be designed holographically to work in coherent light. Experimental results show that holographic lenses can be used advantageously in spatial filtering arrangement due to their light weight, low cost and easier fabrication technique.

References

[1] J.W. Goodman, Introduction to Fourier Optics, 2nd edn. (McGraw-Hill, NewYork, 1968).
[2] D. Gabor, Nature 161, 777 (1948)
[3] S. Prakash and C. Shakher, J. Opt., 28, 1-4 (1997)
[4] N.K. Mohan, Q.T. Islam, P. K. Rastogi, Optics and Lasers in Engineering 44, 871–880 (2006)
[5] R.W. Meier, J. Opt. Soc. Am., 55, 987-991 (1965).
[6] E.B. Champagne, J. Opt. Soc. Am., 57, 51-55 (1967)
[7] A. Ghosh and A.K. Nirala, Opt. Rev. 21, 765–768 (2014)

OSI-ISO 2018 manuscript No.
(160)

Metal Oxide/ Porous Silicon based Devices for Chemical Sensing Application

Priyanka Dwivedi, Saakshi Dhanekar*, Samaresh Das

*E-mail: sdhanekar@care.iitd.ac.in

**Centre for Applied Research in Electronics (CARE),
Indian Institute of Technology (IIT), New Delhi – 110016, India**

Abstract This paper presents fabrication, characterization and testing of metal oxide/porous silicon (PS) based devices for selective detection of volatile organic compounds (VOCs). Electrical detection scheme was applied for sensing VOCs at room temperature. Sensor devices were fabricated using metal oxide like TiO_2 with PS as a sensing material. Electrical electrodes were formed on the sensing surface using standard micro-fabrication techniques. Sensors were tested in presence of ethanol, acetone, IPA and moisture. Various readings were taken at different temperatures to confirm the operating temperature of sensor. Also, sensor was found to be most responsive for ethanol vapors at room temperature. Thus, sensor was found to be selective for ethanol and its best performance was observed at room temperature.

Keywords chemical sensors, metal oxides, TiO_2, selectivity

The need of highly sensitive and selective alcohol sensors has been growing rapidly to prevent and prohibit drinking and driving cases. Different materials are being explored as gas sensors since many years, which include electronic ceramics, metal oxide semiconductors, and conducting polymers [1–3]. Nanostructured transition metal oxides such as ZnO, SnO_2, CuO, WO_3, MoO_3 and TiO_2 etc. are used as potential sensing materials because of high sensitivity, low fabrication costs, durability and reusability. These materials also confront few challenges like selectivity and high operating temperature which makes these materials not compatible for CMOS integration [4–11]. From this point of view ethanol sensor is one of the major components of a breathalyzer used for estimating the alcohol concentration in the human breath. This paper presents the high performance selective ethanol sensor based on TiO_2/porous silicon (PS).

Wafer scale metal oxide/PS was synthesized using RF sputtering in presence of oxygen. The technique used here for TiO_2/PS fabrication is superior in comparison to other methods as this provides on chip scalable and low in cost fabrication process. Electrical electrodes were fabricated on top of TiO_2/PS layer which act as a sensing. These electrodes were used for recording resistive measurements from metal oxide/PS sample in presence of different volatile organic compounds (VOCs). With the effect of metal oxide on PSi, an enhancement in sensitivity and a selective response for ethanol was observed at room temperature. Morphology of the samples investigated using SEM confirms the formation of metal oxide nanostructures on PS. Samples were further analysed using Raman, XRD and XPS.

All samples were tested in presence of different analytes in the wide range of 5-500 ppm. Upon exposure to analytes, a change in resistance was measured through electrical electrodes on the surface. It should be noted that the samples were exposed to different analytes like ethanol, IPA, acetone and moisture, however all were found to be selective to ethanol. The highest response was obtained for ethanol vapors as shown in Fig. 1. Thus sensor can be used

to detect a wide range of ethanol at room temperature. Sensor response obtained from the sample TiO_2/PS in presence of 100 ppm of each test analyte is shown in Fig. 1(a). This sensor was tested for almost two months and almost same response was observed. Hence, this affirms that the sensor exhibits repeatability sensing for ethanol and long stability.

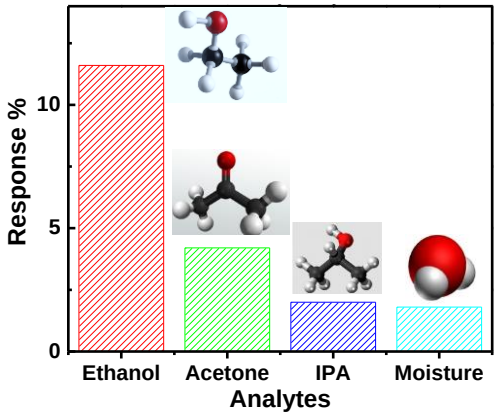

Fig. 1 Sensing Studies of TiO_2/PS Sensor at room temperature (a) selectivity test (b) stability

References

[1] K. Wetchakun, T. Samerjai, N. Tamaekong, C. Liewhiran, C. Siriwong, V. Kruefu, A. Wisitsoraat, A. Tuantranont, S. Phanichphant, Sens. Actuators B Chem. 160 (2011) 580–591.
[2] H. Bai, G. Shi, Gas sensors based on conducting polymers, Sensors 7 (2007) 267–307.
[3] T. Nenov, S. Yordanov, Ceramic sensor device materials, Sens. Actuators B Chem. 8 (1992) 117–122.
[4] N. Gas, Sensors 13 (2013) 865–874.
[5] P. Dwivedi, S. Dhanekar, S. Das, Semicond. Sci. Technol. 31 (2016) 1–7.
[6] A. De Marcellis, G. Ferri, S. Member, P. Mantenuto, S. Member, L. Giancaterini, C. Cantalini, IEEE Sens. J. 13 (2013) 2792–2798.
[7] K. Kalantar-zadeh, J.Z. Ou, ACS Sens. 1 (2016) 5–16.
[8] N.M. Vuong, N.D. Chinh, B.T. Huy, Y. Lee, Sci. Rep. (2016).
[9] C. Li, M. Lv, J. Zuo, X. Huang, Sensors (2015) 3789–3800.
[10] P. Dwivedi, S. Das, S. Dhanekar, ACS Appl. Mater. Interfaces, 9 (2017), 21017−21024
[11] P. Dwivedi, N. Chauhan, P. Vivekanandan, S. Das, D. S. Kumar, S. Dhanekar, Sens. and Actuators B 249 (2017) 602–610.

OSI-ISO 2018 manuscript No.
(161)

Electric-field induced controllable Photoluminescence in rare-earth doped lead-free piezoelectric ceramics- towards paradigm shift in ceramic photonics

Sai Santosh Kumar Raavi, K. R. Kandula, C. Goutham, Abhinav Kumar, Saket Asthana

Abstract: With the advent of Internet of Things (IoT), the requirement for various multifunctional materials is the need of the hour. Sodium bismuth titanate, $Na_{0.5}Bi_{0.5}TiO_3$ (NBT) is a proven candidate showing excellent ferroelectric properties. In particular, it was observed that site-specific substitution with optically active rare-earth (RE) ions resulted in enhanced electrical properties with additional functionality of photoluminescence (PL) making them attractive for promising application. In this report, we focus our attention on obtaining the optimal substitution of RE-ions for enhanced multifunctionality in terms of PL, ferrorelectric and energy storage properties. This work explores substitution of neodymium (Nd^{3+}), Europium (Eu^{3+}), Presoymium (Pr^{3+}) and Holomium (Ho^{3+}) ions into NBT matrix. Most important observation is that obtaining the optimal substitution for obtained highest emission intensity is sufficient to obtain best electrical properties. Our results also indicated that both PL with electrical properties can be modified upon electric poling. In case of Nd, Eu and Ho substituted NBT it is observed that upon poling, PL intensity is observed to be quenched, consistent with the obtained XRD data indicating an electric-field induced structural ordering towards higher symmetry, confirmed with the help of structural refinement. The situation is opposite for Pr-doped NBT. Considering that traditionally, research in ceramics doped with optically active ions have commonly been targeted towards the fabrication of phosphors for fluorescence lamps or lasing applications, we believe the direction of the work presented here offers a paradigm shift in the research of photonics with ceramics.

Keywords Photoluminescence. Lead-free piezoelectric ceramics, rare-earth luminescence, sodium bismuth titanate.

Among, the several lead-free ferro/piezoelectric ceramics $Na_{0.5}Bi_{0.5}TiO_3$ (NBT) has emerged as a potential candidate to replace lead based piezoelectric materials and is chosen as a parent compound for the studies presented. The details of synthesis of NBT can be found elsewhere [2,3]. Polycrystalline NBT compounds with RE^{3+} substitutions (Nd, Eu, Pr, Ho) were synthesized by solid-state route to obtain stoichiometric ratios given as $[Na_{0.5}Bi_{0.5-x}Re_x]TiO_3$, where x is the mol % of the substituent. Phase analysis of the obtained ceramic pellets were performed by using powder X-ray diffractometer over the angle of $20°<2\theta<90°$. The room temperature PL spectrum was measured by photo-exciting with 440 nm (Pr-, Ho-NBT) and 532 nm (for Nd-, Eu-NBT) from cw-DPSS lasers and the subsequent PL is collected by a fiber coupled spectrometer (Avantes). The samples were electrically poled at room temperature in silicon oil bath by applying a DC electric field of 60 kV/cm for 30 min. The hysteresis (P-E) data were performed with TF-Analyzer 2000 on samples of 0.5mm thickness, using silver coated electrodes on both sides.

Dr. Sai Santosh Kumar Raavi
Department of Physics, Indian Institute of Technology Hyderabad, Kandi -502285, Telangana
E-mail: sskraavi@iith.ac.in

As an initial step, the RE substituent concentration is carried out by varying x in the $[Na_{0.5}Bi_{0.5-x}Re_x]TiO_3$ to obtain highest emission intensity. This is important that increasing RE concentration beyond the optimal x, the onset of PL occurs due to concentration quenching. The optimal composition for Nd-NBT, Eu-NBT, Pr-NBT and Ho-NBT are found to be $x = 0.01, 0.025, 0.005\ and\ 0.03$ respectively. As a representation illustration of the performed studies we present Fig -1 (a) that shows the PL spectra obtained for various Eu-NBT with increasing Eu^{3+} concentrations. The most intense spectra is obtained for $x_{Eu} = 0.025$. Figure 1(b) shows the PL quenching observed upon electrical poling. The choice of poling field is done upon performing the hysteresis (P-E) data. Evidently, one can observe changes in both spectral peak position as well as peak intensity upon poling. In case of Eu-NBT, we elucidated this to be as a result of electric-field induced structural ordering to higher symmetry. The structural studies from XRD data corroborated the hypothesis as the poling resulted in transformation of stabilized NBNT phase from monoclinic to orthorhombic structure which has higher symmetry. This explanation is in line with Judd-Oflet theory which is used to estimate the intensities of the transitions for the RE ions. Similar investigations and observations are obtained for Nd-, Pr- and Ho- NBT compounds and will be presented in detail.

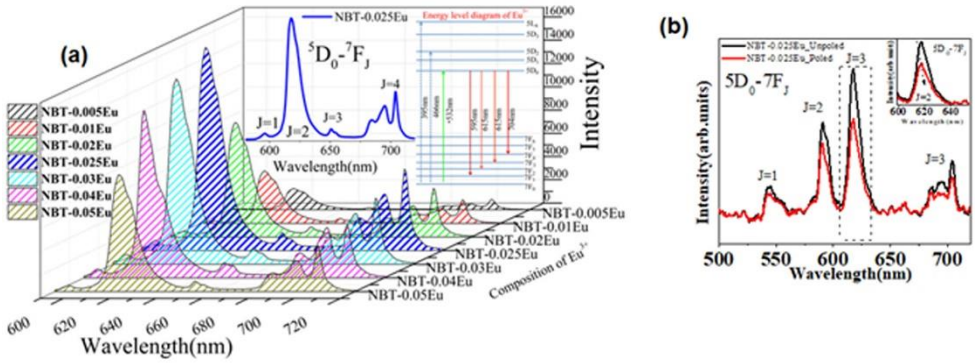

Fig. 1 (a) Photoluminescence spectra of NBET (0<x<0.5) and the inset of the figure represent the area under the curve Vs composition of Eu^{3+}; (b) The comparison of PL spectra of unpoled and poled for optimal concentration of NBET and the inset showed the closed view of $^5D_0$-> ^7F_J.

Further to highlight the application of this optimized RE-substituted NBT, we briefly explain here the results obtained for Nd-substitution [3]. It is found that for the optimized Nd-NBT the electrical characterization revealed a reduction in coercive electric field (E_c) by 12% compared to undoped NBT. The piezoelectricity characterization showed enhanced d_{33} coeffiecint for the optimized NBNT and off-resonance figure of merit (FOM_{off}) for energy harvesting revealed ≈ 30% enhancement. In case of optimized Eu-NBT, the dielectric studies confirm the coexistence of antiferroelectric and ferroelectric and ferroelectric to paraelectric transitions. Similarly, improved electrical properties were observed for the optimized Pr-and Ho-NBT ceramics. To conclude, our results demonstrate that obtaining the optimal RE substitution for highest emission intensity is sufficient to obtain best electrical properties. Therefore, we believe the direction of the work presented here offers a paradigm shift in the research of photonics with ceramics.

References

1. M.K.Niranjan, T.Karthik, S.Asthana,"Theoretical and experimental investigation of Raman modes, ferroelectric and dielectric properties of relaxor $Na_{0.5}Bi_{0.5}TiO_3$." *J Appl. Phys.* Vol. 113, p-194106 (2013).
2. K. Kandula, S. S. K. Raavi, S. Asthana, "Correlation between structural, ferroelectric and luminescence properties through compositional dependence of Nd3+ ion in lead free Na0.5Bi0.5TiO3," J. *Alloy. Comp*, vol. 732, p-233-239 (2018)
3. K. Kandula, S. Asthana, S. S. K. Raavi, "Multifunctional Nd^{3+} substituted $Na_{0.5}Bi_{0.5}TiO_3$ as lead-free ceramics with enhanced luminescence, ferroelectric and energy harvesting properties," RSC Advances, vol. 15282–15289 (2018).

OSI-ISO 2018 manuscript No.
(162)

Laser Induced Breakdown study of Polypropylene (PP) using second harmonic of Nd:YAG Pulsed Laser

Archana Kushwaha, Indrajeet Kumar and Alika Khare

Received: date / Accepted: date

Abstract: Laser induced breakdown study of the safest plastics for daily use, Polypropylene (PP) is carried out. The second harmonic of Nd:YAG Pulsed Laser (λ = 532nm) has been used to create the PP plasma. The PP plasma is analyzed with help of a monochromator and a photo multiplier tube (PMT). Fully resolved CN violet bands are observed with band heads at 388.4 nm, 387.1 nm, 386.0 nm, and 385.5 nm. The temporal evolution of CN band emission in PP plasma is recorded to get the decay time which is estimated by fitting the evolution profile with first order exponential decay function. The decay time of CN band emission is found ~121ns, which is relatively lower and this may be one significance fingerprint to stamp that PP is safe for human being.

Keywords: Laser induced breakdown spectroscopy, Polypropylene, Laser induced plasma, CN band emission.

1. Introduction

Plastics are being used almost in every step of modern life in various forms like water bottles, bags, containers, syringe, medicine containers, food grade plastics, etc[1]. The unprocessed disposal of plastics can pose an adverse effect on human health and will deteriorate our environment. By recycling of these plastic wastes, one can retrieve the useful material and the accumulation of plastics waste can be avoided. Among all the commonly used plastics, Polypropylene (PP) (Recycle code 5) is comparatively safer for human health, as plastic products made by PP, do not leach harmful chemicals into foods or liquids. Polypropylene (PP) is a flexible, hard and semi-transparent and has high resistance to solvents. In this work, spectral response of PP on focusing of a high power pulsed laser is analyzed using Laser Induced Breakdown Spectroscopy (LIBS) technique. LIBS is a very promising technique for in-situ identification of organic materials, as it allows quick and multi-elemental analysis, without contact and prior sample preparation. Many works have been conducted to identify and classify plastics and polymers using the atomic and molecular signal from LIBS[2-5].

2. Experimental Details

For recording the LIBS spectra of PP samples, the schematic of experimental set-up used is shown in Figure 1(a). For formation of laser induced plasma (LIP), the second harmonic of pulsed Nd:YAG laser (quanta system HYL-101, λ = 532nm, τ= 25 ns, f_{rep} =10 Hz) was focused onto the continuously translated sample, with the help of 5 cm focal length lens. The samples used in the experiment were taken from microwave container having recycle code 5. The LIP emission was imaged (1:1) onto the entrance slit of monochromator (SPEX 750M) using a lens of 10 cm focal length. A 532 nm notch filter was placed at the entrance slit in order to avoid the laser scattered light entering into the monochromator. A photo multiplier tube (PMT) attached to monochromator, interfaced with a computer was used to record the spectra. The entrance and exit slit widths of monochromator were kept at 50 μm. To record the CN emission at 388.4 nm, monochromator was scanned from 370 nm to 400 nm. The temporal evolution of the CN emission at 388.4 nm was recorded by displaying the PMT output on to the Digital Storage Oscilloscope (DSO) interfaced with the computer.

Archana Kushwaha
Guest Faculty, Department of Science and Mathematics, IIIT Guwahati, Assam, India
E-mail: archana.kushwaha@gmail.com

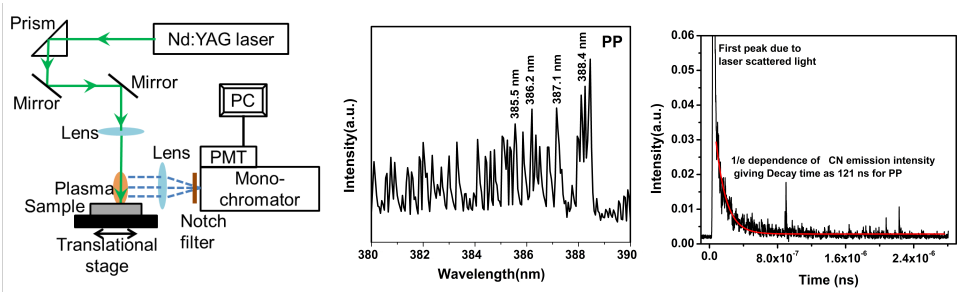

(a) (b) (c)

Fig. 1 (a) Schematic of experimental setup for recording LIBS spectra, (b) CN band emission spectra from LIP of PP, (c) Temporal Evolution of CN emission of PP

3. Result and Discussion

The LIP emission of the plastics is generally having strong ionic and atomic lines because of the relatively higher concentration of carbon in plastics. After termination of the laser pulse, LIP plume expands adiabatically in ambient air. The ambient air also breakdowns in the vicinity of focal volume. Carbon ions and atoms recombine with the ionized nitrogen gas to form CN molecules in the excited states[6]. The excited state relaxes to give CN band emission. In LIP of the taken PP sample, the well resolved CN violet bands ($B^2\Sigma^+ - X^2\Sigma^+$) were observed at 388.4 nm (0, 0), 387.1 nm (1, 1), 386.0 nm (2, 2), 385.5 nm (3, 3) respectively for $\Delta\nu = 0$, where $\Delta\nu = \nu' - \nu''$ is difference between the vibrational quantum numbers of the upper (ν') and lower (ν'') electronic states of corresponding transition. The observed spectrum of CN band emission for PP is shown in Figure 1(b).

Temporal response of the vibrational band of CN molecules is a key parameter for identification and classification of plastics. Therefore, this study was extended to investigate the temporal evolution of CN band emission in PP plasma. The temporal profile of CN emission for PP is shown in Figure 1(c). From temporal evolution, the decay time of CN band can be estimated by fitting temporal profile of the band spectrum to first order exponential decay function, $I(t) = I_0 \exp(-t/\tau)$ where I_0 is the initial intensity immediately after the laser pulse and τ is decay time of the CN emission band for the PP. Exponential fitting is done in Origin 7.0 and is shown in Figure 1(c). It is observed that decay time of CN band emission of PP is ~121 ns, which is relatively lower.

4. Conclusion

LIBS spectra for PP plasma are recorded and analyzed. The well resolved CN violet bands ($B^2\Sigma^+ - X^2\Sigma^+$) were observed at 388.4 nm (0, 0), 387.1 nm (1, 1), 386.0 nm (2, 2), and 385.5 nm (3, 3). The temporal evolution of CN band emission in PP plasma is also investigated. It is found that decay time of CN band emission is ~121ns, which is relatively lower and this may be one major parameter to stamp that PP is safe for human being.

References:

1. M. A. Gondal, M. N. Siddiqui, "Identification of different kinds of plastics using laser-induced breakdown spectroscopy for waste management". Journal of Environmental Science and Health part A, 42, 1989–1997 (2007).
2. J. Anzano, M. Casanova, M. Bermudez, R. Lasheras. "Rapid characterization of plastics using laser-induced plasma spectroscopy (LIPS)". Polymer Testing. 25,623-627 (2006)
3. R. Sattmann, I. Monch, H. Krause,; R. Noll, S. Couris, A. Hatziapostolou, A. Mavromanolakis, C. Fotakis, E. Larrauri, R. Miguel. "Laser-Induced Breakdown Spectroscopy for Polymer Identification". Appl. Spectrosc. 52, 456-461 (1998)
4. J. Anzano, R. Lasheras, J Bonilla, J. Casas, "Classification of polymers by determining of C_1:C_2:CN:H:N:O ratios by laser-induced plasma spectroscopy (LIPS)" Polymer Testing, 27, 705-710 (2008)
5. J. L. Gottfried, F. C. De Lucia, C. A. Munson, A. W. Miziolek. "Laser-induced breakdown spectroscopy for detection of explosives residues: a review of recent advances, challenges, and future prospects". Anal. Bioanal. Chem. 395, 283-300 (2009).
6. A. Kushwaha and R. K. Thareja, Dynamics of laser-ablated carbon plasma: formation of C_2 and CN, applied Optics, 47, G-65-G71 (2008).

OSI-ISO 2018 manuscript No.
(163)

A simple design of metamaterial absorber for large areas fabrication

Raghwendra Kumar[*1,2] **and S. Anantha Ramakrishna**[1]

Abstract We present a simple design of metamaterial absorber for large areas fabrication based on the cavity and guided-mode resonance. The metamaterial absorber consists of tri-layers (Au/ZnS/Au) on the photoresist microstructured. The photoresist micro-structured disk arrays were fabricated using laser interference lithography and followed by sequential deposition of tri-layers using physical vapour deposition technique. Due to the tri-layers deposition on the structured photoresist, there is a formation of cavity and waveguide which enable the absorption of electromagnetic radiation at some specific frequencies. Our proposed design provides polarization and wide-angle insensitive electromagnetic response.

1 Introduction

Electromagnetic metamaterials are artificial nano/micro-structured composites that exhibit unusual electromagnetic responses those are not available in natural materials [1]. These composites usually consist of identically structured unit cells with sub-wavelength sizes, arranged typically in a periodic fashion, and can be considered as bulk homogeneous media described as an effective medium through effective medium parameters. The structures are designed to be resonant at specific frequencies so that the violent dispersion of the material parameters in the neighbourhood of the resonances can be utilized to obtain various effects. Negative refraction, perfect lenses, invisibility cloaking devices and perfect absorbers [2,3] are among some of the applications that have captured the scientific communities' imagination. Spectrally selective perfect/highly intense absorbers have received considerable attention

[1] Department of Physics, Indian Institute of Technology Kanpur, Kanpur 208016, India
[2] Department of Physics, B. N. College, Patna University, 800004, India
E-mail: raghawk@iitk.ac.in

due to their importance for RADAR stealth at microwave and terahertz frequencies, development of sensitive infra-red detectors, micro-bolometer arrays etc.

Here we have used an inexpensive laser interference lithography and physical vapour deposition techniques to fabricate the metamateial absorber over the large area. The fabricated samples were structurally characterized using atomic force microscopy (AFM), and their infra-red properties were characterized using angle-resolved Fourier transformed infra-red spectrometer.

2 Results

Figs. 1(a) and (b) show the AFM topographical maps of the fabricated sample before and after tri-layers deposition with the inset as a 3D view of the corresponding images, respectively. Figs. 1(c) and (d) show normalized measured reflectance spectra of the sample for the TE and TM polarizations, respectively at different incident angles. Due to the single side polished silicon substrate, the transmitted light get diffracted by the roughness on the bottom side of the substrate and hence transmittance cannot be measured and in our case it is almost zero. Thus the absorbance can be calculated as $A(\omega) = 1 - R(\omega)$.

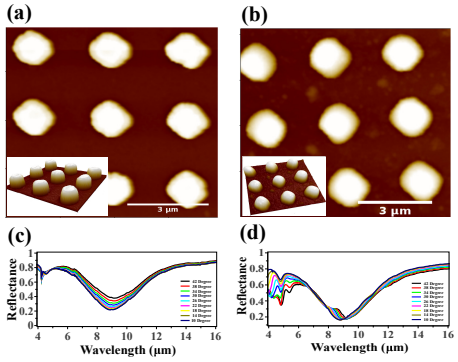

Fig. 1 AFM topographical maps of the fabricated sample (a) before tri-layers deposition, (b) after tri-layers deposition with inset as the 3D view of the corresponding image. The measured reflectance spectra (c) TE polarization, (b) TM polarization at different incident angles.

References

1. Veselago, Viktor G, The electrodynamics of substances with simultaneously negative values of ϵ and μ, Soviet physics uspekhi, **10**, 509 (1968).
2. Landy, N I and Sajuyigbe, S and Mock, JJ and Smith, DR and Padilla, WJ, Perfect metamaterial absorber, Physical Review Letters, **100**, 207402 (2008).
3. Watts, Claire M and Liu, Xianliang and Padilla, Willie J, Metamaterial electromagnetic wave absorbers, Advanced Materials, **24** (2012).

Study for rectification of lateral misalignment of axicon with Controlled Wavefront Distortion

Rajeev Dwivedi[1, 2*], Parag Sharma[1, 2], VK Jaiswal[1, 2] and Ranjana Mehrotra[2]
[1]*Academy of Scientific and Innovative Research (AcSIR), CSIR-NPL Campus, Dr K S Krishnan Marg, New Delhi 110012, India*
[2]*CSIR-National Physical Laboratory, Dr K S Krishnan Marg, New Delhi 110012*
E-mail: raj.dwivedi005@gmail.com
Phone: +91-1145609470

Abstract
Axicon has shown vast applications including laser scanning, laser machining, wavefront sensing, medical diagnostics and corneal eye surgery. The axicon generated hollow beams play a vital role in non-invasive applications, especially, non-contact cornea cutting. A small misalignment induced wavefront distortion in the intensity profile of such hollow beams could lead to catastrophe in such applications. Diagnosing misalignment of axicon in the experimental setup in itself is a tedious task having wide implications in the accuracy of results. We perform a detailed experimental study on these wavefront distortions, to identify the misalignment and its removal in the optical setups. Experiments are performed using both polychromatic and monochromatic partially coherent light sources. It is concluded that the generation of the wavefront distortion is well detectable in partially coherent beams and can be removed in controlled manner by precisely adjusting the lateral position of axicon.
Keyword: Diffractive Optics; Axicon; Dark Hollow Beam; Bessel Beam; Wavefront Distortion

1. Introduction

Axicon is a axially symmetric conical lens, commonly used for producing Bessel beam and hollow beams [1], which has shown significance in the areas including image scanning, wavefront sensing, laser cutting, wavefront sensing medical diagnostics and surgery [2,3]. In many applications namely, corneal eye surgery, axicon generated hollow beam is used for non-invasive cornea cutting, where a small distortion in the intensity profile could severely affect precision of the surgery. Also, in laser cutting and laser scanning wavefront distortion is a bottleneck. Recently, we have studied the appearance of wavefront distortion in the axicon generated beam profiles, arising due to lateral misalignment of axicon (*Dwivedi et al. 2017*), which is inherent in nature. However, recognizing the misalignment of an axicon in experimental setup is a daunting task and also drastically affects the results. We therefore, perform a detailed experimental investigation of these wavefront distortions induced due to the lateral shift of axicon. The experimental study is also carried out with partially coherent monochromatic and polychromatic dark hollow beams. These results are very significant to identify and quantify lateral misalignment of axicon deployed in optical setups which further allow rectification of the misalignment issues in non-invasive applications.

2. Experimental Setup

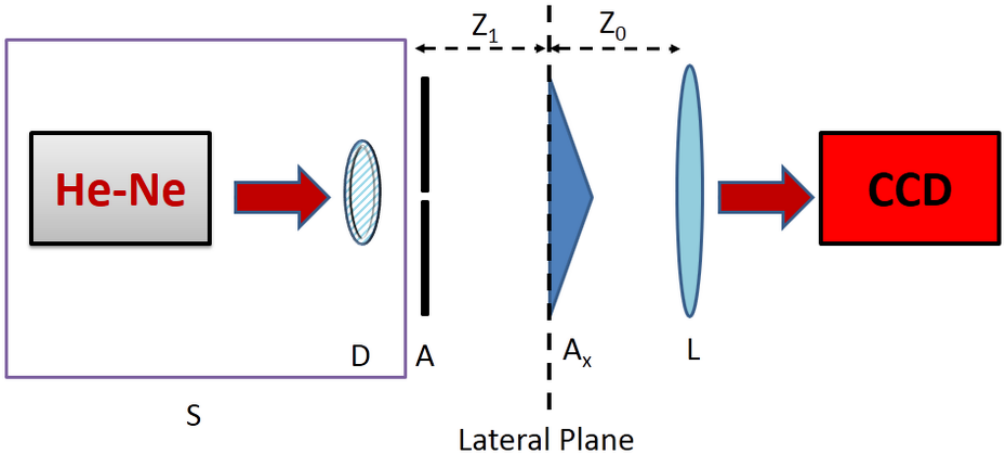

Fig. 1 Schematic diagram of the experimental setup, where light from He-Ne laser (633 nm,1 mw) falls on the rotating diffuser '*D*' followed by a variable pinhole '*d*' for attaining the desired coherence length at the incident plane of axicon. 'Z_1' propagation distance after pinhole. A converging lens '*L*' with focal length f = 120 mm is placed at a distance Z_0 after axicon A_x (having cone angle 'α' = 1° and refractive index 1.515) to generate partially coherent Bessel beam and Dark hollow beam in a controlled manner

3. Results and Discussion

In the case of laterally shifted axicon, appearance of a small wavefront distortion can easily be identified as a growing dark region in the intensity profile (referred by arrows in fig 2 (I) and fig 3 (I)) above the center of the beam for increasing upward lateral shift '*l*' of axicon.

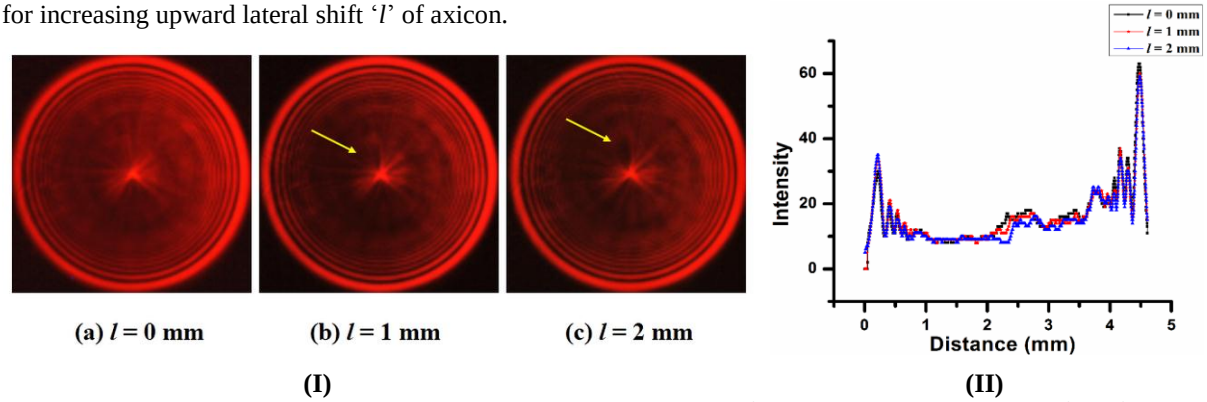

Fig. 2 (I) (a)-(c) CCD image showing variation in the distorted region near the center of the beam with increasing lateral shift '*l*' of axicon placed at *Z* = 140 mm and (II) Shows distortion region appeared in the intensity distribution along the line AB

It is also observed that the wavefront distortion region keeps growing up with *Z* as the hollow beam shapes up with asymmetric annular intensity distribution, evident in fig. 3 (I) and (II). This distortion can be inferred as an indicator and measure of lateral misalignment in the setup and can be removed in controlled manner.

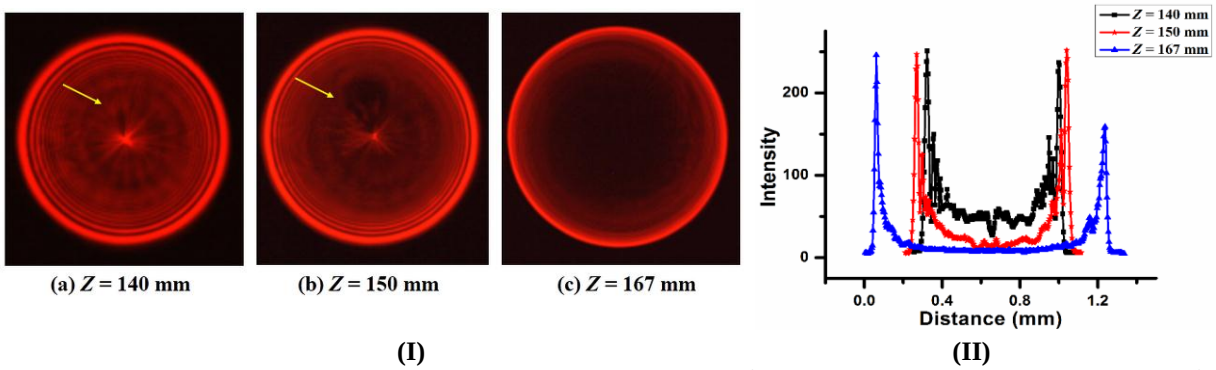

Fig. 3 (I)(a)-(c) CCD image showing variation in the distorted region near the center of the beam with increasing propagation distance 'Z' from axicon-lens assembly for the lateral shift of *l* = 1 mm and (II) Shows distortion region appeared in the intensity distribution along the line CD

The control removal of this type of distortion appearing in the intensity profile can be achieved by precise adjustments in the lateral position of axicon. To investigate effect of wavefront distortion in polychromatic dark hollow beam, we repeat same experiment with polychromatic partially coherent dark hollow beam by replacing '*S*' in fig 1 with a tungsten lamp and observed similar results with additional chromatic aberration effects.

4. Conclusion

In the present study, we performed an in-depth investigation of the generation of wavefront distortion in the beam profile owing to a laterally misaligned axicon setup. It is observed that the wavefront distortion region is easily observable just before the evolution of the dark hollow beam. This study also reveals that the wavefront distortion is easily detectable in the partially coherent beams. The results can be employed in proposing a simpler method to identify and quantify the lateral misalignment of axicon in optical setups.

Acknowledgement

The authors thank the Director, CSIR-National Physical Laboratory for granting the permission and support for this research work.

Reference

1. D. McGloin and K. Dholakia, "Bessel beams: diffraction in a new light," Contemporary Phys 46, 15-28 (2005).
2. O. Ren and R. Birngruber, "Axicon: a new laser beam delivery system for corneal surgery," IEEE J. Quant. Elec. 26, 2305-2308 (1990).
3. B. Vohnsen, S. Castillo, and D. Rativa, "Wavefront sensing with an axicon," Opt. Lett. 36, 846-848 (2011).

Increment of light absorption in periodic structures introducing metallic nano-layer for solar cell applications

Arnab Panda[1], Soumen Maity[2], Rajib Chakraborty[1], Kanik Palodhi[1]
[1] Dept. of Applied Optics and Photonics, University of Calcutta
[2] Dept. of Physics, St. Thomas College of Engineering and Technology
panda1arnab@gmail.com

Abstract: Solar cells are yet to overcome its practical lower efficiency compared to its theoretical potential. One of the most important aspects of enhancing solar efficiency is to increase light trapping within cells for generating more number of carriers. Light trapping within periodic structures can be one of the most promising cost-effective alternative solutions. To increase the optical path length, appropriate insertion of active layers will be critical. In particular, the shape and size of the metallic layers and proper arrangement of periodic structures are vital to increase the optical absorption of the solar cell. In this proceeding, we characterise different metallic layers such as gold, silver and aluminium. Evidently, gold will be a better choice for light trapping considering, its higher absorption and similar absorption property for the entire spectrum.

Keywords: solar cell; light trapping; metallic nano-layer

Solar cells are required for renewable energy applications, particularly, for clean and green energy. A serious challenge, however, is to overcome its practical lower efficiency compared to its theoretical potential. One of the most important aspects of enhancing solar efficiency is to increase light trapping inside the structure for generating more carriers. Light trapping within periodic structures can be the most promising alternative from the cost effectiveness and less material requirement point of view [1]. In this proceeding, our endeavour is describe the effects of change in absorption with change in thickness of layers with different metallic nano-particles introduced inside the periodic structure. This can be partially achieved by introducing metallic nano-layers of appropriate thickness inserted properly inside the structures [2]. Designing periodic structures, in this case, to increase the optical path length inside the active layers will be critical for this purpose. In particular, the shape and size of the metallic layers and proper arrangement of periodic structures, (in this case, bilayers) are vital to increase the optical absorption of the solar cell as well as to reduce the optical absorption by the nano-layers themselves [3, 4]. Here, we prescribe a periodic structure of Silicon (Si) and Titanium dioxide (TiO_2) having several metal nano-particles such as silver (Ag), gold (Au) and aluminium (Al) to enhance the solar light absorption in the visible region. For comparison, Al is also used here, since in room temperature Al behaves similar to noble metals. The schematic of the structure is shown in Fig. 1 for Au-layer, however, for Ag-layer and Al-layer also similar structures are conceived. The thicknesses considered here, as shown in the figure, are obtained from standard literatures [3]. The red dots in the figure simply represent the selection of the layer in FEM software used and does not carry any other physical meaning. In the present proceeding, our emphasis is on the choice of materials, therefore, only one periodic layer on each side of the layer (i.e. Si-TiO_2-metal-Si-TiO_2) is considered. Later, multiple periodic structures can also be explored.

The results arising out these structures are presented in Fig. 2. *Enhanced light trapping is, in effect, increase in absorption and our efforts are to increase absorption in the visible region*, as discussed before. Fig. 2 represents the graphs of absorption vs. wavelength for three metallic layers, Al, Au an Ag. In particular, Fig. 2(a) shows the graphs for nano-layers' thickness to be of 100 nm and Fig. 2(b) shows the same for 50 nm.

From these graphs two important aspects are discussed, here – a) absolute value of absorption and b) relative change in absorption due to different metals. Clearly, variation of thickness from 100 nm to 50 nm for different metallic nano-layers, absolute changes in the value of absorption are negligible. Change in absorption is of the order of 0.1 at 200 nm and this different remains almost same for other wavelengths. Therefore, change of layer thickness will not, significantly, affect light trapping. On the other hand, for three metals used here, clearly, absorption at wavelengths for Al remains low and nearly same. For Ag, though, there is gradual variation, but after 500 nm, it remains nearly saturated. The absorption due to Au, however, remains high and there is an exponential decrease with wavelength though within visible region it remains nearly same. Evidently, gold will be a better choice for light trapping considering, its higher absorption and similar absorption property for the entire spectrum. This high absorption could, possibly, be caused by high absorption resulting from increased electronegativity of gold than other metals considered, here. It also has high electron affinity

compared to other metals considered here for which electrons, and thereby, carriers need to absorb more energy. From a practical point of view also, gold, due to its low oxidation property will be better compared to other materials.

Few immediately possible researches, in this regard, are currently being carried out. First among them is simulation of usage of nano-particles for surface plasmon resonance and secondly, thickness variation for periodic structure will also be incorporated for better results.

References:

1. T. Markvart and L. Castañer, Practical Handbook of Photovoltaics: Fundamentals and Applications, Elsevier, Amsterdam (2003).
2. Nelson J (2003), The Physics of Solar Cells. Imperial College Press, London
3. T. Soga Ed. (2006), Nanostructured materials for solar energy conversion, Elsevier
4. H. A. Atwate and A. Polman, "Plasmonics for improved photovoltaic devices," Nat. Mater. 9(3), 205–213 (2010).

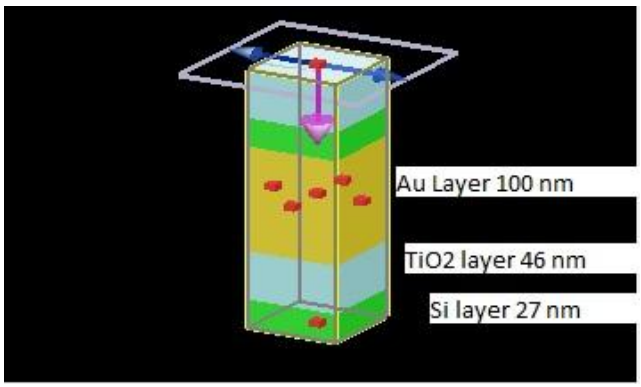

Fig 1 Structure of bilayer with Au metallic nano-layer

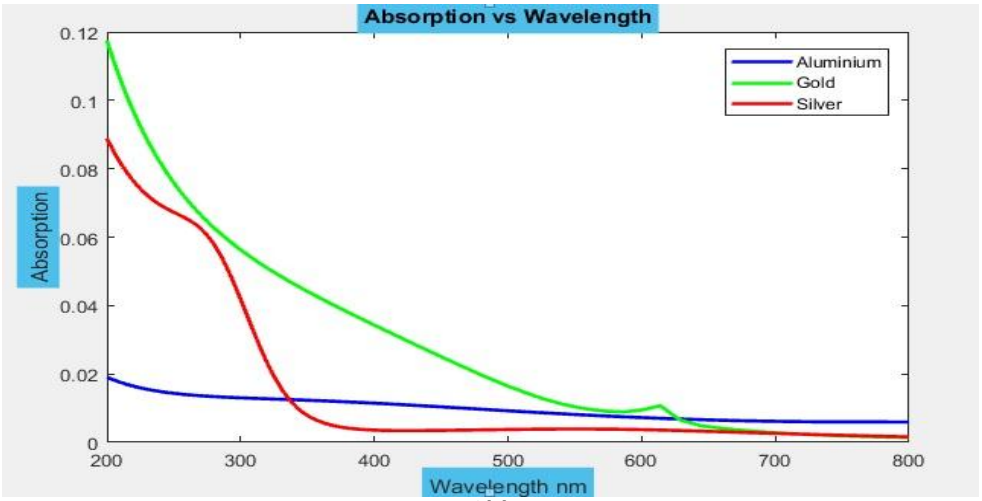

2(a)

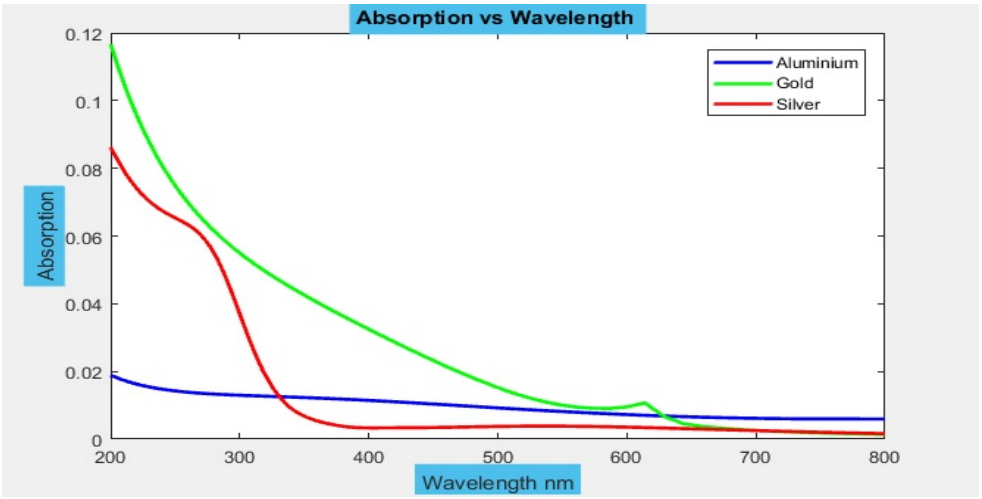

2(b)

Fig 2 Al, Au and Ag defect layers (a) For 100 nm; (b) 50 nm

OSI-ISO 2018 manuscript No.
(166)

Macrobending Loss based Edge Filter using Large Core Graded-index Fiber

Debparna Majumder · Nilotpal Choudhury · Nishant Kr. Shekhar · Ranjan Sen · Mrinmay Pal

Abstract An optimized bend loss based edge filter is presented using a large core graded index fiber with a single turn macrobending structure. A single peak in the Fourier transform of optical spectrum is obtained from the experimental setup on modal decomposition of the fiber and it shows single mode propagation in spite of having a V number greater than 2.405. The structure based on graded index fiber with absorbing coating layer is highly tolerant to whispering gallery modes and produces a bend loss characteristics similar to the fibers with theoretical infinite cladding layer. A linear monotonic change in intensity with discrimination range of 11 dB for a wavelength span 40nm is obtained based on single turn of fiber which can be employed as an edge filter. Novelty in this structure is that, inspite of having a high V number, there is only single mode propagation and transmission spectrum shows a linear monotonic change in intensity with wavelength.

Keywords Fiber edge filter · Graded-index fiber · macrobending loss · wavelength measurement

Introduction

The measurement of unknown wavelength is a common application in optical communication; examples include wavelength monitoring in dense wavelength division multiplexing, and optical sensing using fiber bragg grating and Fabry Perot filters. Bending of fiber causes a reshaping of the guided light which refract the field outwards and for that consequence calculation of bend loss became important since 1970. Marcuse explained that for an optical waveguide with an infinite cladding, bend loss increases as bend radius decrease[1]. The effect of whispering gallery modes in a practical fiber with coating was first explained by Harris and Castle[2]. In 2007, Wang explained an optimized design of macrobending based edge filter using two single mode bare fibers (SMF28, 1060 XP)[3]. Similarly, a different bend loss characteristic was observed in SMF28 with coating layer in wavelength measurement system due to the effect of whispering gallery modes[4]. In the previously published papers, to obtain a monotonic increase in transmission spectra within a wavelength range, fibers had a V number less than 2.405, but the fiber used in this work is having a higher V number. In this paper, a large core graded index fiber is used and its macrobending bend loss effect is utilized to design an edge filter.

Authors acknowledge financial support from CSIR Project MLP0101

Fiber Optics and Photonics Division
CSIR-Central Glass and Ceramic Research Institute, Kolkata
E-mail: dmdeb66@gmail.com

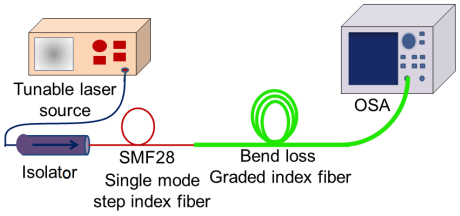

Fig. 1 Schematic of the experimental setup

Experimental Setup and Results

A schematic structure for wavelength measurement edge filter based on macrobending loss using a large core graded index fiber is shown in Fig. 1. Initially, transmission spectra of graded index fiber was measured, to

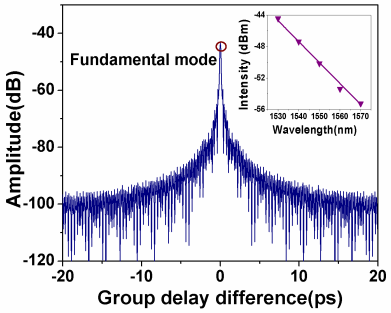

Fig. 2 FFT of the transmission spectra (Inset:Transmission spectrum obtained from OSA with bend radii 3.5cm)

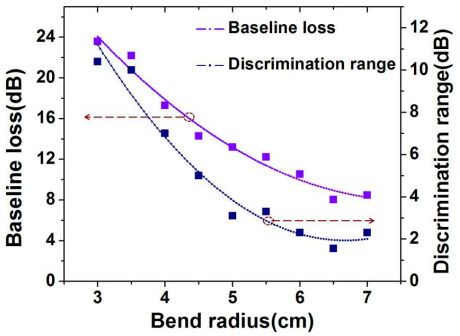

Fig. 3 Baseline loss and discrimination range(single-turn)

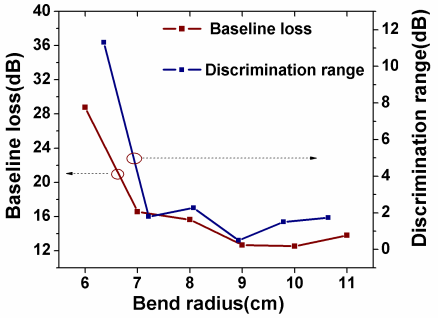

Fig. 4 Baseline loss and discrimination range(multi-turn)

identify the modal decomposition. A single mode step index fiber SMF28(Core diameter 8.2 um, NA:0.14) was spliced to a graded index fiber of core diameter 30um, cladding 125um, NA: 0.07,with parabolic refractive index profile. The transmission spectra of this fiber set-up is measured at the spectrum analyzer from wavelength 1530 to 1570nm at an input power of 6mW(shown in the inset of Fig. 2). Fourier transform of intensity spectrum plotted against group delay differences (shown in Fig.2) explains that maximum power is carried by the fundamental mode with zero group delay, power does not couple to other supported modes. Thus it can be considered that graded index fiber exhibit effective single mode operation inspite of a V value 4.25.

The bend sensitivity of the fiber is measured under different bend radii to obtain certain bend parameters. An edge filter should provide a linear monotonic change of transmission spectrum from a start wavelength to end wavelength, and this linearity is obtained using the graded index fiber for any bend radius. The difference in bend loss between start wavelength and the end wavelength (1530nm to 1570nm) is termed as discrimination range, is 10dB and 7dB for single turn under bend radius 3.5cm and 4cm respectively. The baseline loss(loss at the starting wavelength 1530nm) is nearly 20dB. The fiber with a single turn can give a maximum discrimination range upto 11dB under bend radii 3cm, and below this curvature, the light almost refract outward. The baseline loss and discrimination range follow an exponential trend with the increase of bend radius in a single turn fiber (shown in Fig. 3). At multiple turns, the discrimination range gave random variations inspite of following an exponential trend as shown for single turn of fiber(Fig. 4). This phenomenon can be explained in bending, when radiated field is reflected and forms the whispering gallery modes bend loss characteristics change in a stochastic way. In this case, at 6cm bend radii, discrimination range is 11dB, for multi turn which can be used as an edge filter, but for other radii discrimination range reduces to 2dB. When the fiber is bent in a single turn, whispering gallery modes has no such strong effect on its characteristics. Thus, with the use of graded index fiber using very few number of turns, a 11dB discrimination range can be obtained for a 40nm wavelength span which can be employed as an optimized edge filter.

Conclusion

A optimized fiber bend loss edge filter is developed using a large core graded index fiber based on a single turn macrobending structure.But, with multiple turns effect of whispering gallery modes gets stronger in the fiber. The discrimination range is 11dB for a single turn structure from wavelength 1530 to 1570nm which can be used in wavelength measurement system edge filters.

References

1. Dietrich Marcuse, Curvature loss formula for optical fibers, J. Opt. Soc. Am. 66, 216-220 (1976)
2. Alun J. Harris, Bend Loss Measurements on High Numerical Aperture Single-Mode Fibers as a Function of Wavelength and Bend Radius, J Lightwave Tech., 4 , 34-40 (1986)
3. Pengfei Wang and Gerald Farrell, An Optimized Macrobending-Fiber-Based Edge Filter, IEEE Photonics Technol. Letters 19, 1136-1138 (2007)
4. Qian Wang, Gerald Farrell, Thomas Freir, Ginu Rajan, and Pengfei Wang, Low-cost wavelength measurement based on a macrobending single-mode fiber, Opt. Lett. 31, 1785-1787 (2006)

OSI-ISO 2018 manuscript No.
(167)

Frequency dependent radiation properties of negative permittivity metamaterial reflector antenna

Jovia Jose, Sikha K. Simon, Joe Kizhakooden, Sreedevi P. Chakyar, Anju Sebastian, Nees Paul, Jolly Andrews and Joseph V. P.

Abstract This paper reports a novel type of microwave reflector antenna which uses the frequency dependent properties of epsilon negative (ENG) metamaterial medium. The frequency dependent characteristics of this artificial plasma medium is analyzed using dispersive Auxiliary Differential Equation Finite Difference Time Domain (ADE-FDTD) method by employing a Gaussian pulse and the results are verified experimentally using a plasma medium fabricated by an array of thin conducting wires. The radiation pattern of plain and corner reflector antennas modeled using Drude equations are obtained and are compared with conventional metallic reflector antennas. This new class of plasma antennas show marked variations in radiation pattern for frequencies above and below plasma frequency which may find potential use in various frequency selective applications.

Keywords Artificial Plasma Antenna · Metamaterial · FDTD

Epsilon negative (ENG) medium, a constituent part of metamatrials, has gained importance in microwave and terahertz research fields due to its frequency selective properties. In this paper, we have employed two dimensional ADE-FDTD method [1][2] for a dispersive medium to model frequency dependent reflector antennas using negative permittivity plasma slabs making use of the effective medium theory. Initially we have modeled an artificial plasma medium and its frequency depended behavior is analyzed using a Gaussian pulse[3]. The results are verified by fabricating an artificial ENG sheet using

Jovia Jose
Christ College (Autonomous), Irinjalakuda, University of Calicut, Kerala, India.
Vimala College (Autonomous), University of Calicut, Kerala, India.
Joe Kizhakooden and Nees Paul
Christ College (Autonomous), Irinjalakuda, University of Calicut, Kerala, India.
St. Thomas' College (Autonomous), University of Calicut, Kerala, India.
Sreedevi P Chakyar , Sikha K. Simon ,Jolly Andrews and V P Joseph
Christ College (Autonomous), Irinjalakuda,University of Calicut, Kerala, India.
E-mail: vpj@christcollegeijk.edu.in

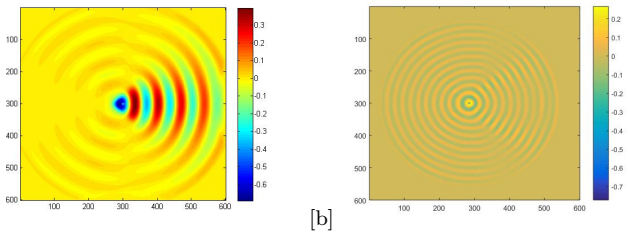

[a] [b]

Fig. 1 Propagation of 3 GHz and 9 GHz sine wave through the corner reflector antenna in the computational domain .

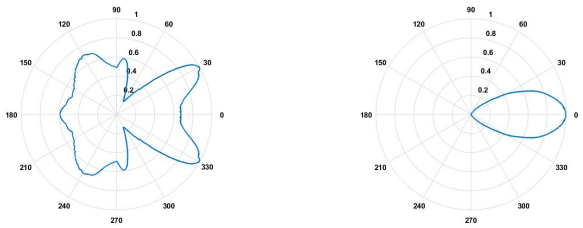

[a] [b]

Fig. 2 Radiation pattern of plasma and the metal corner antenna for 9 GHz

an array of thin copper wires[4]. Reflector antennas of different geometries are quite popular in various microwave applications and in our present work we are introducing a novel type of metamaterial inspired reflector antenna having the frequency selective properties of the plasma medium. The performance of this plasma reflector antenna is compared with the conventional metallic reflector antenna and the results are analyzed. Fig 1 (a) and (b) shows the field distribution for a 90^0 plasma reflector antenna for excitation frequencies below (3 GHz) and above (9 G Hz) the plasma frequency of 4.5 G Hz. The radiation pattern of metallic reflector antenna will be same irrespective of the frequency of operation whereas for our plasma reflector antenna, there is a clear distinction between the patterns obtained above and below the plasma frequency. The plasma frequency related selective properties are clearly observed in the radiation characteristics of this new reflector antenna.

References

1. A. Taflove, S.C. Hagness, M. Piket-May, in *The Electrical Engineering Handbook* (Elsevier Inc., 2005)
2. Y. Hao, R. Mittra, *FDTD modeling of metamaterials: Theory and applications* (Artech house, 2008)
3. J. Jose, S.P. Chakyar, J. Andrews, V. Joseph, in *Numerical Electromagnetic and Multiphysics Modeling and Optimization (NEMO), 2016 IEEE MTT-S International Conference on* (IEEE, 2016), pp. 1–3
4. J.B. Pendry, A. Holden, D. Robbins, W. Stewart, Journal of Physics: Condensed Matter **10**(22), 4785 (1998)

OSI-ISO 2018 manuscript No.
(168)

Refractive index sensing using gold nanohole arrays fabricated by colloidal lithography

Brindhu S Malani · **P. Viswanath**

Abstract We have investigated the optical properties of gold nanohole arrays on silicon substrate fabricated using colloidal lithography. Here, a preformed monolayer of polystyrene spheres is size reduced using reactive ion etching. This is followed by sputtering of gold and removal of polystyrene spheres. Field emission scanning electron microscope images show different degree of ordering and periodicity of gold nanoholes which is found to drastically affect the optical properties. Its application towards sensing is further discussed.

Keywords Colloidal lithography · Plasmonics · Sensing

1 Introduction

Colloidal or nanosphere lithography is a promising approach to pattern hexagonally shaped ordered arrays of spheres which is used as a mask to fabricate large area plasmonic film [1],[2]. Here the size, periodicity and thickness of the gold nanohole arrays is known to affect the optical response to a larger extent. The enhancement in electric field and the sensitivity of the localized surface plasmon resonance modes with refractive index enhances their scope in surface enhanced raman spectroscopy [3] and also in sensing applications [4].

Partial funding from Thematic Projects in frontiers of Nano S&T (TPF-Nano) grant no. SR/NM/TP-25/2016 is acknowledged.

Brindhu S Malani
Centre for Nano and Soft Matter Sciences, P. B. No. 1329, Jalahalli, Bengaluru - 560 013, India.
Department of Physics, Mangalore University, Mangalagangothri, Mangalore, India.

P. Viswanath
Centre for Nano and Soft Matter Sciences, P. B. No. 1329, Jalahalli, Bengaluru - 560 013, India.
E-mail: viswanath@cens.res.in

2 Experimental methods

Close packed polystyrene (PS) spheres (size 1 μm) were formed over silicon substrates using evaporative induced convective self-assembly. Non-close packed (NCP) assembly of PS spheres is obtained from the close packed state by fixing the reactive ion etching parameters (gas flow 6 SCCM, power 7W and pressure 6.3 torr). Gold film of thickness of about 85 nm is sputtered on to this assembly. Post sputtering, the PS spheres were removed from the silicon substrates. The gold nanohole arrays were further characterized using field emission scanning electron microscope (FESEM), optical microscope and uv-visible-near-ir spectroscopy techniques.

3 Results and Discussion

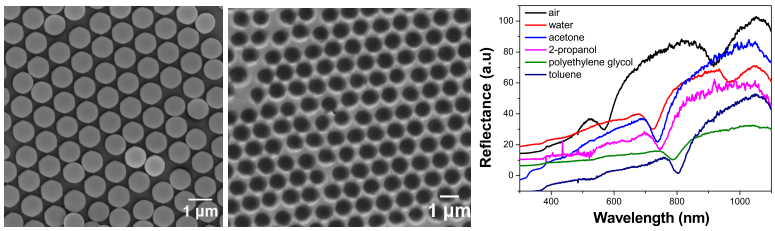

(a) (b) (c)

Fig. 1 FESEM images of a) PS spheres of reduced size in non-close packed state and b) gold nanohole arrays. c) Reflectance spectra of gold nano hole arrays in air and in solvents of different refractive index.

Figure 1(a) shows a representative image of size reduced PS sphere (RIE duration 10 min.) obtained using FESEM where the NCP state of assembly is clearly visible. Optical microscope image of the gold nanohole arrays shows the presence of defects and grain boundary which are intrinsic to the self-assembly process. Further, FESEM image at higher magnification shows hexagonal ordering of the gold nanoholes (Figure 1(b)). Reflectance spectra of the gold nanohole arrays in air and also in solvents of different refractive indices is shown in Figure 1(c). Signatures of coupling of localized surface plasmon resonance and surface plasmon polaritons were seen. We find the former resonance mode tends to red-shift with change in refractive index.

Acknowledgements The authors thank Mr. Arun D for FESEM measurements.

References

1. Deckman, H.W.; Dunsmuir, J.H. *Appl. Phys. Lett.* **41**, 377 (1982).
2. Hulteen, J.C.; Van Duyne, R.P. *J. Vac. Sci. Technol. A* **13**, 1553 (1995).
3. McFarland, A.D.; Young, M.A.; Dieringer, J.A.; Van Duyne, R.P. J. Phys. Chem. B, **109**, 11279 (2005).
4. Haes, A.J.; Van Duyne, R.P. *J. Am. Chem. Soc.*, **124**, 10596 (2002).

OSI-ISO 2018 manuscript No.
(169)

Design Strategy of a Silicon Nano-wire/Array-Waveguide Coupled Section for Spot Size Expansion

Shivani Sital, Niharika Kohli, Nikhil Dhingra and Enakshi Khular Sharma[1]
Department of Electronic Science, University of Delhi South Campus, New Delhi-110021, India
[1]enakshi54@yahoo.co.in

Abstract Due to the high index between Silicon ($n = 3.45$) and SiO_2 ($n = 1.45$), the typical single-moded Silicon waveguide has a dimension $\sim 220 \times 500$ nm^2 while optical waveguides in silica can have dimensions $\sim 2 \times 2$ μm^2. Due to a large mode-mismatch the direct butt coupling of the two leads to huge power loss of more than 90%. We here give a specific design strategy for design of a beam spot size expanding configuration based on complete resonant coupling of optical power from the silicon nano-wire mode to only the fundamental symmetric mode of an Si/SiO_2 array waveguide. The concept is illustrated by design of a nano-wire/5-waveguide array coupled section for coupling from a 220 nm nano-wire to a 2 μm silica waveguide.

Keywords Silicon Waveguides, Coupled Waveguides, SOI waveguides, array waveguides

Introduction

Over the last decade there has been extensive research on silicon based photonic integrated circuits. The optical waveguide used in these photonic circuits is a Silicon core waveguide on a Silicon dioxide (SiO_2) substrate with a cover of SiO_2 or air commonly referred to as a nanowire Due to the high index between Silicon ($n = 3.45$) and SiO_2 ($n = 1.45$), the typical single-moded Silicon waveguide has a dimension $\sim 220 \times 500$ nm^2 and the spot-size of the fundamental propagating mode is ~ 0.11 μm^2. Traditional optical waveguides in silica, including the optical fiber have dimensions $\sim 2 \times 2$ μm^2. Due to a large mode-mismatch the direct coupling of the two leads to huge power loss of more than 90%. Jiang et al [1] and Niharika et al [2] recently proposed a spot-size converter for coupling from a silicon nano-wire to an optical fibre by coupling between the silicon waveguide and fundamental mode of a large dimension waveguide formed by an array of Si/SiO_2 coupled waveguides. However, the two designs [1,2] showed conceptual differences in absence of a specific design strategy for such a spot size expanding configuration. In this paper we discuss the design strategy for such a beam expanding configuration for efficient coupling between a silicon nano-wire and a larger silica waveguide.

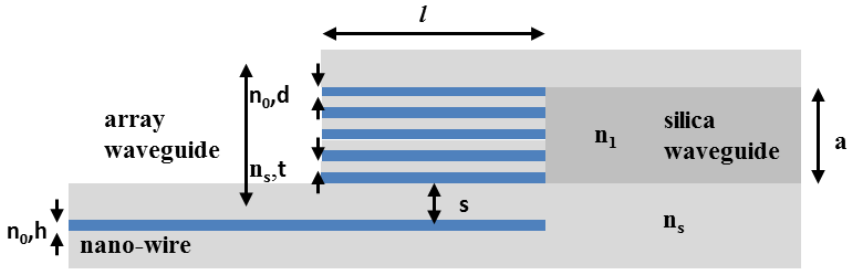

Fig.1 Evanescent coupling between Silicon nanowire and 5-waveguide Si/SiO_2 waveguide array beam expander for efficient coupling to a silica waveguide.

Design of the Coupled Waveguide Array and Optimal Coupling

The Si/SiO_2 waveguide array shown in Fig.(1) consisting of five single-mode waveguides is multi-moded and in general supports five modes. The spacing of the mode

effective indices depends on the thickness, d, of the silicon core and intra-waveguide spacing, t. The spot size expansion is based on complete resonant coupling of optical power from the nano-wire mode to only the fundamental symmetric mode of the array waveguide. In order to achieve this following design criteria need to be satisfied:

1. To ensure that coupling occurs to only one mode at phase matching, the effective indices of the five modes of the array waveguide should be well spaced. This is satisfied by appropriate choice of the intra-waveguide spacing, t. It may be mentioned that higher the spacing, t, higher is the spacing in the effective indices, but this also decreases the mode size expansion factor.
2. For resonant evanescent coupling to the fundamental mode from the nano-wire mode, the two modes have to be synchronous, i.e., have the same propagation constant or effective index. This can be satisfied by estimating the appropriate value of the thickness, d, of the silicon cores of the array waveguide.
3. Once resonant coupling to only one mode is achieved, the fraction of power coupled out of the nano-wire to the array waveguide mode depends on the spacing, s. To ensure complete power transfer this spacing should be large enough to ensure that equal power is coupled into only the first two modes.

Results and Discussion

We considered a typical nano-wire of dimension h = 220 nm, with silicon core index $n_0 = 3.45$ on a silica substrate of index $n_s = 1.45$ at $\lambda = 1550$ nm, which supports a single mode with effective index $n_e = 2.82269$. A study of the array waveguide shows that for t = 200 nm, the effective indices of the five modes are adequately spaced and for d = 189.7 nm, the fundamental mode of the array waveguide is phased matched, i.e., $n_{e1} = 2.82269$. Next, the coupling from the nano-wire mode to the six supermodes of the nano-wire/array-waveguide coupled section was studied. At a value of s = 400 nm, 98.96% power is coupled from the nano-wire into the first two modes of the coupled section and at a length $l = 171$ µm, 96.7% power is obtained in the fundamental mode of the array waveguide due to interference between these two modes as shown in Fig.(2).

Finally, the total power coupling efficiency from the nano-wire waveguide to a silica waveguide of dimension a = 1.75 µm and $n_1 = 1.5$ butt coupled to the array waveguide was obtained as 76.3%. It may be noted that for direct butt coupling of the nano-wire and silica waveguide the coupling is only 24%.

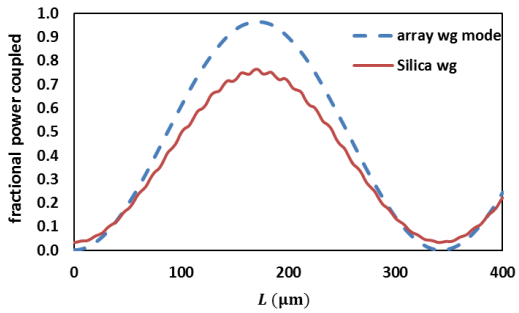

Fig.2 Power coupling between Silicon nanowire to fundamental mode of the 5-waveguide Si/SiO2 waveguide array and silica waveguide as a function of the length of the coupled section.

Acknowledgments

The authors acknowledge the financial support from University Grants Commission (UGC), India, and University of Delhi.

References

1. Weifeng Jiang, Niharika Kohli, Xiaohan Sun and B. M. Azizur Rahman, IEEE Photonics Journal, 8, 6600612, 2016.
2. Niharika Kohli**,** Enakshi K. Sharma and B. M. Azizur Rahman, Journal of Optical and Quantum Electronics 49: 229, 2017.

Study of Two Photon Absorption in Colloidal WS_2 Solution

Prince Sharma[1, 2], Ranjana Mehrotra[1,2] and Parag Sharma[1, 2]

[1]Academy of Scientific and Innovative Research (AcSIR), CSIR-NPL Campus, Dr K S Krishnan Marg, New Delhi 110012, India

[2]CSIR-National Physical Laboratory, Dr K S Krishnan Marg, New Delhi 110012

E-mail: sharmapvats8@gmail.com

Phone: +91-1145608228, Fax: +91-1145609310

Abstract: Two-photon absorption coefficients of a various concentration of colloidal Tungsten disulphide (WS_2) have been investigated and compared. The different concentrations of WS_2were prepared by changing the quantity of Tungsten disulphide in dimethyl sulphoxide. Afterwards, the various solutions of WS_2were examined for their concentration-dependent nonlinear absorption coefficients and refractive index. The nonlinear optical studies have been performed using Nd-YAG pulsed laser of 20ps laser pulses at 532nm as a probing beam in a standard *Z* scan setup. Uv-Visible spectroscopy is used for inferring the linear absorption coefficient of samples. The experimental outcomes revealed that there was a significant nonlinearity at a concentration of 7 mM solution of Tungsten disulphide. This study confirms reverse saturable absorption and two-photon absorption in tungsten disulphide which may find potential applications in optical limiters.

Keywords: *Z* Scan, WS_2, Nonlinear Optics, Colloids

1. Introduction

In last few decades, nonlinear optics has attained a lot of interest due to its numerous applications in diverse areas such as optical modulation, optical switching, optical data storage, frequency shifting, information processing and many more [1]. But the challenge is to find or develop materials which shows high nonlinearity at low power. Among large variety of nonlinear optical materials, 2-D materials such as graphene [2], boron nitride and a new class of materials as TMDs (transition metal dichalcogenides) grew rapidly due to its micro and nanostructures, which shows large nonlinearity at low intensity. They find large applications in electronics and optoelectronics like light emitters, detectors, photovoltaic devices and optical switches. Tungsten disulphide comes under TMDs whose indirect band gap changes to direct band gap on going from bulk to single layer. Due to its direct band gap in the visible region of EM spectra, it is improvised for optoelectronics applications. As its structure changes from bulk to a single layer, there is a change in the width of the band gap from 1.3 ev to 2.1 ev and its properties can be improved on changing its particle size [3]. Even when we work at atomic scale like in quantum dots, there is high tunability of its character due to quantum confinement and size effect [2]. Due to these reasons, WS_2 is an interesting material to work with. Various concentrations of WS_2 in colloidal form has been investigated and thereafter these different solution of WS_2 were compared to examine the concentrations effect on nonlinear absorption coefficients and refractive index. The nonlinear optical studies have been performed using a standard *Z* scan setup [1,4].

2. Experimental Setup

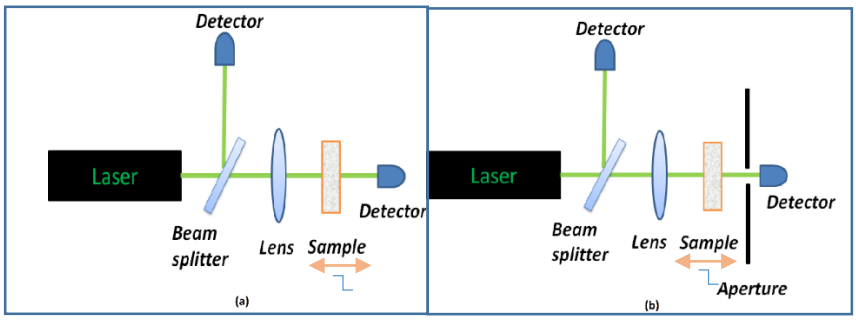

Figure 1. Experimental setup of *Z* scan for study of nonlinear optical properties of sample with Nd-YAG Laser pulsed laser of 20ps laser pulses at 532nm is used, (a) Open aperture for precise determination of nonlinear absorption coefficient and (b) Close aperture setup for precise measurement of nonlinear refractive index

3. Results and Discussions

Z scan technique was used for study of third order nonlinearity. In *Z* scan, experimental data points were fitted by using the equation described below [4]

$$\mathrm{T(z)} = 1 - \frac{-\beta * \mathrm{I0} * \mathrm{Leff}}{2^{3/2} * (1 + (z/\mathrm{z0})^2)} \qquad (1)$$

Where, '*T(z)*' represents the transmission of laser, 'β' is nonlinear absorption coefficient, 'I_0' is peak intensity at focus and $\mathrm{Leff} = \frac{1-\exp(-\mathrm{aL})}{\mathrm{a}}$ where '*a*' is the linear absorption coefficient calculated using UV-Visible spectroscopy, and '*Z*' is the -displacement axis of sample and L is the thickness of cuvette.

This fitted curves gave the two photon absorption coefficient. It was establish that on increasing the molar concentration of WS_2 in colloidal form, the two photon absorption coefficient increases up to a limit and then saturates. It follows the relation as given below

$$\mathrm{Y} = A1 * \exp\left(-\frac{X}{t1}\right) + yo \qquad (2)$$

Where, '*Y'* represents the two photon absorption coefficient, '*X'* represents the concentration and '*A1'*, '*t1'* and '*yo'* are the constants which were determined by fitting the experimental data points.

4. Conclusions

In the present work, we found that different concentration of WS_2 in colloidal form showed variable nonlinearity. It was determined that on increasing the concentration of WS_2, nonlinear absorption coefficient increases and then saturates. It was concluded that on increasing the concentration from 1 mM to 7 mM, there was a maximum enhancement in nonlinearity. The result established that for 7 mM of WS_2 showed the maximum nonlinearity comparative to other concentrations. Further in order to enhance the observed nonlinearity, this optimized concentration of WS_2 will be used for making WS_2 –CNT hybrids. The interaction within the hybrid system will be studied using linear as well as nonlinear characterization techniques. These experimental findings may find applications in various active photonic devices.

5. Acknowledgment

The authors thank Director CSIR-NPL for granting the permission and support for this research work

6. References

1. Strogatz, Steven H. Nonlinear dynamics and chaos: with applications to physics, biology, chemistry, and engineering. CRC Press, 2018.
2. Vermeulen, nathalie, et al. "graphene's nonlinear-optical physics revealed through exponentially growing self-phase modulation." nature communications 9.1 (2018): 2675.
3. Long, hui, et al. "the ws2 quantum dot: preparation, characterization and its optical limiting effect in polymethylmethacrylate." nanotechnology 27.41 (2016): 414005.
4. Sheik-bahae, mansoor, et al. "sensitive measurement of optical nonlinearities using a single beam." ieee journal of quantum electronics 26.4 (1990): 760-769.

Synthetic Aperture White Light Diffraction Phase Microscopy

Vaibhav Bansode, G Hanu Phani Ram, Renu John†

Department of Biomedical Engineering, Indian Institute of Technology Hyderabad

†Corresponding author: renujohn@iith.ac.in

Abstract: We present Synthetic aperture imaging technique based on white light diffraction phase microscopy which completely uses the frequency coverage to improve the field of view. A conventional microscope with a halogen lamp and a Mach-Zehnder interferometer combined to obtain images of the specimen. We have moved the CCD camera through four different positions using a precision translational stage to improve the field of view and Synthetic Aperture is formed. We imaged a microstructure to demonstrate an improved field of view.

Keywords: Microscopy, Quantitative Phase imaging, Synthetic Aperture, white Light Diffraction Phase Microscopy, 3-D imaging

Introduction:

Imaging of transparent specimens using a bright field microscope is challenging as they absorb or scatter light weakly. The phase shift of the transparent specimens can be converted into observable intensity information based on the phase contrast technique developed by Zernike. Quantitative phase imaging (QPI) techniques quantify the phase shift associated with a transparent specimen when light passes through it [1]. QPI can achieve three-dimensional information of the object as it is inherent to the phase information map. White light diffraction phase microscopy (wDPM) is a label-free interferometric QPI modality which produces three-dimensional information of the object non-invasively [2]. In this paper, we developed a Synthetic Aperture white light diffraction phase microscopy with an increased field of view.

Method:

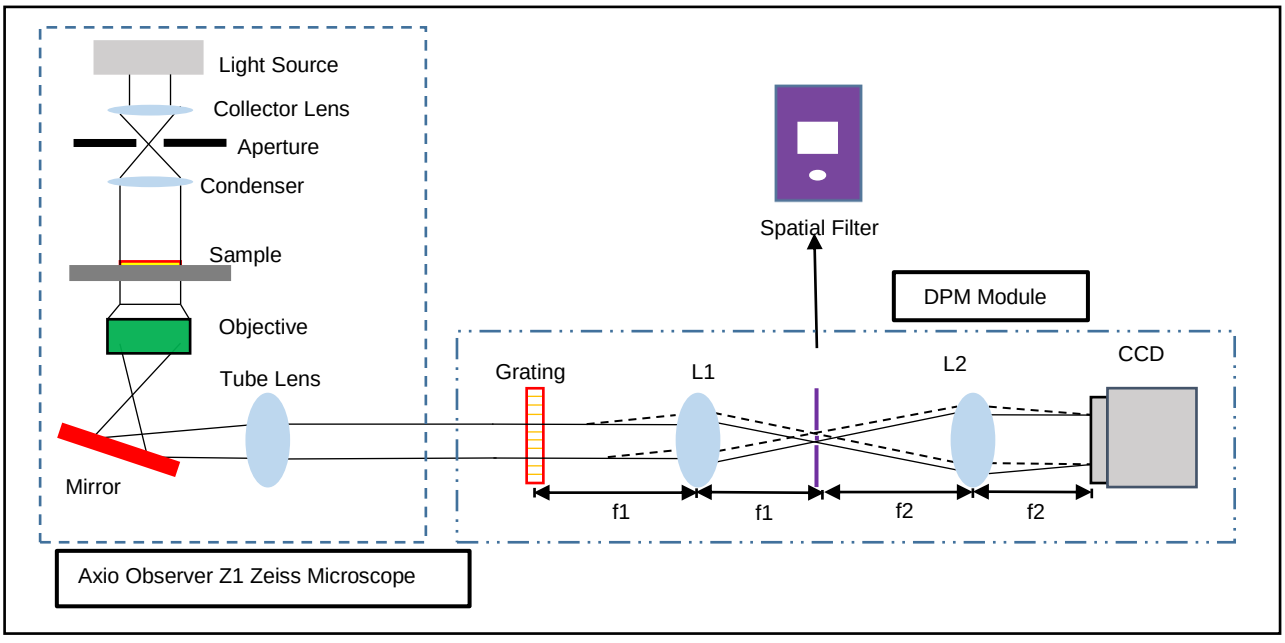

Fig 1. Experimental Set-up wDPM

wDPM systems use a low coherence halogen lamp as a source of illumination. DPM module is an add-on to the inverted microscope Axio Observer Z1, Zeiss. In the proposed work we have used concept of Synthetic aperture radar (SAR) with wDPM for object field of view enhancement. SAR technique combines several low-resolution information to form high-resolution information. The interferogram is recoded using a CCD camera having 1920x2560 pixels and each pixel size $\Delta x = \Delta y = 2.2$ µm. We have recorded four interferogram by using precision translation stage to completely use the frequency coverage. All interferograms are combined using 'efficient sub pixel algorithm' and a single interferogram is formed which enhances the object information and field of view [3]. The phase information of the object has been retrieved using the conventional phase reconstruction algorithms.

Results:

Multiple beam interference technique is used to create a microstructure of a positive photoresist (AZ1518) material having refractive index of 1.623. figure 2 (a, b, c, d) shows the three-dimensional unwrapped phase distribution of four different interferograms and figure 2 (e) shows the three-dimensional unwrapped phase distribution of mosaicked interferogram with *improved field of view* and resolution. Results quantifying the resolution improvement using the new technique will be presented in the full paper.

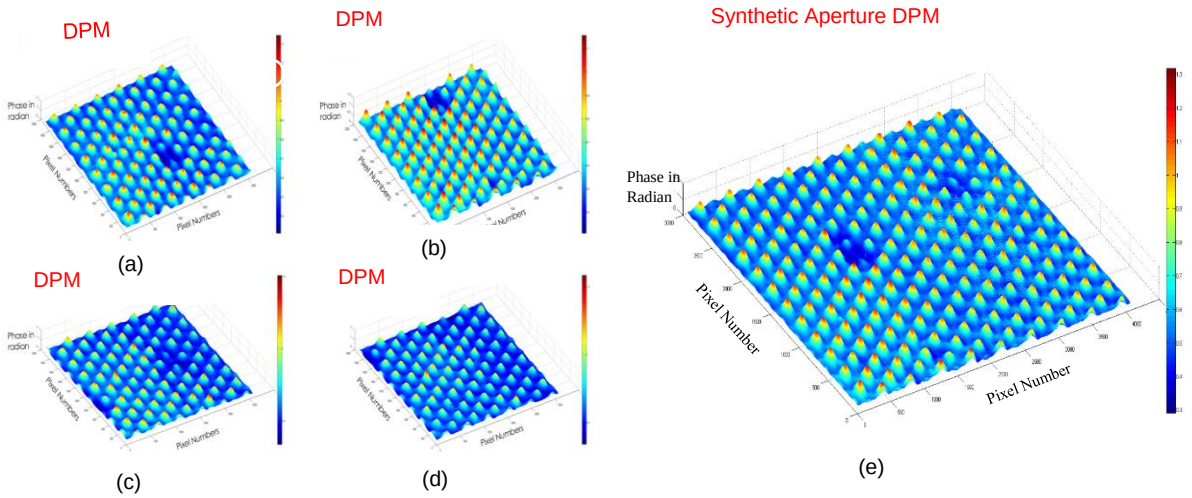

Fig 2. (a), (b), (c), (d) three-dimensional phase map of microstructure and Fig 2. (e) three-dimensional phase map of mosaicked interferogram.

Conclusion:

Synthetic Aperture wDPM enhances the *field of view* and resolution. The simplified interferometric setup has been achieved using small aperture which is needed for phase retrieval and synthetic aperture contributes to improved field of view and allows to achieve resolution therefore suitable for biological microscopic applications.

References:

[1] G.Popescu, Quantitative phase imaging of cells and tissues,(Mcgraw Hill Professional,2011).

[2] B.Bafhuri et al., Diffraction phase microscopy with white light, Optics Letters,vol.37, no.6,pp.1094-1096,(2012).

[3] Manuel Guizar-Sicairos, Samuel T. Thurman, and James R. Fienup, Efficient subpixel image registration algorithms, OPTICS LETTERS / Vol. 33, No. 2 / January 15, (2008)

OSI-ISO 2018 manuscript No.
(173)

Resonance properties of split ring resonators made of polyaniline based conducting polymer

Nees Paul · Sreedevi P Chakyar · Sikha Simon K · Anju Sebastian · Joe Kizhakooden · Umadevi K. S · Jolly Andrews · V P Joseph

Abstract We present the observance of magnetic resonance for the first time in split ring resonators (SRR's) made of polyaniline based conducting polymer and verify our experimental result through simulation. The magnetic resonance behaviour of closed ring resonator (CRR) and SRR of polyaniline - polytetrafluoroethylene (Pani - PTFE) are studied for square and circular shaped rings. This humidity sensitive conducting Pani - PTFE ring, the main characteristics of our novel resonance structure, behaves like lossy conducting ring with wide band resonance behavior whereas the CRR doesnot show any resonant response as is expected for a metallic ring. The results are compared using simulation studies of copper rings of similar dimensions. Resonance absorption of the Pani - PTFE ring resonators are analyzed using the transimission spectra (S_{21}) obtained by arranging the proposed resonator between monopole antennas connected to the transmitting and receiving probes of a Vector Network Analyzer (VNA). The humidity dependence and flexibility of this Pani - PTFE ring can be used for the designing of frequency tunable 3 dimensional resonator and sensors at microwave regime.

Keywords Polyaniline · conducting polymer · split ring resonator · magnetic resonance

Nees Paul · Joe Kizhakooden
Christ College (Autonomous), Irinjalakuda, University of Calicut, Kerala, India.
St. Thomas' College (Autonomous), University of Calicut, Kerala, India.

Sreedevi P Chakyar · Sikha Simon k · Anju Sebastian · Jolly Andrews · V P Joseph
Christ College (Autonomous), Irinjalakuda,University of Calicut, Kerala, India. E-mail: vpj@christcollegeijk.edu.in

Umadevi K. S
Department of Physics, Newmann College, Mahatma Gandhi University, Kerala, India.
Department of Electronics, Prajyothi Nikethan College, University of Calicut, Kerala, India.

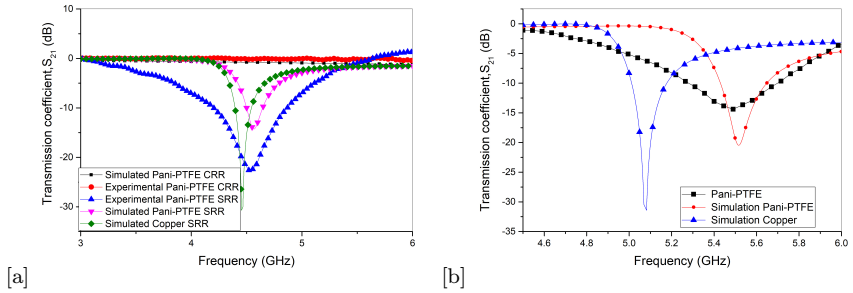

[a] [b]

Fig. 1 (a) Magnetic resonances present in a Copper and Pani-PTFE circular ring of outer diameter = 10 mm, inner diameter = 8 mm, slit = 1.057 mm and thickness t = 2 mm .(b) Magnetic resonances present in a Copper and Pani-PTFE square ring of outer length l_{outer} = 10 mm, inner length l_{inner} = 3.8 mm, split s = 3 mm and thickness t = 1.5 mm.

Protonated chlorine doped polyanilie (Pani) is formed from aniline and ammonium peroxysulphate (APS) using chemical oxidation method. The powdered polyaniline is then turned into sheet form using polytetrafluoroethylene (PTFE) so as to form polyaniline - polytetrafluoroethylene (Pani-PTFE) hybrid sheet.[1,2]The prepared sheets possessing greater conductivity in highly humid conditions are then cut into square and circular rings of specific dimensions.

Figure 1(a) shows the experimental magnetic resonance curves obtained for SRR and CRR of circular geometry made of Pani - PTFE along with the simulation results. Simulated result of circular copper ring with same dimension is also shown in the figure for comparison. The wide band resonance behavior of the Pani - PTFE ring in comparison with its metallic counter part is due to the lower conductivity of the material. The absence of magnetic resonance for CRR is also noticed.[3,4] Figure 1(b) shows the experimental magnetic resonance spectra of a square SRR along with the simulation results where the simulated curve of square metallic ring is also shown. The noticeable shift in the resonance frequency between Pani - PTFE and copper ring may be explained in terms of the higher contribution of displacement current due to the nonignorable dielectric behavior of Pani - PTFE material. The magnetic response of this polymer with tunable conductivity makes it a new candidate for the realisation of left handed materials with attractive features.

References

1. N. Paul, S.P. Chakyar, K. Umadevi, S.K. Sikha, J. Kizhakooden, J. Andrews, V. Joseph, Arabian Journal for Science and Engineering pp. 1–8 (2018)
2. T. Rinku Mariam, K. George, K. Mathew, S. Prathapan, Optimization of preparation techniques and dielectric study of polyanilines in the microwave & high frequency field. Ph.D. thesis, Cochin University of Science & Technology (2005)
3. H. Guo, N. Liu, L. Fu, T.P. Meyrath, T. Zentgraf, H. Schweizer, H. Giessen, Optics express **15**(19), 12095 (2007)
4. E. Ekmekci, G. Turhan-Sayan, Progress In Electromagnetics Research **12**, 35 (2009)

Hydroxyflavone Based Chemosensor for Dual Ion Recognition

Nisha Fatma*, Nupur Pandey, Sanjay Pant,

Photophysics Laboratory, Department of Physics, DSB Campus, Kumaun University, Nainital 263002, Uttarakhand, India

email: noornisha1287@gmail.com

Keywords: ESIPT, 3 Hydroxyflavone, colorimetric, chemosensor

Abstract: A simple ion sensor bearing flavone moiety and hydroxyl group, showed both colorimetric and fluorescence turn–off response towards Cu^{2+} and Fe^{2+} with high sensitivity and selectivity. Meanwhile the distinct color change and the rapid quenching of fluorescence emission provide naked eyes detections.3HF shows great affinity with a wide range of metal ions and the complexation usually occurs at the 3-hydroxy-4-keto binding site(Fig i). In present work 3 Hydroxyflavone was used for the detection of Cu^{2+} and Fe^{2+} ion in aqueous solution. The detection limit of the sensor towards Cu^{2+} and Fe^{2+} was 1.54 µM and 1.98 µM respectively. Moreover, sensor could be used as a quick, simple, visual test strip for Fe^{2+} and Cu^{2+} detection.
This sensor achieved the detection of two ions which does not need to rely on two different probes: utilization of the innate reactivity of only one probe could achieve a dual recognition purpose in a tandem fashion.

Acknowledgement: Authors are thankful to Dr. Mohan Singh Mehata, Laser and Spectroscopy Laboratory, Department of Applied Physics, Delhi Technological University (DTU) for providing steady state measurement facilities.

.

Introduction: Transition metal (TM) ions are caused for concern because of their applications in the field of medicine, catalysis, biology, and environment [1]. Copper is a vital trace element, the third most abundant in humans, and is present at low levels in a variety of cells and tissues with the highest concentrations in the liver. Fast detection of Cu^{2+} in water or physiological samples is of toxicological and environmental concern[3]. Fe^{2+} is one of the most essential metals in oxygen transport and electron transport. Fe^{2+}deficiency in our bodies will lead to low oxygen delivery, which could result in low blood pressure, anemia and decreased immunity. On the contrary, excess Fe^{2+} can result in the formation of reactive oxygen species (ROS), which have damaging effects on lipids, nucleic acids,and proteins [2,3].

Flavonoids are a class of polyphenolic compounds, containing a variety of functional groups including methyl, isopentenyl, and phenolic hydroxyl groups. Studies on the electronic excited—relaxation processes including excited-state proton transfer (ESPT) of flavones, especially for the development of fluorescent probes and sensors have been extensively undertaken [4]. Hydroxyflavones are characterized by low toxicity and extensive pharmacological activity and have become an area for intense study in the field of natural medicines. Here we would like to report on a 3-hydroxyflavone-based fluorescence chemosensor for copper and ferrous ions. [5,6,7]

Experimental: UV-Vis absorption spectra, at room temperature, were recorded by Perkin Elmer Lambda -750 spectrophotometer. Emission spectra were recorded by using Jobin Yvon FL3-22 fluorolog and data were analyzed by related software. 3-Hydroxyflavone of 98-99% purity was purchased from Sigma Aldrich and all the metal salts was purchased from LOBA Chemie and SRL Pvt. Ltd. and both were used without further purification. All the solvents used were of spectroscopic grades and were also checked for their fluorescence purity.

Result and Discussion: On adding the copper and ferrous ions, the probe 3HF showed noticeable naked eye detection of Cu^{2+} and Fe^{2+} ions accompanied by an obvious yellow and brown colour appearing, respectively(Fig ii). Further irradiating 3HF by 345 nm, in MeOH/H_2O, the green emission at 409 nm and a strong band at 510 nm of the long wavelength emission maximum is observed. The recognition ability of the sensor was obtained by mixing it with various metal ions including Ca^{2+}, Mg^{2+}, Al^{3+}, Zn^{2+}, Pb^{2+}, Hg^{2+}, Ag^{2+}, Cu^{2+}, Fe^{2+}, Na^{+}, K^{+} in aqueous solution using the fluorescence titration method (Fig iii). Further on successive addition of $Cu^{2+}$and Fe^{2+}, fluorescence of 3HF was "turned off", whereas no change in wavelength of fluorescence was detected in any of two emission bands. Quenching efficiencies for copper and ferrous ions are found to be 88.35% and 49.07%. Further, the test paper coated with probe 3HF was found to be excellent quick, convenient and visual to detect $Cu^{2+}$and Fe^{2+}ions (Fig iv). The probe is found to be more sensitive towards copper ions.

Conclusion: The sensor 3HF displayed good selectivity, high sensitivity, and low detection limits for the dual ions. The test strips was successfully applied to detect Fe^{2+} and Cu^{2+} ion by a simple test paper. The proposed sensing system can be successfully applicable for determination of Cu^{2+} and Fe^{2+} in waste water samples and onsite analysis showing turn off fluorescence response and for further monitoring of intracellular Cu^{2+} levels in living cells with high sensitivity and selectivity at micromolar level concentrations.

References:

1 L.Wan, D. Ye, W. Li, Y. Liu, L. Li, W. Zhang, L. Ni, Spectrochim. Acta A. 183, (2017), 291–297.
2 Y. Yang, K. Yu, L. Yang , J. Liu, K. Li, S. Luo, Sensors, 15,(2015), 49-58;
3. L. Huang, F. Hou, J. Cheng,; P. Xi, F. Chen, D. Bai, Z. Zeng, Org. Biomol. Chem.10 (2012), 9634–9638.
4. E. Ballesteros, D. Moreno, T. Gomez, T. Rodriguez, J. Rojo, M. Garcia-Valverde, and T. Torroba Org. Lett., 11, (2009).
5. P.K. Sengupta, M. Kasha, Chem. Phys. Lett. 68, (1979), 382–385.
6. M. Voicescu, S. Ionescu, J. Fluoresc, (2013), https://doi.org/ 10.1007/s10895-013-1346.
7.H. Gao, X. Wu , Chem. Heter. Comp. 54(2), 2018, 125–129.

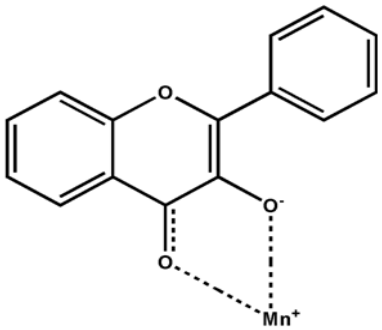

Fig i. Scheme for 3HF metal ion complex

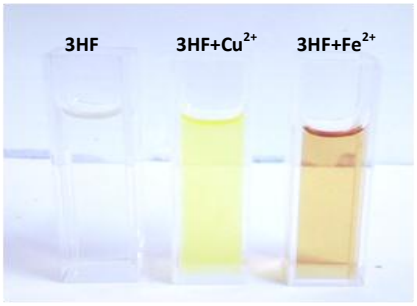

Fig ii. Colorimetric response of 3HF in presensce of Cu^{2+} and Fe^{2+} under visible light

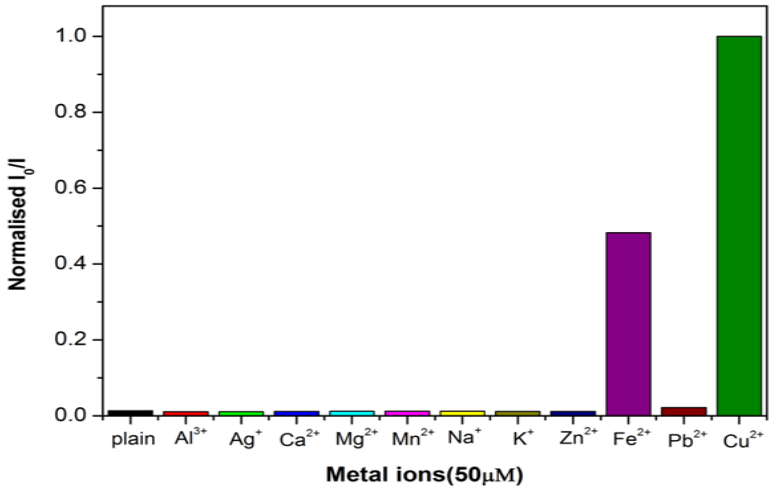

Fig iii. Relative fluorescence intensity of the 3HF(20 μM) in the presence of 50μM of various metal

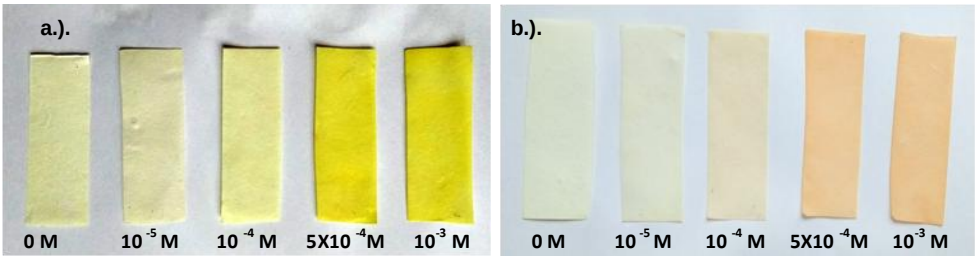

Fig iv. Photographs of 3HF and the response of a.) Cu^{2+} and b.) Fe^{2+} ions on test papers in visible light.

OSI-ISO 2018 manuscript No.
(175)

High Sensitive Mechanical Vibration Sensor using Triangular BCSRR

Sikha K. Simon · C. Bindu · Anju Sebastian · Sreedevi P. Chakyar · Jovia Jose · Nees Paul · Jolly Andrews · V. P. Joseph

Abstract This paper introduces a novel Triangular Broadside Coupled Split Ring Resonator (TBCSRR) metamaterial structure with high Quality factor for the sensitive detection of very weak mechanical vibrations. Instead of fabricating TBCSRR in a conventional manner, we have fixed metallic triangular strips of the resonator on two separate identical low loss thin sheets coaxially, which are capable of changing the spacing between them. Vibration sensor operates on the possible resonance frequency variations of the TBCSRR in relation to the changes in the spacing between rings caused due to amplitude of mechanical vibrations. If the operating frequency of the TBCSRR is selected on the rising or falling slope of the resonance curve, the output amplitude fluctuates in accordance with mechanical vibrations. The resonant absorption curve having very small bandwidth, not reported for earlier structures, makes the proposed TBCSRR a suitable choice for high sensitive vibration measurements. The high Q resonance curve of TBCSRR is experimentally obtained and the result is confirmed using simulation. Using TBCSRR as a sensor probe the amplitude variations caused due to some typical vibrations are presented. The proposed TBCSRR sensor probe may find applications in detecting even very weak vibrations caused due to various man-made and natural sources.

Keywords Metamaterials · Vibration Sensor · BCSRR

Metamaterial TBCSRR structure of different dimensions are fabricated and resonance properties are studied. Fig 1a shows the schematic representation of TBCSRR and Fig 1b shows the experimental and simulated resonance curves

Sikha K. Simon,C. Bindu, Anju Sebastian, Sreedevi P. Chakyar, Jovia Jose, Nees Paul,Jolly Andrews and V. P. Joseph
Department of Physics, Christ College (Autonomous) Irinjalakuda, University of Calicut, Kerala, India.
E-mail: vpj@christcollegeijk.edu.in

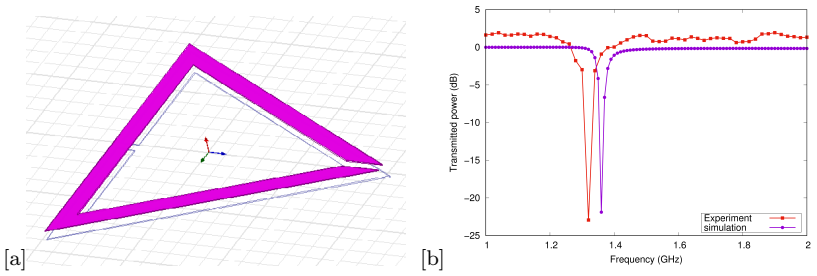

Fig. 1 a) Design of Triangular BCSRR b) Transmission spectra of Triangular BCSRR.

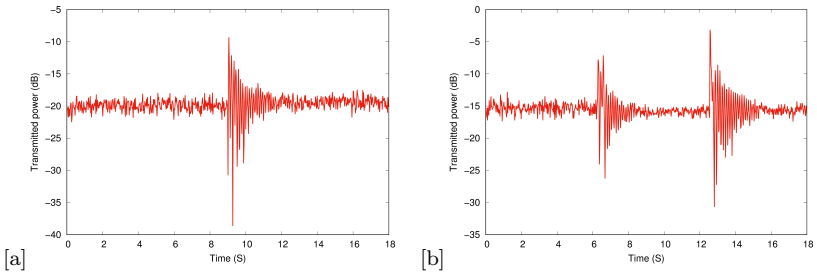

Fig. 2 a) Output vibration pattern due to freely falling standard weight of 2 gm from a height of 10 cm at a distance of 10 cm from the sensor probe. b) Output vibration pattern due to freely falling standard weight of 50 gm and 100 gm from a height of 25 cm at a distance of 2 m from the sensor probe.

of TBCRR having dimensions of length of one side 12 mm ,width 2 mm, silt width 0.5 mm, thickness 0.05 mm and spacing 0.5mm. The experimental set up consists of the newly designed TBCSRR unit with one of its triangular portion fixed on a rigid support whereas the other one is mounted coaxially on a cantilever capable of sensing mechanical vibrations, placed between transmitting and receiving probes of Vector Network Analyser[1,2].

Operating point for the vibration sensor is chosen on the falling edge of the absorption curve at a frequency of 1.31 GHz . In order to verify the sensitivity of the proposed vibration sensor, we have measured vibrations caused due to freely falling standard weights. Typical vibration patterns are shown in Fig 2a and 2b. This proposed high sensitive TBCSRR based vibration sensor can be a suitable choice for the precise detection of very weak vibrations like seismic tremors, vibrations due to hectic transportations, quarrying, pilling etc.

References

1. K. Sikha Simon, S.P. Chakyar, J. Andrews, P. Joseph V, in *American Institute of Physics Conference Series*, vol. 1849 (2017), vol. 1849
2. E. Ekmekci, G. Turhan-Sayan, Applied Physics A **110**(1), 189 (2013)

Focusing Properties Of Azimuthally Polarized Axisymmetric Bessel-Modulated Vortex Gaussian Beam Through A Dielectric Interface

M.Lavanya[1], M. Udhayakumar[2], K.Prabakaran[3], K.B.Rajesh[2*]
[1]*Department of Physics, PSGR Krishnammal College for Women, Coimbatore, Tamilnadu, India.*
[2*]*Department of Physics, Chikkanna Government Arts College, Tiruppur, Tamilnadu, India*
[3]*Department of Physics, Mahendra Arts and Science College (Autonomous), Namakkal, Tamilnadu, India*
Corresponding author Email:rajeskb@gmail.com

Abstract: The tight focusing properties of azimuthally polarized axisymmetric Bessel-modulated Gaussian beam with quadratic radial dependence (QBG beam) in high numerical aperture system through dielectric interface is investigated theoretically by vector diffraction theory. We observed that the generated focal structure is completely transversely polarized and the spot size and focal depth are calculated for different values of μ (beam parameter). It is observed that for complex values of μ, the spot size reduced and the focal depth improved very much. We also observed that presence of annular obstruction further confined the spot size (0.378 λ) and drastically improved the focal depth (31.42λ).

Keywords: Focusing properties, Axisymmetric Bessel-modulated Gaussian, Vector diffraction theory, Dielectric Interface.

1. Introduction

The tight focusing effect of light is an important research due to variety of application such as microscopy [1-3], optical tweezing [4], Raman spectroscopy [5] and fluorescent imaging [6] .These applications demands sub wavelength scale focal spot with ultra long focal depth normally generated using radially polarized beam. However the strong longitudinal component of radially polarized beam suffers discontinuous at the interface of two neighboring media and enlarges the focusing spot in the high-NA medium. This implies that the sub wavelength focused spot with longitudinal polarization is limited in applications such as imaging of silicon integrated circuits[7,8].Hence many methods to generate transversely polarized focal patterns under tight focusing conditions are suggested[9-12].Recently, Caron and Potvliege et.al. Introduced a novel class of beam expressed in cylindrical coordinate system namely, the Bessel-modulated Gaussian beams with quadratic radial dependence (QBG beam) [13]. Belafhal and Dalil-Essakali et. al. studied the propagation properties of QBG beams through an unapertured optical paraxial ABCD system [14]. The tight focusing properties of such a beam are investigated for possible applications in optical trapping and manipulation of particles .In this paper we numerically investigated the tight focusing properties of azimuthally polarized Quadratic Bessel-modulated Gaussian beams through a dielectric interface.

2. Theory

Scheme of the optical system of the proposed system is shown in Fig 1. In the focusing system we investigated, focusing beam is azimuthally polarized axisymmetric QBG beam whose value of transverse optical field is same as that of the scalar axisymmetric QBG beam and is given by [15].

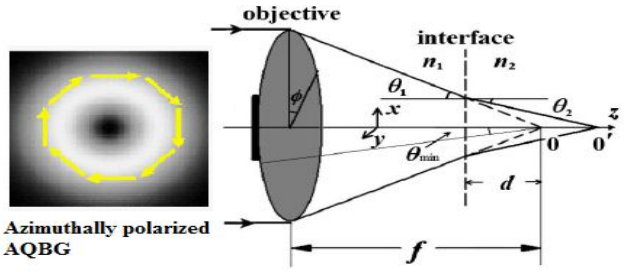

Fig. 1. Scheme of focusing optical system.

$$E_0(r,\varphi,z=0) = J_0\left[\frac{\mu \sin^2(\theta)}{\omega^2 \cdot NA^2}\right] \cdot \exp\left[\frac{\sin^2(\theta)}{\omega^2 \cdot NA^2}\right] \tag{1}$$

For azimuthally polarized beams, the Cartesian components of the electric field vector in the focal region then could be written as [9]

$$E(r,\psi,z) = \begin{bmatrix} E_x(r,\psi,z) \\ E_y(r,\psi,z) \\ E_z(r,\psi,z) \end{bmatrix} = \frac{-iE_0}{\pi} \int_{\delta\cdot\alpha}^{\alpha} \int_0^{2\pi} \exp[-ik_0\Phi(\theta_1,\theta_2)] \times \sin\theta_1 \sqrt{\cos\theta_1} E_0(\theta) \times \tag{2}$$

$$t_p \exp[ik_2 z\cos\theta_2 + ik_1 r\sin\theta_1\cos(\psi-\phi)] \times \begin{bmatrix} -\sin\phi \\ \cos\phi \\ 0 \end{bmatrix} d\phi\, d\theta_1$$

Where $k_i = n_i k_0$ is the wave number, $J_n(x)$ is the Bessel function of the first kind of order n, α = arcsin(NA) is the maximal angle determined by the NA of the objective.

3. Results and Discussion

In the investigation of azimuthally polarized axisymmetric QBG beam, without loss of validity and generality, it is proposed that the numerical aperture of the focusing optical system NA = 0.95 and relative waist width ω=1. We assume here the other parameters are chosen as $\lambda = 632.8\ nm$,$n_1 = 1$, $n_2 = 3.55$, $f = 2\ mm$, $d = 1\lambda$ and $m = 1$.

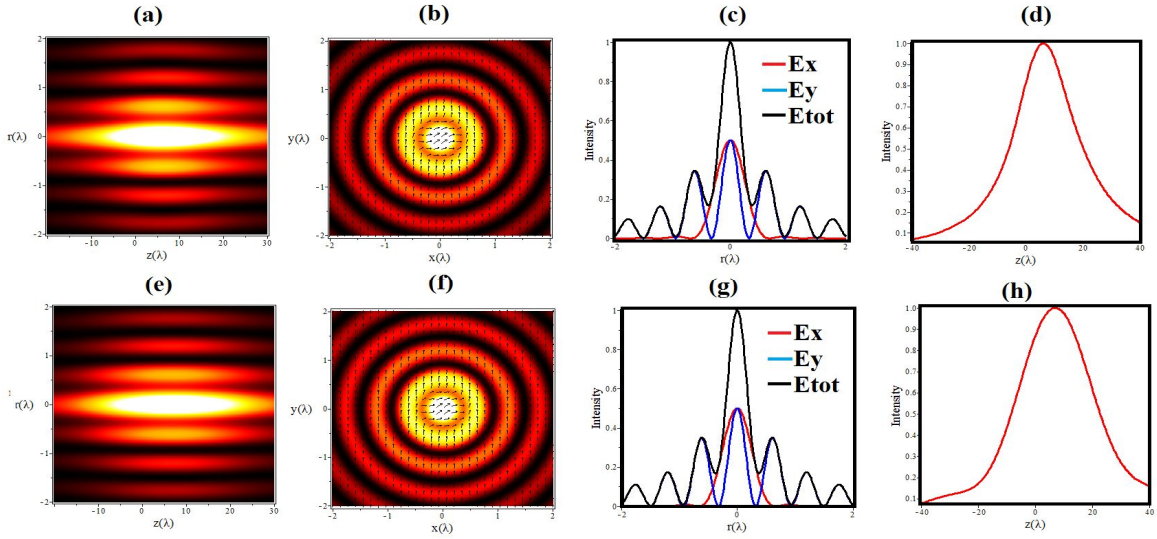

Fig.2. μ=10i using the annular obstruction for δ=0.5 and δ=0.75

In order to improve the focal depth, we tried annular obstruction to the complex value beam parameter μ=10i with δ=0.5 and δ=0.75. It is observed from the Fig.2(a and e) the focal depth of the generated focal structure is improved when using annular obstruction. The DOF achieved for δ=0.5 is 26.1 λ with spot size of 0.426 λ. However for annular obstruction with δ=0.75 the DOF drastically increased to 31.428 λ and spot size decreased to 0.378 λ. The position of maximum intensity corresponding to δ=0.5 is measured as 6.2 λ and for δ=0.75 it is 6.9 λ. We also noted from fig.2(c & g), that the generated focal structure is completely transversely polarized with no longitudinal component. Such a needle of transversely polarized beam is useful in application such as optical recording, optical trapping and semiconductor inspection.

4. Conclusion

The tight focusing properties of azimuthally polarized axisymmetric Bessel-modulated Gaussian beam with quadratic radial dependence (QBG beam) in high numerical aperture system through dielectric interface is analyzed numerically by vector diffraction theory. It is observed that by using annular obstruction with δ=0.5 and δ=0.75 a highly confined transversely polarized focal spot with FWHM around 0.378 λ with large focal depth 31.42λ is obtained for complex valued μ.

Reference

[1] J.W.M. Chon, X. Gan, M. Gu, Appl. Phys. Lett. 81,1576 (2002)
[2] D. Ganic, J.W.M. Chon, M. Gu Appl. Phys. Lett.82,1527 (2003)
[3] P. Munro, P. Török, Opt. Express 13 (18), 6833 (2005)
[4] D. Ganic, X.S. Gan, M. Gu, Opt. Express 13,1260 (2005)
[5] N. Hayazawa, Y. Saito, S. Kawata, Appl. Phys. Lett. 85 (25), 6239 (2004).
[6] L. Novotny, M.R. Beversluis, K.S. Youngworth, T.G. Brown, Phys. Rev. B 68, 115433 (2003)
[7] K. Huang , H.Ye , H. Liu , J.Teng , S P Yeo, C W Qiu arXiv:1406.3823 (2014)
[8] F.Qin , K. Huang, J.Wu , J.Jiao ,X. Luo , C. Qiu , M.Hong Sci. Rep. 5, 1 (2015)
[9] X. Hao, C. F Kuang, T.T Wang, X Liu , Opt. Lett. 35, 3928 (2010)
[10] K. Lalithambigai, P.M. Anbarasan, K.B. Rajesh, Opt. Quantum Electron. 47, 1027 (2015)
[11] P.Suresh , C. Mariyal, K.B.Rajesh, T.V.S Pillai , Z. Jaroszewicz , Appl. Opt. 52, 849 (2013)
[12] C. M. Sundaram, K. Prabakaran, P. M. Anbarasan, K B. Rajesh and A. M. Musthafa, Chin. Phys. Lett.33,064203 (2016).
[13] C. F. R. Caron and R. M. Potvliege, Opt. Commun, 164, 83 (1999)
[14] A. Belafhal, L. Dalil-Essakali, Opt. Commun. 177,181 (2000)
[15] X.Gao ,Q.Zhan, J.Li ,S.Hu, J.Wang, S.Zhuang, Opt Quant Electron. 41,385(2009)

OSI-ISO 2018 manuscript No.
(177)

Temperature Dependence of Complex Permittivity of Flame Retardant Circuit Boards

Sreedevi P. Chakyar · Sherin Thomas · Sikha K. Simon · Nees Paul · Joe Kizhakooden · Anju Sebastian · Jolly Andrews · Joseph V. P.

Abstract The temperature dependence of complex permittivity of flame retardant (FR) printed circuit board (PCB) samples is carried out using a resonance property of metamaterial split ring resonator structure. Different PCB laminates used for the study are placed in close contact with (SRR) test probe and is arranged inside a temperature controllable wooden chamber. The variation in the resonant frequency of the SRR with temperature in presence of the sample is measured by arranging it in between the transmitting and receiving probes of a vector network analyzer (VNA). Using theoretically developed equations the real and imaginary parts of permittivity at different temperature is calculated from the shift in resonance frequency and Q-factor. Results are verified by simulating the resonant frequencies from the calculated values of temperature dependent permittivity.

Keywords Metamaterial · Split Ring Resonator · Flame Retardent boards · Temperature dependent permittivity

Flame retardent (FR) Printed circuit boards (PCBs) are dielectric materials whose electrical properties strongly depend on their composites and fabrication procedure. One desirable condition for the faithful functioning of electromagnetic gadgets is to have thermal stability of the dielectric constant and loss tangent of the PCB laminates. In different electronic circuits the heat produced during operation can affect the performance of the FR board sub-

Sreedevi P. Chakyar, Sherin Thomas, Sikha K. Simon, Jolly Andrews & Joseph V. P.
Department of physics, Christ College (Autonomous), Irinjalakuda, University of calicut, Kerala, India
Nees Paul & Joe Kizhakooden
Department of physics, Christ College (Autonomous), Irinjalakuda, University of calicut, Kerala, India
Department of physics, St. Thomas College (Autonomous),University of Calicut, Kerala, India E-mail: vpjo@christcollegeijk.edu.in

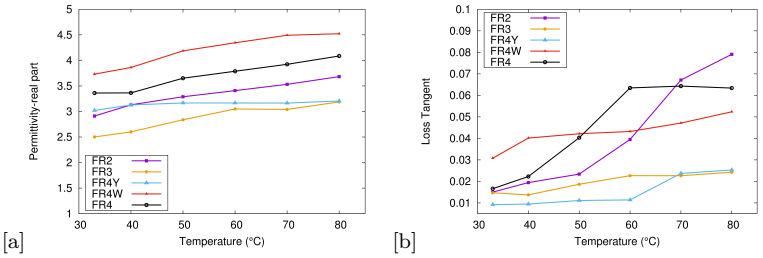

Fig. 1 Variation of (a) real part of permittivity and (b) loss tangent with temperature for five different FR board samples

strate which in turn adversely affect the operation of the circuit as a whole. Hence, the study of dependence of temperature on the electrical properties of the laminates is an important area in designing electronic circuits and antennas. Only a few attempts are found in literature in this regard [1],[2]. But, extensive sample preparation, bulky experimental setup and rigorous calculation methods make them less desirable. In this work we use the dependence of complex permittivity on resonant frequency and Q factor of metamaterial resonating structure SRR to measure the temperature dependent complex permittivity of FR board samples using the equations given in [3].

Five different types of FR boards samples are used for the study. SRR of resonant frequency 3.6 GHz is used as the test probe and is placed between two monopole antennas connected to transmitting and receiving probes of a vector network analyzer (VNA). For uniform heating of the sample, SRR test setup is placed inside a thermally insulated box, which is having an arrangement to increase the temperature using an infrared lamp and having provisions for accurate measurement of temperature.

Figures 1(a) and 1(b) show the variation of the real part of permittivity and loss tangent calculated using equations from the resonant frequencies and Q-factors obtained from the experiments for different temperature. Significant changes in real and imaginary parts are observed even for an experimental band of temperature difference 50 ℃. From the experimentally obtained values of permittivity, the resonant frequencies for different temperatures are simulated and are found to be in agreement with experiment. In various fields employing circuit boards especially in microwave systems, this study may help in the detection and removal of undesirable noise effects which may be more prominent during sudden temperature changes in the environment due to various reasons.

References

1. Y. Kobayashi, J. Yu, in *Microwave Conference, 1992. APMC 92. 1992 Asia-Pacific*, vol. 2 (IEEE, 1992), vol. 2, pp. 859–862
2. H. Li, C. Ra, G. Zhang, W.J. Yoo, J. Korean Phys. Soc **54**, 1096 (2009)
3. S.P. Chakyar, S. K. Simon, C. Bindu, J. Andrews, V. Joseph, Journal of Applied Physics **121**(5), 054101 (2017)

OSI-ISO 2018 manuscript No.
(179)

Analysis of V-slot Bow-tie Optical Antenna

Shubhanshi Sharma · Saawan Kumar Bag · Rajat Kumar Sinha · Shailendra Kumar Varshney

Abstract In this paper, V-slot has been made at the tip of the bow-tie optical antenna. Near field analysis of the antenna has been done for the mid-IR region. It is observed that because of the slot, higher-order resonances occur at the optimized length of 4.5 μm and thickness 375 nm. The maximum electric field intensity of 61.35 $V/\mu m$ and transmittance of -12.98 dB is obtained at the wavelength of 12.8 μm. The designed optical antenna can be used for near-field optical microscopy, IR detection and solar energy harvesting.

Keywords Optical Antenna · Plasmonics · Mid-IR · Localised Surface Plasmons

1 Introduction

In recent times, optical antenna has found many applications in the area of optical microscopy, optical tweezers, thermal imaging and solar energy harvesting. An optical antenna is a device which converts the energy of free propagating electromagnetic waves into localised energy[1]. The optical antennas are generally made of rare metals, such as gold or silver, rested over the Silica glass. When the light of certain frequency is incident on it, localised plasmons are formed at the metal-dielectric interface[2]. As a result, the charge accumulating at the edges generates high electric field at the feed point of the antenna. This paper focuses on the near field analysis of optical antenna where the characteristics of V- slot antenna is studied.

Shubhanshi Sharma · Rajat Kumar Sinha · Shailendra Kumar Varshney
Department of E&ECE, IIT Kharagpur, India
E-mail: shubhanshi0107@gmail.com

Saawan Kumar Bag
Department of Physics, IIT Kharagpur, India

2 Design and Analysis

The optical antenna here is of sectoral bow-tie type which has a slot on its tip which is rested on a silica glass substrate (permittivity of $\varepsilon_r = 2.09$). The design of the device is shown in Fig.1. The antenna arms are made of Gold. The dielectric constant of gold is obtained from the Drude model. The 3D numerical simulation of the proposed design has been done using commercial COMSOL Multiphysics, which works on finite element method. The antenna structure is illuminated from normal direction to the antenna plane with a unity (1 V/m) electric field magnitude and a linear polarisation along the antenna axis. The structure is optimized in terms of antenna length, the thickness of antenna, width and length of the slot to monitor the performance of the antenna in the mid-IR wavelength region. Through simulation, it is found that antenna resonates at multiple wavelengths between 8 μm to 15 μm. The first resonant wavelength is at $\sim$9 μm whereas the second and third resonant wavelengths are 10.6 μm and 12.8 μm, respectively, as shown in Fig.2. The transmission characteristic of the designed antenna is also calculated, which shows a maximum transmission depth of 12.98 dB at 12.8 μm wavelength and greater than 10 dB at $\sim$9 μm.

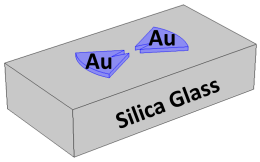

Fig. 1 V-slot gold bow-tie optical antenna placed over Silica Glass

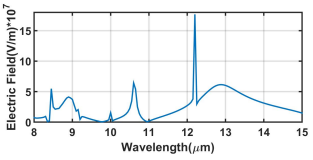

Fig. 2 Electric field for optimised antenna

3 Conclusion

The designed optical antenna works in the mid-IR range of 8 μm to 15 μm. It is observed that because of the slot, higher-order resonances occur at the optimized length of 4.5 μm and thickness 375 nm. The slot is also further optimized for length and width. The maximum electric field intensity of 61.35 $V/\mu m$ and transmittance of -12.98 dB is obtained at the wavelength of 12.8 μm.

References

1. Lukas Novotny and Niek Van Hulst. Antennas for light. *Nature photonics*, 5(2):83, 2011.
2. Vincenzo Giannini, Antonio I Fernández-Domínguez, Susannah C Heck, and Stefan A Maier. Plasmonic nanoantennas: fundamentals and their use in controlling the radiative properties of nanoemitters. *Chemical reviews*, 111(6):3888–3912, 2011.

OSI-ISO 2018 manuscript No.
(180)

Full field birefringence microscopy using a rotating polarizer

Kallol Bhattacharya

Abstract This work aims to provide a novel method to characterize and analyze microscopic birefringent samples in terms of its magnitude of retardance and its fast axis orientation with the help of a rotating analyzer. Moreover, it is possible to estimate the Stokes parameters using a simple algorithm thus developed. The simulated and experimental results thus presented are in good agreement with the proposed theory.

Keywords birefringence measurement, birefringence microscopy, birefringence phase

Theory

If a birefringent material is illuminated by a circularly polarized beam of light, and a polarizer is rotated in the path of the exit beam, the phase difference between the orthogonally polarized components depends on the orientation angle of the polarizer θ, the retardation of the sample and its direction of birefringence ϕ according to the equation

$$I_C(\theta) = 1 + sin\delta\ sin(2\theta - 2\phi) \quad (1)$$

The optimal value of $I_c(\theta)$ can be found by taking the derivative of eqn (1) with respect to θ and equating it to zero. In this way we get the point of inflexion for the function.

$I_C'(\theta) = 0$, which gives $\cos(2\theta_m - 2\phi) = \cos\frac{\pi}{2}$,

i.e., $\phi = \theta_m - \frac{\pi}{4}$ (2)

Also, $I(\phi+45^o)=1+\sin\delta$ (3)

and $I(\phi-45^o)=1-\sin\delta$ (4)

Hence, $\delta = \sin^{-1}\left[\frac{I(\phi+45°)-I(\phi-45°)}{I(\phi+45°)+I(\phi-45°)}\right]$ (5)

Then equations (4) and (5) are used to compute the retardance and the fast axis orientation at each pixel to derive the spatial distribution of retardance of the sample. In case of quantitative evaluation of birefringence in microscopic bio-specimens, the retardance is restricted to well within π radians and as such Eq.5 is sufficient for this purpose. Fig.1 shows plot of Eq.5 for fixed magnitudes of φ and δ as specified in the figures. It is worthwhile to observe that the retardation of the sample controls the amplitude of the periodic oscillations of phase as shown in Fig.1(a) and direction of birefringence controls the position of the inflexion points as evident from Fig.1(b). This provides a clue for complete evaluation of birefringence.

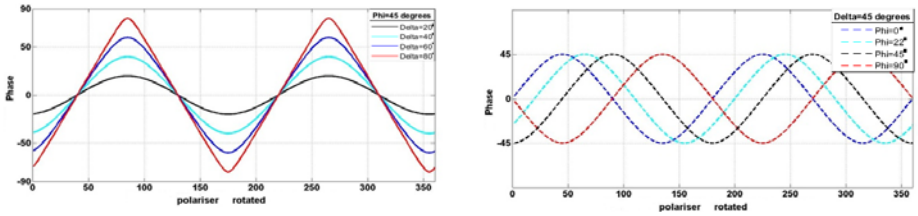

Fig 1. The phase difference between two orthogonal components oriented at θ-45° and θ +45° of the exit beam as obtained when the output polarizer is rotated from 0° to 360° for (a) φ=45° and fixed magnitudes of retardance and (b) and the corresponding changes when the fast axis orientation of the sample is changed in steps of 22.5 degrees, for a sample of retardance π/4.

Kallol Bhattacharya
Department of Applied Optics and Photonics, University of Calcutta, Kolkata 700106
E-mail: kbaop@caluniv.ac.in

EXPERIMENTAL ARRANGEMENT

The experimental set-up is simple as shown as shown in Fig 4. Light from LED is first expanded and collimated and then passed through a circular polarizer (CP) oriented such that circularly polarized light is incident on the birefringent sample, followed by a linear polarizer P_2. Lenses L_1 and L_2 represents the infinity corrected 20X microscope objective and 200 mm focal length tube lens in an afocal arrangement so as to create a sharp image of the sample on the CCD. The second polarizer P_2 is rotated in steps and the resultant intensity variation is recorded on the CCD. Thus in this way a series of frames are generated for full rotation of the polarizerP_2 . These frames were combined give the values of the φ and δ for each and every pixel of the image.

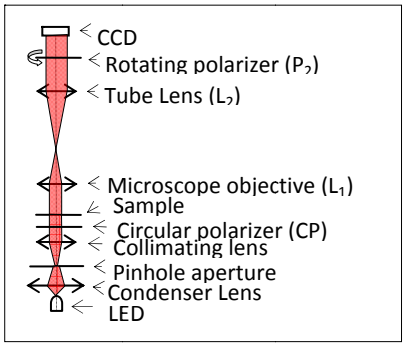

Fig.2. Schematic of the proposed setup

EXPERIMENTAL RESULTS

The results for a nerve from the human brain shown below in Fig.3 (a) to (i). The image of the sample, its retardation map and the map of its fast axis orientation are shown in Figs (a), (b) and (c) respectively. Stokes parameter s_0, and normalized parameters s_1, s_2 and s_3 are depicted in Figs. (d), (e), (f) and (g) respectively and the degrees of linear and circular polarization as shown in Figs. (h) and (i) respectively.

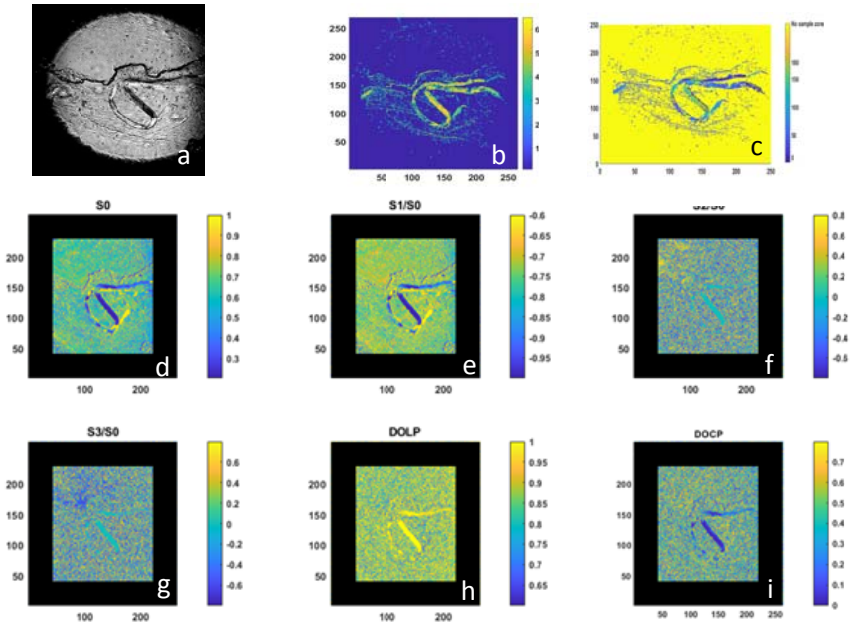

Fig 3(a): Sample consists of a bunch of nervous tissues. (b) Distribution of retardance δ and (c) direction of birefringence φ over the sample zone. (d) Stokes parameter S_o. Normalized Stokes parameters S_1/S_o, S_2/S_o and S_3/S_o shown in Figs (e) to (g) respectively. (h) Degree of linear polarization and (i) Degree of circular polarization.

Conclusion

The technique of birefringence metrology as proposed may be further simplified by generating the plots as shown in Fig.1 from a minimum of five data points and using interpolation techniques. This is presently being investigated.

Hybrid (diffractive/refractive) optics based compact and lightweight optical imaging system for space based remote sensing applications

Shruti Sharma[1,], Amitvikram Kurulkar[1] and M. Senthil Kumar[1]*
[1] Optical System Group, Space Applications Center (ISRO), Ahmedabad 380015, India
[*] Corresponding author: shrutisharma@sac.isro.gov.in

Abstract: Optical and infrared remote sensing using satellite based Earth observation cameras has proved to be an indispensable tool for providing valuable information on natural resources and environment on various spatial and temporal scales. Higher resolution demands larger mirrors/focusing optics and to achieve best image quality, optical aberrations are minimized by using multiple elements in the optical imaging system. This results into increase in weight, size and cost of space based cameras. In this paper, hybrid (diffractive/refractive) optics is proposed as one of the solutions to this problem. Commercially available optical design software ZEMAX, is used to design an eight element refractive optical imaging system (F/5, EFL (effective focal length): 120mm, 500-700nm, $\pm 10^0$ FOV (Field of view)) to achieve diffraction limited performance at 70lp/mm. Two designs have been proposed to reduce weight, size and cost using hybrid optics to meet the same specifications and performance. First design consists of six elements (four refractive lens and two hybrid lens with flat diffractive surface) and second design consists of four elements (two refractive lens and two hybrid lens with curved diffractive surface). Also, in-house fabrication of amplitude and phase binary diffractive lens using Direct Write Laser (DWL) lithography have also been reported in this paper.
Keywords: Diffractive lens, optical design, ZEMAX, remote sensing, hybrid optics, direct write laser lithography

Extended Abstract: Optical and infrared remote sensing using satellite based Earth observation cameras has proved to be an indispensable tool for providing valuable information on natural resources and environment on various spatial and temporal scales. Such observations are crucial and of primary importance in the assessment and monitoring of natural resources, weather and climate system and mitigation of its implications [1].The quality of the imagery reaching the end user from an Earth observation camera depends primarily on the imaging optics, the focal plane detector array and associated electronics and the processing of the raw data. The function of imaging optics is to transfer the radiance from the object space to image plane. The imaging optics for any optical imaging system is chosen from one of three basic configurations – 1. All refractive 2. All reflective 3. A combination of reflective and refractive, called catadioptric. Optical design software is used to optimize the configuration of imaging optics to get the best image quality (measured in terms of MTF and distortion value). Desired performance is achieved by reducing monochromatic and chromatic aberrations which requires optimization of curvatures of optical components and usage of multiple elements [2]. This leads to increase in size and mass of the space based camera. Also, higher and higher resolution is needed to examine distant astronomical objects and also for other applications like earth observation, optical communications etc., which requires larger mirrors/focusing optics which further increases the weight and cost. Since, size and weight is a crucial factor for any object sent into space, solutions are required to reduce the size and weight of space based cameras.

One solution is using a hybrid (diffractive/refractive) lens / optical imaging system i.e. using either diffractive lenses in an optical imaging system or using a hybrid lens (diffractive/refractive) in an optical imaging system. Phase profile of the diffractive surface is modelled by a polynomial, whose coefficients are optimized to achieve the desired performance. Second order phase coefficient is used to establish the power of diffractive lens whereas other higher order coefficients are used to minimize the third order aberrations. Therefore, in diffractive lens, in addition to optimizing the curvature of the surface (on which diffraction pattern is written), we have additional degrees of freedom (higher order phase coefficients) which can be used to control monochromatic aberrations. Additionally, diffractive lenses have large negative dispersion. As such, if diffractive lenses are used together with refractive lenses (positive dispersion) in an optical imaging system (Hybrid system), they can also compensate for chromatic aberration in addition to reducing monochromatic aberrations [3]. Hence, same performance can be achieved with lesser elements, thus reducing the mass and size of an optical imaging system. Also, the value of dispersion for diffractive lenses is much larger, hence chromatic aberration can be compensated in a hybrid system by only a small power of the diffractive element (which means larger focal length and easier fabrication).

In this paper, an all refractive optical imaging system (F/5, 120 mm EFL, wavelength range: 500 – 700nm, $\pm 10^0$ FOV) is designed using commercially available optical design software ZEMAX. System is optimized so as to achieve diffraction limited MTF at 70lp/mm and distortion less than 0.1%. Designed system consists of 8 refractive elements (Refer Fig 1(a)). MTF curves and distortion curves are given in Fig 1(b) and (c) respectively. Optical imaging system with the same specifications is redesigned using ZEMAX to achieve the same image quality using hybrid lenses. In ZEMAX, a diffractive surface is modelled by the following phase profile: $\Phi = M.\sum_{i=1}^{N} A_i \rho^{2i}$,where N is the number of polynomial coefficients in the series, A_i the coefficient on the power of ρ, which is the normalized radial aperture coordinate, and M is the diffraction order. Fig 2(a) shows the design in which diffractive surface is on the flat side of the refractive lens. This system consists of 6 elements (4 refractive lenses and 2 hybrid lenses). Fig 2(b) shows the design in which the diffractive surface is also allowed to be curved resulting in further reduction of elements to 4 elements (2 refractive lenses and 2 hybrid lenses).

Initially, an amplitude (Fig 3(a)) and phase (Fig 3(b)) binary diffractive lens were fabricated in-house, using direct write laser (DWL) lithography. Optimized phase polynomial obtained from ZEMAX is fractured to obtain the transition locations according to the number of levels to be fabricated. Fig 4(a) and 4(b) show the microscopic images of the center rings and side rings of the fabricated

diffractive lens respectively. Fig 4(c) shows the surface profile of the fabricated phase binary diffractive lens from confocal microscope. In the future, fabrication of multilevel (higher efficiency) diffractive lenses and fabrication of hybrid lenses (also with curved diffractive surface) will be undertaken.

Acknowledgements: We acknowledge the support in fabrication work from Mr. Sharad Jain and Mr. Prashant Varma (Microlithography division, SAC (ISRO)).

References:

[1]George Joseph, Fundamentals of Remote Sensing
[2] R. Kingslake, Lens Design Fundamentals (Academic, New York, 1978)
[3] T. Stone and N. George, "Hybrid diffractive-refractive lenses and achromats," Appl. Opt. 27, 2960–2971 (1988)

Figures referenced in text

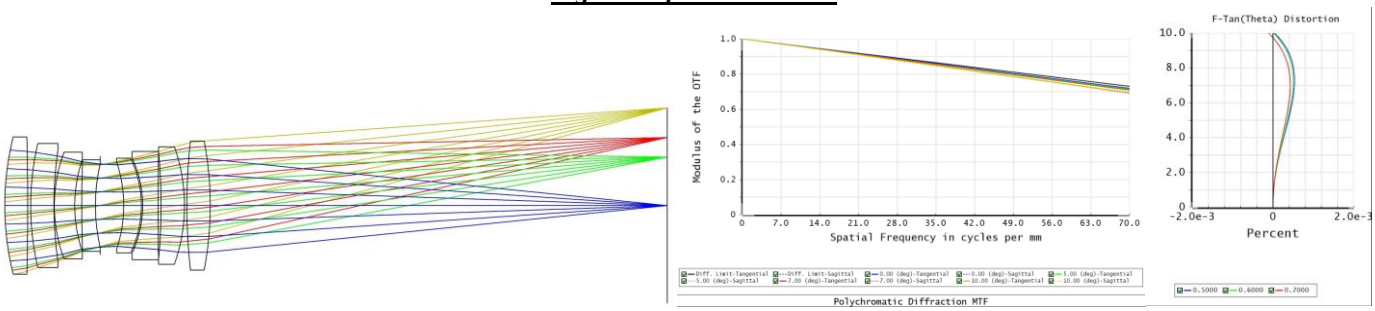

(a) (b) (c)

Fig 1. *Refractive optical imaging system (F/5, EFL:120mm,500-700nm, ±10^0 FOV) (a) Optical system layout consisting of eight refractive elements (b) Polychromatic MTF curve showing diffraction limited performance at 70lp/mm at all fields (sagittal and tangential) (c) Distortion curve for 500nm, 600nm and 700nm as a function of field*

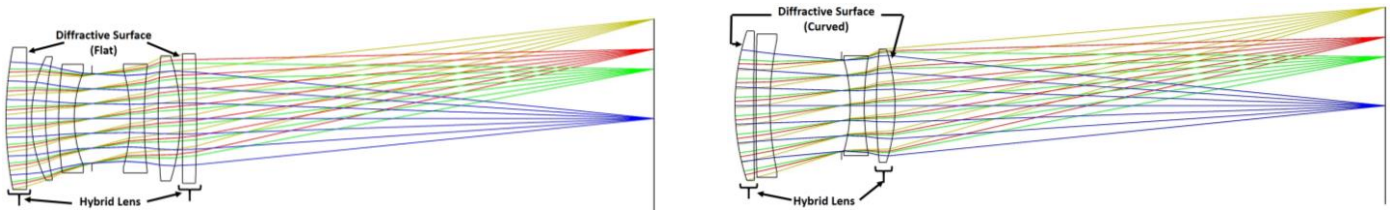

(a) (b)

Fig 2. *Hybrid (diffractive/refractive) optical imaging system (F/5, EFL: 120mm, 500-700nm, ± 10^0 FOV); image quality similar to refractive optical imaging system consisting of 8 elements (as depicted in fig 1) (a) Optical system layout consisting of six elements: 4 refractive lens and 2 hybrid lens with flat diffractive surface (b) Optical system layout consisting of four elements: 2 refractive lens and 2 hybrid lens with curved diffractive surface*

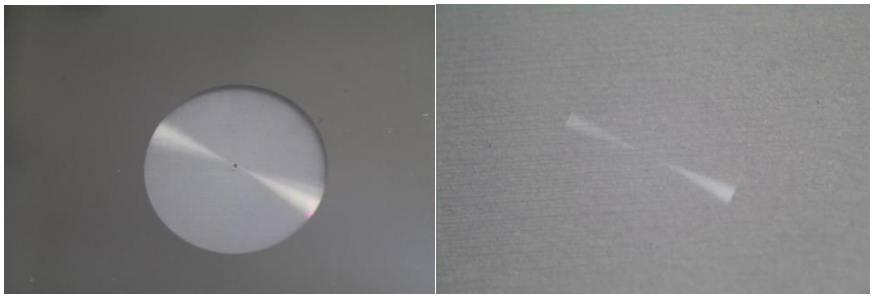

(a) (b)

Fig 3. *Binary diffractive lens fabricated in-house using Direct Write Laser lithography (a) Amplitude (b) Phase*

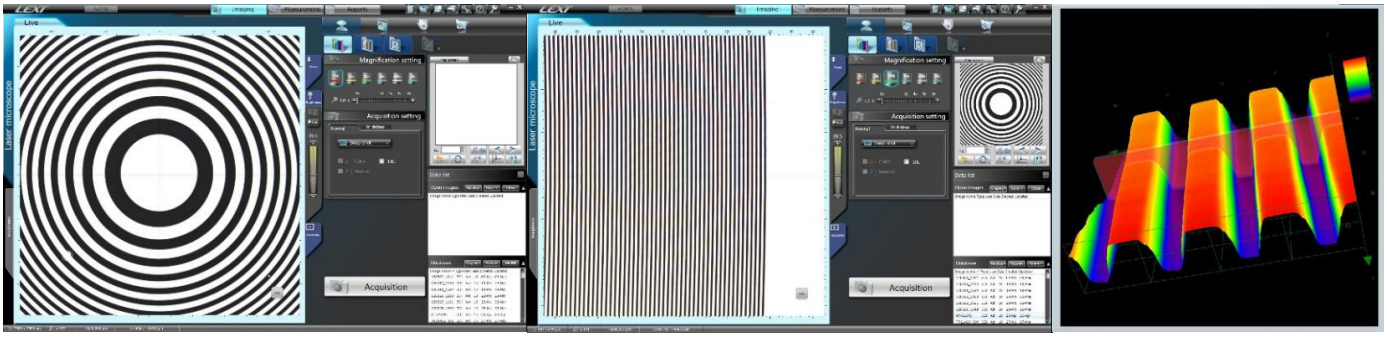

(a) (b) (c)

Fig 4. *Microscopic images of fabricated binary diffractive lens (a) Center rings (b) Side rings (c) Surface profile of phase diffractive lens measured with confocal microscopy. Number of transition points are 1272. Deviation in width of last circle (critical dimension (CD) for fabrication/resolution of diffractive lens), was 3.7% (Targeted CD was 5um, achieved was 4.813um). Achieved etch depth has 2.5% deviation from targeted etch depth (Achieved etch depth is 497nm, while targeted etch depth was 485nm). Deviation in focal length was 0.5% (Design focal length is 200mm). Diffraction efficiency of Phase Binary diffractive lens was 3.5 times more than Amplitude binary diffractive lens.*

TiO_2 nanotubes as photo anode for increased light trapping mechanisms in DSSC

Vaddi Yaswant [1,2], Sarigamala Karthik Kiran[1,2] , Sumit Saxena [2], Shobha Shukla [2*]
[1]Department of Centre for Research in Nanotechnology & Science (CRNTS),Indian Institute of Technology - Bombay.
[2]Nanostructures Engineering and Modeling Laboratory, Department of Metallurgical Engineering and Materials Science, Indian Institute of Technology - Bombay.
[*]sshukla@iitb.ac.in

Abstract

The rapid pace of industrialisation has resulted in increased the consumption of energy up to 520 Quadrillion Btu in 2011[1]. With the sun not dying in near future, solar energy is envisioned to satisfy the energy demands in future. The primary bottleneck in exploiting solar PV power is the cost per unit of electricity. The cost of energy generated using photovoltaics depend on a large number of factors such as conversion efficiency, the lifetime of the solar panels to name a couple of them. First generation solar cells based on crystalline silicon are more efficient and also highly expensive[2],. whereas second and third are cheaper but at the same time suffer from poor efficiencies. One way to increase the efficiencies is to increase the light trapping mechanisms for which TiO_2 nanotubes form potential candidates. The periodic arrangement of nanotubes fabricated on Ti metal arranged as a photonic crystal is expected to increase the light trapping mechanisms. The band gap and density of states available in conduction band are the main parameters to choose an efficient semiconductor[3]. Highly ordered TiO_2 nanotubes fabricated using a nano porous alumina templating method have been used to achieve solar cell efficiencies of 3.5% [4]. Here we propose a technique of fabricating TiO_2 nanotubes with sub wavelength scale pore size using electrochemical anodisation technique. This enables in keeping low fabrication costs and achieve higher efficiencies by increasing light trapping mechanisms because of photonics crystal arrangement.

Keywords

TiO_2 nanotubes, DSSC, light trapping mechanisms, Solar cells.

Introduction

TiO_2 nanotubes have very high surface to volume ratio because of which they are highly used in photocatalysis[5], photo electrolysis[6], and photovoltaics[7]. Several methods have been explored such as deposition into a nano porous alumina template[8], sol–gel method[9], seeded growth[10], and hydrothermal processes[11] to fabricate TiO_2 nanotubes. Of all the methods, fabrication of TiO_2 nanotubes using anodisation of titanium[12] produces more uniform structures. By varying the electrochemical conditions like fluorine content, electrolyte to water ratio, anodisation time and voltage one can control the pore sizes, lengths, and wall thicknesses.

Sample Preparation and Characterisation

TiO_2 nanotubes are prepared using thin Titanium sheet. The Ti foil is cleaned by sonication in ethanol and DI water and later dried with hot air blower. The as such prepared Ti metal is used as anode and platinum gauge (100mesh) as cathode in a two electrode electrochemical cell with 0.5 wt% NH_4F in ethylene glycol and 2 volume % water. During the electrochemical process, anodic oxidation occurs, which converts Ti to TiO_2 and then localised dissolution of oxide occurs because of the fluoride ions resulting in formation of nanotubes [6],. The anodisation is performed at 30V for a period of 24hrs at room temperature. These samples are then cleaned with DI water to remove the contamination and annealed in air at 500^{o}C for 3 hrs at a heating rate of 5^{o}C/min. The SEM image, UV-VIS reflectance spectrum, XRD and PL spectrum are shown in the **Fig.1**.To characterise the electrochemical activity of TiO_2 nanotubes cyclic voltametry was carried out in 1 M Na_2SO_4 solution. The TiO_2 nanotubes grown substrate was polarised from -1.2 to 1.3V vs. SCE. The CV curves exhibit a typical characteristic for anatase structure of titania nanotubes that are characterised with a very low capacitive current in the anodic potential range but in the cathodic range there is a high electrochemical activity. The redox peaks recorded at about −0.7 V could be related with alteration in electronic structure of the oxide, e.g. Incorporation of additional states within the band gap that alter the conductivity and optical properties as well. The cathodic peak could be attributed to Ti^{4+} reduction in conjunction with cation intercalation and is related with substantial variations in the material conductivity. On the other hand, the reduction peak located below −0.5 V was identified as hydrogen evolution despite its generally regarded that this reaction takes place at more negative potentials. The redox activity in the material comes from the internal walls of the nanotubes and also from the top surface of the nano porous structure. The CV is shown in **Fig.2**.

Conclusion

TiO_2 nanotubes are synthesised using two electrode anodisation method and it's SEM, XRD, Reflectance and Photoluminescence spectra are reported. The TiO_2 nanotubes so obtained are expected to show good potential as photo anode under reverse illumination in fabrication of due sensitised solar cells.

Acknowledgments

I would like to acknowledge Council of Scientific and Industrial Research, India and Indian Institute of Technology Bombay for funding my Ph.D. and providing me with required resources.

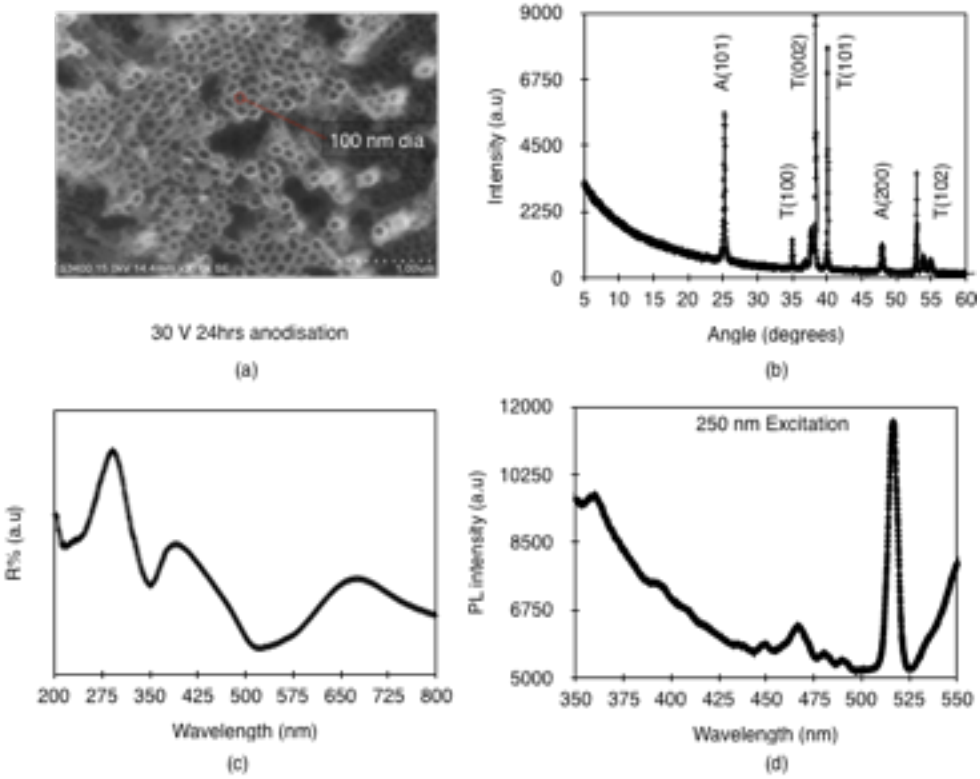

Fig.1 (a) SEM of TiO_2 nanotubes at 30V, 24hrs, (b) XRD of TiO_2 nanotubes, (c) Reflectance of TiO_2 nanotubes, (d) Photoluminescence spectrum of TiO_2 nanotubes.

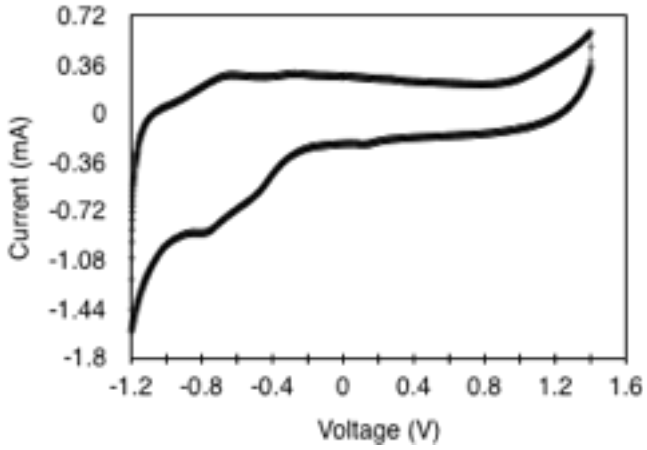

Fig.2 CV measurement of TiO_2 nanotubes

Reference list

1. Kannan, N. & Vakeesan, D. Solar energy for future world: - A review. Renew. Sustain. Energy Rev. 62, 1092–1105 (2016).
2. Mokkapati, S. & Catchpole, K. R. Nanophotonic light trapping in solar cells. *J. Appl. Phys.***112,** 101101 (2012).
3. Cushing, S. K. *et al.* Photocatalytic Activity Enhanced by Plasmonic Resonant Energy Transfer from Metal to Semiconductor. *J. Am. Chem. Soc.***134,** 15033–15041 (2012).
4. Kang, T. S., Smith, A. P., Taylor, B. E., & Durstock, M. F. (2009). Fabrication of highly-ordered TiO2 nanotube arrays and their use in dye-sensitized solar cells. Nano letters, 9(2), 601-606.
5. M. Adachi, Y. Murata, M. Harada, Y. Yoshikawa, Chem. Lett. 29 (2000) 942
6. G.K. Mor, K. Shankar, O.K. Varghese, C.A. Grimes, J. Mater. Res. 19 (2004) 2989.
7. S. Uchida, R. Chiba, M. Tomiha, N. Masaki, M. Shirai, Electrochemistry 70 (2002) 418.
8. P. Hoyer, Langmuir 12 (1996) 1411
9. J.H. Jung, H. Kobayashi, K.J.C. van Bommel, S. Shinkai, T. Shimizu, Chem. Mater. 14 (2002) 1445.
10. Z.R.R. Tian, J.A. Voigt, J. Liu, B. McKenzie, H.F. Xu, J. Am. Chem. Soc. 125 (2003) 12384.
11. T. Kasuga, M. Hiramatsu, A. Hoson, T. Sekino, K. Niihara, Langmuir 14 (1998) 3160.
12. D. Gong, C.A. Grimes, O.K. Varghese, W. Hu, R.S. Singh, Z. Chen, E.C. Dickey, J. Mater. Res. 16 (2001) 3331.

OSI-ISO 2018 manuscript No.
(183)

Spin momentum locking in a tightly focused Gaussian beam

Debapriya Pal · Indrani Bhattacharya · Sourav Islam · Subhasish Dutta Gupta · Nirmalya Ghosh · Ayan Banerjee

Abstract We demonstrate by a simple calculation that tight focusing of a Gaussian beam in optical tweezers leads to spin-momentum locking, where the spin momentum density is rendered independent of helicity while the Poynting vector becomes helicity dependent. We hypothesize that the presence of a stratified medium in the path of the trapping beam would enhance the transverse spin momentum leading to exotic controlled rotation of optically trapped single mesoscopic particles for input circularly polarized light.

Keywords Spin Momentum Locking · Optical Tweezers · Gaussian Beam · Optical Manipulation · Light Matter Interaction

Introduction: Light carries both orbital and spin angular momentum, and the Poynting vector - which is considered to be the vector representative of the flow of energy - has contribution from both the orbital and spin part of the momentum. The spin contribution in Poynting vector, introduced by Belinfante through the equation $\mathbf{p} = \mathbf{p}^o + \mathbf{p}^s$ [1], where $\mathbf{p}^s$ represents the contribution of spin in poynting vector, is rather enigmatic. This is because the term $\mathbf{p}^s$, though being responsible for spin angular momentum, does not contribute to the energy flow, so that it may be considered to be a virtual quantity. On the other hand, $\mathbf{p}^o$ represents canonical momentum that is responsible for generating orbital angular momentum (OAM) ($\mathbf{l} = \mathbf{r} \times \mathbf{p}^o$).

It has recently been discovered that a phase shifted longitudinal component of field plays a major role in the appearance of spin (polarization) dependent transverse momentum and spin (polarization) independent transverse spin angular momentum (SAM) ($\mathbf{p}^s$)[1–4]. This particular feature is well known as spin momentum locking in condensed matter physics in the context of topological insulators [5, 6]. On the surface of a topological insulator, special states exist which fall

Debapriya. Pal, Indrani Bhattacharya, Sourav Islam, Nirmalya Ghosh, Ayan Banerjee
Department of Physical Sciences, Indian Institute of Science Education and Research Kolkata, Mohanpur, India
E-mail: nghosh,ayan@iiserkol.ac.in

Subhasish Dutta Gupta
School of Physical Sciences, Hyderabad Central University, Hyderabad, India

within the bulk energy gap and allow surface metallic conduction [7]. The carriers in these surface states have their spin locked at a right-angle to their momentum (spin-momentum locking) [8]. In optics, this feature is manifested as the transverse component of the Poynting vector - which represents the flow of momentum - being independent of helicity (spin) of the beam [9]. In case of evanescent fields, such non-trivial structures of spin and momentum density have been observed and reported [9]. In fact, such a transversely spinning electric field arising in the case of transverse SAM of light, and resembling the spinning movement of the spokes of a rolling bicycle wheel, has recently been experimentally achieved [10]. It has also been shown that the general solution of Mie scattering from a spherical particle, which has phase-shifted longitudinal component indeed has the helicity dependent transverse component of poynting vector (generally addressed as 'transverse (spin) momentum') and helicity independent transverse spin angular momentum density [11,12]. Thus, keeping in mind that a tightly focused Gaussian beam has a longitudinal field component which is phase shifted from the transverse components, the obvious question that arises is whether a tightly focused Gaussian beam also contains these interesting and exotic properties.

Theory: Tight focusing is well understood with the help of Debye-Wolf diffraction integral method and angular spectrum method. The generation of longitudinal component which is phase shifted from the transverse components is well known. The expression of the tightly focused beam can be written in a matrix formation and be related to input polarization $\mathbf{X}$ [13],

$$\begin{pmatrix} E_x \\ E_y \\ E_z \end{pmatrix} = C \begin{pmatrix} I_0 + I_2 cos2\psi & I_2 sin2\psi & 2iI_1 cos\psi \\ I_2 sin2\psi & I_0 - I_2 cos2\psi & 2iI_1 sin\psi \\ -2iI_1 cos\psi & -2iI_1 sin\psi & I_0 + I_2 \end{pmatrix} \mathbf{X} \tag{1}$$

where $\mathbf{X}$ is Jones polarization vector. I_0, I_1 and I_2 are well known diffraction integrals[13], and C is a constant. Using $\mathbf{X} = [1\ 0\ 0]^T$ as the input Jones matrix for the case of linearly polarized input Gaussian beam and in case of left circular and right circular polarization input (with $\mathbf{X} = [1\ \pm i\ 0]^T$ for L.C.P. and R.C.P. respectively) the output electric field can be calculated.
To calculated magnetic field we exploit the symmetry that tightly focused electric and magnetic field enjoy[14].
The spin momentum density is given in SI units as[2,10,15]

$$\mathbf{S} = \frac{\epsilon \mathbf{E} \times \mathbf{E}^* + \mu \mathbf{H} \times \mathbf{H}^*}{\omega[\epsilon |\mathbf{E}|^2 + \mu |\mathbf{H}|^2]} \tag{2}$$

The Poynting Vector in SI unit is given as:

$$\mathbf{P} = \frac{1}{2}\mathrm{Re}(\mathbf{E} \times \mathbf{H}^*) \tag{3}$$

Next, we calculate the Spin momentum density and Poynting vector. For Right Circularly Polarized light the expressions are:

$$\begin{aligned} S_x &= -4iI_1(I_0 + I_2)\sin(\psi); \\ S_y &= 4iI_1(I_0 + I_2)\cos(\psi); \\ S_z &= -2i(I_0^2 - I_2^2) \end{aligned} \tag{4}$$

$$\begin{aligned} P_x &= 4I_1(I_0 + I_2)\sin(\psi); \\ P_y &= -4I_1(I_0 + I_2)\sin(\psi); \\ P_z &= 2(I_0^2 - I_2^2); \end{aligned} \tag{5}$$

For Left Circularly polarized light the expressions are:

$$\begin{aligned} S_x &= -4iI_1(I_0 + I_2)\sin(\psi); \\ S_y &= 4iI_1(I_0 + I_2)\cos(\psi); \\ S_z &= -2i(I_0^2 - I_2^2); \end{aligned} \tag{6}$$

$$\begin{aligned} P_x &= -4I_1(I_0 + I_2)\sin(\psi); \\ P_y &= 4I_1(I_0 + I_2)\sin(\psi); \\ P_z &= 2(I_0^2 - I_2^2); \end{aligned} \tag{7}$$

In earlier work [16,17], we have demonstrated that the presence of a stratified media in the path of the tightly focused beam in optical tweezers can lead to interesting effects due to spin-orbit interaction of light. This includes an enhanced spin Hall effect [16], which leads to a large transverse spin momentum that causes the formation of intensity lobes of opposite helicities for input linear polarization. We have been able to trap and rotate single particles in opposite directions in this experimental configuration. We therefore hypothesize that the transverse spin angular momentum would be likewise amplified in the presence of the stratified media leading to the generation of exotic effects. We would also like to investigate the behaviour of both P and S for input circular polarization.

Conclusion: It is clear that under the change of helicity from +1 to -1, the transverse component of spin angular momentum remains same, but the transverse components of Poynting Vector flip direction. This confirms that the helicity dependence of the traverse Poynting vector and the helicity-independence of transverse spin angular momentum are properties of a tightly focused Gaussian beam. We believe that both would be amplified in the presence of a stratified media in the path of optical tweezers leading to exotic motion of particles for input circularly polarized light.

Acknowledgements: The author acknowledge the financial support by Indian Institute of Science Education and Research, Kolkata, an autonomous research and teaching institute funded by the Ministry of Human Resource Development, Govt. of India.

References

1. K. Y. Bliokh and A. Y. Bekshaev and F. Nori, Nat. Communications 5, 330 (2014).
2. A. Aiello and P. Banzer and M. Neugebauer G. Leuchs , Nat.Photonics 9, 789 (2015).
3. K. Y. Bliokh and D. Smirnova F. Nori , Science 348, 1448 (2015).
4. A. Y. Bekshaev and K. Y. Bliokh F. Nori , Phys. Rev. X 5, 011039 (2015).
5. M. Z. Hasan et al., Rev. Mod. Phys. 82, 3045 (2010).

6. F. Ortmann and S. Roche and S. Valenzuela, Topological Insulators: Fundamentals and Perspectives (John Wiley and Sons, 2015).
7. F. Zhang and C. L. Kane E. J. Mele, Physical Review B 86(8), 081303 (2012).
8. D. Hsieh and Y. Xia et al., arXiv preprint arXiv:1001.1590 82, 3045 (2010).
9. T. Van Mechelen and Z. Jacob, Optica 3(2), 118-126 (2016).
10. T. Bauer and M. Neugebauer G. Leuchs P. Banzer , Phys. Rev. Lett. 117, 013601 (2016).
11. S. Saha et al., Opt. Lett. 41, 4499 (2016).
12. C. F. Bohren and D. R. Huffman, Wave Optics: Basic Concepts and Contemporary Trends (CRC Press, 2015).
13. S.D. Gupta and N. Ghosh and A. Banerjee, Wave Optics: Basic Concepts and Contemporary Trends (CRC Press, 2015).
14. B. Richards and E. Wolf , Proc. R. Soc. A 253, 358 (1959).
15. M. V. Berry and M. R. Dennis , Proc. R. Soc. A 457, 141 (2001).
16. Basudev Roy et al., Phys. Rev. A 87, 043823 (2013).
17. Basudev Roy et al., New Journal of Physics, 16, 083037 (2014).

OSI-ISO 2018 manuscript no.
(184)

Increment of light absorption in periodic structures introducing metallic nano-layer for solar cell applications

Arnab Panda[1]*, Soumen Maiti[2], Rajib Chakraborty[1], Kanik Palodhi[1]
[1] Dept. of Applied Optics and Photonics, University of Calcutta
[2] Dept. of Physics, St. Thomas College of Engineering and Technology
***Corresponding email:** panda1arnab@gmail.com

Abstract: Solar cells are yet to overcome its practical lower efficiency compared to its theoretical potential. One of the most important aspects of enhancing solar efficiency is to increase light trapping within cells for generating more number of carriers. Light trapping within periodic structures is one of the most promising cost-effective solutions and to increase the optical path length, appropriate insertion of metallic layers is critical. In particular, the shape and size of the metallic layers and proper arrangement of periodic structures are vital to increase the optical absorption of the solar cell. In this proceeding, we *characterise* metallic layers with different metals such as gold, silver and aluminium embedded within a bilayer structure of Titanium dioxide (TiO_2) and Silicon (Si). Evidently from the result, gold becomes the better choice for light trapping considering, superior effective absorption property of structure for the entire spectrum. In another study presented here, comparison of multiple (1-5) gold metallic layer of 5 nm thickness shows that there is significant increase in effective absorption with increase in numbers of layers particularly in the UV spectrum.

Keywords: solar cell; light trapping; metallic nano-layer

Solar cells are required for renewable energy applications, particularly, for clean and green energy. A serious challenge, however, is to overcome its practical lower efficiency compared to its theoretical potential. One of the most important aspects of enhancing efficiency of solar cells is to increase light trapping inside the structure for generating more carriers. Light trapping within periodic structures can be the most promising alternative from the cost effectiveness and less material requirement point of view [1]. In this proceeding, our endeavour is to describe the effects of change in *effective absorption* with change in thicknesses of metallic nano-layers of different metals such as gold (Au), silver (Ag), and aluminium (Al), introduced inside the periodic structure appropriately [2]. By effective absorption, it is meant that this absorption is responsible for carrier generation and not the total absorption within the structure. In particular, the size of the metallic layers and proper arrangement of periodic structures are vital to increase the optical absorption within the solar cell as well as to reduce the losses by the nano-layers themselves [3, 4].

Here, for this study of comparison of different metals, we have designed a simple and well-known periodic structure of TiO_2 and Si having nano-layers of metals to enhance the solar light absorption. The three metals chosen here are commonly used since gold and silver are noble metals and Al behaves similar to noble metals in room temperature. The schematic of the structure is shown in Fig. 1(a) for Au-layer, however, for Ag-layer and Al-layer also similar structures are considered. The thicknesses considered here (50 nm for metallic layers, 46 nm for TiO_2 and 27 nm for Si), as shown in the figure, are obtained from standard literature [3]. The red dots in the figure simply represent the selection of the layer in FEM software used and does not carry any other physical meaning. In the present study, our emphasis is on the choice of metals, therefore, only one periodic layer on each side of the layer (i.e. Si-TiO_2-metal-Si-TiO_2) is considered. The results arising out these structures are presented in Fig. 1(b) that represents the graphs of effective absorption vs. wavelength for three metallic layers with thicknesses of 50 nm. Clearly, absorption at all wavelengths for Al remains low compared to Au and Ag. For Ag, though, there is a gradual variation, but after wavelength 500 nm, it remains nearly saturated. The absorption due to Au, however, remains high and there is an exponential decrease with wavelengths though within visible region it remains nearly same. Evidently, gold will be a better choice for light trapping considering, its higher effective absorption for the entire spectrum. This high absorption could, possibly, be caused by increased electronegativity of gold than other metals considered, here. It also has high electron affinity compared to other metals considered here for which electrons, and thereby, carriers need to absorb more energy. From a practical point of view also, gold, due to its low oxidation property will be better compared to other materials.

From these two graphs two important aspects emerge here- a) possibility of increase in effective absorption with decrease in thickness of metallic layers and increase in number of metallic layers; and b) in all three of the graphs there is higher absorption in UV region. Both of these are going to be examined in the subsequent parts. For studying the effect on absorption due to change in thickness of metallic layer, thickness of gold layer is decreased further to three thicknesses

namely 25 nm, 10 nm and 5 nm without changing the thickness of periodic structure. Corresponding simulation results presented in Fig. 2(a) clearly demonstrates that effective absorption increase with decrease in layer thickness and maximum absorption for 5 nm thickness. The possible reason is decrease in thickness compels the metallic layer to absorb less energy, yet propagate light to semiconductor layers for carrier generation.

We continued our investigation with increase in number of gold layers (keeping 5 nm thickness) separated by bilayers of TiO_2 and Si (as previous) and varied the number from one (1) to five (5). As can be seen from Fig. 2(b), with increase in numbers of layers, effective absorption increases significantly. Evidently, this is due to increase in number of carriers for plasmonic resonance and the phenomenon is particularly strong in the UV region, as described earlier. In fact, all three of the graphs (Fig. 1(b), Fig. 2(a) and Fig. 2(b)) show higher effective absorptions in UV. This is, possibly, due to the fact that the thicknesses of TiO_2 and Si remained constant for all of these cases and that is the determining factor in light trapping in around the wavelength region (UV).

In conclusion, we presented a brief study on characterisation of usage of metallic layers within a periodic structure of TiO_2 and Si by changing the materials (Au, Ag and Al), thicknesses (25 nm, 10 nm and 5 nm) and numbers (1–5) for obtaining maximum effective absorption leading to maximum carrier generation. The study shows that using multiple metallic layers of gold with 5 nm thickness, higher effective absorption can be achieved. This can lead to designing more efficient solar cells in future.

References:

1. T. Markvart and L. Castañer, Practical Handbook of Photovoltaics: Fundamentals and Applications, Elsevier, Amsterdam (2003).
2. Nelson J (2003), The Physics of Solar Cells. Imperial College Press, London
3. T. Soga Ed. (2006), Nanostructured materials for solar energy conversion, Elsevier
4. H. A. Atwate and A. Polman, "Plasmonics for improved photovoltaic devices," Nat. Mater. 9(3), 205–213 (2010).

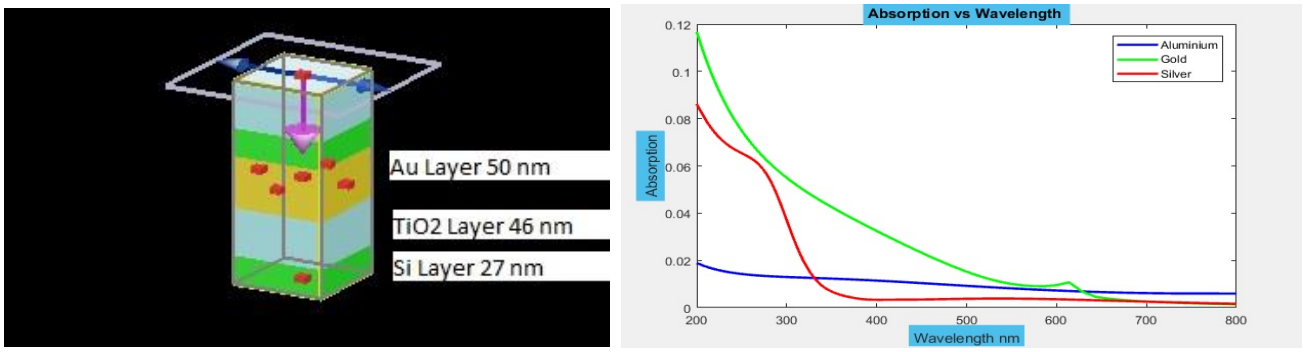

1(a) **1(b)**

Fig 1 Comparison of different metals (a) Structure with Au metallic nano-layer (b) effective absorption due to Al, Au and Ag metallic layers of 50 nm

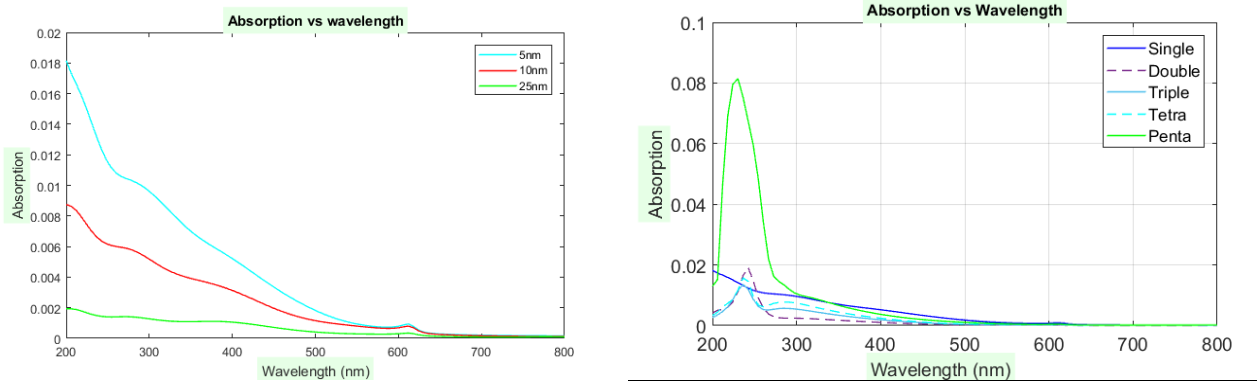

2(a) **2(b)**

Fig 2 (a) Comparison of change in thickness of gold (b) effective absorption due to multiple Au metallic layer of 5 nm thickness

OSI-ISO 2018 manuscript No.
(186)

'Seeing' quantum correlations in two-level atomic system

Mithilesh K. Parit · Shaik Ahmed · P. Anantha Lakshmi · Prasanta K. Panigrahi · Sourabh Singh

Abstract We study the behavior of intensity pattern and photon statistics for the coupled two-level atomic system in the far-field domain which shows two distinct regimes, one with uniform intensity and other with non-uniform intensity. The effect of transition frequency on the radiation intensity is explicitly demonstrated at finite temperature in two phases. Radiated intensity is shown to exhibit periodic variation from super to sub-radiant as a function of observation angle. It persists at higher temperatures with reduced intensity, even in the absence of entanglement but with non-zero quantum discord, showing the physical realization of quantum discord.

Keywords Two-level atoms · Superradiance · Quantum correlation · Photon-photon correlation

Mithilesh K. Parit
Department of Physical Sciences, Indian Institute of Science Education and Research Kolkata, Mohanpur 741246, West Bengal, India
E-mail: mithilesh.parit@gmail.com

Shaik Ahmed
Department of Humanities and Science, MLR Institute of Technology, Dundigal, Hyderabad-500043, Telangana, India
E-mail: shaiq786@gmail.com

P. Anantha Lakshmi
School of Physics, University of Hyderabad, Hyderabad - 500046, Telangana, India
E-mail: palsp@uohyd.ernet.in

Prasanta K. Panigrahi
Department of Physical Sciences, Indian Institute of Science Education and Research Kolkata, Mohanpur 741246, West Bengal, India
E-mail: pprasanta@iiserkol.ac.in

Sourabh Singh
epartment of Physical Sciences, Indian Institute of Science Education and Research Kolkata, Mohanpur 741246, West Bengal, India
E-mail: sourabh.showstopper@gmail.com

1 Introduction

The atomic system of coupled two-level atoms is an ideal venue to 'see' the effect of different quantum correlation (QCs) on the emitted light. The far field radiation pattern, faithfully reveals the effect of entanglement and discord on the pattern of emitted light. More importantly, the angular distribution and 'statistics' of light quanta can be controlled through the system parameters. We investigate this physical system in the presence of a realistic environment and demonstrate the effect of temperature on different QCs influencing the observed radiation pattern.

We consider a three identical coupled two-level atomic system. The system is non-interacting with environment and surroundings. The Hamiltonian for such a system of two-level atoms is given by [1],

$$H = \sum_{i=1}^{3} \omega_i S_i^z + \sum_{i \neq j=1}^{3} \Omega_{ij} \; S_i^+ S_j^-. \tag{1}$$

The first term describes the energy difference between ground and excited state of an isolated atom and the second term represents the interaction between the ground state of one atom and the excited state of another atom, with Ω_{ij} is the coupling strength. The interaction is prohibited between two atoms which are both in excited/ground state. In the above, $S_i^+ = (|1\rangle\langle 0|)_i$ and $S_i^- = (|0\rangle\langle 1|)_i$ are the raising and lowering operators of the i^{th} atom in the spin representation. The presence of the coupling, Ω_{ij}, between the atoms causes mixing of the energy levels leading to the creation of states with different correlations. The characteristics of radiation intensity with constant coupling is extensively dealt in [2], for two topologically distinct configurations, namely, line and loop configurations, for the first time at finite temperature and as a function of transition frequency.

We now take into account the thermal effects, where, at finite temperature, the expectation value of an observable $\left\langle \hat{A} \right\rangle$ takes the form,

$$\left\langle \hat{A} \right\rangle = Tr\left(\hat{\rho}\hat{A}\right), \tag{2}$$

with $\hat{\rho}$ being the thermal density operator given by,

$$\hat{\rho} = \frac{\sum_{i=1}^{8} |\psi_i\rangle \langle\psi_i| \, e^{-\beta\epsilon_i}}{Tr\left(\sum_{i=1}^{8} |\psi_i\rangle \langle\psi_i| \, e^{-\beta\epsilon_i}\right)}. \tag{3}$$

Here $|\psi_i\rangle$ is an eigenstate with ϵ_i its eigenvalue. For pairwise thermal entanglement, one can obtain the reduced density matrices ρ_{ij} by taking partial trace of $\rho = \rho_{ijk}$ with respect to k, given by

$$\rho_{ij} = Tr_k\left(\rho_{ijk}\right). \tag{4}$$

The normalized intensity in the far field domain is given by [1–3],

$$I(\mathbf{r}) = \left\langle \hat{E}^{(-)}\hat{E}^{(+)} \right\rangle = \sum_{i,j} \langle \hat{S}_i^{+}\hat{S}_j^{-} \rangle e^{i(\phi_i - \phi_j)}. \tag{5}$$

Here ϕ_j is the relative optical phase accumulated by a photon emitted at $\mathbf{R}_j$ and detected at $\mathbf{r}$. In the subsequent sections, we investigate the behavior of intensity pattern and photon-photon correlation (also known as intensity-intensity correlation), resulting from the line configuration as a function of the system parameters, as well as observation angle at finite temperature.

2 The characteristics of radiation intensity in the line configuration

In the line configuration, a system of three identical coupled two-level atoms are placed symmetrically along a line with equal spacing d between adjacent atoms. For simplicity, we consider all transition frequencies of three atoms to be the same, $\omega_1 = \omega_2 = \omega_3 = \omega$ and the nearest neighbour interactions $\Omega_{12} = \Omega_{23} = \Omega = 1$ and next nearest interaction $\Omega_{13} = 0$. For this topology the phase ϕ_j the relative optical phase accumulated by a photon emitted at $\mathbf{R}_j$ and detected at $\mathbf{r}$ is,

$$\phi_j(\mathbf{r}) \equiv \phi_j = k\mathbf{n}.\mathbf{R}_j = jkd\sin\theta, \tag{6}$$

with $k = \frac{\lambda}{2}$, where λ is wavelength of observed radiation.

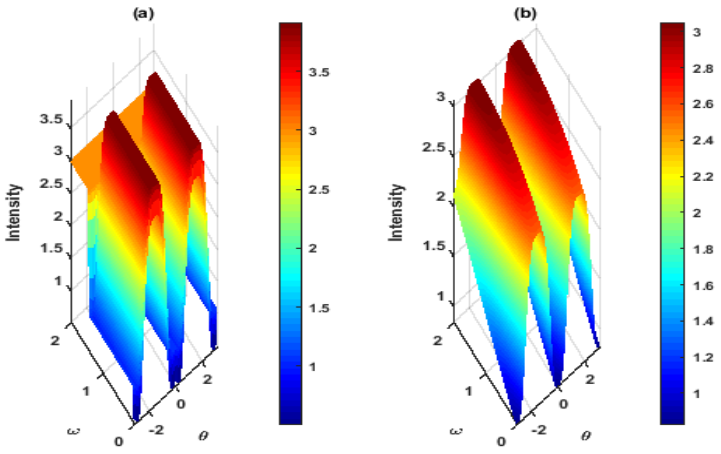

Fig. 1 (Color online) Panels a and b show the radiation intensity for fixed inter-atomic spacing ($d = \frac{\lambda}{2}$) as a function of observation angle and transition frequency for two different temperatures (a) $T = 0.005$ and (b) $T = 1.0$, respectively, clearly revealing two distinct phases and interference effect.

Fig. 1 shows the variation of the intensity pattern as a function of transition frequency and observation angle. The behavior of intensity from super

to sub-radiant is observed with respect to observation angle. This reflects the subtle interference effects present in the three particle system. At low temperatures, as transition frequency increases a phase with uniform light emission is seen, separated from a non-uniform intensity with periodic modulations. The uniform phase of radiation arises when both entanglement and discord vanish, as is evident from Fig. 1(a). The uniform phases vanish at higher temperatures is shown in Fig. 1(b).

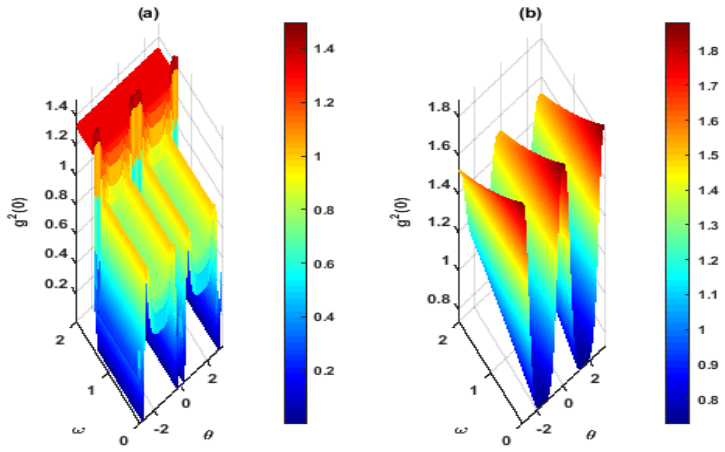

Fig. 2 (Color online) Panels a and b show the variation of photon-photon correlation at fixed inter-atomic spacing ($d = \frac{\lambda}{2}$) as a function of observation angle and transition frequency for two different temperatures (a) T=0.005 and (b) T=1, respectively.

We have investigated the photon-photon correlation as a function of observation angle and transition frequency for two different temperatures as shown in Fig. 2, revealing the sub- and super-Poissonian statistics of emitted radiation. The value of $g^2(0) < 1$ represents sub-Poissonian and $g^2(0) > 1$ super-Poissonian photon statistics.

3 Conclusion

In conclusion, the QCs in an entangled atomic ensemble leave their signature on emitted radiation. This can be quantitatively estimated, showing the precise effect of QCs on the nature of emitted radiation in different parameter domain. The emitted intensity is found highly super-radiant depending on system parameters. Further, photon-photon correlation shows sub- and super-Poissonian statistics as a function of observation angle and system parameters.

4 Acknowledgements

Authors gratefully thank Prof. G. S. Agarwal for his suggestions. Mithilesh K. Parit acknowledges discussion with Dr. Chiranjib Mitra.

References

1. G. S. Agarwal, *Quantum Optics* (Cambridge University Press, Cambridge, UK).
2. M. K. Parit, S. Ahmed, S. Singh, P. A. Lakshmi, P. K. Panigrahi, Quantum Light on Demand, pre-print: arxiv.org/abs/1805.08642 (2018).
3. R. Wiegner, J. von-Zanthier, and G. S. Agarwal, Quantum-interference-initiated superradiant and subradiant emission from entangled atoms, Phy. Rev. A **84**, 023805 (2011).

Existence of Critical wavelengths in the Transmission Spectrum of Directional Coupler Employing Non-Identical Single Mode Fibers

Garima Bawa and Saurabh Mani Tripathi

Abstract We examine the existence of two *critical* wavelengths in the transmission-spectrum of a Directional Coupler (DC), employing two non-identical single mode fibers. One fiber consists of a core with GeO_2-doped SiO_2 and the other with both B_2O_3 and GeO_2 doping in SiO_2 host.

Keywords Directional coupler, Integrated optics, *Critical* wavelength, Fiber Optics, Fiber

I.INTRODUCTION

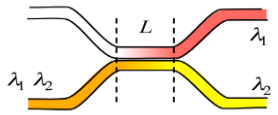

Fig 1 Schematic Diagram of a Directional Coupler

RECENTLY the existence of a *critical* wavelength has been predicted and subsequently demonstrated in the transmission spectrum of fiber-optic single-multi-mode structures and DCs [1,2]. The *critical* wavelength has two distinct properties (*i*) the spectral shift of transmission spectrum is of opposite nature on either side of the critical wavelength, and (*ii*) sensitivity is highest for transmission maximum/minimum nearest to the *critical* wavelength. In this paper we theoretically demonstrate that in DCs employing non-identical single mode fibers there exist two *critical* wavelengths both of which are of mutually opposite nature.

II.Theoretical Analysis

We consider a directional coupler consisting of two non-identical optical fibers, with their core regions made of 3.1 mole% GeO_2 doped SiO_2, and 7.7 mole% B_2O_3 and 9.1 mole% GeO_2 doped in SiO_2, respectively, with their core diameters selected using the phase-matching condition [3] to increase the power transfer at a particular wavelength and their axial separation being 2.5 μm, schematically shown in Fig1. The cladding region is considered to be made of fused SiO_2. For theoretical analysis, a master wave equation was solved for the super-modes supported by the DC to obtain the propagation constants and field distribution of the super-modes [3]. For our analysis we have considered strictly single-moded optical fibers i.e. l =0. The modal fields of the fibers have been taken as follows [3]

$$\psi(r,\phi) = \begin{cases} \frac{A}{J_l(U)} J_l\left(\frac{Ur}{a}\right) \begin{bmatrix}\cos l\phi \\ \sin l\phi\end{bmatrix}; for\ r \le a \\ \frac{A}{K_l(W)} K_l\left(\frac{Wr}{a}\right) \begin{bmatrix}\cos l\phi \\ \sin l\phi\end{bmatrix}; for\ r \ge a \end{cases} \quad (1)$$

We incorporated the wavelength dependence in the refractive indices of the fibers using Sellmeier relation [4].

III.Results and Discussions

The powers carried by the first ($|a(z)|^2$) and the second ($|b(z)|^2$) SMFs of the DC are obtained using the coupled mode theory and are given by [3]

$$|a(z)|^2 = 1 - \frac{k^2}{\frac{1}{4}\Delta\beta^2 + k^2} sin^2[(\frac{1}{4}\Delta\beta^2 + k^2)^{\frac{1}{2}}z] \quad (2)$$

$$|b(z)|^2 = \frac{k^2}{\frac{1}{4}\Delta\beta^2 + k^2} sin^2[(\frac{1}{4}\Delta\beta^2 + k^2)^{\frac{1}{2}}z \quad (3)$$

here $\Delta\beta = \beta_1 - \beta_2$, and z is the interaction length.

The length $L_c = \frac{h}{2} = \pi/2(\frac{1}{4}\Delta\beta^2 + k^2)^{1/2}$ is the coupling length of the directional coupler and corresponds to the minimum length required for the maximum energy transfer between the two fibers. In our simulations the interaction length is taken as 3400 μm.

The transmission spectrums at two different temperature variations i.e. ΔT=0℃ and 50℃ are plotted in Fig.2(a), showing the existence of two critical wavelengths at 0.92 μm and

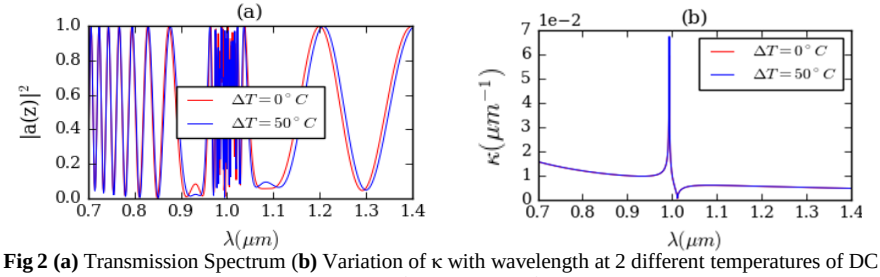

Fig 2 (a) Transmission Spectrum (**b)** Variation of κ with wavelength at 2 different temperatures of DC consisting of non-identical fibers.

1.08 μm, respectively. We also observe that the nature of spectral shifts around these two critical wavelengths is opposite. To explain this peculiar behavior, in Fig.2(b) we have plotted the spectral variation of κ (= βs− βa) i.e. variation of the propagation constant difference of the symmetric- and anti-symmetric super modes with changes in wavelength. Since the propagation constant of the super modes is a function of both the operating wavelength as well as perturbation parameter (here temperature), we can write the variations in phase difference of the super modes ($\varphi = \kappa L$) as,

$$\Delta\varphi = \frac{\partial\varphi}{\partial\lambda}\Delta\lambda + \frac{\partial\varphi}{\partial T}\Delta T \quad (4)$$

In order to obtain the wavelength shift of a given peak/dip due to change in temperature, we put $\Delta\varphi = 0$, as a particular peak/dip corresponds to a fixed phase difference. This gives

$$\frac{\Delta\lambda}{\Delta T} = -\frac{\partial\varphi}{\partial T}\frac{1}{L}(\frac{\partial k}{\partial\lambda})^{-1} \quad (5)$$

From Fig.2(b) we see that ∂κ /∂λ is negative (positive) and ∂φ/∂T is positive (positive) on the lower (higher) wavelength side of the first *critical* wavelength, resulting in a positive (negative) spectral shift of the transmission maxima/minima on the lower (higher) wavelength side, while its vice-versa for the second *critical* wavelength.

IV. Conclusions

In conclusion, we theoretically demonstrate the existence of two *critical* wavelengths in the transmission-spectrum of a Directional Coupler (DC), employing two non-identical single mode optical. These two wavelengths are of utmost importance to enhance the sensitivity of a sensor based on directional coupler. Owing to the fact that the sensitivity is inversely proportional to the slope of the phase mismatch curve (Eq.(5)), an infinite sensitivity can be achieved by operating the DC at the critical wavelengths.

V. References

1. S. M. Tripathi, A. Kumar, R. K. Varshney, Y. B. P. Kumar, E. Marin, J. P. Meunier, "Strain and temperature sensing characteristics of single-mode–multimode–single-mode structures", IEEE J. Lightw. Technol. 27, pp. 2348-2356 (2009). 2. S. M. Tripathi, A. Kumar, E. Marin, J.P. Meunier,
2. G. Bawa and S. M. Tripathi, "*Critical Wavelength in the Transmission Spectrum of a Directional Coupler Employing GeO2-doped Single ModeFibers*," Eprint: 035214, 2017.
3. A. K. Ghatak and K. Thyagarajan, Introduction to Fiber Optics, (U.K.: Cambridge Univ. Press, 1998).
4. M. J. Adams, *An Introduction to Optical Waveguide*, (John Wiley & Sons Inc., 1981).

OSI-ISO 2018 manuscript No.
(189)

Build-up Dynamics of Mode-locked like Pulses in a Linear Cavity with Frequency Shifted Feedback

Nishant Kr. Shekhar[1] · Mrinmay Pal[1] · Chandan Guha[2] · Ranjan Sen[1]

Abstract The transient state dynamics of sub-hundred nanosecond mode-lock like pulses in a frequency shifted feedback cavity with ytterbium doped active fiber as gain medium is studied. The feedback provided to the linear cavity is the Doppler upshifted frequency of the diffracted light from an intracavity acousto-optic modulator. The pulses evolve through three distinct optical regimes classified as passive Q-switching, continuous-wave and multiple-pulse mode locking. Each of these regions are inherently stable in separate windows of the input pump power. The regions have distinct spectral and temporal characteristics which has been investigated in this paper.

Keywords Frequency shifted feedback laser · Passive Q-switching · Mode-locking · Linear cavity

Introduction

Frequency shifted feedback (fsf) lasers have long challenged the researchers with theoretical difficulty of explaining the pulsed output from them. In an effort to comprehend its behaviour C. C. Cutler [1] created a computational model and associated the mode-lock like output to a moving comb of coherent frequencies. Later, L.P. Yatsenko et.al [2] showed that the discrete comb model of a traditional mode-lock laser is equivalent to the model by Cutler in a time frame of multiple output pulses or put simply in periodic state of pulse generation. In 2011, H. Guillet de Chatellus et.al [3] commented on the universal validity of the moving comb model restricting its usefulness to a subset of observations. The statement was based on the quadratic spectral phase that the modes have in a fsf cavity to the constant one of the traditional mode-locked lasers. The quadratic spectral phase in the conventional mode-lock cavities is an outcome of Kerr non-linearity while these are inherent to the Doppler shifting mechanisms of an acousto-optic modulator(AOM) that are mostly employed in fsf cavities. In order to reduce the dilemma of the current situation an exhaustive experimental data is required both in stationary and transient phases of these lasers.

Authors acknowledge financial support from CSIR Project MLP0101

[1] Fiber Optics and Photonics Division
CSIR-Central Glass and Ceramic Research Institute, Kolkata
E-mail: nishantkumarshekhar@gmail.com

[2] Chemical Engineering Department
Jadavpur University, Kolkata

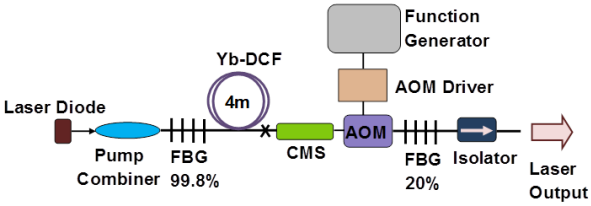

Fig. 1 Schematic layout of the experimental setup

Experimental Setup and Results

The experimental setup of the fsf fiber laser is shown in Fig.1. The cavity comprises of a double-clad Yb-fiber (core diameter: 8.9 um, core NA: 0.1) of length 4 meter, a pair of FBGs of reflectivity 99% and 20% with Bragg wavelength at 1064nm (3dB bandwidth 3nm and 1nm respectively). A fiber pigtailed AOM (operating wavelength: 1030 to 1090 nm) is placed inside the cavity. The AOM driver was supplied a DC waveform from an

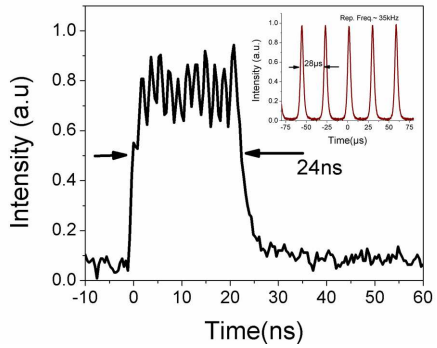

Fig. 2 Multiple-pulsing output (Inset: Passive Q-switched pulses)

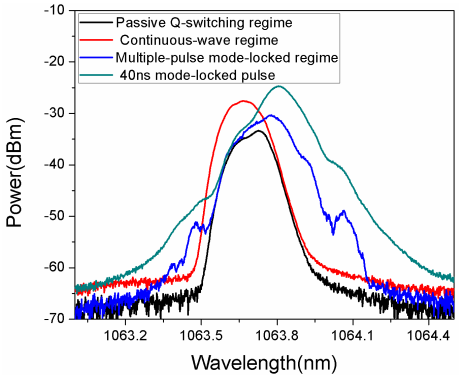

Fig. 3 Spectral output of different regimes

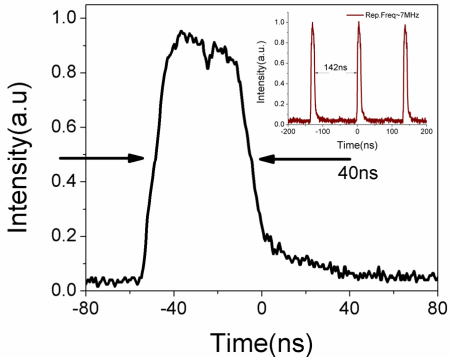

Fig. 4 Mode-locked pulse of 40ns (Inset: Repetition frequency of output)

arbitrary function generator (Agilent 81150A). The total cavity length was about 14 m. Active Yb-fiber was pumped by MM 976nm pump diode through a pump combiner. An isolator was placed at the output end to prevent back-reflection. Spectral and temporal characteristics were acquired by an optical spectrum analyser (Yokogawa-AQ6370D) and an oscilloscope (Tektronix-DPO7254C) respectively.

The passive Q-switched pulses that emanate from the regenerative amplification of spontaneous emission is shown in Fig 2 (inset).The AOM driver when driven with a DC waveform feeds a sinusoidal frequency of 150 MHz and creates a moving diffraction grating in the AOM whose 1st-order diffracted beam is connected to the cavity. This causes a feedback of 150 MHz upshifted frequency to the cavity that fails to provide enough gain to any of the Fabry-Perot modes and thus ensues generation of stable relaxation oscillations. These pulses were tunable from 25 kHz to 39 kHz with increasing pump power. At about 2W of pump power the acquired phase correlation is disrupted which makes the passive Q-switched pulses disappear and a continuous-wave (CW) laser gets generated. The beginning of the CW regime was also marked by a shift in peak wavelength of the spectra as shown in Fig. 3, signifying the dominance of Doppler up-shifted frequency in the cavity. Fig.3 also provides spectral information of the other regimes. On further increment of pump power to about 2.2W, multiple burst of sub-nanosecond pulses in a rectangular shaped envelope of 24 ns were formed as depicted in Fig.2. These changed to a 10 ns pulse on small increment of 100 mW of pump power. With further increments of pump power the 10 ns pulse broadens and attains a width of 40 ns running at a repetition frequency of 7 MHz which is shown in Fig. 4 and in its inset. The pulse breaks thereafter with further increment of pump power. The formation of such mode-locked like pulses could be hypothesized with the argument that since the reciprocal of the round trip time of the cavity is 7 MHz and feedback frequencies are 150 MHz apart, the Fabry-Perot modes that would get reinforced lie approximately at a difference of 1 GHz. This lowers the probability of phase locking of a large number of cavity modes and with few modes that develops a phase correlation generates the nano-second mode-lock like pulses.

Conclusion

Since a large number of experimental data on ring cavities are already available, the authors preferred to study the less researched linear fsf cavity in the emission area of ytterbium doped silica fibers and have documented the results.

References

1. C. C. Cutler, Why does linear phase shift cause mode locking?, IEEE Journal of Quantum Electronics 28 (1), 282-288 (1992)
2. L.P. Yatsenko, B.W. Shore, K. Bergmann, Theory of a frequency-shifted feedback laser, Optics Communications 236(1–3), 183-202(2004)
3. H. Guillet de Chatellus, E. Lacot, W. Glastre, O. Jacquin, O. Hugon, The hypothesis of the moving comb in frequency shifted feedback lasers, Optics Communications 284 (20), 4965-4970 (2011)

Design and Performance Evaluation of Extended Depth of Focus IR Camera

M P Singh, K K Pant, Ajay Kumar, L M Pant, Amitava Ghosh
Instruments research & Development Establishment
email: mpsingh@irde.drdo.in

Abstract: A design of extended depth of focus Infrared camera using wavefront coding is described herein. The phase mask is designed and optimized so that the PSF and subsequently the MTF remains invariant to the range of defocus/temperature range. This provides advantage over traditional infrared imaging system, where athermalization increases complexity and cost of the imaging system. The image is blurred due to introduction of phase mask but it is recovered digitally by using suitable image deconvolution technique. The effect of detector sampling, deconvolution method and noise enhanced by deconvolution process is studied and techniques to improve the performance are reported.
OCIS codes: (110.2960) image analysis; (110.7348) wavefront coding

1. Introduction

The depth of focus of any optical imaging system depends on the aperture of the optical system and there is a tradeoff between the performance and depth of focus. The wavefront coding imaging technology increases the depth of focus without compromising the performance with lesser number of optical elements [1]. The technology gives advantages in terms of reducing aberrations and defocus caused by the temperature change as well as errors due to the assembly, along with reduction in weight, size and cost of imaging systems. The cubic phase mask can be represented as

$$P = \exp[i\alpha(x^3 + y^3)] \tag{1}$$

where α is the strength of phase mask. Traditional optical systems have a depth of focus defined by Rayleigh criterion according to which optical path difference on the edge of the aperture should be within a quarter of wavelength. However the wavefront imaging system significantly increases the depth of focus depending on the strength of the phase mask. The approximate extension ratio in depth of focus is given by [2]

$$M = \frac{3\alpha}{\pi} \tag{2}$$

2. Optical design of IR system

A LWIR infrared system was designed with F#1.4, focal length 50mm and total system length was less than70 mm. The detector used has 640X480 pixels with 17 µm pitch. The optical system consists of a two lens (Petzval type design) system. . Optical design of the wavefront coded IR system was done on a ray tracing software written in Matlab. The MTF of the system is nearly diffraction limited throughout the field and range of wavelengths. The corresponding plot of MTF is shown in the figure 1.

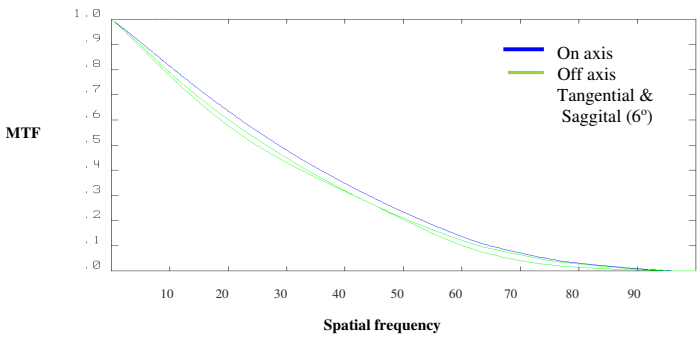

Fig.1 MTF at different field positions

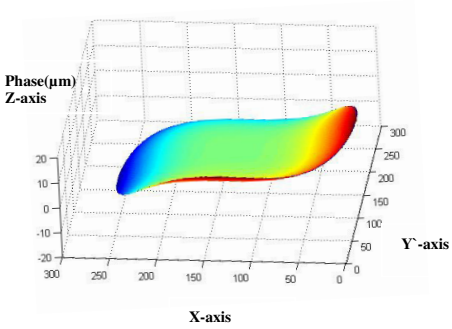

Fig 2 a) Phase mask

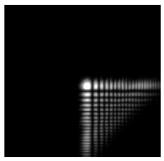

b) PSF

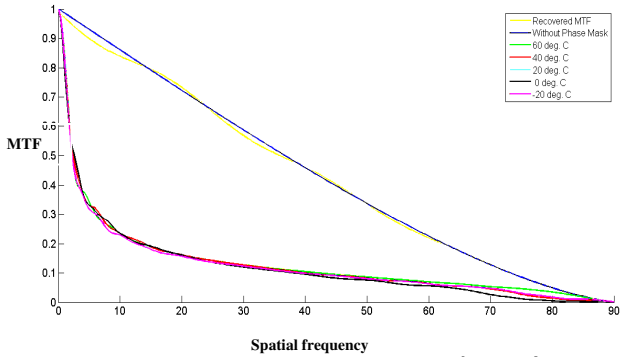

c) MTF at different temperatures from -20 ^{0}C to 60 ^{0}C

The cubic phase mask was designed and optimised by comparing the focused image without phase mask to the images recovered for the temperature range (-20 ^{0}C to 60 ^{0}C) using phase mask in a least squares manner and the optimized phase mask was obtained by minimizing the least squares error. The optimized phase mask strength comes out to be 2.88 waves (λ=10µm). The MTF has non-zero values at required spatial frequencies (Detector cut off 30 line pair/mm) of the optical system.

3. Image restoration

The image of a Siemens star pattern was taken as an input image. Figure 3.1 shows the image for optical system without phase mask at different temperature/defocus. Figure 3.2 shows the image for optical system with phase mask applied for same range of temperatures For image restoration Weiner filter [4] was used. Figure 3.3 shows the restored images after deconvolution. The recovered images are not affected by the variation of temperature.

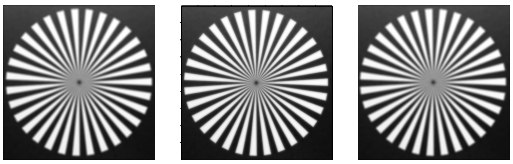

(a (b) (c)

Fig 3.1 Without phase mask a) at -20 ^{0}C b) at 20 ^{0}C c) at 60 ^{0} C

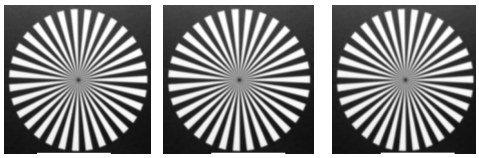

(a) (b) (c)

Fig 3.2 With phase mask a) at -20 ^{0}C b) at 20 ^{0}C c) at 60 ^{0} C

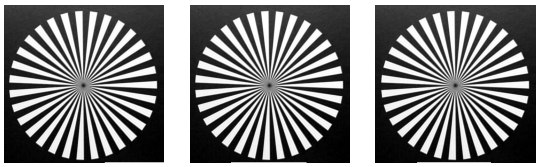

(a) (b) (c)

Fig 3.3 Recovered image a) at -20 ^{0}C b) at 20 ^{0}C c) at 60 ^{0} C

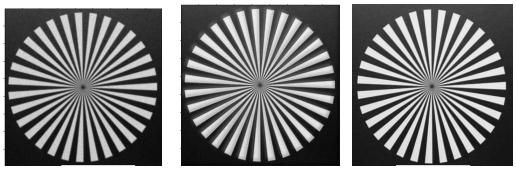

(a) (b) (c)

Fig 3.4 a) noisy image b) recovered image c)after noise reduction

4. Conclusion

It is observed that the wavefront coding reduces the aliasing effects and the detector sampling does not affect the image restoration quality. The noise characteristics of the recovered image were also studied. It was found that the noise enhanced during the convolution process can be reduced significantly by minimizing the total variation in the image(Fig 3.4). The work will help in development of low cost light weight athermalized imaging systems for firefighting applications, night driving and airborne applications.

5. References

[1] Edward R. Dowski, Jr. and W. Thomas Cathey. "Extended depth of field through wave-front coding". Appl.Opt., 34(11):1859-1866(1995).

[2] T. Zhao and F. Yu, " Point spread function analysis of a cubic phase wavefront coding system with a circular pupil"., Optics express 20(3), 2408-2419(2012)

[3 P. E. X. Silveira and R. Narayanswamy, "Signal-to-noise analysis of task-based imaging systems with defocus," Appl. Opt. 45, 2924- 2934 (2006).

[4] J.W.Goodman. "Introduction to Fourier Optics, (Third Edition)", New York: Roberts and Company Publishers Inc., 2005

OSI-ISO 2018 manuscript No.
(191)

Rapid phase calibration of a spatial light modulator using novel phasemasks

Amar Deo Chandra · Dibyendu Nandy · Ayan Banerjee

Abstract The phase response of a reflective spatial light modulator (SLM) is measured using interferometry. The conventional method is cumbersome and we suggest a new method using novel phasemasks for faster characterisation of the SLM. This new method is threefold faster than the conventional method for phase measurements.

Keywords spatial light modulator · interferometry · phase measurement · novel phasemasks · fast characterization

1 Introduction

Spatial Light Modulators (SLMs) are dynamic optical elements which can be used to modulate the amplitude or the phase of the incident light beam. They have myriad applications in the field of aberration correction in microscopy [1], beam shaping [2], optical trapping [2–4], super-resolution imaging [5] and wavefront correction [6]. In order to use the SLM for any phase measurement applications, it is essential to characterise the phase response of the device. There are many methods discussed in literature such as intensity correlation [7]

Amar Deo Chandra
Center of Excellence in Space Sciences India, Indian Institute of Science Education and Research, Kolkata

Ayan Banerjee and Dibyendu Nandy
Department of Physical Sciences, Indian Institute of Science Education and Research, Kolkata
Center of Excellence in Space Sciences India, Indian Institute of Science Education and Research, Kolkata
E-mail: ayan@iiserkol.ac.in

and interferometry [8] to calibrate the SLM. We use a Michelson interferometer setup to characterise the phase response of our reflective SLM. This method is time-consuming and we report a new method using novel phasemasks which can enable threefold faster measurements without modifying any hardware in the experimental setup.

2 Methods

We set up a Michelson interferometer as shown in the schematic diagram (fig. 1) for measuring phase shifts by varying gray values on the SLM. The mirror in one arm of the interferometer is replaced by the reflective SLM from Holoeye (LC-R 1080) [9]. We study and characterise the phase response of the SLM at 671 nm.

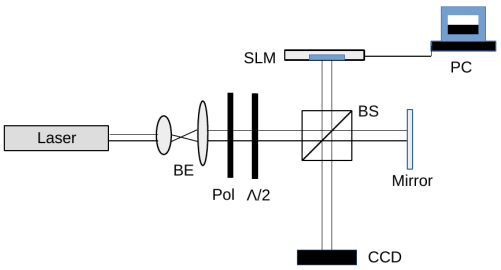

Fig. 1 Michelson interferometer setup for phase calibration of a reflective SLM.

We use a half-wave plate to rotate the incident polarisation of the laser beam to align along the molecular director of the liquid crystal molecules to achieve phase mostly modulation. Phase measurements are very accurate but are prone to vibrations and local variations in the refractive index of air. To mitigate this problem, we generate phase masks horizontally divided into variable graylevel (top half) and fixed reference graylevel (bottom half) at zero which are then displayed on the monitor. We vary grayvalues from 0-255 in steps of 10 (15 for the last step) and record twenty interferograms for each step. Fig. 2 shows some interferograms (top panel) obtained for grayvalues of 0, 140, 190 and 255 respectively and the corresponding phasemasks (bottom panel) displayed on the SLM. This shows that differential phase shifts are produced on varying grayvalues in the phase mask displayed on the SLM.

In order to measure phase shifts at each displayed grayvalue, we developed a semi-automated pipeline in python and shell to analyze all 520 interferograms. The first step in the analysis is to smoothen each interferogram and then make an appropriate 1-D cut in the interferogram at two locations viz. one in the top half and the other in the bottom half of the interferogram. These values are kept fixed for all interferograms. A peak detection algorithm then detects

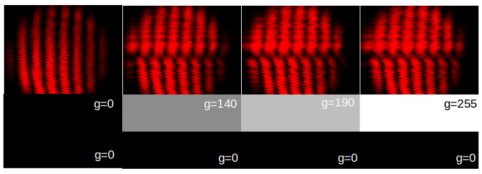

Fig. 2 Interferograms (top panel) obtained for different phasemasks (shown in bottom panel). The lower half of each phase mask is kept fixed at reference grayvalue of zero while the variable graylevel shown in top half of each mask is 0, 140, 190 and 255 respectively.

the number of specified peaks in the fringe pattern and finds the relative shift between the upper half (variable graylevel) and lower half (reference graylevel) of the fringe pattern (fig. 3).

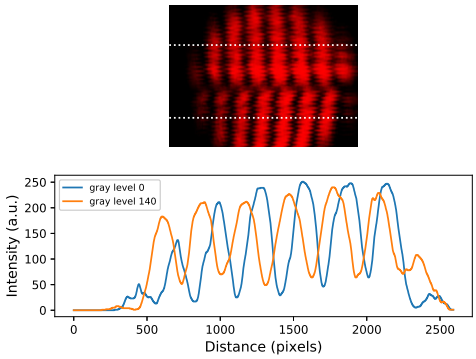

Fig. 3 Fringes showing relative phase shifts between desired graylevel and reference graylevel for grayvalues of 140 and 0 respectively. Rows selected for plotting profiles in top half and bottom half of each interferogram are shown by white dotted lines.

This process of calibration is cumbersome and we suggest an improved method of calibration which is three times faster that the current method and does not involve disturbing any component in the experimental setup (no moving parts). We construct a new phasemask made up of three different graylevel stripes embedded on reference graylevel of zero. We record the interferogram using the same setup and simultaneously measure differential phase shifts for three different graylevels with respect to the reference graylevel (fig. 4).

3 Results and Discussions

We obtain the phase shift vs grayvalue curve as shown in fig. 5. The phase shift in pixels is converted into phase shift in radians by normalizing each phase shift

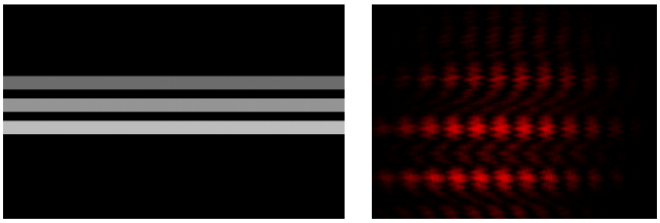

Fig. 4 The novel phase mask used in our experiment (left panel) showing three different graylevels (top to bottom: 110, 150 and 190) superimposed on reference graylevel and the corresponding interferogram (right panel) exhibiting simultaneous phase shifts obtained using our phasemask.

by the number of pixels between consecutive bright fringes corresponding to phase shift of 2π radians. We observe that the maximum phase sweep achieved by the SLM is about 0.8π which is less than about 1π phase depth claimed by the manufacturer at visible wavelengths. The phase response of the SLM is non-linear and the linear region of operation of the SLM is from grayvalue 90 to about grayvalue 160.

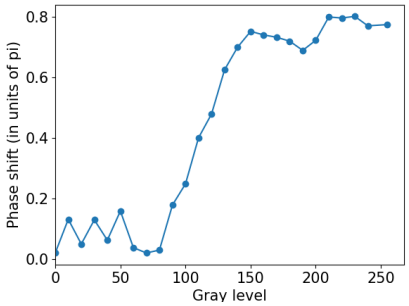

Fig. 5 Phase shift vs grayvalue curve for SLM obtained by interferometric calibration.

4 Conclusions

We calibrate a reflective SLM using interferometric measurements and implement a new rapid phase measurement scheme using novel phasemasks. Our method is three times faster than the conventional method and can be useful for fast phase calibration and sensing applications.

Acknowledgements This work was supported by the Center of Excellence in Space Sciences India (CESSI) and the Indian Institute of Science Education and Research, Kolkata, funded by the Ministry of Human Resource Development, Govt. of India. A.D.C. acknowledges support from the INSPIRE fellowship of the DST, Govt. of India.

References

1. K. D. Wulff *et al.*, Optics Express **14**, 4169 (2006).
2. D. G. Grier, nature **424**, 810 (2003).
3. M. Padgett and R. Di Leonardo, Lab on a Chip **11**, 1196 (2011).
4. K. Dholakia and T. Čižmár, Nature Photonics **5**, 335 (2011).
5. N. A. Ochoa and C. Pérez-Santos, Optics letters **38**, 5389 (2013).
6. G. D. Love, Applied optics **36**, 1517 (1997).
7. H. Yue *et al.*, Applied optics **51**, 4457 (2012).
8. B. Villalobos-Mendoza, F. S. Granados-Agustín, D. Aguirre-Aguirre, and A. Cornejo-Rodríguez, Applied optics **54**, 7997 (2015).
9. *https://holoeye.com/*.

OSI-ISO 2018 manuscript No.
(192)

Directed self assembly of bio-inspired peptide microrods and their optical waveguiding properties

Roshan Tiwari[1], Krishnendu Manjhi[2] ,Subir Ray[1] , Subhrokoli Ghosh[1], Nirmalaya Ghosh[1], Debashish Haldar[2]

and Ayan Banerjee[1]

[1]Department of Physical Sciences, Indian Institute of Science Education and Research, Kolkata

e-mail address:ayan@iiserkol.ac.in

[2]Department of Chemical Sciences, Indian Institute of Science Education and Research, Kolkata

Abstract: Significant research activity has happened recently on the development of microrod-shaped waveguides from the self-assembly of the diphenylalanine (FF) moiety depending on various fabrication conditions. However, the reported self-assembly is without any external stimuli, and is also not directed. We have developed a new method of directed self-assembly of such microrod waveguides on a glass substrate by the use of laser induced microbubbles which also leads to the formation of ring-like structures which display wave-guiding properties. In addition, we have observed Fano resonances in the case of single FF micro-rod irradiated by broadband light. We also demonstrate that the asymmetry of the Fano resonances is modified in the presence of a dye in contact with the waveguides, which clearly proves the suitability of these structures for sensing applications.
Keywords*: diphenyl-alanine, directed self-assembly, optical tweezers, waveguides, Fano resonance*

Introduction: Self-assembly is ubiquitous in nature, scaling from molecular to planatery systems. Desired patterns and functions can be engineered by understanding the interactions governing the self-assembly of the building blocks. Practical limitations of lithography and other top-down techniques have spurred interest in bottom-up approaches, where building blocks self-assemble into desired structures. Over a few decades, a lot of attention is given in this approach to develop new strategies. In this context, peptides as building blocks have become possible candidates for fabricating novel functional material. Among peptides, diphenylalanine(FF) has been extensively investigated due to its structural simplicity , functional versatility, biocompatibility and broad applications in biology .

In recent times, considerable research has been carried out on the development of microrod shaped waveguides [3,4], ranging from the self assembly of the FF moiety by tuning different parameters like concentration like concentration of FF, sonication time, nature of solvent, environmental conditions[2,3] etc. But precise control and formation of the complex structures like ring, torroids etc. by just spontaneous self-assembly has proved difficult.

In this paper, we report a method of directed self-assembly which uses laser induced micro-bubbles [2]. The process is fast (seconds in contrast to hours), and controllable both in terms of morphology as well as spatial location. Thus, we have demonstrated the formation of both microrods and micro-ring like structures of FF using such micro-bubbles which are generated on pre-existing patterns of soft oxometalates (SOMs) [2] on glass that are absorptive at the wavelength of a tightly focused laser that forms a thermo-optic tweezers [2]. We have controlled the size of the microrods and rings by varying the laser power as well as exposure time. In addition,

Roshan Tiwari
Indian Institute of Science Education and Research Kolkata
Email : rt14ip045@iiserkol.ac.in
Ayan Banerjee
Indian Institute of Science Education and Research Kolkata
Email : ayan@iiserkol.ac.in

we have obtained clear signatures of wave-guiding in rods [3,4] and ring structures when irradiated with both monochromatic and broadband, both visually and by using a spectrometer. Finally, we report Fano-resonances [7] observed in the case of single FF microrods irradiated by broadband light. These are understandably induced by the coupling of the waveguide mode and the background broadband scattering profile. It is well known that Fano resonances – that are characterised by asymmetric resonance spectral profiles – have promising applications in multifarious directions including sensing, switching and non-linear optical devices etc. [5,6,8]. We obtain clearly different values of the asymmetry parameter q for orthogonal polarizations. We have also demonstrated that the asymmetry is modified in the presence of a dye in contact with the waveguides, which clearly proves the suitability of these structures for sensing applications.

Materials and methods:

2.1. *Microrod preparation:* FF rods were prepared by dissolving the L-diphenylalanine (FF) peptide (Bachem) in distilled water at an initial concentration of 10^{-2} M and then sonicating for 30 min.

2.2 *Molybdenum-Based Soft-Oxometalate*: The SOM was prepared by dispersing 817.6 mg of ammonium heptamolybdate tetrahydrate (from Sigma-Aldrich) in 4 mL of water which was warmed until a homogeneous dispersion was obtained. This dispersion was then cooled to room temperature

2.3. *Thermo-optical Tweezer:* The thermo-optical tweezers is constructed around an inverted microscope (IX71 Olympus). A 100X, 1.4 N.A. oil immersion microscope objective (plano-apochromat, infinity corrected) is used to couple 1064 nm from a diode laser (Laser LSR1064 ML) into the sample holder to attain a spot size of waist radius ~500 nm. The laser power can be varied from 0 to 100 mW after the objective.

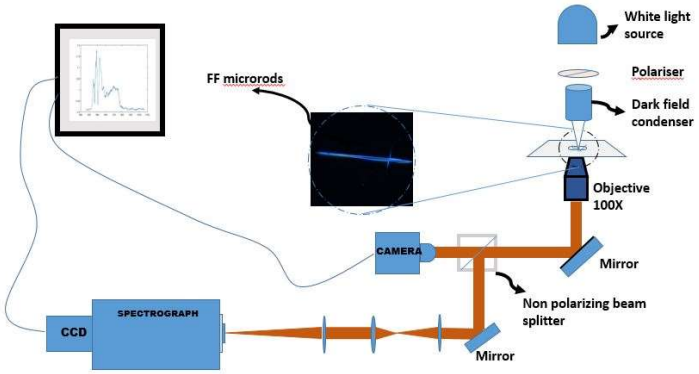

Fig. 1 Experimental setup for spectral response of FF rod

Results and Discussions

Ring Pattern Formation:

We used a substrate which was pre-patterned by soft oxometalates using the techniques described in Ref. [2]. The SOM patterns were washed with methanol to reduce their thickness and width so as to cause minimum contamination of the FF. The FF solution of concentration 10^{-2} M was drop-casted on the coverslip and the trail was focused with 1064 nm laser such that a microbubble is nucleated. This bubble due to the difference in surface tension generates convective flows which assemble the FF moiety at the base of the bubble in form of a ring. We observed that as we increase the laser power, the ring size increases due to increased size of bubble as evident from Fig 2 (a) and (b). Also the size of the ring increases with increasing the time of irradiationas evident from Fig 2 (c) and (d), for which self-assembly happens.

2. Wave-guiding in FF

The wave-guiding property of the FF micro- ring and FF cluster was then investigated by a laser as shown in Fig 3(a), and broadband light in Fig 3(b), respectively. When the laser at 780 nm is focused at a certain region of the micro-ring the light is guided along the periphery of the resonator, resulting in guiding the light along the ring, as shown in Fig. 3(a).When the FF cluster was excited by broadband light, only particular k vectors of light fulfill the coupling conditions into the waveguide so that a particular wavelength is propagated along the waveguide, as shown in Fig3(c). Understandably, this coupling depends on different geometric properties of the cavity.

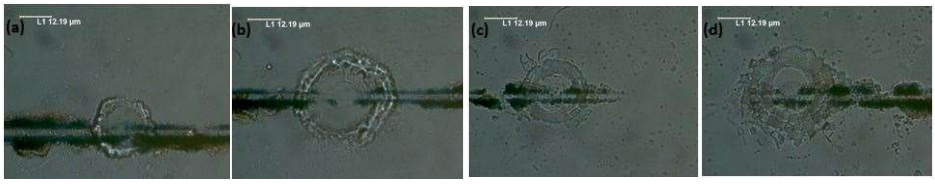

Fig. 2 CCD images of rings assembled for 1min at (a) 10 mW (b) 60 mW .CCD images of rings assembled at 60 mW power for (c) 30 sec (d) 1.5 min

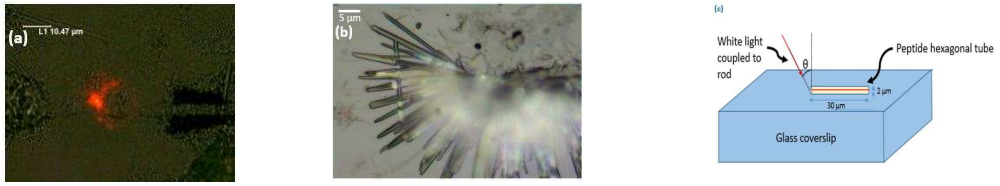

Fig. 3 (a) FF ring clusters formed on the trail of SOM's, acting as a waveguide when excited at 671 nm.(b) FF cluster showing wave-guiding for broadband excitation.(c) Schematic diagram showing the coupling of k vector into the micro-rod cavity.

3. Anisotropic Fano Resonance in a Waveguided FF microrod:

The Fano resonance line-shape is due to interference between two scattering amplitudes, one due to scattering within a continuum of states (the background process) and the second due to an excitation of a discrete state (the resonant waveguide process). The resulting expression for the scattered intensity can be written as

$$I_S = |E_s(\omega)|^2 \approx \frac{(q+\epsilon)^2}{(1+\epsilon^2)} + \frac{B}{(1+\epsilon^2)} \qquad (1)$$

The first term represents the Fano-type asymmetric spectral line shape with an effective asymmetry parameter q. The second term corresponds to a Lorentzian background. The FF rod acting as a waveguide, oriented horizontally, on top of a glass coverslip is shown in Fig 4(c). The scattering polarization response from the FF waveguide crystal sample were recorded for orthogonal polarizations using a spectrometer integrated with a dark-field microscope. Focused annular-shaped white light was used as an excitation source in this arrangement. Typical SEM images of a FF rod on a glass substrate are shown in Fig (4a.). We observe that for such FF waveguides the background broadband can couple to the guided mode.

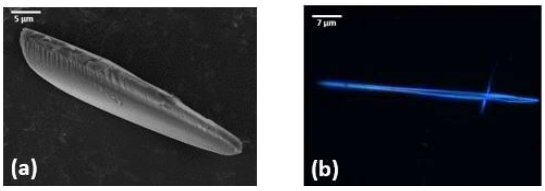

Fig 4 a. SEM image of a FF microrod on a glass substrate, b. Dark field image of a FF microrod

In Fig. 5(a) and 5(b), we demonstrate the different spectra obtained for a single FF rod irradiated with incident orthogonal polarizations. We fit the data with eq.1 in Fig 5(c) which yields the asymmetry parameter q are $q_x = 0.015$ for TM (blue) and $q_y = 0.071$ for TE (red) mode, respectively. Thus, clearly are $q_x \neq q_y$.The corresponding parameters in a similar FF rod doped with Congo red dye (10^{-2} M) are $q_x = 0.009$ for TM and $q_y = 0.030$ for TE mode respectively as shown in Fig 7(b). This also implies for the anisotropy of the q parameters. Also, in presence of the dye, there is an appreciable change in the q parameter due to change in the refractive index of cavity, which establishes the possibility of the use of such waveguides for sensing using Fano resonances.

Fig.5 The spectral variation of scattered intensity (**a)**TM- x polarization (**b)**TE-y polarization **(c)** For a single rod .Theoretical fits of the spectra with q_x=0.015 and q_y=0.071 for TM and TE polarization respectively. **(d)** A dye-doped FF rod. Theoretical fits of the spectra with q_x= 0.009 and q_y=0.030 for TM and TE polarisation respectively

Conclusion: In conclusion, we have developed a novel method of directed self-assembly which results in the formation of micro-rods and rings of different sizes and at different spatial locations of a glass substrate. The structures display clear wave-guiding properties for both laser and broadband excitation. For the latter, we obtain Fano resonances with the asymmetry parameter q being modified for incident orthogonal polarizations. We show that the value of q also changes in the presence of a dye in contact with the waveguide, thus demonstrating the possible application of these structures for precision sensing. We would like to extend the applications of these devices towards the development of display lighting systems and the sensing of bio-analytes.

Acknowledgments: The author acknowledge the financial support by Indian Institute of Science Education and Research, Kolkata, an autonomous research and teaching institute funded by the Ministry of Human Resource Development, Govt. of India.

References:

1.Jiarui Chen , Shuyu Qin , Xinglong Wu, and Paul K. Chu, ACS Nano, 10,832-838, 2016
2. Basudev Roy, Manish Arya, Preethi Thomas, Julius Konstantin Ju rgschat, K.Vasudev Rao, Ayan Banerjee, Chilla Malla Reddy, and Soumyajit Roy, Langmuir,,29,14733-14742,2013
3. Qi Li, Yi Jia, Luru Dai,Yang Yang, and Junbai Li, ACS Nano,9,2689-2695,2015
4.Q. Li, Dr. H. Ma, Y. Jia, Prof. J. Li Q. Li, Dr. H. Ma, Y. Jia, Prof. J. Li, Adv. Optical Mater. 2015, 3, 194–198
5. B. Luk'yanchuk, N.I. Zheludev , S.A.Maier, N.J.Halas,P.nordlander,H.Giessen and C.T Chong, Nature Matter. 9, 707-715(2010)
6. Anker, J. N.; Hall, W. P.; Lyandres, O.; Shah, N. C.; Zhao, J.; Van Duyne, R. P. Biosensing with Plasmonic Nanosensors. Nat. Mater. 7, 442−453,2008
7. Subir Ray, Shubham Chandel, Ankit Singh, Abhishek Kumar, Arpita Mondal, Subhradeep Misra ,Partha Mitra, and Nirmalaya Ghosh, ACS Nano,11,1641-1648, 2017
8 Shafiei, C. Wu, Y. Wu, A.B. Khanikaev, P. Putzke, A. Singh, X. Li, and G. Shvets, Nature Photon. 7, 367-372,2013

Ultrafast Excitonic Recombination in MoS_2 Nano-crystals:Observed through Time Resolved Non-linear Pump, Linear Probe Spectroscopy

Manobina Karmakar [a,*], Sayantan Bhattacharya [a,†], Subhrajit Mukherjee [b,†], Rup Kumar Chowdhury[a], Samit K. Ray [a,c] and Prasanta Kumar Datta [a]

[a] Department of Physics, [b] Advanced Technology Development Centre, Indian Institute of Technology, Kharagpur, India 721302; [c] S.N. Bose National Centre for Basic Sciences, Kolkata, India 700106.

Abstract: We have utilized single and two-photon pump excitation in femtosecond transient absorption spectroscopy to probe C exciton dynamics in MoS_2nano-crystals. We observe valance band depletion and Pauli blocking effects in the probe absorption of A and B excitons under linear photo- excitation regime. In presence of non- linear pump, the Pauli blocking effect disappears due to a trapped state in the nano-crystals. The excitons created by later technique undergo ten times faster relaxation than that of the excitons created by single photon absorption.

Keywords: Transient absorption spectroscopy, Molybdenum disulphide, Transition metal dichalcogenides, Excitons.

1.Introduction:

Transient absorption spectroscopy is an efficient tool in probing carrier dynamics in a semiconducting system in a time window of few hundred femtoseconds to a few nanoseconds. Apart from the inter-band transitions, this non-equilibrium spectroscopic technique can shed light onto different processes namely bandgap renormalization, Pauli blocking, many-body exciton interactions etc. [1-3] which occur as a result of Coulombic interactions. Carrier and quasi-particle dynamics in such materials become extremely important because of application in opto-electronic devices. Here we have chosen a transition metal dichalcogenide material- molybdenum disulphide (MoS_2) and study its excitonic transitions upon quantum confinement. We propose a technique to identify two-photon pumping in this dual–beam spectroscopy. Using two-photon absorption (TPA) in a trapped state of MoS_2 nanocrystals, we could differentiate photo bleaching effect and Pauli blocking in conduction band.

2. Sample Preparation:

Starting from bulk MoS_2 (99%, 2 μm in size), we have prepared nano-sheets and nano-crystals by a combination of sonication and gradient centrifugation using N, N dimethylformamide (DMF) as solvent [4]. A simple sono-chemical exfoliation technique comprised of sonication and gradient centrifugation is used to exfoliate the 2D layers from its bulk. We procured sample "NF", nano-sized flakes of MoS_2 (lateral dimension 10-100 nm) andsample "NC", which is MoS_2 nano-crystals (of average diameter 2 nm) inter-dispersed in nano-sheets (lateral dimension 10-100 nm).

3. Results and Discussion:

Steady state optical absorption spectra of the sample NC shows well-known A, B and C excitonic peaks, centered around 665 nm (1.86 eV), 610 nm (2.03 eV) and 435 nm (2.85 eV). Comparing these values in NF we observe a blue-shift in all three features, maximum shift is for the C peak ~106 meV. There is also a maximum in absorption spectrum around 305 nm, whose origin is not yet known. We hypothesize this transition as a trapped state stemming fromlateral confinement; as the absorbance at this particular wavelength is seen to be enhanced in the NC sample (Fig. 1).

We excite the sample NC with 405 nm(~180 eV blue-detuned to C excitation) and and 610 nm pump (in resonance to the B excitons) inducing a carrier density of $2*10^{13}cm^{-2}$and probe its differential absorbance ($\Delta OD(\lambda,t) = A^{pump}(\lambda,t) - A^{no\ pump}(\lambda)$; where A is absorbance) in the visible range through a broadband supercontinuum probe with variable delay from 200 fs to a few ns. To understand whether the pump absorption is single-photon or two-photon, we calculate the gradient of the ΔOD with respect to pump fluence. Considering the fact that Fermi-Dirac distribution of valance band is perturbed by pump excitation, it

† These authors contributed equally to the work.

can be easily shown that Log(ΔOD) = Log(a) + η1∗Log(N) ,where η1=1 for linear absorption and Log(ΔOD) = Log(b) +η2*Log(N) for two-photon absorption, η2 being 2. N is number of pump photons per pulse and 'a' is a constant proportional to linear absorption cross-section and 'b' is that of TPA. These conditions will be satisfied only when the absorbance of the material is less than 1, which we had maintained throughout our experiment. We track this gradient (η) for 500 nm probe wavelength and find that it is ~1 for 405 nm and ~2 for 610 nm pumping. We repeat the same calculations at different delay times and result was the same. We also changed the tracking wavelength and calculated η1 and η2 varying from430 nm, 650 nm and the results were as before. This is quite surprising because the probe is always in the linear regime (verified by varying probe intensity). η being 2 in broadband region reflects the fact that the population in the valance band has been depleted by two-photon absorption. As there is a sharp peak in the absorption spectra at 305 nm trapped state, the TPA is observed in this particular pump wavelength (610 nm).

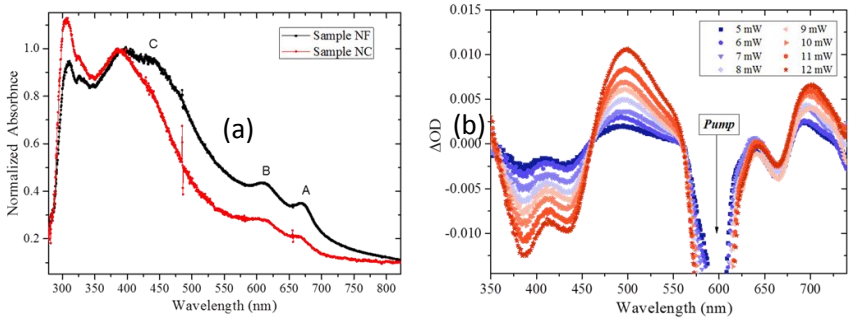

Fig.1: (a) Steady state absorption spectrum of sample NF and NC, (b) Differential absorption spectra at 5 ps delay for varying pump powers.

We observe the decay dynamics of the C exciton resonance peak for both the cases and fit with tri-exponential decaying functions (*Linear*: T1: 1.01±0.05 ps, T2= 73±17, T3=900±250 ps; *Nonlinear*: T1: 0.3±0.02 ps, T2= 7±1, T3=132±25 ps). The recombination rates for TPA is one order less than that of the single-photon pump absorption. This is because of the fact that upon TPA, photons in the trapped states do not scatter onto the conduction band and hence effect of Pauli blocking is absent. In this condition, the reduction of probe absorbance is an outcome of the valance band depletion, which is removed through faster relaxation. On the other hand, for 405 nm pump excitation (linear regime) the exciton bleaching is due to both valance band depletion and Pauli blocking. This results in a slower relaxation rate of the excitons.

4. Conclusion:

We have prepared MoS_2 nano-crystals in dispersion and studied its transient absorption upon linear and two- photon non- resonant pump excitation. We distinguished processes of valance band depletion and Pauli blocking in this semiconductor and found out the time-scales of those processes.

5. Acknowledgements:

The authors acknowledge the equipment grant of UPM (SGDRI) project of IIT Kharagpur.

6. References:

[1]N.Peyghambarian, H. M.Gibbs, J. L.Jewell, A. Antonetti, A. Migus, D. Hulin, and A.Mysyrowicz, "Blue Shift of the Exciton Resonance due to Exciton-Exciton Interactions in a Multiple-Quantum-Well Structure", Phys. Rev. Lett. **53**, 2433 (1984)

[2]Alexey Chernikov, Claudia Ruppert, Heather M. Hill, Albert F. Rigosi & Tony F. Heinz, "Population inversion and giant bandgap renormalization in atomically thin WS2 layers",Nature Photonics volume 9, pages 466–470 (2015)

[3] Xiaoxi Wu, M. Tuan Trinh, and X.-Y. Zhu, "Excitonic Many-Body Interactions in Two-Dimensional Lead IodidePerovskite Quantum Wells",J. Phys. Chem. C, 119, 14714−14721 (2015)

[4] S. Mukherjee, R. Maiti, A. Midya, S. Das, and S. K. Ray, "Tunable Direct Bandgap Optical Transitions in MoS2 Nanocrystals for Photonic Devices", ACS Photonics , 2, 760−768 (2015)

OSI-ISO 2018 manuscript No.
(195)

Tunable OMIT and OMIA in a double cavity hybrid optomechanical system

Nikhil Pramanik, Krishna Chaitanya Yellapragada, Suneel Singh and P. Anantha Lakshmi.

Abstract

We study switching from optomechanically induced transparency (OMIT) to optomechanically induced absorption (OMIA) of the weak probe field, by tuning the control fields driving each of the cavities, in a tunnel coupled double cavity system. The system consists of two tunnel-coupled optomechanical cavities, each driven by a coupling field. A probe field is injected through one of the cavities, the transmission characteristics of which are studied. A systematic study of the probe transmission in different parameter regimes is carried out, which also incorporates the case in which the cavity detunings and the atomic detunings are all distinct. This is different from the previous studies [1,2] where all these detunings are assumed to be equal to the mirror oscillation frequency, which resulted in considerable simplification. Our analysis enables separating out the contribution arising from different frequency components clearly.

In the case of a weak photon tunneling rate from the first cavity to the second, combined with a strong optomechanically coupling of the first cavity, it is seen that the effect of the second cavity is negligible, thus giving rise to OMIT. For moderate values of the tunnel coupling strengths, the effect of the second cavity gives rise to modification in the transmission spectrum. However, for the case of a strong optomechanical coupling in the second cavity, combined with a weak optomechanically coupled first cavity, we observe OMIA. From a study carried out through an extensive parameter regime, it is observed that while the first cavity induces OMIT, the second cavity is responsible for the observed OMIA in the transmission spectrum. The OM coupling strength can be tuned either by changing the cavity lengths or the power of the control fields. It is also seen that switching from OMIT to OMIA can be seen by introducing atomic ensembles in the cavities.

Keywords Optomechanics, Coherent effects, OMIT, OMIA, Double cavity

Model

The hybrid OM system studied here is shown in Fig.1, consisting of two optomechanical cavities filled which two level atomic ensembles. Each cavity consists of a (perfectly reflecting) fixed mirror and a (partially transmitting) movable mirror, with a tunnel

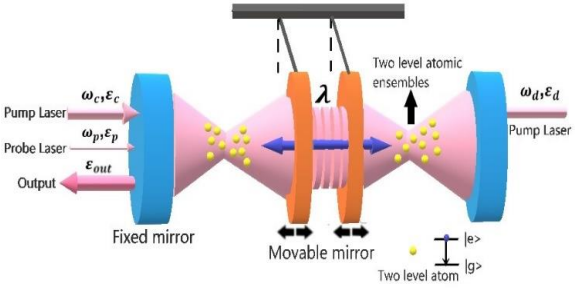

Fig. 1 Schematic diagram of a tunnel coupled double cavity hybrid optomechanical system

coupling rate of λ, which is proportional to the transmittance of the oscillating mirrors, with their effective mass, frequency and mechanical decay rates given by m_i , ω_{mi} and γ_{mi} (i=1,2), respectively. L_i (i=1,2) are the lengths of the cavities, ω_0 and κ are the frequency and the cavity decay rate, assumed to be equal for both cavities.

Each of these cavities is driven by a laser field of frequency ω_i (i = c, d), with input powers P_c and P_d respectively. A probe beam with frequency ω_p is injected into the left cavity. The Hamiltonian taking into account various interactions is constructed and the Heisenberg equations of motion for the operators are solved under appropriate approximations and representative results for the transmission spectrum are presented in the following.

Shift of OMIA TO OMIT by tuning the input pump laser field

Pumping the left cavity with a laser field gives rise to OMIT as shown (blue solid curve) in Fig. 2 (a), corresponding to weak optomechanical coupling regime for the right cavity and thus has negligible effect on the output spectrum. The OM coupling of left cavity g_{m1} being strong, we obtain OMIT at the line centre. Similarly pumping the right cavity gives rise to OMIA (red dotted curve) [1].

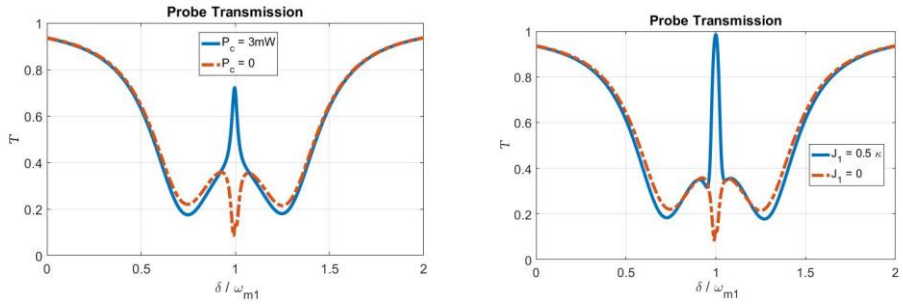

Fig. 2 Probe transmission spectrum as a function of normalized probe detuning (δ/ω_{m1}). (a) OMIT (blue curve) for Pc = 3 mW; OMIA (red dotted curve) for Pc=0. (b) OMIT (blue curve) with J_1=0.5*k*, OMIA (red dotted curve) for J_1=0.

From fig. 2 (b) it is clearly seen that OMIA in the transparency spectrum can be altered to OMIT by introducing two level atoms in the left cavity[2]. Here, the atoms couple to the cavity field, which in turn couples to the mechanical modes of the movable mirror, thus enhancing the overall effective OM coupling, giving rise to OMIT at the line centre. These results demonstrate that tunability from OMIT to OMIA and vice versa can be achieved by modifying the pump laser powers and/or by introduction of atomic ensemble into the left cavity.

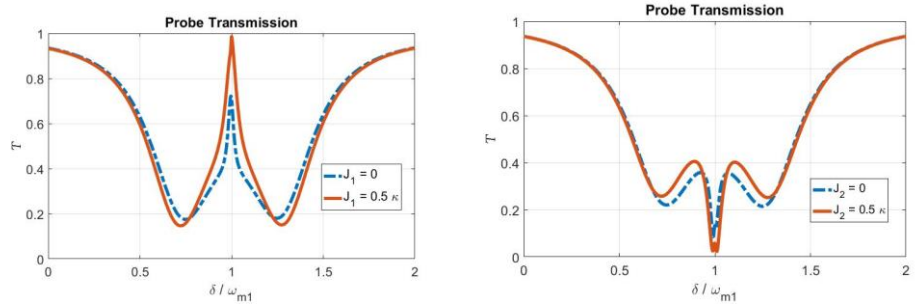

Fig. 3 Probe transmission spectrum as a function of normalized probe detuning (δ/ω_{m1}). (a) Enhanced OMIT (Red) at J_1 = 0.5 κ, (Blue dotted curve) for J_1=0. (b) Increased OMIA (red curve) with J_2=0.5 κ, (blue dotted curve) J_2=0.

Furthermore we observe enhancement of probe transmission by introducing atoms in the left cavity which is shown by the red solid curve in Fig. 3 (a). An increase in probe absorption at line center can be observed (red curve in Fig. 3(b)) when atoms are added to the right cavity.

References

1. B. P. Hou, L. F. Wei and S. J. Wang, Optomechanically induced transparency and absorption, in hybridized optomechanical systems, Phy. Rev. A 9, 033829 (2015)
2. Wen-Qing Xia, Ya-Fei Yu and Zhi-Ming Zhang, Adjustable quantum coherence effects in a hybrid optomechanical system, Chinese Physics B, Volume 26, Number 5 (2017)

SPONSORS

Abstract book created by-
Kajal Chaudhary and Gagandeep Kaur